PROBING NONEQUILIBRIUM QUANTUM MATTER WITH TWO-TIME CORRELATION FUNCTIONS

ALEXANDER SCHUCKERT

Technische Universität München
Fakultät für Physik
Lehrstuhl für kollektive Quantendynamik

PROBING NONEQUILIBRIUM QUANTUM MATTER WITH TWO-TIME CORRELATION FUNCTIONS

ALEXANDER SCHUCKERT

Vollständiger Abdruck der von der Fakultät für Physik der Technischen Universität München zur Erlangung des akademischen Grades eines

Doktors der Naturwissenschaften (Dr. rer. nat.)

genehmigten Dissertation.

Vorsitzender:
Prof. Dr. Alexander Holleitner
Prüfende der Dissertation:
1. Prof. Dr. Michael Knap
2. Prof. Dr. Frank Pollmann

Die Dissertation wurde am 31.08.2021 bei der Technischen Universität München eingereicht und durch die Fakultät für Physik am 22.10.2021 angenommen.

"The behavior of large and complex aggregates of elementary particles is not to be understood in terms of a simple extrapolation of the properties of a few particles. Instead, at each level of complexity entirely new properties appear, and the understanding of the new behaviors requires research as fundamental in its nature as any other."

— P.W. Anderson (1923 – 2020)
in *More is different*

ABSTRACT

We study the thermalization dynamics of many-body quantum systems, ranging from many-body chaos close to a phase transition over eigenstate thermalization in quantum simulators and gauge theories to the emergence of superdiffusive transport in long-range systems. We also develop non-equilibrium probes of phases of matter, including spin spiral order, a Hartree Fock theory of the disordered Coulomb gas and a time dependent spectroscopy protocol for spinon excitations.

KURZZUSAMMENFASSUNG

Wir untersuchen die Thermalisierungsdynamik von Quantensystemen, vom Vielteilchenchaos in der Nähe eines Phasenübergangs über Eigenzustandsthermalisierung in Quantensimulatoren und Eichtheorien bis zum superdiffusiven Transport in langreichweitig wechselwirkenden Systemen. Wir entwickeln auch Nichtgleichgewichtsproben für Materiephasen, einschließlich des Zerfalls von Spinspiralen, einer Hartree-Fock-Theorie des ungeordneten Coulomb-Gases und eines zeitabhängigen Spektroskopieprotokolls für Spinonanregungen.

SUMMARY

How do closed many-body quantum systems prepared in a non-equilibrium state relax to thermal equilibrium? In this thesis, we study this question through the lens of two-time correlation functions, which allow to identify the underlying mechanisms in detail. We study several stages of the thermalization process and develop protocols to probe them via two-time correlators in quantum simulators.

At the earliest times, quantum information is spread quickly through the system. We use the two-time out-of-time-ordered correlation function to quantify the spreading of many-body chaos in a relativistic scalar field theory. We find that close to the thermal phase transition, chaos spreads quickest. This is contrary to the expectation that dynamics are in general slowed down on approach to criticality.

The eigenstate thermalization hypothesis (ETH) has been conjectured to be the mechanism underlying the thermalization process. We find a way of probing the off-diagonal part of ETH in quantum simulators without any theory input via two-time correlators, enabling the study of thermalization in a regime inaccessible to numerical methods. In systems which do not thermalize fast, we show how to identify non-thermal excitations directly in experiment.

We furthermore develop a non-equilibrium quantum field theory method for quantum electrodynamics in one spatial dimension. We characterize thermalization of a string via two-time correlators, finding several distinct time scales in the relaxation.

At the latest times, classical hydrodynamic transport of conserved quantities is expected to dominate the dynamics as the quantum system has effectively dephased itsself. However, this regime is challenging to capture both numerically and in quantum simulation experiments as it only appears at late times. We show that non-equilibrium quantum field theory methods can access the hydrodynamic regime. In particular, we find that long-range interacting systems exhibit superdiffusive emergent transport at late times by calculating the two-time correlation function related to the conserved quantity. We test our predictions by comparing our theoretical results to a quantum simulation experiment with trapped ions, finding agreement.

The universality of these thermalization phenomena become apparent when considering the range of physical implementations which we study in this thesis, ranging from non-relativistic to relativistic systems, from fermionic over bosonic species to spin systems, and from short- over long-range to gauge-boson-mediated interactions.

In the second part of the thesis, we use some of these results to probe equilibrium phases of matter. First, in the Heisenberg model, we characterize the instabilities of spin spiral states related to sought-after spin superfluids, showing that they decay via the build-up of transverse fluctuations. Second, we develop a Hartree-Fock method which includes screening to describe the three dimensional disordered Coulomb gas. Third, we develop a protocol to measure time-dependent angle-resolved-photoemission spectra, a two-time function, with cold atoms. In particular, we show that unoccupied spinon states can be excited by a magnetic field gradient and imaged by our spectroscopy method, enabling more detailed studies of spinon Fermi seas appearing in spin liquids.

ZUSAMMENFASSUNG

Wie relaxieren geschlossene Vielteilchenquantensysteme, die sich in einem Nichtgleichgewichtszustand befinden? In dieser Arbeit untersuchen wir diese Frage aus dem Blickwinkel der Zwei-Zeiten-Korrelationsfunktionen, die es ermöglichen, die zugrunde liegenden Mechanismen im Detail zu identifizieren. Wir untersuchen verschiedene Phasen des Thermalisierungsprozesses und entwickeln Protokolle, die die Untersuchung von Thermalisierung mit Hilfe von Zwei-Zeiten-Korrelatoren in Quantensimulatoren ermöglichen.

Zu den frühesten Zeitpunkten wird Quanteninformation schnell durch das System verbreitet. Wir verwenden die zeitlich ungeordnete Korrelationsfunktion, um die Ausbreitung von Vielteilchenchaos in einer relativistischen Skalarfeldtheorie zu quantifizieren. Wir stellen fest, dass sich in der Nähe des thermischen Phasenübergangs das Chaos am schnellsten ausbreitet. Dies steht im Gegensatz zu der Erwartung, dass die Dynamik bei Annäherung an den kritischen Punkt im Allgemeinen verlangsamt wird.

Die Eigenzustandsthermalisierungshypothese (ETH) beschreibt den zugrundeliegenden Mechanismus für Thermalisierung. Wir haben einen Weg gefunden, den Nebendiagonalteil der ETH in Quantensimulatoren ohne die Zuhilfenahme von numerischen Ergebnissen über Zwei-Zeiten-Korrelatoren zu untersuchen. Dies ermöglicht die Untersuchung der Thermalisierung in einem Bereich, der für numerische Methoden unzugänglich ist. In Systemen, die nicht schnell thermalisieren, zeigen wir, wie man nichtthermische Anregungen direkt im Experiment identifizieren kann.

Darüber hinaus entwickeln wir eine Nichtgleichgewichtsquantenfeldtheoriemethode für die Quantenelektrodynamik in einer räumlichen Dimension. Wir charak-

terisieren die Thermalisierung eines Strings mit Hilfe von Zwei-Zeiten-Korrelatoren und finden mehrere unterschiedliche Zeitskalen in der Relaxation.

Es wird erwartet, dass zu den spätesten Zeitpunkten die Dynamik vom klassischen hydrodynamischen Transport von Erhaltungsgrößen dominiert wird, da das Quantensystem sich selbst effektiv dekoheriert hat. Es ist jedoch schwer, dieses Regime sowohl numerisch als auch in Quantensimulationsexperimenten zu erfassen, da es erst zu späten Zeitpunkten auftritt. Wir zeigen, dass Methoden der Nichtgleichgewichtsquantenfeldtheorie den Zugang zum hydrodynamischen Regime ermöglichen. Insbesondere stellen wir fest, dass langreichweitig wechselwirkende Systeme superdiffusiven emergenten Transport zu späten Zeiten entwickeln, indem wir die Zwei-Zeiten-Korrelationsfunktion in Bezug auf die Erhaltungsgröße berechnen. Wir testen unsere Vorhersagen, indem wir unsere theoretischen Ergebnisse mit einem Quantensimulationsexperiment mit gefangenen Ionen vergleichen und Übereinstimmung feststellen.

Die Allgemeingültigkeit dieser Thermalisierungsphänomene wird deutlich, wenn man die Bandbreite der physikalischen Implementierungen betrachtet, die wir in dieser Dissertation untersuchen: von nichtrelativistischen bis zu relativistischen Systemen, von fermionischen über bosonische Spezies bis hin zu Spinsystemen und von kurz über langreichweitige bis hin zu eichbosonvermittelten Wechselwirkungen.

Im zweiten Teil der Dissertation nutzen wir einige dieser Ergebnisse, um Gleichgewichtsphasen von Materie zu untersuchen. Zunächst charakterisieren wir im Heisenbergmodell die Instabilitäten von Spin-Spiral-Zuständen, die mit Spinsupraflüssigkeiten zusammenhängen, und zeigen, dass sie durch den Aufbau von Transversalfluktuationen zerfallen. Zweitens entwickeln wir eine Hartree-Fock-Methode, die Abschirmung beinhaltet, um das dreidimensionale ungeordnete Coulomb-Gas zu beschreiben. Drittens entwickeln wir ein Protokoll zur Messung von zeitabhängigen und winkelaufgelösten Photoemissionsspektren, einer Zwei-Zeiten-Funktion, mit kalten Atomen. Insbesondere zeigen wir, dass unbesetzte Spinonzustände durch einen Magnetfeldgradienten angeregt und mit unserer Spektroskopiemethode abgebildet werden können, was detailliertere Studien von Spinonfermiseen in Spinflüssigkeiten ermöglicht.

PUBLICATIONS

Parts of this thesis have been previously published or uploaded to a preprint server. All preprints have been handed in for peer review. The corresponding chapters are extended versions of these publications. We indicate unpublished sections in the beginning of these chapters. Chapters 5 and 7 have not been published at the time this thesis was written. Chapter 2 represents a review-like reformulation of non-equilibrium quantum field theory which has not been published in this form elsewhere, except section 2.2.3, which is based on

- **Alexander Schuckert**, Asier Pineiro-Orioli, Jürgen Berges:
  "Nonequilibrium quantum spin dynamics from two-particle irreducible functional integral techniques in the Schwinger boson representation"
  – Phys. Rev. B 98, 224304 (2018) [arXiv:1806.02347].

Chapter 3 is based on

- **Alexander Schuckert**, Michael Knap:
  "Many-body chaos near a thermal phase transition"
  – SciPost Phys. 7, 022 (2019) [arXiv:1905.00904].

Chapter 4 is based on

- **Alexander Schuckert**, Michael Knap:
  "Probing eigenstate thermalization in quantum simulators via fluctuation-dissipation relations"
  – Phys. Rev. Research 2, 043315 (2020) [arXiv:2007.10347].

Chapter 6 is based on

- **Alexander Schuckert**, Izabella Lovas, Michael Knap:
  "Non-local emergent hydrodynamics in a long-range quantum spin system"
  – Phys. Rev. B 101, 020416(R) (2020) [arXiv:1909.01351],

- M. K. Joshi, F. Kranzl, **A. Schuckert**, I. Lovas, C. Maier, R. Blatt, M. Knap, C. F. Roos:
  "Observing emergent hydrodynamics in a long-range quantum magnet"
  – [arXiv:2107.000331].

Chapter 8 is based on

- Joaquin F. Rodriguez-Nieva, **Alexander Schuckert**, Dries Sels, Michael Knap, Eugene Demler:
  "Transverse instability and universal decay of spin spiral order in the Heisenberg model"
  – [arXiv:2011.07058].

Chapter 9 is based on

- **Alexander Schuckert***, Annabelle Bohrdt*, Eleanor Crane, Fabian Grusdt:
  "Visualizing spinon Fermi surfaces with time-dependent spectroscopy"
  – Phys. Rev. B (2021) [arXiv:2105.13366].

Apart from the topics related to non-equilibrium dynamics of closed quantum systems covered in this thesis, I have contributed to work on quantum computation in dopant atoms in silicon which will not be covered here. For the record, I summarize our results here. In

- Eleanor Crane, Thomas Crane, **Alexander Schuckert**, Nguyen H. Le, Kristian Stockbridge, Steven Chick, and Andrew J. Fisher:
  "Optically controlled entangling gates in randomly doped silicon"
  – Phys. Rev. B 100, 064201 (2020) [arXiv:1902.00288]

we explored the feasibility of implementing a quantum computer in the solid state in the absence of precision placement of qubits. We calculated optimal doping densities, in particular for multi-species gates in which one species controls the other for entangling gate operation. We also propose to use this platform as a simulator of two-spin-species Heisenberg dynamics and predict its dynamics with the moving average cluster expansion. In

- Eleanor Crane, **Alexander Schuckert**, Nguyen H. Le, Andrew J. Fisher:
  "Rydberg Entangling Gates in Silicon"
  – Phys. Rev. Research 3, 033086 (2021) [arXiv:2008.11736]

we port entangling gates originally invented for cold atom platforms to the donor platform and show their feasibility by simulating the gate operation in the presence of decoherence.

* indicates equal contribution.

Who is the third who walks always beside you?
When I count, there are only you and I together
But when I look ahead up the white road
There is always another one walking beside you.

— from T.S. Eliot - The Waste Land

ACKNOWLEDGMENTS

The single author on the cover of this document hides the fact that science (and life in general) is a collaborative effort. None of the results presented here would have been obtained without the enduring help and advise from teachers, colleagues, family and friends both in the past four years and before.

First of all, I would like to thank Prof. Michael Knap for accommodating me in his group. Thank you, Michael, for letting me explore my own ideas as well as giving me the flexibility to largely work remotely before COVID made that mainstream. I very much appreciate your close and time-intense mentoring, giving me the opportunity to not only learn physics from you (especially your deep intuition for experiments) but also the social aspects of science.

I also thank Prof. Frank Pollmann for many insightful discussions and comments. Your unshakeably positive spirit and your curiosity-driven approach to science were inspiring to witness.

I very much appreciated the lively community in the condensed matter theory group. Much credit goes to the PIs (Apart from Michael and Frank also Prof. Johannes Knolle and Dr. Sergej Moroz) for co-creating this spirit by putting a lot of effort into inviting speakers and creating discussions in and around black-board seminars, journal clubs and retreats.

In my first and second year, I was fortunate enough to attend several lecture series by Prof. Wilhelm Zwerger. It was an honour to learn the basics of the field of cold atoms from one of its pioneers and most distinguished teachers. I am still impressed by the fact that he sometimes gave lectures with only me being present and the stories and insights he spread at lunchtime in the IPP canteen taught me about the twists and turns behind the shiny surface of big science discoveries.

Most crucial to the community spirit at TUM was of course the peer group. I am especially thankful for the very warm and supportive welcome by Simon Weidinger, who calmly answered and helped me with all sorts of questions ranging from teaching over numerics to physics. Thank you, Johannes Feldmeier, for being the "Ruhepol" of the group, for many lunch-food-coma discussions and for joining in

with all sorts of sports. Thank you, Clemens Kuhlenkamp, for being as keen for 2PI as I am and for being the only other person with the "correct" dialect in this group. Thanks also to Nepomuk Ritz and Ansgar Burchards for many interesting discussions about 2PI. Thank you, Izabella, for collaborating on the part of this thesis I am now most proud of, especially for keeping us on track to not get lost in the details. Thanks to all the people from the wider group for creating so many interesting discussions in and around the seminars, especially to Claudio Benzoni, Julian Bibo, Umberto Borla, Johannes Hauschild (the TeNPy hero), Tibor Rakovszky, Pablo Sala, Adam Smith, and Ruben Verresen.

Thank you, Annabelle and Fabian Bohrdt, for many amazing bike rides and uncountably many occasions of crucial advice about being a couple in physics. Thank you, Fabian, for giving me much needed advice from an advanced postdoc. And thank you, Annabelle, for pushing me to keep moving forwards, especially with regards to writing this thesis and answering all of my annoying questions with regards to the hand-in process and physics.

It was a pleasure to "grow up" in the wider Munich Quantum Physics community, and especially being part of the graduate school IMPRS-QST. I thank Ignacio Cirac for guiding the purpose of this school: foster exchange between each other and with other quantum centres. The person probably most responsible for the spirit of IMPRS-QST is Sonya Gzyl. Thank you, Sonya, for taking on all of the annoying tasks of organizing events and travels so that we could focus on science and getting to know each other and for listening for when things did not go ideally. A big thanks to all the fellow IMPRS people, Margret Heinze, Antonio Rubio-Abadal, Karen Wintersperger, Dominik Irber, Noelia Fernández, Patrick Emonts, Caroline de Groot, Jan Dziewor, Sebastian Huber, Johannes Knörzer, Dimitri Pimenov, and many others for creating so many interesting and fun events.

Thank you to all the people who were involved in parts of the research presented here, especially to Joaquin Rodriguez-Nieva and Manoj Joshi, who lead two of the projects whose results I present here.

Thank you also to Prof. Andrew Fisher for so openly including me in the research at the LCN, and for enabling Ella and me to work together in the same place.

A quick (but loud) shout-out to the "Freiheit"-crew Nicola Pancotti, Henrik Dreyer and Ruben Verresen, who know so well how to have deep discussions around Alice and Bob.

Thank you, Asier, for your continued mentoring from the very first theoretical physics courses during the Bachelor's. Thank you for being my friend and teacher. I hope we will collaborate both in physics and/or other life projects for many years to come!

The immediacy of the most recent step in one's education makes it easy to forget the steps before. I enjoyed having supportive mentors and teachers from a very young age. I thank my primary school teacher Mr. Maisack for trying to meet my insatiable joy for calculating (sometimes even against the school's rules) and who showed me that numbers and computers belong together in a time when most people were still wary of these machines. Dr. Lang, Mr. Günther and Mrs. Schneider took over in high school (Gymnasium) to introduce more advanced math, and finally, Dr. Zepper and Mr. Trein showed me the power of physics to explain nature with mathematical formulae. I especially remember the troubling experience of seeing the dichotomy of particle and wave picture in the double slit experiment with single electrons, performed live by Mr. Trein in class. I also would like to thank my Geology and Geography teacher Mr. Schober to show that a physical explanation of the world does not stop at a fundamental level. At Heidelberg University, I would like to thank my professors for their efforts to convey the basic concepts used in modern physics. I am especially thankful to all the student tutors who relentlessly answered all of our questions while trying to solve problem sheets. The inspiring lectures by Prof. Bartelmann (I still remember him deriving Einstein's field equations without any script!) encouraged me to choose him as my mentor for the Bachelor thesis, which offered me a first glimpse into modern field theory approaches and a first contact with research in general. My second supervisor, Prof. Weidemüller, awakened my interest in the world of cold atoms. I am very thankful for having had the opportunity to explore the experimental part of this field during my short research stay at the Centre for Quantum Technologies in Singapore with Prof. Dieckmann and Dr. Debatin. During my Erasmus stay at University College London, Prof. Olaya-Castro and Prof. Oppenheim finally introduced the more advanced notions of quantum physics to me. The "Bell's inequality" lesson of the latter will stay with me forever - Prof. Oppenheim's tweet with a photo of the class saying "these people's life is about to change forever" was indeed not an understatement. During my Master's thesis, Prof. Berges and Asier Pineiro-Orioli taught me the non-equilibrium field theory techniques that I would go on to apply in this thesis. I feel very fortunate to having had the chance to be properly part of a research group during my Bachelor's and Master's thesis', which is not a given. Thanks especially to my then-office mates Torsten Zache and Oscar Garcia-Monteiro who helped me both then and in occasional discussions during my PhD.

I was lucky enough to have friends and family who not only supported me along my path but also made life worth living.
Thank you, LBC crew, for keeping me on the ground.
Thank you, Manu, for countless discussions about physics and showing me that there are other interesting things to explore.

Thank you, Max and Felix, for having created this enormous anchor in our youth, which I can always look back to in darker times.
Thank you, Simon and Nicci, for giving me a home on the other side of the earth and for being the critical voice asking whether my path is helping anybody.
Thank you, Richard, for showing me that everything is possible if one pushes hard enough. And how to live a diverse life. I will miss you.
Thank you, Michèle, for welcoming me in your homes, for helping me stay on track despite you going through the darkest of times, and for bringing art to my life.
Thank you, Tom, for asking questions and for creating.
Thank you, Mattie, for not letting anything disturb your pursuit of happiness.
Thank you, Onkel Hermann, for keeping your interest in math and your humour.
Thank you, Tante Elke, for being so caring.
Thank you, Buba, for teaching me to be kind, patient and content with what I have.
Thank you, Gulasch-Omi, for showing me what it means to have lived for helping others.
Thank you, Emi-Opa. I feel like having learnt so much from you despite never having met you.
Thank you, Bücher-Omi, for bringing beauty, nature and music to my life and for helping me to understand myself.
Thank you, Maxi, for being so focused, for struggling with the same things as I do, for always being there if I need a helping hand with yet another move and simply for being my brava.
Thank you, Papi, for your endless optimism and unconditional support and for showing me how to push for a life goal with endurance, stability and ritual.
Thank you, Mami, for keeping me on track in times of great distraction, for letting me make my own mistakes, and for guiding me in exploring the chaos of my teenage mind in countless “Küchengespräche”.
Thank you, Ella, for being my teacher, partner, collaborator, friend, for explaining my emotions to me, for exploring our joint ideas and for pushing us to take the road less travelled by. Because that makes all the difference.

CONTENTS

LIST OF FIGURES

ACRONYMS

OTOC out-of-time-ordered correlation function

2PI two-particle irreducible effective action method

spin-2PI two-particle irreducible effective action method for spin systems

dTWA discrete truncated Wigner approximation

GOE Gaussian orthogonal ensemble

FDR fluctuation dissipation relation

LTFI long-range transverse field Ising model

ETH eigenstate thermalization hypothesis

MPS matrix product state

ARPES angle-resolved photoemission spectroscopy

tdARPES time-dependent angle-resolved photoemission spectroscopy

1

INTRODUCTION

1.1 THERMALIZATION OF CLOSED MANY-BODY SYSTEMS

1.1.1 *Classical mechanics*

Scientists have been fascinated for centuries by a process called *thermalization*, the fundamental mechanism of how non-equilibrium states relax toward thermal equilibrium. Famously, Boltzmann [1] and Loschmidt [2] discussed in a fiery exchange how macroscopic, irreversible, *thermo*dynamics with an apparent arrow of time [3] emerge from the microscopic, reversible dynamics described by Newton's equations. One important hall-mark of thermal equilibrium is that only very little information is needed to accurately describe the macroscopic behaviour. Only a single function, for example the free energy, needs to be known to determine macroscopic observables such as specific heat or susceptibilities. Contrastingly, the location and velocity of every single constituent particle, or in case of quantum physics, the wavefunction of the system, needs to be known to specify the microscopic state of the system. The thermalization process is hence accompanied by a drastic reduction of the amount of information needed to describe the macroscopic properties of the system. This observation marks thermalization as a classic example of an *emergent* phenomenon as termed by Anderson [4], and, in the context of ecology, by Haber [5]: the interaction between many microscopic constituents can lead to an entirely different effective description of the macroscopic behaviour. For example, it is not necessary to understand the quantum physics of every single molecule to describe the behaviour of living cells. However, how emergence works in detail is unknown despite the ubiquity of this concept and understanding emergence in specific circumstances is one of the most challenging problems in science in general. For example, the emergence of human consciousness from the seemingly simple mechanics of neural networks belongs to this class of problems. Similarly, thermalization is the process of the emergence of statistical mechanics from Newton's equations. It is clear that this process must involve some ignorance from the observer's perspective: If they could follow every single particles' trajectory, reversibility would always be retained as Newton's equations would allow a perfect recovery of the initial state [6], i.e. the dynamics are reversible. On the contrary, thermodynamics is irreversible as postulated in the second law. Boltzmann thought he had found a theorem proving

the approach to equilibrium [1], now called the "H-theorem" because of the capital letter he used for the quantity corresponding to the entropy. He showed this quantity to increase with time as demanded by the second law of thermodynamics. However, his way of introducing "ignorance" into the description, molecular chaos (*Stoßzahlansatz*), later was identified to artificially introduce irreversibility. Modern explanations of thermalization in classical systems are based on two assumptions, which are partially based on analytical and numerical evidence [1], dynamical chaos and the ergodic hypothesis.

CHAOS The discovery of dynamical chaos [8] in numerical simulations gave some explanation for the emergence of an effective arrow of time. Chaos is the observation that the distance between two states initially prepared close to each other increases very quickly with time. As we cannot know the initial state with arbitrary precision, this means that following the state of a large system of particles is close to impossible. This effect has also been termed the "butterfly effect": In principle, a small difference in how a butterfly flaps its wings could mean the difference between a storm being created on the other end of the world, or not. Dynamical chaos is a result of the non-linearity of classical interacting systems, leading to the potential of large forces being created by a small perturbation. See Refs. [9, 10] for more thorough introductions into this field.

ERGODICITY The ergodic hypothesis [11] is the other cornerstone of explaining the emergence of statistical mechanics in classical systems. It formulates the expectation that the time evolved state visits every possible phase space point during the dynamics. This assumption serves as a way to make the ensemble formulation of statistical mechanics plausible: Despite the fact that a physical system only exists once, statistical mechanics calculates its properties from many realizations of the same system, the ensemble. In the microcanonical ensemble, for instance, all phase space configurations within a small shell of the conserved quantities such as energy and particle number serve as members of the ensemble, where every state is assumed to be equally probable. The ergodic hypothesis replaces the ensemble picture with a time evolution: As it assumes that the time evolving system visits every single phase space point (under the constraints of conserved quantities) and spends the same time in each state, observing a single system over a long time is the same as averaging over all states. Although the ergodic hypothesis has been proven in some systems [12–15], its practical implications are weakened by the fact that the time it takes to explore the whole phase space of the system scales exponentially

1 The presentation in the remainder of this subsection as well as the following subsection is based on Ref. [7]

with its size. Moreover, following the ergodic hypothesis, only the *time averaged* state would look thermal, but not the state at every instance of time. However, it is clear from both experiments and our everyday experience that thermalization is in general faster than exponential and macroscopic objects are in equilibrium even for one instance of time. One may hence formulate a different hypothesis: One does not need to observe all phase space points of a system in order to find agreement with the ensemble average. Instead, a single phase space point suffices because macroscopic observables take similar values in most phase space points. Hence, thermalization only amounts to reaching a "typical" phase space point rather than exploring all possible phase space points and averaging over all of them. "Typical" in this case means that macroscopic observables agree between typical phase space points. While this hypothesis makes sense intuitively, it is hard to rigorously formulate in classical mechanics. As we will see in the following, quantum mechanics enables the definition of thermalization in much more concrete terms, related to a similar notion of typicality of states, despite initial difficulties in porting the concepts of ergodicity and chaos to the quantum world.

1.1.2 *Quantum mechanics*

With the advent of quantum mechanics, explaining irreversibility from microscopic laws seemed even more difficult than in classical mechanics. Dynamical chaos is absent in the Schrödinger equation when employing a straight-forward generalization of the classical concept. To see this, consider two initial states $|\Psi_1\rangle$ and $|\Psi_2\rangle$ and define the "distance" between the two states as $||\Psi_1\rangle - |\Psi_2\rangle|^2 = 2(1 - \mathrm{Re}(\langle\Psi_1|\Psi_2\rangle))$. The states evolved under a time-independent Hamiltonian $\hat{H}$ are given by $|\Psi_{1/2}(t)\rangle = e^{-i\hat{H}t}|\Psi_{1/2}\rangle$. Therefore, the distance measure between the two time evolved states does not diverge exponentially but is in fact *constant*, as $\langle\Psi_1(t)|\Psi_2(t)\rangle = \langle\Psi_1|\Psi_2\rangle$. Of course, this is a quite naive generalization of classical dynamical chaos, relying on the intuition that the components of the wavefunction are the generalization of classical phase space. However, the wavefunction of a macroscopically large system is not measurable as it would require exponentially many measurements in system size/number of particles. Similarly, the ergodic hypothesis is difficult to generalize to quantum systems as even the notion of trajectories is ambiguous due to two reasons: On the one hand, the momentum and position of a particle can not be measured at the same time due to the uncertainty principle. On the other hand, particles are indistinguishable and hence their trajectory can not be traced individually. While Wigner-Weyl quantisation offers a generalization of phase space to quantum systems, the resulting phase-space

function can be negative and therefore can not be interpreted as a probability distribution, contrary to the classical phase space distribution. Finally, it has been explicitly shown that most states of the exponentially large Hilbert space are only reached in exponential time under time evolution [16]. Hence, the notion of ergodicity is not useful in practice. Von Neumann already recognized these difficulties in a pioneering work aimed at generalizing Boltzmann's H-theorem to quantum mechanics [17, 18]. He proposed to focus on *observables* rather than the wave function when discussing thermalization, similar in spirit to the "typical phase space point" approach we discussed in the context of classical systems. However, it took another major innovation to put this picture on more sturdy feet: random matrix theory.

QUANTUM CHAOS The application of the theory of random matrices [19, 20] to the study of quantum Hamiltonians is often called "quantum chaos", despite it being unrelated to dynamical chaos in classical systems. Loosely speaking, however, they share the common concept of introducing randomness through complexity. In the case of dynamical chaos, complexity is introduced by the non-linear equations of motion. In quantum chaos, the exponentially large Hilbert space leads to the Hamiltonian having statistical properties resembling those of a random matrix. Wigner introduced this hypothesis in the context of studying the energy levels of large nuclei [21]. More generally, interacting, time-reversal symmetric quantum systems show statistical properties resembling a Gaussian orthogonal ensemble (GOE)[2]. It is defined by the probability distribution

$$P(\hat{H}) \propto \exp\left(-\frac{1}{2\sigma^2}\mathrm{Tr}\left(\hat{H}^2\right)\right), \tag{1.1}$$

where σ^2 sets the variance, i.e. the energy scale and $\hat{H}$ are real symmetric matrices. A frequently used statistic to compare non-random Hamiltonians of many-body systems to random matrices is the ratio of consecutive levelspacings

$$r_i = \frac{\min(E_{i+1} - E_i)}{\max(E_{i+1} - E_i)}, \tag{1.2}$$

where E_i are the sorted eigenvalues. For the GOE, the probability distribution of the r_i is approximately given by

$$P_{\mathrm{GOE}}(r) = \frac{27}{4}\frac{r + r^2}{(1 + r + r^2)^{5/2}}. \tag{1.3}$$

One of the most important features of this distribution is that $\lim_{r\to 0} P_{\mathrm{GOE}}(r) = 0$, which is often referred to as *level repulsion*[3]. It is the many-body generalization

2 The Gaussian orthogonal ensemble is replaced by the Gaussian unitary ensemble if time-reversal symmetry is broken, e.g. in the presence of a magnetic field.

3 In order to see random matrix behaviour in non-random Hamiltonians, one needs to look at a sufficiently small energy window as well as resolve all symmetries. We will discuss the first requirement

of avoided crossings induced by off-diagonal elements in a 2×2 matrix and is therefore usually attributed to the presence of many-body interactions [4]. Contrarily, a non-interacting system has been conjectured by Berry and Tabor [23] to have a nearest-neighbour level spacing statistic following the one of a Poisson distribution, $P_{\mathrm{POI}}(r) = 2/(1+r)^2$. Crucially, this distribution has its maximum at vanishing level spacing. This means that free systems have an energy level statistic as if energy levels were simply sprinkled on an interval. Contrarily, interacting systems show correlations between energy levels, reducing the probability for them to be close in energy. The emergence of random matrix behaviour has been tested in many circumstances and we will show one specific example in section 6.2.

One of the most intriguing features of random matrices is the structure of the matrix elements of Hermitian matrices $\hat{A} = \sum_k A_k |k\rangle \langle k|$ (i.e. observables) with respect to the eigenstates $|n\rangle$ of random matrices,

$$\langle m|\hat{A}|n\rangle \approx \bar{A}\delta_{mn} + \sqrt{\frac{\overline{A^2}}{\mathcal{D}}} R_{mn}, \tag{1.4}$$

where $\overline{A^l} = \frac{1}{\mathcal{D}} \sum_k A_k^l$, $\mathcal{D}$ is the dimension of the Hilbert space and R_{mn} are random numbers with vanishing mean and variance 1 (off-diagonal elements) or 2 (diagonal elements). As $\overline{A^l}$ is a $\mathcal{D}$-independent number, the above expression shows that for random matrices, the ensemble average over many matrices is equivalent to the "infinite volume limit" $\mathcal{D} \to \infty$ in a fixed random matrix - in both cases, the off-diagonal matrix elements vanish. This is similar to the corresponding assumption in traditional statistical mechanics.

EIGENSTATE THERMALIZATION For a non-random many-body Hamiltonian $\hat{H}$ it is clear that the random matrix theory result for matrix elements of operators (1.4) must be modified to include an energy dependence of the right hand side as microcanonical expectation values depend on energy. In particular, the off-diagonal elements must be adapted to account for the energy dependence of the density of states. In a seminal paper [24], Srednicki proposed the following ansatz based on previous works [25, 26], now known as the eigenstate thermalization hypothesis:

$$\langle n|\hat{A}|m\rangle = A(\bar{E})\delta_{nm} + e^{-S(\bar{E})/2} f_A(\bar{E}, E_m - E_n) R_{nm}, \tag{1.5}$$

where $A(\bar{E})$ is the microcanonical expectation value of operator $\hat{A}$ at energy $\bar{E} = (E_n + E_m)/2$, S is the thermodynamic entropy, R_{nm} are random numbers with mean

in detail when introducing the eigenstate thermalization hypothesis. The second requirement comes from the fact that states in two symmetry sectors do not have any reason for repelling each other as the two symmetry sectors do not interact. Hence, level repulsion would be artifically reduced.

4 See Ref. [22] for a short introduction to level repulsion and its generalization to the interaction of a single level with a continuum.

zero and unit variance. $f_A(\bar{E}, E_m - E_n)$ and $A(\bar{E})$ are smooth functions of their arguments. To see the implications for thermalization of the ETH ansatz, consider the expectation value of $\hat{A}$ with respect to a time evolved state,

$$\langle \Psi(t)|\hat{A}|\Psi(t)\rangle = \sum_m |\langle m|\Psi\rangle|^2 \langle m|\hat{A}|m\rangle + \sum_{m,n\neq m} \langle m|\Psi\rangle \langle \Psi|n\rangle \langle n|\hat{A}|m\rangle e^{-i(E_m-E_n)t}. \tag{1.6}$$

In order to show thermalization, this expectation value needs to agree with the microcanonical expectation, i.e. $A(E_\Psi)$, where $E_\Psi = \langle \Psi|\hat{H}|\Psi\rangle$ is the energy of the initial state. In a system without extensive degeneracies, the second, time-dependent term is expected to average to zero due to dephasing between the oscillating terms, which may be enforced by taking the long time average. Then, inserting the ETH ansatz, we get

$$\langle \Psi(t)|\hat{A}|\Psi(t)\rangle \overset{t\to\infty}{\longrightarrow} \sum_m |\langle m|\Psi\rangle|^2 A(E_m) \equiv \bar{A}. \tag{1.7}$$

This agrees with the microcanonical expectation value if the energy fluctuations of the $|\langle m|\Psi\rangle|^2$ are small (i.e. subextensive), because the function A(E) in the ETH ansatz is assumed to be smooth. Energy fluctuations are indeed small for most physical initial states, see e.g. Ref. [27] for a proof that product states fulfill this condition. Put differently, the overlaps with the initial state $|\langle m|\Psi\rangle|^2$ represent a new thermodynamic ensemble which agrees with the microcanonical one due to the vanishing energy fluctuations.

In a similar way, it can be shown from ETH that fluctuations around the long-time value are small,

$$\left(\langle \Psi(t)|\hat{A}|\Psi(t)\rangle^2 - \bar{A}^2\right) \overset{t\to\infty}{\longrightarrow} \sum_{m,n\neq m} |\langle m|\Psi\rangle|^2 |\langle n|\Psi\rangle|^2 |\langle n|\hat{A}|m\rangle|^2 \tag{1.8}$$

$$\leq \max |\langle n|\hat{A}|m\rangle|^2 \tag{1.9}$$

$$\propto e^{-S(\bar{E})/2} \tag{1.10}$$

$$\overset{L\to\infty}{\longrightarrow} 0 \tag{1.11}$$

due to the extensivity of the thermodynamic entropy. Hence, the diagonal part of ETH dictates that expectation values of operators in a time evolved state agree with the microcanonical expectation and the off-diagonal part leads to vanishing fluctuations of the time-evolved expectation values. Experimentally, the diagonal part of ETH can hence be probed by preparing an initial state and seeing whether the time evolved state agrees with the microcanonical expectation. The off-diagonal part is however harder to probe due to it being vanishingly small. Moreover, even the microcanonical expectation values are in general hard to calculate for quantum

many-body systems. It is one of the achievements of this thesis to show how the off-diagonal part of ETH can be experimentally probed by using two-time correlation functions without the need of any theory input, see chapter 4. While initially, eigenstate thermalization was proposed as a sufficient condition for thermalization, it has recently been proposed [28] that it is in fact also a necessary condition.

APPROACH TO EQUILIBRIUM While ETH can make remarkably precise statements about the long-time value of expectation values and their agreement with the thermal expectation, the temporal approach to this value can not be predicted by ETH. In the discussion above, we always used either the infinite time limit or an average over infinitely long times, similar in spirit to the long-time average envisioned in the classical ergodic hypothesis. The actual dephasing process between many-body eigenstates naively takes exponentially long time as the level spacing is exponentially small in system size. In numerical simulations and quantum simulation experiments, it has nevertheless been shown that thermalization is indeed a fast process, with the thermalization time often even independent of system size. For example, Rigol et al. [27] studied this question for a very small system containing just four particles. Importantly, not only the approach to equilibrium was confirmed in this work, but also that ETH is indeed the mechanism which leads to thermalization. In a recent experiment, the emergence of many-body behaviour has been impressively shown by the appearance of a Fermi sea for as few as five fermions [29]. Numerous methods have been developed to study the non-equilibrium dynamics of quantum systems and to confirm ETH. In section 1.2, we will introduce some of these methods in more detail and the results obtained by them.

SCRAMBLING While it is so far not possible to predict just from the Hamiltonian describing a specific system how quickly it will thermalize, some progress has been made recently to further characterize the approach to equilibrium and the processes involved. At the center stage is the question of how quickly quantum information is spread throughout the system. The half-system entanglement entropy, for instance, grows linearly with time in most systems [30], indicating an efficient loss of the details of the initial state [5]. Some of the most general results on entanglement spreading come from a time-dependent generalization of random matrix theory, random unitary circuits, where random entangling gates are acted on a set of qubits. They serve as generic, time-discretized models of time evolution in quantum systems. For instance, the linear growth of the entanglement entropy has been

5 Of course, the entanglement entropy of the whole system stays constant due to the unitary of the dynamics

shown to fulfill the Kardard-Parisi-Zhang equation [31–33], which was later also confirmed in a Hamiltonian model [34]. A second notion of information spreading is the *scrambling* of operators. This has been termed in the context of the thermalization of black holes [35] and constitutes a semi-classical generalization of the ideas behind classical dynamical chaos to quantum dynamics. Instead of studying trajectories of the wavefunctions, scrambling describes the process of operator spreading in the Heisenberg picture, i.e. how correlated a time evolved operator is with an operator at the initial time. In systems with a well-defined semi-classical limit involving a "small parameter" playing the role of the reduced Planck's constant $\hbar$, this spreading does indeed happen exponentially quickly in time [36–39]. Moreover, these systems show a ballistic spreading of chaos without a broadening of the wavefront. Systems without a semi-classical limit, such as spin $1/2$ systems and bosonic systems with a fixed particle number, do not show exponential growth of many-body chaos [33, 40]. Instead, the presence of an upper bound of the chaos measure leads to a quick saturation to the maximally possible value. Moreover, the ballistic wavefront broadens diffusively. In random unitary circuits, the scrambling process and the two limits discussed above has been studied to great depth and in some cases even analytically [41–43]. We will study in section 3 how scrambling happens near a thermal phase transition, where in principle, slow dynamics are expected.

EMERGENT CLASSICAL TRANSPORT Scrambling is a fast process, leading to the evolving quantum system looking essentially classical as if it was dephased by an environment. On the contrary, the spreading of conserved quantities such as the energy density or particle number need to fulfill the continuity equation and hence are much slower processes. In general, it is hence expected that slow, classical transport emerges as the latest stage in the thermalization of quantum systems. Establishing this assumption and, furthermore, determining the transport coefficients of the hydrodynamic theory for specific quantum systems is a hard problem, due to the absence of controlled analytical approaches and the amount of computational resources required to model the quantum entanglement present in the time evolved state [30, 32, 40, 44, 45]. In recent years, Feynman's idea of using *quantum* computational resources to simulate quantum systems has been established to realize and explore quantum systems (see section 1.2). However, it remains an open challenge to precisely track the evolution to the late-time hydrodynamic regime, as large, coherent quantum systems are required. In chapter 6 we will use field theoretical methods (which we introduce in chapter 2) as well as a quantum simulation realized in a collaboration with the trapped ions group in Innsbruck

to show that hydrodynamics indeed emerges in the thermalization dynamics of closed quantum systems.

DETOURS TO OR ABSENCE OF EQUILIBRIUM While most many-body systems relax to equilibrium in the way we discussed above, many cases have been discovered recently in which thermalization either happens very slowly, not at all or only via a detour. Prethermalization [46–48] is a phenomenon in the presence of two very different time scales in the system, which induce an approximately conserved quantity. Only after times exponentially long in the inverse size of the term breaking the conservation does the system relax to its true equilibrium. Even more extremely, highly excited bosonic systems can first approach a fixed point of the dynamics which is not thermal equilibrium, termed a non-thermal-fixed-point [49–51]. These dynamics are characterized by turbulent transport as well as algebraically slow, self-similar dynamics. Disordered, one-dimensional systems have been shown to exhibit many-body-localization[52–57], where an extensive set of local integrals of motion lead to emergent integrable dynamics and the system fails to thermalize on accessible timescales. Most recently, special many-body eigenstates termed many-body scars [58, 59] have been discovered in systems with dynamical constraints [60–62], leading to extremely slow, "glassy" relaxation[6]. Furthermore, conservation of multipole moments lead to a fragmentation of the Hilbert space into extensively many blocks [61], creating a failure to thermalize. If the fragmentation is perturbed, a subdiffusive approach to equilibrium has been shown [65].

In this section we have introduced some of the established notions to explain why many-body systems reach thermal equilibrium, most importantly the eigenstate thermalization hypothesis. Before we move to the main part of this thesis, we discuss some of the methods used to study quantum many-body dynamics and the challenges met in doing so.

6 In classical systems, such slow dynamics can for example occur in glasses [63, 64], which is why slow relaxation to equilibrium is often referred to as "glassy dynamics".

1.2 SIMULATING QUANTUM-MANY-BODY DYNAMICS

1.2.1 *Classical simulation*

WHY TIME EVOLVING QUANTUM MANY-BODY SYSTEMS IS HARD. The dynamics of non-relativistic quantum many-body systems is described by the Schrödinger equation[7]

$$i\frac{d}{dt}|\psi\rangle = \hat{H}|\psi\rangle\,. \tag{1.12}$$

Although the formal solution of this equation is easy to write down in terms of a matrix exponential,

$$|\psi(t)\rangle = e^{-i\hat{H}t}|\psi(0)\rangle\,, \tag{1.13}$$

solving this equation in practice is in general a hard problem. This is because of two reasons. On the one hand, the dimension of the state $|\psi\rangle$ expanded in a suitable basis in general scales exponentially in the size of the problem, i.e. the system size and/or particle number. For example, spin $1/2$ degrees of freedom have local Hilbert space dimension 2 consisting of the states $|\uparrow\rangle, |\downarrow\rangle$. A state describing a system comprising of L such sites then has a total Hilbert space dimension of 2^L. As the amplitudes of the state are in general complex, representing such a state on a classical computer with double precision takes $2^L \times 16$ bytes of memory. Hence, even a state describing a system with just 32 sites would already exhaust the memory of most current laptop computers, requiring 69 Gigabytes of RAM just to store the state. Moreover, the Hamiltonian expressed in the same basis is a $(2^L)^2$ matrix and would therefore require even more memory to be stored. Luckily, it turns out that for most problems the Hamiltonian is a sparse matrix such that only the non-zero elements have to be stored. For slightly larger problems than the ones accessible by exact diagonalization, this enables the use of Trotterization and efficient sparse matrix-vector multiplications [66] to solve Eq. 1.13 by

$$|\psi(t)\rangle \approx (e^{-i\hat{H}(t/n)})^n|\psi(0)\rangle\,. \tag{1.14}$$

However, this procedure has an error increasing with the time step (t/n) as well as the total number of steps n, limiting its general range of applicability to short times. This is a first manifestation of the second problem of evolving quantum many-body systems: reaching long times.

It turns out that the "reaching long times" problem is in fact almost the same problem as "reaching large systems". This becomes more apparent if one formulates

7 In this chapter and throughout the thesis we will work in units where $\hbar = 1 = k_B$.

time evolution in the context of "traditional" computer science complexity classes. An example for a difficult classical problem is the famous travelling salesman problem, which is in the complexity class NP-complete [67]. This means that the solution can be verified in a time polynomial in the size of the problem, but finding this solution takes a superpolynomial time. Moreover, finding a solution to the traveling salesman problem is equivalent to finding a solution to any other problem in NP-complete as problems in this class can be translated to each other with a polynomial overhead. Finding an efficient solution to NP-complete problems is one of the biggest outstanding challenges in computer science [8].

Where does time evolving a quantum system fit into these complexity considerations? The first observation is that classical computer science problems do not need exponential memory, but only exponential time, whereas the quantum time evolution algorithm quoted above takes exponential memory, but only linear time, so a direct comparison seems difficult. However, there exist algorithms which trade the exponential memory with exponential time. The simplest one is called "Feynman algorithm" [68–70]. It follows a similar procedure as the construction of the path integral formulation of quantum mechanics [71–73] by trading the n multiplications of the $2^L \times 2^L$ matrix $e^{-i\hat{H}(t/n)}$ on the 2^L statevector with a sum over the $(2^L)^{n-1}$ possible histories or paths. This is done by inserting a complete basis set between the applications of $e^{-i\hat{H}(t/n)}$. This way, the transition probability from one of the basis states to another can be computed without storing the full initial state. Using that $\hat{H}$ is local, matrix elements of $e^{-i\hat{H}(t/n)}$ between basis states can also be computed without explicitly constructing $\hat{H}$, showing that we have successfully traded exponential memory with exponential time. From this first look, the computational resources needed to time evolve many-body quantum systems scales as unfavourably with the system size n as some of the hardest problems known in computer science. We note however, that to our knowledge this hardness is not proven so far, i.e. there may be an efficient classical algorithm which has simply not been found yet.

Even more troubling than this exponential requirement for resources is that contrary to problems in NP, there is no obvious way to check the consistency of the result of the computation. This means, in a sense, that quantum time evolution is even harder than NP problems. In practice, this means that we need to cross-check results between different approximate methods, hoping that agreement between two complementary methods signals proximity to the exact solution. However, we of course do not have a guarantee that we get the correct solution if two approximate solutions agree. Throughout this thesis, we will try to compare as many numerical

8 So much so that whoever "simply" proves whether or not this is possible (known as the "P=NP or P≠NP" problem) will get awarded a million dollars by the Clay Mathematics Institute.

methods and analytical results as were accessible to us to gain confidence about our results.

Many methods exist to somewhat alleviate the exponential resources required for evolving many-body quantum systems. Most of them rely on the observation that the full amplitude vector $|\psi\rangle$ contains a lot of information which is not directly relevant to local observables, i.e. $|\psi\rangle$ contains information which is not realistically measurable in experiment. In the last years, at least two major ways have been established to use this observation: In the first, the state is compressed by using some measure of "complexity" and only taking into account the most relevant contributions. In the second, the notion of a state is entirely scrapped and local observables are evolved *directly*.

Starting with Yuri Manin's [74] and Richard Feynman's [75] visions, a new possibility to simulate the dynamics of quantum systems has been established in recent years: the simulation with another quantum system which can be highly controlled. We will discuss below that this can in fact be done in two ways: In a "digital" approach, time evolution is broken down to basic building blocks, called gates in analogy to classical computation, which are then acted on discrete quantum degrees of freedom. In "analogue" approaches, a certain Hamiltonian $\hat{H}$ is implemented with high confidence and the time evolution of an initial state is studied by observing the system after some time.

In the following, we will first discuss the state-of-the-art method to evolving low-dimensional lattice systems in time by compressing the state using the entanglement entropy as a complexity measure, matrix product state (MPS) methods. Then, we will discuss methods based on directly evolving observables in time. In chapter 2 we will introduce one method in this class in more depth: non-equilibrium quantum field theory. Afterwards, we will introduce digital as well as analogue quantum simulation methods.

MATRIX PRODUCT STATES One of the major advances in the study of strongly correlated quantum systems has been the discovery of the density matrix renormalization group [76], whose efficiency to find ground states of gapped Hamiltonians is based on the fact that such states obey the so-called "area law" [77, 78]. This means that the entanglement entropy, a measure for the complexity of the state, only grows with the size of the boundary of the system, rather than the system size itself. In particular, in 1D this means that the entanglement entropy of the ground state of a gapped Hamiltonian is constant as a function of system size. MPS have been shown to capture this type of "low complexity" state very efficiently. Moreover, they contain a "tuning knob" with which the complexity that the MPS can capture can be increased. In fact, *any* quantum state can be represented by

an MPS. This would however again need a memory scaling exponentially in the system size. More specifically, the MPS ansatz for the wave function can be written as [79]

$$|\psi\rangle = \sum_{i_1,\ldots,i_L=1}^{d} \prod_{\alpha=1}^{L} M_{i_\alpha}^{\alpha} |i_1,\ldots,i_L\rangle\,, \tag{1.15}$$

where d is the local Hilbert space dimension (e.g. $d = 2$ for the spin $1/2$ electron example used above) and $|i_1,\ldots,i_L\rangle$ are the product states spanning the Hilbert space. On each site, there are d matrices of dimension $\chi_\alpha \times \chi_{\alpha+1}$ which are multiplied together to yield the state coefficient. χ_α is called the bond dimension of the matrix product state. It can be shown that the maximum entanglement entropy that a matrix product state can capture scales logarithmically with the bond dimension χ_α. As generic states follow the volume law, i.e. entanglement entropy scaling linearly in the number of sites L, this means that the bond dimension needed to express a generic state scales exponentially in the size of the system. However, as mentioned above, ground states of gapped Hamiltonians in 1D follow an area law and hence can be described by a matrix product state with *finite* bond dimension. For us, it is important to know that the entanglement entropy in general increases linearly with time [30]. This means that, starting from a low entanglement initial state, the maximum time to which an MPS can be evolved to scales logarithmically in the bond dimension.

In most of the cases we are going to be interested in during this thesis, the initial state will be given by a product state, which can be represented by an MPS of bond dimension 1. For example, a Néel state in a 1D spin model, $|{\downarrow}{\uparrow}\cdots{\downarrow}{\uparrow}\rangle$ can be written with 4 matrices as

$$M_0^{2i} = 0, \quad M_1^{2i} = 1, \tag{1.16}$$

$$M_0^{2i+1} = 1, \quad M_1^{2i+1} = 0, \text{ with } i \leq L/2. \tag{1.17}$$

There are many algorithms to time evolve matrix product states, for example the time-dependent-variational principle [80, 81] (most suitable for systems with long range interactions [44, 82]), the WI/WII matrix-product-operator algorithm [83] (suited for evolution of two-dimensional systems in a cylinder geometry and long-range systems, e.g. for calculating spectral functions [84–86] and single excitation dynamics [87]). One of the most widely used algorithms is time evolving block decimation [88], which is well-adapted for one-dimensional problems with nearest-neighbour interactions. We will be employing this algorithm in chapter 8 in this thesis. It relies on a Trotterization of the time evolution operator $\hat{U} = (e^{-i\hat{H}dt})^n \equiv (U_{\mathrm{dt}})^n$ with $dt = t/n$, similarly to the sparse matrix method discussed above.

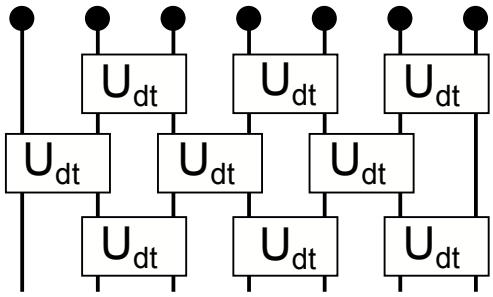

Figure 1.1: Schematic depiction of the TEBD algorithm. The blobs indicate the sites i_α of the system while time proceeds from top to bottom.

However, it goes one step further by assuming a nearest-neighbour form of the Hamiltonian $\hat{H} = \sum_i \hat{h}_{i,i+1}$. In this case, a single time step can be decomposed as

$$e^{-i\hat{H}dt} \approx \prod_{i\,\text{odd}} e^{-i\hat{h}_{i,i+1}dt} \prod_{i\,\text{even}} e^{-i\hat{h}_{i,i+1}dt}. \tag{1.18}$$

In Fig. 1.1 we give a schematic of this algorithm. After application of a single time step, the bond dimension of the matrices will have increased due to the entanglement created by the two-site gates. Usually, a maximum bond dimension $\chi_{\max}$ is defined, to which the matrices are truncated after each time step by performing a Schmidt decomposition (technically done by using the singular value decomposition) and only keeping the largest $\chi_{\max}$ values. Expectation values of observables can then be obtained by representing the operators in a matrix product form. Finally, $\chi_{\max}$ is increased until convergence, where the needed $\chi_{\max}$ increases with time due to the growth of entanglement during the time evolution. See Ref. [89] for a more complete and thorough introduction.

EVOLVING OBSERVABLES INSTEAD OF WAVEFUNCTIONS All previous methods to calculating or simulating quantum dynamics were based on evolving the Schrödinger equation (1.12). This yields the complete wavefunction $|\psi(t)\rangle$ as a function of time. From the wavefunction, arbitrary observables can be evaluated. However, one can also follow a different approach by directly evolving expectation values of observables in time. The obvious starting point for such an approach are the Heisenberg equations of motion for a closed system for the observables $\hat{A}$,

$$-i\partial_t \hat{A} = [\hat{H}, \hat{A}]. \tag{1.19}$$

Evaluating the commutator and taking the expectation value, we can then evaluate the time evolution of $\langle \hat{A}(t) \rangle$ as a function of a different observable [9], $\langle [\hat{H}, \hat{A}] \rangle$. To

9 This procedure is related to matrix product operator (MPO) techniques [79, 90–95]. However, in MPO methods, the full operator is evolved and could then in principle be evaluated with respect to any initial state. Here, we discuss directly evolving expectation values of operators by starting with the initial value of the observable in a specific initial state.

solve these equations, we need to evaluate the time evolution of $\langle[\hat{H}, \hat{A}]\rangle$ which is determined by yet another observable, $\langle[\hat{H}, [\hat{H}, \hat{A}]]\rangle$. It is obvious that this hierarchy of equations of motion does not close in general for interacting systems and an infinite number of coupled equations of motions need to be solved simultaneously. This hierarchy of equations of motion is also called the Bogoliubov-Born-Green-Kirkwood-Yvon (BBGKY) hierarchy [96–101]. As exactly solving the hierarchy is not possible in general, the prime goal in this approach to quantum dynamics is to find a way to close this hierachy in a controlled manner. Most importantly, this needs to be done in a *self-consistent* way. To see this [10], consider a naive perturbative expansion of $\hat{A}(t)$ using the Baker-Campbell-Hausdorff formula,

$$\hat{A}(t) = \hat{A}(0) + it[\hat{H}, \hat{A}(0)] + \frac{t^2}{2}[\hat{H}, [\hat{H}, \hat{A}(0)]] + \mathcal{O}(t^3). \tag{1.20}$$

It is immediately clear that such an expansion will fail at times $t \approx 1$ if $||\hat{H}|| = 1$. Hence, in order to go to non-perturbatively long times, a possible approximation to the right hand side of the Heisenberg equation of motion needs to be dependent on the value of $\hat{A}$ at time t. In chapter 2 we will show how to introduce such a *self-consistent* approximation scheme using non-equilibrium quantum field theory.

1.2.2 *Digital quantum simulation*

Quantum computers are machines which can perform a "universal" set of operations on qubits, which are nothing else than the spin 1/2 degrees of freedom we discussed so far. "Universal" means in this case that any unitary operator $\hat{U}$ can be implemented using only a given set of operations. It was shown [103], that any such unitary can be decomposed into a sequence of single qubit and two-qubit operations. Hence, performing a quantum computation has a similar "brick-wall" structure as the TEBD algorithm represented in Fig. 1.1, albeit without a truncation step and with different gates in every layer. Conversely, this means that a quantum computer can perform time evolution of a spin 1/2 quantum system using Trotterization and a decomposition into single and two-qubit gates. As no truncation is performed in this case, a quantum computer can in principle efficiently evolve a quantum system in time, using only $\mathcal{O}(L \times n)$ two-qubit gates, i.e. it scales both linearly with system size and the maximum time [104–106]. In particular, it has been shown that all states that are reached via time evolution with a local Hamiltonian in polynomial time can be efficiently represented by a quantum circuit [16].

However, today's quantum computers are still very noisy, meaning that gates can not be performed with perfect efficiency. This introduces an error in the calculation

10 See also section 1.1.1. in Ref. [102] for an illustrative example why non-self-consistent approximations fail for dynamics.

with every time step and therefore limits the maximum time until the quantum computer can precisely evolve the quantum system. This gate error plays an analogous role to the truncation step in the MPS TEBD algorithm, as it reduces the amount of entanglement captured by the computer. This argumentation has recently been used in reverse to construct an MPS algorithm which limits the entanglement akin to noise [45]. The analogy between noise in a quantum computer and MPS truncation has also recently been studied [107] in order to compare their performance. The authors show that a quantum computer with a one-dimensional (nearest-neighbour) geometry and a two-qubit fidelity of no better than 99% can be simulated with matrix product state methods with a linear cost in both L and n. This shows that while quantum computers hold the promise of efficiently solving the time evolution of quantum systems, classical computational schemes will stay competitive until error correction [108–110] can be widely implemented. While we only discussed the most straight-forward way of simulating quantum many-body dynamics with quantum computers, other algorithms have been developed. For example, a recent hybrid quantum-classical algorithm optimizes a variational state during the time evolution, reaching far longer times than naive trotterization [111]. Moreover, representing an infinite MPS opens up the possibility to simulate infinitely large systems on a quantum computer with a finite number of qubits [112, 113].

1.2.3 *Analogue quantum simulation*

Analogue quantum simulators realize a specific Hamiltonian, which is connected to the microscopic dynamics in the experiments. Crucially, the Hamiltonian is precisely known and the parameters can be tuned within certain limits. Initial states are prepared as ground or thermal states of some extreme limit of the parameters, and time evolution is probed by rapidly changing the parameters. This is also called a "quench" experiment, in analogy to experiments on glasses, where the temperature is rapidly changed to bring the system out of equilibrium. The last crucial ingredient for studying time evolution is the measurement of observables. Here, again, the possible measurements are related to the specific platforms. It is one crucial goal of this thesis to expand the range of observables which can be studied in quantum simulators, see chapters 4, 6, and 9.

Historically, analogue quantum simulators were the first step towards digital approaches. In their famous visions, Yuri Manin [74] and Richard Feynman [75] proposed a simulator based on the "analogue" intuition described above: In order to simulate a quantum mechanical system governed by a Hamiltonian $\hat{H}_{\text{system}}$, find a different quantum mechanical system, the simulator, which can be more

easily controlled and is governed by the same, or a related Hamiltonian $\hat{H}_{\text{simulator}}$. Take, for example, the cuprate materials as our "system" we would like to learn about. They exhibit a vast range of quantum mechanical phases including a Mott insulating state [114] with anti-ferromagnetic spin order and high temperature superconductivity [115]. The main features of these materials are conjectured to be described by the two-dimensional Fermi-Hubbard model [116, 117]

$$\hat{H}_{\text{Hubbard}} = -t \sum_{\langle i,j\rangle,\sigma} (\hat{c}^{\dagger}_{i\sigma}\hat{c}_{j\sigma} + h.c.) + U \sum_{i} \hat{n}_{i\downarrow}\hat{n}_{i\uparrow}, \tag{1.21}$$

where $c_{i,\sigma}$ are electronic annihilation operators of spin σ and $n_{i\sigma} = c^{\dagger}_{i\sigma}c_{i\sigma}$ is the density operator of electrons with spin σ at site i. t, U denote hopping between nearest-neighbour sites and on-site interactions strength, which result from Coulomb repulsion between electrons [118]. In the cuprates, the scale of the hopping is on the order of 0.5 eV [119], corresponding to a timescale of 10 femtoseconds, rendering it challenging to observe electronic dynamics in a time-resolved way [120]. Moreover, disorder as well as subleading couplings render it difficult to compare theory to experiment. Lastly, the coherence time of the system is generally quite short such that time evolution of *closed* quantum systems is difficult to study in materials. In an analogue quantum simulator, on the contrary, the Hamiltonian $H_{\text{simulator}}$ is known very well and couplings to the environment are small compared to intrinsic time scales. In the following, we will briefly discuss how cold atoms in optical lattices enable the observation of dynamics in the Hubbard model before moving on to the quantum simulation of spin systems in Rydberg atoms and trapped ions. We finish with a brief overview over other platforms for quantum simulation of dynamics.

COLD ATOM QUANTUM SIMULATION The observation of a Bose Einstein condensate [121, 122] in laser cooled Alkali atoms impressively showed the potential of quantum optics experiments to probe many-body states of matter in a well-controlled way [123, 124]. Another milestone towards quantum simulation was the observation [125] of the superfluid-Mott insulator transition in cold atoms in optical lattices [126], showing that they are indeed excellent simulators of Hubbard models. As atoms are neutral, one might at first think that the the on-site term can not be implemented. Here, however, the "analogue" aspect of the simulator becomes most apparent: The physical mechanism leading to a certain term in the Hamiltonian is irrelevant, what matters is only that the Hamiltonian is exactly the one aimed for. In cold atoms, the on-site term can for example be implemented by representing the spin degree of freedom with two long-lived hyperfine levels of the ground state. Scattering between two atoms is at low temperatures dominated by s-wave scattering, which is local. In an optical lattice, this means that

atoms on a single site interact, leading to the sought-after on-site term. Interactions between neighbouring sites, contrarily, are negligible due to the neutrality of the atoms. Cold atom simulators can also tune the ratio t/U by changing the depth V of the lattice: while $U \sim V^{3/4}$, the hopping scales as $t \sim V^{3/4} \exp -2V^{1/2}$ [126]. Therefore, t/U is exponentially sensitive to changes of the lattice depth and can hence be tuned over a wide range. In the extreme limit of $U/t \to \infty$ and unit filling, i.e. one atom per site, the system enters a Mott-insulating phase, i.e. each atom is localized on one lattice site. In terms of dynamics, this result has been used ten years later to prepare a global quantum quench by removing an atom on every second lattice site, producing a charge density wave product state [127]. The time evolution of this charge density wave was then probed by simply taking pictures of the position of the atoms as a function of time. Of course, in a solid, trying to image the dynamics of an electronic charge density wave would be very challenging because electrons are about 10^5 times lighter and therefore move much faster. Moreover, the lattice spacing in cold atoms is much larger, given by the wavelength of the light which traps the atoms and hence on the order of 1 μm. This means that tunneling is suppressed. In total, tunneling times are on the order of a millisecond [127], making it possible to picture the time evolution with a simple CCD camera when making the atoms fluoresce [11]. The time evolution of the charge density wave state was shown to match a matrix product state simulation remarkably well, which only took into account coherent quantum dynamics. As the MPS simulation had to be stopped at times earlier than those accessible by the quantum simulator, this experiment was an early example of "quantum advantage" for studying non-equilibrium dynamics [127]. Other experimental studies of nonequilibrium dynamics in cold atoms in optical lattices include the observation of prethermalization [47], many-body-localization [129], and the observation of integrable dynamics [130–132]

Another major milestone for quantum simulation in cold atoms was the development of the "quantum gas microscope" [133–139], enabling single site resolution. This lead to a whole range of significant advances in studying strongly correlated phases, including the observation of anti-ferromagnetic order in the Mott-insulating state [140], bad metallic transport in the attractive ($U < 0$) Hubbard model [141], the detection of string patterns in the doped system [142, 143]. See Ref. [144, 145] for a more complete overview over the advances in studying equilibrium phases with cold atoms. Moreover, quantum gas microscopy enabled the time and space resolved observations of closed quantum many-body dynamics in Hubbard mod-

11 In studies of equilibrium properties, however, the small hopping comes at a price: reaching temperatures T that are small in units of the hopping is very challenging [128] as typical tunnelings corresponds to nanokelvin temperatures.

els, including the measurement of the growth of the entanglement entropy [146], the propagation of holes in an antiferromagnet [147, 148], Floquet prethermalization [149], slow dynamics [150, 151], and more detailed studies of many-body localization [152–155, 155–159].

QUANTUM SIMULATION OF SPIN SYSTEMS IN COLD ATOMS Cold atoms in optical lattices can also study the dynamics of spin systems by using the superexchange mechanism in a Mott-insulator: single particle hops are detuned by the large on-site interactions while second order processes of two atoms exchanging position are resonant. This way, it is possible to implement the Heisenberg model

$$\hat{H}_{\text{Heisenberg}} = J \sum_{\langle i,j \rangle} \left(\hat{S}_i^x \hat{S}_j^x + \hat{S}_i^y \hat{S}_j^y + \Delta \hat{S}_i^z \hat{S}_j^z \right), \tag{1.22}$$

where $\hat{S}_i^\alpha$ are the spin operators fulfilling $\left[\hat{S}_i^\alpha, \hat{S}_j^\beta\right] = i\epsilon^{\alpha\beta\gamma}\hat{S}_j^\gamma$ as well as $\mathbf{S}^2 = S(S+1)$. Importantly, the anisotropy Δ can be tuned by the intra and interspecies interactions using a magnetic Feshbach resonance. Motivated by experiments using this mechanism [160–163], we will study the dynamics of spin spirals in chapter 8.

RYDBERG ATOMS Another approach, which has progressed rapidly in the last years, is to use strong interactions between atoms that are highly excited to a large principal quantum number n, so-called Rydberg atoms. In particular, the second order Van-der-Waals interactions scale with n^{11}, leading to interaction time scales on the order of 10 nanoseconds with lifetimes in the range of microseconds [59]. There are many ways to encode a spin 1/2 in atoms. One possibility is to use the ground and Rydberg level, which enables the study of coherent dynamics in the long-range transverse field Ising model in a longitudinal field,

$$\hat{H}_{\text{Ising}} = \sum_{i,j} J_{ij} \hat{S}_i^z \hat{S}_j^z + \Omega \sum_i \hat{S}_i^x + \Delta \sum_i \hat{S}_i^z, \tag{1.23}$$

where $J_{ij} \sim 1/|i-j|^6$ for Van-der-Waals interactions and Ω, Δ are Rabi frequency and detuning of the ground-Rydberg transition [12]. Experiments also studied spin dynamics in disordered systems by exciting atoms in a cloud to two different Rydberg states, which leads to a different encoding of a spin 1/2 than the one above [164, 165]. Resonant dipole interactions between these levels, falling off with distance as $J_{i,j} \sim 1/|i-j|^3$, leads to the implementation of an XY model instead of the transverse field Ising model quoted above. Due to the blockade effect, two Rydberg excitations are separated by several micrometers, leading to well-separated atoms despite the fact that a cloud of atoms was considered. Due to the strong

12 In this notation, the detuning contains a shift due to the Van-der-Waals interactions.

interactions, the movement of the cold atoms was also negligible, leading to a lattice model with positional disorder. The advent of arrays of optical tweezers [166, 167] (Nobel prize 2018) lead to the removal of disorder, enabling almost arbitrary lattices [168, 169]. This enabled the observation of quantum phases [170], including a topological spin liquid [171], as well as the discovery of constrained dynamics due the presence of many-body scars [59]. Moreover, Kibble-Zurek dynamics across a quantum phase transition [172] have been observed. Rydberg interactions can also be used to "dress" the dynamics of ground orbital state atoms, which has been used in several experiments on dynamics of spin systems dynamics with long-range interactions [173]. Some of the protocols we will discuss in chapter 4 will be aimed at the Rydberg platform or contain the tweezer technology as a probe of cold atoms in optical lattices.

TRAPPED IONS A third quantum simulation platform which we will be heavily motivated by is ions trapped in electromagnetic fields [174, 175]. In the most widely used linear Paul trap, a time-varying quadrupole field in radial direction is combined with a static electric field in the axial direction to confine a string of ions in an anisotropic three-dimensional harmonic potential. Due to the repulsion between the ions, they form a regular Coulomb crystal, i.e. a regular chain in the case of a Paul trap and a triangular lattice in the case of two-dimensional traps. As in the case of cold atoms, a spin $1/2$ degree of freedom can be encoded by using two long-lived internal states of the ions, e.g. hyperfine levels of the electronic ground state (e.g. in Yb^+) or a combination of electronic ground state and a metastable electronic excited state (e.g. in Ca^+). This choice also determines how local control is implemented: hyperfine levels have transition frequencies in the radio-frequency regime and therefore focussed light beams cannot be used to address locally due to the typical distances between ions being far smaller than the wavelength of the light. More involved techniques such as a combination of optical pumping and a stimulated Raman transition have to be used in this case to establish local addressing. Contrarily, encoding a spin in electronic states enables direct addressing with tightly focussed laser beams, which is the approach our collaborators used in the experiment we report on in chapter 6. A coupling between the ions in the string can be induced by using the phonon modes of the ion crystal. When exciting an ion with a bichromatic laser, the momentum of the photon is absorbed by the lattice, creating a phonon. This phonon can in turn be absorbed by a different ion, which de-excites its internal state. In the regime of strong detuning from this transition, the phonons are only virtually occupied and can hence be integrated out. It can then be shown [174] that this coupling effectively implements the long-range

transverse field Ising model[13] in equation (1.23). While the form of the Hamiltonian is the same as in the case of Rydberg atoms, the couplings J_{ij} are different and depend on the laser and phonon properties. Importantly, by changing the detuning of the bichromat from the different phonon modes, the form of the J_{ij} can be tuned. The couplings approximately follow a power-law behaviour $J_{ij} \sim 1/|i-j|^{\alpha}$, with long-range exponent $\alpha \in [0, 3]$.

The tunability of the long-range exponent in trapped ions is a remarkable feature of the system which sparked research into the dynamics of such systems, not only experimentally but also theoretically. Of central importance is the question of how quickly quantum information and excitations spread and how this spread depends on the long range exponent α, which only recently got settled for $\alpha > 1$. Early experiments studied the propagation of correlations [176], which sparked intensive research into the modification of Lieb-Robinson bounds [177] for short range systems. Recently, this question was settled at least for $\alpha > 1$, and it was shown that faster-than-linear light cones appear for $\alpha < 3$ [178]. Other dynamical phenomena studied in trapped ions include many-body localization [179], pair creation in the Schwinger model [180], dynamical quantum phase transitions [181, 182], prethermalization [183], measurement induced phase transitions [184], environment-assisted transport [185], scrambling [186] and quasiparticle propagation [187]. In chapter 6 of this thesis, we will show that transport of a conserved quantity is also strongly modified in the presence of long-range interactions, both theoretically and in collaboration with the trapped ions group in Innsbruck also experimentally.

OTHER SYSTEMS In the previous sections, we focussed on the most commonly employed analogue quantum simulators for studying dynamics, and those which we will have in mind in the following chapters. However, also other platforms exist which have shown significant progress over the last years. In particular, solid state platforms hold the promise to generalize the way ordinary computers are built to quantum computers. For example, superconducting qubits [129], which employ LC circuits with a Josephson junction as non-linear element [188, 189], are not only considered to be one of the most promising platforms for digital quantum computation [190–192], but have also been used for analogue quantum simulation of dynamics in the Bose-Hubbard model [193, 194]. Other solid state systems include quantum dots [195], where electrostatic gates create a box potential to trap single electrons and which can access the extreme regime of very strong on-site interactions where Nagaoka ferromagnetism [196] becomes important [197]. While quantum dots are rather large objects, where the confinement of electrons in

13 S^yS^y and S^zS^z couplings can in principle be implemented by applying two other pairs of beams onto the system in the two other spatial directions. This has however to our knowledge not been done yet.

an electrostatic well leads to quantization, *single* dopant atoms can also be "trapped" in the silicon lattice [198]. This enables a rather direct analogy to Rydberg atoms, as group V donors act similarly in the silicon lattice as alkali atoms in vacuum [199]. For example, I have been involved in a study showing that the Rydberg entangling gates developed for cold atom implementations can be ported to this platform [200]. Donors also enable the study of the Hubbard model at far lower temperatures than the ones accessible in cold atoms [201]. Similarly, nitrogen vacancy centers in diamond offer clean two-level-system dynamics which can even be optically addressed. The inevitably present disorder in these systems can be characterized well and the coherence times of the NV centers is remarkably long. This enabled the observation of time crystalline phases [202] as well as hydrodynamic transport in a very large spin system [203]. Cold atoms have also been used in new settings and different species. For instance, cavities have been employed to mediate long-range interactions between cold atoms [204, 205] and magnetic atoms have enabled the study of supersolid phases in which short and long-range interactions compete. Similarly, dipolar molecules promise the study of dipolar magnetism in very large arrays [206, 207] as well as continuum systems [208].

CONCLUSION While digital quantum simulators can universally simulate any dynamics they meet the challenge of gate errors. Analogue simulators can only simulate specific Hamiltonians $\hat{H}$, however their purpose-built design means that longer times and larger systems can already be reached, even accessing regimes that are challenging for numerical methods. The majority of experiments probing thermalization dynamics have been of the analogue kind and all protocols we will develop in this thesis will be aimed at these approaches.

1.3 OUTLINE OF THE THESIS

After having introduced some of the main concepts which this thesis will be revolving around, we give a brief overview over its contents:

- In chapter 2 we will introduce non-equilibrium quantum field theory, one of the most frequently employed methods in this thesis.
- In part i we will explore several aspects of the thermalization dynamics of many-body quantum systems. The chapters describe several phases in the approach of the quantum system toward equilibrium. They are roughly ordered by the time these processes appear during the dynamics. Exemplifying the universality of the processes, the models discussed in the chapters will

be very diverse, including relativistic, nonrelativistic, bosonic, fermionic and spin models with short, long range and gauge-boson-mediated interactions.

  - First, we investigate the scrambling of quantum information during the first, "many-body chaos" stage of the thermalization process in chapter 3. In particular, we will investigate how this process behaves in the vicinity of a thermal phase transition in a relativistic scalar field theory. We employ a semi-classical method in this chapter.
  - In chapter 4, we discuss how the off-diagonal part of the eigenstate thermalization hypothesis can be probed in analogue quantum simulators by measuring two-time correlation functions and by testing the emergence of the fluctuation dissipation relations (FDRs). We develop protocols to measure the latter in quantum gas microscopes, Rydberg atom spin simulators, trapped ions and superconducting qubits. We apply our methods to not only characterize thermalization but also its temporary absence in the case of a "prethermal" state and the presence of confined excitations. The numerical results in this chapter are obtained with exact diagonalization.
  - In chapter 5, we use the lessons learnt in the previous chapter to study thermalization in a 1+1 dimensional lattice gauge theory. We use non-equilibrium quantum field theory, introduced in chapter 2, to study thermalization of strings in this model. Furthermore, we extend these methods to directly study spectral functions at infinite temperature and develop a $1/N$ expansion to study thermalization in SU(N) symmetric, non-abelian gauge theories.
  - In chapter 6 we study the last stage of the thermalization dynamics: The slow transport of conserved quantities across the system. In particular, we study how conventional diffusion is altered by the presence of long-range interactions. We test our results from analytical, semi-classical methods and spin 2PI (introduced in chapter 2) in a collaboration with a quantum simulation experiment with trapped ions.

- In part ii we apply some of the intuitions and methods we found while studying the non-equilibrium dynamics of quantum systems to learning about phases of matter, i.e. *equilibrium* phases. A central role will be taken by identifying the relevant excitations and we will use out-of-equilibrium or near-equilibrium techniques to do so.
  - In chapter 7 we aim to describe a recently discovered new state of matter termed the "marginal Fermi glass", found by two-dimensional

spectroscopy measurements. We use a screened Hartree Fock theory and an effective description of particle hole states.

- Chapter 8 contains an analysis of the stability of spin spiral states in the Heisenberg model. We employ a Holstein Primakoff analysis to identify the excitations relevant for its decay as well as semiclassical, spin 2PI and MPS techniques to verify our description.
- In chapter 9 we show how to implement time-dependent angle-resolved photoemission spectroscopy (tdARPES) in quantum gas microscopes and investigate spinon excitations not occupied in the ground state with a quench protocol within exact diagonalization.

2

NON-EQUILIBRIUM QUANTUM FIELD THEORY

In this chapter, we will introduce the two-particle-irreducible effective action approach [209, 210]. It enables a systematic way to derive self-consistent approximations for the non-equilibrium dynamics of quantum systems. We will first introduce the formalism for fermions before moving on to spins, which are more challenging to describe. For both cases, we will give some benchmarks, showing that these methods can qualitatively describe many important non-equilibrium phenomena, sometimes even with quantitative precision.

2.1 FERMIONS

Fermions are defined by their anticommutation relations $\left\{\hat{c}_i, \hat{c}_j^\dagger\right\} = \delta_{ij}$. We consider the general normal ordered Hamiltonian

$$\hat{H} = \sum_{ij} J_{ij} \hat{c}_i^\dagger \hat{c}_j + \frac{1}{2} \sum_{ij} U_{ij} \hat{c}_i^\dagger \hat{c}_j^\dagger \hat{c}_j \hat{c}_i, \tag{2.1}$$

In general, J_{ij} may contain a diagonal component $h_i \delta_{ij}$, for example in the presence of a disordered external field. While at first glance, we restrict ourselves to spinless fermions, the Hamiltonian is in fact more general. Spins σ can for example be introduced by redefining the index $i \to (i, \sigma)$ and considering a suitable form of the interaction U_{ij}. However, we assume that there are no pairing terms $\sim \hat{c}^\dagger \hat{c}^\dagger + h.c.$ and that there is no pairing in the initial state. While this section is not oriented along the lines of a specific source, the reviews by Schluenzen et al. [211] and Berges [210] as well as the book by Stefanucci and Van Leeuwen [212] are very good primers into the field.

2.1.1 *Equations of motion from the 2PI effective action*

CLOSED TIME CONTOUR Field theory is usually formulated in terms of correlation functions, as we outlined in section 1.2.1. Of central importance is the two-time correlation function

$$\left\langle \hat{c}_i(t_1) \hat{c}_j^\dagger(t_2) \right\rangle, \tag{2.2}$$

with the expectation value taken with respect to the initial state. This function will turn out to be the natural basic building block of approximations within

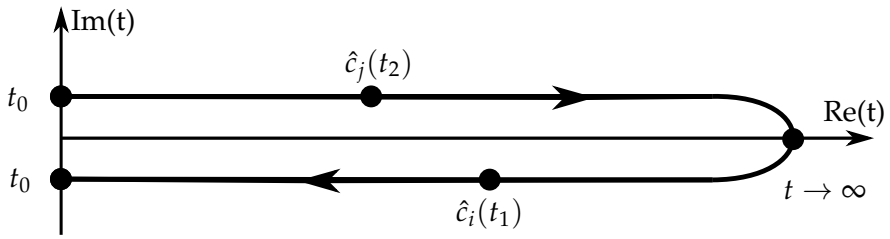

Figure 2.1: Closed time contour depiction of a two point correlation function.

nonequilibrium QFT. By explicitly expanding the time evolution of the Heisenberg operators, $\langle \hat{c}_i^\dagger(t_1)\hat{c}_j(t_2)\rangle = \langle e^{i\hat{H}t_1}\hat{c}_i e^{-i\hat{H}(t_1-t_2)}\hat{c}_j^\dagger e^{-i\hat{H}t_2}\rangle$, we see that read from the right, time evolution proceeds from the initial state to time t_2, then from t_2 to t_1 and from t_1 back to the initial time. This can be visualized in the closed time contour depicted in Fig. 2.1, where the two branches are extended to imaginary time for better visibility.

GENERATING FUNCTIONAL With the notion of a closed time contour at hand, we can now formulate a generating functional for non-equilibrium correlation functions, given by

$$Z[R] = \left\langle T_\mathcal{C} \exp\left\{ i \int_\mathcal{C} dt_1 dt_2 \sum_{ij} \hat{c}_i(t_1) R_{ij} \hat{c}_j^\dagger(t_2) \right\} \right\rangle, \tag{2.3}$$

where $T_\mathcal{C}$ denotes time ordering along the closed time contour and $\int_\mathcal{C}$ an integration along this contour. Correlation functions can now be obtained from Z by functional derivation with respect to the source field R. In particular, the Green's function $D_{ij}(t_1,t_2) = \langle \mathcal{T}_\mathcal{C} \hat{c}_i(t_1)\hat{c}_j^\dagger(t_2)\rangle$ is given by

$$\frac{\delta Z}{i\delta R_{ij}(t_1,t_2)} = D_{ij}(t_1,t_2) \tag{2.4}$$

To make contact with field theory, we reformulate Z in terms of a Grassmann path integral by trotterizing the time ordered exponential and inserting fermion coherent state identities inbetween the time steps [1] (see e.g. [210] for a detailed derivation). This leads to

$$Z[R] = \int \mathcal{D}\bar{c}\mathcal{D}c \exp\left\{ i\big(S[c,\bar{c}] + \int_\mathcal{C} dt_1 dt_2 \sum_{ij} c_i(t_1) R_{ij} \bar{c}_j(t_2)\big) \right\}, \tag{2.5}$$

where we assumed that the initial state is a fermionic Gaussian state by absorbing its value into the initial value of the source field R. The action S on the closed time contour $\mathcal{C}$ corresponding to the Hamtilonian $\hat{H}$ is given by

$$S[c,\bar{c}] = \int_\mathcal{C} dt \sum_{ij} \left[\bar{c}_i \left\{ i\partial_t \delta_{ij} - h_{ij} \right\} c_j - \frac{1}{2} U_{ij} \bar{c}_i \bar{c}_j c_j c_i \right], \tag{2.6}$$

1 The Hamiltonian needs to be normal ordered for this procedure. Above we have already assumed this form.

where the operators $\hat{c}, \hat{c}^\dagger$ have been replaced with Grassmann numbers $c, \bar{c}$.

2PI EFFECTIVE ACTION The generating functional Z is formulated in terms of the source field R. In analogy to thermodynamic potentials, we can change the quantities with respect to which the theory is formulated by Legrende transformation. The so-called two-particle-irreducible effective action $\Gamma[D]$ can be found in this way by a Legrende transformation

$$\Gamma[D] = -i \ln(Z[R]) - \int_{\mathcal{C}} dt_1 dt_2 \sum_{ij} R_{ij}(t_1, t_2) D_{ij}(t_1, t_2) \tag{2.7}$$

The 2PI effective action can be written into a sum of the one-loop part and a "rest" Γ_2,

$$\Gamma[D] = -i \operatorname{Tr} \ln D^{-1} - i \operatorname{Tr}\left\{ D_0^{-1} D \right\} + \Gamma_2[D] + \text{const.}, \tag{2.8}$$

where $\Gamma_2[D]$ contains all two-particle irreducible diagrams with propagator lines represented by the full Green's function D [209]. The free correlator D_0 may be read off from the action by noting that $S_{U=0} = \int_{\mathcal{C}} \mathrm{d}t_1 \int_{\mathcal{C}} \mathrm{d}t_2 \sum_{ij} \bar{c}_i i D_0^{-1} c_j$, such that

$$i D_{0,ij}^{-1}(t_1, t_2) = \left(i\partial_t \delta_{ij} - J_{ij} \right) \delta_{\mathcal{C}}(t_1 - t_2). \tag{2.9}$$

The equations of motions of the correlator are obtained from the variation of the effective action, $\delta\Gamma / \delta D = 0$ and results in

$$D_{ij}^{-1}(t_1, t_2) = D_{0,ij}^{-1}(t_1, t_2) - \Sigma_{ij}(t_1, t_2), \tag{2.10}$$

with the self energy defined as [2]

$$\Sigma_{ij}(t_1, t_2) = -i \frac{\delta \Gamma_2[D]}{\delta D_{ji}(t_2, t_1)}. \tag{2.11}$$

Convoluting Eq. (2.10) from the right with D, we get equations of motion for the correlator,

$$\left[i\partial_{t_1} \delta_{ik} - J_{ik} \right] D_{kj}(t_1, t_2) = i\delta_{ij} \delta_{\mathcal{C}}(t_1 - t_2) + i \int_{\mathcal{C}} dt \Sigma_{ik}(t_1, t) D_{kj}(t, t_2). \tag{2.12}$$

These equations are not yet amenable to a numerical procedure due to the reference to the closed time contour. In order to get rid of the latter, we decompose D into spectral and statistical components

$$D_{ij}(t_1, t_2) = F_{ij}(t_1, t_2) - \frac{i}{2} \operatorname{sgn}_{\mathcal{C}}(t_1 - t_2) \rho_{ij}(t_1, t_2), \tag{2.13}$$

2 Note that the indices are switched around in the denominator. This is because $\frac{\delta}{\delta D_{ab}} f(D) = f'(D)_{ba}$. For example, suppressing time indices, $\frac{\delta}{\delta D_{ab}} \operatorname{Tr}(D_0^{-1} D) = \frac{\delta}{\delta D_{ab}} \sum_{cd} D_{0,cd}^{-1} D_{dc} = \sum_{cd} D_{0,cd}^{-1} \delta_{ad} \delta_{bc} = D_{0,ba}^{-1}$.

with

$$F_{ij}(t_1,t_2) = \frac{1}{2}\left\langle \left[\hat{c}_i(t_1), \hat{c}_j^\dagger(t_2)\right]\right\rangle, \tag{2.14}$$

$$\rho_{ij}(t_1,t_2) = i\left\langle \left\{\hat{c}_i(t_1), \hat{c}_j^\dagger(t_2)\right\}\right\rangle. \tag{2.15}$$

We arrive at the Kadanoff-Baym equations

$$\left(i\partial_{t_1}\delta_{ik} - \tilde{J}_{ik}(t_1)\right)F_{kj}(t_1,t_2) = \int_0^{t_1} \mathrm{d}t \Sigma^\rho_{ik}(t_1,t)F_{kj}(t,t_2) - \int_0^{t_2} \mathrm{d}t \Sigma^F_{ik}(t_1,t)\rho_{kj}(t,t_2), \tag{2.16}$$

$$\left(i\partial_{t_1}\delta_{ik} - \tilde{J}_{ik}(t_1)\right)\rho_{kj}(t_1,t_2) = \int_{t_2}^{t_1} \mathrm{d}t \Sigma^\rho_{ik}(t_1,t)\rho_{kj}(t,t_2). \tag{2.17}$$

Above, we separated a time-local part of the self-energy, according to $\Sigma(t_1,t_2) = -i\Sigma^{(0)}(t_1)\delta_{\mathcal{C}}(t_1-t_2) + \Sigma^F(t_1,t_2) - \frac{i}{2}\,\mathrm{sgn}_{\mathcal{C}}(t_1-t_2)\Sigma^\rho(t_1,t_2)$ and absorbed it into the quadratic part of the Hamiltonian according to $J_{ij} \to \tilde{J}_{ij}(t_1) = J_{ij} + \Sigma^{(0)}_{ij}(t_1)$.

INTERPRETATION OF F AND ρ The physical meaning of F and ρ becomes clear when considering the equilibrium limit. In this case, both F and ρ do not depend on central time $(t_1+t_2)/2$ and we can Fourier transform with respect to the relative time, $\rho(\omega) = \int d(t_1-t_2)e^{i\omega(t_1-t_2)}\rho(t_1-t_2)$. Considering for the moment also a translationally invariant situation and transforming to momentum space $\mathbf{p}$, we find by inserting complete sets of many-body eigenstates that

$$\rho_{\mathbf{p}}(\omega) = \frac{i}{Z}\sum_n e^{-\beta E_n}\Bigg(\sum_m \delta(\omega-(E_m-E_n))|\left\langle m|c^\dagger_{\mathbf{p}}|n\right\rangle|^2 + \sum_m \delta(\omega+(E_m-E_n))|\left\langle m|c_{\mathbf{p}}|n\right\rangle|^2\Bigg). \tag{2.18}$$

The spectral function hence gives direct access to many-body excitations, with the matrix element dictating that both "particle" and "hole" excitations are probed. The meaning of F can be found from the fluctuation-dissipation relation which connects it to ρ by

$$F_{ij}(\omega) = -i\left(\frac{1}{2} - n^F_{\beta,\mu}(\omega)\right)\rho_{ij}(\omega), \tag{2.19}$$

with the Fermi-Dirac distribution $n^F_{\beta,\mu}(\omega) = 1/\left(e^{\beta(\omega-\mu)}+1\right)$ at inverse temperature β and chemical potential μ. Hence, F also contains information about the *occupation* of the many-body-eigenstates which motivates its name "statistical function". We emphasize however, that F and ρ are independent of each other in non-equilibrium settings. Lastly, we note that in angle-resolved-photoemission spectroscopy experiments, which we will discuss in one of the later chapters in this thesis, the "hole/occupied spectral function" $A = \langle c^\dagger c\rangle$ is measured, which can

be obtained from F and ρ by $A = \frac{-i}{2}\rho - F$. In equilibrium, $A = n^F\rho$, i.e. only the occupied states are visible in this technique.

For a given approximated self energy, the Kadanoff-Baym equations of motion can be solved numerically by employing initial conditions for a product state,

$$F_{ij}(0,0) = \left(\frac{1}{2} - \langle \hat{n}_i(0)\rangle\right)\delta_{ij}, \tag{2.20}$$

$$\rho_{ij}(0,0) = i\delta_{ij}, \tag{2.21}$$

where the latter is a consequence of the commutation relations. The time evolution of the occupation numbers can then be read out according to

$$\langle \hat{n}_i(t)\rangle = \left(\frac{1}{2} - F_{ii}(t,t)\right). \tag{2.22}$$

The Kadanoff-Baym equations are exact if the exact expression for Σ is known. In general, this is not the case. In the following, we will discuss two approximation schemes for Σ: a perturbative loop expansion and the non-perturbative GW approximation.

2.1.2 *Loop expansion*

The 2PI effective action consists out of all two-particle irreducible, connected vacuum diagrams. To perform a loop expansion, we identify the interaction part of the action by

$$iS_{int} = \int_{\mathcal{C}} \mathrm{d}t \sum_{ij}\left(-i\frac{U_{ij}}{2}\right)\bar{c}_i\bar{c}_j c_j c_i. \tag{2.23}$$

We then proceed as if we were making a perturbative loop expansion, with vertex factors given by $-i\frac{U_{ij}}{2}$, propagator lines by D and the 2PI effective action carries an overall factor of $(-i)$. The overall sign of each diagram is determined by the number L of loops with more than one vertex as $(-1)^L$.

TWO LOOPS The expansion of Γ_2 up to two loops is given by

$$\Gamma_2^{2\,\mathrm{loop}} = (-i)\int_{\mathcal{C}} \mathrm{d}t \sum_{ij}(-i\frac{U_{ij}}{2})\big[-D_{ji}(t,t)D_{ij}(t,t) + D_{ii}(t,t)D_{jj}(t,t)\big]. \tag{2.24}$$

The self energy up to two loops is hence given by

$$\Sigma_{ij}^{2\,\mathrm{loop}}(t_1,t_2) = i\Big(\sum_k D_{kk}(t_1,t_1)U_{ik}\delta_{ij} - U_{ij}D_{ij}(t_1,t_1)\Big)\delta_{\mathcal{C}}(t_1-t_2), \tag{2.25}$$

where we used $U_{ij} = U_{ji}$. At equal times, the construction of the path integral in terms of coherent states [3] dictates $D_{ij}(t,t) = F_{ij}(t,t) - \frac{1}{2}\delta_{ij}$. Hence, it follows for the time local part of the self energy

$$\Sigma_{ij}^{(0),2\,\mathrm{loop}}(t) = -\left(\sum_k \left(F_{kk}(t,t) - \frac{1}{2}\right) U_{ik}\delta_{ij} - U_{ij}F_{ij}(t,t)\right). \tag{2.26}$$

Moreover, $\Sigma_F = 0 = \Sigma^\rho$, showing that to this order the memory integrals vanish. The two loop approximation is also known as self-consistent Hartree-Fock approximation.

THREE LOOPS The contributions to Γ_2 with three loops are given by

$$\begin{aligned}\Gamma_2^{3\,\mathrm{loop}} = (-i)\frac{1}{2!}(-i)^2 \sum_{ijkl} \frac{U_{ij}}{2}\frac{U_{kl}}{2} \int_{\mathcal{C}} \mathrm{d}t_1 \int_{\mathcal{C}} \mathrm{d}t_2 \times \\ \times \Big[-2D_{li}(t_2,t_1)D_{ik}(t_1,t_2)D_{kj}(t_2,t_1)D_{jl}(t_1,t_2) \\ + 2D_{ik}(t_1,t_2)D_{ki}(t_2,t_1)D_{jl}(t_1,t_2)D_{lj}(t_2,t_1)\Big].\end{aligned} \tag{2.27}$$

The self-energy follows as

$$\begin{aligned}\Sigma_{nm}^{3\,\mathrm{loop}}(t_4,t_3) = \sum_{jk} U_{nj}U_{km}\big(-D_{nk}(t_4,t_3)D_{kj}(t_3,t_4)D_{jm}(t_4,t_3) \\ + D_{nm}(t_4,t_3)D_{kj}(t_3,t_4)D_{jk}(t_4,t_3)\big).\end{aligned} \tag{2.28}$$

3 Here we argue why $D_{ij}(t,t) = F_{ij}(t,t) - \frac{1}{2}\delta_{ij}$. Above we implicitly constructed a (Grassmann) coherent state path integral to get our action S, see Ref. [213] for an explicit derivation. In order to do so, resolutions of the identity from the coherent states $|\eta\rangle$ get inserted between trotterized time evolution operators. Then, the relations $\langle\eta|\,\hat{c}^\dagger = \langle\eta|\,c^*$, $\hat{c}\,|\eta\rangle = c\,|\eta\rangle$, are used to replace operators with Grassmann numbers in the path integrals. Therefore, $\hat{c}^\dagger$ operators always need to act on an infinitesimally later time slice than the $\hat{c}$ operators. Hence, when evaluating $G(t,t')$ for $t = t'$, the time t' corresponding to the $\hat{c}^\dagger$ operator is in fact given by $t + \epsilon$. Hence, when using the decomposition in Eq. (2.13) for $t = t'$, the contour sign function does not vanish as naively expected, but return $\mathrm{sgn}_{\mathcal{C}}(t - (t+\epsilon)) = -1$ and we get using the equal-time commutation relations that $G_{ij}(t,t) = F_{ij}(t,t) + \frac{i}{2}\rho_{ij}(t,t) = F_{ij}(t,t) - \frac{1}{2}\delta_{ij}$.

Decomposition into F/ρ components yields

$$\Sigma^{F,3\,\text{loop}}_{nm} = \frac{1}{4}\sum_{jk} U_{nj}U_{km}\left(\rho_{nk}\rho^*_{jk}F_{jm} + \rho_{nk}F^*_{jk}\rho_{jm} + F_{nk}\rho^*_{jk}\rho_{jm} - 4F_{nk}F^*_{jk}F_{jm}\right) - \left(\rho_{nm}\rho^*_{jk}F_{jk} + \rho_{nm}F^*_{jk}\rho_{jk} + F_{nm}\rho^*_{jk}\rho_{jk} - 4F_{nm}F^*_{jk}F_{jk}\right), \tag{2.29}$$

$$\Sigma^{\rho,3\,\text{loop}}_{nm} = -\sum_{jk} U_{nj}U_{km}\left(\rho_{nk}F^*_{jk}F_{jm} + F_{nk}\rho^*_{jk}F_{jm} + F_{nk}F^*_{jk}\rho_{jm} - \frac{1}{4}\rho_{nk}\rho^*_{jk}\rho_{jm}\right) - \left(\rho_{nm}F^*_{jk}F_{jk} + F_{nm}\rho^*_{jk}F_{jk} + F_{nm}F^*_{jk}\rho_{jk} - \frac{1}{4}\rho_{nm}\rho^*_{jk}\rho_{jk}\right), \tag{2.30}$$

where we omitted the time arguments (all the same).

2.1.3 *GW approximation - effective Bose-Fermi mixture*

The loop expansion discussed in the previous section is only valid at small interaction strengths. Here, we discuss the non-perturbative "GW" approximation, which resums part of the perturbative series. It can be derived by reorganizing the diagrammatic series by introducing a Hubbard-Stratonovich field, which introduces a new bosonic, non-dynamical field. In this effective Bose-Fermi mixture, the quartic vertex is replaced by a cubic Yukawa-type vertex. The GW approximation then corresponds to keeping only the diagram with two vertices, i.e. the lowest order in Bose-Fermi interactions.

HUBBARD-STRATONOVICH FIELD IN DENSITY CHANNEL We introduce a real bosonic Hubbard-Stratonovich field ψ by using the identity $\int \mathcal{D}\psi e^{\frac{i}{2}\sum_{ij}\left[U^{-1}\right]_{ij}\psi_i\psi_j} = \text{const}$. A shift $\psi_i \to \psi_i - \sum_k U_{ik}\bar{c}_k c_k$ then leads to the action

$$S[c,\bar{c},\psi] = \int_{\mathcal{C}} dt \sum_{ij}\bar{c}_i\left\{i\partial_t\delta_{ij} - h_{ij}\right\}c_j + \frac{1}{2}\sum_{ij}\left[U^{-1}\right]_{ij}\psi_i\psi_j - \sum_j \psi_j\bar{c}_j c_j. \tag{2.31}$$

We have hence traded the four-point fermionic interaction with a Yukawa-type interaction between the non-dynamical density field ψ and the fermions. We can now proceed as in the case for a purely fermionic theory, constructing the 2PI effective action, deriving the equations of motion and finally constructing the approximation from a loop expansion in Bose-Fermi interactions.

2PI EFFECTIVE ACTION The 2PI effective action corresponding to the above classical action is given by

$$\begin{aligned}\Gamma[\bar{\psi}, G, D] =& S[\bar{\psi}] + \frac{i}{2}\operatorname{Tr}\ln G^{-1} + \frac{i}{2}\operatorname{Tr}\{G_0^{-1}G\} \\ & - i\operatorname{Tr}\ln D^{-1} - i\operatorname{Tr}\{D_0^{-1}[\bar{\psi}]D\} + \Gamma_2[D, G],\end{aligned} \tag{2.32}$$

where $\bar{\psi}_i(t_1) = \langle\psi_i(t_1)\rangle$, $G_{ij}(t_1,t_2) = \langle\mathcal{T}_\mathcal{C}\psi_i(t_1)\psi_j(t_2)\rangle = G_{ji}(t_2,t_1)$, $D_{ij}(t_1,t_2) = \langle\mathcal{T}_\mathcal{C}c_i(t_1)\bar{c}_j(t_2)\rangle = D^*_{ji}(t_2,t_1)$. Note that there are no cross-correlators between bosonic and fermionic fields because $\langle c\rangle = 0$ (for a discussion, see Refs. [214, 215]). Γ_2 includes all two-particle irreducible vacuum diagrams formed by the vertex $iS_{int} = -i\sum_j \psi_j\bar{c}_jc_j$ and the propagators G, D. The free propagators are given by

$$iD^{-1}_{0,ij}(t_1,t_2) = \left(i\partial_t\delta_{ij} - (J_{ij} + \bar{\psi}_j(t_1)\delta_{ij})\right)\delta_\mathcal{C}(t_1 - t_2), \tag{2.33}$$

$$iG^{-1}_{0,ij}(t_1,t_2) = \left[U^{-1}\right]_{ij}\delta_\mathcal{C}(t_1 - t_2). \tag{2.34}$$

As before, the equations of motion for the mean field $\bar{\psi}$ and the propagators D,G are obtained from evaluating the effective action at an extremum, $\delta\Gamma = 0$. Contrary to before, we now also get an equation of motion for the mean field from $\delta\Gamma/\delta\bar{\psi} = 0$. From this we get

$$\bar{\psi}_j(t) = \sum_k U_{jk}D_{kk}(t,t), \tag{2.35}$$

$$\begin{aligned}\left[i\partial_{t_1}\delta_{ik} - (J_{ik} + \bar{\psi}_i(t_1)\delta_{ik})\right]D_{kj}(t_1,t_2) =& \, i\delta_{ij}\delta_\mathcal{C}(t_1 - t_2) \\ & + i\int_\mathcal{C} dt\Sigma_{ik}(t_1,t)D_{kj}(t,t_2),\end{aligned} \tag{2.36}$$

$$\begin{aligned}G_{ij}(t_1,t_2) =& \, iU_{ij}\delta_\mathcal{C}(t_1 - t_2) \\ & + iU_{ik}\int_\mathcal{C} dt\Pi_{kl}(t_1,t)G_{lj}(t,t_2),\end{aligned} \tag{2.37}$$

where the fermionic and bosonic self energies are given as

$$\Sigma_{ij}(t_1,t_2) = -i\frac{\delta\Gamma_2}{\delta D_{ji}(t_2,t_1)}, \qquad \Pi_{ij}(t_1,t_2) = 2i\frac{\delta\Gamma_2}{\delta G_{ji}(t_2,t_1)}. \tag{2.38}$$

As we are only interested in the real-time part of the contour, we decompose the correlators into spectral and statistical (a.k.a. Keldysh) components according to

$$D_{ij}(t_1,t_2) = F_{ij}(t_1,t_2) - \frac{i}{2}\operatorname{sgn}_\mathcal{C}(t_1 - t_2)\rho_{ij}(t_1,t_2), \tag{2.39}$$

$$G_{ij}(t_1,t_2) = iU_{ij}\delta_\mathcal{C}(t_1 - t_2) + U_{ik}\left(\chi^F_{kl}(t_1,t_2) - \frac{i}{2}\operatorname{sgn}_\mathcal{C}(t_1 - t_2)\chi^\rho_{kl}(t_1,t_2)\right)U_{lj}, \tag{2.40}$$

where we split off the time-singular part of the bosonic correlator. We denote the time-non-singular part with χ and split off the interactions for later convenience.

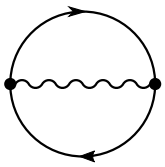

Figure 2.2: Diagram with smallest number of loops formed by the vertex $\sim \psi\bar{c}c$. Wiggled line corresponds to the bosonic propagator G, solid arrow line to the fermionic propagator D.

The equation for the mean field becomes

$$\bar{\psi}_j(t) = \sum_k U_{jk}\left(F_{kk}(t,t) - \frac{1}{2}\right), \tag{2.41}$$

where we used that $D_{ij}(t,t) = F_{ij}(t,t) - \frac{\delta_{ij}}{2}$. Inserting this into the effective Hamiltonian and using that $F_{kk} = \frac{1}{2} - \langle \hat{n}_k \rangle$ we recognise that this corresponds to the familiar Hartree term.

The equations of motion for the fermionic correlators then become

$$\big(i\partial_{t_1}\delta_{ik} - \tilde{h}_{ik}(t_1)\big)F_{kj}(t_1,t_2) = \int_0^{t_1} \mathrm{d}t \Sigma^{\rho}_{ik}(t_1,t)F_{kj}(t,t_2) - \int_0^{t_2} \mathrm{d}t \Sigma^{F}_{ik}(t_1,t)\rho_{kj}(t,t_2), \tag{2.42}$$

$$\big(i\partial_{t_1}\delta_{ik} - \tilde{h}_{ik}(t_1)\big)\rho_{kj}(t_1,t_2) = \int_{t_2}^{t_1} \mathrm{d}t \Sigma^{\rho}_{ik}(t_1,t)\rho_{kj}(t,t_2), \tag{2.43}$$

where we introduced the effective Hamiltonian $\tilde{h}_{ij}(t) = h_{ij} + \bar{\psi}_i(t)\delta_{ij} + \Sigma^{(0)}_{ij}(t)$, where a possible time local part of the self energy was introduced by decomposing $\Sigma(t_1,t_2) = -i\Sigma^{(0)}(t_1)\delta_{\mathcal{C}}(t_1-t_2) + \Sigma^F(t_1,t_2) - \frac{i}{2}\operatorname{sgn}_{\mathcal{C}}(t_1-t_2)\Sigma^{\rho}(t_1,t_2)$. Similarly, the equations of motion for the bosonic correlator are given by

$$\begin{aligned}\chi^F_{ij}(t_1,t_2) = -\Pi^F_{ij}(t_1,t_2) &+ \int_0^{t_1} \Pi^{\rho}(t_1,t)_{ik}U_{kl}\chi^F_{lj}(t,t_2) \\ &- \int_0^{t_2} \Pi^F(t_1,t)_{ik}U_{kl}\chi^{\rho}_{lj}(t,t_2)\end{aligned} \tag{2.44}$$

$$\chi^{\rho}_{ij}(t_1,t_2) = -\Pi^{\rho}_{ij}(t_1,t_2) + \int_{t_2}^{t_1} \Pi^{\rho}(t_1,t)_{ik}U_{kl}\chi^{\rho}_{lj}(t,t_2), \tag{2.45}$$

where we again decomposed $\Pi(t_1,t_2) = \Pi^F(t_1,t_2) - \frac{i}{2}\operatorname{sgn}_{\mathcal{C}}(t_1-t_2)\Pi^{\rho}(t_1,t_2)$.

APPROXIMATION As discussed before, the GW approximation corresponds to taking into account the diagram with the smallest number of loops given in Fig. 2.2. The corresponding Γ_2 is given by

$$\Gamma_2 = (-i)(-i)^2\frac{1}{2!}\int_{\mathcal{C}} dt_1 \int_{\mathcal{C}} dt_2 \sum_{ij} D_{ij}(t_1,t_2)D_{ji}(t_2,t_1)G_{ij}(t_1,t_2), \tag{2.46}$$

where one factor of $(-i)$ comes from the definition of the effective action, $(-i)^2$ comes from the two vertices and $\frac{1}{2!}$ comes from the expansion of the exponential.

After decomposition into time-local, spectral and statistical components, the self energies are given by

$$\Sigma^{(0)}_{ij}(t) = -U_{ij}F_{ij}(t,t), \tag{2.47}$$

$$\Sigma^{F}_{ij}(t_1,t_2) = \sum_{kl} U_{ik}U_{lj}\left(F_{ij}(t_1,t_2)\chi^{F}_{kl}(t_1,t_2) - \frac{1}{4}\rho_{ij}(t_1,t_2)\chi^{\rho}_{kl}(t_1,t_2)\right), \tag{2.48}$$

$$\Sigma^{\rho}_{ij}(t_1,t_2) = \sum_{kl} U_{ik}U_{lj}\left(F_{ij}(t_1,t_2)\chi^{\rho}_{kl}(t_1,t_2) + \rho_{ij}(t_1,t_2)\chi^{F}_{kl}(t_1,t_2)\right), \tag{2.49}$$

$$\Pi^{F}_{ij}(t_1,t_2) = \frac{1}{4}|\rho_{ij}(t_1,t_2)|^2 - |F_{ij}(t_1,t_2)|^2, \tag{2.50}$$

$$\Pi^{\rho}_{ij}(t_1,t_2) = -F_{ij}(t_1,t_2)\rho^{*}_{ij}(t_1,t_2) - \rho_{ij}(t_1,t_2)F^{*}_{ij}(t_1,t_2). \tag{2.51}$$

Note that the bosonic self energies Π correspond to the fermionic bubble $\Pi \sim DD^*$, such that the equations of motion for χ correspond to the RPA resummation of fermionic bubbles. Moreover, $\Sigma^{(0)}$ corresponds to the Fock contribution and the term $\bar{\chi}$ appearing in the free correlator $D^{(0)}$ is equivalent to the Hartree contribution. Hence, the GW approximation contains the full 2-loop contribution discussed above.

As a last remark, we note that the GW theory discussed here can be immediately adapted to describe mixtures with dynamical bosonic degrees of freedom, i.e. situations with a term $\bar{\psi}i(\partial_t - J^{B}_{ij})\psi$ in the action. This would replace the free correlator G_0^{-1} of the bosons as well as turn the equations for $\chi^{F/\rho}$ into integro-differential equations. The GW approximation then corresponds to a two-loop approximation for the interactions between fermions and bosons. See e.g. Ref [216] for a study of a relativistic mixture.

2.1.4 *Observables*

The 2PI Formalism gives access to a wide variety of observables, some of which are difficult to access even for numerically exact methods.

SINGLE PARTICLE DENSITY MATRIX AND LOCAL OCCUPATIONS F contains information about the single particle occupations and coherences. At equal times, we can obtain the single particle density matrix via

$$\langle \hat{c}^{\dagger}_i(t)\hat{c}_j(t)\rangle = -F_{ji}(t,t) + \frac{1}{2}\delta_{ij}, \tag{2.52}$$

where for equal sites, we obtain the local occupations via

$$\langle \hat{n}_i(t)\rangle = \frac{1}{2} - F_{ii}(t,t). \tag{2.53}$$

SPECTRA In time-dependent angle-resolved-photoemission-spectroscopy, a probe we will discuss more in depth in chapter 9, a correlation function of the form

$A^< \sim \langle c^\dagger c \rangle$ is probed, i.e. the hole spectral function. More specifically, we can obtain the spectrum from F and ρ by transforming to central time $T = (t_1 + t_2)/2$ and relative time $\tau = t_1 - t_2$ and Fourier transforming with respect to relative time. Moreover, in a translationally invariant system, we transform from the lattice indices to momentum $\mathbf{p}$. Using the definitions of F and ρ in terms of the (anti-)commutator, Eqs. (2.14), (2.15), we find

$$A^<_{\mathbf{p}}(T,\omega) = \int d\tau e^{i\omega\tau} \left(\frac{-i}{2}\rho_{\mathbf{p}}(T,\tau) - F_{\mathbf{p}}(T,\tau) \right) \tag{2.54}$$

for the time, frequency and momentum resolved hole spectrum measured in ARPES.

Equivalently, the particle spectrum $A^>$ measured in angle resolved inverse photoemission spectropy (ARIPES), can be obtained via

$$A^>_{\mathbf{p}}(T,\omega) = \int d\tau e^{i\omega\tau} \left(\frac{-i}{2}\rho_{\mathbf{p}}(T,\tau) + F_{\mathbf{p}}(T,\tau) \right). \tag{2.55}$$

DENSITY-DENSITY EQUAL-TIME CORRELATIONS We can obtain density correlations via

$$\sum_k U_{ik} \langle \hat{n}_k(t)\hat{n}_i(t) \rangle = -i\partial_{t_1} F_{ii}(t_1,t_2)\big|_{t_1=t_2} + \sum_j J_{kj}F_{jk}(t_1,t_1) + \frac{1}{2}\sum_j U_{jk} \langle \hat{n}_j \rangle . \tag{2.56}$$

This equation is in particular interesting for a spinful Hubbard model with only on-site interactions between up and down fermions. In this case, this equation directly yields the double occupation $\langle \hat{n}_{i\uparrow}\hat{n}_{i\downarrow} \rangle$ [217]. Interpreting our lattice system as the discretized version of a continuum Fermi gas, the double occupation directly yields the Tan contact, one of the most crucial quantities determining the properties of such systems [218–221]. In the case of nearest neighbour interactions, we can obtain the nearest-neighbour density correlations in this way.

In the following, we will show this identity. Consider the Heisenberg equations of motion for the annihilation operator,

$$i\partial_t c_k = \left[\hat{c}_k, \hat{H}\right] \tag{2.57}$$

$$= \sum_j J_{kj}\hat{c}_j + \sum_j U_{kj}\hat{c}_j^\dagger \hat{c}_j \hat{c}_k. \tag{2.58}$$

Multplying $\hat{c}_l^\dagger(t_2)$ from the right, we get

$$i\partial_{t_1}\hat{c}_k(t_1)\hat{c}_l^\dagger(t_2) = \sum_j J_{kj}\hat{c}_j(t_1)\hat{c}_l^\dagger(t_2) + \sum_j U_{kj}\hat{c}_j^\dagger(t_1)\hat{c}_j(t_1)\hat{c}_k(t_1)\hat{c}_l^\dagger(t_2). \tag{2.59}$$

Together with the equivalent equation by multplying $\hat{c}_l^\dagger(t_2)$ from the left, we find

$$i\partial_{t_1}F_{kl}(t_1,t_2)\big|_{t_1=t_2,k=l} = \frac{i}{2}\partial_{t_1}\left(\langle \hat{c}_k(t_1)\hat{c}_l^\dagger(t_2) - \hat{c}_l^\dagger(t_2)\hat{c}_k(t_1) \rangle \right)\big|_{t_1=t_2,k=l} \tag{2.60}$$

$$= \sum_j J_{kj}F_{jk}(t_1,t_1) + \frac{1}{2}\sum_j U_{kj} \langle \hat{n}_j \rangle - \sum_j U_{kj} \langle \hat{n}_j\hat{n}_k \rangle . \tag{2.61}$$

Rearranging terms, we find the above result.

ENERGY Using the result for the density correlations, we can also get the total energy, i.e. the expectation value of the Hamiltonian, by

$$\langle \hat{H} \rangle = -\frac{i}{2} \sum_j \partial_{t_1} F_{jj}(t_1, t_2)\big|_{t_1=t_2} + \frac{1}{4} \sum_{jk} U_{kj} \langle \hat{n}_j \rangle - \frac{1}{2} \sum_{jk} J_{kj} F_{jk}(t_1, t_1) + \frac{1}{2} \sum_j J_{jj}. \quad (2.62)$$

By separating off the contributions to the energy resulting from the quadratic part as well as the Hartree-Fock contribution, a *correlation* energy can be defined, quantifying the part of the energy arising from beyond-mean-field correlations. This formula is also valid in cases where $\hat{H}$ is not constant. In Ref. [222] this was used to study heating in a periodically driven system.

TWO-PARTICLE TWO-TIME CORRELATIONS FROM THE AUXILIARY FIELD CORRELATOR Here we show that in the exact theory, the auxiliary field correlators χ^F and χ^ρ appearing in the GW approximation represent the two-time density correlations. To do so, we follow the procedure in App. D of Ref. [215] of the author, and introduce a source field coupling to the auxiliary field into the action in Eq. (2.31) via

$$S[c, \bar{c}, \psi] \to S[c, \bar{c}, \psi] + \int_{\mathcal{C}} dt \sum_j \eta_j \psi_j. \quad (2.63)$$

Completing the square and integrating out the auxiliary field, we find

$$Z[\eta] \propto \int \mathcal{D}\bar{c}\mathcal{D}c \exp\left[iS[\bar{c}, c] + i \int_{\mathcal{C}} dt \sum_{ij} U_{ij} \left(\eta_i \bar{c}_j c_j - \frac{1}{2} \eta_j \eta_j \right) \right]. \quad (2.64)$$

Using this expression, we can obtain the correlation functions of ψ in terms of $\bar{c}$, c via functional differentiation. As a first check, the one-point-function

$$\langle \psi_i(t) \rangle = \frac{1}{Z} \frac{\delta Z}{i\delta\eta_i(t)}\bigg|_{\eta=0} = \sum_j U_{ij} \langle \bar{c}_j c_j \rangle, \quad (2.65)$$

is in agreement with Eq. (2.41), which was obtained from the equations of motion.

For the two-point function, we find

$$\langle T_{\mathcal{C}} \psi_i(t_1) \psi_j(t_2) \rangle = \frac{1}{Z} \frac{\delta Z}{i\delta\eta_j(t_2)\delta\eta_i(t_1)}\bigg|_{\eta=0} \quad (2.66)$$

$$= iU_{ij}\delta_{\mathcal{C}}(t_1 - t_2) + \sum_{kl} U_{ik} U_{jl} \langle \bar{c}_k(t_1) c_k(t_1) \bar{c}_l(t_2) c_l(t_2) \rangle. \quad (2.67)$$

Using that the left-hand-side is equivalent to $G_{ij}(t_1, t_2) + \bar{\psi}_i(t_1)\bar{\psi}_j(t_2)$, we find together with the definition of χ^F, χ^ρ in Eq. (2.40) that

$$\chi^F_{ij}(t_1, t_2) = \frac{1}{2} \langle \{ \hat{n}_i(t_1), \hat{n}_j(t_2) \} \rangle, \quad (2.68)$$

$$\chi^\rho_{ij}(t_1, t_2) = i \langle [\hat{n}_i(t_1), \hat{n}_j(t_2)] \rangle. \quad (2.69)$$

Hence, the density two-point correlators can be probed via the auxiliary field correlators. We note however, that the above equations only strictly hold in the exact theory as we used the equivalence of operator expectation values and path integral expectation values, which can fail in the presence of 2PI approximations [214]. This can lead for example to violations of sum rules. Most notably, the identity

$$\chi^F_{ii}(t,t) = \langle (\hat{n}_i(t))^2 \rangle = \langle \hat{n}_i(t) \rangle \tag{2.70}$$

can be violated as this relies on the "crossing symmetry" $\langle \hat{c}_i^\dagger \hat{c}_i \hat{c}_i^\dagger \hat{c}_i \rangle = \langle \hat{c}_i^\dagger (1 - \hat{c}_i^\dagger \hat{c}_i) \hat{c}_i \rangle$, which is in general broken for conserving approximations [223].

2.1.5 *Numerical solution and benchmark*

The Kadanoff-Baym equations are causal integro-differential equations which can be solved by discretizing both the derivative using a finite-difference expression and the integral using Newton-Cotes discretisation. This needs to be done in a way which does not hamper the conservation of conserved quantities, in particular the particle number conservation. Predictor-corrector methods enable such a conserving evolution of the equations of motion and they have been established as a "gold-standard" to solving non-relativistic Kadanoff-Baym equations. For more details on the implementation, see App. F of Ref. [215] of the author. For a particularly elegant scheme suited for large quadratic terms in the Hamiltonian, see App. B of Ref. [212]. For relativistic theories, a symmetric discretization of the second order time derivative leads to a simpler, also conserving evaluation of the equations of motion [210].

To benchmark the method, we compare 2PI to exact diagonalization results for a four site Hubbard model with nearest neighbour hoppings and interactions, $U_{ij} = U\delta_{\langle i,j \rangle}$, $J_{ij} = -\delta_{\langle i,j \rangle}$ with a relatively large interaction strength $U = 1$. We prepare the system in an inital charge density wave, i.e. $\langle \hat{n}_i \rangle = 1$ on even sites and zero otherwise. In Fig. 2.3 we show the comparison for the three different approximations discussed above, the two perturbative ones (2 loop/Hartree Fock and 3 loop) and the non-perturbative GW approximation. We study the imbalance of the system $\sum_{i=0}^{3} (-1)^i \langle \hat{n}_i \rangle$. It is clearly visible that all approximations are successfull in describing the short time dynamics, while deviations occur at longer times. Remarkably, all three approximations are almost exact up to times $Jt \sim 2$, which is about a factor of two longer than the validity of non-self-consistent time-dependent perturbation theory, which diverges at roughly $Jt \approx 1$. Moreover, we can see that going further in the perturbative expansion elongates the times in which 2PI is exact to about $Jt \approx 3.5$. Lastly, even though deviations occur at longer times in all approximations, the qualitative behaviour resembles the exact dynamics. The GW

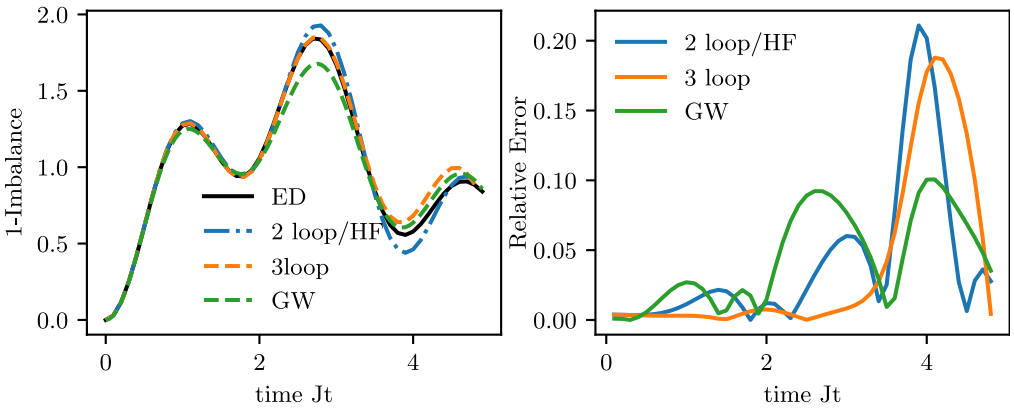

Figure 2.3: Comparison between 2PI and exact diagonalization for a four site spinless Fermi-Hubbard model starting from a charge density wave initial state.

approximation only contains one of the two 3-loop diagrams and hence deviates earlier from the exact results. However, for longer times its partial inclusion of higher orders of the perturbation series becomes visible as the deviations increase slower than for the other two approximations. For a more in-depth comparison of 2PI methods to exact numerics, see Ref. [217].

2.1.6 *Thermal equilibrium*

The 2PI formalism can also be used to obtain equilibrium properties of many-body systems. In particular, it enables the calculation of dynamical correlation functions directly in real-time, which is challenging in the imaginary time Matsubara formalism due to the nececessity to perform analytic continuation. While the Matsubara formalism can also be used in conjunction with 2PI by adding an additional imaginary part to the real time contour (see e.g. [212]), we here only discuss a formalism directly in real time by using simplifications introduced by thermal equilibrium.

They are given by

- TIME-TRANSLATIONAL INVARIANCE Two time functions only depend on the relative time, e.g. $F(t_1, t_2) = F(t_1 - t_2)$. We can then Fourier transform with respect to time via $F(t) = \int \frac{d\omega}{2\pi} e^{-i\omega t} F(\omega)$. Similarly, one-time functions are independent of time, in particular the effective single particle Hamiltonian $\tilde{h}$.

- FLUCTUATION-DISSIPATION RELATIONS Spectral and statistical components are related by the fluctuation-dissipation relations

$$F(\omega) = -i\left(\frac{1}{2} - n^F_{\beta,\mu}(\omega)\right)\rho(\omega), \tag{2.71}$$

$$\chi^F(\omega) = -i\left(\frac{1}{2} + n^B_{\beta}(\omega)\right)\chi^\rho(\omega), \tag{2.72}$$

with the Fermi-Dirac distribution $n^F_{\beta,\mu}(\omega) = 1/\left(e^{\beta(\omega-\mu)}+1\right)$ and Bose-Einstein distribution $n^B_\beta(\omega) = 1/\left(e^{\beta\omega}-1\right)$ with inverse temperature β and chemical potential μ. Note that in the case of the GW approximation, the latter does not enter the bosonic fluctuation-dissipation relation as χ corresponds to a correlator of fermionic bilinears, which are not the raising/lowering operators corresponding to a conserved quantity. fermionic/bosonic fluctuation-dissipation relations similarly relate the fermionic/bosonic self energies Σ/Π.

In order to transform the equations of motion to frequency space, we first send the initial time to the distant past $t_0 \to -\infty$ and introduce the retarded Green's functions

$$D^R(t_1 - t_2) = \Theta(t_1 - t_2)\rho(t_1 - t_2), \tag{2.73}$$

$$\chi^R(t_1 - t_2) = \Theta(t_1 - t_2)\chi^\rho(t_1 - t_2) \tag{2.74}$$

One can then show that

$$D^R(\omega) = -\left[\omega - \tilde{h} - \Sigma^R(\omega)\right]^{-1}, \tag{2.75}$$

$$\chi^R(\omega) = -\left[\mathbb{1} - \Pi^R(\omega)U\right]^{-1}\Pi^R(\omega). \tag{2.76}$$

The self energies are most conveniently calculated in real time, where

$$\tilde{h}_{ij} = J_{ij} + \sum_k U_{jk}\left(F_{kk}(t=0) - \frac{1}{2}\right) - U_{ij}F_{ij}(t=0), \tag{2.77}$$

$$\Sigma^R_{ij}(t) = \sum_{kl} U_{ik}U_{lj}\left(F_{ij}(t)\chi^R_{kl}(t) + D^R_{ij}(t)\chi^F_{kl}(t)\right), \tag{2.78}$$

$$\Pi^R_{ij}(t) = -F_{ij}(t)(D^R_{ij}(t))^* - D^R_{ij}(t)(F_{ij}(t))^*. \tag{2.79}$$

After initializing D^R, e.g. with the free solution, the self-consistency loop proceeds as follows:

1. Calculate spectral function from

$$\rho_{ij}(\omega) = D^R_{ij}(\omega) - \left(D^R_{ji}(\omega)\right)^*. \tag{2.80}$$

and calculate F from fluctuation-dissipation relation, Eq. (2.71). Note that ρ is *not* proportional to the imaginary part of D^R (only for $i = j$). Do the same for χ^ρ and χ^F.

2. Fourier transform F and D^R to real time and calculate effective Hamiltonian $\tilde{h}$ from Eq. (2.77), as well as the bosonic self energy from Eq. (2.79).

3. Fourier transform bosonic self energy to frequency space and evaluate χ^R from Eq. (2.76)

4. Fourier transform χ^R to real time and evaluate Σ^R from Eq. (2.78). Finally, Fourier transform Σ^R to frequency space and evaluate D^R from Eq. (2.75).

An alternative approach would be to Fourier transform the spectral function to real time, evaluating Σ^ρ, Π^ρ, multiply with the $\Theta(t)$ function to get the retarded components and then transform back to frequency space.

The thus obtained thermal equilibrium state can also be used as an initial state for the real-time evolution under a different Hamiltonian than the one used for calculating the equilibrium state. To do so, all correlation functions are transformed back to a two-time form, where they are constant along the central time axis. The thus obtained two-time blocks are then inserted into the non-equilibrium Kadanoff-Baym equations and convergence with respect to the size of the block needs to be checked.

2.2 SPINS

In this section, we discuss the recently developed [48] extension of 2PI techniques to spin Hamiltonians of the form

$$\hat{H} = \frac{1}{2}\sum_{ij}\sum_{\alpha\beta} J_{ij}^{\alpha\beta}\hat{S}_i^\alpha \hat{S}_j^\beta, \tag{2.81}$$

where the spin operators fulfill $[\hat{S}_i^\alpha, \hat{S}_j^\beta] = i\delta_{ij}\epsilon^{\alpha\beta\gamma}\hat{S}_i^\alpha$ and $\sum_\alpha (\hat{S}_i^\alpha)^2 = \frac{3}{4}$.

As spin operators can not easily be translated into a coherent state path integral [4], we need to first use a mapping to either bosons or fermions in order to use the procedure developed in the previous section. We will discuss both alternatives in the following two sections.

2.2.1 *Majorana fermion mapping*

The original formulation [48] uses a mapping to Majorana fermions $\hat{\eta}_i^\alpha$ by

$$\hat{S}_i^\alpha = -\frac{i}{2}\epsilon^{\alpha\beta\gamma}\hat{\eta}_i^\beta\hat{\eta}_i^\gamma. \tag{2.82}$$

4 While spin coherent states and a corresponding path integral can be constructed [224], the resulting form is not directly amenable to 2PI techniques due to the presence of Berry phase terms.

The anticommuation relations $\{\hat{\eta}_i^\alpha, \hat{\eta}_j^\beta\} = \delta^{\alpha\beta}\delta_{ij}$ automatically guarantee both the spin commutation relations and the length constraint $\sum_\alpha (\hat{S}_i^\alpha)^2 = \frac{3}{4}$.

In the following, we will discuss the derivation of the spin 2PI equations for Majorana fermions. While it follows similar steps as Ref. [48], we will use the formulation in terms of spectral and statistical components of the Green's function rather than greater/lesser components to make the derivation coherent with our previous discussion of fermions.

CLASSICAL AND EFFECTIVE ACTION The closed-time path action corresponding to the spin Hamiltonian $\hat{H}$ expressed in terms of Majoranas is given by

$$S[\eta] = \int_{\mathcal{C}} dt \left\{ \frac{1}{2}\sum_j \eta_j^\alpha(t) i\partial_t \eta_j^\alpha(t) + \frac{1}{8}\sum_{ij} J_{ij}^{\alpha\beta}\epsilon^{\alpha\delta_1\delta_2}\epsilon^{\beta\gamma_1\gamma_2}\eta_i^{\delta_1}(t)\eta_i^{\delta_2}(t)\eta_j^{\gamma_1}(t)\eta_j^{\gamma_2}(t) \right\}, \tag{2.83}$$

where from now on we imply summation over repeated indices. As J is the only scale in the problem, a loop expansion is problematic. Therefore, we seek to perform a GW approximation as discussed in the previous section. To do so, we introduce a real bosonic Hubbard Stratonovich field χ, giving the action

$$S[\eta,\chi] = \int_{\mathcal{C}} dt \left\{ \frac{1}{2}\sum_j \eta_j^\alpha(t) i\partial_t \eta_j^\alpha(t) + \frac{1}{2}\sum_{ij} [J^{-1}]_{ij}^{\alpha\beta}\chi_i^\alpha\chi_j^\beta + \frac{i}{2}\sum_i \chi^\alpha(t)\epsilon^{\alpha\beta\gamma}\eta_i^\beta(t)\eta_i^\gamma(t) \right\}. \tag{2.84}$$

The 2PI effective action corresponding to this action is given by

$$\Gamma[D,G] = S[\bar{\chi}] - \frac{i}{2}\operatorname{Tr}\ln D^{-1} - \frac{i}{2}\operatorname{Tr}\{D_0^{-1}D\} + \frac{i}{2}\operatorname{Tr}\ln G^{-1} + \frac{i}{2}\operatorname{Tr}\{G_0^{-1}G\} + \Gamma_2[G,D], \tag{2.85}$$

where $D_{ij}^{\alpha\beta}(t_1,t_2) = \langle T_{\mathcal{C}}\eta_i^\alpha(t_1)\eta_j^\beta(t_2)\rangle$ and $G_{ij}^{\alpha\beta}(t_1,t_2) = \langle T_{\mathcal{C}}\chi_i^\alpha(t_1)\chi_j^\beta(t_2)\rangle$. Note also the symmetry properties $G_{ij}^{\alpha\beta}(t_1,t_2) = G_{ji}^{\beta\alpha}(t_2,t_1)$ and $D_{ij}^{\alpha\beta}(t_1,t_2) = -D_{ji}^{\beta\alpha}(t_2,t_1)$.

EQUATIONS OF MOTION The equations of motion for the correlators G, D and the mean field $\bar{\chi}$ follow from varying the effective action $\delta\Gamma = 0$, giving

$$\bar{\chi}_i^\alpha(t) = -\frac{i}{2}\sum_k J_{ik}^{\alpha\gamma}\epsilon^{\gamma\delta\beta}D_{kk}^{\delta\beta}(t,t), \tag{2.86}$$

$$\left(i\partial_t\delta^{\alpha\delta} + i\epsilon^{\alpha\delta\gamma}\bar{\chi}_i^\gamma(t_1)\right) D_{ij}^{\delta\beta}(t_1,t_2) = i\delta_{ij}\delta_{\mathcal{C}}(t_1-t_2) + i\int_{\mathcal{C}} dt\Sigma_{ik}^{\alpha\gamma}(t_1,t)D_{kj}^{\gamma\beta}(t,t_2), \tag{2.87}$$

$$G_{ij}^{\alpha\beta} = iJ_{ij}^{\alpha\beta}\delta_{\mathcal{C}}(t_1-t_2) + iJ_{ik}^{\alpha\gamma}\int_{\mathcal{C}} dt\Pi_{kl}^{\gamma\delta}G_{lj}^{\delta\beta}(t,t_2), \tag{2.88}$$

where $\Sigma = -2i\frac{\delta\Gamma_2}{\delta D}$, $\Pi = 2i\frac{\delta\Gamma_2}{\delta G}$ are the Majorana and auxiliary field self energies.

We decompose the Majorana correlator into spectral and statistical parts by $D(t_1,t_2) = F(t_1,t_2) - \frac{i}{2}\,\mathrm{sgn}_{\mathcal{C}}(t_1-t_2)\rho(t_1,t_2)$, yielding

$$\left(i\partial_t\delta^{\alpha\delta} + i\epsilon^{\alpha\delta\gamma}\bar{\chi}_i^{\gamma}(t_1)\right)F_{ij}^{\delta\beta}(t_1,t_2) = \int_0^{t_1} dt\Sigma_{ik}^{\rho,\alpha\gamma}(t_1,t)F_{kj}^{\gamma\beta}(t,t_2) - \int_0^{t_2} dt\Sigma_{ik}^{F,\alpha\gamma}(t_1,t)\rho_{kj}^{\gamma\beta}(t,t_2), \tag{2.89}$$

$$\left(i\partial_t\delta^{\alpha\delta} + i\epsilon^{\alpha\delta\gamma}\bar{\chi}_i^{\gamma}(t_1)\right)\rho_{ij}^{\delta\beta}(t_1,t_2) = \int_{t_2}^{t_1} dt\Sigma_{ik}^{\rho,\alpha\gamma}(t_1,t)\rho_{kj}^{\gamma\beta}(t,t_2). \tag{2.90}$$

Similarly, we decompose the auxiliary field correlator as $G(t_1,t_2) = iJ\delta_{\mathcal{C}}(t_1-t_2) + J[\chi^F(t_1,t_2) - \frac{i}{2}\,\mathrm{sgn}_{\mathcal{C}}(t_1-t_2)\chi^{\rho}(t_1,t_2)]J$, with which we get

$$\chi_{ij}^{F,\alpha\beta}(t_1,t_2) = -\Pi_{ij}^{F,\alpha\beta}(t_1,t_2) + \int_0^{t_1}\Pi_{ik}^{\rho,\alpha\gamma}(t_1,t)J_{kl}^{\gamma\delta}\chi_{lj}^{F,\delta\beta}(t,t_2) - \int_0^{t_2}\Pi_{ik}^{F,\alpha\gamma}(t_1,t)J_{kl}^{\gamma\delta}\chi_{lj}^{\rho,\delta\beta}(t,t_2), \tag{2.91}$$

$$\chi_{ij}^{\rho,\alpha\beta}(t_1,t_2) = -\Pi_{ij}^{\rho,\alpha\beta}(t_1,t_2) + \int_{t_2}^{t_1}\Pi_{ik}^{\rho,\alpha\gamma}(t_1,t)J_{kl}^{\gamma\delta}\chi_{lj}^{\rho,\delta\beta}(t,t_2). \tag{2.92}$$

GW APPROXIMATION We use the approximation with the smallest number of vertices, given by

$$\Gamma_2[G,D] = \frac{i}{4}\epsilon^{\alpha\gamma\delta}\epsilon^{\alpha'\gamma'\delta'}\int_{\mathcal{C}}dt_1\int_{\mathcal{C}}dt_2 G_{ij}^{\alpha\alpha'}(t_1,t_2)D_{ij}^{\gamma\gamma'}(t_1,t_2)D_{ij}^{\delta\delta'}(t_1,t_2), \tag{2.93}$$

where the overall prefactor is comprised out of $(-1/2)^2$ from the two vertex prefactors, $1/2!$ from the expansion of the exponential, $(-i)$ from the definition of Γ_2, (-1) from one fermion loop and a factor of 2 for the two equivalent possibilities to form this loop.

The self energies follows as

$$\Sigma_{ij}^{F,\alpha\alpha'}(t_1,t_2) = -\epsilon^{\alpha\beta\gamma}\epsilon^{\alpha'\beta'\gamma'}\left(J_{ik}^{\beta\delta}\chi_{kl}^{F,\delta\xi}J_{lj}^{\xi\beta'}F_{ij}^{\gamma\gamma'} - \frac{1}{4}J_{ik}^{\beta\delta}\chi_{kl}^{\rho,\delta\xi}J_{lj}^{\xi\beta'}\rho_{ij}^{\gamma\gamma'}\right), \tag{2.94}$$

$$\Sigma_{ij}^{\rho,\alpha\alpha'}(t_1,t_2) = -\epsilon^{\alpha\beta\gamma}\epsilon^{\alpha'\beta'\gamma'}\left(J_{ik}^{\beta\delta}\chi_{kl}^{\rho,\delta\xi}J_{lj}^{\xi\beta'}F_{ij}^{\gamma\gamma'} + J_{ik}^{\beta\delta}\chi_{kl}^{F,\delta\xi}J_{lj}^{\xi\beta'}\rho_{ij}^{\gamma\gamma'}\right), \tag{2.95}$$

$$\Pi_{ij}^{F,\alpha\alpha'}(t_1,t_2) = -\frac{1}{2}\epsilon^{\alpha\beta\gamma}\epsilon^{\alpha'\beta'\gamma'}\left(F_{ij}^{\beta\beta'}F_{ij}^{\gamma\gamma'} - \frac{1}{4}\rho_{ij}^{\beta\beta'}\rho_{ij}^{\gamma\gamma'}\right), \tag{2.96}$$

$$\Pi_{ij}^{\rho,\alpha\alpha'}(t_1,t_2) = -\frac{1}{2}\epsilon^{\alpha\beta\gamma}\epsilon^{\alpha'\beta'\gamma'}\left(F_{ij}^{\beta\beta'}\rho_{ij}^{\gamma\gamma'} + \rho_{ij}^{\beta\beta'}F_{ij}^{\gamma\gamma'}\right), \tag{2.97}$$

where we omitted a Fock-type contribution $\Sigma \propto J_{ij}G_{ij}\delta_{\mathcal{C}}(t_1-t_2)$ as this will turn out to vanish for physical initial states.

Solving the above set of equations, we can extract the time evolution of spin expectation values by

$$\langle\hat{S}_i^{\alpha}(t)\rangle = -\frac{i}{2}\epsilon^{\alpha\beta\gamma}F_{ii}^{\beta\gamma}(t,t). \tag{2.98}$$

PHYSICAL INITIAL STATES AND TRANSLATIONAL INVARIANCE The initial value of ρ is given by the Majorana anticommutation relations as

$$\rho_{ij}^{\alpha\beta}(0,0) = i\delta^{\alpha\beta}\delta_{ij}. \tag{2.99}$$

The initial value of F results from the initial spin expectation values as

$$F_{ij}^{\alpha\beta}(0,0) = i\epsilon^{\alpha\beta\gamma}\left\langle \hat{S}_j^{\gamma}\right\rangle \delta_{ij}. \tag{2.100}$$

Therefore, physical initial states imply $D_{ij}(0,0) \sim \delta_{ij}$, and therefore $\Sigma_{ij} \sim \delta_{ij}$ and $\Pi_{ij} \sim \delta_{ij}$. Moreover, for translational invariant initial states, $D, \Sigma, \Pi, \bar{\chi}$ become independent of lattice site and D_{ij}, J_{ij} are only dependent on the relative coordinate. In Fourier space, we write $J_{\mathbf{k}} = \frac{1}{N}\sum_{ij} e^{i\mathbf{k}(\mathbf{r}_i - \mathbf{r}_j)} J_{ij}$, and the resulting set of equations of motions is

$$\bar{\chi}^{\alpha}(t) = -\frac{i}{2} J_{\mathbf{k}=0}^{\alpha\gamma}\epsilon^{\gamma\delta\beta}F^{\delta\beta}(t,t), \tag{2.101}$$

$$\left(i\partial_t\delta^{\alpha\delta} + i\epsilon^{\alpha\delta\gamma}\bar{\chi}^{\gamma}(t_1)\right)F^{\delta\beta}(t_1,t_2) = \int_0^{t_1} dt\Sigma^{\rho,\alpha\gamma}(t_1,t)F^{\gamma\beta}(t,t_2) - \int_0^{t_2} dt\Sigma^{F,\alpha\gamma}(t_1,t)\rho^{\gamma\beta}(t,t_2), \tag{2.102}$$

$$\left(i\partial_t\delta^{\alpha\delta} + i\epsilon^{\alpha\delta\gamma}\bar{\chi}^{\gamma}(t_1)\right)\rho^{\delta\beta}(t_1,t_2) = \int_{t_2}^{t_1} dt\Sigma^{\rho,\alpha\gamma}(t_1,t)\rho^{\gamma\beta}(t,t_2), \tag{2.103}$$

$$\chi_{\mathbf{k}}^{F,\alpha\beta}(t_1,t_2) = -\Pi^{F,\alpha\beta}(t_1,t_2) + \int_0^{t_1}\Pi^{\rho,\alpha\gamma}(t_1,t)J_{\mathbf{k}}^{\gamma\delta}\chi_{\mathbf{k}}^{F,\delta\beta}(t,t_2) - \int_0^{t_2}\Pi^{F,\alpha\gamma}(t_1,t)J_{\mathbf{k}}^{\gamma\delta}\chi_{\mathbf{k}}^{\rho,\delta\beta}(t,t_2), \tag{2.104}$$

$$\chi_{\mathbf{k}}^{\rho,\alpha\beta}(t_1,t_2) = -\Pi^{\rho,\alpha\beta}(t_1,t_2) + \int_{t_2}^{t_1}\Pi^{\rho,\alpha\gamma}(t_1,t)J_{\mathbf{k}}^{\gamma\delta}\chi_{\mathbf{k}}^{\rho,\delta\beta}(t,t_2). \tag{2.105}$$

The self energies then become

$$\Sigma^{F,\alpha\alpha'}(t_1,t_2) = -\epsilon^{\alpha\beta\gamma}\epsilon^{\alpha'\beta'\gamma'}\frac{1}{N}\sum_{\mathbf{k}} J_{\mathbf{k}}^{\beta\delta}J_{\mathbf{k}}^{\tilde{\xi}\beta'}\left(\chi_{\mathbf{k}}^{F,\delta\tilde{\xi}}F^{\gamma\gamma'} - \frac{1}{4}\chi_{\mathbf{k}}^{\rho,\delta\tilde{\xi}}\rho^{\gamma\gamma'}\right), \tag{2.106}$$

$$\Sigma^{\rho,\alpha\alpha'}(t_1,t_2) = -\epsilon^{\alpha\beta\gamma}\epsilon^{\alpha'\beta'\gamma'}\frac{1}{N}\sum_{\mathbf{k}} J_{\mathbf{k}}^{\beta\delta}J_{\mathbf{k}}^{\tilde{\xi}\beta'}\left(\chi_{\mathbf{k}}^{\rho,\delta\tilde{\xi}}F^{\gamma\gamma'} + \chi_{\mathbf{k}}^{F,\delta\tilde{\xi}}\rho^{\gamma\gamma'}\right), \tag{2.107}$$

$$\Pi^{F,\alpha\alpha'}(t_1,t_2) = -\frac{1}{2}\epsilon^{\alpha\beta\gamma}\epsilon^{\alpha'\beta'\gamma'}\left(F^{\beta\beta'}F^{\gamma\gamma'} - \frac{1}{4}\rho^{\beta\beta'}\rho^{\gamma\gamma'}\right), \tag{2.108}$$

$$\Pi^{\rho,\alpha\alpha'}(t_1,t_2) = -\frac{1}{2}\epsilon^{\alpha\beta\gamma}\epsilon^{\alpha'\beta'\gamma'}\left(F^{\beta\beta'}\rho^{\gamma\gamma'} + \rho^{\beta\beta'}F^{\gamma\gamma'}\right). \tag{2.109}$$

EXCTRACTING SPIN-SPIN CORRELATIONS Repeating the same line of argumentation as in section 2.1.4, we find that we can extract spin-spin correlations from the auxiliary field correlators via

$$\chi^{F,\alpha\beta}_{\mathbf{k}}(t_1,t_2) = \frac{1}{2}\left\langle\langle \hat{S}^{\alpha}_{\mathbf{k}}, S^{\beta}_{\mathbf{k}}\rangle\right\rangle, \tag{2.110}$$

$$\chi^{\rho,\alpha\beta}_{\mathbf{k}}(t_1,t_2) = i\left\langle\left[\hat{S}^{\alpha}_{\mathbf{k}}, S^{\beta}_{\mathbf{k}}\right]\right\rangle. \tag{2.111}$$

As we will see in chapter 8, the usage of these identities is hampered by the violation of sum rules, which appear as a result of the approximation used.

2.2.2 *Schwinger boson mapping*

The author of this thesis developed an alternative formulation in terms of Schwinger bosons [215], employing

$$\hat{S}^{\alpha}_i = \frac{1}{4}\hat{\varphi}^a_i \mathcal{K}^{\alpha}_{ab}\hat{\varphi}^b_i, \tag{2.112}$$

where $[\hat{\varphi}^a_i, \hat{\varphi}^b_j] = \delta_{ij}\delta^{ab}$ defines the bosonic operators. Here, $a \in \{0,1,2,3\}$, such that the above definition needs to be supplemented by a constraint on the occupation of the bosons on each site [215]. The matrices $\mathcal{K}$ are defined as

$$\mathcal{K}^{\alpha} = [\sigma^x \otimes \mathbb{1}]\,\delta^{\alpha x} + [\sigma^y \otimes \mathbb{1}]\,\delta^{\alpha y} + [\sigma^z \otimes \mathbb{1}]\,\delta^{\alpha z}. \tag{2.113}$$

Rather than deriving the Schwinger boson spin 2PI equations, we note that they can be obtained from the Majorana version by comparing the two definitions for the spin operators in Eqs. (2.82), (2.112). This implies a prescription following

$$\epsilon^{\alpha\beta\gamma} \to \frac{i}{2}\mathcal{K}^{\alpha}_{bc}, \tag{2.114}$$

along with replacing the (3×3) matrices $(F, \rho, \Sigma^F, \Sigma^\rho, \Pi^F, \Pi^\rho)$ with (4×4) matrices. Moreover, we need to replace the time derivative $i\partial_t\delta^{ab}$ in Eqs. (2.102), (2.103) with $-i[\mathbb{1}\otimes\sigma^y]^{ab}$ to account for the different type of species. Comparing the thus obtained equations of motion, we indeed find the Schwinger boson spin 2PI equations derived in Ref. [215]. Note that the initial conditions are now given by

$$\rho^{ab}_{ij}(0,0) = -[\mathbb{1}\otimes\sigma^y]^{ab}\delta_{ij} \tag{2.115}$$

and

$$F_{ij}(0,0) = \delta_{ij}\begin{pmatrix} \langle\hat{S}^z_i\rangle + S + \frac{1}{2} & 0 & \langle\hat{S}^x_i\rangle & \langle\hat{S}^y_i\rangle \\ 0 & \langle\hat{S}^z_i\rangle + S + \frac{1}{2} & -\langle\hat{S}^y_i\rangle & \langle\hat{S}^x_i\rangle \\ \langle\hat{S}^x_i\rangle & -\langle\hat{S}^y_i\rangle & -\langle\hat{S}^z_i\rangle + S + \frac{1}{2} & 0 \\ \langle\hat{S}^y_i\rangle & \langle\hat{S}^x_i\rangle & 0 & -\langle\hat{S}^z_i\rangle + S + \frac{1}{2} \end{pmatrix}. \tag{2.116}$$

The spin expectation values can be read out by

$$\langle \hat{S}_i^\alpha(t) \rangle = \frac{1}{4} \mathcal{K}_{ab}^\alpha F_{ii}^{ab}(t,t). \tag{2.117}$$

2.2.3 *Benchmark: Relaxation dynamics and signatures of many body localization in the XXZ chain*

This section is based on the publication

- Alexander Schuckert, Asier Pineiro-Orioli, Jürgen Berges:
  "Nonequilibrium quantum spin dynamics from two-particle irreducible functional integral techniques in the Schwinger boson representation"
  – Phys. Rev. B 98, 224304 (2018) [arXiv:1806.02347]

Structure and text have been rearranged and adapted here.

The question of whether and how the far-from-equilibrium dynamics on different sides of a quantum critical point (QCP) are connected to the underlying quantum phase transition [225] has recently gained much attention from the perspective of dynamical phase transitions [181, 226–228]. In this section, we investigate whether this field of study may be addressed by the Schwinger boson spin 2PI method. Here, we consider a model studied before in this context [225, 226], the antiferromagnetic nearest-neighbor interacting XXZ chain with periodic boundary conditions defined by the Hamiltonian

$$\hat{H} = J \sum_i \left(\hat{S}_i^x \hat{S}_{i+1}^x + \hat{S}_i^y \hat{S}_{i+1}^y + \Delta \hat{S}_i^z \hat{S}_{i+1}^z \right), \tag{2.118}$$

where we choose $J > 0$ and Δ denotes the anisotropy. This model exhibits a quantum phase transition from a gapless Luttinger liquid phase with quasi-long-range order for $|\Delta| < 1$, to an antiferromagnetic (ferromagnetic) phase with long-range order for $\Delta > 1$ ($\Delta < -1$) [225].

We study the evolution of the staggered magnetization,

$$\sum_i (-1)^i \langle S_i^z(t) \rangle, \tag{2.119}$$

in a spin chain initialized with classical Néel order, i.e.

$$|\Psi_0\rangle = |\uparrow\downarrow\uparrow \cdots \uparrow\downarrow\rangle, \tag{2.120}$$

for different anisotropies Δ. The time evolution of this initial state has been extensively studied with a numerically accurate method (iMPS) in the infinite length limit [225, 229]. Those studies show different dynamical behaviour of this non-equilibrium initial state depending on Δ. One finds exponentially damped oscillations with near constant oscillation period for $\Delta \leq 1$, a simple exponential decay

for $\Delta > 1$, and an algebraic decay for $\Delta = 0$. This behaviour was later attributed to an underlying dynamical quantum phase transition [226].

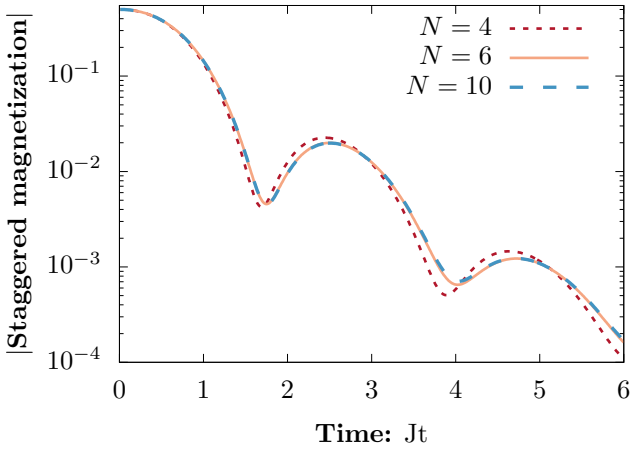

Figure 2.4: Comparison of different system sizes in the dynamics of the staggered magnetization starting in the classical Néel state in the XXZ chain at the Heisenberg point $\Delta = 1.0$. A fast convergence to the thermodynamic limit is found as chain length 6 shows no sizeable difference to chain length 10.

Evaluation in the infinite length limit

Using our 2PI approach, we first compare in Fig. 2.4 the effect of varying the system size on the dynamics of the staggered magnetization for $\Delta = 1$. Remarkably, we find no significant changes in the dynamics for the times considered when increasing the chain length from $N = 6$ to $N = 10$. This suggests that results with a system size of just $N = 6$ can already be taken as a good approximation to the thermodynamic limit in this particular problem. Moreover, we observed a similarly fast convergence to the thermodynamic limit in two spatial dimensions (not shown), which indicates that this method is also well-suited for the study of quantum dynamics of spin systems in the infinite volume limit in higher dimensions. This fast convergence to the thermodynamic limit is a feature resulting from the field-theoretic nature of our method and was also found in Ref. [48]. We note that we do not use a memory cut here as we found it to lead to an unphysical leveling-off of the exponential damping.

Dynamics of the Néel ordered state on different sides of the QCP

Fig. 2.5 shows the time evolution of the staggered magnetization for different values of Δ below and above the transition as obtained from our 2PI approximation. Re-

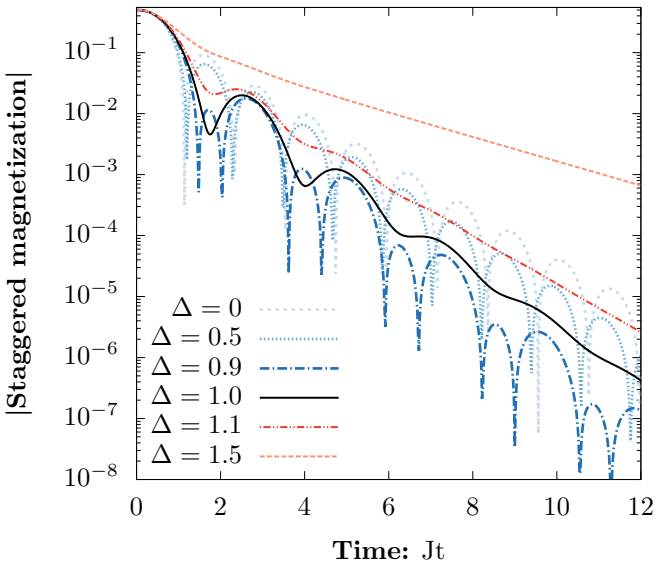

Figure 2.5: Time evolution of the modulus of the staggered magnetization in the XXZ chain with different anisotropies Δ, tuning across the (dynamical) quantum phase transition at $\Delta = 1$. The dynamics exhibit an oscillating exponentially damped behaviour for $\Delta < 1$ and a pure exponential damping for $\Delta > 1$, which was previously found with MPS [225]. Note that in mean field/LO the staggered magnetization stays constant for all times and hence all features seen here are solely obtained from the NLO approximation.

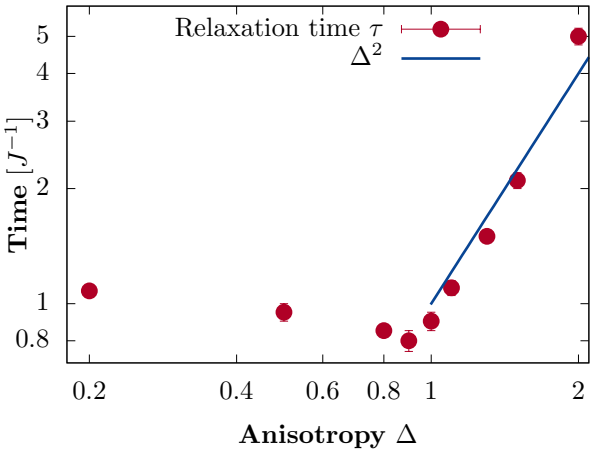

Figure 2.6: Relaxation time as obtained from an exponential fit to the data in Fig. 2.5 as a function of anisotropy. As the QCP around $\Delta = 1$ is approached the dynamics becomes faster, which is the anomalous behaviour found before in this model. Furthermore, the relaxation time changes asymetrically as the QCP is approached from above/below. The errors result from the fitting procedure and are smaller than the dot size for most data points. The blue line (not a fit) indicates the Δ^2 behaviour previously found for the approach to the QCP from above[225].

markably, our method captures the qualitative behavior expected [225]. For $\Delta < 1$ we obtain exponentially damped oscillations, whereas for $\Delta > 1$ the damping becomes exponential and non-oscillatory. This represents a considerable improvement compared to previous mean-field treatments based on a mapping to a spinless fermion model [225], which found spurious algebraic decay of the staggered magnetization for $\Delta < 1$ and a constant oscillatory behaviour for $\Delta > 1$. Note that such a mean-field approximation does not correspond to our LO approximation, which is equivalent to mean-field in the original spin variables and which does not show *any* dynamics here.

Fitting an exponentially damped function $f(t) \sim \exp(-t/\tau)$ to our data, where the proportionality factor contains an oscillatory function for $\Delta < 1$, we extract the relaxation time τ as a function of the anisotropy, see Fig. 2.6. As the critical point at $\Delta = 1$ is approached from below we observe a fall-off of the relaxation time, which is the behaviour expected in this model. Note that this constitutes a rather anomalous behavior compared to the usual critical slowing down close to quantum critical points [225, 230]. As $\Delta = 1$ is approached from above, an algebraic dependence $\tau(\Delta) \sim \Delta^2$ has been previously found in Ref. [225]. Fig. 2.6 shows that our results are compatible with such a quadratic dependence in the regime just above $\Delta = 1$[5].

While all of the above results are in agreement with those found in Ref. [225] with iMPS, the damping rates inferred do not agree quantitatively with the iMPS results. Moreover, the quantum critical point seems to be slightly shifted away from $\Delta = 1$ in our approximation, as evidenced by the simple exponential damping of the $\Delta = 1$ curve shown in Fig. 2.5, instead of the oscillations around zero found in Ref. [225]. Other features not well reproduced by our approximation include the approximate Δ-independence of the oscillation periods found for $\Delta < 1$ and the algebraic decay expected for $\Delta = 0$.

Despite these quantitative inaccuracies, which may be improved in the next order of the $1/N$ expansion, it is remarkable that our 2PI approximation is able to reproduce most generic features of the relaxation dynamics around the QPT of the XXZ chain, even in the strongly interacting regime around $\Delta = 1$. In particular, it greatly outperforms previous mean-field treatments built on a mapping to spinless fermions which show a qualitatively different behavior. The results presented here open up the possibility to study dynamical quantum phase transitions in lattice spin systems in regimes in which methods such as iMPS or other DMRG related methods fail, e.g. in higher dimensions as previously done in the $O(N)$ model [231].

5 While the line in this figure is not a fit we checked that vastly different power laws such as $\sim \Delta$ and $\sim \Delta^3$ are clearly inconsistent with the data.

For this purpose, our results suggest that one would not need to simulate large system sizes owing to the fast convergence to the thermodynamic limit shown here.

Signatures of Many Body Localization

In the first applications, we have shown that the Schwinger boson spin-2PI method is able to reproduce generic features of thermalization dynamics in interacting spin models. In this section, we give some indicative results that it is also able to capture the dynamics of local observables in a system which refuses to thermalize: a many-body localized (MBL) system [52–54, 154, 179, 232]. The model best studied in this context is the Heisenberg chain with nearest-neighbour interactions in a random field [57, 233, 234]

$$\hat{H} = J \sum_i \left(\hat{S}_i^x \hat{S}_{i+1}^x + \hat{S}_i^y \hat{S}_{i+1}^y + \hat{S}_i^z \hat{S}_{i+1}^z \right) + \sum_i h_i \hat{S}_i^z, \tag{2.121}$$

where the h_i are numbers drawn from a uniform random distribution in the interval $[-\Theta, \Theta]$. Note that this Hamiltonian becomes the model (2.118) studied in the previous section for $\Delta = 1$ and $\Theta = 0$. This model can be transformed to a Hubbard-type model using the Jordan-Wigner transformation. In Ref. [235] this has been used to develop a Hartree-Fock theory of the many-body-localization transition. As before, we consider as initial state the classical Néel state in Eq. (2.120) and study the dynamics of the staggered magnetization, Eq. (2.119), in a system with periodic boundary conditions. For the purpose of localization it is useful to note that for this particular initial state, the staggered magnetization can be interpreted as quantifying the correlations with the initial state by means of

$$\sum_i \langle \hat{S}_i^z(t) \hat{S}_i^z(0) \rangle = \frac{1}{2} \sum_i (-1)^i \langle S_i^z(t) \rangle \,. \tag{2.122}$$

For thermalizing systems with initial state in the zero-magnetization sector, such as the Néel state, the correlation with the initial state, and hence the staggered magnetization, should go to zero as a relaxing system effectively forgets its initial state. In a localized system, however, memory of the initial state is retained and therefore the above quantity tends to a nonzero constant in a fully many-body localized system.

Fig. 2.7 shows the time evolution of the staggered magnetization in a chain of six spins initialized in a Néel ordered state for various disorder strengths Θ. The results displayed are averaged over 26 disorder realizations. Based on the finite-size discussion of the previous section for the case without disorder (see Fig. 2.4), we expect them to capture at least some qualitative features of the system in the thermodynamic limit. For very weak disorder ($\Theta = 0.01$), we observe that the time

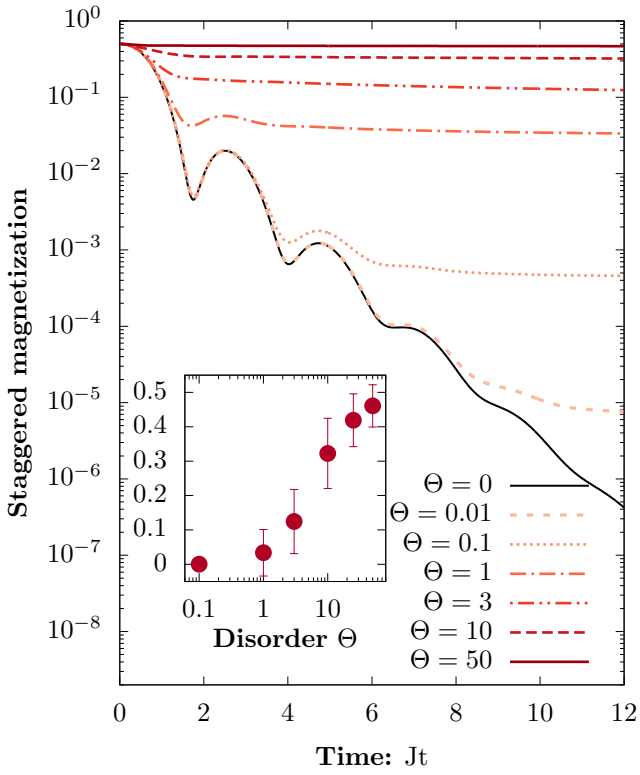

Figure 2.7: Time evolution of the staggered magnetization in a Heisenberg chain of 6 spins with a random field for different disorder strengths Θ, averaged over 26 realizations of the disorder. As the disorder increases, the dynamics slow down from exponentially fast relaxation to a full arrest on the observed timescales. Inset: Latest value of the staggered magnetization as a function of disorder strength. Error bars are defined as the standard deviation of the disorder average.

evolution is indistinguishable from the case of no disorder for early times and the relaxation slows down at around $Jt = 8$. For larger disorder strengths, a plateau is approached and the value of the staggered magnetization at the plateau is found to increase with increasing disorder. For $\Theta = 50$ no time evolution of the staggered magnetization is visible on the observed timescale. In the inset, we show the latest value of the staggered magnetization as a function of the disorder. A crossover from thermalization at low disorder strength to no relaxation at strong disorder is visible (see inset in Fig. 2.7), where the inflexion point resulting from interpolating between the points is consistent with the value $\Theta \approx 3.5$ obtained in Ref. [236] for the location of the MBL transition.

While these observations are in agreement with previous numerical studies of MBL in this system, we note that the observed timescales as well as the system size are not large enough to conclusively demonstrate that this method is able to describe this phenomenon. Future studies would, however, be immediately able to generalize results to higher dimensions and more exotic interactions (such as long-range interactions), where other standard numerical methods become inapplicable. Moreover, it is useful to note that in contrast to conventional field-theoretic treatments of disordered systems [237], the disorder is taken into account without further approximations as it is quadratic in the Schwinger boson operators.

Part I

THERMALIZATION OF CLOSED QUANTUM MANY-BODY SYSTEMS

In this part we will study various aspects of the thermalization dynamics of many-body quantum systems, ranging from many-body chaos near a phase transition over the use of fluctuation-dissipation relations to characterize eigenstate thermalization to the emergence of transport dynamics in the late-time relaxation of long-range spin systems.

3

MANY-BODY CHAOS NEAR A THERMAL PHASE TRANSITION

This chapter is based on the publication

- Alexander Schuckert, Michael Knap: "Many-body chaos near a thermal phase transition" – SciPost Phys. 7, 022 (2019) [arXiv:1905.00904]

Structure and text have been rearranged and adapted here. Section 3.8 as well as subsection 3.7.2 have not been published yet.

We study many-body chaos in a (2+1)D relativistic scalar field theory at high temperatures in the classical statistical approximation, which captures the quantum critical regime and the thermal phase transition from an ordered to a disordered phase. We evaluate out-of-time-ordered correlation functions (OTOCs) and find that the associated Lyapunov exponent increases linearly with temperature in the quantum critical regime, and approaches the non-interacting limit algebraically in terms of a fluctuation parameter. OTOCs spread ballistically in all regimes, also at the thermal phase transition, where the butterfly velocity is maximal. This chapter contributes to the understanding of the relation between quantum and classical many-body chaos. As an outlook, we show that our method can be applied to other field theories dominated by classical modes at long wavelengths and generalized to situations far-from-equilibrium.

3.1 INTRODUCTION

Thermalization in classical many-body systems can be understood from the perspective of dynamical chaos: details of the initial state are effectively forgotten by the exponential divergence of trajectories. In quantum many-body systems, the same picture can not be immediately applied as the Schrödinger equation is a linear differential equation and therefore does not directly give rise to chaos. However, parts of the system may look thermal if their surrounding provides a thermalizing environment, as put forward by the eigenstate thermalization hypothesis [25–27]. Thermalization can be directly probed by evaluating fluctuation-dissipation relations far from equilibrium as well [48, 238, 239]. Yet, a dynamical mechanism of thermalization in quantum systems comparable in generality to the one offered by chaos in classical systems has remained elusive so far.

Recently, OTOCs [240, 241] have been proposed as a generalization of classical dynamical chaos to quantum systems. As motivated from the perspective of operator scrambling in strongly coupled field theories with a gravity dual [242–246], they have been shown to exhibit exponential growth in many field theories [36–38, 247–250]. Moreover, OTOCs spread (in general) ballistically in space with a "butterfly velocity" quantifying the speed of scrambling, which has been also found in non-relativistic lattice systems [34, 40–42, 251–256]. Such ballistic spreading is to be expected in systems with well-defined quasiparticles [257], but even strongly coupled systems without quasiparticles exhibit a well-defined butterfly velocity. While these results show many analogies to dynamical chaos in classical systems [258–261], the exact relation between exponential growth in OTOCs and classical chaos remains unclear.

Here, we study a self-interacting real scalar field theory in the strongly correlated regime in which classical modes are expected to dominate: at high temperatures and around a second-order thermal phase transition. While the critical dynamics are notoriously hard to study with diagrammatic techniques [262], the classical statistical approximation provides reliable results for the order parameter dynamics in these regimes [263–267]. Furthermore, it has recently been shown that also the leading behaviour of the OTOC is captured within semi-classical approximations [268] and we conjecture this result to generalize to our case. Hence, we numerically obtain both the spectral function and the OTOC by evolving the classical field equations of motion of an infinitesimal perturbation and averaging over thermal initial states. The zero-momentum spectral function exhibits algebraically slow relaxation near the critical point as a consequence of critical slowing down, but possesses well-defined quasi-particles at higher momentum or away from the critical point. By contrast, we do not find signatures of critical slowing down in the OTOC even though the studied time scales are well within the temporal correlation length. Instead, the OTOC exhibits ballistic spreading and exponential growth in the whole considered parameter regime. By matching the quantum field theory in the quantum critical regime to the classical field theory via dimensional reduction, we find the Lyapunov exponent to reproduce the linear-in-temperature scaling, that has been found in other strongly coupled theories in accordance with the Maldacena-Shenker-Stanford (MSS) bound [243]. Furthermore, it approaches the non-interacting limit algebraically in a fluctuation parameter and exhibits a cusp at the phase transition. The butterfly velocity is significantly smaller than the speed of light and shows a global maximum near the phase transition. Lastly, the temporal fluctuations of the OTOC follow a self-similar behaviour in agreement with the Kardar-Parisi-Zhang (KPZ) universality class [269].

This chapter is organized as follows. First, we introduce the real scalar field theory, how to obtain the classical statistical approximation from dimensional reduction and our numerical methods. Secondly, we discuss the long wavelength excitations obtained from the spectral function at zero momentum. Finally, we show that the dynamics of the OTOC display qualitatively different perspective on the thermalization dynamics compared to the spectral function.

3.2 REAL SCALAR FIELD THEORY AT HIGH TEMPERATURE

MODEL. We study a real scalar field theory in $d = 2$ spatial dimensions given by the Hamiltonian

$$H = \int \mathrm{d}^2\mathbf{x} \left[\frac{1}{2}\pi^2 + \frac{1}{2}\left(\nabla\varphi\right)^2 + \frac{1}{2}m^2\varphi^2 + \frac{\lambda}{4!}\varphi^4 \right], \tag{3.1}$$

with bare mass m^2 and interaction constant λ. $\pi = \partial_t\varphi$ is the canonically conjugate momentum of the real scalar fields φ. This model exhibits a finite temperature phase transition from a disordered paramagnetic phase with $\langle\varphi\rangle = 0$ to a symmetry broken phase with $\langle\varphi\rangle \neq 0$ in the universality class of the 2D Ising model.

THE CLASSICAL STATISTICAL APPROXIMATION. At high temperatures and close to the phase transition, the two dimensional classical statistical field theory given by the Hamiltonian in Eq. (3.1) can be interpreted as an effective field theory for the corresponding (2+1)D finite temperature quantum field theory for long-wavelength, long-distance properties. This may be allegorically understood from the fact that in the high-T regime and close to a thermal phase transition, dominant long wavelength excitations have frequency $\omega \ll T$ and hence the Bose-Einstein distribution reduces to the classical Rayleigh-Jeans law

$$\frac{1}{\exp(\omega/T) - 1} \approx \frac{T}{\omega} \gg 1. \tag{3.2}$$

For long wavelength observables, the quantum field theory is therefore expected to be dominated by these highly occupied modes and reduces to a classical statistical field theory. The two-dimensional classical theory may then be matched to the corresponding $(2+1)$ dimensional quantum field theory by inserting the mass m^2 and coupling λ obtained from dimensional reduction, i.e., by integrating out all non-zero Matsubara frequencies. This procedure is based on the fact that the latter have larger thermal masses than the zero Matsubara mode to lowest order in an $\epsilon = 3 - d$ expansion [267] and hence may be integrated out to obtain the long-distance properties of the theory. While it was previously shown that this procedure can also be used to obtain the order parameter dynamics [267, 270, 271],

we conjecture in this chapter that it also captures the leading chaotic scrambling dynamics in the OTOC at times shorter than the Ehrenfest time. This assumption was previously shown to be valid in semi-classical calculations in the Bose-Hubbard model [268]. Furthermore, a diagrammatic approach to the related O(N) model has found the OTOC to be dominated by momenta $p < T$, i.e., the classical modes at high temperature [37].

In the following, we will discuss the above arguments more in-depth, from dimensional reduction to a dynamical argument.

Dimensional reduction

We are interested in a real scalar quantum field theory at finite temperature described by the partition function

$$Z = \int \mathcal{D}\phi(x,\tau)\exp\left(-S\right) \tag{3.3}$$

with Euclidean action

$$S[\phi] = \int_0^{1/T} \mathrm{d}\tau \int \mathrm{d}^2\mathbf{x} \left\{ \frac{1}{2}\left(\partial_\tau \phi\right)^2 + \frac{1}{2}\left(\nabla_{\mathbf{x}}\phi\right)^2 + \frac{1}{2}(r_c + r)\phi^2 + \frac{g}{4!}\phi^4 \right\}. \tag{3.4}$$

Above we have introduced the deviation r of the quadratic coupling from the (quantum) critical coupling r_c and the quartic coupling g.

The procedure of dimensional reduction reduces the above $(2+1)$ dimensional quantum field theory to the two dimensional classical statistical field theory discussed above. To do so, we mainly follow the line of argumentation in Refs. [230, 262, 267].

FREE THEORY. To motivate the general procedure, consider for a moment $g = 0$. Introducing the fields $\phi(\tau,\mathbf{x}) = \sum_{n\in\mathbb{R}} e^{i\omega_n\tau}\phi_n(\mathbf{x})$ in Matsubara space, the action becomes

$$S^{U=0}[\phi] = \frac{1}{T}\sum_n \int \mathrm{d}^2\mathbf{x} \left\{ \frac{1}{2}\left(\nabla_{\mathbf{x}}\phi_n\right)^2 + \frac{1}{2}(r_c + r + 4\pi^2 n^2 T^2)\phi_n^2 \right\}. \tag{3.5}$$

At high temperature, the masses of the non-zero Matsubara modes become very large. As these determine the inverse correlation length, the low momentum properties are entirely dominated by the $n = 0$ mode. Hence, all modes with $n \neq 0$ may be omitted and the theory is described by a two dimensional classical statistical theory involving only the $n = 0$ mode.

INTERACTING THEORY. For $g \neq 0$, it is expected that the non-zero Matsubara modes have thermal masses of order of at least T. The same procedure may hence

be followed in cases in which the $n = 0$ mode has a thermal mass smaller than T, which is especially true near a thermal phase transition [230]. Then, we can perturbatively integrate out all non-zero Matsubara modes, replacing the bare couplings in the action by renormalized ones in an expansion with respect to the in general small mass of the $n = 0$ mode in units of temperature. We denote these by $r + r_c \to m^2$ and $g \to \lambda$. In order to render the thermal mass of the zero mode smaller than T, we use the results from Ref. [267]. There, a $\epsilon = 3 - d$ expansion was used, resulting in $m^2 \sim \epsilon T^2 \ll T^2$. After removing the only UV divergence in this theory by introducing a one loop renormalized mass M^2 according to Eq. (3.11) below, the couplings to be inserted into the classical effective theory result to lowest order as

$$M^2 = \left(\frac{\sqrt{2}}{3}\pi T\right)^2, \tag{3.6}$$

$$\mathcal{G} = 8\sqrt{2}\pi \approx 35.5 \tag{3.7}$$

in the high-T quantum critical regime in $d = 2$.

DYNAMICS. While these arguments are strictly only valid for static properties, it has been shown that low frequency, low momentum dynamical properties such as the damping rate of the quasiparticle in the spectral function yields the same result in quantum and classical field theory after matching only *static* quantities [270, 271]. To do so, a canonically conjugate field momentum term $\pi = \partial_t \varphi$ needs to be introduced as done in Eq. (3.1). Although it is natural to choose the same form of the field momentum in the classical theory as in the quantum theory, this is not a unique choice as dynamical and static properties are independent in classical field theory [272]. In the following, we give a complementary discussion of the range of validity of the classical statistical approximation for the field dynamics from the perspective of the equilibrium limit of non-equilibrium quantum field theory.

Equilibrium classical field theory from nonequilibrium quantum field theory

Classical statistical field theory is a good approximation for quantum field theory in regimes in which the statistical fluctuations, given by the anticommutator of fields $F = \left\langle \frac{1}{2}\{\hat{\varphi}, \hat{\varphi}\}\right\rangle - \langle\hat{\varphi}\rangle^2$, are much larger than the quantum fluctuations, given by the commutator of fields (i.e. the spectral function) $\rho = i\left\langle[\hat{\varphi}, \hat{\varphi}]\right\rangle$,

$$|F(t_1, t_2; \mathbf{x}_1, \mathbf{x}_2)| \gg |\rho(t_1, t_2; \mathbf{x}_1, \mathbf{x}_2)|. \tag{3.8}$$

This classicality condition can be motivated from a slightly more restrictive, but rigorous condition derived from two-particle irreducible effective action meth-

ods in (non-)relativistic scalar field theories [265, 273] and is applicable both in equilibrium and far-from-equilibrium. In thermal equilibrium, F and ρ are only dependent on relative coordinates $t_1 - t_2$ and $\mathbf{x_1} - \mathbf{x_2}$ and are linked by the fluctuation-dissipation relations in temporal frequency space, $F = -i(1/2 + n_T)\rho$, where $n_T(\omega) = 1/(\exp(\omega/T) - 1)$ is the Bose-Einstein distribution. Although the classicality condition in Eq. (3.8) must strictly be fulfilled for all $(t_1, t_2; \mathbf{x}_1, \mathbf{x}_2)$, one may argue that a theory already behaves classically if it is dominated by modes fulfilling this condition. Consequently, a theory in thermal equilibrium behaves classically if the spectral function is dominated by momentum modes $\mathbf{p}$ with energy $\omega \ll T$ as then $n_T(\omega) \approx T/\omega \gg 1$, i.e. the Bose-Einstein distribution reduces to the classical Rayleigh-Jeans law.

In the presence of well-defined quasiparticles, ρ is strongly peaked at frequency $\omega \approx \sqrt{m^2 + \mathbf{p}^2}$ (neglecting the momentum dependence of the effective mass). At zero momentum, Eq. (3.8) can therefore then be specified to the condition

$$m^2 \ll T^2, \tag{3.9}$$

which coincides with the condition for dimensional reduction discussed above.

Moreover, directly at the phase transition $\mathcal{G} = \mathcal{G}_c$, the classicality condition above is exactly fullfilled as the zero-momentum spectral function diverges as $\omega \to 0$. This justifies why zero-momentum, zero-frequency properties of quantum field theories at finite temperature phase transitions are rigorously described by classical field theory [263].

Having discussed the validity of the classical statistical approximation, we discuss how to evaluate observables at finite temperature.

3.3 OBSERVABLES AT FINITE TEMPERATURE

We evaluate all observables $\mathcal{O}$ in thermal equilibrium according to the classical phase space average

$$\langle \mathcal{O}(\mathbf{x}, t) \rangle_{\mathrm{cl}} = \frac{1}{Z_{\mathrm{cl}}} \int \mathcal{D}\varphi_0 \mathcal{D}\pi_0 \mathcal{O}(\mathbf{x}, t) \exp\left(-H/T\right), \tag{3.10}$$

where $Z_{\mathrm{cl}} = \int \mathcal{D}\varphi_0 \mathcal{D}\pi_0 \exp\{-H/T\}$ is the classical partition sum at temperature T and the phase space measure at the initial time is given by $\mathcal{D}\varphi_0 \mathcal{D}\pi_0 = \Pi_{\mathbf{x}} \mathrm{d}\varphi(\mathbf{x}, t = 0) \mathrm{d}\pi(\mathbf{x}, t = 0)$. Numerically, we regularize the model on an $N \times N$ lattice with lattice spacing a_s and sample the canonical distribution with a hybrid Monte Carlo method. For details on the implementation, see section 3.4.

All ultraviolet divergences of the classical field theory are cancelled after lattice regularization [274] by introducing a one-loop renormalized mass[1] M according to

$$m^2 = M^2 - \frac{\lambda T}{2} \int \frac{\mathrm{d}^2\mathbf{p}}{(2\pi)^2} \frac{1}{\mathbf{p}^2 + M^2}, \tag{3.11}$$

which is the classical limit of the corresponding result in thermal quantum field theory [264, 267].

Furthermore, we use M as our unit and introduce dimensionless variables according to $\tilde{\mathbf{x}} = \mathbf{x}M, \tilde{t} = tM, \tilde{\varphi}_a = \varphi_a T^{-1/2}, \tilde{\pi}_a = \pi_a M^{-1} T^{-1/2}$. As a result, the theory only depends on a single dimensionless variable

$$\mathcal{G} = \frac{\lambda T}{M^2} \tag{3.12}$$

and results in the continuum, infinite volume limit are obtained by taking $a_s \to 0$, $N \to \infty$.

The fluctuation parameter $\mathcal{G}$ interpolates smoothly between the paramagnetic phase (for small $\mathcal{G}$), the high-T quantum critical regime (around $\mathcal{G} \approx 35$) [267], the finite temperature phase transition line at $\mathcal{G}_c \approx 61.44$,[2] and the symmetry broken phase for $\mathcal{G} > \mathcal{G}_c$. We confirmed this value in our Monte Carlo simulations by studying both the Binder cumulant, a measure for non-Gaussian fluctuations of the order parameter (see section 3.5), and critical behaviour of the spectral function near $\mathcal{G}_c$ in section 3.6.

DYNAMICAL CORRELATION FUNCTIONS. The dynamics of the field can be obtained from its equation of motion

$$\partial_{\tilde{t}}^2 \tilde{\varphi} = \Delta\tilde{\varphi} - \frac{m^2}{M^2}\tilde{\varphi} - \frac{\mathcal{G}}{6}\tilde{\varphi}^3 \tag{3.13}$$

on the lattice, with initial conditions obtained from Monte Carlo sampling. In the classical limit, the spectral function $\rho_{\mathrm{q}}(t, \mathbf{x}) = i\langle[\hat{\varphi}(\mathbf{x}, t), \hat{\varphi}(\mathbf{0}, 0)]\rangle$ is given in terms of the Poisson bracket according to $\rho(t, \mathbf{x}) = -\langle\{\varphi(\mathbf{x}, t), \varphi(\mathbf{0}, 0)\}_{PB}\rangle_{\mathrm{cl}}$ and can be obtained from the two-point correlation function using the classical fluctuation-dissipation relation [263, 264, 267] (FDR)

$$\rho(t, \mathbf{x}) = -\frac{1}{T}\partial_t \langle\varphi(t, \mathbf{x})\varphi(0, \mathbf{0})\rangle_{\mathrm{cl}}. \tag{3.14}$$

1 M is in general not the *full* renormalized mass, in particular it does not vanish at the phase transition. In the perturbative regime at small coupling and high temperatures (small $\mathcal{G}$), M is however very close to the full renormalized mass as pointed out in [274] and shown in section 3.6.

2 Note that this value is independent of the cut-off for the latter being small enough as we have removed all ultraviolet divergences with our renormalization procedure [275]. See Ref. [267] for a discussion of the behaviour of $\mathcal{G}$ across the phase diagram.

The spectral function can also be directly obtained from the Poisson bracket (PB),

$$\rho(\mathbf{x},t) = -\int \mathrm{d}^d\mathbf{z} \left\langle \left(\frac{\delta\varphi(\mathbf{x},t)}{\delta\varphi(\mathbf{z},0)} \frac{\delta\varphi(\mathbf{0},0)}{\delta\pi(\mathbf{z},0)} - \frac{\delta\varphi(\mathbf{x},t)}{\delta\pi(\mathbf{z},0)} \frac{\delta\varphi(\mathbf{0},0)}{\delta\varphi(\mathbf{z},0)} \right) \right\rangle_{\mathrm{cl}} \tag{3.15}$$

$$= \left\langle \frac{\delta\varphi(\mathbf{x},t)}{\delta\pi(\mathbf{0},0)} \right\rangle_{\mathrm{cl}}. \tag{3.16}$$

The latter functional derivative can be evaluated numerically by evolving the linearized field equations of motion in parallel,

$$\partial_t^2 \delta\tilde{\varphi} = \Delta\delta\tilde{\varphi} - \frac{m^2}{M^2}\delta\tilde{\varphi} - \frac{\mathcal{G}}{2}\tilde{\varphi}^2\delta\tilde{\varphi}, \tag{3.17}$$

which can also be interpreted as evolving a second field configuration with slightly perturbed initial momenta $\tilde{\pi}(0,\mathbf{x}) \to \tilde{\pi}(0,\mathbf{x}) + \epsilon\delta\tilde{\pi}(0,\mathbf{x})$ in the limit $\epsilon \to 0$. In section 3.4 we show that obtaining the spectral function numerically with Eq. (3.16) is equivalent to Eq. (3.14). In fact, Eq. (3.16) has some advantages over the FDR method as it does not show finite time-step pathologies for short times. Moreover, it can be used to evaluate the spectral function in regimes in which the FDR does not hold, such as for out-of-equilibrium initial states, as it is related to the numerical linear response theory introduced in Ref. [276, 277].

OTOC. The classical limit of the OTOC $-\langle[\hat{\varphi}(\mathbf{x},t),\hat{\varphi}(\mathbf{0},0)]^2\rangle$ can similarly be obtained by replacing commutators with Poisson brackets, giving

$$C(\mathbf{x},t) = \left\langle \{\varphi(\mathbf{x},t),\varphi(\mathbf{0},0)\}_{PB}^2 \right\rangle_{\mathrm{cl}} \tag{3.18}$$

$$= \left\langle \left(\frac{\delta\varphi(\mathbf{x},t)}{\delta\pi(\mathbf{0},0)} \right)^2 \right\rangle_{\mathrm{cl}}. \tag{3.19}$$

Hence, the only difference to the evaluation of the spectral function in Eq. (3.16) is to square the Poisson bracket *before* averaging over the thermal initial conditions. This means that fluctuations between individual realizations do not cancel out and the chaotic growth of initial perturbations is revealed.

In our simulations, we initialize the perturbation of the momentum as $\delta\pi(\mathbf{x},0) = c\delta(\mathbf{x})$ with a random number c uniformly drawn from a small interval centred around zero, while the field perturbation vanishes initially. Subsequently, we observe the growth of the latter by evolving Eqs. (3.13,3.17) in parallel. We found that choosing an initial condition with $\delta\pi(\mathbf{x},0) = 0$, $\delta\varphi(\mathbf{x},0) = c\delta(\mathbf{x})$ as initial condition, i.e. the OTOC $\langle\{\varphi(\mathbf{x},t),\pi(\mathbf{0},0)\}^2\rangle$, gives similar results as the one in Eq. (3.19).

3.4 NUMERICAL IMPLEMENTATION

DISCRETIZATION. The Hamiltonian in Eq. (3.1) in terms of the rescaled variables discretized on an $N \times N$ square lattice with rescaled lattice spacing $\tilde{a}_s = a_s M$ is given by

$$H/T = \frac{1}{2}\tilde{a}_s^2 \sum_{\mathbf{x}} \left[\tilde{\pi}_{\mathbf{x}}^2 - \tilde{\varphi}_{\mathbf{x}} \frac{1}{\tilde{a}_s^2} \sum_{\mathbf{e}_i} (\tilde{\varphi}_{\mathbf{x}+\mathbf{e}_i} - 2\tilde{\varphi}_{\mathbf{x}} + \tilde{\varphi}_{\mathbf{x}-\mathbf{e}_i}) + \frac{m^2}{M^2}\tilde{\varphi}_{\mathbf{x}}^2 + \frac{\mathcal{G}}{12}\tilde{\varphi}_{\mathbf{x}}^4 \right], \quad (3.20)$$

where we have partially integrated the gradient term in order to write it in terms of a second order discretization of the resulting Laplacian. In the latter, $\mathbf{e}_i$ denote the lattice unit vectors. The bare mass squared is given in terms of the discretized gap equation (Eq. (3.11)) as

$$\frac{m^2}{M^2} = 1 - \frac{\mathcal{G}}{2V} \sum_{\mathbf{p}} \frac{1}{\mathbf{p}^2 + 1}, \quad (3.21)$$

where the lattice momenta are given by[210]

$$\mathbf{p}^2 = \sum_{i=1}^{2} \frac{4}{\tilde{a}_s^2} \sin^2\left(\frac{\pi n_i}{N}\right) \quad (3.22)$$

with $n_i \in \{0, .., N-1\}$.

We use a leapfrog discretization with time step $d\tilde{t} = dtM$ for the equations of motion of the field,

$$\begin{aligned} &\frac{\tilde{\varphi}_{\mathbf{x}}(t+1) - 2\tilde{\varphi}_{\mathbf{x}}(t) + \tilde{\varphi}_{\mathbf{x}}(t-1)}{d\tilde{t}^2} \\ &= \left[\frac{1}{\tilde{a}_s^2} \sum_{\mathbf{e}_i} (\tilde{\varphi}_{\mathbf{x}+\mathbf{e}_i}(t) - 2\tilde{\varphi}_{\mathbf{x}}(t) + \tilde{\varphi}_{\mathbf{x}-\mathbf{e}_i}(t)) - \frac{m^2}{M^2}\tilde{\varphi}_{\mathbf{x}}(t) - \frac{\mathcal{G}}{6}\tilde{\varphi}_{\mathbf{x}}^3(t) \right], \end{aligned} \quad (3.23)$$

as well as for the equations of motion of the field perturbation,

$$\begin{aligned} \delta\tilde{\varphi}_{\mathbf{x}}(t+1) = 2\delta\tilde{\varphi}_{\mathbf{x}}(t) - \delta\tilde{\varphi}_{\mathbf{x}}(t-1) + d\tilde{t}^2 \times \\ \left[\frac{1}{\tilde{a}_s^2} \sum_{\mathbf{e}_i} (\delta\tilde{\varphi}_{\mathbf{x}+\mathbf{e}_i}(t) - 2\delta\tilde{\varphi}_{\mathbf{x}}(t) + \delta\tilde{\varphi}_{\mathbf{x}-\mathbf{e}_i}(t)) - \frac{m^2}{M^2}\delta\tilde{\varphi}_{\mathbf{x}}(t) - \frac{\mathcal{G}}{2}\tilde{\varphi}_{\mathbf{x}}^2(t)\delta\tilde{\varphi}_{\mathbf{x}}(t) \right]. \end{aligned} \quad (3.24)$$

The initial state of the fields are given by Monte Carlo sampling as described below whereas we initialize the perturbation of the momenta as

$$\delta\tilde{\pi}_{\mathbf{x}}(0) = c\delta_{\mathbf{x}\mathbf{0}} \quad (3.25)$$

where c is a random number drawn uniformly from the interval $[-0.1, 0.1]$ and the field perturbation $\delta\tilde{\varphi}_{\mathbf{x}}(0) = 0$. We have checked that the results for the Lyapunov exponent and the butterfly velocity do not depend on the choice of interval.

DISCRETIZED OTOC. As we need to prepare an initial state for the perturbation $\sim \delta(\mathbf{x})$ in the continuum, and therefore $\sim \frac{1}{\tilde{a}_s^d}\delta_{\mathbf{x0}}$ on the d-dimensional lattice, the lattice spacing dependence is given as

$$\left(\frac{\delta\tilde{\varphi}(t,\mathbf{y})}{\delta\tilde{\pi}(0,\mathbf{x})}\right)^2 \to \tilde{a}_s^{2d}\left(\frac{\delta\tilde{\varphi}_{\mathbf{y}}(t)}{\delta\tilde{\pi}_{\mathbf{x}}(0)}\right)^2, \tag{3.26}$$

i.e. the results obtained with the initial state in Eq. (3.25) have to be *divided* by $\tilde{a}_s^{2d}$ to obtain results independent of the lattice spacing. We have furthermore tested that using double or quadruple computer precision does not result in a considerable difference.

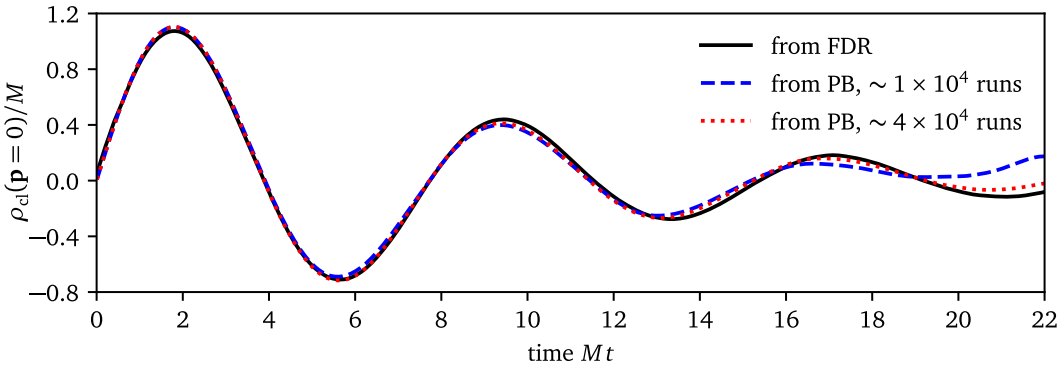

Figure 3.1: **Comparison of two different numerical approaches to obtain the spectral function.** Spectral function at zero momentum for $\mathcal{G} = 20$ as obtained from the fluctuation-dissipation relations (FDR) (Eq. (3.14)) and the Poisson Bracket (PB) (Eq. (3.16)), where the former is fully converged with respect to the number of runs. The latter converges to the FDR result as the number of runs is increased. Deviations at early times are due to the finite time step (see text).

SPECTRAL FUNCTION FROM FDR AND PB. In Fig. 3.1 we compare the spectral function as obtained from the fluctuation dissipation relation (Eq. (3.14)) and the Poisson bracket (Eq. (3.16)). Both methods converge for intermediate and late times as the number of runs is increased. Deviations occur at early times as the spectral function obtained from the FDR, opposed to the one from the PB, does not exactly vanish at initial time due to the finite time step [264].

CRITICAL SPECTRAL FUNCTION. In order to obtain enough statistics to evaluate the critical spectral function in Fig. 3.5, we exploit time-translational invariance [263] of thermal equilibrium by transforming to Wigner coordinates $\rho(t_1,t_2) = \rho(T = \frac{1}{2}(t_1+t_2), \tau = t_1 - t_2)$ and averaging over the 'center of mass time' T. To transform

to Fourier space with respect to the relative coordinate τ, we used the antisymmetry of ρ to perform the discrete sine transform

$$\rho(t, \mathbf{p} = 0) = \frac{a_s^d}{N^d} \sum_{\mathbf{x}} \left(2 \int d\tau \rho_{\mathbf{x}}(\tau) \sin(\omega\tau) \right), \tag{3.27}$$

where d is the spatial dimension. We have also used a Gaussian filter to reduce finite-time oscillations in the Fourier transformed spectra, but have checked that the overall behaviour is robust against change of filter window.

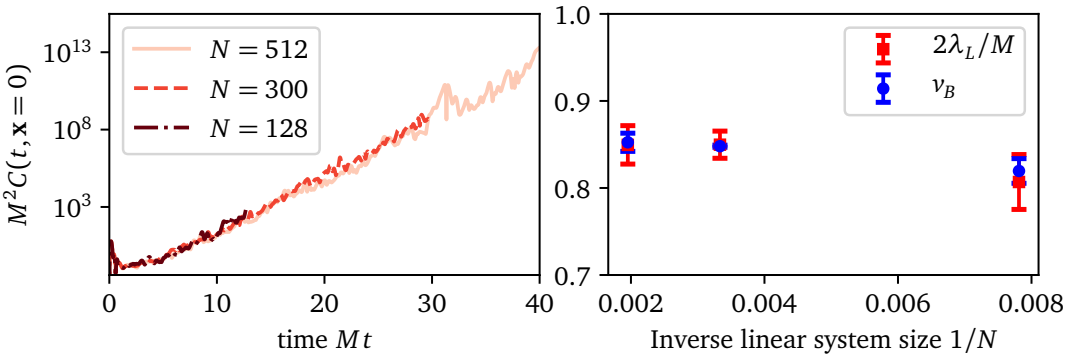

Figure 3.2: **Convergence of the OTOC at $\mathcal{G} = 61.5$ with system size.** Both the convergence of the local OTOC (left) as well as butterfly velocity and lyapunov exponent (right) with respect to system size indicate that there are no considerable finite size effects for $N = 300$, the system size chosen for most data shown here. We stopped the simulations at times $t \sim Na_s$ to avoid boundary effects.

HYBRID MONTE CARLO. We start the Monte Carlo algorithm by initializing the fields in a state drawn from the thermal state of the free theory ($\mathcal{G} = 0$) with a Gaussian of zero mean and standard deviation $1/\sqrt{(\tilde{a}_s(m^2/M^2))^2 + d}$, with $d = 2$ being the spatial dimension [210]. This initialization has lead a much shorter thermalization time compared to initialization with a standard deviation independent of $\mathcal{G}$. We then iterate the following Hybrid/Hamiltonian Monte Carlo (HMC) step introduced in the context of lattice QCD [278, 279].

1. Draw some initial $\tilde{\pi}(\mathbf{x})$ from a Gaussian distribution with zero mean and standard deviation $1/\sqrt{\tilde{a}_s}$. Evaluate the Hamiltonian, giving the energy E_1/T.

2. Evolve this state in time using Eq. (3.23) with step size $d\tilde{t} = \epsilon$ for a number of time steps N_t.

3. Evaluate the Hamiltonian again, giving E_2/T.

4. Accept the new configuration with probability $\min(1, \exp(-(E_2/T - E_1/T))$.

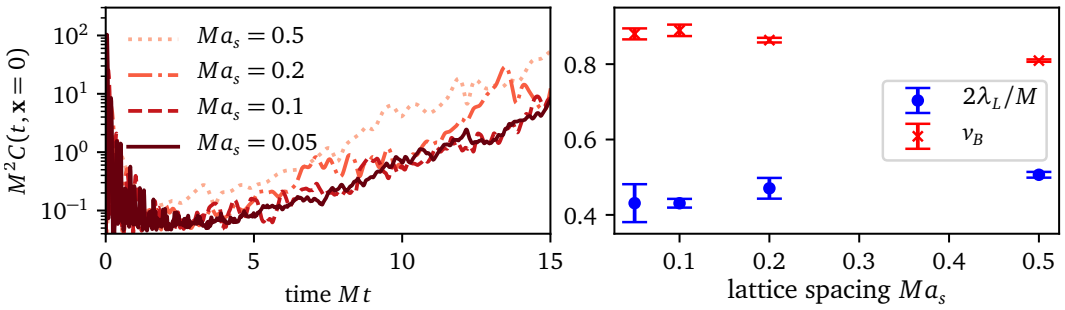

Figure 3.3: **Convergence of the out-of-time ordered correlator with lattice spacing.** (left) Although quantitative differences between lattice spacings are visible in the out-of-time correlator at $\mathcal{G} = 35$, they show the same qualitative behaviour with lattice spacings $Ma_s \leq 0.1$ oscillating around an exponential growth. The oscillations become smaller when increasing the number of Monte Carlo runs (not shown). (right) Butterfly velocity and Lyapunov exponent as a function of lattice spacing. Both quantities are independent of lattice spacing within error bars at around $Ma_s = 0.2$, the value chosen for all simulations shown in the following.

We have usually chosen $\epsilon \approx 0.01\tilde{a}_s$ and $\epsilon N_t \approx 1$, yet large values of $\mathcal{G}$ required slightly smaller ϵ. Furthermore, the number of time steps was randomized by $\pm 10\%$ in order to circumvent possible periodicities of the trajectories. We started the measurement runs from a pre-equilibrated state obtained after approximately $1000 - 5000$ Monte Carlo steps (thermalization as monitored from the convergence of the energy was usually reached after ≈ 50 steps for small $\mathcal{G}$ and took longer for larger $\mathcal{G}$ due to critical slowing down). Measurements were taken after approximately $30 - 50$ steps, where the autocorrelation of the fields with the initial (pre-equilibrated) state was negligible. This turned out not to be the case in the symmetry broken phase due to the difficulty of escaping one of two deep minima of the effective potential. We hence used independently thermalized MC initial conditions with approx 5000 Monte Carlo steps. Furthermore, we checked for several values of $\mathcal{G}$ that we averaged over enough realizations (usually $10^3 - 10^4$) by checking convergence of Jackknife errors for the butterfly velocity and Lyapunov exponent from a binning analysis [280].

CONVERGENCE WITH SYSTEM SIZE AND LATTICE SPACING. In Figs. 3.3,3.2 we compare the time evolution of the local OTOC $C(\mathbf{x} = 0, t)$ as well as the butterfly velocity and Lyapunov exponent for different lattice spacings and system sizes. No considerable dependency on those two parameters is seen around the conventionally chosen ones ($Ma_s = 0.2, N = 300$). We find a tendency for larger differences between different lattice spacings than between different system sizes, indicating that the

OTOC and its properties have a stronger dependence on the UV than the infrared cut-off. This also holds near the phase transition, since the OTOC is not sensitive to critical slowing down.

JACKKNIFE BINNING ANALYSIS. In order to estimate errors and convergence with respect to sample size, we employed a jackknife binning analysis. Dividing up the ensemble of samples into M blocks of size k, it proceeds by calculating an observable $\mathcal{O}$ (such as the Lyapunov exponent) of an ensemble-average in which one of those blocks has been omitted. Denoting $\langle\mathcal{O}\rangle$ the observable calculated on the whole ensemble and $\langle\mathcal{O}\rangle_i$ the one where block i has been removed before averaging, the jackknife estimate for the mean and standard deviation are given by [281]

$$\langle\mathcal{O}\rangle_{JK} = \langle\mathcal{O}\rangle - (M-1)\left(\frac{1}{M}\sum_{i=1}^{M}\langle\mathcal{O}\rangle_i - \langle\mathcal{O}\rangle\right), \tag{3.28}$$

$$\Delta\mathcal{O} = \sqrt{\frac{M-1}{M}\sum_{i=1}^{M}\left(\langle\mathcal{O}\rangle_i - \frac{1}{M}\sum_{i=1}^{M}\langle\mathcal{O}\rangle_i\right)}. \tag{3.29}$$

In order to check convergence of the errors with respect to the sample size, the standard deviation needs to be plotted as a function k for a fixed sample size. If the standard deviation converges, then so has the sample average.

3.5 PHASE TRANSITION

The model considered in this chapter (c.f. Eq. (3.1)) exhibits an equilibrium phase transition from a symmetric phase with $\langle\varphi\rangle = 0$ to a symmetry broken phase with $\langle\varphi\rangle \neq 0$. Due to our renormalization procedure, the critical value of $\mathcal{G}$ does not strongly depend on the lattice spacing and can be found by standard finite size scaling procedures at a small enough, but fixed a_s. Here, we study the Binder cumulant B_4 [282] given by

$$B_4 = 1 - \frac{\langle\varphi^4\rangle}{3\langle\varphi^2\rangle^2} \tag{3.30}$$

with limits $B_4 \to \frac{2}{3}$ for $\mathcal{G} \to \infty$ and $B_4 \to 0$ for $\mathcal{G} \to 0$ and a universal value $B_{4,c} \approx 0.6104$ [283] at the phase transition. In above expression, $\varphi = \frac{1}{N^2}\sum_{\mathbf{x}}\varphi_{\mathbf{x}}$ denotes the volume averaged field.

In Fig. 3.4 we determine the critical Binder cumulant $B_{4,c}$ as well as fluctuation parameter $\mathcal{G}_c$ from the intersection of $B_4(\mathcal{G})$ of the three largest system sizes considered. We find $\mathcal{G}_c = 61.38 \pm 0.16$ and $B_{4,c} = 0.604 \pm 0.004$ consistent with previous results [275, 283] and with errors mainly resulting from residual finite-size

effects. Furthermore, we show the finite size collapse of system sizes $N \geq 32$, assuming that B_4 is directly a finite size scaling function of the form $B_4 = B_4((\mathcal{G} - \mathcal{G}_c)N^{1/\nu}, \dots)$.

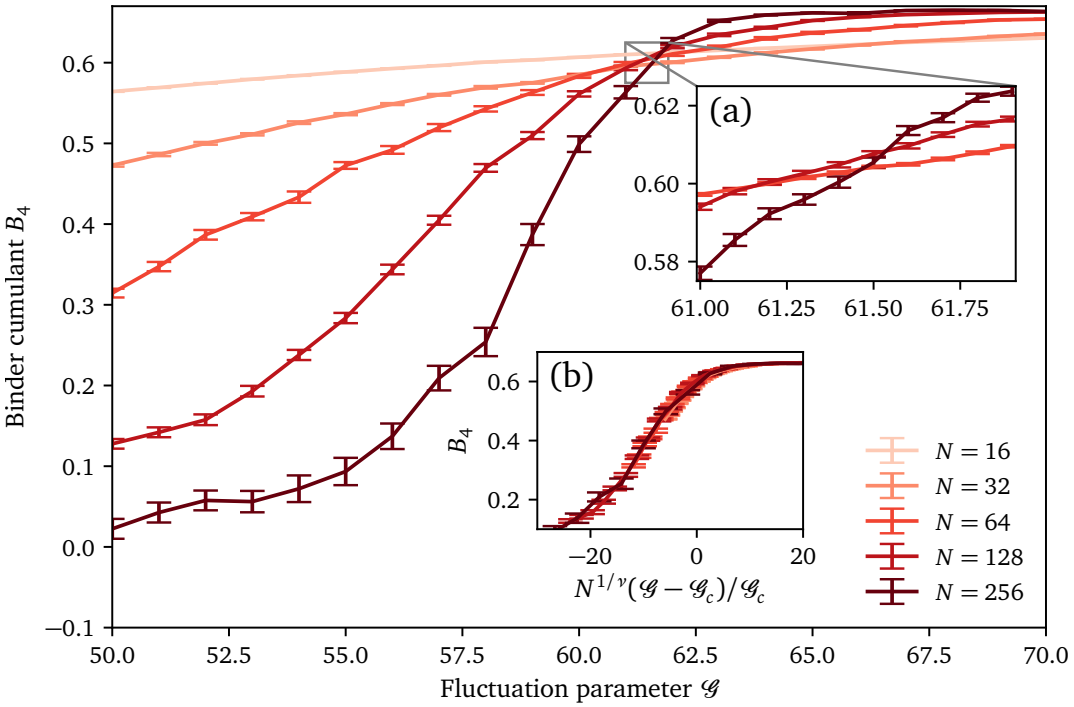

Figure 3.4: **Phase transition.** Binder cumulant as defined in Eq. (3.30) as a function of the fluctuation parameter $\mathcal{G}$ for different system sizes, where the inflexion point as determined from the largest system sizes in inset (a) reveals the critical fluctuation parameter to be $\mathcal{G}_c \approx 61.4$ in agreement to previous studies [275]. Rescaling all curves as shown in inset (b) with the known critical exponent $\nu = 1$ for the 2D Ising universality class leads to a good collapse over a large parameter regime. Lines connecting data points are solely a guide for the eyes. Error bars are obtained from a jackknife binning analysis.

3.6 QUASIPARTICLES AND CRITICAL BEHAVIOUR IN THE SPECTRAL FUNCTION

Many properties of a many-body system can be deduced from the nature of its elementary excitations and one might expect scrambling and the spreading of OTOCs to be primarily determined by their properties. We discuss in the next section that this is in fact not the case. Before doing so, we study the spectral function, discussing the qualitatively different regimes for small $\mathcal{G}$ and near the phase transition at $\mathcal{G}_c$.

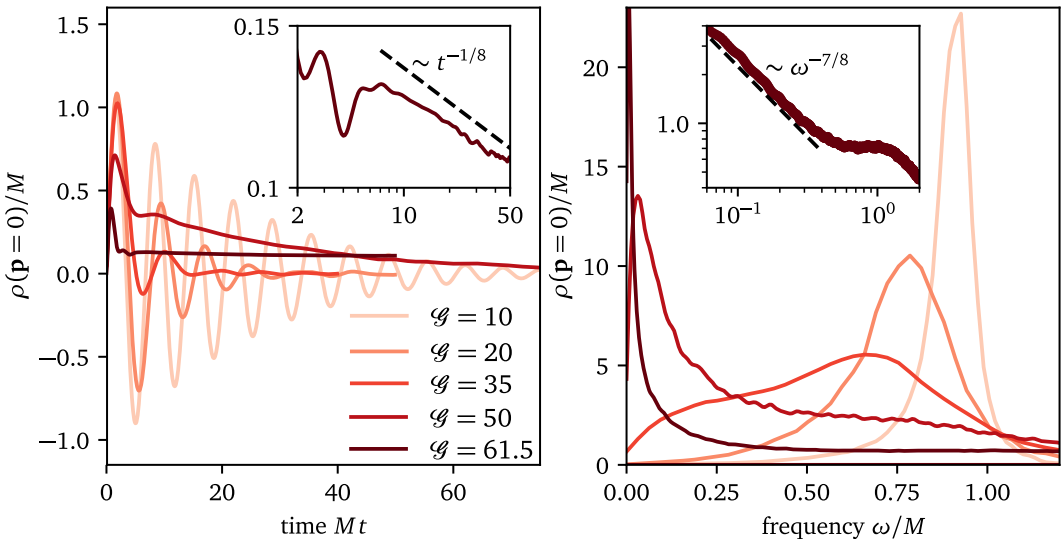

Figure 3.5: **Spectral function in real time (left) and frequency (right).** For small $\mathcal{G}$, the real time spectral function exhibits weakly damped oscillations, corresponding to a sharp quasiparticle peak with mass gap approximately given by the one-loop renormalized mass M. As $\mathcal{G}$ is increased, higher loop corrections become important, leading to stronger damping and a shift of the maximum away from M. At $\mathcal{G} = 50$, the spectral function already exhibits critical behaviour, showing an exponential decay with correlation length $\xi_t \approx 30M$. Close to the phase transition, $\mathcal{G} = 61.5$, critical algebraic decay becomes apparent both in time and frequency space as ξ_t is larger than the studied timescales (insets). Dashed lines correspond to the expectations from the 2D static Ising universality class and assuming a dynamic critical exponent $z = 2$. In this plot, $N = 128, a = 0.2$ except for $\mathcal{G} = 61.4$, where $N = 256$. Some regimes of this figure have been previously studied in Refs. [263, 264, 267].

WELL DEFINED QUASIPARTICLES AT SMALL $\mathcal{G}$. In weakly interacting theories and in the absence of instabilities, the effective low-energy excitations are generically given by quasiparticles with masses and lifetimes modified by interactions. In real scalar field theory described by the Hamiltonian in Eq. (3.1), free relativistic bosonic excitations with dispersion $\omega(\mathbf{p}) = \sqrt{\mathbf{p}^2 + m^2}$ are dressed by classical statistical (thermal) fluctuations[3]. To make this statement more explicit, consider the spectral function $\rho(\omega, \mathbf{p})$, which can be written as [264, 284]

$$\rho(\omega, \mathbf{p}) = \frac{-2\,\mathrm{Im}\Sigma(\omega, \mathbf{p})}{[\omega^2 + \mathbf{p}^2 + m^2 - \mathrm{Re}\Sigma(\omega, \mathbf{p})]^2 + [\mathrm{Im}\Sigma(\omega, \mathbf{p})]^2} \tag{3.31}$$

in terms of the (retarded) self-energy $\Sigma(\omega, \mathbf{p})$.

When $\Sigma \to 0$, the spectral function exhibits δ peaks at the free particle excitation energies $\pm\sqrt{\mathbf{p}^2 + m^2}$. When $\Sigma \neq 0$, sharp peaks still dominate the spec-

3 In the dimensionally reduced theory, quantum fluctuations only enter through the effective couplings M and $\mathcal{G}$ chosen in the classical Hamiltonian.

tral function as long as the damping rate $-\mathrm{Im}\Sigma(\omega,\mathbf{p})/\omega$ is much smaller than $\mathbf{p}^2+m^2-\mathrm{Re}\Sigma(\omega,\mathbf{p})$. The spectral function can then be approximated by a relativistic Breit-Wigner function, reading at zero momentum,

$$\rho_{QP}(\omega,\mathbf{p}=\mathbf{0})=\frac{2\omega\Gamma}{(\omega^2-m_R^2)^2+\omega^2\Gamma^2}, \tag{3.32}$$

where $m_R^2=m^2+\mathrm{Re}\Sigma$ is the renormalized mass of the quasiparticle (QP) state and $\Gamma=-\mathrm{Im}\Sigma/m_R$ is its inverse lifetime.

In Fig. 3.5 we display the real-time and real-frequency spectral function obtained from the classical FDR in Eq. (3.14). For $\mathcal{G}=10$, exponentially damped oscillations in the real-time domain correspond to a quasiparticle peak with Breit-Wigner line shape in the frequency domain, with oscillation frequency and damping rate corresponding to the position and width of the peak, respectively. Fitting the line shape in Eq. (3.32) to the data, we determine the mass of the quasiparticle as $m_R\approx 0.91M$ and the damping rate (inverse lifetime) as $\Gamma\approx 0.09/M$. By studying the spectral function with $\mathbf{p}>0$ (not shown in plot) we furthermore find that the effective dispersion of the quasiparticles is given by $\approx\sqrt{m_R^2+\mathbf{p}^2}$, i.e. the momentum dependence of the effective mass can be approximately neglected in this regime. However, both the height of the peak and the damping rate becomes smaller as $\mathbf{p}$ is increased, which is primarily a result of the sum rule $\int_0^\infty \mathrm{d}\omega/(2\pi)\omega\rho(\omega,\mathbf{p})=1$ (i.e. the equal-time commutation relations) as discussed in Ref. [284]. We can conclude that in this regime, well-defined quasiparticles are present, with self-energy corrections beyond the one-loop contribution in Eq. (3.11) only playing a minor role. For $\mathcal{G}=20$, the quasiparticle peak broadens and shifts to smaller frequencies as higher-loop corrections become more important, with fit parameters resulting as $m_R\approx 0.78M$ and $\Gamma\approx 0.24/M$. On the $N=100$ lattice, we find the height of the quasiparticle peak at the first nonzero lattice momentum (not shown in plot) to be already an order of magnitude smaller. This shows that the field dynamics are dominated by small momentum excitations.

At $\mathcal{G}=35$ (the value corresponding to the high-T quantum critical regime), the spectral function exhibits overdamped behaviour in real time and a double peak structure is present in the frequency domain. Apart from the remnant of the quasiparticle peak at larger frequencies, a smaller contribution at near-zero frequencies anticipates the low-frequency behaviour of the spectral function near the critical point. This double-peak structure indicates an intricate interplay between diffusive modes dominating at the critical point and the quasiparticle remnant from the paramagnetic phase, leading to strongly correlated dynamics [264].

Finally we note that the classical spectral functions obtained here are directly related to the ones in the high-T quantum theory by the matching procedure

described in chapter 3.2: Inserting the renormalized mass M obtained from dimensional reduction leads to the quantum results for m_R and the damping rate as shown in Refs. [266, 270].

UNIVERSAL BEHAVIOUR NEAR $\mathcal{G}_c$. At a phase transition, the spectral function exhibits a qualitatively different behaviour by acquiring a universal scaling form [263]

$$\rho(t, \mathbf{p} = 0) = t^{\frac{2-\eta}{z}-1} g\left(\frac{t}{\xi_t}\right), \tag{3.33}$$

with anomalous dimension η, and dynamic critical exponent z, which in principle is independent of static critical exponents near thermal (i.e. classical) phase transitions [272]. The universal scaling function g is expected to behave as

$$g\left(\frac{t}{\xi_t}\right) \sim \exp\left(-\frac{t}{\xi_t}\right), \tag{3.34}$$

with a diverging temporal correlation length ξ_t at the critical point. With the exactly known static critical exponent [285] $\eta = 0.25$ and the previously found dynamic critical exponent $z = 2$ in this model [263, 286], we expect an algebraic behaviour $\rho(t, \mathbf{p} = 0) \sim t^{-1/8}$ and $\rho(\omega, \mathbf{p} = 0) \sim \omega^{-7/8}$ for long times and small frequencies at the critical point $\mathcal{G}_c$.

In the insets of Fig. 3.5, we display the critical spectral function at $\mathcal{G} = 61.5 \approx \mathcal{G}_c$ on a double logarithmic scale, recovering the expected algrebraic behaviour of the spectral function with exponents in rough agreement with the expected values (black dashed lines). As we find no exponential decay on the observed time scales we conclude that $\xi_t \gg 50/M$ for $\mathcal{G} = 61.5$, with the algebraic decay setting in at around $Mt = 10$. Remarkably, we already find near-critical behaviour of the spectral function for $\mathcal{G} = 50$, however, with the exponential decay of $g(t/\xi_t)$ dominating the dynamics. From a fit to an exponential for times $Mt > 20$ we find $\xi_t \approx 30/M$. The oscillatory behaviour before the algebraic/exponential decay is related to short-time high-momentum physics, that are remnants of quasi-particles [263]. At higher momentum (not plotted), we indeed find well-defined quasiparticle peaks even at $\mathcal{G}_c$ with a linear dispersion $\mathbf{!} = |\mathbf{p}|$, i.e. with a group velocity equal to the speed of light, albeit with drastically reduced weight compared to the zero-frequency, zero-momentum peak.

ORDERED PHASE $\mathcal{G} > \mathcal{G}_c$. In the symmetry broken phase (not plotted) we again find a quasiparticle peak, however with a significantly higher renormalized mass $m_R \approx 3.5M$ and a large broadening of $\Gamma \approx 1.5/M$ at $\mathcal{G} = 90$. These gapped excitations correspond to the amplitude fluctuations in the minima of the effective

potential. There are no gapless Goldstone modes due to the discrete $\mathbb{Z}_2$ symmetry of the order parameter.

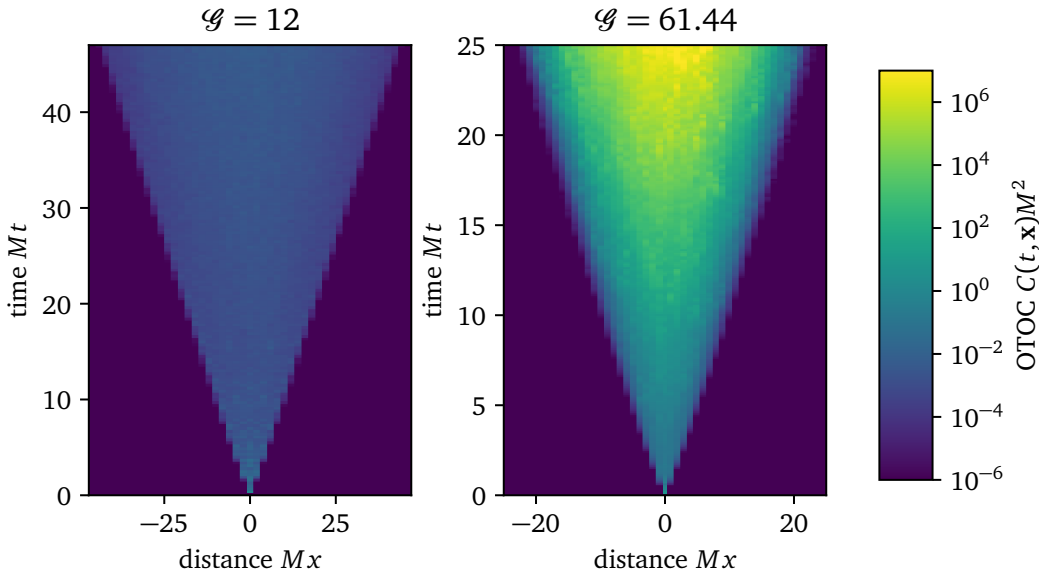

Figure 3.6: **Ballistic spreading of OTOC.** Cut of the OTOC along one axis. For all values of $\mathcal{G}$ (left: $\mathcal{G} = 12$,, right: $\mathcal{G} = 61.44$) studied in this chapter, we have found ballistic spreading of the OTOC. However, both the butterfly velocity and the Lyapunov exponent associated with the exponential growth within the lightcone showed a strong dependence on $\mathcal{G}$. Due to the ambiguity of the color scale, it is not possible to read off the butterfly velocity directly from this plot. For a detailed discussion see Sec. 3.7.2.

3.7 MANY-BODY CHAOS

By studying the spectral function we have found qualitatively distinct regimes characterized by the presence of well-defined quasiparticles for small $\mathcal{G}$, a cross-over to a broad spectrum at $\mathcal{G} \approx 35$ and universal, algebraic low-frequency behaviour near $\mathcal{G}_c$ without well-defined quasiparticle excitations at zero momentum. In this section, we study the dependence of the OTOC $C(\mathbf{x}, t)$ on $\mathcal{G}$.

BALLISTIC SPREADING FOR ALL $\mathcal{G}$. In Fig. 3.6 we display a cut of the OTOC $C(\mathbf{x}, t)$ along one real-space axis for small $\mathcal{G}$ and near $\mathcal{G}_c$, showing ballistic spreading. The same holds for all other values of $\mathcal{G}$ studied in this chapter. Furthermore, we find perturbations to spread throughout the lightcone. As indicated by the logarithmic color scale, we also find exponential growth of the OTOC within the light-cone, with the Lyapunov exponent λ_L associated to that growth being strongly dependent on

the fluctuation parameter $\mathcal{G}$. The ballistic spreading needs to be contrasted with the emergent non-relativistic dynamic exponent $z = 2$ found from the spectral function at the phase transition as the OTOC still shows a "$z = 1$" behaviour.

ABSENCE OF CRITICAL SLOWING DOWN IN THE OTOC. In Fig. 3.7, we show the time evolution of the local OTOC for several values of $\mathcal{G}$. The short time behaviour ($Mt < 2$) is not dependent on $\mathcal{G}$ and is merely related to the initial conditions chosen: The initially non-vanishing momentum perturbation at the origin is converted into a δ-function-like shape of the field perturbation as $\delta\pi = \partial_t \delta\varphi^4$. Subsequently, the dynamics is dominated by the large gradient to neighbouring lattice sites, i.e. the Laplacian in the equations of motion (see Eq. (3.17)) is far larger than the other terms. As soon as the differences to neighbouring lattice sites are washed out, the non-linear dynamis created by the interplay between the term proportional to the mass squared and the one including the coupling to the field dominates. Importantly, we find that for all values of $\mathcal{G}$ these late-time dynamics are given by an exponential growth of $C(\mathbf{x} = 0, t)$, with an approximately constant exponent for late times. This behaviour has to be contrasted with the spectral function, for which we found algebraically slow decay for $Mt \gtrsim 10$ at $\mathcal{G} = \mathcal{G}_c$ (see Fig. 3.5). For $\mathcal{G} \gtrsim 50$, the temporal correlation length is larger than $Mt = 30$ such that the time scales shown in Fig. 3.7 are well within the regime showing exponential damping in the spectral function, where the decay rate diverges as the phase transition is approached. The OTOC instead *grows* exponentially with an increasing exponent as $\mathcal{G}$ increases.

To assess these findings more quantitatively, we study the Lyapunov exponent of the exponential growth, the space-time shape of the OTOC, the butterfly velocity associated to the ballistic spreading and fluctuations of the OTOC in the following. We have checked in section 3.4 that all our results are independent of both lattice spacing and system size and thus determine the chaotic properties of the continuum field theory in the thermodynamic limit.

3.7.1 *Lyapunov exponent*

Lyapunov exponents are a standard measure of chaos in classical dynamics [287], quantifying the rate of separation between two neighbouring trajectories. In general, the number of Lyapunov exponents is equal to the number of degrees of freedom, quantifying the rate of change associated with a perturbation in every direction of phase space. In our case, the number of degrees of freedom is given by $2 \times$

4 This explains why the OTOC $\langle\{\varphi(\mathbf{x}, t), \pi(\mathbf{x}, 0)\}\rangle$ gives the same results as the one studied here.

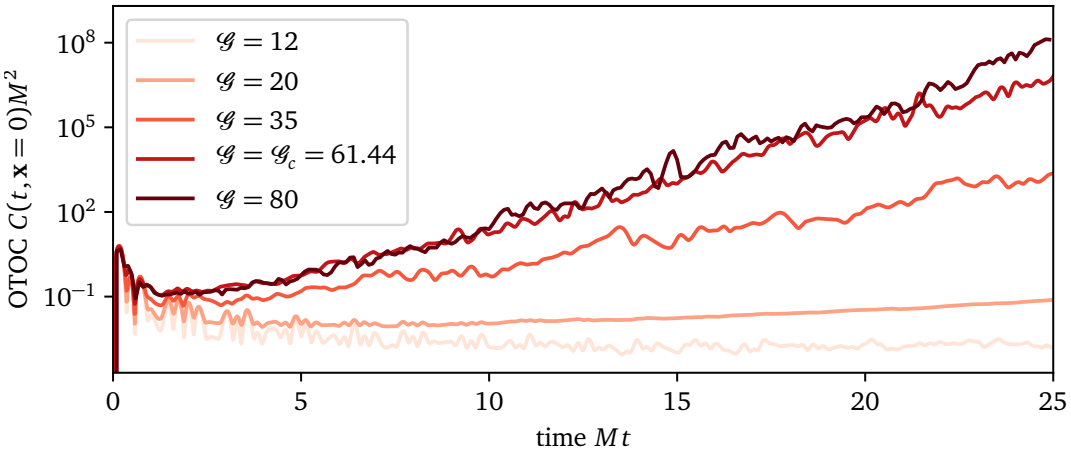

Figure 3.7: **Local OTOC.** After the trivial short-time dynamics related to the spreading of a sharply peaked momentum-field perturbation, chaotic exponential growth sets in with late time behaviour dominated by the largest Lyapunov exponent, which is strongly dependent on the value of the fluctuation parameter $\mathcal{G}$. For the smallest value $\mathcal{G} = 12$, exponential growth only sets in after the time scale shown here; we hence evolved larger systems to longer times to determine the Lyapunov exponent in that case.

$N^2 \approx 10^5$ for the typical lattice sizes, so that determining the whole Lyapunov spectrum (scaling quadratically with the number of degrees of freedom [288]) is not constructive. We hence focus on the largest Lyapunov exponent λ_L (in the following simply called "the Lyapunov exponent") by defining

$$\lambda_L = \lim_{t\to\infty} \frac{1}{2t} \ln C(\mathbf{x} = 0, t). \tag{3.35}$$

Here the limit of vanishing perturbation is implicit in this definition as we are evaluating the OTOC directly in this limit, c.f. Eq. (3.17). In practice, we determine the Lyapunov exponent by a fit with an exponential to $C(\mathbf{x} = 0, t)$ at late times. Note that in this semi-classical model the OTOC is not expected to saturate, whereas, in a full quantum theory the OTOC is expected to deviate from the semi-classical exponential growth around the Ehrenfest time [268]. Our classical theory may hence be viewed as an effective theory for a quantum system at high temperatures such that the time scales studied here are below the Ehrenfest time of the corresponding quantum theory. Similar conclusions have been drawn previously from the perspective of semi-classical trajectories [268] and for fidelity-OTOCs in the Dicke model[289]: In regimes dominated by classical modes, the exponential growth of the OTOC is described by the classical statistical approximation. Further evidence may be obtained from the large-N, high T calculation in Ref. [37]. There, it was found that the rungs in the Bethe-Salpeter equation for the OTOC contributing to the exponential growth are dominated by classical modes with $\mathbf{p} < T$. This may

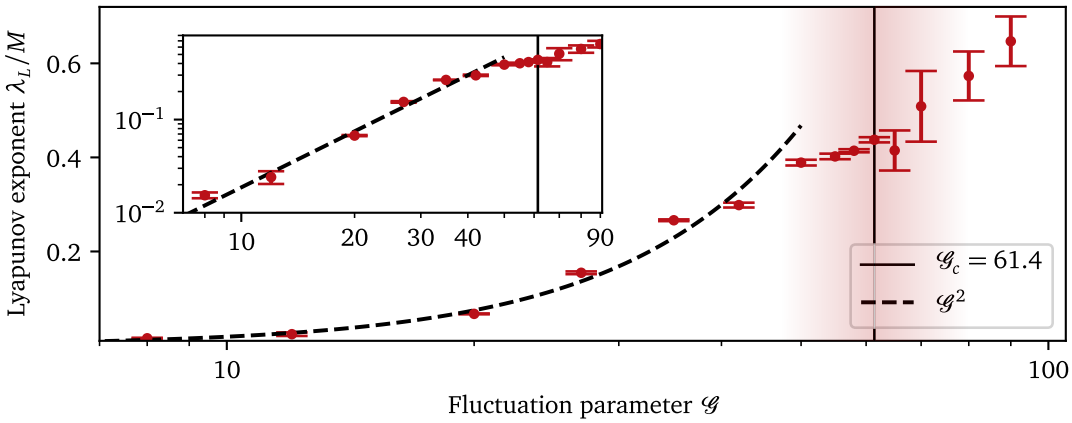

Figure 3.8: **Lyapunov exponent.** The Lyapunov exponent λ_L increases as a function of $\mathcal{G}$, with a different approach to the phase transition from above and below. The red shading indicates the range of $\mathcal{G}$ in which critical slowing down was found in the spectral function. An approximate power-law behaviour $\sim \mathcal{G}^2$ is found for $\mathcal{G} \lesssim 40$ (see inset). Error bars are statistical errors obtained from a jackknife binning analysis detailed in section 3.4.

be understood from the fact that the "Wightman" correlators responsible for the chaotic contributions of those rungs are at $T \gg \omega$ proportional to the correlation functions $\langle\varphi\varphi\rangle$, which are hence strongly peaked at $\omega \approx \sqrt{m_R^2 + \mathbf{p}^2}$ and have a weight strongly decreasing with $\mathbf{p}$ (due to the FDR, c.f. the discussion of the finite $\mathbf{p}$ behaviour of the spectral function in chapter 3.6). While we determined λ_L from the local OTOC at position $\mathbf{x} = 0$, we found exponential growth with the same λ_L for all $\mathbf{x}$ as long as the light-cone has passed, i.e. for times $Mt > |M\mathbf{x}|/v_B$, where v_B is the butterfly velocity studied below. This implies that the Lyapunov exponent can equivalently be defined as $\lambda_L = \lim_{t\to\infty} \frac{1}{2t} \ln C(\mathbf{p} = 0, t)$.

LOCAL, STATIC APPROXIMATIONS FAIL TO REPRODUCE EXPONENTIAL GROWTH. As we are determining the Lyapunov exponent from a local quantity, one could suspect from the equations of motion of the perturbation (see Eq. (3.17)) that the chaotic exponential growth can be related to an instability of independent anharmonic oscillators on each lattice site with an (in general complex) frequency given in terms of the static value of the volume average of $\tilde{\varphi}^2$. However, in this approximation we have found *stable* oscillations for all values of $\mathcal{G}$ considered here. Hence, they can not reproduce the exponential growth of the OTOC, which is a genuine dynamical many-body effect in this theory.

ALGEBRAIC APPROACH OF λ_L TO NONINTERACTING LIMIT. In Fig. 3.8 we show the Lyapunov exponent as defined in Eq. (3.35) as a function of the fluctuation parameter $\mathcal{G}$. For small $\mathcal{G}$, we find an approximate power law behaviour $\sim \mathcal{G}^2$,

where $\mathcal{G} = 0$ is the non-interacting limit in which $\lambda_L = 0$. Algebraic approach of a non-chaotic limit has been previously found[5] in many other classical dynamical models [287, 291].

LINEAR-IN-T BEHAVIOUR IN QUANTUM CRITICAL REGIME. By employing the matching procedure described in section 3.2 we can relate the results for the classical theory to the corresponding quantum theory at high temperatures in the quantum critical regime, in which $\mathcal{G} \approx 35$ and $M = \sqrt{2}\pi T/3$ [267]. Inserting our numerical result for $\mathcal{G} \approx 35$ and using that we measure λ_L in units of M we get

$$\lambda_L^{\text{quantum crit.}} \approx (0.12 \pm 0.01)\pi T. \tag{3.36}$$

This linear-in-T scaling was conjectured to be the universal behaviour in strongly correlated quantum systems and in particular, our result is within the conjectured MSS bound[6] $\lambda_L \leq \pi T$ [243]. In a recent large-N $d = 2$ calculation in the $O(N)$ model (for which ours is the $N = 1$ variant) the linear-in-T behaviour was also reproduced, but with a substantially larger prefactor. We note however, that $N = 1$ is special in $d = 2$ due to the presence of a finite-temperature phase transition related to the discrete symmetry of the field. The case of $N = 1, d = 2$ was also shown to be special in far-from-equilibrium phenomena [292] otherwise universal for all N and $d \leq 3$ [50]. It would hence be interesting to study the $N \gg 1$ limit within the classical statistical approximation and compare with the diagrammatic approach.

SIGNATURES OF A CROSSOVER NEAR THE PHASE TRANSITION. We find that the $\mathcal{G}^2$ behaviour found for small $\mathcal{G}$ crosses over to a slower increase for large $\mathcal{G}$, with the point of the crossover between the two behaviours approximately corresponding to $\mathcal{G}_c$. Previously, a cusp-like behaviour has been found at the phase transition of a classical XY model [293]. A maximum of the Lyapunov exponent near second-order phase transitions found in some other models[291, 294] has later been attributed [288] to the divergence of the specific heat near the phase transition, i.e. the Lyapunov function to be a smooth function of the energy. We find a similar behaviour in our case (not shown in plot), with the Lyapunov exponent *decreasing* as a function of $\langle H \rangle / VT$, with large $\mathcal{G}$ corresponding to small $\langle H \rangle / VT$, and with

5 One is inclined to put the recently found algebraic behaviour $T^{0.48}$ of the Lyapunov exponent in a classical spin system [259] more into the perspective of this classical order-to-chaos transition rather than the conjectured connection to the linear-in-T bound in quantum many-body chaos, especially as in many classical dynamical models the exponent was found to be given by the Feigenbaum constant ≈ 0.449 [290].

6 Note that we define the Lyapunov exponent by a factor of two differently to the authors of the bound.

no apparent special feature near the energy density corresponding to $\mathcal{G}_c$. Directly at the phase transition we find

$$(\lambda_L/M)\big|_{\mathcal{G}=\mathcal{G}_c} = 0.44 \pm 0.01. \tag{3.37}$$

We note that $M > 0$ in the dimensional reduction scheme discussed here [267] and in particular it stays finite at the phase transition[7].

ORDERED PHASE $\mathcal{G} > \mathcal{G}_c$. Even though λ_L is numerically difficult to obtain in this region (see section 3.4), we found λ_L to continue to rise for $\mathcal{G} > \mathcal{G}_c$, however somewhat slower than below the phase transition. In order to find more conclusive results in the ordered phase, a description in terms of a "dual" weakly coupled classical field theory [267, 295] might lead to further insights into the chaotic properties of the ordered phase and make numerical simulations considerably easier.

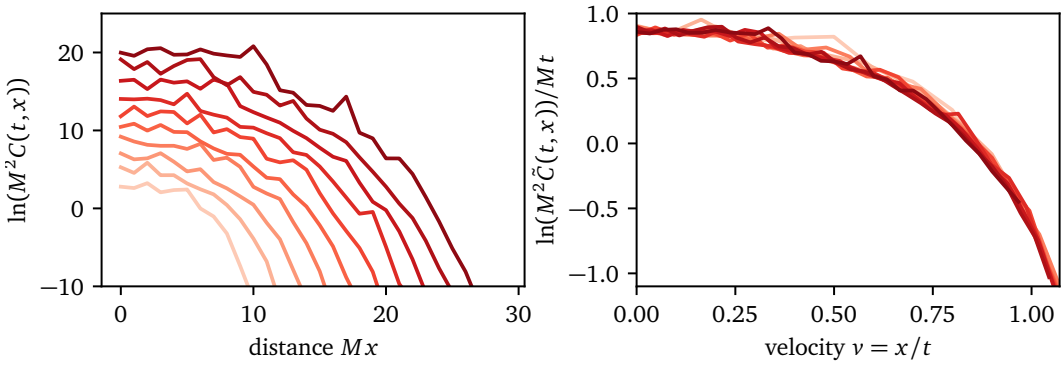

Figure 3.9: **Scaling collapse of the OTOC.** On the left we display equally spaced time slices in the interval $Mt \in [10, 30]$ for $\mathcal{G} = 61.44$ along one spatial axis, with times increasing from bright to dark colours. The collapse in the right plot indicates that $C(t,x) \sim \exp(\lambda(v)t)$, with a scaling function $\lambda(v) = \lambda(x/t)$. The OTOC $C(t,x) \to 0$ outside the causal lightcone $v/c = 1$ in the limit $a_s \to 0$, which we checked numerically.

3.7.2 *OTOC exponential growth from local field fluctuations*

One may be tempted to try obtaining at least the qualitative features in Fig. 3.8 from approximating each lattice site $\mathbf{x}$ as an independent anharmonic oscillator, with growth resulting from local field fluctuations. In this section we show that this is not possible and conclude that the exponential growth observed is a genuine dynamical many-body effect.

7 It is the mass renormalized by classical statistical fluctuations m_R which vanishes at the phase transition, as visible from the study of the spectral function in chapter 3.6.

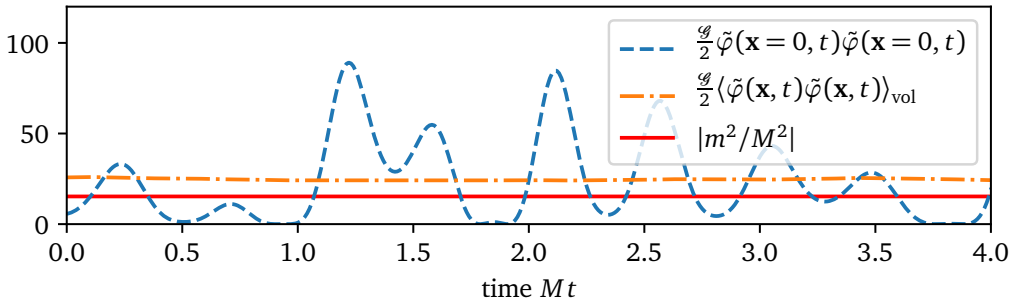

Figure 3.10: **Competition between mass term and order parameter fluctuations.** Time evolution of the field squared at one lattice site in a *single* run at $\mathcal{G} = 61.44$ alongside the nearly constant volume average of the same quantity. While the latter is always larger than the negative mass squared, the former is over a large timespan smaller, leading to exponential growth of the perturbations.

INDEPENDENT OSCILLATORS AT EACH LATTICE POINT We start by neglecting the spatial dependence by not taking into account the Laplacian on the right hand side of the equations of motion of the perturbation, which we reproduce here for convenience:

$$\partial_t^2 \delta\tilde{\varphi} = \Delta\delta\tilde{\varphi} - \frac{m^2}{M^2}\delta\tilde{\varphi} - \frac{\mathcal{G}}{2}\tilde{\varphi}^2\delta\tilde{\varphi}. \tag{3.38}$$

This independent anharmonic oscillator approximation may be motivated by the observation from Fig. 3.7 that the exponential growth only sets in after some time $Mt \approx 3$, presumably enough to homogenize the immediate surrounding of $\mathbf{x} = 0$ and render gradients small[8]. As a second approximation, we decouple the field evolution from the perturbation by the mean-field type approximation $\tilde{\varphi}(t)\tilde{\varphi}(t)\delta\tilde{\varphi}(t) \to \langle\tilde{\varphi}(t)\tilde{\varphi}(t)\rangle\delta\tilde{\varphi}(t)$. By replacing ensemble with volume average, we can furthermore write $\langle\tilde{\varphi}(t)\tilde{\varphi}(t)\rangle \approx \frac{1}{N^2}\langle\tilde{\varphi}_i(t)\tilde{\varphi}_i(t)\rangle_{\text{vol}}$. Finally, we numerically find that the latter quantity is approximately constant, but dependent on $\mathcal{G}$ as can be guessed from the fact that it is related to the transverse momentum [296], a conserved quantity in this model [297].

Under these assumptions, we can reduce the equations of motion of the perturbation at each lattice site to the one of an harmonic oscillator with solution

$$\delta\tilde{\varphi}(t) = \frac{\delta\pi_0}{\omega_{HO}}\sin(\omega_{HO}t)\,, \quad \text{with}\,\omega_{HO} = \sqrt{\frac{m^2}{M^2} + \frac{\mathcal{G}}{2}\langle\tilde{\varphi}\tilde{\varphi}\rangle}, \tag{3.39}$$

where we made use of the numerical result that $\omega_{HO} \in \mathbb{R}$ in the regime $7 < \mathcal{G} < 200$ for $N = 300$, $a_s = 0.2$ and used as initial conditions $\delta\phi(t=0) = 0$, $\delta\pi(t=0) = \delta\pi_0$.

8 Neglecting this term does not neglect all other lattice points completely as there is still the momentum sum in the one-loop mass in Eq. (3.11).

This approximation therefore fails completely to predict the exponential growth of perturbations found by evaluating the exact equations of motion. We furthermore find that the mass term $\sim m^2/M^2$ is negative for $\mathcal{G} \gtrsim 7$, therefore competing against the 'fluctuation term' $\sim \mathcal{G}\langle\tilde{\varphi}\tilde{\varphi}\rangle > 0$, which we find numerically to be always larger in magnitude than the mass term.

LOCAL DYNAMICAL FIELD FLUCTUATIONS LEAD TO EXPONENTIAL GROWTH

The above findings provoke reconsidering the approximations made, especially using the volume average of the fluctuations of the local field seems too restrictive. Indeed, in Fig. 3.10 we find the local field at one location and a single run to fluctuate wildly as a function of time. In particular, it drops *below* $|m^2/M^2|$ for a large time span in the evolution. Using our above harmonic approximation as an instantaneous approximation, we find that ω_{HO} becomes imaginary, leading to exponential growth of $\delta\tilde{\varphi}(t)$. At this point, also the approximation of independence of neighbouring space point breaks down as sudden exponential growth at one point leads to large gradients to neighbouring points.

We have also checked that evolving the full equations of motion for the anharmonic oscillator (i.e. $N = 1$) with m^2/M^2 given by the result in a $300x300$ lattice (but with Monte Carlo sampling for $N = 1$) leads to $\lambda_L = 0$ for all $\mathcal{G}$. Hence each lattice site is in a non-chaotic regime of the corresponding anharmonic oscillators.

We can therefore conclude that the exponential growth of perturbations observed in this chapter is a genuine dynamical many-body effect as both the assumptions of static fluctuations driving the growth and independence of neighbouring lattice points are not able to explain the observed phenomenology and we find indications that fluctuations in the local equal-time field fluctuations lead to the observed exponential growth.

While so far having mainly focussed on the time evolution of the local OTOC, we extend our analysis to the full space-time dependence in the following. After showing that the OTOC follows an approximately self-similar time evolution, we define the butterfly velocity unambiguously via the resulting scaling function. Lastly, we show that the butterfly velocity exhibits a global maximum at the phase transition.

SPACE-TIME DEPENDENCE OF THE OTOC. Cuts of the OTOC along one axis of the 2D spatial plane are shown in Fig. 3.9 for several times. The scaling collapse obtained on the right side of the plot indicates that the OTOC follows a self-similar time evolution of the form

$$C(\mathbf{x}, t) \sim \exp(\lambda(v)t), \tag{3.40}$$

with a velocity-dependent Lyapunov exponent $\lambda(v) \equiv \lambda(|\mathbf{x}|/t)$ [34, 39, 298–300] and where the exact functional form of $\lambda(v)$ in general depends on $\mathcal{G}$. We however qualitatively found it to be similar for all values of $\mathcal{G}$. In particular, it smoothly crosses zero at some finite v and hence wave front broadening as obtained in chaotic quantum lattice models is not present here [34, 39, 41, 42]. In order to obtain the scaling collapse, we plot $\tilde{C}(t,x) = C(t,x) - \text{const.}$, where the constant is the intersection with the y-axis of the linear fit to $\ln(C(t, x = 0))$ for $Mt > 10$ and is related to the non-universal time evolution for $Mt < 10$.

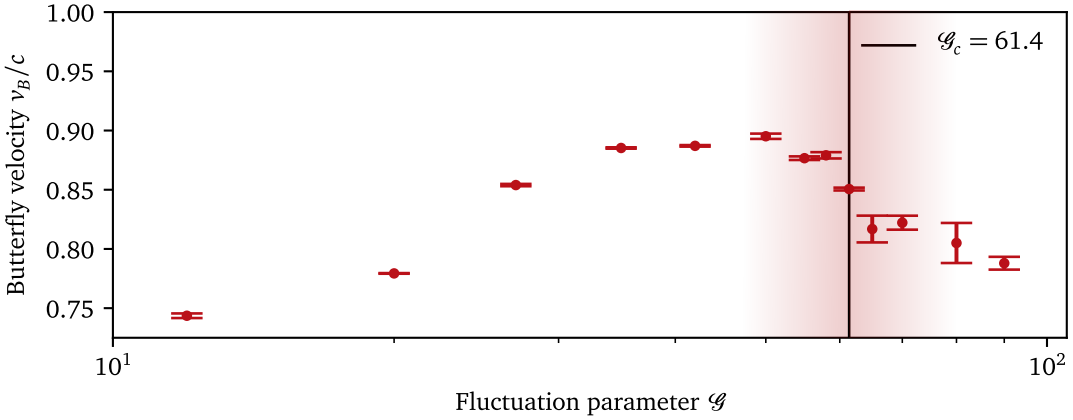

Figure 3.11: **Butterfly velocity.** The velocity associated to the ballistic spreading of the OTOC exhibits a global maximum on approach to the phase transition at $\approx 0.89c$, and is considerably smaller than the speed of light c for a wide range of values for $\mathcal{G}$. Different behaviour is seen on both sides of the phase transition: While the butterfly velocity is slowly rising upon approaching the phase transition from the paramagnetic phase, it steeply decreases as one moves away from it into the symmetry broken phase. The red shading indicates the range of $\mathcal{G}$ in which critical slowing down was found in the spectral function. Error bars are obtained from a jackknife binning analysis.

BUTTERFLY VELOCITY. The above finding of a self-similar evolution of the OTOC in space-time motivates the definition of the butterfly velocity as the velocity v_B by

$$\lambda(v = v_B) = 0, \tag{3.41}$$

corresponding to the "slice" of constant velocity v at which the OTOC neither grows nor decays with time.

In Fig. 3.11 we show the butterfly velocity as a function of the fluctuation parameter $\mathcal{G}$. We find that v_B is always significantly smaller than the speed of light c. In particular, in the high temperature quantum critical regime, $\mathcal{G} = 35$, of the corresponding quantum field theory we have

$$v_B^{\text{quantum crit.}} = (0.853 \pm 0.001)c, \tag{3.42}$$

which is significantly smaller than $v_B \approx c$ found in the high-T phase of the O(N) model at large N [37]. As the phase transition is approached from the paramagnetic phase, the butterfly velocity saturates around $\mathcal{G} = 50$ at the maximum value of approximately $0.89c$ before dropping sharply just at the phase transition as one moves into the symmetry broken phase.

The maximum of the butterfly velocity and hence maximally fast spreading of OTOCs at the phase transition is in sharp contrast to the diffusively slow order parameter dynamics found in the spectral function. This shows the qualitatively different behaviour of many-body chaos and transport and shows that the former is a new, in general independent measure of thermalization. We note however, that λ_L and v_B might not be completely independent parameters as a universal relation between the diffusion constant, λ_L and v_B has been conjectured [244, 248].

3.7.3 *Fluctuations*

Previous studies in quantum lattice models [34, 41, 42] showed that the growth of the $(D-1)$ dimensional OTOC *front* can be mapped to interface growth in the $(D-1)$ KPZ universality class (in 1D, diffusive behaviour of the front is found). Classical spin chains in 1D [260], however, found indications that the effective equations of motion of the OTOC itsself follows KPZ universality, i.e. that its run-to-run fluctuations have a self-similar behaviour with universal exponents. In a (2+1)D classical spin model, no such behaviour was however found [259].

Here, we study the run-to-run fluctuations of the time-dependent height variable

$$h(t) = \ln\left(\{\varphi(\mathbf{x}=\mathbf{0},t),\varphi(\mathbf{0},0)\}^2_{PB}\right)/2, \tag{3.43}$$

which is the single-run generalization of $\ln(C(t)/2)$. Therefore, the slope of $h(t)$ is the single-run generalization of the Lyapunov exponent λ_L. In general, however, $\langle h(t)\rangle_{\mathrm{cl}} \neq \ln(C(t)/2)$ due to the non-commutativity of sample average and logarithm (see Ref. [301]). We study the time evolution of the probability distribution of $h(t)$ to quantify fluctuations of the local OTOC.

In Fig. 3.12 we show that the probability distribution $P(h,t)$ follows the (in time) self-similar scaling form

$$P(h,t) = t^{-\alpha} P_S\left(\frac{h-\langle h\rangle(t)}{t^\alpha}\right). \tag{3.44}$$

In order to estimate the exponents for the scaling collapse of the fluctuations above, we performed a χ^2 analysis. First, we change the definition of the scaling ansatz in Eq. (3.44) slightly by introducing a reference time t_{ref},

$$P_{\mathrm{resc}}(t,\bar{h}) = \left(\frac{t}{t_{\mathrm{ref}}}\right)^{-\alpha} P\left(t, \left(\frac{t}{t_{\mathrm{ref}}}\right)^{-\alpha}\bar{h}\right), \tag{3.45}$$

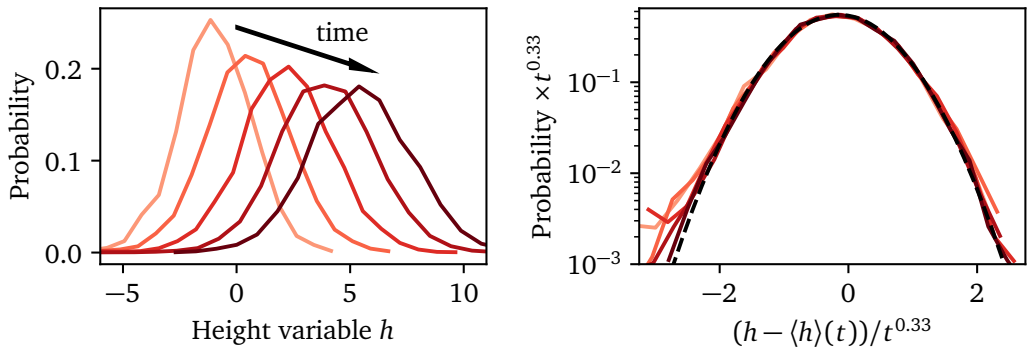

Figure 3.12: **Self-similarity in the run-to-run fluctuations of the OTOC.** Time dependent probability distribution of $h(t)$ at $\mathcal{G} = 61.44$, near the phase transition. All curves collapse after a rescaling with t^{α}, $\alpha = 0.33 \pm 0.06$. The scaling function is close to a Gaussian (dashed black line), with residual deviations from scaling and Gaussianity vanishing as time progresses. Times increase from bright to dark lines and are given by $Mt \in \{11, 16, 21, 26, 30\}$.

where we also introduced $\bar{h} = h - \langle h\rangle(t)$. Usually, we chose $Mt_{\text{ref}} = 11$, i.e. the beginning of the regime in which almost no deviation from self-similar behaviour is visible. According to this definition, a perfect scaling collapse would correspond to

$$\Delta P = P_{\text{resc}}(t, \bar{h}) - P(t_{\text{ref}}, \bar{h}) = 0 \quad \forall t \in \text{scaling regime}. \tag{3.46}$$

In order to quantify deviations from scaling, we define the error function

$$\chi^2(\alpha) = \frac{1}{N_t} \sum_{t=t_{\text{ref}}}^{t_{\text{max}}} \frac{1}{\int d\bar{h}} \int d\bar{h} \left(\frac{\Delta P(t, \bar{h})}{P(t_{\text{ref}}, \bar{h})} \right)^2, \tag{3.47}$$

where N_t is the number of times in the interval $[t_{\text{ref}}, t_{\text{max}}]$, in our case usually $Mt_{\text{max}} = 30$ and $N_t = 20$. Integrals over $\bar{h}$ were numerically evaluated with the trapezoidal rule as in our case $P(t, \bar{h})$ is given in terms of discrete bins from a histogram. We furthermore interpolated $P(t_{\text{ref}}, \bar{h})$ linearly to evaluate it at the arguments of $P_{\text{resc}}(t, \bar{h})$.

Finally, we minimized $\chi^2(\alpha)$ to get the most likely value $\bar{\alpha}$ of the scaling exponent. The error is then given by the standard deviation σ of the corresponding likelihood function, i.e. $\sigma = \sqrt{\chi^2(\bar{\alpha})}$.

$$\alpha = 0.33 \pm 0.06 \tag{3.48}$$

from a χ^2 analysis which we discuss below. This value of α is in accordance with the (1+1)D KPZ universality class and hence the scenario of a fluctuating OTOC front also found in quantum lattice models [34, 41, 42]. We however can not fully exclude the OTOC itsself fluctuating, as found in 1D classical spin chains [260], as

(2+1)D KPZ behaviour with exponent 0.24 is within 1.5 standard deviations of our result.

The scaling distribution P_S closely follows a Gaussian with mean -0.16 and variance 0.77. Note that in the regime accessible here, a Gaussian is not distinguishable from a Tracy-Widom distribution expected from KPZ universality [302].

SHORT TIME BEHAVIOUR. Times earlier than $Mt \approx 3$ deviate substantially from the self-similar scaling form in Eq. (3.44), exhibiting large (negative) skewness as well as a shift of the maximum towards larger h, corresponding to the local maximum in the time evolution visible in Fig. 3.7. In the range $3 < Mt < 10$, the distribution is still substantially skewed, but approximately coincides with the scaling form around the maximum. A leftover of this evolution is visible in the rescaled plot in Fig. 3.12 for times $Mt > 10$, where deviations in the tails of the distribution from the scaling form become smaller as time progresses.

In this chapter, many-body chaos in the self-interacting $\lambda\varphi^4$ real scalar field theory has been discussed at high temperatures and near its second order thermal phase transition. By employing dimensional reduction we reduced this quantum field theory to a classical statistical field theory and argued why dynamical and chaotic properties may be captured by this approximation. Subsequently, we employed a numerical method motivated from linear-response theory to study the classical equivalent of the out-of-time-ordered correlator (OTOC) and used the classical fluctuation-dissipation relations to study the spectral function.

Opposed to the diffusive order parameter transport near the phase transition we found ballistic spreading of OTOCs in the whole parameter regime. The Lyapunov exponent exhibits the linear-in-T behaviour conjectured to be universal in the quantum critical regime. Furthermore, we found some indications of a different functional form of the approach to the critical fluctuation strength on both sides of the phase transition. Most importantly, we found the butterfly velocity to have a global maximum near the phase transition, indicating that OTOCs spreads quickest in this strongly correlated regime. We contrasted these findings with the order parameter dynamics from the spectral function and argued how many-body chaos offers an independent characterization of thermalization dynamics.

While temporal fluctuations of the OTOC were found to be consistent with the KPZ universality class, further investigations would be necessary to fully confirm this. Especially spatial fluctuations could be studied, as well as the dependence of the exponents on the dimensionality.

While we argued here that many aspects of quantum many-body chaos can be captured by the classical statistical approximation and reproduced many results from diagrammatic quantum field theory calculations, it would be advantageous to

test these assumptions within a unified framework. A possible route to do so would be to use a Bethe-Salpeter equation on a doubled Keldysh contour obtained from the two-particle-irreducible effective action [210] in some analogy to the calculation of the shear viscosity [303] as classical and quantum contributions can be naturally identified in this formalism [273]. This could also offer a route to benchmarking the non-perturbative approximations (such as the $1/N$ expansion) frequently employed to diagrammatically studying OTOCs in field theories [37, 248, 265].

Furthermore, it would be interesting to investigate the connection of chaos to the hydrodynamic modes, in this model the transverse momentum, a diffusive mode, and the pressure, a damped ballistic mode. It has been previously shown that the diffusion constant stays finite at the phase transition [286]. It would hence be interesting to study whether the conjectured connection [244] $D = v_B^2/\lambda_L$ between the diffusion constant D, the Lyapunov exponent and the butterfly velocity also holds in this model as previously found in other classical models [259] and quantum field theories [248].

3.8 OUTLOOK: MANY-BODY-CHAOS FAR-FROM-EQUILIBRIUM

Our method of obtaining the OTOC can be straightforwardly applied to other bosonic field theories in the classical statistical regime at high occupations. Here, we adapt the methods discussed above to situations far-from-equilibrium, for both the O(N)-model, the generalization of the theory discussed above to N field components, and an interacting non-relativistic Bose gas. This opens the possibility to study many-body-chaos close to non-thermal-fixed points [304] or the early stages after a heavy-ion collision by adapting our methods to classical Yang-Mills theory [305].

O(N)-MODEL The O(N) model is an N-component real scalar field theory in d spatial dimensions given by Hamiltonian

$$H = \int \mathrm{d}^d\mathbf{x} \left[\frac{1}{2}\pi_a^2 + \frac{1}{2}\left(\nabla\varphi_a\right)^2 + \frac{1}{2}m^2\varphi_a^2 + \frac{\lambda}{4!N}(\varphi_a^2)^2 \right], \tag{3.49}$$

with bare mass m^2 and interaction constant λ. $\pi_a = \partial_t\varphi_a$ is the canonically conjugate momentum of the real scalar fields φ_a. A sum over the field index a is implied. The equations of motion of the field are given by

$$\partial_t^2\varphi_a = \Delta\varphi_a - m^2\varphi_a - \frac{\lambda}{6N}\varphi_b^2\varphi_a. \tag{3.50}$$

and the linearized equations of motion for the perturbation around trajectories given by

$$\partial_t^2\delta\varphi_a = \Delta\delta\varphi_a - m^2\delta\varphi_a - \frac{\lambda}{6N}\left(\varphi_b^2\delta\varphi_a + \varphi_a\varphi_b\delta\varphi_b\right). \tag{3.51}$$

We are primarily interested in the field averaged spectral function, given by

$$\rho(\mathbf{x},\mathbf{x}';t,t') = i\frac{1}{N^2}\sum_{a,b}\left\langle[\varphi_a(\mathbf{x},t),\varphi_b(\mathbf{x}',t')]\right\rangle \tag{3.52}$$

and the field averaged OTOC

$$C(\mathbf{x},\mathbf{x}';t,t') = -\frac{1}{N^2}\sum_{a,b}\left\langle[\varphi_a(\mathbf{x},t),\varphi_b(\mathbf{x}',t')]^2\right\rangle. \tag{3.53}$$

In classical statistical simulations, we can obtain above quantities by replacing $-i$ times the commutator with the Poisson bracket [273], i.e.

$$-i\left[\varphi_a(\mathbf{x},t),\varphi_b(\mathbf{x}',t')\right] \to \sum_c\int \mathrm{d}^d\mathbf{z}\left(\frac{\delta\varphi_a(\mathbf{x},t)}{\delta\varphi_c(\mathbf{z},0)}\frac{\delta\varphi_b(\mathbf{x}',t')}{\delta\pi_c(\mathbf{z},0)} - \frac{\delta\varphi_a(\mathbf{x},t)}{\delta\pi_c(\mathbf{z},0)}\frac{\delta\varphi_b(\mathbf{x}',t')}{\delta\varphi_c(\mathbf{z},0)}\right). \tag{3.54}$$

The Poisson bracket can be evaluated numerically by evolving the equations of motion of the perturbation in Eq. (3.17) in parallel with the field equations of motion in Eq. (3.13).

INTERACTING BOSE GAS An interacting Bose gas described by a complex field $\Psi(\mathbf{x},t)$ evolves according

$$i\partial_t\Psi(\mathbf{x},t) = -\frac{\nabla^2}{2m}\Psi(\mathbf{x},t) + g|\Psi(\mathbf{x},t)|^2\Psi(\mathbf{x},t) \tag{3.55}$$

with the coupling strength $g = 4\pi a/m$ given in terms of the mass m, scattering length a in the dilute regime in which $na^3 \ll 1$ with density n.
Accordingly, the linearized equations of motion are given by

$$i\partial_t\delta\Psi(\mathbf{x},t) = -\frac{\nabla^2}{2m}\delta\Psi(\mathbf{x},t) + 2g|\Psi(\mathbf{x},t)|^2\delta\Psi(\mathbf{x},t) + g\Psi(\mathbf{x},t)^2\delta\Psi^\dagger(\mathbf{x},t). \tag{3.56}$$

The observables of interest are again given by the spectral function

$$\rho(\mathbf{x},\mathbf{x}';t,t') = i\left\langle[\Psi(\mathbf{x},t),\Psi^\dagger(\mathbf{x}',t')]\right\rangle \tag{3.57}$$

and the OTOC

$$C(\mathbf{x},\mathbf{x}';t,t') = -\left\langle[\Psi(\mathbf{x},t),\Psi^\dagger(\mathbf{x}',t')]^2\right\rangle. \tag{3.58}$$

Because the canonically conjugate field of Ψ is given by $i\Psi^\dagger$, the Poisson bracket becomes

$$-i\left[\Psi(\mathbf{x},t),\Psi^\dagger(\mathbf{x}',t')\right] \to \sum_c\int \mathrm{d}^d\mathbf{z}\left(\frac{\delta\Psi(\mathbf{x},t)}{\delta\Psi(\mathbf{z},0)}\frac{\delta\Psi^\dagger(\mathbf{x}',t')}{i\delta\Psi^\dagger(\mathbf{z},0)} - \frac{\delta\Psi(\mathbf{x},t)}{i\delta\Psi^\dagger(\mathbf{z},0)}\frac{\delta\Psi^\dagger(\mathbf{x}',t')}{\delta\Psi(\mathbf{z},0)}\right). \tag{3.59}$$

Alternatively, the field operator Ψ can be split into real and imaginary components to evaluate the Poisson bracket, as done in [273].

NUMERICAL IMPLEMENTATION We discuss the numerical implementation for the O(N) model, with the interacting Bose gas following analogously. Assuming a discretization on an N_s^d hypercubic lattice with lattice spacing a_s (i.e. volume $V = (a_s N_s)^d$) and periodic boundary conditions, the spectral function is given by

$$\begin{aligned} &-\rho_{\mathrm{cl}}(\mathbf{x}-\mathbf{x}';t,t') \\ &= \left\langle \sum_c a_s^d \sum_{\mathbf{z}} \left\langle \left\langle \left(\frac{\delta\varphi_a(\mathbf{x},t)}{\delta\varphi_c(\mathbf{z},0)} \frac{\delta\varphi_b(\mathbf{x}',t')}{\delta\pi_c(\mathbf{z},0)} - \frac{\delta\varphi_a(\mathbf{x},t)}{\delta\pi_c(\mathbf{z},0)} \frac{\delta\varphi_b(\mathbf{x}',t')}{\delta\varphi_c(\mathbf{z},0)} \right) \right\rangle_{\mathbf{x}+\mathbf{x}'} \right\rangle_{a,b} \right\rangle_{\mathrm{cl}}, \end{aligned} \tag{3.60}$$

where we have denoted the average over the initial field configurations with subscript 'cl' and the average over the center of mass coordinate with subscript $\mathbf{x}+\mathbf{x}'$. Note that care has to be taken for the latter - the number of values averaged over depends on $\mathbf{x}-\mathbf{x}'$.

The protocol then proceeds as follows:

1. For each initial state sample, perform two runs, one in which $\delta\varphi_c(\mathbf{z},0) \neq 0$ and one in which $\delta\pi_c(\mathbf{z},0) \neq 0$ for some randomly chosen $\mathbf{z}$ and c, saving $\frac{\delta\varphi_a(\mathbf{x},t)}{\delta\pi_c(\mathbf{z},0)}$ and $\frac{\delta\varphi_a(\mathbf{x},t)}{\delta\varphi_c(\mathbf{z},0)}$ for all $\mathbf{x}, t, a$.

2. After the time evolution of both runs, calculate

$$\left\langle \left\langle \left(\frac{\delta\varphi_a(\mathbf{x},t)}{\delta\varphi_c(\mathbf{z},0)} \frac{\delta\varphi_b(\mathbf{x}',t')}{\delta\pi_c(\mathbf{z},0)} - \frac{\delta\varphi_a(\mathbf{x},t)}{\delta\pi_c(\mathbf{z},0)} \frac{\delta\varphi_b(\mathbf{x}',t')}{\delta\varphi_c(\mathbf{z},0)} \right) \right\rangle_{\mathbf{x}+\mathbf{x}'} \right\rangle_{a,b}. \tag{3.61}$$

3. Average over $\mathbf{z}$, c and initial conditions at the same time, effectively performing a Monte Carlo evalutation of the integral over $\mathbf{z}$ and the sum over c.

As we need to prepare an initial state for the perturbation $\delta\varphi_c(\mathbf{x},0) = c\delta(\mathbf{x}-\mathbf{z})$ in the continuum, and therefore $\sim \frac{1}{\tilde{a}_s^d}\delta_{\mathbf{xz}}$ on the d-dimensional lattice, the lattice spacing dependence is given as

$$\left(\frac{\delta\varphi(t,\mathbf{y})}{\delta\pi(0,\mathbf{x})} \right) \to a_s^d \left(\frac{\delta\varphi_{\mathbf{y}}(t)}{\delta\pi_{\mathbf{z}}(0)} \right), \tag{3.62}$$

i.e. the results obtained with the above prescription have to be *divided* by $\tilde{a}_s^d$ to obtain results independent of the lattice spacing.

Compared to the linear response protocol used in Refs. [276, 277] the present one has the advantage of not involving a small perturbing field as the equations of motion for the perturbation in Eq. (3.17) are already evaluated in the limit $\epsilon \to 0$. Therefore one can evaluate the spectral function for all (t,t') in a single run.

OTOC The generalization of the OTOC is simply given by squaring the Poisson bracket before averaging over initial conditions, i.e.

$$
\begin{aligned}
&C_{\mathrm{cl}}(\mathbf{x}-\mathbf{x}';t,t') \\
&= \Bigg\langle \sum_{c'}\sum_{c} a_s^{2d} \sum_{\mathbf{z}}\sum_{\mathbf{z}'} \Bigg\langle \Bigg\langle \left(\frac{\delta\varphi_a(\mathbf{x},t)}{\delta\varphi_c(\mathbf{z},0)} \frac{\delta\varphi_b(\mathbf{x}',t')}{\delta\pi_c(\mathbf{z},0)} - \frac{\delta\varphi_a(\mathbf{x},t)}{\delta\pi_c(\mathbf{z},0)} \frac{\delta\varphi_b(\mathbf{x}',t')}{\delta\varphi_c(\mathbf{z},0)} \right) \times \\
&\qquad \times \left(\frac{\delta\varphi_a(\mathbf{x},t)}{\delta\varphi_{c'}(\mathbf{z}',0)} \frac{\delta\varphi_b(\mathbf{x}',t')}{\delta\pi_{c'}(\mathbf{z}',0)} - \frac{\delta\varphi_a(\mathbf{x},t)}{\delta\pi_{c'}(\mathbf{z}',0)} \frac{\delta\varphi_b(\mathbf{x}',t')}{\delta\varphi_{c'}(\mathbf{z}',0)} \right) \Bigg\rangle_{\mathbf{x}+\mathbf{x}'} \Bigg\rangle_{a,b} \Bigg\rangle_{\mathrm{cl}} .
\end{aligned}
\tag{3.63}
$$

This means that four runs have to be evolved for a given initial field configuration, one each with $\delta\varphi_c(\mathbf{z},0) \neq 0$, $\delta\pi_c(\mathbf{z},0) \neq 0$, $\delta\varphi_{c'}(\mathbf{z}',0) \neq 0$, $\delta\pi_{c'}(\mathbf{z}',0) \neq 0$.

4

PROBING EIGENSTATE THERMALIZATION IN QUANTUM SIMULATORS VIA FLUCTUATION-DISSIPATION RELATIONS

This chapter is based on the publication

- Alexander Schuckert, Michael Knap: "Probing eigenstate thermalization in quantum simulators via fluctuation-dissipation relations" – Phys. Rev. Research 2, 043315 (2020) [arXiv:2007.10347]

Structure and text have been rearranged and adapted here.

The eigenstate thermalization hypothesis (ETH) offers a universal mechanism for the approach to equilibrium of closed quantum many-body systems. So far, however, experimental studies have focused on the relaxation dynamics of observables as described by the diagonal part of ETH, whose verification requires substantial numerical input. This leaves many of the general assumptions of ETH untested. Here, we propose a theory-independent route to probe the full ETH in quantum simulators by observing the emergence of fluctuation-dissipation relations, which directly probe the off-diagonal part of ETH. We discuss and propose protocols to independently measure fluctuations and dissipations as well as higher-order time ordered correlation functions. We first show how the emergence of fluctuation dissipation relations from a nonequilibrium initial state can be observed for the 2D Bose-Hubbard model in superconducting qubits or quantum gas microscopes. Then we focus on the long-range transverse field Ising model (LTFI), which can be realized with trapped ions. The LTFI exhibits rich thermalization phenomena: For strong transverse fields, we observe prethermalization to an effective magnetization-conserving Hamiltonian in the fluctuation dissipation relations. For weak transverse fields, confined excitations lead to non-thermal features resulting in a violation of the fluctuation-dissipation relations up to long times. Moreover, in an integrable region of the LTFI, thermalization to a generalized Gibbs ensemble occurs and the fluctuation-dissipation relations enable an experimental diagonalization of the Hamiltonian. This chapter presents a theory-independent way to characterize thermalization in quantum simulators and paves the way to quantum simulate condensed matter pump-probe experiments.

4.1 INTRODUCTION

The long coherence time scales accessible in quantum simulators made it possible to experimentally observe thermalization in isolated quantum systems [127, 146, 162, 306], the absence thereof in the presence of disorder [129, 152, 154, 179, 307] and integrability in reduced dimensions [47, 308]. Typically, these observations were based on probing *equal-time* correlation functions [309–311], concluding the observation of equilibration by comparison to the expected microcanonical expectation values at the same energy density as the initial state. This approach in particular requires viable theory input to compare with. However, in order to show full thermalization also the *fluctuations* around the equilibrium expectation value as well as the *response* of the system to small perturbations need to match the expectation in thermal equilibrium. This can be understood from the ETH [24–27, 312], via its Ansatz for the matrix elements of observables $\hat{A}$ with respect to many-body eigenstates $|n\rangle$ with energy E_n:

$$\langle n|\hat{A}|m\rangle = A(\bar{E})\delta_{nm} + e^{-S(\bar{E})/2} f_A(\bar{E},\omega) R_{nm}, \tag{4.1}$$

where $\bar{E} = (E_n + E_m)/2$, $\omega = E_m - E_n$, $A(\bar{E})$ is the value of $\langle \hat{A} \rangle$ in the microcanonical ensemble at energy $\bar{E}$, $S(\bar{E})$ is the thermodynamic entropy (i.e. the number of states in a small interval around energy $\bar{E}$) and R_{nm} are Gaussian random numbers. Measuring equal-time correlation functions in experiment only probes the first ("diagonal") term as in the long time limit $\langle \hat{A}(t) \rangle \equiv \langle \psi_0 | \hat{A}(t) | \psi_0 \rangle \to \bar{A} \equiv \sum_n |\langle \psi_0 | n \rangle|^2 \langle n|\hat{A}|n\rangle$. While temporal fluctuations of equal-time correlation functions around the steady-state value can in principle be used to probe the off-diagonal part of ETH as $\langle \hat{A}(t) \rangle^2 - \bar{A}^2 \to \sum_{m\neq n} |\langle \psi_0|n\rangle|^2 |\langle m|\psi_0\rangle|^2 |\langle m|\hat{A}|n\rangle|^2$, they are exponentially small in system size since the thermodynamic entropy is extensive. Hence, it becomes impractical to observe them in large systems [313, 314]. Equal-time correlation functions therefore only probe the diagonal part of ETH while requiring substantial theory input to conclude thermalization in experiment as they require a comparison with an equilibrium expectation value.

Here, we propose to measure *two-time correlation functions* of the form $\langle \hat{A}(t_1)\hat{B}(t_2) \rangle$ to probe thermalization in quantum simulators. They are entirely determined by the off-diagonal part of ETH while staying of $\mathcal{O}(1)$ in the thermodynamic limit, hence offering a route to experimentally probe the entirety of eigenstate thermalization. Moreover, two-time correlation functions offer a completely *theory-independent* route to do so by testing the fluctuation dissipation relation (FDR) [48, 239, 277, 315–317]. FDRs relate the anticommutator (statistical) two-time function

$$F(t_1,t_2) = \frac{1}{2}\langle \{\hat{A}(t_1), \hat{B}(t_2)\} \rangle - \langle \hat{A}(t_1) \rangle \langle \hat{B}(t_2) \rangle, \tag{4.2}$$

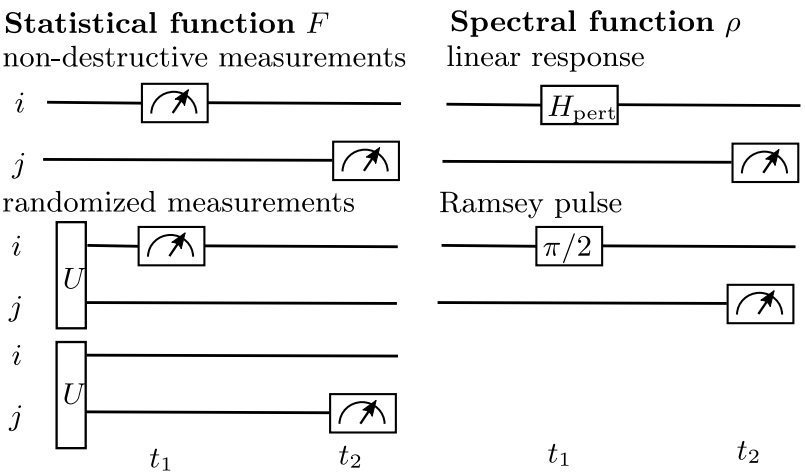

Figure 4.1: **Measuring two-time correlation functions out of equilibrium.** The statistical function F can be measured by employing a non-destructive measurement on site i at time t_1 before measuring site j at time t_2. The measurement at t_1 can be deferred to t_2 by shelving. Alternatively, measurements of two independent experimental realizations can be combined to yield F by averaging over global random unitaries U acted on the initial state. The spectral function ρ can be measured by non-equilibrium linear-response (e.g. Bragg or tweezer spectroscopy), employing light pulses on lattice site i at time t_1 before measuring at time t_2. Alternatively, a Ramsey-type sequence works similarly. The protocols for F and ρ can be realized in quantum simulators of spin models such as trapped ion experiments as well as simulators of Bose- and Fermi-Hubbard models such as quantum gas microscopes and superconducting qubits. The non-destructive measurement and Ramsey protocols can be combined to measure higher-order time ordered correlation functions.

which quantifies fluctuations of the system, with the commutator (spectral function)

$$\rho(t_1, t_2) = \langle [\hat{A}(t_1), \hat{B}(t_2)] \rangle \,, \tag{4.3}$$

quantifying dissipation of energy [1]. Once local thermal equilibrium is approached at late times, the fluctuations and dissipations are independent of the central time $T = (t_1 + t_2)/2$ due to time-translational invariance. Fourier transforming the relative time $\tau = (t_1 - t_2)$ to frequencies ω, we obtain the FDR

$$F(\omega) = n_\beta(\omega)\rho(\omega). \tag{4.4}$$

The Bose-Einstein distribution (plus the "quantum half")

$$n_\beta(\omega) = \frac{1}{2} + \frac{1}{\exp(\beta\omega) - 1} \tag{4.5}$$

at inverse temperature β links fluctuations and dissipation; see App. 4.2 for a short derivation of the FDRs and App. 4.3 for the connection between ETH and FDRs. As the FDR is completely independent of microscopic details and the initial state, measuring F and ρ independently from each other out-of-equilibrium and testing the FDRs provides a universal and theory-independent way of probing thermalization in quantum simulators. Moreover, from the FDR one can extract the temperature of the many-body system, which is usually challenging to determine experimentally [320, 321].

While the ETH implies the fulfillment of FDRs, physical initial states are always superpositions of many eigenstates such that the FDR of single eigenstates are challenging to probe in experiments [2]. However, the energy density variance of initial states prepared as the ground state of some Hamiltonian can be shown to vanish in the thermodynamic limit [27]. Hence, such initial states can be seen as a superposition of eigenstates in a small energy shell. As the ETH functions $A(\bar{E})$ and $f_A(\bar{E}, \omega)$ are assumed to be smooth functions of $\bar{E}$, the vanishingly small energy variance of physical initial state implies that probing an initial state with energy $\bar{E}$ and probing an arbitrary eigenstate with the same energy yields the same result at long times.

In this chapter, we propose protocols for measuring fluctuations and dissipations independently from each other out-of-equilibrium in quantum simulators of spin systems as well as fermionic and bosonic quantum gas microscopes employing protocols based on Ramsey pulses [323], non-destructive projective measurements [323, 324], randomized measurements [325] and linear response, including

1 Heating rates in the linear response regime of periodically driven systems are determined by ρ [318] and hence can also be used to probe the off-diagonal part of ETH [319]. However, heating rates are challenging to measure in experiment [149].

2 A recent protocol has shown how to prepare eigenstates in finite size systems [322].

non-equilibrium Bragg [326] and "tweezer" spectroscopy. We then discuss applications of the protocols in Sec. 4.7. As a first example, we show that the FDRs can be probed in current quantum gas microscopes as well as superconducting qubit experiments implementing the Bose-Hubbard model. Going beyond the case of fast thermalization, we show that in trapped ion experiments several examples of prethermalization [46] can be probed in the LTFI. At large transverse fields, a single approximately conserved quantity leads to thermalization to a prethermal Hamiltonian, which can be directly observed by testing the FDRs. In an integrable sector of the LTFI, extensively many conserved quantities lead to thermalization to a generalized Gibbs ensemble, which can again be observed by a generalized FDR [327]. In turn, measuring two-time correlations enable an experimental diagonalization of the quadratic Hamiltonian. Finally, at small transverse fields, confined excitations can be directly observed in the spectral function and lead to genuine non-thermal features including a violation of the FDR observable up to long times.

Before presenting our measurement protocols, we first derive the fluctuation-dissipation relation and show that they are implied by the eigenstate thermalization hypothesis.

4.2 FLUCTUATION-DISSIPATION RELATIONS

The fluctuation-dissipation relations are a consequence of the cyclicity of the trace and the interpretation of two-time correlators in terms of spectral and statistical components, which follow from the commutation relations.

KUBO-MARTIN-SCHWINGER (KMS) CONDITION IN THERMAL EQUILIBRIUM. The KMS condition for a correlation function of two operators $\hat{A}(t_1)$ and $\hat{B}(t_2)$ evaluated in the Heisenberg picture with Hamiltonian $\hat{H}$ is a simple property of the thermal density matrix:

$$\begin{aligned} \mathrm{Tr}\left[e^{-\beta\hat{H}}\hat{A}(t_1)\hat{B}(t_2)\right] &= \mathrm{Tr}\left[e^{-\beta\hat{H}}e^{\beta\hat{H}}\hat{B}(t_2)e^{-\beta\hat{H}}\hat{A}(t_1)\right] \\ &= \mathrm{Tr}\left[e^{-\beta\hat{H}}\hat{B}(t_2-i\beta)\hat{A}(t_1)\right], \end{aligned} \tag{4.6}$$

where we only used the cyclicity of the trace. In particular, the above relation does not depend on the commutation relations of $\hat{A}$ and $\hat{B}$ (This is in general not true if above relations are defined in terms of a path integral as then all correlation functions are automatically time ordered and the fermionic relation (i.e. for $\hat{A}$,$\hat{B}$ being fermionic creation/annihiliation operators) acquires a minus sign [210].)

Defining the two Wightman functions by using time-translational invariance of thermal equilibrium,

$$G^{>}(t_1 - t_2) = \frac{1}{Z} \operatorname{Tr}\left[e^{-\beta \hat{H}} \hat{A}(t_1) \hat{B}(t_2)\right] \tag{4.7}$$

$$G^{<}(t_1 - t_2) = \frac{1}{Z} \operatorname{Tr}\left[e^{-\beta \hat{H}} \hat{B}(t_2) \hat{A}(t_1)\right], \tag{4.8}$$

with $Z = \operatorname{Tr} e^{-\beta \hat{H}}$, and Fourier transforming with respect to $t_1 - t_2$, $G^{>}(\omega) = \int \mathrm{d}t e^{i\omega t} G^{>}(t)$, the KMS condition simply becomes

$$G^{>}(\omega) = e^{\beta\omega} G^{<}(\omega). \tag{4.9}$$

FLUCTUATION DISSIPATION RELATIONS (FDRS). FDRs may be obtained from the KMS condition by combining the Wightman functions into (bosonic or fermionic) spectral (ρ) and statistical (F) components as

$$\rho(\omega) := G^{>}(\omega) \mp G^{<}(\omega) \tag{4.10}$$

$$F(\omega) := \frac{1}{2}\left(G^{>}(\omega) \pm G^{<}(\omega)\right), \tag{4.11}$$

where the upper (lower) sign corresponds to bosons (fermions), respectively. These definitions respect the proper interpretation of ρ as a spectral function as may be motivated from the sum rule $\int \frac{d\omega}{2\pi} \rho(\omega) = \rho(t = 0) = \langle [\hat{A}, \hat{B}]_{\mp} \rangle$, i.e., the equal-time (anti-)commutation relations.

Inserting the KMS condition in Fourier space into above definitions, we find the FDRs

$$F(\omega) = n_\beta(\omega) \rho(\omega), \tag{4.12}$$

with $n_\beta(\omega) = \frac{1}{2} \pm 1/(\exp(\beta\omega) \mp 1)$ the Bose-Einstein/Fermi-Dirac distribution at inverse temperature β. We emphasize that whether bosonic or fermionic FDRs are obtained is not a mathematical property of the operators $\hat{A}$ and $\hat{B}$ but of the physical interpretation of the (anti-)commutator as the spectral/statistical function. In particular, this interpretation is ambiguous in the case of spin operators due to the sum rules differing between equal-site and un-equal site operators. For example, the raising/lowering operators $\hat{\sigma}_i^{\pm}$ anticommute for equal sites but commute for un-equal sites. Conventionally, bosonic FDRs are used for spin systems [48], which we also follow here.

We furthermore note that the FDR is not defined at $\omega = 0$ as the KMS condition in Eq. (4.9) implies $\rho(\omega = 0) = 0$, with $F(\omega = 0)$ left unconstrained.

KMS CONDITION AND FDR IN THE PRESENCE OF A CONSERVED QUANTITY In a grand-canonical equilibrium set-up with an additional conserved quantity $\hat{N}$

(defined by $[\hat{H}, \hat{N}] = 0$) and corresponding chemical potential μ, the KMS condition may be obtained according to

$$\begin{aligned} \operatorname{Tr} e^{-\beta(\hat{H}-\mu\hat{N})}\hat{A}(t_1)\hat{B}(t_2) &= \operatorname{Tr} e^{-\beta(\hat{H}-\mu\hat{N})}e^{\beta(\hat{H}-\mu\hat{N})}\hat{B}(t_2)e^{-\beta(\hat{H}-\mu\hat{N})}\hat{A}(t_1) \\ &= \operatorname{Tr} e^{-\beta(\hat{H}-\mu\hat{N})}e^{-\beta\mu\hat{N}}\hat{B}(t_2 - i\beta)e^{\beta\mu\hat{N}}\hat{A}(t_1). \end{aligned} \tag{4.13}$$

Whether or not a simple relation such as the one in Eq. 4.9 emerges crucially depends on the operator $\hat{B}$. For example, if $[\hat{N}, \hat{B}] = 0$, such as the case for the densities $\hat{n}_i$ defined by $\hat{N} = \sum_i \hat{n}_i$, the above relation returns again Eq. 4.9. Moreover, if $[\hat{B}, \hat{N}] = \hat{B}$, such as the case for an annihilation operator $\hat{a}_i$, defined by $\hat{n}_i = \hat{a}_i^\dagger \hat{a}_i$, we get

$$e^{-\beta\mu\hat{N}}\hat{B}e^{\mu\hat{N}} = e^{\beta\mu}\hat{B}. \tag{4.14}$$

and hence

$$G^>(\omega) = e^{\beta(\omega-\mu)}G^<(\omega). \tag{4.15}$$

Similar relations follow for the creation operator $\hat{a}_i^\dagger$. For the FDR of the annihilation operator with some other operator we then get

$$F(\omega) = \left(\frac{1}{2} \pm n_{\beta,\mu}(\omega)\right)\tilde{\rho}(\omega) \tag{4.16}$$

with $n_{\beta,\mu}(\omega) = 1/(\exp(\beta(\omega-\mu)) \mp 1)$ the Bose-Einstein/Fermi-Dirac distributions in the presence of a chemical potential.

Crucially, if $\hat{B}$ fulfills neither of the above simple commutation relations with the conserved quantity $\hat{N}$, *no* FDR is obtained as then there is no simple KMS condition.

4.3 FDRS AND THE EIGENSTATE THERMALIZATION HYPOTHESIS

Here we summarize the arguments in Ref. [7] to show that the ETH implies the FDRs, and that the experimental test of FDRs directly tests the off-diagonal part of ETH. We supplement the analytical arguments by showing the FDR on the level of individual eigenstates in the two-dimensional Bose Hubbard model.

To prove these statements, we assume $\hat{B} = \hat{A}^\dagger$, which is the case for all functions evaluated in the main text. For general $\hat{B} \neq \hat{A}$ additional assumptions not contained in the ETH have to be made [7]. For late times T, all T dependent terms in the Lehmann representation of the spectral and statistical functions are expected to dephase (c.f. Eq. (4.91)), such that

$$\lim_{T\to\infty} F(T,\omega) \equiv F(\omega) = \sum_n |\langle\psi_0|n\rangle|^2 F_{nn}(\omega), \tag{4.17}$$

$$\lim_{T\to\infty} \rho(T,\omega) \equiv \rho(\omega) = \sum_n |\langle\psi_0|n\rangle|^2 \rho_{nn}(\omega). \tag{4.18}$$

with the eigenstate spectral/statistical functions given by

$$F_{nn}(\omega) = \frac{1}{2}\sum_{l\neq n} |\langle n|\hat{A}|l\rangle|^2(\delta(\omega-(E_l-E_n))+\delta(\omega+(E_l-E_n))) \tag{4.19}$$

$$\rho_{nn}(\omega) = \sum_{l\neq n} |\langle n|\hat{A}|l\rangle|^2(\delta(\omega-(E_l-E_n))-\delta(\omega+(E_l-E_n))). \tag{4.20}$$

These expressions makes explicit that the long-time value of the spectral and statistical functions is entirely determined by the off-diagonal matrix elements of $\hat{A}$. Comparing with the corresponding equilibrium expressions,

$$F_{\text{equ.}}(\omega) = \frac{1}{Z}\sum_n e^{-\beta E_n} F_{nn}(\omega) \tag{4.21}$$

$$\rho_{\text{equ.}}(\omega) = \frac{1}{Z}\sum_n e^{-\beta E_n} \rho_{nn}(\omega), \tag{4.22}$$

one may first be lead to believe that the $|c_n(0)|^2$ must correspond to the weights in thermal equilibrium, $\frac{1}{Z}e^{-\beta E_n}$, in order for the equilibrium FDR to hold. This is however in general not true, as the $|c_n(0)|^2$ do not resemble any of the thermal ensembles [328] for most physical initial states. The eigenstate thermalization hypothesis offers a different route to thermalization in the sense of FDRs: *each eigenstate fulfills an FDR individually* and hence the weighted sum over the initial state distribution $|c_n(0)|^2$ does so, too.

Now, consider the Fourier transformed correlation function of a single eigenstate,

$$C_n(\omega) = \int \mathrm{d}\tau e^{i\omega\tau} \langle n|\hat{A}(\tau)\hat{A}^\dagger(0)|n\rangle \tag{4.23}$$

$$= 2\pi\sum_m \delta(\omega-(E_m-E_n))|\langle n|\hat{A}|m\rangle|^2. \tag{4.24}$$

The ETH Ansatz [24] demands that

$$\langle n|\hat{A}|m\rangle = A(\bar{E})\delta_{nm} + e^{-S(\bar{E})/2} f_A(\bar{E}, E_m-E_n) R_{nm}, \tag{4.25}$$

where $A(\bar{E})$ is the microcanonical expectation value of operator $\hat{A}$ at energy $\bar{E} = (E_n+E_m)/2$, S is the thermodynamic entropy, R_{nm} are random numbers with mean zero and unit variance and $f_A(\bar{E}, E_m-E_n)$ and $A(\bar{E})$ are smooth functions of their arguments $\bar{E}$. Inserting this ansatz into the eigenstate correlation function and replacing the sum over energies by an integral $\sum_m \to \int d(E_m-E_n)\exp[S(E_n+(E_m-E_n))]$ and using that the $|R_{nm}|^2$ average out under the sum, we then arrive at

$$C_n(\omega)/2\pi = |A(\bar{E})|^2\delta(\omega) + e^{S(E_n+\omega)-S(E_n+\omega/2)}|f_A(E_n+\omega/2,\omega)|^2. \tag{4.26}$$

As argued in Ref. [7] both S and f_A can be Taylor expanded around $\omega = 0$ if $\hat{A}$ is a local few-body operator, such that

$$C_n(\omega)/2\pi = |A(\bar{E})|^2\delta(\omega) + e^{\beta\omega/2}|f_A(E_n,\omega)|^2, \tag{4.27}$$

where we used that $dS(E)/dE = \beta$ with $\beta = \beta(E)$ the inverse temperature. We construct the eigenstate spectral and statistical functions from $C_n(\omega)$ by using $|f_A(E_n,\omega)|^2|R_{nm}|^2 = |f_{A^\dagger}(E_n,-\omega)|^2|R_{mn}|^2$, resulting in

$$F_{nn}(\omega)/2\pi = \cosh(\beta\omega/2)|f_A(E_n,\omega)|^2, \tag{4.28}$$

$$\rho_{nn}(\omega)/2\pi = 2\sinh(\beta\omega/2)|f_A(E_n,\omega)|^2. \tag{4.29}$$

Both F and ρ are hence entirely determined by f_A and the inverse temperature corresponding to the eigenenergy E_n. Moreover, we finally find that the FDR holds on the level of a single eigenstate,

$$F_{nn}(\omega) = n_\beta(\omega)\rho_{nn}(\omega) \tag{4.30}$$

with $n_\beta(\omega) = \frac{1}{2} + 1/(\exp(\beta\omega) - 1)$.

From this result we can now deduce the conditions on the initial state for the FDR. Inserting the eigenstate FDR into the long-time limit of the non-equilibrium statistical function (c.f. Eq. (4.17)),

$$F(\omega) = \sum_n |c_n|^2 n_{\beta(E_n)}(\omega)\rho_{nn}(\omega) \tag{4.31}$$

$$\stackrel{?}{=} n_\beta(\omega)\rho(\omega), \tag{4.32}$$

we clearly see that the second equality can only be true if the $|c_n|^2$ are concentrated around a region in which $\beta(E_n)$ is not a strongly varying function.

NUMERICAL VERIFICATION OF THE ETH SCENARIO. In Fig. 4.2 we verify the FDR for a single eigenstate of the 2D Bose Hubbard model. The inverse temperature β extracted from the FDR matches the expectation from the corresponding eigenenergy, i.e. from solving $E_n = \frac{1}{Z}\mathrm{Tr}[e^{-\beta\hat{H}}\hat{H}]$ for β. See Ref. [329] for an in-depth analysis of finite size effects in the FDR from the perspective of ETH.

4.4 MEASURING TWO-TIME CORRELATIONS IN SPIN MODEL SIMULATORS

Solving the quantum many-body problem is equivalent to obtaining all time ordered correlation functions [309] $\langle T\hat{A}(t_1)\hat{B}(t_2)\hat{C}(t_3)\cdots\rangle$. Here, we propose protocols to measure such correlation functions in quantum simulators of lattice models by using their decomposition into nested (anti-) commutators [330]. In particular, we will focus on the two-time correlation function which can be decomposed into the anti-/commutator (i.e. the statistical/spectral function) according to $\langle T\hat{A}(t_1)\hat{B}(t_2)\rangle = F + \frac{1}{2}\mathrm{sgn}(t_1 - t_2)\rho$. In the following, we present several protocols to measure F and ρ independently from each other in quantum simulators of spin (in this

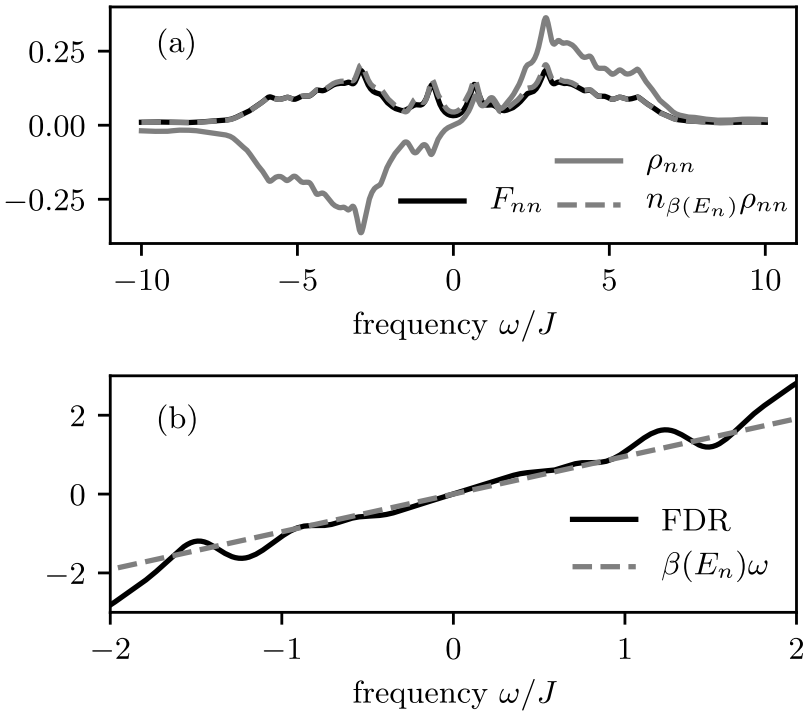

Figure 4.2: **FDR for a single eigenstate.** (a) Eigenstate statistical F_{nn} and spectral functions ρ_{nn} as well as the right-hand-side of the FDR $n_\beta \rho_{nn}$ for an eigenstate n with eigenenergy $E_n \approx -9.06J$ in the 2D Bose Hubbard model at $U/J = 4$ with the same initial state and operator proped as in Fig. 4.4 in the main text. The corresponding inverse temperature $\beta(E_n) \approx 0.95J$ expected in thermal equilibrium is set by the eigenenergy of the state via Eq. (4.64). To evaluate Eq. (4.24) we used a Lorentzian broadening with FWHM of $0.2J$. (b) FDR function as defined in Eq. (4.63) for low frequencies, showing the expected linear behaviour with a slope matching the inverse temperature.

section) and Bose-/Fermi-Hubbard models (in the next section) and indicate how to generalize them to higher order time ordered correlation functions. Our protocols are summarized in Fig. 4.1.

Ramsey protocol for spectral function ρ

Many-body Ramsey interferometry has been shown to be probe spectral functions in quantum simulators of spin models [323, 324] using local spin rotations of the form

$$R_i^\alpha(\theta) = \cos(\theta/2)\hat{\mathbb{1}}_i - i\sin(\theta/2)\hat{\sigma}_i^\alpha, \tag{4.33}$$

where $\hat{\sigma}^\alpha$ are the Pauli matrices [3]. The protocol proceeds as follows: Starting from some initial state $|\Psi_0\rangle$, evolve for time t_1, apply a local rotation $R_i^\alpha(\theta)$ at site i, subsequently evolve for a time $(t_2 - t_1)$ and finally measure $\hat{\sigma}_j^\beta$ [4]. The result can be written as

$$\begin{aligned}\langle\hat{\sigma}_j^\beta(t_2)\rangle_\theta = \cos^2(\theta/2)\,\langle\hat{\sigma}_j^\beta(t_2)\rangle + \frac{i}{2}\sin\theta\,\langle[\hat{\sigma}_i^\alpha(t_1),\hat{\sigma}_j^\beta(t_2)]\rangle \\ + \sin^2(\theta/2)\,\langle\hat{\sigma}_i^\alpha(t_1)\hat{\sigma}_j^\beta(t_2)\hat{\sigma}_i^\alpha(t_1)\rangle\,,\end{aligned} \tag{4.34}$$

where all expectation values are written in the Heisenberg picture. The spectral function can then be obtained by combining two runs with opposite angle $\theta = \pm\pi/2$ by

$$\langle[\hat{\sigma}_i^\alpha(t_1),\hat{\sigma}_j^\beta(t_2)]\rangle = -i\,\langle\hat{\sigma}_j^\beta(t_2)\rangle_{\pi/2} + i\,\langle\hat{\sigma}_j^\beta(t_2)\rangle_{-\pi/2}\,. \tag{4.35}$$

Projective measurement protocol for F.

The statistical function F has been shown to be probed by replacing the pulses in the Ramsey protocol for ρ with non-destructive projective measurements [323, 324], which have for example been demonstrated in superconducting qubits [331], Rydberg tweezer arrays [332] and trapped ions [333, 334]. In this protocol, a measurement of $\hat{\sigma}_i^\alpha$ at time t_1 (without disturbing the rest of the system) and a subsequent measurement of $\hat{\sigma}_j^\beta$ at time $t_2 - t_1$ is combined to yield

$$\frac{1}{2}\,\langle\{\hat{\sigma}_i^\alpha(t_1),\hat{\sigma}_j^\beta(t_2)\}\rangle = P_{ij}^{+\alpha+\beta} + P_{ij}^{-\alpha-\beta} - P_{ij}^{+\alpha-\beta} - P_{ij}^{-\alpha+\beta}, \tag{4.36}$$

3 While Rabi pulses only directly implement pulses in the x-y plane of the Bloch sphere, a pulse around the z axis can be implemented by $\hat{R}_i^z(\theta) = \hat{R}_i^x(\pi/2)\hat{R}_i^y(\theta)\hat{R}_i^x(-\pi/2)$ [174].

4 Measurements of $\hat{\sigma}^{x/y}$ can be implemented by applying local pulses before measuring $\hat{\sigma}^z$, for example $\hat{\sigma}^y = -\hat{R}^x(-\frac{\pi}{2})\hat{\sigma}^z\hat{R}^x(\frac{\pi}{2})$.

where $P_{ij}^{+\alpha+\beta}$ is the joint probability of measuring $+1$ for $\hat{\sigma}_i^{\alpha}(t_1)$ and $+1$ for $\hat{\sigma}_j^{\beta}(t_2)$.

The non-desctructive projective measurement can be replaced by spin shelving as noted in Ref. [323]. In this variant, the measurement at time t_1 is replaced by a π pulse between one of two spin levels at site i and a third level, which does not participate in the many-body dynamics. At time t_2 this third level gets measured as well, effectively projecting the state onto one of the two measurement outcomes at time t_1. This variant of the protocol has a speed advantage as single-site pulses are usually much faster than measurements and the many-body dynamics.

Randomized measurement protocol for F.

We propose statistical correlations between randomized measurements [307, 325, 335–338] as an alternative to measure the statistical correlation function F in small systems. It relies on acting with global random unitaries $\hat{u}$ on the initial state $|\Psi_0\rangle$. After time evolving for a time t_1, $\hat{A}$ is measured. Preparing the same initial state (with the same unitary $\hat{u}$) to measure $\hat{B}$ after evolving for time t_2 as well as measuring the overlap $\langle\rho_0\rangle_u \equiv |\langle\Psi_0|\hat{u}|\Psi_0\rangle|^2$ of the initial state with $\hat{u}|\Psi_0\rangle$ in a separate measurement, one can then extract F by averaging over random unitaries as

$$\langle\{\hat{A},\hat{B}\}\rangle = \mathcal{N}_H^3\overline{\langle\hat{A}(t_1)\rangle_u\langle\hat{B}(t_2)\rangle_u\langle\rho_0\rangle_u} - \mathcal{N}_H C(t_1,t_2), \tag{4.37}$$

where $\mathcal{N}_H \gg 1$ is the Hilbert space dimension, the overline denotes averaging over random unitaries and we assumed $\hat{A}$, $\hat{B}$ to be traceless. The second term is the infinite temperature correlation function

$$\begin{aligned} C(t_1,t_2) &\equiv \frac{1}{\mathcal{N}_H}\mathrm{Tr}(\hat{A}(t_1)\hat{B}(t_2)) \\ &= \mathcal{N}_H\overline{\langle\hat{A}(t_1)\rangle_u\langle\hat{B}(t_2)\rangle_u}, \end{aligned} \tag{4.38}$$

which is interesting in its own right as it quantifies thermalization and transport in the middle of the spectrum in systems with a bounded local Hilbert space. Note that both F and C can be obtained from the same experimental data. Moreover, if $\hat{A} = \hat{B}$ only a *single* time trace needs to be measured for every unitary u (along with $\langle\rho_0\rangle_u$).

Global random unitaries can be implemented by adding local quenched disorder to a many-body Hamiltonian [325, 339].

We present the proofs of Eqs. (4.37) and (4.38) below. They follow straightforwardly from the ones presented in Ref. [338] for the out-of-time-ordered correlation function (OTOC). We also present a generalization to operators which are not traceless and a simplification of the protocol in case of thermal equilibrium $\hat{\rho}_0 \propto e^{-\beta\hat{H}}$. In

the proofs, we assume u to be a unitary 3-design, i.e. moments up to the third order have to match the circular unitary ensemble (C can be measured with 2-designs).

PROOF OF EQ. (4.38). In Ref. [338] it was shown from the properties of u that $\overline{\langle\hat{A}\rangle_u \langle\hat{B}\rangle_u} = \frac{1}{\mathcal{N}_H c}\sum_{\tau\in S_2}\mathrm{Tr}(\tau\hat{A}\otimes\hat{B})$, where S_n is the permutation group on n letters and $c = \mathcal{N}_H + 1$. For $n = 2$, $S_2 = \{\mathbb{1}, \mathrm{SWAP}\}$, where the SWAP operator acts as $\mathrm{SWAP}(|a\rangle\otimes|b\rangle) = |b\rangle\otimes|a\rangle$. By acting with τ to the left when writing out the trace as a sum over basis states and using that $\mathrm{Tr}(\hat{A}\otimes\hat{B}) = \mathrm{Tr}(\hat{A})\,\mathrm{Tr}(\hat{B})$, it follows that

$$\overline{\langle\hat{A}\rangle_u \langle\hat{B}\rangle_u} = \frac{1}{\mathcal{N}_H c}\left(\mathrm{Tr}(\hat{A})\,\mathrm{Tr}(\hat{B}) + \mathrm{Tr}(\hat{A}\hat{B})\right). \tag{4.39}$$

Using that $\hat{A}$,$\hat{B}$ are traceless and inserting $\hat{A}\to\hat{A}(t_1)$, $\hat{B}\to\hat{B}(t_2)$ we arrive at Eq. (4.38), where we assumed $\mathcal{N}_H \gg 1$.

PROOF OF EQ. (4.37). Similarly, it was shown in Ref. [338] that $\overline{\langle\hat{A}\rangle_u \langle\hat{B}\rangle_u \langle\hat{C}\rangle_u} = \frac{1}{c'}\sum_{\tau\in S_3}\mathrm{Tr}(\tau\hat{A}\otimes\hat{B}\otimes\hat{C})$, where $c' = \mathcal{N}_H(\mathcal{N}_H+1)(\mathcal{N}_H+2)$. Summing over all possible permutations τ, inserting $\hat{C} = \rho_0$, $\mathrm{Tr}\,\rho_0 = 1$ and $\hat{A}\to\hat{A}(t_1)$, $\hat{B}\to\hat{B}(t_2)$ we get

$$\begin{aligned}
&\overline{\langle\hat{A}(t_1)\rangle_u \langle\hat{B}(t_2)\rangle_u \langle\rho_0\rangle_u} \\
&= \frac{1}{c'}\Big(\mathrm{Tr}\,\hat{A}\,\mathrm{Tr}\,\hat{B} + \mathrm{Tr}\,\hat{A}\,\mathrm{Tr}\,(\rho_0\hat{B}(t_2)) + \mathrm{Tr}\,\hat{B}\,\mathrm{Tr}\,(\rho_0\hat{A}(t_1)) \\
&+ \mathrm{Tr}\,(\hat{A}(t_1)\hat{B}(t_2)) + \mathrm{Tr}\,\rho_0\hat{A}(t_1)\hat{B}(t_2) + \mathrm{Tr}\,\rho_0\hat{B}(t_1)\hat{A}(t_2)\Big).
\end{aligned} \tag{4.40}$$

Assuming that the terms in the first row vanish for traceless $\hat{A}$,$\hat{B}$, we arrive at Eq. (4.37), where we assumed $\mathcal{N}_H \gg 1$.

SPECIAL CASE: THERMAL EQUILIBRIUM. The above protocol can also be used to measure the equilibrium structure factor $F(t_1 - t_2)$ by inserting $\rho_0 = \rho_\beta = (1/Z)e^{-\beta\hat{H}}$, which via the FDR then yields the equilibrium spectral function of the operators $\hat{A}$ and $\hat{B}$. In cold atom experiments, this protocol may be used to obtain the density-density (particle-hole) spectral function for $\hat{A} = \hat{B} = \hat{n}$. For platforms in which it is difficult to prepare thermal states, but moments of the many-body Hamiltonian can be measured (such as trapped ions), finite temperature spectral functions may still be measured in a high temperature expansion [338]. ‘

4.5 MEASURING TWO-TIME CORRELATIONS IN BOSE- AND FERMI-HUBBARD SIMULATORS

By generalizing the previously discussed protocols for spin systems we show how to measure n-time correlation functions of the local density operator $\hat{n}_i$ in quantum simulators of bosonic or fermionic lattice models.

Ramsey protocol for spectral function ρ.

A pulse operator $\hat{R}_i(\theta)$ analogous to the spin model protocol can be introduced by noting that the local density operator can be written as $\hat{n}_i = (\sigma_i^z - \mathbb{1})/2$ if the occupations are restricted to zero and one as the case for fermions and "hard-core" bosons, i.e. bosons in the presence of large on-site interactions. An off-resonant light field induces an AC Stark shift described by the Hamiltonian $\hat{H}_{\mathrm{L}} = -h_i \hat{n}_i$, which in a quantum gas microscope can be implemented by a "tweezer" laser shone on a single lattice site i, for example through a spatial light modulator [154]. In a superconducting circuit, this Hamiltonian can be implemented by a change in the frequency detuning of the superconducting oscillator representing lattice site i [193, 194]. In any case, applying the field for a duration t implements the operator

$$\hat{R}_j(\theta) = \left(\cos(\theta/2)\mathbb{1} + i\sin(\theta/2)\hat{\sigma}_j^z\right)\exp(i\theta/2), \tag{4.41}$$

with $\theta = h_j t$ and we assumed $\hat{H}_L$ to be dominating the dynamics during the pulse. Proceeding as in the spin system protocol, i.e. evolving until time t_1, applying $R_i(\theta)$, evolving for a time $(t_2 - t_1)$ and measuring $\hat{n}_j$, we get

$$\begin{aligned}\langle \hat{n}_j(t_2)\rangle_\theta &= \langle \hat{n}_j(t_2)\rangle - i\sin(\theta)\,\langle\left[\hat{n}_i(t_1), \hat{n}_j(t_2)\right]\rangle \\ &+ 2\sin^2(\theta/2)\left[2\,\langle \hat{n}_i(t_1)\hat{n}_j(t_2)\hat{n}_i(t_1)\rangle - \langle\left\{\hat{n}_i(t_1), \hat{n}_j(t_2)\right\}\rangle\right],\end{aligned} \tag{4.42}$$

from which the spectral function can be extracted by choosing $\theta = \pm\pi/2$,

$$\langle\left[\hat{n}_k(t_1), \hat{n}_j(t_2)\right]\rangle = \frac{i}{2}\left(\langle \hat{n}_j(t_2)\rangle_{\pi/2} - \langle \hat{n}_j(t_2)\rangle_{-\pi/2}\right). \tag{4.43}$$

Non-equilibrium linear response protocols for spectral function ρ.

In non-equilibrium linear response, the spectral function may be obtained without restrictions on the occupation numbers. Here, we apply a small perturbation $\hat{V}$ during the dynamics and compare the measurement of an observable $\hat{A}$ at time t_1 to

an evolution without perturbation. In general, the outcome of such an experiment is

$$\langle \hat{A}(t_1)\rangle_{V\neq 0} - \langle \hat{A}(t_1)\rangle_{V=0} = -i\int_{t_0}^{t_1} dt\, \langle \left[\hat{A}(t_1), \hat{V}(t)\right]\rangle\,. \tag{4.44}$$

We now specify this expression to a local (real-space) and non-local (momentum-space) density perturbation.

LOCAL DENSITY PERTURBATION. Applying a short pulse (compared to the many-body dynamics) with an off-resonant light field on lattice site j such that $\hat{V}(t) = h_j \hat{n}_j \delta(t - t_2)$, where h_j is the pulse area, we can measure the real space density-density spectral function via

$$\langle \left[\hat{n}_k(t_1), \hat{n}_j(t_2)\right]\rangle = \frac{i}{h_j}\left(\langle \hat{n}_k(t_1)\rangle_{h\neq 0} - \langle \hat{n}_k(t_1)\rangle_{h=0}\right), \tag{4.45}$$

where $t_1 > t_2$ due to causality and contrary to the Ramsey protocol, h_j needs to be much smaller than the parameters of the many-body Hamiltonian.

In the above protocol, separate experimental runs for different sites j need to be conducted. By contrast, we can evaluate all j simultaneously using a disordered global perturbation $\hat{V}(t) = \delta(t - t_2)\sum_k h_k \hat{n}_k$ [277], with $\overline{h_i} = 0$ and $\overline{h_i h_k} = \sigma_h^2 \delta_{ik}$, where the overline denotes averaging over realizations of the random potentials with variance σ_h^2. The local spectral function can then be evaluated by post-processing as

$$\langle \left[\hat{n}_k(t_1), \hat{n}_j(t_2)\right]\rangle = \frac{i}{\sigma_h^2}\overline{h_j\left(\langle \hat{n}_k(t_1)\rangle_{h\neq 0} - \langle \hat{n}_k(t_1)\rangle_{h=0}\right)}, \tag{4.46}$$

where σ_h^2 needs to be small in order to be in the linear response regime.

STIMULATED BRAGG SPECTROSCOPY. In Bragg spectroscopy [326, 340–342], two lasers are shone onto the lattice, with the atoms absorbing a photon from one of the two and emitting into the other. The momentum transfer $\hbar\mathbf{q}$ and the energy $\hbar\omega$ are defined by the angle between the two lasers and their frequency difference, respectively. The coupling to the atoms is given by

$$\hat{V}_I(t) = \frac{V_0}{2}\left(\hat{n}_{-\mathbf{q}}(t)e^{-i\omega t} + \hat{n}_{\mathbf{q}}(t)e^{i\omega t}\right) s(t), \tag{4.47}$$

where $\hat{n}_{\mathbf{q}} = \sum_j e^{i\mathbf{q}\mathbf{r}_j}\hat{n}_j$ is the Fourier transform of the local occupation numbers (i.e. the particle-hole excitation annihilation operator), V_0 is proportional to the laser intensity and $s(t)$ is the pulse envelope function. We consider measuring $\hat{n}_{\mathbf{q}}$ by using a quantum gas microscope to measure the local occupation numbers $\hat{n}_j$ and Fourier transforming afterwards. In the following, we specify this protocol to two pulse shapes $s(t)$.

Assuming a delta-like pulse, $s(t_1 - t_p) \sim \delta(t_1 - t_p)$, we get

$$\langle \hat{n}_{\mathbf{q}}(t) \rangle - \langle \hat{n}_{\mathbf{q}}(t) \rangle_{V=0} = -\frac{iV_0}{2} \left\langle \left[\hat{n}_{\mathbf{q}}(t), \hat{n}_{-\mathbf{q}}(t_p) + \hat{n}_{\mathbf{q}}(t_p) \right] \right\rangle , \tag{4.48}$$

i.e. the analogous expression to Eq. (4.45) in momentum space. The Bragg pulses duration can be much slower than typical tunneling times in optical lattices, such that the δ-form of the pulse is valid [341].

For a constant pulse, $s(t_1) = 1$, a Laplace transform with respect to t evaluated at the same frequency ω results in

$$\begin{aligned} &\langle \hat{n}_{\mathbf{q}}(\omega) \rangle - \langle \hat{n}_{\mathbf{q}}(\omega) \rangle_{V=0} = \\ &-\frac{iV_0}{2} \int_0^\infty dt \int_0^t dt_1 \Big\langle \left[\hat{n}_{\mathbf{q}}(t), \hat{n}_{-\mathbf{q}}(t_1) e^{-i\omega(t_1 - t)} \right. \\ &\qquad \left. + \hat{n}_{\mathbf{q}}(t_1) e^{i\omega(t_1 + t)} \right] \Big\rangle, \end{aligned} \tag{4.49}$$

which is related to the spectral function Fourier transformed with respect to the relative time.

Projective measurement protocol for F

The projective measurement protocol for spin systems crucially relies on the fact that spin operators have exactly two eigenvalues. In simulators of Fermi-Hubbard models, the spin system protocol can therefore be straightforwardly generalized to the measurement of the local density $\hat{n}_{i\sigma}$ of hyperfine/spin component σ on site i. However, in Bose-Hubbard model simulators, this condition is only fulfilled when the onsite-interaction is sufficiently large and occupations are low, such that the parity of particle number, $\sum_n |2n\rangle \langle 2n|$ is almost equal to the particle number.

Keeping these limitations in mind, the protocol proceeds as the one for spin systems: After having evolved the initial state $|\Psi(0)\rangle$ under Hamiltonian $\hat{H}$ for time t_1 and subsequently having measured $\hat{n}_i$ we get for the post-measurement state

$$|\Psi'(t_1)\rangle = \begin{cases} \frac{1}{\sqrt{1 - \langle \Psi(t_1) | \hat{n}_i | \Psi(t_1) \rangle}} (1 - \hat{n}_i) |\Psi(t_1)\rangle & \text{for } |0\rangle_{t_1} \\ \frac{1}{\sqrt{\langle \Psi(t_1) | \hat{n}_i | \Psi(t_1) \rangle}} \hat{n}_i |\Psi(t_1)\rangle & \text{for } |1\rangle_{t_1} \end{cases} , \tag{4.50}$$

where $|0\rangle / |1\rangle$ denotes having measured occupation zero/one. Subsequently time evolving for time $t_2 - t_1$, we find for the final measurement of $\hat{n}_j$ that

$$\begin{aligned} &\langle \hat{n}_j(t_2) \rangle \Big|_{|0\rangle, |1\rangle} = \\ &\begin{cases} \frac{1}{1 - \langle \hat{n}_i(t_1) \rangle} \langle (1 - \hat{n}_i(t_1)) \hat{n}_j(t_2) (1 - \hat{n}_i(t_1)) \rangle & \text{for } |0\rangle_{t_1} \\ \frac{1}{\langle \hat{n}_i(t_1) \rangle} \langle \hat{n}_i(t_1) \hat{n}_j(t_2) \hat{n}_i(t_1) \rangle & \text{for } |1\rangle_{t_1} , \end{cases} \end{aligned} \tag{4.51}$$

where we switched to the Heisenberg picture. Rearranging terms, we get

$$\langle\{\hat{n}_i(t_1), \hat{n}_j(t_2)\}\rangle = \\ \langle\hat{n}_j(t_2)\rangle_{|1\rangle} \langle\hat{n}_i(t_1)\rangle - \langle\hat{n}_j(t_2)\rangle_{|0\rangle} (1 - \langle\hat{n}_i(t_1)\rangle) + \langle\hat{n}_j(t_2)\rangle\,, \tag{4.52}$$

where with $\langle\hat{n}_j(t_2)\rangle_{|1\rangle}$ we denoted the expectation value of $\hat{n}_j$ at time t_2 conditioned on having measured occupation one at time t_1. The last term is the expectation value of $\hat{n}_j$ at time t_2 without having measured at time t_1.

Non-destructive projective measurement in optical lattices using tweezers

The simplest scheme to implement non-destructive local projective measurements may be executed in quantum gas microscopes might be using fluorescence imaging [343, 344], which would however require a selective illumination of the lattice, e.g. by a tweezer. We present several other schemes in the following.

BILAYER MICROSCOPY. This recently developed technique [321, 345, 346] might enable such measurements in a spinful Hubbard model. There, the dynamics can be effectively stopped at time t_1 by splitting the spin up/down components from each other and simultaneously increasing the lattice depth. After a fluorescence measurement of one of the components (without measuring the other, which can be done by selecting the layer with the focus of the microscope [345]), the two layers are reunited to resume the dynamics before splitting them again to measure at a second time t_2. This way, a measurement of $\sum_{i,j}\langle\{\hat{n}_{i\sigma}(t_1), \hat{n}_{j\sigma'}(t_2)\}\rangle$ with $\sigma, \sigma' \in \{\uparrow, \downarrow\}$ can be made.

Similarly to the spin protocol, the measurement at time t_1 can be deferred until time t_2 by mapping the occupation of a site to a tweezer or a different layer of the optical lattice and subsequently measuring whether or not an atom was present at time t_1 by measuring the tweezer's occupation at time t_2.

SHINING A TWEEZER ON THE LATTICE. Following Ref. [347], a tightly focussed tweezer can be used to map the occupation of a site in the 2D optical lattice to the one of the tweezer. Moving the tweezer away from the lattice then makes it possible to measure the occupation without disturbing the rest of the system. For this protocol to work, moving the tweezer should be faster than any time scale in the many-body system, especially the tunneling. Tunneling times are on the order of ms in optical lattices [125] which is longer than the typically 100μs it takes to move an optical tweezer over the distance of one lattice site [169].

BRINGING A TWEEZER NEXT TO THE LATTICE. Alternatively to shining a tweezer directly on the optical lattice, one may bring it close to a given lattice site [348], which induces tunnelling of strength J_t between the tweezer and the site. Writing the state of an atom being in the tweezer as $|t\rangle$, we can write the effective Hamiltonian as $\hat{H} = J_t(|t\rangle\langle 1| + |1\rangle\langle t|)$, with $|1\rangle$ denoting the site being occupied. Keeping the tweezer for a time t next to the site induces a "pulse"

$$U = \exp(iHt) = \cos(J_t t)\mathbb{1} + i\sin(J_t t)(|t\rangle\langle 1| + |1\rangle\langle t|). \tag{4.53}$$

Choosing $t = \pi/J_t$ induces a "π-pulse", mapping the occupation of the site to the initially empty tweezer. Here, J_t needs to be much larger than the energy scales in the Bose-Hubbard model, $J_t \gg J, U$, i.e. the distance of the tweezer from the lattice must be smaller than the lattice spacing (although not much smaller due to the exponential dependence of the tunneling amplitude on the distance [126]).

Randomized measurement protocol for F

The protocol employing randomized measurements presented for spin systems can be applied to Hubbard simulators without any adapations, where the necessary implementation of disorder has been demonstrated in both quantum gas microscopes [153, 154, 159] and superconducting qubits [193, 194].

4.6 MEASURING HIGHER ORDER TIME ORDERED CORRELATION FUNCTIONS

Here, we generalize the previously known protocols for two-time functions [323, 324] to multi-time correlation functions. A specific three-point correlation function can be directly read off of Eq. (4.34):

$$\langle\hat{\sigma}_j^\beta(t_2)\rangle_{\pi/2} + \langle\hat{\sigma}_j^\beta(t_2)\rangle_{-\pi/2} = \langle\hat{\sigma}_i^\alpha(t_1)\hat{\sigma}_j^\beta(t_2)\hat{\sigma}_i^\alpha(t_1)\rangle\,, \tag{4.54}$$

with $t_2 > t_1$ as demanded by causality. In order to reconstruct the complete three point time ordered correlation function, we need to additionally measure all possible (anti-)commutator nestings [330]. These can be obtained by combining the projective measurement and Ramsey protocols as we show below. For example, a measurement of $\hat{\sigma}_i^\alpha$ at time t_1 followed by a pulse $R_j^\beta(\theta)$ at time t_2 and a measurement of $\hat{\sigma}_k^\gamma$ at time t_3 can be combined to obtain

$$\begin{aligned}
&\langle\Psi(t_1)|\,\hat{P}_i^{+\alpha}\,|\Psi(t_1)\rangle\,\langle\hat{\sigma}_j^\beta(t_2)\rangle_{+\alpha,\theta=\pi/4} \\
&+ \langle\Psi(t_1)|\,\hat{P}_i^{-\alpha}\,|\Psi(t_1)\rangle\,\langle\hat{\sigma}_j^\beta(t_3)\rangle_{-\alpha,\theta=-\pi/4} \\
&= \frac{1}{4}\,\langle\{\hat{\sigma}_i^\alpha(t_1), [\hat{\sigma}_k^\gamma(t_2), \hat{\sigma}_j^\beta(t_3)]\}\rangle\,,
\end{aligned} \tag{4.55}$$

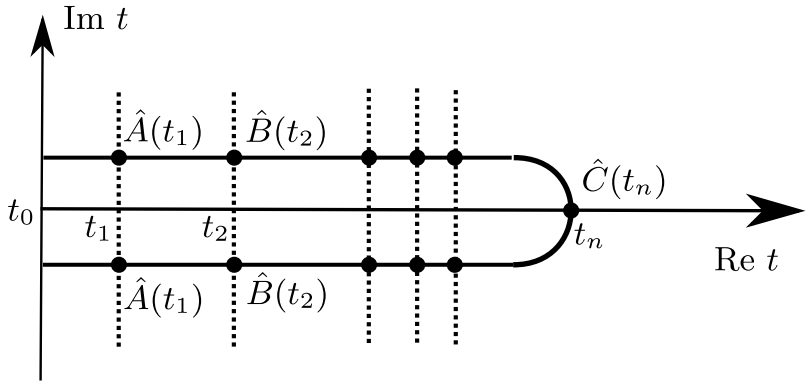

Figure 4.3: **Closed time contour depiction of the subclass of $(2n+1)$ point correlation functions accessible via protocols with n π-pulses.** Starting from the initial time t_0, operators are inserted along the contour at times $t_1, t_2, \ldots, t_n$ by local pulses. At t_{n+1} the operator $\hat{C}$ gets measured and the evolution is stopped. The operator measured by the protocol can then be obtained by starting from t_0 on the upper branch up to t_{n+1} and then backward on the lower branch back to t_0, i.e. $\langle \hat{A}(t_1)\hat{B}(t_2)\cdots\hat{C}(t_{n+1})\cdots\hat{B}(t_2)\hat{A}(t_1)\rangle$. Note that this is only a subclass of the correlation functions obtainable by the protocols presented in this section and all operators are given by Pauli matrices.

where $\hat{P}_i^{\pm\alpha} = \frac{1}{2}(\hat{\mathbb{1}} \pm \hat{\sigma}_i^{\pm\alpha})$ is the projection operator corresponding to eigenvalue +1/-1 of $\hat{\sigma}^{\alpha}$ [5]. As we see above, a projective measurement/pulse results in the appearance of an anticommutator/commutator. We hence argue that this procedure generalizes to all n-point time ordered correlation functions by decomposing them into nested anti-/commutators.

In the following we show in more detail how to generalize the projective measurement/Ramsey protocols to measure higher order time-ordered correlation functions by using more than one pulse/projection before the final measurement. Here we present the case for two pulses and two projections. We show that from this sequence *all* three point time ordered correlation functions can be obtained. These are given by the nested (anti-) commutators $\langle\{A(t_1),\{B(t_2),C(t_3)\}\}\rangle$, $\langle\{A(t_1),[B(t_2),C(t_3)]\}\rangle$, $\langle[A(t_1),\{B(t_2),C(t_3)\}]\rangle$ and $\langle[A(t_1),[B(t_2),C(t_3)]]\rangle$. The appearance of a anticommutator or commutator is obtained by a projection/pulse, respectively.

Apart from all three point correlators, also a subclass of four point and five point functions can be obtained from the two pulse/projection protocol. Furthermore, we show for arbitrary n that a particular $(2n+1)$-point correlation function can be obtained from an n pulse sequence.

5 While projections on $\hat{\sigma}^z$ are directly implemented by measurements of the level population, projection operators in the other directions of the Bloch sphere may be implemented by precluding the measurement with appropriate pulses, $\hat{P}^{\pm y} = \hat{R}^x(\pi/2)\hat{P}^{\pm z}\hat{R}^x(-\pi/2)$ and $\hat{P}^{\pm x} = \hat{R}^y(\pi/2)\hat{P}^{\pm z}\hat{R}^y(-\pi/2)$.

TWO PULSES. By using a two-pulse generalization of the commutator protocol discussed in the main text, i.e. evolve until time t_1, apply local rotation $\hat{R}_i^\alpha(\theta)$, evolve until time $(t_2 - t_1)$, apply a local rotation $\hat{R}_k^\gamma(\theta)$, evolve until time $(t_2 - t_3)$ and finally measure $\hat{\sigma}_j^\beta$, one can show that

$$\begin{aligned}\frac{1}{2}\left(\langle\hat{\sigma}_j^\beta\rangle_\theta + \langle\hat{\sigma}_j^\beta\rangle_{-\theta}\right) &= \cos^4\left(\frac{\theta}{2}\right)\langle\hat{\sigma}_j^\beta(t_3)\rangle \\ &- \sin^2\left(\frac{\theta}{2}\right)\cos^2\left(\frac{\theta}{2}\right)\big(\langle[\hat{\sigma}_i^\alpha(t_1),[\hat{\sigma}_k^\gamma(t_2),\hat{\sigma}_j^\beta(t_3)]]\rangle \\ &- \langle\hat{\sigma}_i^\alpha(t_1)\hat{\sigma}_j^\beta(t_3)\hat{\sigma}_i^\alpha(t_1)\rangle - \langle\hat{\sigma}_k^\gamma(t_2)\hat{\sigma}_j^\beta(t_3)\hat{\sigma}_k^\gamma(t_2)\rangle\big) \\ &+ \sin^4\left(\frac{\theta}{2}\right)\langle\hat{\sigma}_i^\alpha(t_1)\hat{\sigma}_k^\gamma(t_2)\hat{\sigma}_j^\beta(t_3)\hat{\sigma}_k^\gamma(t_2)\hat{\sigma}_i^\alpha(t_1)\rangle\,, \end{aligned} \tag{4.56}$$

which can be used to extract a five-point function of the form depicted in Fig. 4.3 by using $\theta = \pi$. The knowledge of this five-point-function as well as the one point function and the part of the three point correlation function obtainable from the one pulse commutator protocol can then be used to extract the nested commutator in the second row. Similarly, a nested four-point commutator may be obtained by noting that

$$\begin{aligned}&\frac{1}{2}\left(\langle\hat{\sigma}_j^\beta\rangle_\theta - \langle\hat{\sigma}_j^\beta\rangle_{-\theta}\right) \\ &= i\sin\left(\frac{\theta}{2}\right)\cos^3\left(\frac{\theta}{2}\right)\big(\langle[\hat{\sigma}_i^\alpha(t_1),\hat{\sigma}_j^\beta(t_3)]\rangle \\ &\qquad\qquad + \langle[\hat{\sigma}_k^\gamma(t_2),\hat{\sigma}_j^\beta(t_3)]\rangle\big) \\ &+ i\sin^3\left(\frac{\theta}{2}\right)\cos\left(\frac{\theta}{2}\right)\big(\langle[\hat{\sigma}_i^\alpha(t_1),\hat{\sigma}_k^\gamma(t_2)\hat{\sigma}_j^\beta(t_3)\hat{\sigma}_k^\gamma(t_2)]\rangle \\ &+ \langle\hat{\sigma}_i^\alpha(t_1)[\hat{\sigma}_k^\gamma(t_2),\hat{\sigma}_j^\beta(t_3)]\hat{\sigma}_i^\alpha(t_2)\rangle\big), \end{aligned} \tag{4.57}$$

which is however only a subclass of all possible four-point nested commutators (with others expected to appear with a higher number of pulses).

N PULSES. While the exact structure of the obtained commutators for arbitrary rotation angles θ is difficult to obtain for the general case of n pulses, it can be seen that

$$\begin{aligned}&\frac{1}{2}\left(\langle\hat{\sigma}_j^\beta\rangle_{\theta=\pi} + \langle\hat{\sigma}_j^\beta\rangle_{\theta=-\pi}\right) = \langle\hat{\sigma}_j^\beta\rangle_{\theta=\pi} \\ &= \langle\hat{\sigma}_i^\alpha(t_1)\hat{\sigma}_k^\gamma(t_2)\cdots\hat{\sigma}_j^\beta(t_{n+1})\cdots\hat{\sigma}_k^\gamma(t_2)\hat{\sigma}_i^\alpha(t_1)\rangle\,, \end{aligned} \tag{4.58}$$

where t_{n+1} is the time of the measurement after n pulses at times t_n. This $(2n+1)$-point-correlation function can be visualized on the closed time contour, see Fig. 4.3.

TWO PROJECTIONS. The same argumentation can be repeated for the case when pulses are replaced by projections, which in general leads to a replacement of com-

mutators with anticommutators. More specifically, for the case of two projections, we get with analogous notation to the two-pulse case

$$\begin{aligned}
&\langle\Psi(t_1)|\,\hat{P}_i^{+\alpha}\,|\Psi(t_1)\rangle\,\langle\Psi(t_2)|\,\hat{P}_k^{+\alpha}\,|\Psi(t_2)\rangle\,\langle\hat{\sigma}_j^{\beta}(t_2)\rangle_{+\alpha}\\
&-\langle\Psi(t_1)|\,\hat{P}_i^{-\alpha}\,|\Psi(t_1)\rangle\,\langle\Psi(t_2)|\,\hat{P}_k^{-\alpha}\,|\Psi(t_2)\rangle\,\langle\hat{\sigma}_j^{\beta}(t_3)\rangle_{-\alpha}\\
&=\frac{1}{8}\Big(\,\langle\{\hat{\sigma}_j^{\beta}(t_3),\hat{\sigma}_k^{\gamma}(t_2)+\hat{\sigma}_i^{\alpha}(t_1)\}\rangle\\
&+\langle\hat{\sigma}_i^{\alpha}(t_1)\{\hat{\sigma}_k^{\gamma}(t_2),\hat{\sigma}_j^{\beta}(t_3)\}\hat{\sigma}_i^{\alpha}(t_1)\rangle\\
&+\langle\{\hat{\sigma}_i^{\alpha}(t_1),\hat{\sigma}_k^{\gamma}(t_2)\hat{\sigma}_j^{\beta}(t_3)\hat{\sigma}_k^{\gamma}(t_3)\}\rangle\,\Big),
\end{aligned}\tag{4.59}$$

and

$$\begin{aligned}
&\langle\Psi(t_1)|\,\hat{P}_i^{+\alpha}\,|\Psi(t_1)\rangle\,\langle\Psi(t_2)|\,\hat{P}_k^{+\alpha}\,|\Psi(t_2)\rangle\,\langle\hat{\sigma}_j^{\beta}(t_2)\rangle_{+\alpha}\\
&+\langle\Psi(t_1)|\,\hat{P}_i^{-\alpha}\,|\Psi(t_1)\rangle\,\langle\Psi(t_2)|\,\hat{P}_k^{-\alpha}\,|\Psi(t_2)\rangle\,\langle\hat{\sigma}_j^{\beta}(t_3)\rangle_{-\alpha}\\
&=\frac{1}{8}\Big(\,\langle\hat{\sigma}_j(t_3)\rangle+\langle\{\hat{\sigma}_i^{\alpha}(t_1),\{\hat{\sigma}_k^{\gamma}(t_2),\hat{\sigma}_j^{\beta}(t_3)\}\}\rangle\\
&+\langle\hat{\sigma}_i^{\alpha}(t_1)\hat{\sigma}_j^{\beta}(t_3)\hat{\sigma}_i^{\alpha}(t_1)\rangle\\
&+\langle\hat{\sigma}_k^{\gamma}(t_2)\hat{\sigma}_j^{\beta}(t_3)\hat{\sigma}_k^{\gamma}(t_2)\rangle\\
&\qquad+\langle\hat{\sigma}_i^{\alpha}(t_1)\hat{\sigma}_k^{\gamma}(t_2)\hat{\sigma}_j^{\beta}(t_3)\hat{\sigma}_k^{\gamma}(t_2)\hat{\sigma}_i^{\alpha}(t_1)\rangle\,\Big),
\end{aligned}\tag{4.60}$$

which indeed are the analogous expressions to the two pulse case with commutators replaced by anticommutators. In particular, the nested double anticommutator three point function can be obtained from the last equation.

PROJECTION FOLLOWED BY PULSE. A projection at time t_1 can also be followed by a pulse at time t_2. Different linear combinations of the expectation value of $\hat{\sigma}_j^{\beta}(t_3)$ for $\pm\alpha$ and $\pm\theta$ give access to different correlation functions. Here we only note that a nested anticommutator/commutator three point function can be obtained by

$$\begin{aligned}
&\langle\Psi(t_1)|\,\hat{P}_i^{+\alpha}\,|\Psi(t_1)\rangle\,\langle\hat{\sigma}_j^{\beta}(t_2)\rangle_{+\alpha,\theta=\pi/4}\\
&+\langle\Psi(t_1)|\,\hat{P}_i^{-\alpha}\,|\Psi(t_1)\rangle\,\langle\hat{\sigma}_j^{\beta}(t_3)\rangle_{-\alpha,\theta=-\pi/4}\\
&=\frac{1}{4}\,\langle\{\hat{\sigma}_i^{\alpha}(t_1),[\hat{\sigma}_k^{\gamma}(t_2),\hat{\sigma}_j^{\beta}(t_3)]\}\rangle\,.
\end{aligned}\tag{4.61}$$

PULSE FOLLOWED BY PROJECTION. Similarly, if a pulse at time t_1 is followed by a projection at time t_2,we get

$$\begin{aligned}&\langle\Psi(t_1)|\,\hat{P}_i^{+\alpha}\,|\Psi(t_1)\rangle\,\langle\hat{\sigma}_j^{\beta}(t_2)\rangle_{+\alpha,\theta=\pi/4}\\&+\langle\Psi(t_1)|\,\hat{P}_i^{-\alpha}\,|\Psi(t_1)\rangle\,\langle\hat{\sigma}_j^{\beta}(t_3)\rangle_{-\alpha,\theta=-\pi/4}\\&=\frac{1}{4}\,\langle[\hat{\sigma}_i^{\alpha}(t_1),\{\hat{\sigma}_k^{\gamma}(t_2),\hat{\sigma}_j^{\beta}(t_3)\}]\rangle\,,\end{aligned}\tag{4.62}$$

i.e. commutator and anticommutator are exchanged compared to projection and pulse being in reverse order.

We hence showed that all possible combinations of (anti-)commutator nestings are measurable on the level of three point functions, which means that the complete time ordered three point function can be reconstruncted. Furthermore, we saw that a projector/commutator always leads to an (anti-)commutator. We therefore expect that the structure remains for higher order correlation functions such that all possible (anti-)commutator nestings can be obtained by appropriate combinations of pulses and projections and hence all time ordered n point correlation functions can be accessed.

4.7 CHARACTERIZING THE EMERGENCE OF FLUCTUATION-DISSIPATION RELATIONS

After having introduced measurement protocols for F and ρ, we now show that FDRs can be used to characterize thermalization in current quantum simulation platforms. We test the emergence of the FDR in Eq. (4.4) by defining the function

$$\mathrm{FDR}(T,\omega)=\log\left(\frac{1}{F(T,\omega)/\rho(T,\omega)-1/2}+1\right),\tag{4.63}$$

where $\rho(T,\omega)=\int dt e^{i\omega t}\rho(T+t/2,T-t/2)$ is the two-time spectral function at central time $T=(t_1+t_2)/2$. The FDR demands that $\mathrm{FDR}(T,\omega)=\beta\omega$ in equilibrium with the inverse temperature β set by the energy of the initial state

$$\langle\psi_0|\hat{H}|\psi_0\rangle=\mathrm{Tr}\left(\frac{\exp(-\beta\hat{H})}{Z}\hat{H}\right).\tag{4.64}$$

All numerical results have been obtained using exact diagonalization. We introduce our efficient numerical calculation of two-time correlations in the following.

EVALUATING F AND ρ IN EXACT DIAGONALIZATION. In order to calculate the correlation functions $F=\frac{1}{2}\left\langle\left\{\hat{A}(t_1),\hat{B}(t_2)\right\}\right\rangle$ and $\rho=\left\langle\left[\hat{A}(t_1),\hat{B}(t_2)\right]\right\rangle$ in general, we first time evolve the initial state $|\Psi\rangle$ to $|\Psi(t)\rangle=U(t)\,|\Psi\rangle\equiv\exp(-i\hat{H}t)\,|\Psi\rangle$ for all times t at which the two-time correlation function should be evaluated. Then,

we create a set of four states by acting with $\hat{A}, \hat{B}$ and their Hermitian conjugates onto $|\Psi(t)\rangle$ and evolve them back for every point in time t, such that we arrive at $|\Psi_A(t)\rangle = \hat{A}(t)|\Psi\rangle$,$|\Psi_{A'}(t)\rangle = \hat{A}^\dagger(t)|\Psi\rangle$,$|\Psi_B(t)\rangle = \hat{B}(t)|\Psi\rangle$ and $|\Psi_{B'}(t)\rangle = \hat{B}^\dagger(t)|\Psi\rangle$, where $\hat{A}(t) = U^\dagger(t)\hat{A}U(t)$.

From these states we can then calculate F and ρ by evaluating

$$F(t_1,t_2) = \frac{1}{2}\left(\langle\Psi_{A'}(t_1)|\Psi_B(t_2)\rangle + \langle\Psi_{B'}(t_1)|\Psi_A(t_2)\rangle\right),$$
$$\rho(t_1,t_2) = \left(\langle\Psi_{A'}(t_1)|\Psi_B(t_2)\rangle - \langle\Psi_{B'}(t_1)|\Psi_A(t_2)\rangle\right). \tag{4.65}$$

for all times t_1 and t_2.

Simplifications occur if $\hat{B}^\dagger = A$ such as for creation/annihilation or σ^+,σ^- operators, and as then only two states have to be evolved. If additionally $\hat{A}^\dagger = \hat{A}$, only a single state needs to be evolved and F and $-(i/2)\rho$ correspond to the real/imaginary parts of the correlation function $\langle\Psi_A(t_1)|\Psi_A(t_2)\rangle$.

EFFICIENT NUMERICAL EVALUATION. Eq. (4.65) can be evaluated efficiently by writing the states $|\Psi_A(t_1))\rangle$ into a matrix P_A, where states for different times are the rows of P_A. Then, Eq. (4.65) can be evaluated by the matrix product as $\langle\Psi_A(t_1)|\Psi_B(t_2)\rangle = [P_A^* P_B^T]_{t_1 t_2}$.

When using full diagonalization, i.e. obtaining the vector of eigenenergies $\mathbf{E}$ and the matrix U with the eigenvectors as its columns, the forward-backward evolution described above can be efficiently obtained by writing the times t_1 into a vector $\mathbf{T}$. By repeating the initial state $\dim(\mathbf{T})$ times in a matrix P_{ini}, the time evolved states follow as

$$P_A = U\exp(i\mathbf{E}\otimes\mathbf{T})\odot U^\dagger A U\exp(-i\mathbf{E}\otimes\mathbf{T})\odot U^\dagger P_{\text{ini}}, \tag{4.66}$$

where $\odot$ denotes the Hadamard product (element-wise multiplication) and the exponential is understood element-wise.

4.8 THERMALIZATION IN THE BOSE HUBBARD MODEL

One of the first demonstrations of the relaxation of equal-time observables towards their equilibrium expectation values was given in an experiment simulating the Bose-Hubbard model [127], hence effectively probing the diagonal part of ETH. Here we study the fluctuation-dissipation relations and hence test the validity of the off-diagonal part of ETH.

We study a two-dimensional Bose-Hubbard model with open boundary conditions, given by Hamiltonian

$$\hat{H} = -J\sum_{<i,j>}(\hat{a}_i^\dagger\hat{a}_j + \hat{a}_j^\dagger\hat{a}_i) + \frac{U}{2}\sum_i \hat{n}_i(n_i - 1), \tag{4.67}$$

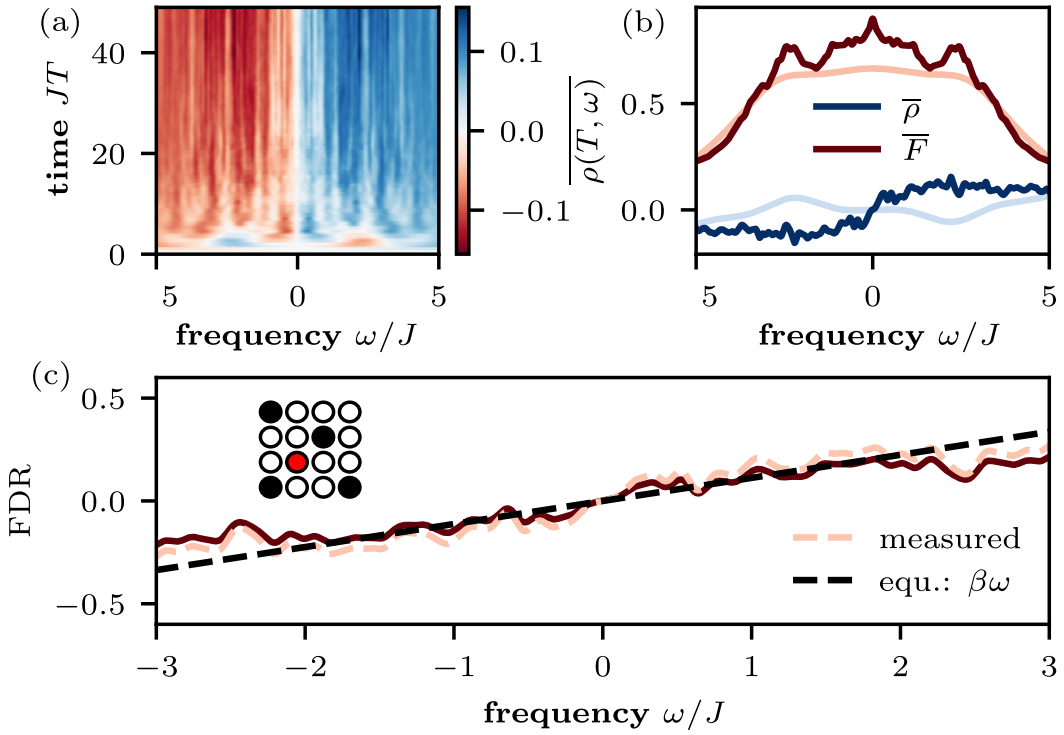

Figure 4.4: **Emergence of FDRs in the 2D Bose Hubbard model.** (a) Central-time averaged equal-site density-density spectral function ρ as a function of central time JT and frequency. (b) Late time spectral and statistical functions ($JT = 40$, dark) compared to early times ($JT = 2$, bright). (c) Fluctuation dissipation relation function defined in Eq. (4.63) at time $JT = 40$ compared to the equilibrium expectation (dashed black line), with the inverse temperature β set by energy of the initial state according to Eq. (4.64). While the dark red line shows the ideal result, the bright dashed line is the result measured by the linear response and non-destructive projective measurement schemes. The inset shows the location of the initially occupied sites (black) and the probed lattice site (red) on the 4×4 lattice. The on-site repulsion is given by $U/J = 6$. We used a Gaussian frequency broadening with standard deviation $\sigma_\omega = 0.05J$ for the Fourier transform.

where $[\hat{a}_i, \hat{a}_j^\dagger] = \delta_{ij}$, $\hat{n}_i = \hat{a}_i^\dagger \hat{a}_i$ and we truncate the local Hilbert space dimension to three states. In Fig. 4.4 we show the central time averaged statistical and spectral function defined as $\overline{\rho(T,\omega)} = \frac{1}{T}\int_0^T dt\rho(t,\omega)$ for the local density, i.e. $\hat{A} = \hat{B} = \hat{n}_i$ with the probed lattice site i indicated in red in Fig. 4.4c). In Fig. 4.4a) we show that $\overline{\rho}$ (and equally $\overline{F}$, not shown) becomes approximately independent of central time for $JT \gtrsim 20$, indicating that a steady-state has been reached. In order to test whether this steady-state displays the correct connection between F and ρ expected in equilibrium, we plot the FDR function, Eq. (4.63), showing that indeed $\mathrm{FDR}(T,\omega) \sim \beta\omega$. The inverse temperature β extracted from the FDR matches the expectation from the energy of the initial state (c.f. Eq. 4.64), indicating that the correct equilibrium state has been reached. Moreover, in Fig. 4.4c) we display the FDR function as obtained from an experiment employing non-equilibrium linear response to measure the density-density spectral function ρ and the projective measurement protocol to measure the parity-parity statistical function F, which agrees reasonably well with the temperature obtained in the FDR from the ideal case and we find better agreement as the on-site repulsion U is increased.

Here, we showed that full thermalization (i.e. both the diagonal and off-diagonal parts of ETH) can be observed in Hubbard models by probing the emergence of FDRs between the density-density fluctuations and dissipations. In the following, we will discuss cases in which more intricate transient dynamics not contained in the ETH can be observed and characterized via two-time correlation functions.

4.9 PRETHERMALIZATION IN THE LONG-RANGE TRANSVERSE FIELD ISING MODEL

While ETH provides a universal mechanism for how quantum systems reach a thermal steady state at long times, long-lived transient non-thermal states not described by ETH can arise in the dynamics due to a competition of different terms in the Hamiltonian or the presence of non-thermal eigenstates. Here, we will discuss how two-time functions and the FDR can be used to characterize several examples of such *prethermal* steady-states in the long-range transverse field Ising chain (LTFI) implemented in trapped ion quantum simulators

$$\hat{H} = \sum_{i<j} \frac{J}{|i-j|^\alpha} \hat{\sigma}_i^x \hat{\sigma}_j^x + \frac{g}{2} \sum_i \hat{\sigma}_i^z \tag{4.68}$$

with chain length L, long-range exponent α and transverse field strength g. We will discuss how three generic examples of prethermalization can be observed in the FDR, using the LTFI to demonstrate the principle. In the first case, a large transverse field g leads to the classic version of prethermalization as introduced by Berges

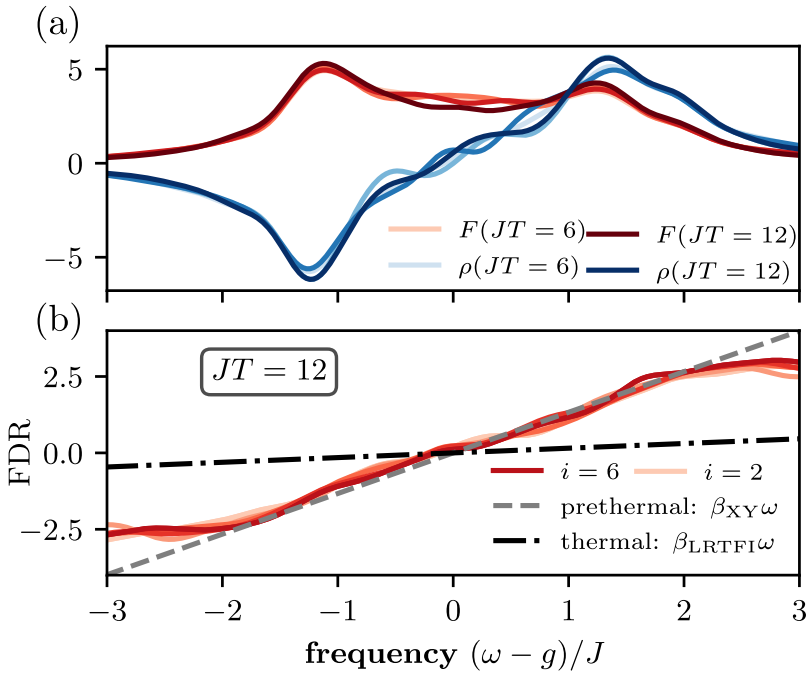

Figure 4.5: **Prethermal FDRs in the long-range transverse field Ising model.** (a) The equal-site spectral and statistical functions ρ, F of the local spin raising operators $\hat{\sigma}_i^+$ with initial state $|\psi_0\rangle = |\uparrow\downarrow\cdots\downarrow\uparrow\rangle_x$ and $i = 2$. Central times JT increase from bright to dark. (b) Fluctuation-dissipation relation for different lattice sites i (increasing from bright to dark) along with the expected inverse temperatures β in thermal equilibrium of the LTFI and the prethermal Hamiltonian (XY model). We used a Gaussian broadening with standard deviation $\sigma_\omega = 0.2J$ for the Fourier transform. Parameters used are $L = 13$ (open boundary conditions), long-range exponent $\alpha = 1.5$, transverse field $g = 12J$.

et al. [46], where a single quasi-conserved quantity prevents full thermalization up to exponentially long times in J/g [349] and prethermalization to an effective Hamiltonian can be observed in the FDR. In the second example, we show that the generalization of this phenomenon to an *extensive* number of approximately conserved quantities in an integrable sector of the LTFI [327] can be used to experimentally diagonalize the Hamiltonian. In the third case, we discuss quenches from a polarized state at $g = 0$ to small g and show how emergent confined excitations can be identified by genuine non-equilibrium features in the two-time functions and by a violation of the FDR up to long times.

4.9.1 *Prethermalization due to an approximate conservation law*

Here we study the LTFI in the regime of large transverse field, $g = 12J$, and choose the local spin raising/lowering operators $\hat{A} = \hat{\sigma}_i^+ = \hat{B}^\dagger$ as operators in the two-time functions, with $\hat{\sigma}^\pm = \frac{1}{2}(\hat{\sigma}^x \pm i\hat{\sigma}^y)$. In Fig. 4.5a) we show F and ρ starting from the

initial state $|\psi_0\rangle = |\uparrow\downarrow\cdots\downarrow\uparrow\rangle_x$, showing that for central times as small as $JT = 6$ a steady state has been reached. However, contrary to the case in the Bose-Hubbard model, they are not centred around $\omega = 0$. Moreover, the FDR function, shown in Fig. 4.5b), approximately shows the linear-in-frequency behavior expected in equilibrium, but with the inverse temperature β not matching the expectation from inserting the LTFI into Eq. (4.64). Both of these features are explained by the phenomenon of prethermalization [46]. Here, the large value of g energetically disfavors all terms in the Hamiltonian changing the total transverse magnetization $\hat{S}^z = \frac{1}{2}\sum_i \hat{\sigma}_i^z$, i.e. terms $\sim \sigma^+\sigma^+, \sigma^-\sigma^-$. This leads to an almost conservation of the transverse magnetization and the system effectively evolves under the Hamiltonian $\hat{H}_{\text{eff}} = \hat{H}_{XY} + g\hat{S}^z$ with $\hat{H}_{XY} = \sum_{i<j} \frac{J}{|i-j|^\alpha}(\hat{\sigma}_i^+\hat{\sigma}_j^- + h.c.)$. The shift of the frequency-space two-time functions follows from the fact that $\hat{\sigma}^\pm$ are the raising/lowering operators corresponding to the approximate conservation law, i.e. $[\hat{S}^z, \hat{\sigma}^\pm] = \pm\hat{\sigma}^\pm$. Using that $[\hat{H}_{XY}, \hat{S}^z] = 0$, we find that the term $\sim S^z$ in H_{eff} then leads to a precession of the two time functions of $\sigma^\pm$, i.e. $\hat{\sigma}^+(t_1)\hat{\sigma}^-(t_2) = e^{ig(t_1-t_2)}\hat{\sigma}'^+(t_1)\hat{\sigma}'^-(t_2)$, with the $'$ indicating the remaining non-trivial time evolution with $\hat{H}_{XY}$. After the Fourier transform with respect to $t_1 - t_2$, this precession leads to the shift $\omega \to \omega + g$ in the two-time functions and is a direct consequence of the approximate conservation law [6]. From this picture, we moreover expect the system to thermalize to a grand-canonical equilibrium state $e^{-\beta(\hat{H}_{XY} - \mu\hat{S}^z)}$ instead of $e^{-\beta\hat{H}}$ on short timescales, where $\mu = 0$ for our initial state. This behavior is directly reflected in the temperature found in the FDR: The temperature obtained from inserting $\hat{H}_{XY}$ into Eq. (4.64) agrees well with the time evolved quasi steady-state (grey dashed line in Fig. 4.5). We note that at exponentially long times in J/g, prethermalization to $e^{-\beta\hat{H}_{XY}}$ would ultimately give way to full thermalization to the LTFI, however we did not find this for our finite-size system on the studied timescales.

In this section, we have shown that the presence of a prethermal conserved quantity can be observed by measuring the FDR corresponding to the raising/lowering operators of the conserved quantity. In the following, we show that this scheme can be generalized to the case of an extensive number of conserved quantities in an integrable model.

4.9.2 *Prethermalization in the vicinity of integrability: Generalized Gibbs ensemble FDR*

Integrable models possess an extensive (and complete) set of local conserved quantities $\hat{\mathcal{I}}_q$, which prevents them from thermalizing in the sense of the ETH [27].

6 In general, one would also expect such a shift if the (pre-)thermal steady state has non-zero chemical potential. In our case, however, the chemical potential corresponding to the initial state vanishes such that the shift is solely due to the precession induced by term $\hat{S}^z$ in the Hamiltonian.

However, integrable models are still expected to fulfill Jayne's maximum entropy principle [350] and hence be described by a "generalized Gibbs ensemble"

$$\hat{\rho}_{GGE} \sim \exp\left(-\sum_q \lambda_q \hat{\mathcal{I}}_q\right) \tag{4.69}$$

at late times with the Lagrange multipliers λ_q determined by the initial condition according to $\langle\psi_0|\hat{\mathcal{I}}_q|\psi_0\rangle \stackrel{!}{=} \mathrm{Tr}(\hat{\rho}_{\mathrm{GGE}}\hat{\mathcal{I}}_q)$.

It was shown [327, 351] that the reasoning for deriving the FDR in App. 4.2 while replacing the canonical density matrix $\frac{1}{Z}e^{-\beta\hat{H}}$ with ρ_{GGE} leads to a "generalized Gibbs ensemble FDR". We summarize the reasoning in the following.

GENERALIZED KMS CONDITION AND FDRS. Thermalization to the GGE implies that two-time correlation functions of operators $\hat{A}$ and $\hat{B}$ fulfill a generalized KMS condition

$$\mathrm{Tr}\left(\hat{\rho}_{\mathrm{GGE}}\hat{A}(t_1)\hat{B}(t_2)\right) = \mathrm{Tr}\left(\hat{\rho}_{\mathrm{GGE}}\hat{B}'(t_2)\hat{A}(t_1)\right), \tag{4.70}$$

with $\hat{B}'(t_2) = e^{\sum_k \lambda_k \hat{\mathcal{I}}_k}\hat{B}(t_2)e^{-\sum_k \lambda_k \hat{\mathcal{I}}_k}$. The resulting FDR then crucially depends on the operator $\hat{B}$. For example, for $\hat{B} = \hat{\mathcal{I}}_k$ it follows that $\hat{\mathcal{I}}'_k(t_2) = \hat{\mathcal{I}}_k(t_2)$ and therefore the commutator vanishes, $\rho = \langle[\hat{A}(t_1), \hat{\mathcal{I}}_k(t_2)]\rangle_{\mathrm{GGE}} = 0$, rendering the FDR meaningless as the anticommutator $\tilde{F} = \frac{1}{2}\langle\{\hat{A}(t_1), \hat{\mathcal{I}}_k(t_2)\}\rangle_{\mathrm{GGE}}$, i.e. F in Eq. (4.2) without subtracting the disconnected part, is in general non-zero.

An FDR of the expected form is however obtained for $\hat{B} = \hat{d}_k$, defined by $\hat{\mathcal{I}}_k = \hat{d}_k^\dagger\hat{d}_k$ as then $\hat{d}'_k(t_2) = e^{-\lambda_k}\hat{d}_k(t_2)$ and hence $\langle\hat{A}(t_1)\hat{d}_k(t_2)\rangle = e^{-\lambda_k}\langle\hat{d}_k(t_2)\hat{A}(t_1)\rangle$. Therefore we find the FDR

$$\tilde{F}(t_1, t_2) = \left(\frac{1}{2} + n_{\lambda_k}\right)\rho(t_1, t_2), \quad \text{with} \quad n_{\lambda_k} = \frac{1}{e^{-\lambda_k} - 1}. \tag{4.71}$$

For a non-interacting model of the form

$$\hat{H} = \sum_q \epsilon_q \hat{d}_q^\dagger\hat{d}_q, \tag{4.72}$$

the spectral and statistical functions for $\hat{A} = \hat{d}_q = \hat{B}^\dagger$ trivially fulfill the GGE FDR for all times and initial states. We will show in the following that the GGE FDR is observable in an integrable sector of the LTFI [7].

7 In Ref. [327, 352] a similar reasoning was followed, however focussing on density-density (two-particle) correlations from which only linear combinations of the λ_q can be extracted. Here, we show instead that the λ_q can be directly extracted from the single-particle two-time correlation functions while additionally enabling the extraction of the Bogoliubov angles.

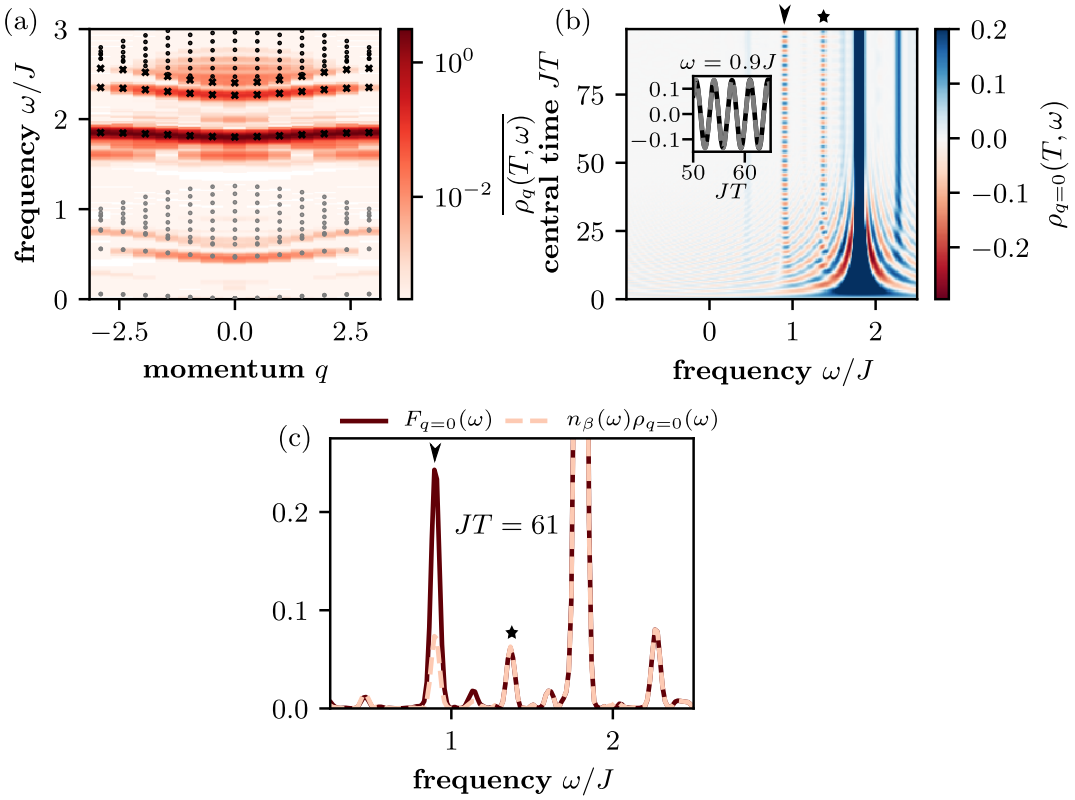

Figure 4.6: **Violation of the FDR due to confined excitations in the LTFI.** (a) Two-domain wall spectral function averaged over central time T starting from a completely x-polarized state. Black dots and crosses indicate the difference $E_n - E_0$ of the eigenenergies E_n with the ground state energy E_0, grey dots are $E_n - E_1$. (b) Time and frequency resolved spectral function. Black arrow and star indicate oscillatory features, which are non-thermal as depend on central time. Inset: The oscillation frequency of the peak at $\omega = 0.9J$ (black) matches the energy difference between the first and second excited state (sinusoidal fit with fixed frequency in dashed grey). (c) Test of the FDR by comparing $F_{q=0}(T,\omega)$ with the corresponding right hand side of the FDR in Eq. (4.4) for a fixed time $JT = 61$. The black arrow/star indicates the location of the two non-thermal features in b). For all subplots, we used a Gaussian broadening with standard deviation $40/J$ in time and do not plot very small frequencies in c) due to artefacts from the Fourier transform. Here, the transverse field is $g = 0.53J$ and the long range exponent $\alpha = 2.3$.

INTEGRABLE LIMIT OF THE LTFI. If the initial state has only a few n on top of the fully polarized state in the direction of the field, $|\Psi_0\rangle = |\uparrow\uparrow\cdots\uparrow\rangle$ or $|\Psi_0\rangle = |\downarrow\downarrow\cdots\downarrow\rangle$, the dynamics can be accurately described within linear spin-wave theory [183, 187, 353, 354]. Employing a Holstein-Primakoff transformation $\hat{\sigma}_i^z \to 2\hat{a}_i^\dagger\hat{a}_i - 1$, $\hat{\sigma}_i^+ \to \hat{a}_i^\dagger\sqrt{1-\hat{a}_i^\dagger\hat{a}_i} \approx \hat{a}_i^\dagger$, we can map the LTFI Hamiltonian of length L to

$$\hat{H} = \sum_{i,j} J_{ij}\left(\hat{a}_i^\dagger\hat{a}_j + \frac{1}{2}\left(\hat{a}_i^\dagger\hat{a}_j^\dagger + \hat{a}_i\hat{a}_j\right)\right) + g\sum_i \hat{a}_i^\dagger\hat{a}_i \tag{4.73}$$

in the regime where $\max(J_{ij}) \ll g$ at low filling such that the pairing terms are suppressed and hence the spin-wave approximation stays valid in the dynamics. For a single spin flip on top of the fully polarized state, this mapping becomes exact as $\max(J_{ij})/g \to 0$.

We diagonalize the spatial degree of freedom by employing an orthogonal transformation $UU^T = \mathbb{1}$, such that $\sum_{i,j} = U_{ik}J_{ij}U_{jk'} = \nu_k\delta_{kk'}$, which introduces a conjugate coordinate k via $\hat{a}_k = \sum_i U_{ik}\hat{a}_i$ and ν_k are the eigenvalues of the interaction matrix J_{ij} ($J_{ii} = 0$) [183]. The Hamiltonian then reads

$$\hat{H} = \sum_k (\nu_k + g)\hat{a}_k^\dagger\hat{a}_k + \frac{1}{2}\nu_k(\hat{a}_k^\dagger\hat{a}_k^\dagger + \hat{a}_k\hat{a}_k) \tag{4.74}$$

and can be diagonalized via a Bogoliubov transformation $\hat{a}_k = \cosh(\Theta_k)\hat{d}_k - \sinh(\Theta_k)\hat{d}_k^\dagger$, $\Theta_k = \frac{1}{2}\operatorname{arctanh}\left(\nu_k/(\nu_k+g)\right)$ such that

$$\hat{H} = \sum_k \epsilon_k\hat{d}_k^\dagger\hat{d}_k \quad \text{with} \quad \epsilon_k = \sqrt{g(g+2\nu_k)}. \tag{4.75}$$

The explicitly diagonalized Hamiltonian in Eq. (4.75) shows that the LTFI has extensively many conserved quantities $\hat{\mathcal{I}}_k = \hat{n}_k \equiv \hat{d}_k^\dagger\hat{d}_k$ in this regime, implying that the equilibrium state is described by a GGE (c.f. Eq. (4.69)). The Lagrange multipliers λ_k to which an initial state $|\Psi_0\rangle$ is expected to thermalize to are determined by the condition $\langle\Psi_0|\hat{n}_k|\Psi_0\rangle \equiv \langle\hat{n}_k\rangle_0 \overset{!}{=} \frac{1}{Z}\operatorname{Tr}\left[\hat{\rho}_{\mathrm{GGE}}\hat{n}_k\right]$. Evaluating both sides then leads to

$$\lambda_k = -\ln\left(\frac{1}{\langle\hat{n}_k\rangle_0} + 1\right), \tag{4.76}$$

with $\langle\hat{n}_k\rangle_0 = \cosh(2\Theta_k)\sum_{i,j} U_{ik}U_{jk}\langle\hat{a}_i^\dagger\hat{a}_j\rangle_0 + \sinh^2(\Theta_k)$.

FDRS IN INTEGRABLE REAL-TIME DYNAMICS. Here we show explicitly that the GGE-FDR in Eq. (4.71) emerges in the non-equilibrium dynamics under the Hamiltonian in Eq. (4.75). In the Heisenberg picture, the rotated operators $\hat{d}_k$ evolve

according to $\hat{d}_k(t) = e^{i\hat{H}t}\hat{d}_k e^{-i\hat{H}t} = e^{-i\epsilon_k t}\hat{d}_k$. Hence, it follows for the two-time correlation functions

$$\tilde{F} = \frac{1}{2}\left\langle\left\{\hat{d}_k(t_1), \hat{d}_k^\dagger(t_2)\right\}\right\rangle_0 = e^{-i\epsilon_k(t_1-t_2)}\left(\frac{1}{2} + \langle\hat{n}_k\rangle_0\right), \tag{4.77}$$

$$\rho = \left\langle\left[\hat{d}_k(t_1), \hat{d}_k^\dagger(t_2)\right]\right\rangle_0 = e^{-i\epsilon_k(t_1-t_2)}, \tag{4.78}$$

which explicitly shows that Eq. (4.71) is fulfilled for all times t_1, t_2 as $\langle\hat{n}_k\rangle_0 = \langle\hat{n}_k\rangle_{\mathrm{GGE}} = n_{\lambda_k}$ by definition of the GGE. In the sense of the FDR, this integrable model is therefore instantly thermalized to the GGE.

Similarly, one can also calculate the two-time correlation functions of the number operator $\hat{n}_k$, which are commuting constants of motion and hence

$$rho = \langle[\hat{n}_k(t_1), \hat{n}_{k'}(t_2)]\rangle_0 \tag{4.79}$$

$$= \langle[\hat{n}_k, \hat{n}_{k'}]\rangle_0 = 0. \tag{4.80}$$

However,

$$\tilde{F} = \langle\{\hat{n}_k(t_1), \hat{n}_{k'}(t_2)\}\rangle_0 - \langle\hat{n}_k(t_1)\rangle\langle\hat{n}_{k'}(t_2)\rangle \tag{4.81}$$

$$= \langle\hat{n}_k\hat{n}_{k'}\rangle_0 - \langle\hat{n}_k\rangle\langle\hat{n}_{k'}\rangle \neq 0 \tag{4.82}$$

in general and hence there is only an FDR in the sense $\rho/\tilde{F} = 0$.

GGE FDR IN EXPERIMENTALLY OBSERVABLE OPERATORS. Here we show that a GGE FDR is also obtained for the experimentally accessible operators $\hat{a}_k$. First of all, we note that

$$\hat{a}_k(t) = \cosh(\Theta_k)e^{i\epsilon_k t}\hat{d}_k - \sinh(\Theta_k)e^{-i\epsilon_k t}\hat{d}_k^\dagger, \tag{4.83}$$

from which it follows that

$$\tilde{F} = \frac{1}{2}\left\langle\left\{\hat{a}_k(t_1), \hat{a}_k^\dagger(t_2)\right\}\right\rangle \tag{4.84}$$

$$\begin{aligned} &= \frac{1}{2}\left(\cosh^2(\Theta_k)e^{-i\epsilon_k(t_1-t_2)} + \sinh^2(\Theta_k)e^{i\epsilon_k(t_1-t_2)}\right) \\ &\quad\times\left(1 + 2\langle\hat{d}_k^\dagger\hat{d}_k\rangle_0\right) \\ &\quad - \sinh(\Theta_k)\cosh(\Theta_k) \\ &\quad\times\left(e^{-i\epsilon_k(t_1+t_2)}\langle\hat{d}_k\hat{d}_k\rangle_0 + e^{i\epsilon_k(t_1+t_2)}\langle\hat{d}_k^\dagger\hat{d}_k^\dagger\rangle_0\right), \end{aligned} \tag{4.85}$$

$$\rho = \cosh^2(\Theta_k)e^{-i\epsilon_k(t_1-t_2)} - \sinh^2(\Theta_k)e^{i\epsilon_k(t_1-t_2)}, \tag{4.86}$$

where one can show that $\langle\hat{d}_k\hat{d}_k\rangle_0 = \langle\hat{d}_k^\dagger\hat{d}_k^\dagger\rangle_0 = \cosh(\Theta_k)\sinh(\Theta_k)(1 + 2\langle\hat{a}_k^\dagger\hat{a}_k\rangle_0)$.

In the limit where the central time $T = \frac{1}{2}(t_1 + t_2)$ is large, we can apply the rotating wave approximation and neglect the fast rotating terms in $\tilde{F}$. Fourier transforming with respect to the relative time $t_1 - t_2$, we find

$$\rho(\omega) = 2\pi\big(\cosh^2(\Theta_k)\delta(\omega - \epsilon_k) - \sinh^2(\Theta_k)\delta(\omega + \epsilon_k)\big), \tag{4.87}$$

$$\tilde{F}(\omega, T \to \infty) = 2\pi\left(\frac{1}{2} + \langle \hat{d}_k^\dagger \hat{d}_k \rangle_0\right) \times \big(\cosh^2(\Theta_k)\delta(\omega - \epsilon_k) + \sinh^2(\Theta_k)\delta(\omega + \epsilon_k)\big). \tag{4.88}$$

Therefore, we can read off the GGE parameter λ_k from the peak at $\omega = \epsilon_k$ by

$$\lambda_k = \ln\left(\frac{1}{\frac{\tilde{F}(\omega=\epsilon_k)}{\rho(\omega=\epsilon_k)} - \frac{1}{2}} + 1\right). \tag{4.89}$$

This procedure also works if observation or coherence times are finite and so the δ-peaks are broadened as the peaks in both $\tilde{F}$ and ρ get broadened equally with the area under the curves staying constant.

The dispersion of the diagonalized Hamiltonian ϵ_k can be read off from the position of the peaks in ρ, whereas the ratio of the two peak heights yields the Bogoliubov angle Θ_k. Hence, from a measurement of this two-time function the Hamiltonian can be "experimentally diagonalized". Moreover, the two-time functions of the *rotated* degrees of freedom can now be obtained from the unrotated two-time functions via

$$\begin{aligned}
&\langle \hat{d}_k(t_1)\hat{d}_k^\dagger(t_2)\rangle \\
&= \cosh^2(\Theta_k)\,\langle \hat{a}_k^\dagger(t_1)\hat{a}_k(t_2)\rangle + \sinh^2(\Theta_k)\,\langle \hat{a}_k(t_1)\hat{a}_k^\dagger(t_2)\rangle \\
&- \cosh(\Theta_k)\sinh(\Theta_k)\left(\langle \hat{a}_k^\dagger(t_1)\hat{a}_k^\dagger(t_2)\rangle + \langle \hat{a}_k(t_1)\hat{a}_k(t_2)\rangle\right).
\end{aligned} \tag{4.90}$$

This leads to an alternative method to obtain the λ_k: the FDRs of the *rotated* degrees of freedom can be obtained and the λ_k extracted from Eq. (4.71). This alternative procedure has the advantage of only involving the relative time $t_1 - t_2$ even when starting from non-equilibrium initial states, such that we can set $t_2 = 0$, reducing the experimental effort as only one-point functions have to be measured.

Note that "thermalization to a GGE" is in practice only a transient phenomenon as there are always integrability-breaking terms present in experiment [47, 308], leading to thermalization to a (grand-)canonical ensemble at late times. This is why the case discussed here is a direct generalization of the prethermalization discussed in the previous section, with the single additional conservation law replaced with extensively many.

4.9.3 *Prethermalization due to confined excitations*

So far, we showed that the nature of the (pre-)thermal steady state can be elucidated from measuring FDRs, hence showing their potential to test the assumptions of the ETH. In the following, we will show that information contained in F and ρ can also be used to identify the relevant excitations for the thermalization dynamics in a case in which violations of the FDR (and therefore the ETH) survive up to long times.

At small transverse fields, $g < J$, the LTFI shows confinement of domain wall excitations [355], which leads to non-thermal eigenstates in the spectrum [356] and and long thermalization times [357–359]. Here, we will show that this effect reminiscent of the confinement between quarks in QCD [360] leads to non-thermal features in two-time correlation functions, including a violation of the FDR (and hence ETH) up to long times. The proposal discussed here for characterizing confined excitations by two-time correlations may be used in the future to characterize unknown non-thermal eigenstates directly in experiment.

We prepare the totally x-polarized initial state $|\psi_0\rangle = |\uparrow \cdots \uparrow\rangle_x$, which is close to one of the two ground states due to $g < J$. We directly probe the confined excitations by calculating the two-domain-wall spectral and statistical function in momentum space by choosing $\hat{A} \equiv \hat{\sigma}_2^+ = (\hat{\sigma}_q^z + i\hat{\sigma}_q^y)/2 = \hat{B}^\dagger$, which flips a spin and hence creates two domain walls. In Fig. 4.6a) we show the central-time averaged non-equilibrium spectral function for $\alpha = 2.3$, $g = 0.53J$ and periodic boundary conditions (replacing the distance $|i-j|$ in Eq. (4.68) with $\min(|i-j|, L-|i-j|)$). Three nearly dispersionless sharp excitations (linewidth limited by the numerical broadening) between $\omega \approx 1.9J$ and $\omega \approx 2.3J$ are clearly visible along with a continuum of excitations above them. These correspond to excitations within and outside of the confining potential, respectively [358], as we show by plotting the difference between the excited state eigenenergies and the ground state energy $E_n - E_0$ (black crosses for confined excitations, black dots for continuum). Moreover, we find some spectral weight *below* the gap ($\omega \approx 1.9J$), at frequencies corresponding to the energy difference of the eigenenergies with the first excited state $E_n - E_1$. Moreover, we find oscillations of the spectral weight as a function of central time in Fig. 4.6b) (marked by an arrow and a star), indicating that an equilibrium state has not yet been reached up to times as along as $JT = 100$ [8]. This is further substantiated by a violation of the FDR at the location of some of these oscillatory features (Fig. 4.6c)). In the following, we will show that these non-thermal features are a direct consequence of the large overlap of the initial state with sharp excitations and show that their properties can be read off from the two-domain-wall nonequilibrium

8 Oscillations for times JT<30 around the peak at $\omega/J = 1.9$ are artifacts of the Fourier transform (Gibbs phenomenon).

spectral function. First, note that the Lehmann representation of the spectral function can be split into a time dependent and time independent part [235], resulting in

$$\rho(T,\omega) = \sum_n |\langle\psi_0|n\rangle|^2 \rho_{nn}(\omega) + \sum_{n,m\neq n} \langle\psi_0|n\rangle\langle m|\psi_0\rangle e^{i(E_n-E_m)T}\rho_{nm}(\omega) \tag{4.91}$$

with the eigenstate spectral functions

$$\rho_{nm}(\omega) = \sum_l \langle n|\hat{\sigma}_2^+|l\rangle\langle l|\hat{\sigma}_2^-|m\rangle\delta(\omega - (E_l - \frac{E_m+E_n}{2})) - \langle n|\hat{\sigma}_2^-|l\rangle\langle l|\hat{\sigma}_2^+|m\rangle\delta(\omega + (E_l - \frac{E_m+E_n}{2})). \tag{4.92}$$

From the time independent/diagonal part we can directly explain the spectral weight below the gap: Because of the large overlap of the initial state with the first excited state $|1\rangle$, also $\rho_{11}(\omega)$ contributes, which contains delta-peaks at frequencies $E_n - E_1$. Furthermore, the only central time-dependence is contained in an oscillatory term with frequency $E_n - E_m$, which appear at frequencies ω' given by a superposition of *three* eigenergies, $\omega' = \pm(E_l - (E_m + E_n)/2)$. We can use this observation to analyse the oscillatory features found in the non-equilibrium spectral function. At $\omega' \approx 0.9$ (marked by an arrow) and $\omega' \approx 1.4$ (marked by a star) we find that the central time oscillation frequency is in perfect agreement with $E_0 - E_1$, indicating that $m, n \in 0, 1$. From the frequency location ω', we can furthermore identify that $l = 0, 1$ and $l = 3$ are the contributions in Eq. (4.92) leading to the features at $\omega' \approx 0.9$, $\omega' \approx 1.4$, respectively. This shows that the central time oscillations arise solely from the two lowest excited states corresponding to confined excitations [9]. In general, one would expect such central-time oscillations to dephase rapidly. Here, however, the fact that the initial state has a strongly peaked overlap with eigenstates well isolated in energy leads to a long lifetime of the central-time oscillations.

While any such central-time dependent contribution leads to a deviation from the diagonal ensemble (which is the first term in Eq. (4.91)) and hence a lack of thermalization, the FDR is not necessarily violated if ρ and F are shifted equally (assuming the individual eigenstates fulfill the FDR). Indeed, as visible in Fig. 4.6c), the oscillatory feature at $\omega \approx 0.9J$ violates the FDR while the one at $\omega \approx 1.4J$ does not, despite having the same oscillation amplitude and frequency. This is explained

9 Note that the two lowest eigenstates are doubly degenerate, leading to the non-zero matrix elements between states of equal energy needed to give a non-zero contribution in Eq. (4.92). To illustrate this, consider the two ground states $|0\rangle, |0'\rangle$ (given by $|\uparrow\cdots\uparrow\rangle_x$, $|\downarrow\cdots\downarrow\rangle_x$ for $g = 0$), $\langle 0|\hat{\sigma}_2^+|0'\rangle \neq 0$ because $\hat{\sigma}_2^+$ flips a spin, $\hat{\sigma}_2^+|\uparrow\rangle = |\downarrow\rangle$ and the resulting state has non-zero overlap with the other ground-state because of $g \neq 0$.

by comparing the expression in Eq. (4.92) with the corresponding one for F, given by

$$F(T,\omega) = \sum_n |\langle\psi_0|n\rangle|^2 F_{nn}(\omega) + \sum_{n,m\neq n} \langle\psi_0|n\rangle\langle m|\psi_0\rangle e^{i(E_n-E_m)T} F_{nm}(\omega) \tag{4.93}$$

with the eigenstate statistical functions

$$F_{nm}(\omega) = \frac{1}{2}\sum_l \langle n|\hat{\sigma}_2^+|l\rangle\langle l|\hat{\sigma}_2^-|m\rangle\delta(\omega - (E_l - \frac{E_m+E_n}{2})) + \langle n|\hat{\sigma}_2^-|l\rangle\langle l|\hat{\sigma}_2^+|m\rangle\delta(\omega + (E_l - \frac{E_m+E_n}{2})). \tag{4.94}$$

The only difference to ρ is an overall factor $1/2$ (which would get compensated on the right-hand-side of the FDR by $n_\beta(\omega) \approx 1/2$ at low temperatures) and the two terms in the first and second line in Eq. 4.94 get added instead of subtracted. By explicitly analyzing the contributions in Eq. (4.92), we found that for the feature at $\omega \approx 1.4J$ the first term dominates, which has the same sign in the expressions for F and ρ such that both get shifted equally compared to the diagonal ensemble expectation and the FDR is fulfilled. Contrastingly, for the feature at $\omega \approx 0.9J$, the second term dominates, which has a different sign in F and ρ such that the FDR is violated. In Fig. 4.6c), we find a second FDR-violating feature around $\omega \approx 1.1J$, with an oscillation frequency matching $E_2 - E_0$, corresponding to contributions from the ground state and second confined state, $n, m, l \in 0, 2$. Note that the violation of the FDR we observe here can not be explained by an effective, i.e. frequency independent temperature differing from the one expected from the energy of the initial state, which for example occurs in periodically driven systems [318]. Such an effective non-thermal temperature would manifest its-self in a mismatch of F and the right-hand-side of the FDR, $n_\beta(\omega)\rho$, for all frequencies low enough to show the β dependence of $n_\beta(\omega)$ (i.e. such that $n_\beta(\omega)$ differs significantly from $1/2$). This is however not the case here: in Fig. 4.6c) a peak at frequency $\omega \approx 0.25J$ *fulfilling* the FDR is clearly visible, showing that the violations of the FDR discussed here indeed occur at isolated frequencies and cannot be explained by a non-thermal effective temperature.

For most of the interpretations given above, no additional numerics apart from the calculation of the two-time functions were needed and the same conclusions could have been made only given an experimental measurement of the two-time functions. Therefore, this provides a general procedure how to extract information about long lived prethermal (or even non-thermal) excitations completely independently of numerical calculations: Central time oscillations indicate their presence while the central time oscillation frequency and frequency location ω' can be used to extract

their energy. The property that the FDR is violated or not at the location of the peak can then be used to extract information about the matrix elements and hence about the nature of the excitation itself, where the latter can be refined by probing two-time correlations of different operators and initial states.

4.10 CONCLUSIONS AND OUTLOOK

We have shown how to probe the off-diagonal part of eigenstate thermalization with two-time functions in quantum simulators, which is an open experimental challenge. We discussed and introduced measurement protocols in quantum simulators of spin and Hubbard models for the two-time spectral function ρ and statistical function F, which are in general independent of each other out of equilibrium. We have shown that probing the link between the statistical function F and the spectral function ρ via the fluctuation-dissipation relations can be used to probe the off-diagonal part of ETH independently of both microscopic details and theory input, thus providing a general route to probing thermalization in quantum simulators. Going beyond testing thermalization of the steady-state at long times, we showed that the FDRs can also be used to characterize prethermal steady states, which can lead to modifications of the FDR in the case of almost conserved quantities and can even lead to a violation of the FDR in the presence of confined excitations.

Our scheme can be used to probe multiple aspects of thermalization. By preparing initial states with energy densities covering the whole spectrum (for example spin spirals [48, 161–163], thermalization of a many-body Hamiltonian across its whole energy spectrum could be probed. Individual eigenstates could be prepared by a recently proposed protocol employing weak measurements [322]), thus opening the route to directly test the off-diagonal part of ETH in terms of individual eigenstates with the FDR. In many-body localized systems, a uniform late-time temperature is not expected, however, local temperatures can be defined [361] and could be measured by using the FDRs as a local thermometer. Two-time functions show aging in classical glasses [60, 362], their measurement could hence probe the analogy to glasses made in quantum systems with slow relaxation [164, 363]. Furthermore, the non-thermal oscillatory features we found for confined excitations could be used to characterize other non-thermal states such as many-body scars [58, 59]. Our measurement protocols could also be used to show violations of the FDR due to transport processes near non-thermal fixed points [277]. Lastly, our protocols offer a route to quantum simulate pump-probe experiments on solids such as optical spectroscopy [364] (measuring ρ) and optical noise spectroscopy [317] (measuring F) by using the analogy between the light-matter couplings and the resulting linear-

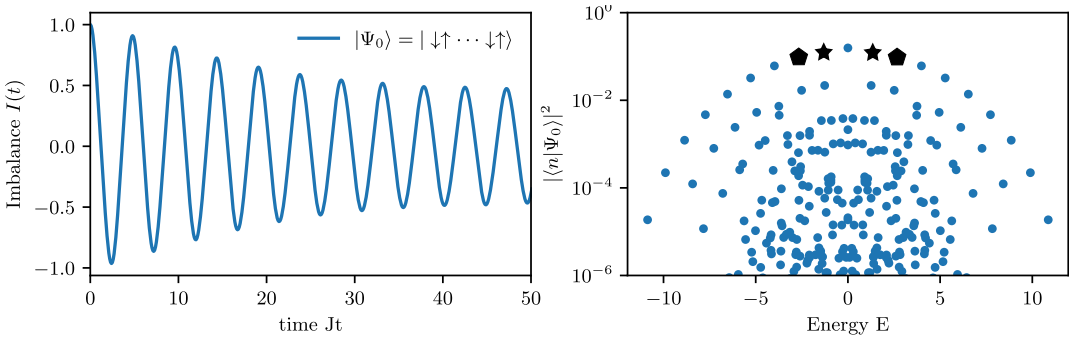

Figure 4.7: **Slow relaxation in the PXP model due to scars.** (left) Anomalously slow decay of the staggered magnetization. (right) Overlap of the staggered initial state with the many-body eigenstates. System size $L = 18$.

response correlation functions. While in the solid state, the non-zero charge of the electron leads to a coupling of the current density to the light field, in cold (neutral) atom platforms, the dipolar coupling leads to a coupling of the atom number density to the light. Hence, the measurement of density-density two-time functions proposed here is analogous to the current-current functions of optical measurements in the solid state.

4.11 OUTLOOK: MANY-BODY SCAR SPECTROSCOPY

In section 4.9 we showed that two-time correlation functions can be used to study confined excitations in the long-range transverse field Ising model. These are *low-energy* excitations which show anomalous non-thermal behaviour and are therefore only visible when starting from an initial state sufficiently close to the ground state. Recently, cases have been found in which non-thermal behaviour can also be found when starting from initial states in the middle of the energy spectrum, implying long relaxation times even at infinite temperature. One long-known example is many-body localization, in which disorder leads to a localization of the whole many-body spectrum even at finite interaction strength, at least in one spatial dimension. Very recently, dynamics with slow relaxation have also been discovered in the absence of disorder, caused by dynamical constraints which drastically reduce the connectivity of the Hilbert space [59]. Here, we discuss the model in which such dynamics have been seen first [59], a chain of Rydberg atoms in a regime in which strong Van-der-Waals interactions lead to the blockade effect: despite the continuous operation of a laser exciting the ground to the Rydberg state, not all atoms can be excited at the same time as the interactions shift neighbours of an already excited atom out of resonance. As the Van-der-Waals interaction decays as

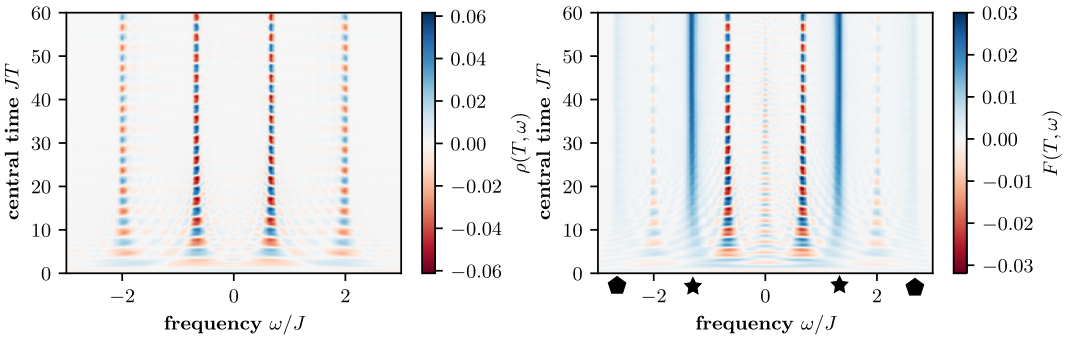

Figure 4.8: **Scars in the two time correlations.** Spectral and connected statistical functions ρ and F starting from the Néel state. Operators probed are local magnetizations, $\hat{A} = \sigma_i^z$, $\hat{B}_j = \hat{\sigma}_j^z$ with $i = 5$, $j = 8$. System size $L = 18$. The energies marked with a star and polygon refer to the correspondingly marked states in Fig. 4.7.

$\sim 1/r^6$ with distance r, the blockade is strongest for nearest-neighbours, such that an effective model for the dynamics can be written as

$$\hat{H} = J \sum_i \hat{P}_{i-1} \hat{\sigma}_i^x \hat{P}_{i+1}, \qquad \text{with} \qquad \hat{P}_i = |\uparrow\rangle \langle\uparrow|_i , \tag{4.95}$$

known as the "PXP" model. Here, $|\uparrow\rangle$ is the Rydberg state and $|\downarrow\rangle$ is the ground state.

In Fig. 4.7 we show the decay of the staggered magnetization after starting from a Néel initial state, $|\Psi_0\rangle = |\uparrow\downarrow \cdots \downarrow\uparrow\rangle$, showing anomalously slow decay. This initial state is has zero energy and hence corresponds to an infinite temperature state due to the particle-hole symmetry of the Hamiltonian. For such states, very rapid decay is usually expected. We also show the overlaps of the initial state with the eigenstates of the system. Crucially, there is a band of states with high overlap, which are also called scar states [58].

In Fig. 4.7 we show that these states are directly identifyable by measuring two-time correlations. In the statistical function, time-independent peaks mark the energy of the scar states, which we can directly trace back to the states with the highest overlap in Fig. 4.7. Moreover, pure oscillating peaks inbetween the time-independent peaks are visible. These correspond to similar beating terms as observed in section 4.9.3 for confined states. Their central time oscillation frequency corresponds to the difference in energy between the scar states. Their non-equilibrium character can be seen from two signs. First of all, a central time dependence indicates non-thermal behaviour. Secondly, the spectral function at infinite temperature should strictly vanish due to the cyclicity of the trace. However, we find similar oscillating peaks in the spectral function as in the statistical function, albeit no time-independent ones.

Here we have given a first peek into how two-time correlations could be used to identify mid-spectrum non-thermal states. Further questions remain. For example,

measuring F and ρ for different operators could elucidate the structure of the non-thermal states by getting an indication for their matrix element structure. By comparison, we found by using a spin flip operator in section 4.9.3 that the confined excitations are of two-domain-wall character.

5

THERMALIZATION IN (1+1)D LATTICE GAUGE THEORIES

We study thermalization dynamics in (1+1) dimensional SU(N) lattice gauge theories interacting with matter fields [1]. We employ non-equilibrium quantum field theory techniques, which in previous attempts have failed to accurately describe gauge theory dynamics due to violations of the gauge constraint [365]. Here, we use a reformulation of the theory in entirely in terms of fermions, circumventing these problems. In the Schwinger model, the U(1) symmetric version of the same model, we study the emergence of fluctuation-dissipation relations (FDRs) within a weak coupling expansion. Starting from an initial state with a string on top of the vacuum of the strongly interacting theory, we demonstrate that the Hartree-Fock/Gaussian state approximation is unsuitable to describe thermalization. Employing the next-to-leading order in the weak-coupling approximation, the system thermalizes and FDRs are quickly fulfilled for all ratios of mass m and interaction strength g. The effective temperature T and chemical potential μ both depend on time, showing an exponential relaxation towards equilibrium. We find that the spectral function quickly thermalizes, indicating the emergence of a kinetic regime. At the same time, site-dependent temperatures agree with each other while local chemical potentials between antimatter and matter sites disagree. At the true thermalization time, site dependent temperatures and chemical potentials finally agree and become independent of time. We study the parameter dependence of the thermalization time, finding that it increases with increasing final state temperature. Finally, we present two approaches to extend the use of non-equilibrium quantum field theory. We derive a method to directly study infinite-temperature dynamics, enabling the evaluation of high-temperature spectral functions. We furthermore present a systematic approximation for (1+1)D SU(N) gauge theories in $1/N$, opening the possibility to study thermalization in non-abelian lattice gauge theories with a well-controlled expansion parameter.

1 This project was conceived with Pablo Sala who I also thank for many helpful discussions with regards to the interpretation of the data.

5.1 MODEL AND METHODS

We study a (1+1)D SU(N) symmetric lattice gauge theory [366] with staggered fermions. Crucially, in one spatial dimension, the gauge fields can be integrated out, leading to a Hamiltonian only in terms of the Fermions given by

$$H = \epsilon \sum_n \left(\mathbf{c}_n^\dagger \mathbf{c}_{n+1} + h.c. \right) + m \sum_n (-1)^n \mathbf{c}_n^\dagger \mathbf{c}_n + \frac{g^2}{2} \sum_a \sum_{n,m} \mathcal{Q}_n^a V_{nm} \mathcal{Q}_m^a \tag{5.1}$$

as shown in Ref. [367]. In above Hamiltonian, $\mathcal{Q} = \boldsymbol{Q} + \boldsymbol{q}$ is the total charge consisting out of the static (external) charge $\boldsymbol{q}$ and the dynamical charge

$$Q_n^a = \mathbf{c}_n^\dagger T^a \mathbf{c}_n \tag{5.2}$$

with the $N^2 - 1$ SU(N) generators T^a and the N-component spinor $\mathbf{c}_n$. For $N = 1$, the dynamical charge is given by $Q_n = c_n^\dagger c_n - \frac{1}{2}(1 - (-1)^n)$. Note that here, $n = 1, \ldots, L$. m and g are mass and coupling strength and we use $\epsilon = 1$ as our unit of energy. The form of the effective interactions between the fermions V_{nm} depends on the boundary conditions. For open boundary conditions, the Coulomb interaction is given by $V_{nm} = -|n-m|/2$, indicating the linearly confining potential between charges. For periodic boundary conditions (for which also a term $\mathbf{c}_L^\dagger \mathbf{c}_0 + h.c.$ is added), the potential changes to [368]

$$V_{nm} = -\frac{g^2}{2} \left(\frac{L-3}{L-2} \right) \times \left\{ \begin{array}{ll} |n-m|, & \text{for } |n-m| = 0, 1 \\ |n-m| + \frac{|n-m|^2 - 3|n-m| + 2}{2-L}, & \text{for } 2 \leq |n-m| \leq \frac{L}{2} - 1 \\ \frac{L^2-8}{4(L-3)}, & \text{for } |n-m| = \frac{L}{2} \end{array} \right\}. \tag{5.3}$$

The electric field E_n^a can be obtained from the charges by

$$E_n^a = \sum_k^n Q_k^a \tag{5.4}$$

in the absence of external sources (all $q_l = 0$).

The above Hamiltonian only contains terms quadratic and quartic in fermion operators. This means that we can directly use the 2PI effective action techniques we introduced in chapter 2 without any immediate additional difficulty due to the presence of gauge fields. This is opposed to previous attempts to using self-consistent methods for gauge theories, were it has been shown that the gauge constraint leads to difficulties in the interpretation of the 2PI correlators [365, 369–372].

EFFECTIVE WEAK COUPLING FOR OPEN BOUNDARIES Inserting the staggered charge for the case of $N = 1$ and reordering terms, we find for open boundary conditions

$$H_{U(1)} = \epsilon \sum_n \left(c_n^\dagger c_{n+1} + h.c. \right) - \frac{g^2}{4} \sum_{n,m} c_n^\dagger c_n |n-m| c_m^\dagger c_m + \sum_n \left(m(-1)^n - \frac{g^2}{4} \sum_l |l-n| \left(2q_l - (1-(-1)^l \right) \right) c_n^\dagger c_n \tag{5.5}$$

This rewriting shows that the staggered formulation leads to a "renormalization" of the mass. In particular, for open boundary conditions this means that even for large g, the quadratic terms in the Hamiltonian are much larger than the quartic ones, enabling a weak-coupling approximation. This may partially explain the efficacy of the Gaussian state ansatz in Ref. [367], where it was shown to capture the ground state properties remarkably well in comparison to exact MPS techniques. Some qualitative features of the dynamics were shown to be captured by the Gaussian state approximation as well. However, it is clear that due to the lack of true scattering, thermalization can not be described within this approximation [373]. Contrarily, for periodic boundary conditions, the local fields do not show the same behaviour, i.e. they stay of order m throughout the system. We note that the Gaussian state method is equivalent to the the two-loop approximation on the level of the effective action we showed in chapter 2, as can be seen by directly comparing the resulting equations of motion. In the following, we will therefore use "Gaussian state", "two-loop approximation" and "Hartree-Fock" interchangeably as they correspond to the same approximation.

While it is difficult to systematically improve the Gaussian state approximation, here we use the 2PI formalism to do so. We will include the next order in the weak-coupling approximation [239] as well as the GW approximation to study thermalization in the Schwinger model. In the following, we will always consider periodic boundary conditions, using the expression for the potential derived in chapter 4B of Ref. [368] and stated above.

5.2 STRING DYNAMICS IN THE SCHWINGER MODEL AT WEAK COUPLING

In the limit of large couplings $g \gg 1$, the Schwinger model can be solved analytically and the groundstate is given by

$$|\psi_0\rangle = |10101010...\rangle\,, \tag{5.6}$$

which we call "strong coupling vacuum" in the following. If we create a pair of opposite charges onto the strong coupling vacuum, a "string" of electric field

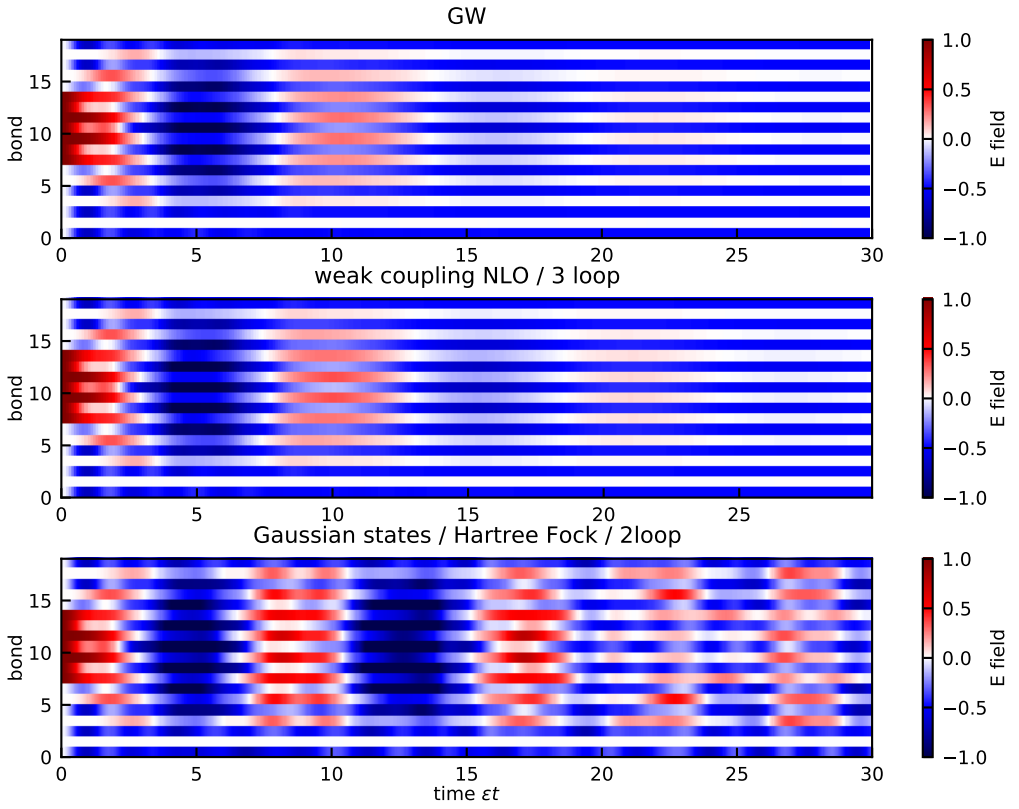

Figure 5.1: Breaking and relaxation of a string on top of the strong coupling vacuum. Mass $m = 0.1\epsilon$, coupling strength $g = 1\epsilon$.

connects the two and the potential energy rises linearly with increasing distance. At some threshold distance, the potential energy however stops to rise as the energy becomes high enough to create electron-positron pairs out of the vacuum which screen the two charges. Dynamically, it was shown that this "pair-creation" is visible in the dynamics of the electric field if a pair of (either dynamical or static) charges is placed at large enough distance [180, 367].

It was shown that some non-trivial dynamics are captured within the two-loop approximation in Ref. [367], specifically the creation of particle-antiparticle pairs as well as string-antistring configurations. In Fig. 5.1 we show the time evolution of the electric field starting from a string on top of the strong coupling vacuum for mass $m = 0.1\epsilon$, coupling strength $g = 1\epsilon$ and compare the results obtained from 2 loops, 3 loops and the GW approximation with periodic boundary conditions. In all methods, we find oscillations between the string configuration (leading to a positive electric field connecting the charges) and the anti-string configuration (leading to the opposite sign of the electric field). Moreover, at short times, pairs of particles and antiparticles are created, visible by the oscillation of the electric field in-between the two ends of the spatially spreading string. While in 2loop, the oscillations continue and become more fractured due to interference, we find damping of the oscillations

within the 3 loop and GW approximations. Within the two loop approximation, there is an artificial extensive number of conserved quantities, which correspond to the momentum space occupation numbers for periodic boundary condition. As the initial state is a superposition of these conserved quantities, the late time interference pattern corresponds to a dephasing process between these conserved quantities. However, there is no scattering between momentum modes, hampering the approach to true thermal equilibrium. Hence, late-time thermalization can not be described within the 2 loop approximation [239]. The 3 loop and GW approximation break this spurious conservation, enabling the approach to a thermal equilibrium state. We note that there is no qualitative difference between the 3 loop and the GW approximation in this regime. Merely the renormalization of the string-antistring oscillation frequency as well as the decay constant are slightly different. As they can directly be related to the real and imaginary part of the self-energy, respectively, we conclude that the higher order bubble diagrams included in the GW approximation are not very relevant for the dynamics in this regime.

In the following, we will investigate the thermalization dynamics in more detail from the perspective of two-time correlation functions and the fulfillment of the fluctuation-dissipation relations.

5.3 THERMALIZATION

We discussed in chapter 4 a possible mechanism for how quantum systems thermalize: the eigenstate thermalization hypothesis (ETH). ETH is an ansatz for the matrix elements of observables, consisting of a diagonal and off-diagonal part. The diagonal part dictates the thermalization of single-time observables: They decay to the value expected from the microcanonical ensemble corresponding to the energy density of the initial state. Contrarily, the off-diagonal part dictates the thermalization of two-time correlation functions as we discussed in-depth in chapter 4. In the following, we will probe the thermalization of the two-time correlation functions

$$F_{ij}(t_1, t_2) = \frac{1}{2} \left\langle \left[\hat{c}_i(t_1), \hat{c}_j^\dagger(t_2) \right] \right\rangle , \tag{5.7}$$

$$\rho_{ij}(t_1, t_2) = i \left\langle \left\{ \hat{c}_i(t_1), \hat{c}_j^\dagger(t_2) \right\} \right\rangle , \tag{5.8}$$

which signify the statistical and spectral function, respectively. Frequently, we will transform to central time $T = (t_1 + t_2)/2$ and relative time $\tau = t_1 - t_2$ and Fourier transform with respect to relative time, $\rho_{ij}(T, \omega) = \int d\tau e^{i\omega\tau} \rho_{ij}(T, \tau)$. ETH implies [2]

2 See chapter 4 for a proof.

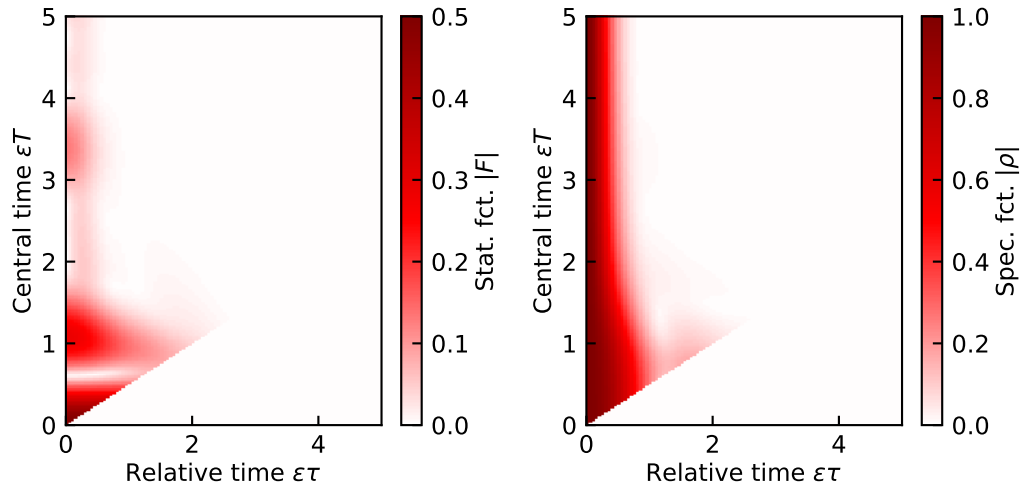

Figure 5.2: Equal site statistical and spectral functions ρ_{ii} and F_{ii} as a function of central and relative time. Middle site of the chain, mass $m = 0.1\epsilon$, interaction strength $g = 1\epsilon$, system size $L = 20$.

that at late times T the spectral and statistical functions are not independent of each other but connected via the fluctuation dissipation relations as

$$F_{ij}(\omega) = -i\left(\frac{1}{2} - n_{\beta,\mu}(\omega)\right)\rho_{ij}(\omega), \tag{5.9}$$

where $n_{\beta,\mu} = \frac{1}{e^{\beta(\omega-\mu)}+1}$ is the Fermi-Dirac distribution at inverse temperature β and chemical potential μ. Note that one can transform this "fermionic" FDR into the "bosonic" one introduced in chapter 4 by inserting the different definition of F and ρ. In the following, we use 2PI methods to calculate F and ρ for the 1+1 dimensional lattice gauge theory and probe the fulfillment of the fluctuation-dissipation relations as a stringent test of the eigenstate thermalization hypothesis.

5.3.1 *Spectral and statistical correlations*

In Fig. 5.2 we show the equal-site spectral and statistical functions as a function of relative and central time for the same parameters as in Fig. 5.1. We find that both F and ρ decay rapidly as a function of relative time, indicating that there are no long-lived single particle excitations present. Moreover, this means that we can cut the memory integral in the 2PI formalism - in principle, the whole history of the dynamics would have to be stored in order to solve the Kadanoff-Baym equations in Eqs. (5.25), (5.26). Due to the rapid decay of the correlation functions, the memory integrals can be cut to the recent history. Here, we use a memory time of $\epsilon t_{\text{mem}} = 10$ and checked convergence. A second interesting feature is that the

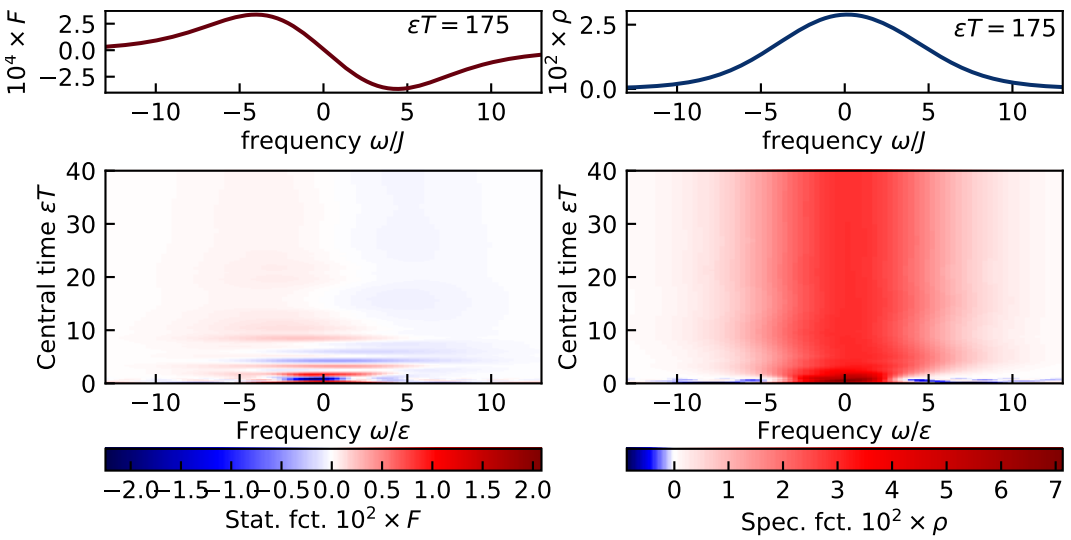

Figure 5.3: Equal site spectral and statistical functions ρ_{ii} and F_{ii} as a function of central time and frequency. Middle site of the chain $i = 9$, mass $m = 0.1\epsilon$, interaction strength $g = 1\epsilon$, system size $L = 20$.

decay with relative time becomes quicker as a function of central time. In particular, the spectral function ρ shows almost no central time dependence after about $\epsilon T \approx 2$.

In frequency space, the fast relaxation of ρ becomes even more apparent, see Fig. 5.3. While ρ relaxes on time scales of a few $1/\epsilon$, the statistical function still shows oscillations of its zero crossing on time scales as large as $\epsilon T \approx 10$. After these oscillations have settled, the overall scale of F still evolves, as visible from comparing the scale of $\approx 10^{-2}$ at $\epsilon T = 40$ with the scale of $\approx 10^{-4}$ at times $\epsilon T = 175$. This is a first indication that there are at least three time scales involved in the dynamics: First, the spectral function ρ thermalizes, then the statistical function F obtains its final form and thirdly, the overall scale of F reaches the equilibrium value. In the following, we will study how these time scales are reflected in the fluctuation-dissipation relations.

5.3.2 *Emergence of fluctuation-dissipation relations*

We test the emergence of the fluctuation-dissipation relation by defining the "fluctuation-dissipation relation function"

$$\mathrm{FDR}(T,\omega) = \ln\left[\left(\frac{1}{2} - \frac{iF(T,\omega)}{\rho(T,\omega)}\right)^{-1} - 1\right]. \tag{5.10}$$

In equilibrium, $\mathrm{FDR}(T,\omega)$ becomes independent of T and is equal to $\beta\omega$. In Fig. 5.4 we show this function for the spectral and statistical functions displayed in the previous subsection. At early times (bright colour), the FDR is clearly not fulfilled as

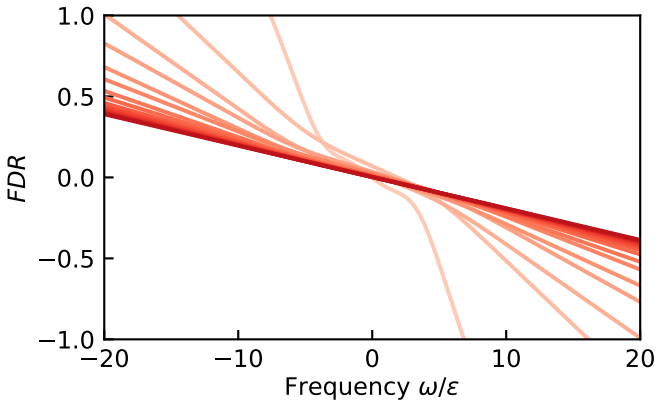

Figure 5.4: Time evolution of the FDR function, Middle site of the chain $i = 9$, mass $m = 0.1\epsilon$, interaction strength $g = 1\epsilon$, system size $L = 20$. Time increases from bright to dark, the colour hue indicates the linearly spaced time, $2.5 \leq \epsilon T < 75$.

the FDR function is not a straight line. The FDR is first fulfilled for small frequencies and then for larger frequencies. At very late times, a straight line is visible ranging over all displayed frequencies, however with a slope which is gradually changing.

In Fig. 5.5, we study this time dependence in more detail. We extract the time dependent inverse temperatures $\beta(T)$ and chemical potentials $\mu(T)$ by fitting a linear function to the FDR function to the central region $-5 \leq \omega/\epsilon \leq 5$ and for different sites i, where the even sites represent particles and uneven sites the antiparticles. At short times, both the temperature and chemical potential show erratic behaviour, with the chemical potential showing some oscillations, which reflect the oscillations of the zero-crossing of F. They have roughly the same oscillation frequency as the particle-antiparticle oscillations in the electric field in Fig. 5.1. At times $\epsilon T \approx 10$, the site-dependent temperatures start to agree between themselves while the site-dependent chemical potentials do not agree. However, particle sites roughly agree between themselves while they disagree with the antiparticle sites. After this initial behaviour, both temperature and chemical potential relax exponentially to their final equilibrium value. At these late times, the chemical potentials of particle and antiparticle sites also agree with each other. In order to extract a decay time as well as the final values of chemical potential and temperature, we fit a function

$$\beta(T) = \beta_\infty - a \exp(-\Gamma_\beta T), \tag{5.11}$$

to the time-dependent temperatures and similarly to the chemical potentials. For this parameter set ($m = 0.1$, $g = 1.0$) we find $\beta_\infty \epsilon \approx -0.019$, $\mu_\infty \approx -0.06$ and $\Gamma_\beta/\epsilon \approx \Gamma_\mu/\epsilon = 0.07$. Furthermore, we characterize the intermediary oscillations of the chemical potential by subtracting the fit from the data, see inset in Fig. 5.5. We find exponentially decaying oscillations which exactly correspond to the oscillations

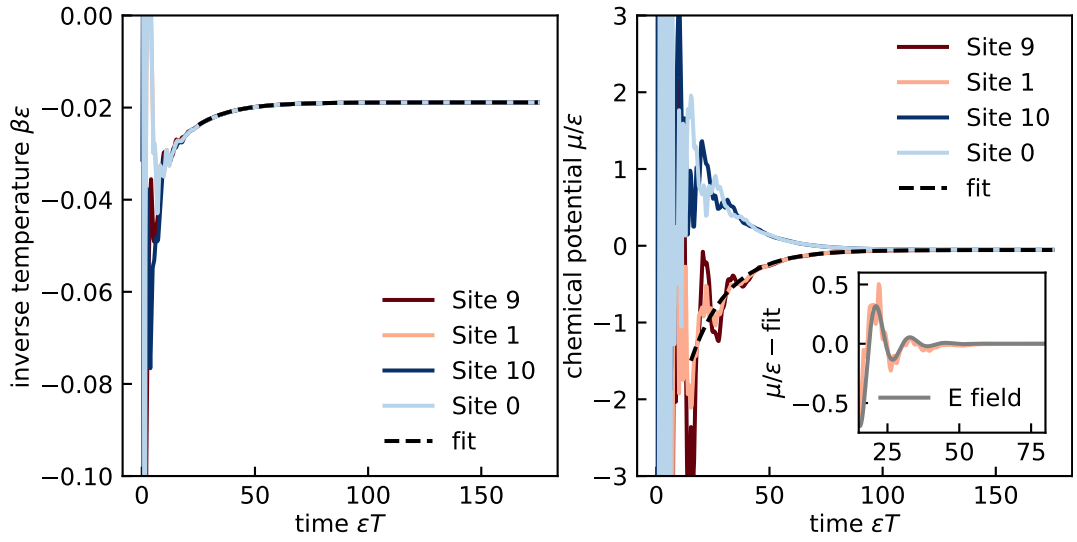

Figure 5.5: Time dependence of local temperatures and chemical potential, mass $m = 0.1\epsilon$, interaction strength $g = 1\epsilon$, system size $L = 20$. Inset: Difference between μ/ϵ at site 1 and the fit. The grey line is the electric field shown in Fig. 5.1 on bond 11 (bond 1 oscillates similarly, we chose bond 11 for a cleaner signal) multiplied by a factor of 4 for better comparison.

of the electric field. A fit to a function $a + b\cos(\omega T + \phi)\exp(-\gamma T)$ results in $\omega/\epsilon \approx 0.13$ and $\gamma/\epsilon \approx 0.5$. Hence, these oscillations die out on a timescale almost an order of magnitude faster than the approach to global equilibrium.

Hence, the three stages of thermalization mentioned previously can be characterized as follows from the perspective of the FDR: First, the site dependent temperatures thermalize between themselves. Then, the oscillations of the chemical potentials of (anti-)particle sites damp out, which are related to string and anti-string oscillations. Lastly, the now globally defined temperatures and (anti-) particle chemical potentials relax to their final value, with particle and antiparticle μ agreeing at late times.

Having characterized the thermalization process for a single parameter set of m and g, we now analyze how final temperature, chemical potential and relaxation rates depend on these parameters.

5.3.3 *Thermalization rates*

In Fig. 5.6 we display the final temperatures and thermalization rates as a function of mass and interaction strength. We find that the final temperature increases as the interaction strength increases, which may at first seem puzzling because we created the string on top of the $g \to \infty$ vacuum and hence the temperature should decrease. However, as g increases, the energy introduced by the string also increases due to

the interaction term, which increases the final temperature. Our results imply that in this competition, the latter effect dominates. However, at large g our perturbative method is not very reliable any more such that we cannot exclude that at higher orders a different behaviour might emerge. Contrastingly, the final temperature decreases as the mass increases for fixed interaction strength, in particular crossing the infinite temperature point $\beta = \infty$ at around $m/\epsilon \approx 0.25$.

In general, we find the thermalization rate to show analogous behaviour to the final temperature: As β_∞ decreases, the thermalization rate increases. This is somewhat expected: As the temperature increases, more excitations are available which can scatter to reach equilibrium faster. These excitations are however not necessarily of single-particle nature as we discussed in subsection 5.3.1: the spectral function has a very broad peak, indicating the absence of quasiparticles. It is an interesting question how the thermalization rate scales as a function of final temperature in this case. It has been conjectured [374, 375], that in general $\Gamma \propto \frac{1}{\beta_\infty}$ and has also been confirmed in the strongly interacting SYK model [376]. To test this hypothesis in our model, we plot in Fig. 5.7 the thermalization rate as a function of final temperature and fixed $g = \epsilon$. We indeed find a behaviour roughly compatible with a linear increase, however with a very small prefactor. Moreover, the temperatures accessible in our quenches are very high. Lower temperatures could be accessed in our method by preparing the true interacting vacuum of the theory before introducing the charges, such that we could test the conjecture $\Gamma \propto \frac{1}{\beta_\infty}$ down to lower temperatures.

We note that we did not find signs of confinement in our non-equilibrium results - in all cases, the string relaxed exponentially fast at long times. While this might be a result of our method as confinement is in general interpreted as a non-perturbative phenomenon, it might also be due to the high temperatures we probed in our quenches: confinement is in principle a ground state or close-to-ground state phenomenon. Here, we studied the dynamics of strings created on top of the strong-coupling vacuum and not on top of the interacting vacuum of the theory as for example done in Refs. [367, 377]. This means that we simultaneously quenched the system in two ways: In a global way by quenching the breakground and in a (more) local way by creating charges. To discern effects coming from one or the other, the thermalization of the strong-coupling vacuum without creating charges could be studied in the future.

This high-temperature perspective on the Schwinger model can be brought to the extreme by studying the infinite temperature spectral function. In the following, we develop a novel method to calculate infinite temperature dynamics from 2PI.

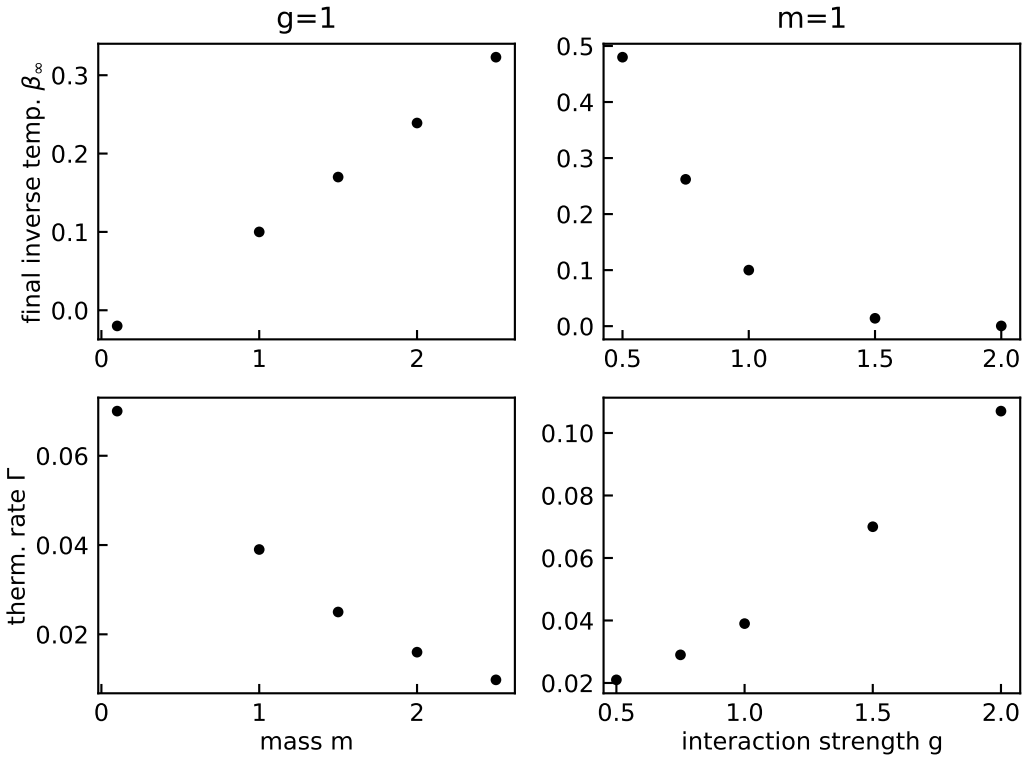

Figure 5.6: Final temperatures (first row) and thermalization rates as a function of mass, for fixed $g = 1$ (first column) and interaction strength, for fixed mass $m = 1$ (second column). All quantities in units of ϵ.

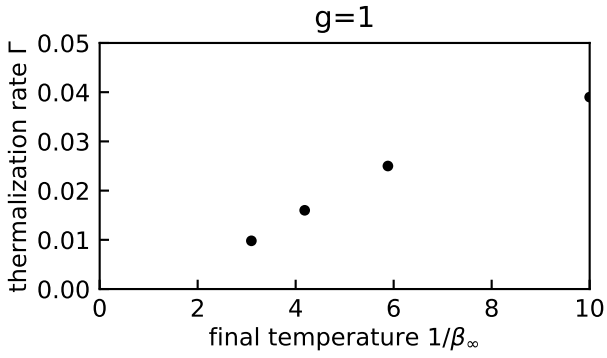

Figure 5.7: Thermalization rate as function of final temperature for a fixed $g = \epsilon$, varying the mass.

5.4 INFINITE TEMPERATURE SPECTRAL FUNCTION

The infinite temperature correlation function in principle contains information about excitations of the whole many-body spectrum as it averages over all many-body eigenstates. However, it will be dominated by the states in the middle of the spectrum as the density of states is largest there. We will use this fact in chapter 6 to measure this function in experiment more efficiently and within spin 2PI by sampling product states. Here, we develop a more direct route to probing infinite temperature dynamics in 2PI.

5.4.1 *Infinite temperature fluctuation-dissipation relation*

Consider the fluctuation dissipation relation

$$F_{ij}(\omega) = (-i)\left(\frac{1}{2} \pm n_{\beta,\mu}(\omega)\right)\rho_{ij}(\omega) \tag{5.12}$$

with the Bose-Einstein/Fermi-Dirac distribution given by

$$n_{\beta,\mu}(\omega) = \frac{1}{e^{\beta(\omega-\mu)} \mp 1}, \tag{5.13}$$

which is the generalization to both Bose and Fermi systems of the FDR we quoted above. The statistical/spectral function in the grand canonical ensemble are defined as

$$F_{ij}(\omega) = \frac{1}{2}\int d(t_1-t_2)e^{i\omega(t_1-t_2)}\frac{1}{Z}\,\mathrm{Tr}\left\{e^{-\beta(\hat{H}-\mu\hat{N})}\left(c_i(t_1)c_j^\dagger(t_2) \pm c_j^\dagger(t_2)c_i(t_1)\right)\right\}, \tag{5.14}$$

$$\rho_{ij}(\omega) = \int d(t_1-t_2)e^{i\omega(t_1-t_2)}\frac{1}{Z}\,\mathrm{Tr}\left\{e^{-\beta(\hat{H}-\mu\hat{N})}i\left(c_i(t_1)c_j^\dagger(t_2) \mp c_j^\dagger(t_2)c_i(t_1)\right)\right\}, \tag{5.15}$$

where the time dependent functions do not depend on the central time $(t_1+t_2)/2$ due to time-translational invariance in equilibrium.

The total particle number density in equilibrium is fixed by the relation

$$\begin{aligned}
\langle\hat{n}\rangle &= \frac{1}{V}\sum_j \frac{1}{Z}\,\mathrm{Tr}\left\{e^{-\beta(\hat{H}-\mu\hat{N})}c_j^\dagger c_j\right\} && (5.16)\\
&= \mp\frac{1}{2} \pm \int\frac{d\omega}{2\pi}\frac{1}{V}\sum_j F_{jj}(\omega) && (5.17)\\
&= \mp\frac{1}{2} \mp i\int\frac{d\omega}{2\pi}\left(\frac{1}{2} \pm n_{\beta,\mu}(\omega)\right)\frac{1}{V}\sum_j \rho_{jj}(\omega) && (5.18)\\
&= -i\int\frac{d\omega}{2\pi}n_{\beta,\mu}(\omega)\frac{1}{V}\sum_j \rho_{jj}(\omega), && (5.19)
\end{aligned}$$

where V is the system volume and in the last step we used the equal-time (anti-)commutation relations $\int \frac{d\omega}{2\pi}\rho_{jj}(\omega) = i\langle c_j(t)c_j^\dagger(t) \mp c_j^\dagger(t)c_j(t)\rangle = i$.

In the infinite temperature limit $\beta \to 0$, the chemical potential needs to be determined self-consistently from Eq. (5.19) in order to keep the total particle number fixed. This means that the product $\beta\mu$ needs to stay finite when taking the limit $\beta \to 0$ in the Bose-Einstein/Fermi-Dirac distribution,

$$\lim_{\substack{\beta\to 0 \\ \beta\mu\to\text{const.}}} n_{\beta,\mu}(\omega) = \frac{1}{e^{-\beta\mu} \mp 1}. \tag{5.20}$$

As $n_{\beta,\mu}$ is now frequency independent, we can solve Eq. (5.19) for $\beta\mu$, again using the sum rule $\int \frac{d\omega}{2\pi}\rho_{jj}(\omega) = i$,

$$\langle \hat{n} \rangle = \frac{1}{e^{-\beta\mu} \mp 1} \tag{5.21}$$

$$\leftrightarrow \beta\mu = \log\left(\frac{1}{\langle \hat{n} \rangle^{-1} \pm 1}\right). \tag{5.22}$$

This relation fixes the chemical potential and the FDR reduces to

$$F_{ij}(\omega) = (-i)\left(\frac{1}{2} \pm \langle \hat{n} \rangle\right)\rho_{ij}(\omega) \tag{5.23}$$

with total number density $\langle \hat{n} \rangle$. Therefore, F and ρ are directly proportional to each other both in time and frequency space, significantly reducing the complexity of the problem.

5.4.2 *2PI at infinite temperature*

In field theory calculations, F and ρ usually appear as independent variables. As we just showed, at infinite temperature, they are related by a simple time and frequency independent prefactor and should hence be exchangeable. This simplifications becomes most apparent for fermions at half filling, $\langle \hat{n} \rangle = 1/2$, for which the FDR in Eq. (5.23) shows that the statistical function vanishes identically,

$$F_{ij}(\omega) = 0. \tag{5.24}$$

.

More generally, we can show this simplifcation in the Kadanoff-Baym equations for F and ρ

$$\left(i\partial_{t_1}\delta_{ik} - \tilde{J}_{ik}(t_1)\right)F_{kj}(t_1,t_2) = \int_0^{t_1} \mathrm{d}t \Sigma^\rho_{ik}(t_1,t)F_{kj}(t,t_2) - \int_0^{t_2} \mathrm{d}t \Sigma^F_{ik}(t_1,t)\rho_{kj}(t,t_2), \tag{5.25}$$

$$\left(i\partial_{t_1}\delta_{ik} - \tilde{J}_{ik}(t_1)\right)\rho_{kj}(t_1,t_2) = \int_{t_2}^{t_1} \mathrm{d}t \Sigma^\rho_{ik}(t_1,t)\rho_{kj}(t,t_2) \tag{5.26}$$

with (Hartree-Fock renormalized) single particle Hamiltonian $\tilde{J}_{ij}$. Note that these equations are a complete description of the problem as the imaginary part of the equilibrium contour is shrunk to zero at infinite temperature and hence no Matsubara/mixed Green's functions appear. By using the (infinite T) FDR for the statistical/spectral self energies Σ^F, Σ^ρ,

$$\Sigma^F_{ij}(\omega) = (-i)\left(\frac{1}{2} \pm \langle \hat{n} \rangle\right) \Sigma^\rho_{ij}(\omega). \tag{5.27}$$

and replacing the statistical components in Eq. (5.25) by using Eqs. (5.27), (5.23), we directly reproduce Eq. (5.26), showing that both equations yield a redundant description of the problem.

We can simplify the solution of the problem further by using time-translational invariance in equilibrium, yielding

$$\left(i\partial_t \delta_{ik} - \tilde{J}_{ik}\right) \rho_{kj}(t) = \int_0^t \mathrm{d}t' \Sigma^\rho_{ik}(t-t')\rho_{kj}(t') \tag{5.28}$$

with the initial condition is fixed by the equal-time commutation relations by $\rho_{ij}(0) = i\delta_{ij}$. Note that the occupation of the system enters through the time-independent Hartree-Fock-Hamiltonian $\tilde{J}_{ij}$, which is given by

$$\tilde{J}_{ij} = J_{ij} - \left(\sum_k \left(F_{kk}(0) - \frac{1}{2}\right) U_{ik}\delta_{ij} - U_{ij}F_{ij}\right). \tag{5.29}$$

Inserting the infinite T FDR as well as $F_{ij}(0) = \int d\omega F_{ij}(\omega)$, we get $F_{ij}(0) = \delta_{ij}\left(\frac{1}{2} \pm \langle \hat{n} \rangle\right)$ and hence

$$\tilde{J}_{ij} = J_{ij} - \left(\pm \langle \hat{n} \rangle \sum_k U_{ik} - U_{ii}\left(\frac{1}{2} \pm \langle \hat{n} \rangle\right)\right)\delta_{ij}. \tag{5.30}$$

FREQUENCY SPACE FORMULATION Introducing the retarded Green's function $G^R(t) = \Theta(t)\rho(t)$ and self energy $G^R(t) = \Theta(t)\Sigma^\rho(t)$, we can rewrite this equation in frequency space as

$$G^R(\omega) = -[\omega - \tilde{J} - \Sigma^R(\omega)]^{-1}. \tag{5.31}$$

The problem can then be solved by the following self-consistency loop (in analogy to the one use in Ref. [376]), starting from a random guess for $\rho(\omega)$, fulfilling $\int d\omega \rho_{ij}(\omega) = i\delta_{ij}$.

5.4.3 *Numerical solution of infinite temperature 2PI*

In order to solve t use the algorithm proposed in [378], which transforms into the "rotating frame" of the quadratic part of the Hamiltonian according to

$$\rho(t) = U(t)\tilde{\rho}(t), \quad U(t) = e^{-iJt}, \tag{5.32}$$

where in the following all quantities are matrices in lattice site space. Inserting this into Eq. 5.28, a timestep $t \to t + \Delta$ can be exactly written as

$$\rho(t+\Delta) = U(\Delta)\left(\rho(t) - i\int_t^{t+\Delta} U(t-t')I(t')dt'\right), \tag{5.33}$$

where $I(t) = \int_0^t dt' \Sigma^\rho(t-t')\rho(t')$ is the right hand side of Eq. 5.28. This expression is amenable to a predictor-corrector scheme. In the predict step we set $I(t') = I(t)$, such that

$$\rho(t+\Delta) = U(\Delta)\rho(t) - V(\Delta)I(t), \tag{5.34}$$

with $V(\Delta) = J^{-1}(\mathbb{1} - U(\Delta))$. In the correct step, we replace $I(t) \to \frac{1}{2}(I(t) + I(t+\Delta))$ to re-evaluate $\rho(t+\Delta)$, which can be iterated until convergence of some error threshold. Note that $U(\Delta), V(\Delta)$ only need to be calculated once for a fixed time step Δ. The integral $I(t)$ can be calculated with some quadrature rule such as the trapezoidal rule.

5.5 SU(N) LATTICE GAUGE THEORIES: 2PI 1/N EXPANSION

Most results discussed in the previous sections were based on a weak coupling approximation or the non-perturbative, but somewhat poorly motivated GW approximation. In this section, we develop a systematic expansion for non-Abelian SU(N) lattice gauge theories in the inverse number of "colours" N. In this section, we denote the coupling g in the Hamiltonian (5.1) with $\tilde{g}$, i.e. $g \to \tilde{g}$ and introduce the t'Hooft coupling $g^2 = \tilde{g}^2 N$. This will enable us to perform a $1/N$ expansion while keeping $N\tilde{g}^2$ fixed. We also use the identity

$$\sum_a T^a_{\alpha\beta} T^a_{\gamma\delta} = \frac{1}{2}\left(\delta_{\alpha\delta}\delta_{\beta\gamma} - \frac{1}{N}\delta_{\alpha\beta}\delta_{\gamma\delta}\right). \tag{5.35}$$

Inserting this into the interaction part $\hat{H}_{\text{int}} \equiv \frac{g^2}{2N}\sum_a \sum_{nm} \mathcal{Q}^a_n V_{nm} \mathcal{Q}^a_m$ of the Hamiltonian we get

$$\begin{aligned}\hat{H}_{\text{int}} = &\frac{g^2}{4N}\sum_{nm} V_{nm} \sum_\alpha c^\dagger_{\alpha n} c_{\alpha n} - \frac{g^2}{4N}\sum_{nm} V_{nm} \sum_{\alpha\beta} c^\dagger_{\alpha n} c_{\alpha m} c^\dagger_{\beta m} c_{\beta n} \\ &- \frac{g^2}{4N^2}\sum_{nm} V_{nm} \sum_{\alpha\beta} c^\dagger_{\alpha n} c_{\alpha n} c^\dagger_{\beta m} c_{\beta m}.\end{aligned} \tag{5.36}$$

We can now decouple the two interaction terms by introducing Hubbard Stratonovich fields by adding the terms

$$H_\psi = \frac{1}{2}\frac{2N}{g^2}\sum_{nm} (V_{nm})^{-1} \psi^\dagger_{nm}\psi_{nm}, \tag{5.37}$$

$$H_\chi = \frac{1}{2}\frac{2N^2}{g^2}\sum_{nm} [V^{-1}]_{nm}\chi_n\chi_m \tag{5.38}$$

to the Hamiltonian. Also note that $\psi^\dagger_{nm} = \psi_{mn}$. $(V_{nm})^{-1}$ denotes the inverse of the nm element of V whereas $[V^{-1}]_{nm}$ denotes the nm element of the inverse matrix. Shifting those fields by

$$\psi_{nm} \to \psi_{nm} + \frac{g^2}{2N} V_{nm} \sum_\alpha c^\dagger_{\alpha m} c_{\alpha n} \tag{5.39}$$

$$\chi_n \to \chi_n + \frac{g^2}{2N^2} \sum_m V_{nm} \sum_\alpha c^\dagger_{\alpha m} c_{\alpha m} \tag{5.40}$$

then cancels out the two four-point terms and we finally arrive at the interaction Hamiltonian

$$\begin{aligned}\hat{H}_{\text{int}} =& \frac{N}{g^2} \sum_{nm} (V_{nm})^{-1} \psi^\dagger_{nm} \psi_{nm} + \frac{N^2}{g^2} \sum_{nm} [V^{-1}]_{nm} \chi_n \chi_m + \frac{g^2}{4N} \sum_{nm} V_{nm} c^\dagger_{\alpha n} c_{\alpha n} \\ &+ \sum_{n \neq m} \sum_\alpha c^\dagger_{\alpha n} c_{\alpha m} \psi_{nm} + \sum_n \sum_\alpha c^\dagger_{\alpha n} c_{\alpha n} \chi_n .\end{aligned} \tag{5.41}$$

The full closed-time-path action is then given by

$$\begin{aligned}S[c, \psi, \chi] = \int_{\mathcal{C}} \mathrm{d}t \, \Bigg\{ & \sum_{nm} c^\dagger_{\alpha n} \left(i\partial_t \delta_{nm} - h_{nm} \right) c_{\alpha m} - \frac{N}{g^2} V^{-1}_{nm} \psi^\dagger_{nm} \psi_{nm} \\ & - \frac{N^2}{g^2} \sum_{nm} [V^{-1}]_{nm} \chi_n \chi_m - \sum_{n \neq m} c^\dagger_{\alpha n} c_{\alpha m} \psi_{nm} - \sum_n c^\dagger_{\alpha n} c_{\alpha n} \chi_n \Bigg\}\end{aligned} \tag{5.42}$$

with single particle Hamiltonian

$$h_{ij} = \left(\epsilon \delta_{j,i+1} + \left(m(-1)^i + \frac{g^2}{4N} \sum_k V_{ik} \right) \delta_{ij} \right). \tag{5.43}$$

The χ field in this action corresponds to the Hubbard Stratonovich field used in the GW approximation, i.e. the above action reduces to Eq. 2.31 when setting $N = 1$. In the 1/N expansion, a second auxiliary field ψ enters, which couples to creation/annihilation operators at different sites. Hence, the ψ correlator will have the form of an effective vertex with four lattice indices and it will turn out, that it corresponds to the particle-particle T-matrix [211].

Equations of motion

The free propagators are defined from writing the free action as $S_0 = \int dt c^\dagger i D_0^{-1} c + \bar{\psi}^\dagger i G_0^{-1} \bar{\psi} + \bar{\chi} i K_0^{-1} \bar{\chi}$, with $\bar{\psi} = \langle \psi \rangle$ resulting in

$$iD^{-1,\alpha\beta}_{0,ij}(t_1, t_2) = \left(i\partial_{t_1} \delta_{ij} - h_{ij} - \bar{\psi}_{ij} - \bar{\chi}_i \delta_{ij} \right) \delta_{\mathcal{C}}(t_1 - t_2) \delta^{\alpha\beta} \tag{5.44}$$

$$iG^{-1}_{0,(ij)(kl)}(t_1, t_2) = -\frac{N}{g^2} V^{-1}_{(ij)} \delta_{(ij),(kl)} \delta_{\mathcal{C}}(t_1 - t_2), \tag{5.45}$$

$$iK^{-1}_{0,ij}(t_1, t_2) = -\frac{2N^2}{g^2} [V^{-1}]_{ij} \delta_{\mathcal{C}}(t_1 - t_2), \tag{5.46}$$

where for the G propagator we introduced a superindex (ij) to rewrite the four-leg tensor as a matrix. Note that there are no free propagators mixing the fields.

The 2PI effective action is then given by

$$\Gamma[D,G,K,\bar{\psi},\bar{\chi}] = S[\bar{\psi},\bar{\chi}] - i\,\mathrm{Tr}[D_0^{-1}[\bar{\chi},\bar{\psi}]D] - i\,\mathrm{Tr}[\ln D^{-1}] + i\,\mathrm{Tr}[G_0^{-1}G] + i\,\mathrm{Tr}[\ln G^{-1}] + \frac{i}{2}\,\mathrm{Tr}[K_0^{-1}K] + \frac{i}{2}\,\mathrm{Tr}[\ln K^{-1}] + \Gamma_2[D,G,K], \tag{5.47}$$

where the last term are all two-particle irreducible diagrams consisting out of the propagators D,G and K.

The equations of motion for the mean fields follow from extremezing the 2PI effective action, giving

$$\frac{\delta\Gamma}{\delta\bar{\psi}_{(nm)}(t)} = -\frac{N}{g^2}V^{-1}_{nm}\bar{\psi}_{(mn)}(t) + D^{\alpha\alpha}_{mn}(t,t) = 0 \tag{5.48}$$

$$\Rightarrow \qquad \bar{\psi}_{(mn)}(t) = \frac{g^2}{N}V_{nm}D^{\alpha\alpha}_{mn} \tag{5.49}$$

$$\frac{\delta\Gamma}{\delta\bar{\chi}_n(t)} = -\frac{N^2}{g^2}\sum_m([V^{-1}]_{mn} + [V^{-1}]_{nm})\bar{\chi}_m(t) + D^{\alpha\alpha}_{nn}(t,t) = 0 \tag{5.50}$$

$$\Rightarrow \qquad \bar{\chi}_n(t) = \frac{g^2}{2N^2}\sum_m V_{nm}D^{\alpha\alpha}_{mm} \tag{5.51}$$

Similarly, extremizing the effective action with respect to the propagators yields Schwinger-Dyson equations

$$D^{-1} = D_0^{-1} - \Sigma \tag{5.52}$$

$$G^{-1} = G_0^{-1} - \Pi \tag{5.53}$$

$$K^{-1} = K_0^{-1} - \Xi, \tag{5.54}$$

where the self energies are defined as

$$\Sigma^{\alpha\beta}_{ij}(t_1,t_2) = -i\frac{\delta\Gamma_2}{\delta D^{\beta\alpha}_{ji}(t_2,t_1)} \tag{5.55}$$

$$\Pi_{(ij)(kl)}(t_1,t_2) = i\frac{\delta\Gamma_2}{\delta G_{(kl)(ij)}(t_2,t_1)} \tag{5.56}$$

$$\Xi_{ij}(t_1,t_2) = 2i\frac{\delta\Gamma_2}{\delta K_{ji}(t_2,t_1)}. \tag{5.57}$$

Convoluting the Schwinger-Dyson equation from the right with D, we can derive their integro-differential form (also known as Kadanoff-Baym equations), giving

$$\sum_k (i\partial_{t_1}\delta_{ik}\delta^{\alpha\gamma} - \tilde{J}_{ik}^{\alpha\gamma}) D_{kj}^{\gamma\beta}(t_1,t_2) = i\delta_{ij}\delta^{\alpha\beta}\delta_{\mathcal{C}}(t_1-t_2) + i\sum_{kl}\int_{\mathcal{C}} dt \Sigma_{ik}^{\alpha\gamma}(t_1,t) D_{kj}^{\gamma\beta}(t,t_2), \tag{5.58}$$

$$G_{(ij),(kl)}(t_1,t_2) = -\frac{g^2}{N} V_{ij} i\delta_{(ij),(kl)}\delta_{\mathcal{C}}(t_1-t_2) - i\frac{g^2}{N} V_{(ij)} \sum_{(mn)} \int_{\mathcal{C}} dt \Pi_{(ij),(mn)}(t_1,t) G_{(mn),(kl)}(t,t_2), \tag{5.59}$$

$$K_{ij}(t_1,t_2) = -\frac{g^2}{2N^2} V_{ij} i\delta_{ij}\delta_{\mathcal{C}}(t_1-t_2) - i\frac{g^2}{2N^2}\sum_{kl} V_{ik}\int_{\mathcal{C}} dt \Xi_{kl}(t_1,t) K_{lj}(t,t_2), \tag{5.60}$$

where we defined the effective single-particle Hamiltonian $\tilde{J}_{ik}^{\alpha\beta} = h_{ik}^{\alpha\beta} - \bar{\psi}_{ik}\delta^{\alpha\beta} - \bar{\chi}_i\delta_{ik}\delta^{\alpha\beta} + \Sigma_{ik}^{0,\alpha\beta}$, including a possible time-local part of the fermion self-energy.

Symmetries of correlators

The correlators used above are defined as

$$D_{kj}^{\gamma\beta}(t_1,t_2) = \langle T_{\mathcal{C}} c_{\gamma k}(t_1) c_{\beta j}^\dagger(t_2)\rangle \tag{5.61}$$

$$G_{(ij),(kl)}(t_1,t_2) = \langle T_{\mathcal{C}} \psi_{(ij)}(t_1)\psi_{(kl)}^\dagger(t_2)\rangle \tag{5.62}$$

$$K_{ij}(t_1,t_2) = \langle T_{\mathcal{C}} \chi_i(t_1)\chi_j(t_2)\rangle\,. \tag{5.63}$$

From this we can follow the following identities:

$$(D_{kj}^{\gamma\beta}(t_1,t_2))^* = D_{jk}^{\beta\gamma}(t_2,t_1), \tag{5.64}$$

$$G_{(ij),(kl)}(t_1,t_2) = G_{(lk),(ji)}(t_2,t_1), \tag{5.65}$$

$$(G_{(ij),(kl)}(t_1,t_2))^* = G_{(kl),(ij)}(t_2,t_1) = G_{(ji),(lk)}(t_1,t_2), \tag{5.66}$$

$$K_{ij}(t_1,t_2) = K_{ji}(t_2,t_1). \tag{5.67}$$

1/N expansion

The diagrams in Γ_2 are all two-particle-irreducible *vacuum* diagrams built from propagators G, D, K and vertices $iS_{int} = -i\sum_{n\neq m} c_{\alpha n}^\dagger c_{\alpha m}\psi_{nm} - i\sum_n c_{\alpha n}^\dagger c_{\alpha n}\chi_n$. Hence, all diagrams must be singlets in colour space. The possible $SU(N)$ singlets are given by

$$\mathrm{Tr}(D^n), G, K, \tag{5.68}$$

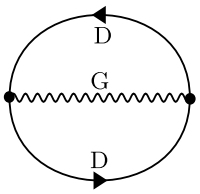

Figure 5.8: The only NLO diagram contributing to Γ_2. The fermion loop contributes a factor of N whereas $G \sim 1/N$, leading to an overall scaling of 1.

with n an arbitrary integer and $\mathrm{Tr}(D^n) \sim N$. From the equations 5.59 and 5.60 we can furthermore see that $G \sim 1/N$ and $K \sim 1/N^2$. Moreover, $\bar{\psi} \sim 1$ and $\bar{\chi} \sim 1/N$. Therefore, the leading order term in $1/N$ in the full effective action is the term where $\bar{\psi}$ is contracted with D, leading to an overal scaling of N (second term in Eq. 5.47). At next-to-leading order, the $\bar{\chi}$ contribution in the same term (giving $N \times 1/N = 1$) contributes as well as the diagram depicted in Fig. 5.8. Note that the propagator K only contributes at NNLO, such that to NLO, $\Xi = 0$.

To NLO, Γ_2 is therefore given by

$$\Gamma_2^{\mathrm{NLO}} = (-i)\frac{1}{2!}(-i)^2 \int_{\mathcal{C}} dt_1 \int_{\mathcal{C}} dt_2 \sum_{n\neq m} \sum_{l\neq k} D^{\alpha\beta}_{ml}(t_1,t_2) D^{\beta\alpha}_{kn}(t_2,t_1) G_{(nm),(kl)}(t_1,t_2). \tag{5.69}$$

If initially, the propagator of the fermions is diagonal in spinor space i.e. $D^{\alpha\beta}_{nm} = \langle c^\dagger_{\alpha n} c_{\beta m}\rangle = D_{nm}\delta_{\alpha\beta}$ then both interactions will not mix different components and the symmetry is conserved.

The self-energies follow as

$$\Pi_{(ij),(mn)}(t_1,t_2) \equiv i\frac{\delta\Gamma_2}{\delta G_{(mn),(ij)}(t_2,t_1)} \tag{5.70}$$

$$= -\frac{1}{2} D^{\alpha\beta}_{nj}(t_2,t_1) D^{\beta\alpha}_{im}(t_1,t_2), \tag{5.71}$$

$$\Sigma^{\alpha\beta}_{ij}(t_1,t_2) \equiv -i\frac{\delta\Gamma_2}{\delta D^{\beta\alpha}_{ji}(t_2,t_1)} \tag{5.72}$$

$$= \sum_{kn} D^{\alpha\beta}_{kn}(t_1,t_2) G_{(nj),(ki)}(t_1,t_2). \tag{5.73}$$

Spectral and statistical components

We decompose

$$D^{\alpha\beta}_{kj}(t_1,t_2) = F^{\alpha\beta}_{kj}(t_1,t_2) - \frac{i}{2}\mathrm{sgn}_{\mathcal{C}}(t_1-t_2)\rho^{\alpha\beta}_{kj}(t_1,t_2) \tag{5.74}$$

$$\begin{aligned} G_{(ij),(kl)}(t_1,t_2) &= -\frac{g^2}{N}V_{ij}i\delta_{(ij),(kl)}\delta_{\mathcal{C}}(t_1-t_2) \\ &\quad + \frac{g^2}{N}V_{(ij)}\left(G^F_{(ij),(kl)}(t_1,t_2) - \frac{i}{2}\mathrm{sgn}_{\mathcal{C}}(t_1-t_2)G^{\rho}_{(ij),(kl)}(t_1,t_2)\right)\frac{g^2}{N}V_{(kl)}, \end{aligned} \tag{5.75}$$

leading to the equations of motion

$$\sum_k \left(i\partial_{t_1}\delta_{ik}\delta^{\alpha\gamma} - \tilde{J}^{\alpha\gamma}_{ik}(t_1)\right)F^{\gamma\beta}_{kj}(t_1,t_2) = \sum_k \int_0^{t_1} \mathrm{d}t \Sigma^{\rho,\alpha\gamma}_{ik}(t_1,t)F^{\gamma\beta}_{kj}(t,t_2) \tag{5.76}$$

$$- \sum_k \int_0^{t_2} \mathrm{d}t \Sigma^{F,\alpha\gamma}_{ik}(t_1,t)\rho^{\gamma\beta}_{kj}(t,t_2), \tag{5.77}$$

$$\sum_k \left(i\partial_{t_1}\delta_{ik}\delta^{\alpha\gamma} - \tilde{J}^{\alpha\gamma}_{ik}(t_1)\right)\rho^{\gamma\beta}_{kj}(t_1,t_2) = \sum_k \int_{t_2}^{t_1} \mathrm{d}t \Sigma^{\rho,\alpha\gamma}_{ik}(t_1,t)\rho^{\gamma\beta}_{kj}(t,t_2), \tag{5.78}$$

for the fermion correlators and

$$\begin{aligned} G^F_{(ij),(kl)} &= -\Pi^F_{(ij),(kl)} - \frac{g^2}{N}\sum_{mn}\int_0^{t_1}\mathrm{d}t \Pi^{\rho}_{(ij),(mn)}V_{(mn)}G^F_{(mn),(kl)} \\ &\quad + \frac{g^2}{N}\sum_{mn}\int_0^{t_2}\mathrm{d}t \Pi^{F}_{(ij),(mn)}U_{(mn)}G^{\rho}_{(mn),(kl)}, \end{aligned} \tag{5.79}$$

$$\begin{aligned} G^{\rho}_{(ij),(kl)} &= -\Pi^{\rho}_{(ij),(kl)} \\ &\quad - \frac{g^2}{N}\int_{t_2}^{t_1}\sum_{mn}\mathrm{d}t \Pi^{\rho}_{(ij),(mn)}U_{(mn)}G^{\rho}_{(mn),(kl)}. \end{aligned} \tag{5.80}$$

for the auxiliary field correlators. The K propagator can be decomposed analogously, it corresponds to the density correlator in the GW approximation discussed in section 2.1.3 of the introduction. We refrain from discussing it in the following, as it only appears at NNLO in 1/N. We also note that $VG^{Frho}V$ correspond to the spectral/statistical components of the particle-particle T-matrix, which can be explicitly seen by comparing the expressions to the ones given in Ref. [211].

The auxiliary field self energies follow as

$$\Pi^F_{(ij),(mn)}(t_1,t_2) = -\frac{1}{2}\left(F^{\beta\alpha}_{im}(t_1,t_2)(F^{\beta\alpha}_{jn}(t_1,t_2))^* - \frac{1}{4}\rho^{\beta\alpha}_{im}(t_1,t_2)(\rho^{\beta\alpha}_{jn}(t_1,t_2))^*\right), \tag{5.81}$$

$$\Pi^{\rho}_{(ij),(mn)}(t_1,t_2) = -\frac{1}{2}\left(F^{\beta\alpha}_{im}(t_1,t_2)(\rho^{\beta\alpha}_{jn}(t_1,t_2))^* + \rho^{\beta\alpha}_{im}(t_1,t_2)(F^{\beta\alpha}_{jn}(t_1,t_2))^*\right), \tag{5.82}$$

while the fermionic self energies are given as

$$\Sigma^{(0),\alpha\beta}_{ij}(t_1,t_2) = \frac{g^2}{N}\sum_k V_{jk}\left(F^{\alpha\beta}_{kk} - \frac{1}{2}\right)\delta_{ij}, \tag{5.83}$$

$$\Sigma^{F,\alpha\beta}_{ij}(t_1,t_2) = \frac{g^4}{N^2}\sum_{nk} V_{nj}V_{ki}\Big(F^{\alpha\beta}_{kn}(t_1,t_2)G^F_{(nj),(ki)}(t_1,t_2) - \frac{1}{4}\rho^{\alpha\beta}_{kn}(t_1,t_2)G^{\rho}_{(nj),(ki)}(t_1,t_2)\Big), \tag{5.84}$$

$$\Sigma^{\rho,\alpha\beta}_{ij}(t_1,t_2) = \frac{g^4}{N^2}\sum_{nk} V_{nj}V_{ki}\Big(F^{\alpha\beta}_{kn}(t_1,t_2)G^{\rho}_{(nj),(ki)}(t_1,t_2) + \rho^{\alpha\beta}_{kn}(t_1,t_2)G^F_{(nj),(ki)}(t_1,t_2)\Big). \tag{5.85}$$

In this form, we can finally solve the equations of motion for the correlators as discussed in the introduction. Note that in this form, the equations scale as N_c^3 with the number of colours (where the equations for F, ρ are the bottleneck) and N_s^6 with the number of lattice sites (bottleneck given by equations for G^F and G^ρ). The former can be reduced to $O(1)$ by starting in a colour-symmetric initial state with $D^{\alpha\beta} \sim \delta^{\alpha\beta}$. Then, only a single component needs to be evolved in time. The scaling with the number of sites can be reduced by considering translationally invariant initial states.

5.6 CONCLUSIONS AND OUTLOOK

In this chapter we have studied thermalization dynamics in the lattice Schwinger model, i.e. one-dimensional quantum electrodynamics, with non-equilibrium quantum field theory. We studied the breaking of strings on top of the strong coupling vacuum at weak coupling, showing that previously used Hartree-Fock/Gaussian state methods are insufficient to describe the approach to equilibrium. At three loop order, we found good agreement of the dynamics with the GW approximation, which resums bubble diagrams to infinite order in the interaction strength. Strings always relaxed on the relatively short time scales we studied, which we attributed to the fact that we used a high-energy initial state. We studied the two-time correlation functions to test the off-diagonal part of eigenstate thermalization as proposed in chapter 4. We found at least three time scales in the dynamics, corresponding to a fast relaxation of the spectral function, over the establishment of a global local temperature to the global relaxation of the temperature to its final value. Finally, we presented two new non-equilibrium quantum field theory methods which will enable a further study of this problem. On the one hand, the evaluation of spectral functions directly at infinite temperature could enable further insights into mid-spectrum properties of the Schwinger model, especially about the (non-)existence of

well-defined quasiparticles in this high temperature regime. On the other hand, we derived a controlled 1/N expansion for SU(N) lattice gauge theories, which enables the study of thermalization in non-abelian settings. In particular, an experimental study of the latter model could be enabled by using the implementation of the Schwinger model with Bose-Fermi mixtures [379–382] with alkaline-earth atoms, which have SU(N) symmetric interactions [383] with N as large as 10. The early establishment of a near-constant spectral function indicates that kinetic approaches could be successful to describe the dynamics. They could be directly derived from the methods we used here [210, 384] and offer novel insights into transport phenomena in gauge theories. Last but not least, a study of the non-equilibrium dynamics of confinement would be enabled by first preparing a low temperature state of the interacting theory before creating a string, which could be done by the methods we discussed in chapter 2. Doing so would also enable answering the question whether a weak coupling expansion is enough to reproduce a near-stable string at low temperatures or whether non-perturbative approximations such as the GW approximation are necessary to capture this phenomenology.

6

NON-LOCAL EMERGENT HYDRODYNAMICS IN A LONG-RANGE QUANTUM SPIN SYSTEM

This chapter is based on the publications

- Alexander Schuckert, Izabella Lovas, Michael Knap: "Non-local emergent hydrodynamics in a long-range quantum spin system" – Phys. Rev. B 101, 020416(R) (2020) [arXiv:1909.01351]
- M. K. Joshi, F. Kranzl, A. Schuckert, I. Lovas, C. Maier, R. Blatt, M. Knap, C. F. Roos: "Observing emergent hydrodynamics in a long-range quantum magnet" – [arXiv:2107.000331]

Structure, text and figures have been rearranged and adapted here. The discrete truncated Wigner approximation (dTWA) results were obtained by Izabella Lovas. The experimental results were obtained by M. K. Joshi, F. Kranzl, C. Maier, R. Blatt, C. F. Roos.

Generic short-range interacting quantum systems with a conserved quantity exhibit universal diffusive transport at late times. We employ non-equilibrium quantum field theory and semi-classical phase-space simulations to show how this universality is replaced by a more general transport process in a long-range XY spin chain at infinite temperature with couplings decaying algebraically with distance as $r^{-\alpha}$. While diffusion is recovered for $\alpha > 1.5$, longer-ranged couplings with $0.5 < \alpha \leq 1.5$ give rise to effective classical Lévy flights; a random walk with step sizes drawn from a distribution with algebraic tails. We find that the space-time dependent spin density profiles are self-similar, with scaling functions given by the stable symmetric distributions. As a consequence, for $0.5 < \alpha \leq 1.5$ autocorrelations show hydrodynamic tails decaying in time as $t^{-1/(2\alpha-1)}$ and linear-response theory breaks down. We compare our theoretical results to a quantum simulation experiment with 51 individually controlled ions, in which our Lévy flight picture is confirmed by measuring the space-time resolved correlation functions in an infinite temperature state.

6.1 INTRODUCTION

Universality in equilibrium asserts that microscopic details are irrelevant for the emergent quantum phases of matter and their transitions. Rather, symmetries and topology determine the essential macroscopic properties. By contrast, all scales, from low to high energies, are relevant for quantum systems which are driven far from their thermal equilibrium. Recent experimental progress in engineering coherent and interacting quantum systems made it possible to create and explore exotic non-equilibrium states, which can exhibit unconventional relaxation dynamics [47, 59, 150, 306, 385, 386], dynamical phases [51, 129, 146, 179, 307, 387], and transitions between them [181, 182].

Despite this wealth of observed quantum phenomena, a common anticipation is that classical hydrodynamics of a few conserved quantities emerges universally for any complex quantum system, as strong interactions entangle and effectively mix local degrees of freedom [40, 388]. This is because in quantum many-body systems, macroscopic inhomogeneities in a conserved quantity must be transported across the whole system to reach an equilibrium state. As this process constrained by a continuity equation, it is in general slow in the absence of long-lived quasi-particle excitations [40, 43, 44, 388–392]. The universality of this effective classical description may be understood from the central limit theorem: in the regime of incoherent transport, short range interactions lead to an effective random walk with a finite variance of step sizes, leading to a Gaussian distribution at late times. This universality is broken when quantum coherence is retained, such as in integrable models [393–399] or in the vicinity of a many-body localized phase, where rare region effects give rise to subdiffusive transport [54–56, 152, 233, 400].

However, verifying this assumption, and furthermore determining the non-universal transport coefficients of the emergent hydrodynamic theory for specific systems is challenging. Recently, enormous efforts have been devoted to detect hydrodynamic transport in quantum gases [141, 401–403] and condensed matter systems [203, 404–406]. While transport is generally expected to be diffusive, a variety of largely unexplored classes of hydrodynamics have been theoretically predicted including anomalous subdiffusive [65, 407] and superdiffusive transport [408–410].

In this chapter, we show how this universal diffusive transport in short range interacting systems is replaced by a more general, non-local effective hydrodynamical description in systems with algebraically decaying long-range interactions. We use semi-analytical non-equilibrium quantum field theory calculations (the two-particle irreducible effective action method for spin systems (spin-2PI)) and dTWA simulations to show that in a long-range interacting XY spin chain, spin

transport at infinite temperature effectively obeys a classical master equation with algebraically decaying transition amplitudes. This effective description can be reformulated as a classical random walk with infinite variance of step sizes, giving rise to a generalized central limit theorem and to a late-time description in terms of classical Lévy flights [411], an example for *super*diffusive anomalous transport. As a result, we demonstrate that the full spatio-temporal shape of the correlation function $C(j,t) = \langle \hat{S}^z_j(t)\hat{S}^z_0(0)\rangle$, and in particular, the exponent of the hydrodynamic tail in the autocorrelation function $C(j=0,t)$, depends strongly on the long-range exponent α. While for $\alpha > 1.5$ we recover classical diffusion, the autocorrelation function shows hydrodynamic tails with an exponent $1/(2\alpha-1)$ for $0.5 < \alpha \leq 1.5$. Furthermore, $C(j,t)$ possesses a self-similar behavior, with the scaling function covering all stable symmetric distributions as a function of α, smoothly crossing over from a Gaussian at $\alpha = 1.5$ over a Lorentzian at $\alpha = 1$ to an even more sharply peaked function as $\alpha \to 0.5$. We also extract the generalized diffusion coefficient D_α from the scaling functions, and explain its α dependence by Lévy flights; quantum effects are incorporated in a many-body time scale depending only weakly on α. For $\alpha \leq 0.5$ no emergent hydrodynamic behavior is found as the system relaxes instantaneously in the thermodynamic limit [412].

We compare our theoretical results to an experiment in a trapped ion quantum simulator, confirming the Lévy flight transport process. Throughout this chapter, we will show theoretical results alongside the experimental results, giving a complete characterization of the transport process. This cross-method verification establishes both the theoretical tools of nonequilibrium quantum field theory and discrete truncated Wigner simulations as well as experimental quantum simulation as efficient tools to study transport phenomena in the thermalization dynamics of quantum many-body systems.

6.2 MODEL

We study the long range interacting quantum XY chain with open boundary conditions, given by the Hamiltonian

$$\hat{H} = -\frac{1}{2}\sum_{i\neq j=-L/2}^{L/2} \frac{J}{\mathcal{N}_{L,\alpha}|i-j|^\alpha}\left(\hat{S}^x_i\hat{S}^x_j + \hat{S}^y_i\hat{S}^y_j\right). \tag{6.1}$$

Here, $\hat{S}^\alpha = \frac{1}{2}\hat{\sigma}^\alpha$ denotes spin-$\frac{1}{2}$ operators given in terms of Pauli matrices, L is the (odd) length of the chain [1], and we set $\hbar = 1$. The interaction strength J is rescaled with the factor $\mathcal{N}_{L,\alpha} = \sqrt{\sum_{j\neq 0}|j|^{-2\alpha}}$ in order to remove the L and α dependence of the time scale associated with the perturbative short time dynamics of the central

1 We always assume integer divisions when we write $\frac{L}{2}$.

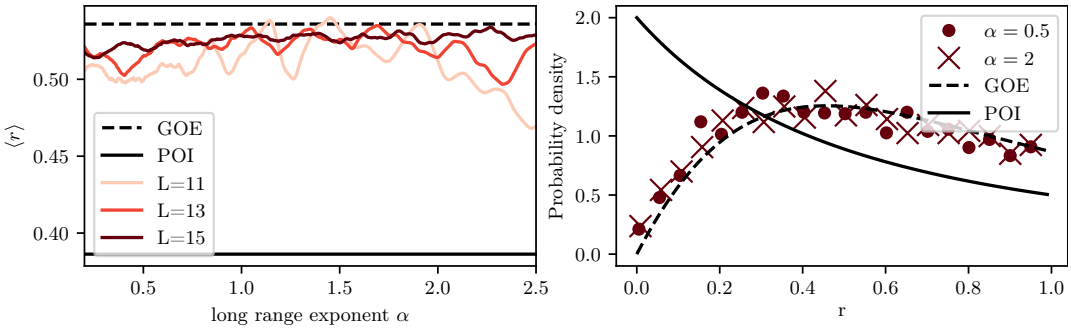

Figure 6.1: **Level statistics.** (left) Mean of ratio of consecutive level spacings r and (right) probability distribution of r for $L = 15$, showing convergence to the expectation from the GOE as $L \to \infty$ for all values of α studied here. For the mean we used a moving average over α values in a window of approx. 0.11 to smoothen the curves, amounting to 41 values in our scanning resolution. No such averaging was done for the probability distribution.

spin at $i = 0$. The above model and is an effective description of the long-range transverse field Ising model for large fields [179, 187]. In the following, we show that it shows chaotic (Wigner-Dyson) level statistics for the whole range of α considered here ($0.5 \leq \alpha \leq 2$) and is therefore expected to thermalize.

LEVEL STATISTICS. We consider the subsector with total magnetization one and even parity and plot in Fig. 6.1 the histogram of the ratio of consecutive levelspacings

$$r_i = \frac{\min(E_{i+1} - E_i)}{\max(E_{i+1} - E_i)}, \quad r_i \in [0, 1]. \tag{6.2}$$

For exemplary values $\alpha = 0.5$ and $\alpha = 2$, the histogram follows the expectation from the Gaussian orthogonal ensemble (GOE) $P_{\text{GOE}}(r) = ((27/4)(r + r^2))/((1 + r + r^2)^{5/2})$ and is in particular far from the Poisson distribution(POI) $P_{\text{POI}}(r) = 2/(1 + r)^2$ expected in integrable models. Moreover, we plot the mean of the distribution $\langle r \rangle$ as a function of α, with random matrix expectations $\langle r_{\text{GOE}} \rangle \approx 0.54$, $\langle r_{\text{POI}} \rangle \approx 0.39$. We find values in agreement with the GOE for $0.2 < \alpha < 2.5$, showing that all values of α considered are non-integrable.

DYNAMICS IN DIFFERENT SPIN SUBSECTORS. The long-range XY model conserves the total S^z magnetization, with product states in the S^z basis evolving radically differently depending on the complexity of the corresponding magnetization sector. For just a few spin flips on top of the completely polarized state, the dynamics can be exactly solved and are described in terms of ballistically propagating spin waves, with a diverging group velocity at $\alpha = 1$ [176, 187, 413] related to the algebraic leakage of the Lieb-Robinson bound [177, 414–416]. In contrast, here

we show that the exponentially large Hilbert space sector for an extensive number of spin flips gives rise to rich transport phenomena, driven by the long-range nature of the interactions.

6.3 METHODS

In the following, we demonstrate the emergence of effective transport dynamics in the quantum dynamics of the Hamiltonian (6.1) by studying the unequal time correlation function

$$C(j,t) := \mathrm{Tr}\left[\hat{S}^z_j(t)\hat{S}^z_0(0)\right]_{|\mathrm{j}=0\rangle=|\uparrow\rangle}. \tag{6.3}$$

Here, we perform the trace over product states in the S^z basis, restricted to the Hilbert space sector with $\sum_i S^z_i = \frac{1}{2}$, such that $\langle S^z_i(t=0)\rangle = \frac{1}{2}\delta_{0,i}$ for all spins i. This way, we probe the transport of a single spin excitation moving in an infinite temperature bath with vanishing total magnetization.

We employ two complementary, approximate methods to study the dynamics at long times and for large system sizes, in a regime that is challenging to access by numerically exact methods [417]. Schwinger boson spin-2PI [48, 215], a non-equilibrium quantum field theory method, employs an expansion in the inverse coordination number $1/z$ to reduce the many-body problem to solving an integro-differential equation that scales algebraically in system size. As the effective coordination number is large in a long-range interacting system, we expect this approximation to be valid for small α. The dTWA evolves the classical equations of motion, while introducing quantum fluctuations by sampling initial states from the Wigner distribution [418–421] and was shown to be particularly well suited for studying long-range interacting systems [165, 420]. If not stated otherwise, all our results have been converged with respect to system size in the theoretical methods, for which we employed chains with $201 - 601$ sites.

In the trapped ion quantum simulator, (pseudo-)spins are realized with two electronic states of the $^{40}Ca^+$ ion: $|S_{1/2}, m = +1/2\rangle$ as $|\downarrow\rangle$ and $|D_{5/2}, m = +5/2\rangle$ as $|\uparrow\rangle$. The quantum state of individual ions is controlled by a tightly focused, steerable laser beam capable of addressing any ion in the string, in conjunction with a laser beam that collectively interacts with the ions. A two-tone laser field realizes approximately power-law decaying Ising interactions between the (pseudo-)spins by off-resonantly coupling motional and electronic degrees of freedom of the ion chain. Application of a strong transverse field energetically penalizes spin non-conserving contributions [187]. The effective dynamics is then described by the long-range XY model in Eq. (6.1), where J and α can be tuned by varying the amplitude and

frequency of the two-tone laser field. Experimentally, the Hamiltonian is often written in a slightly different convention [175] to Eq. 6.1, given by

$$\hat{H}_{\text{exp}} = \sum_{i<j} \frac{J_{\text{exp}}}{|i-j|^{\alpha}} (\hat{\sigma}_i^+ \hat{\sigma}_j^- + \hat{\sigma}_i^- \hat{\sigma}_j^+). \tag{6.4}$$

This definition can be obtained from Eq. (6.1) by inserting $\hat{S}^{\alpha} = \frac{1}{2}\hat{\sigma}^{\alpha}$ and $J = 2J_{\text{exp}}\mathcal{N}_{\alpha}$. Correspondingly, the correlation function differs by a prefactor of $1/4$ when written in terms of Pauli matrices. We will employ $\hat{H}_{\text{exp}}$ whenever we discuss experimental data.

$4C_j(t) = \langle \hat{\sigma}_j^z(t)\hat{\sigma}_0^z \rangle_{T=\infty} \sim \langle \phi_1|\sigma_j^z(t)|\phi_1\rangle + \langle \bar{\phi}_1|\sigma_j^z(t)|\bar{\phi}_1\rangle + \langle \phi_2|\sigma_j^z(t)|\phi_2\rangle + \cdots$

Figure 6.2: **Initial state preparation in the trapped ion quantum simulator.** Infinite-temperature correlations are measured by averaging over initial product states while preparing the central ion deterministically in the same state (blue box). Picture of three exemplary initial states in a chain of $^{40}Ca^+$ ions ($|\uparrow\rangle$ dark spots, $|\downarrow\rangle$ bright spots). White squares (circles) indicate the intended preparation of $|\uparrow\rangle$ ($|\downarrow\rangle$), achieved with 99% fidelity per ion.

6.3.1 *Product state sampling of the trace*

Preparing an infinite temperature state is difficult both in our theory methods and in the quantum simulator. We overcome this challenge by expressing the infinite temperature expectation value as an equally weighted trace over product states $|\phi\rangle$ in the $\hat{\sigma}^z$ basis. To do so, we first express the infinite temperature correlation function in Eq. (6.3) as

$$4C_j(t) = \langle \hat{\sigma}_j^z(t)\hat{\sigma}_0^z(0)\rangle_{T=\infty} \tag{6.5}$$

$$= \frac{1}{Z}\text{Tr}\left[e^{-\hat{H}/T}\hat{\sigma}_j^z(t)\hat{\sigma}_0^z(0)\right]\Big|_{T=\infty} \tag{6.6}$$

$$= \frac{1}{Z}\text{Tr}\left[\hat{\sigma}_j^z(t)\hat{\sigma}_0^z(0)\right], \tag{6.7}$$

with the partition sum $Z = \text{Tr}[e^{-\hat{H}/T}]|_{T=\infty} = 2^L$ for systems of size L. We expand the trace in the $\hat{\sigma}^z$ basis to obtain

$$4C_j(t) = \frac{1}{Z}\sum_{\sigma_{-\frac{L}{2}},\ldots,\sigma_{\frac{L}{2}}} \langle \sigma_{-\frac{L}{2}}\ldots\sigma_{\frac{L}{2}}|\hat{\sigma}_j^z(t)\hat{\sigma}_0^z(0)|\sigma_{-\frac{L}{2}}\ldots\sigma_{\frac{L}{2}}\rangle \tag{6.8}$$

$$= \frac{1}{Z}\sum_{\sigma_{-\frac{L}{2}},\cdots,\sigma_{\frac{L}{2}}} \sigma_0 \langle \sigma_{-\frac{L}{2}}\cdots\sigma_{\frac{L}{2}}|\hat{\sigma}_j^z(t)|\sigma_{-\frac{L}{2}}\ldots\sigma_{\frac{L}{2}}\rangle, \tag{6.9}$$

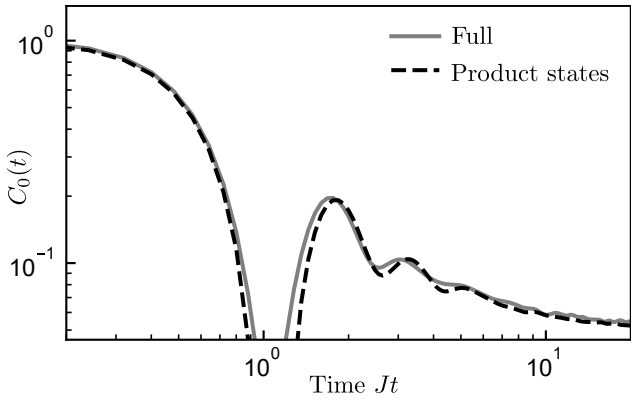

Figure 6.3: **Comparison of full trace to product state sampling.** Data obtained from exact diagonalization on an $L = 19$ chain with $\alpha = 1$. For product state sampling, we used $M = 240$ initial states, for full trace we used 10 Haar-random states. The saturation at late times is a finite size effect.

where $\sigma_j = \pm 1$. We have therefore reduced the evaluation of a two-time correlation function to the weighted sum of single-time functions using product initial states, which can be realized in the experiment, see Fig. 6.2. In order to evaluate Eq. (6.9) exactly, all 2^L product states in the z-basis would have to be prepared, time evolved and measured to then obtain $C_j(t)$ from the weighted sum. Moreover, when only averaging over a small number of initial states, large statistical fluctuations are expected in the measured correlations, such that a sampling of the sum with a finite number of states seem challenging. We remove these fluctuations by sampling pairs of conjugate product states, $|\phi\rangle$ and $|\overline{\phi}\rangle$, where in the second configuration all spins are flipped except for the central one. For each pair of product states, initial correlations are unity in the center of the system while being zero elsewhere, reproducing directly this property of the full trace; see first two initial states in Fig. 6.2. With this procedure, convergence is already achieved for a small number of initial product states. In the experiment, for $\alpha = 0.9$ and 1.1 ($\alpha = 1.5$), 60 (120) initial product state configurations were created, each of which was realized, evolved, and measured for 50 to 200 times in the quantum simulation. In spin-2PI simulations we used $4 - 16$ different initial states, while in dTWA the averaging over initial states is performed in parallel with the Monte Carlo averaging over the Wigner distribution; here we typically use $\sim 10^5$ samples. We furthermore only consider the largest sector with magnetization ~ 0. In Fig. 6.3 we compare the sampling of the largest sector to the exact results of the thermal expectation value. The full trace is evaluated using the typicality approach [422], which involves evolving Haar-random states $|\psi_r\rangle$ in the entire Hilbert space and then averaging over $5 - 10$ such states.

6.4 EFFECTIVE STOCHASTIC DESCRIPTION OF LONG-RANGE TRANSPORT

Before evaluating the infinite temperature correlation function introduced above, we first construct the expected classical transport process by evaluating the corresponding Master equation and studying its properties in detail.

As the model in Eq. (6.1) is equivalent to long-range hopping hard core bosons, we conjecture the effective classical equation of motion for the transported local density $f_j(t)$, in our case $\left\langle \hat{S}^z_j(t) \right\rangle + \frac{1}{2}$, to be of the form [2]

$$\partial_t f_j(t) = \sum_{i \neq j} \left(W_{i\to j}\, f_i(1-f_j) - W_{j\to i}\, f_j(1-f_i) \right) \tag{6.10}$$

Here, the transition rate $W_{i\to j}$ is determined by the microscopic transport processes present in the Hamiltonian, in our case the long-range hopping of spins. More specifically, from Fermi's golden rule the transition rate for a flip flop process between spins i and j is proportional to $|\langle \uparrow_i \downarrow_j |\hat{H}| \downarrow_i \uparrow_j \rangle|^2$, and hence we phenomenologically set

$$W_{i\to j} = W_{j\to i} = \frac{\lambda}{|i-j|^{2\alpha}}, \tag{6.11}$$

where λ^{-1} is a characteristic time scale determined by the full many-body Hamiltonian.

Due to the symmetry of the transition matrix elements $W_{i\to j} = W_{j\to i} \equiv W_{ij}$, the Master equation is linear,

$$\partial_t f_j = \sum_{i \neq j} W_{ij}(f_i - f_j) \tag{6.12}$$

and can be solved by taking the Fourier transform. This gives

$$\partial_t f(k) = [W(k) - W(k=0)]\, f(k), \tag{6.13}$$

where

$$f(k) = \sum_{j=-L/2}^{L/2} e^{-ikj} f_j, \tag{6.14}$$

and

$$W(k) - W(k=0) = \lambda \left[\sum_{j=-L/2}^{-1} + \sum_{j=1}^{L/2} \right] \left(e^{-ikj} - 1 \right) / |j|^{2\alpha} \tag{6.15}$$

$$\approx 2\lambda \int_1^{L/2} dx\, \left(\cos kx - 1 \right) / x^{2\alpha}, \tag{6.16}$$

2 A Master equation in terms of a local *probability* density may be obtained by normalizing the local density.

with $k = 2\pi n/L$, $n = -L/2, ..., L/2$.

The long time behavior is dominated by large wavelengths $k \ll 1$. For $0.5 < \alpha < 1.5$ the integral remains convergent when we remove both the upper and lower cutoffs, leading to the following approximation in the regime $k \ll 1$,

$$\begin{aligned} W(k) - W(k=0) &\approx 2\lambda \int_0^{L/2} dx\ (\cos kx - 1)\ /x^{2\alpha} - 2\lambda \int_0^1 dx\ (\cos kx - 1)\ /x^{2\alpha} \\ &\approx 2\lambda \int_0^{\infty} dx\ (\cos kx - 1)\ /x^{2\alpha} + \lambda k^2 \int_0^1 dx\, x^{2-2\alpha} \\ &= \left(-c_\alpha\, |k|^{2\alpha-1} + \frac{k^2}{3-2\alpha}\right) \lambda. \end{aligned} \tag{6.17}$$

Here

$$c_\alpha = -2 \int_0^{\infty} dz\ (\cos z - 1)\ /z^{2\alpha} = -2\,\Gamma(1-2\alpha)\sin(\alpha\pi), \tag{6.18}$$

with Γ denoting the gamma function. Note that $c_\alpha > 0$ for $0.5 < \alpha < 1.5$.

For $0.5 < \alpha < 1.5$, the first term in Eq. (6.17), $\sim |k|^{2\alpha-1}$, will dominate the long time behavior, leading to

$$\partial_t f(k) \approx -\lambda c_\alpha\, |k|^{2\alpha-1} \quad \Rightarrow \quad f(k,t) = f(k,0)\, e^{-\lambda c_\alpha |k|^{2\alpha-1} t}. \tag{6.19}$$

In particular, taking an initial state with a single localized excitation, $f_j(t=0) = \delta_{j,0}/4$ and hence $f(k,0) \equiv 1/4$ with the factor $1/4$ stemming from $(\hat{S}^z)^2 = 1/4$, we arrive at the scaling ansatz

$$f_j(t) \approx \frac{1}{4} \int \frac{dk}{2\pi}\ \exp\left(ikj - \lambda\, t\, c_\alpha\, |k|^{2\alpha-1}\right) = (\lambda c_\alpha t)^{-1/(2\alpha-1)}\, F_\alpha\left(\frac{|j|}{(\lambda c_\alpha t)^{1/(2\alpha-1)}}\right), \tag{6.20}$$

with $F_\alpha(y)$ given by

$$F_\alpha(y) = \frac{1}{4} \int \frac{\mathrm{d}k}{2\pi} \exp(-|k|^{1/\beta_\alpha}) \exp(iyk). \tag{6.21}$$

DIFFUSION FOR $\alpha > 1.5$. While we used $\alpha < 1.5$ in the derivation of Eq. (6.17), the expression is in fact valid for all $\alpha > 0.5$. This can be shown by evaluating the following integral exactly,

$$W(k) - W(k=0) \approx 2\lambda\, |k|^{2\alpha-1} \int_{|k|}^{\infty} dz\ (\cos z - 1)\ /z^{2\alpha},$$

and expanding the resulting expression around $k = 0$. Noting that for $\alpha > 1.5$ the $|k|^{2\alpha-1}$ term is subdominant, we arrive at

$$f_j^{\alpha>1.5}(t) \approx \frac{1}{4} \int \frac{dk}{2\pi}\ \exp\left(ikj - \frac{\lambda}{2\alpha-3} k^2 t\right) = (D_\alpha t)^{-1/2}\ G\left(\frac{|j|}{(D_\alpha t)^{1/2}}\right), \tag{6.22}$$

reproducing diffusive behaviour for $\alpha > 1.5$ with diffusion coefficient $D_\alpha = \lambda/(2\alpha - 3)$ and a Gaussian $G(y) = \exp(-y^2/4)/8\sqrt{\pi}$.

EXPONENTIAL LATE TIME DECAY OF THE AUTOCORRELATION FUNCTION. For finite system sizes L, approximating the discrete Fourier sums by integrals eventually breaks down at very long times. In this regime the time evolution will be dominated by the two smallest non-zero wave-numbers, $k = \pm 2\pi/L$, leading to an exponential decay

$$f_j(t) \approx \frac{1}{L}\left[f(k=0,t) + \sum_{k_0=\pm 2\pi/L} e^{ik_0 j} f(k_0,t)\right] \tag{6.23}$$

$$= \frac{1}{4L}\left[1 + 2\cos(2\pi j/L) e^{-\lambda t c_\alpha (2\pi/L)^{2\alpha-1}}\right] \tag{6.24}$$

for the case of $\alpha \leq 1.5$. The exponent of this exponential decay is hence expected to scale with the system size as $\sim (1/L)^{2\alpha-1}$. This prediction is in agreement with our spin-2PI numerical results. Moreover, this result can be used to extract the diffusion coefficient $D_\alpha = \lambda c_\alpha$ from finite size data.

In the following, we will discuss several physical consequences of the hydrodynamic scaling functions derived from the classical Master equation, ranging from the divergence of the spin conductivity to the breakdown of linear-response theory.

6.4.1 *Spin conductivity*

In this section we examine the spin conductivity $\sigma(q,\omega)$, as calculated from linear-response theory, and show that the DC conductivity $\sigma_{\mathrm{DC}} = \lim_{\omega\to 0}\lim_{q\to 0}\sigma(q,\omega)$ diverges in the superdiffusive region $\alpha < 1.5$.

First we deduce $\sigma(q,\omega)$ in frequency space from the spin correlation function $C(q,t)$ in real time. We assume that $C(q,t)$ decays as

$$C(q,t) = C(q)\exp(-D_\alpha |q|^{2\alpha-1} t). \tag{6.25}$$

For the initial state discussed there, $C(q) \equiv C(q,t=0) = 0.25$, which coincides with the spin susceptibility at infinite temperature.

Performing a Laplace transform $\tilde{C}(q,z) = \int_0^\infty dt e^{izt} C(q,t)$, we arrive at

$$\tilde{C}(q,z) = \frac{i}{z + iD_\alpha |q|^{2\alpha-1}} C(q). \tag{6.26}$$

The above equation makes the crossover from diffusive over ballistic to superballistic transport explicit as the power of $|q|$ in the pole of $\tilde{C}(q,z)$ determines this property. Also note that there is no damping of these hydrodynamic modes.

Moreover, one can show that $C(q,\omega) = 2\mathrm{Re}(\tilde{C}(q,z+i0^+)$ [423] from $\tilde{C}(q,z) = \int \frac{\mathrm{d}\omega}{2\pi i} C(q,\omega)/(\omega - z)$ and the fact that $C(q,t)$ is real and even (although not explicit

in Eq. (6.25), which is only defined for $t > 0$, this may be seen from $C(x,t) = \mathrm{Tr}(S^z(x,t)S^z(0,0)) = \frac{1}{2}(\mathrm{Tr}(S^z(x,t)S^z(0,0)) + \mathrm{Tr}(S^z(0,0)S^z(x,t)))$.). Hence,

$$C(q,\omega) = C(q)\frac{2D_\alpha|q|^{2\alpha-1}}{\omega^2 - (D_\alpha|q|^{2\alpha-1})^2}. \tag{6.27}$$

Finally, we assume that a continuity equation of the form

$$\partial_t S^z(x,t) + \partial_x j(x,t) = 0 \tag{6.28}$$

holds, where $j(x,t)$ is the spin current density, which is in general non-local in the case of long-range interactions [424]. In the limit of high temperatures T, the spin conductivity is given by $\sigma(q,\omega) = \frac{1}{2T}\int \mathrm{d}t \int \mathrm{d}x\, e^{i\omega t - iqx}\langle j(x,t)j(0,0)\rangle$ (here we set $k_B = 1$). It follows that

$$T\sigma(q,\omega) = \frac{\omega^2}{2q^2}C(q,\omega) \tag{6.29}$$

$$= C(q)\frac{D_\alpha\omega^2|q|^{2\alpha-3}}{\omega^2 - (D_\alpha|q|^{2\alpha-1})^2}. \tag{6.30}$$

For the DC conductivity we then get

$$T\sigma_{\mathrm{DC}} = \begin{cases} \infty & \text{for } \alpha < 1.5 \\ D_\alpha C(q) & \text{for } \alpha = 1.5 \end{cases}, \tag{6.31}$$

showing that σ_{DC} diverges in the superdiffusive regime while it follows the Einstein relation in the diffusive regime. Note that this divergence is qualitatively different to the one observed in a metal: There, the AC conductivity diverges only at $\omega = 0$ due to the Drude term, but is finite for any finite ω. Here, however, the conductivity diverges for any frequency ω as $q \to 0$, i.e. $\sigma(\omega, q \to 0) = \infty$. This is a result of the non-local character of spin transport in this model.

6.4.2 *Breakdown of linear-response for Lévy flights*

In this section we argue that linear-response theory breaks down for long-range interacting models displaying Lévy flight behavior, in agreement with the discussion of the previous section. Instead, we find a non-linear relation between the (spin) current $\mathcal{J}$, and the field E [424],

$$\mathcal{J} \sim E^{2\alpha-2}. \tag{6.32}$$

To arrive at Eq. (6.32), we add a small static homogeneous magnetic field gradient to the Hamiltonian,

$$\hat{H}(E) = -\frac{1}{2}\sum_{i\neq j=-L/2}^{L/2}\frac{J}{\mathcal{N}_{L,\alpha}|i-j|^\alpha}\left(\hat{S}_i^x\hat{S}_j^x + \hat{S}_i^y\hat{S}_j^y\right) - E\sum_{j=-L/2}^{L/2} j\,\hat{S}_j^z, \tag{6.33}$$

and we proceed by writing down a classical master equation, expected to capture the behavior of $\hat{H}(E)$,

$$\partial_t f_j = \sum_{i \neq j} \left[W_{i\to j}(E)\, f_i\,(1-f_j) - W_{j\to i}(E)\, f_j\,(1-f_i) \right]. \tag{6.34}$$

According to Fermi's golden rule, $W_{i\to j}(E)$ is proportional to $|i-j|^{-2\alpha}$ based on the matrix element connecting the initial and final states. Moreover, in the presence of field E and at finite temperatures T, the transition rates for hops to the left and right directions differ in such a way that the right hand side of Eq. (6.34) vanishes for the new equilibrium state of Hamiltonian Eq. (6.33), $f_i^{eq}(E)$. These considerations lead to a ratio determined by the different Boltzmann weights associated with these processes,

$$\frac{W_{i\to j}(E)}{W_{j\to i}(E)} = \frac{f_j^{eq}(E)(1-f_i^{eq}(E))}{f_i^{eq}(E)(1-f_j^{eq}(E))} = \exp\left[(j-i)E/T\right]$$

resulting in a modified ansatz. In principle $\lambda \to \lambda(E)$ could still weakly depend on $(i-j)^2 E^2$, but this would result in a subleading renormalization of the current compared to the leading order behavior discussed below.

$$W_{i\to j}(E) = \frac{e^{(j-i)E/(2T)}}{\cosh[(j-i)E/(2T)]} \frac{\lambda}{|i-j|^{2\alpha}}.$$

We evaluate the current response by linearizing the Fourier transform of the master equation in occupation numbers $f(k)$, resulting in

$$\partial_t f(k) = \left[W(k;E)W(k=0;E)\right] f(k) \equiv r(k;E)\, f(k),$$

with a field dependent decay rate

$$r(k;E) = \lambda \int_1^{L/2} dx \left[\frac{e^{xE/(2T)}}{\cosh(xE/(2T))} \frac{e^{-ikx}-1}{x^{2\alpha}} + \frac{e^{-xE/(2T)}}{\cosh(xE/(2T))} \frac{e^{ikx}-1}{x^{2\alpha}} \right].$$

The broken left / right symmetry gives rise to a non-zero drift velocity, evaluated as

$$v_{drift} = i \left.\frac{dr(k;E)}{dk}\right|_{k=0} = 2\lambda \int_1^{L/2} dx\, x^{1-2\alpha} \tanh(xE/(2T)). \tag{6.35}$$

We can distinguish three different regimes based on the behavior of v_{drift}. For very long-ranged interactions $\alpha < 1$, v_{drift} diverges in the thermodynamic limit, resulting in a diverging current response $\mathcal{J}$ for arbitrarily small fields E. On the other hand, in the regime of standard diffusion, $\alpha > 3/2$, Eq. (6.35) is dominated by small distances $x = O(1)$, where we can use the expansion $\tanh(xE/(2T)) \approx xE/(2T)$, yielding

$$v_{drift}^{diff} \approx \lambda E/T \int_1^{\infty} dx\, x^{2-2\alpha} = \frac{\lambda}{3-2\alpha} E/T = D_\alpha E/T.$$

We thus recover the standard linear-response

$$\mathcal{J} = v_{drift}\, f(k=0,0) \approx D_\alpha E/(4T),$$

yielding a DC conductivity $\sigma_{DC} \approx D_\alpha/(4T)$ in agreement with (6.31) obtained from linear-response theory in the previous section.

The two regions discussed above are separated by a regime displaying an anomalous non-linear-response, $1 < \alpha < 3/2$. Here we can remove both the lower and upper cutoffs from Eq. (6.35), resulting in

$$\begin{aligned} v_{drift} &\approx 2\lambda \int_0^\infty dx\, x^{1-2\alpha} \tanh(xE/(2T)) \\ &= 2\lambda\, (E/(2T))^{2\alpha-2} \int_0^\infty dy\, y^{1-2\alpha} \tanh(y), \end{aligned}$$

indeed giving rise to anomalous scaling $\mathcal{J} \sim (E/T)^{2\alpha-2}$ for $1 < \alpha < \frac{3}{2}$.

6.4.3 *Classical master equation in dimension $d > 1$*

In the following, we extend the results of the classical Master equation to spins at locations $\mathbf{r}_i$ in d dimensions. The Master equation (6.12) then reads

$$\partial_t f_{\mathbf{r}_j} = \sum_{i \neq j} W_{|\mathbf{r}_i - \mathbf{r}_j|}(f_{\mathbf{r}_i} - f_{\mathbf{r}_j}), \qquad \text{with} \qquad W_{|\mathbf{r}_i-\mathbf{r}_j|} = \frac{\lambda}{|\mathbf{r}_i - \mathbf{r}_j|^{2\alpha}}. \tag{6.36}$$

Fourier transforming again diagonalizes the differential equation, yielding

$$f(|\mathbf{k}|,t) = f(|\mathbf{k}|,0) \exp\{(W(|\mathbf{k}|) - W(|\mathbf{k}| = \mathbf{0})t)\}. \tag{6.37}$$

TWO SPATIAL DIMENSIONS D=2. Denoting $k \equiv |\mathbf{k}|$ in the following, we evaluate the Fourier transform of the transition amplitudes in continuous space with both an IR (system size L) and UV (lattice spacing $a = 1$) cutoff, yielding

$$W(k) - W(k=0) = \lambda \int_1^L \mathrm{d}r\, r \int_0^{2\pi} \mathrm{d}\theta \left(e^{-ikr\cos(\theta)} - 1\right) \frac{1}{r^{2\alpha}} \tag{6.38}$$

$$= \lambda\, 2\pi \int_1^L \mathrm{d}r\, r^{1-2\alpha} \left(\mathcal{J}_0(kr) - 1\right), \tag{6.39}$$

with $\mathcal{J}_0(kr)$ denoting the zeroth order Bessel function of the first kind. For $\alpha < 1$ we get a divergence in the thermodynamic limit $L \to \infty$, hence we expect the dynamics to be described by the infinite ranged mean field model in that regime. Concentrating on $\alpha \geq 1$, we can remove the IR cutoff and arrive at

$$W(k) - W(k=0) \approx 2\pi\lambda \int_1^\infty \mathrm{d}r\, r^{1-2\alpha} \left[\mathcal{J}_0(kr) - 1\right] \tag{6.40}$$

$$\approx 2\pi\lambda \left[k^{2\alpha-2} \int_0^\infty \mathrm{d}x\, x^{1-2\alpha} \left(\mathcal{J}_0(x) - 1\right) + \frac{k^2}{4} \int_0^1 r^{3-2\alpha} \mathrm{d}r\right], \tag{6.41}$$

$$W(k) - W(k=0) \approx \lambda \left[-c_\alpha k^{2\alpha-2} + \frac{k^2\,\pi}{2(4-2\alpha)} \right], \tag{6.42}$$

with

$$c_\alpha = 2\pi \int_0^\infty \mathrm{d}x\, x^{1-2\alpha}\,(1-\mathcal{J}_0(x)) = -\frac{2^{2-2\alpha}\,\pi\Gamma(1-\alpha)}{\Gamma(\alpha)} \quad \text{for} \quad 1<\alpha<2. \tag{6.43}$$

We see that a superdiffusive solution is obtained for $1 < \alpha \leq 2$, where the first term $\sim k^{2\alpha-2}$ dominates. Neglecting all other terms, we hence arrive at the scaling ansatz for a localized excitation $f(k, t=0) = \frac{1}{4}$

$$f_{\mathbf{r}}(t) = (\lambda c_\alpha\, t)^{-\frac{2}{2\alpha-2}} F_\alpha^{2D}\left(\frac{|\mathrm{r}|}{(\lambda c_\alpha\, t)^{\frac{1}{2\alpha-2}}} \right), \tag{6.44}$$

with

$$F_\alpha^{2D}(y) = \frac{1}{8\pi} \int_0^\infty \mathrm{d}k\, k\, \mathcal{J}_0(ky)\, e^{-k^{2\alpha-2}}. \tag{6.45}$$

THREE SPATIAL DIMENSIONS D=3. We similarly get

$$W(k) - W(k=0) = 2\pi\lambda \int_1^L \mathrm{d}r\, r^2 \int_0^\pi \mathrm{d}\theta\, \sin\theta \left(e^{-ikr\cos(\theta)} - 1 \right) \frac{1}{r^{2\alpha}} \tag{6.46}$$

$$= 4\pi\lambda \int_1^L \mathrm{d}r\, r^{2-2\alpha} \left(\frac{\sin(kr)}{kr} - 1 \right), \tag{6.47}$$

where we get an IR divergence and hence expect mean-field behavior for $\alpha < 3/2$. Considering only $\alpha \geq 3/2$, we set $L \to \infty$ and get for small k

$$W(k) - W(k=0) \approx \lambda \left[-c_\alpha k^{2\alpha-3} + \frac{k^2\, 2\pi}{3(5-2\alpha)} \right], \tag{6.48}$$

with

$$c_\alpha = -4\pi \sin(\pi\alpha)\Gamma(2-2\alpha) \quad \text{for} \quad 1.5 < \alpha < 2.5. \tag{6.49}$$

Now superdiffusive behavior is seen for $1.5 < \alpha < 2.5$ with a scaling ansatz in real space for a localized excitation

$$f_{\mathbf{r}}(t) = (\lambda c_\alpha\, t)^{-\frac{3}{2\alpha-3}} F_\alpha^{3D}\left(\frac{|\mathrm{r}|}{(\lambda c_\alpha\, t)^{\frac{1}{2\alpha-3}}} \right), \tag{6.50}$$

with

$$F_\alpha^{3D}(y) = \frac{1}{8\pi^2 y} \int_0^\infty \mathrm{d}k\, k \sin(ky)\, e^{-k^{2\alpha-3}}. \tag{6.51}$$

6.4.4 *Summary and discussion of results for the classical Master equation.*

Starting from an initial state with a single excitation in the center of the chain, we found the solution of the Master equation in Eq. (6.12) by

$$f_j(t) \approx \begin{cases} (D_\alpha t)^{-1/2} G\left(\frac{|j|}{(D_\alpha t)^{1/2}}\right) & \text{for } \alpha > 1.5 \\ (D_\alpha t)^{-\beta_\alpha} F_\alpha\left(\frac{|j|}{(D_\alpha t)^{\beta_\alpha}}\right) & \text{for } 0.5 < \alpha \leq 1.5 \end{cases} \tag{6.52}$$

in the limit of long times and large system sizes. Here, $G(y) = \exp(-y^2/4)/8\sqrt{\pi}$ denotes the Gaussian distribution, indicating normal diffusion for $\alpha > 1.5$ with diffusion constant $D_\alpha \propto \lambda$. For $0.5 < \alpha \leq 1.5$, $G(y)$ is replaced by the family of stable, symmetric distributions $F_\alpha(y)$, given by

$$F_\alpha(y) = \frac{1}{4} \int \frac{\mathrm{d}k}{2\pi} \exp(-|k|^{1/\beta_\alpha}) \exp(iyk), \tag{6.53}$$

with the constant prefactor $D_\alpha = \lambda c_\alpha$ constituting a generalized diffusion coefficient [3]. We found $c_\alpha = -2\Gamma(1-2\alpha)\sin(\pi\alpha)$ from the classical Master equation, with Γ denoting the gamma function. Furthermore, the exponent of the hydrodynamic tail β_α is given by

$$\beta_\alpha = \frac{1}{2\alpha - 1}. \tag{6.54}$$

The Fourier transform in Eq. (6.21) only leads to elementary functions for $\alpha = 3/2$ and $\alpha = 1$, resulting in a Gaussian and a Lorentzian distribution, respectively [4]. The scaling functions $F_\alpha(y)$ are the fixed point distributions in the generalized central limit theorem [426] of i.i.d. random variables with heavy tailed distributions. Importantly, $F_\alpha(y)$ has diverging variance for $\alpha < 1.5$, undefined mean for $\alpha \leq 1$, and displays heavy tails $\sim |y|^{-2\alpha}$. The classical Master equation hence predicts a cross-over from diffusive ($\alpha \geq 1.5$) over ballistic ($\alpha = 1$) to super-ballistic ($0.5 < \alpha < 1$) transport.

When adding a linear magnetic field gradient $\sim E \sum_i i\hat{S}_i^z$ to the Hamiltonian, the resulting classical Master equation predicts the spin current to depend non-linearly on the arbitrarily weak E for $\alpha < 1.5$, indicating a breakdown of linear-response theory [424], as we show in section 6.4.2. Calculating the current response function from Eq. (6.52), we found a diverging response for vanishing momentum $q \to 0$ for every value of the frequency ω [423].

3 The prefactor $1/4$ accounts for the normalization of the correlation function, $C(j, t=0) = \delta_{0,j}/4$. Furthermore, reinstating a lattice spacing a, the units of D_α depend on α, in particular it is a velocity for $\alpha = 1$.

4 Other closed form solutions exist [425], for example for $\alpha = 1.25$ in terms of hypergeometric functions.

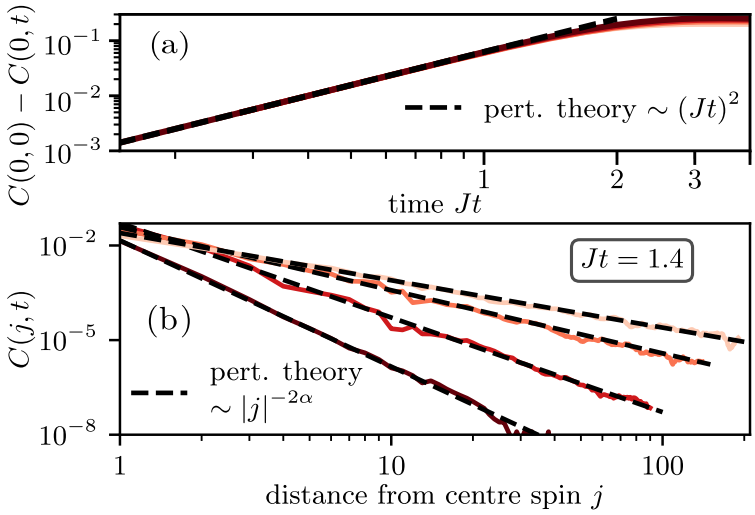

Figure 6.4: **Short time dynamics.** We compare spin-2PI results with second order perturbation theory, Eq. (6.61). (a) The collapse of the autocorrelator for different exponents α shows that the short time evolution is independent of α and L when the Hamiltonian is rescaled with $\mathcal{N}_{\alpha,L}$. (b) The un-equal-time correlation function for $\alpha \in \{0.75, 1, 1.5, 2\}$ (from top to bottom), shows algebraic tails that are entirely captured by second order perturbation theory. We used a moving average over $5 - 10$ lattice sites to smoothen the results.

6.5 PERTURBATIVE SHORT TIME DYNAMICS

Before the emergent classical transport process kicks in, the many-body system first has to dephase coherence contained in the initial state. As we discussed in chapter 3, this proceeds very quickly due to the presence of many-body chaos. Here, we only discuss the very initial stages of the dephasing process within the perturbative short time regime, which holds as long as $Jt \ll 1$. We will see that even in this seemingly trivial regime, the long-range nature of the interactions has important consequences for the spin correlations.

Here we calculate the short time dynamics of

$$\mathrm{Tr}\{\hat{S}_i^z(t) S_m^z(0)\} \tag{6.55}$$

while not rescaling the Hamiltonian, i.e. $\mathcal{N} = 1$ in the notation in Eq. (6.1).

We start by calculating the dynamics of $\hat{S}_i^z(t)$ in the Heisenberg picture,

$$\begin{aligned}\hat{S}_i^z(t) &= e^{i\hat{H}t} \hat{S}_i^z e^{-i\hat{H}t} \\ &\approx \hat{S}_i^z + iJt \left[\frac{\hat{H}}{J}, \hat{S}_i^z\right] + \frac{(iJt)^2}{2!} \left[\frac{\hat{H}}{J}, \left[\frac{\hat{H}}{J}, \hat{S}_i^z\right]\right] + \mathcal{O}((Jt)^3).\end{aligned}$$

The (nested) commutators turn out to be

$$\left[\hat{H}, \hat{S}_i^z\right] = i \sum_{k \neq i} J_{ik} \left(\hat{S}_i^x \hat{S}_k^y - \hat{S}_k^x \hat{S}_i^y\right), \tag{6.56}$$

$$\begin{aligned}\left[\hat{H}, \left[\hat{H}, \hat{S}_i^z\right]\right] = &-\frac{1}{2} \sum_{j \neq k, k \neq i} J_{ik} J_{kj} \left(\hat{S}_j^x \hat{S}_i^x \hat{S}_k^z + \hat{S}_i^x \hat{S}_j^x \hat{S}_k^z + \hat{S}_j^y \hat{S}_i^y \hat{S}_k^z + \hat{S}_i^y \hat{S}_j^y \hat{S}_k^z\right) \\ &+ \frac{1}{2} \sum_{k \neq i, j \neq i} J_{ik} J_{ij} \left(\hat{S}_j^x \hat{S}_k^x \hat{S}_i^z + \hat{S}_k^x \hat{S}_j^x \hat{S}_i^z + \hat{S}_j^y \hat{S}_k^y \hat{S}_i^z + \hat{S}_k^y \hat{S}_j^y \hat{S}_i^z\right).\end{aligned} \tag{6.57}$$

When evaluating the trace as a sum over product states in the z-basis, one directly sees that only terms survive with $\hat{S}_j^{x/y} \hat{S}_i^{x/y} \sim \delta_{ij}$. Hence the first order contribution vanishes and we get

$$\mathrm{Tr}\{\hat{S}_i^z(t) S_m^z(0)\} = \frac{t^2}{4} \sum_{k \neq i} J_{ik}^2 \left(\mathrm{Tr}\{\hat{S}_k^z \hat{S}_m^z\} - \mathrm{Tr}\{\hat{S}_i^z \hat{S}_m^z\}\right) + \mathrm{Tr}\{\hat{S}_i^z \hat{S}_m^z\}. \tag{6.58}$$

Furthermore, $\mathrm{Tr}\{\hat{S}_k^z \hat{S}_m^z\} = \frac{1}{4}\delta_{km}$ and hence

$$\mathrm{Tr}\{\hat{S}_i^z(t) \hat{S}_m^z(0)\} = \begin{cases} \frac{1}{4}(1 - \frac{t^2}{4} \sum_{i \neq k} J_{ik}^2) & \text{for } i = m \\ \frac{t^2}{16} J_{im}^2 & \text{for } i \neq m \end{cases}. \tag{6.59}$$

PERTURBATIVE TIME SCALE. The above expression for the autocorrelator $i = m$ provokes the definition of a perturbative inverse time scale

$$\mathcal{N}_{L,\alpha} = \sqrt{\sum_j \left|\frac{L}{2} - j\right|^{-2\alpha}}, \tag{6.60}$$

which we used to rescale the Hamiltonian in Eq. (6.1) to render the short time evolution of the autocorrelator of the spin in the middle of the chain independent of α and L. Notably, in the thermodynamic limit $L \to \infty$, this time scale approaches a constant for $\alpha > 0.5$ while it goes to zero as $L^{\alpha - 0.5}$ for $\alpha < 0.5$. For $\alpha = 0.5$, we find asymptotically $\mathcal{N}_{L \to \infty, \alpha = 0.5} \sim \sqrt{\log(L^2)}$.

Furthermore, the more general perturbative time scale $\sqrt{\sum_{i \neq k} J_{ik}}$ is dependent on the reference spin i, showing that the spins away from the center evolve slower than the middle spin. As $L \to \infty$, this effect goes away for $\alpha > 0.5$ (however very slowly as a function of L for small α), but remains for $\alpha < 0.5$.

Inserting this perturbative time scale, we find

$$\mathrm{Tr}\left[\hat{S}_j^z(t) \hat{S}_0^z(0)\right] \approx \begin{cases} \frac{1}{4}(1 - \frac{J^2 t^2}{4}) & \text{for } j = 0 \\ \left(\frac{Jt}{4\mathcal{N}_{L,\alpha}}\right)^2 \frac{1}{|j|^{2\alpha}} & \text{for } j \neq 0 \end{cases}. \tag{6.61}$$

Physically, in this regime each spin is precessing in the effective magnetic field created by all other spins. The autocorrelation function is independent of α and L due to our choice of the normalization factor $\mathcal{N}_{L,\alpha}$, ensuring that the typical

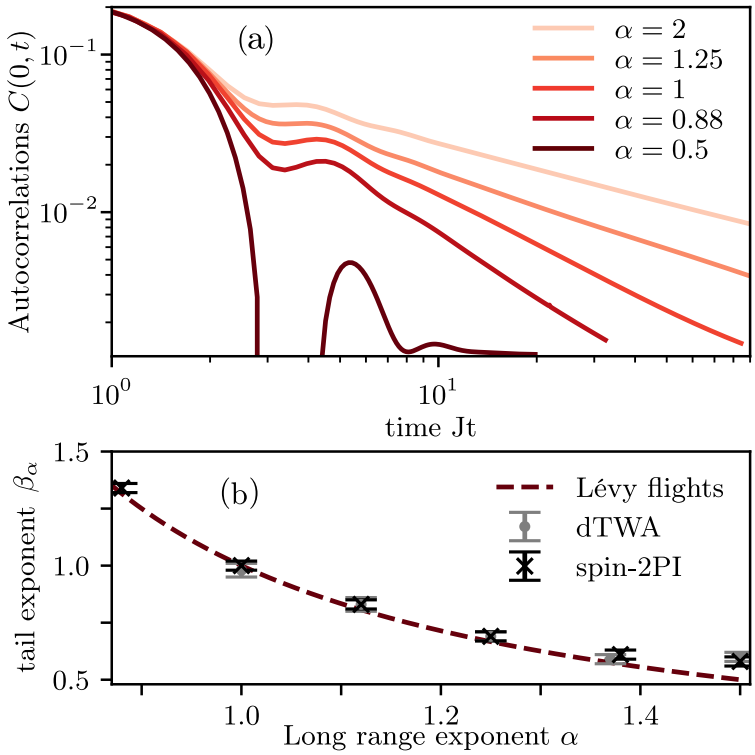

Figure 6.5: **Hydrodynamic tails in the spin autocorrelator.** (a) For long-range coupling exponents $\alpha > 0.5$, autocorrelations decay algebraically at late times with an exponent that depends on α. By contrast for $\alpha \leq 0.5$ hydrodynamic tails are absent. (b) The exponents β_α of the hydrodynamic tail obtained from two different approaches (symbols) agree with the predictions from classical Lévy flights in the thermodynamic limit (dashed curve). Deviations at large α are due to finite time corrections to scaling which can also be understood from Lévy flights.

magnetic field at the center of the chain remains of the order of J. The spatial correlation function at a fixed time inherits the algebraic behavior of the interaction strength, falling off as $|j|^{-2\alpha}$ between spins of distance j, which is reproduced by both dTWA (not shown) and spin-2PI, see Fig. 6.4.

6.6 EMERGENT HYDRODYNAMIC TRANSPORT FROM QUANTUM DYNAMICS

In this section we will show that the superdiffusive transport expected from the classical master equation does indeed occur in the long-range XY model. We will do so by employing both spin 2PI simulations and the discrete truncated Wigner approximation and comparing our theoretical results to experimental ones obtained in the trapped ion quantum simulator.

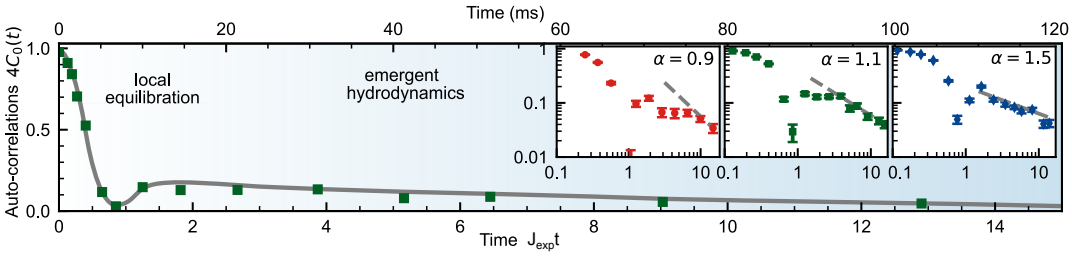

Figure 6.6: **Measured auto-correlations** (green squares) for 51 ions and $\alpha = 1.1$ (gray line: guide to the eye). Error bars, denoting the standard error of the mean are smaller than the symbols. At short times (red shading), the spin excitation quickly relaxes to a local equilibrium state. At late times (blue shading) global conservation laws constrain the relaxation of spin excitations, leading to a slow power-law decay of the auto-correlations. Insets: Auto-correlations on a double logarithmic scale for different values of α highlighting the tunable transport. Gray dashed lines are power laws with the predicted exponent from Lévy flights. Here, $J_{\text{exp}} = 248$ rad/s, 129 rad/s, and 116 rad/s for $\alpha = 0.9$ (51 ions), $\alpha = 1.1$ (51 ions), and $\alpha = 1.5$ (25 ions).

6.6.1 *Hydrodynamic tails*

The scaling form from classical Lévy flights in Eq. (6.52) implies the presence of a hydrodynamic tail in the autocorrelation function $C(j = 0, t)$ with exponent $\beta_\alpha = 1/(2\alpha - 1)$, which replaces the universal exponent $1/2$ for diffusion in 1D, see Fig. 6.5 for our field theory results. For $\alpha \to 1.5$ we find slight deviations from β_α, these can however be explained by a subtle finite-time effect also present in classical Lévy flights, see Sct. 6.7. For $\alpha < 0.5$ we find no hydrodynamic tail for the numerically accessible system sizes $L < 601$. This matches the expectation that the system relaxes instantaneously in the thermodynamic limit [412], which is also indicated by the fact that the perturbative short time scale diverges, $\mathcal{N}_{L\to\infty,\alpha} = \infty$, for $\alpha \leq 0.5$. On even longer time scales, the discretized Fourier transform underlying the derivation of Eq. (6.52) is dominated by the smallest wavenumber in finite chains, and the hydrodynamic tail is replaced by an exponential convergence towards the equilibrium value $0.25/L$ with a rate $\sim (1/L)^{2\alpha-1}$. The trapped ion experimental data, Fig. 6.6, is also consistent with the hydrodynamic theory of Eq. (6.52). We show the coherence of the simulator by comparing its results with exact simulations in Fig. 6.7.

6.6.2 *Spreading of correlations*

A more stringent test of the emergent hydrodynamics is obtained from the full spatial correlation profile. In Fig. 6.8 we show the spreading of $t^{\beta_\alpha} C(j, t)$ for two

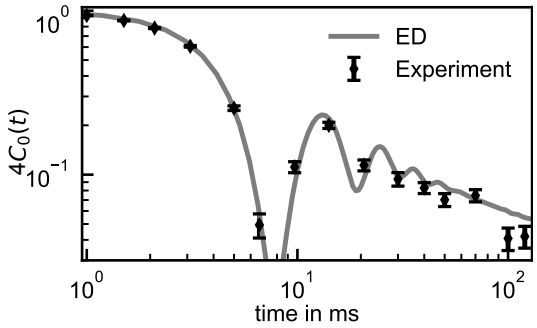

Figure 6.7: **Auto-correlation function from experiment and exact diagonalization (ED).** In ED we used the experimental J_{ij} matrix for $\alpha = 1.5$ and $L = 25$ as well as the 240 initial states used in the experiment.

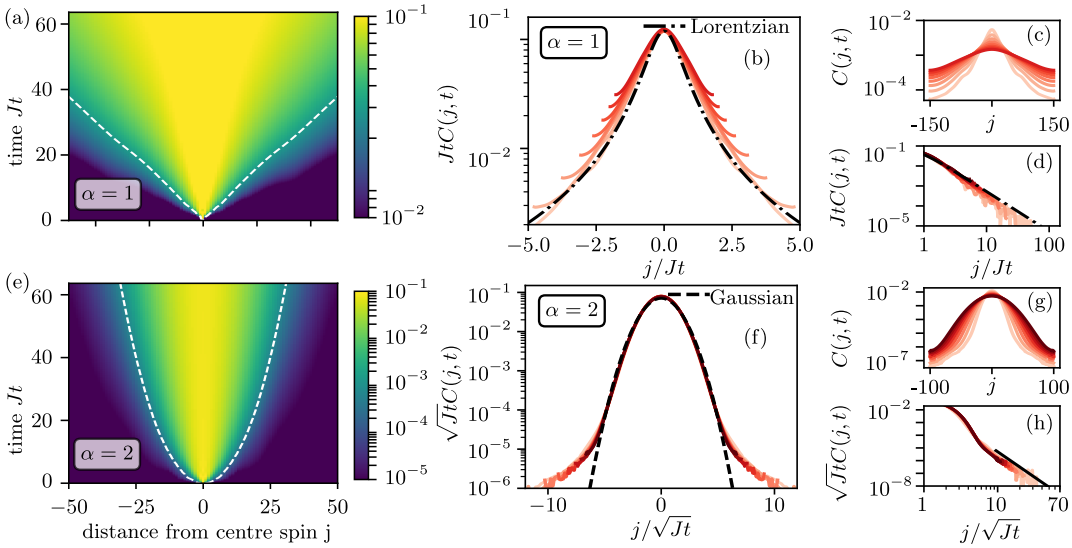

Figure 6.8: **Emergent self-similar time evolution.** The correlation function $C(j,t)$ obtained from spin-2PI for chains of lengths $L = 201$ ($\alpha = 2$, subfigures (e-h)), $L = 301$ ($\alpha = 1$, subfigures (a-d)). (a,e) $C(j,t)$ multiplied by $t^{1/(2\alpha-1)}$ to account for the overall decay expected from Lévy flights shows a diffusive cone for $\alpha = 2$, whereas for $\alpha = 1$ a ballistic light-cone emerges. The contour lines for $\alpha = 1, 2$ correspond to values $t^{1/(2\alpha-1)}C(j,t) = 0.03, 10^{-4}$, respectively. (b,f) Rescaling of linearly spaced time slices for $23 \leq Jt \leq 84$ ($\alpha = 1$) and $42 \leq Jt \leq 226$ ($\alpha = 2$) (lines become darker as time increases) for the same data as in (a,e) agrees well with the scaling function expected from classical Lévy flights, Eq. (6.52). The only fitting parameter is the generalized diffusion coefficient. (d,h) Rescaled time slices ($2 \leq Jt \leq 28$) on a double-logarithmic scale reveal for $\alpha = 1$ the heavy tail $\sim y^{-2}$ expected from Lévy flights (Eq. (6.52)), where the dashed-dotted line is the same fit as in (b). The tail $\sim y^{-4}$ (thick black line) for $\alpha = 2$ ($8 \leq Jt \leq 85$) is a finite time effect also present in classical Lévy flights. (c,g) Unscaled data.

values of α obtained from spin 2PI. While for $\alpha = 2$ a diffusive cone is visible, the spreading for $\alpha = 1$ is ballistic as expected from the Master equation. In

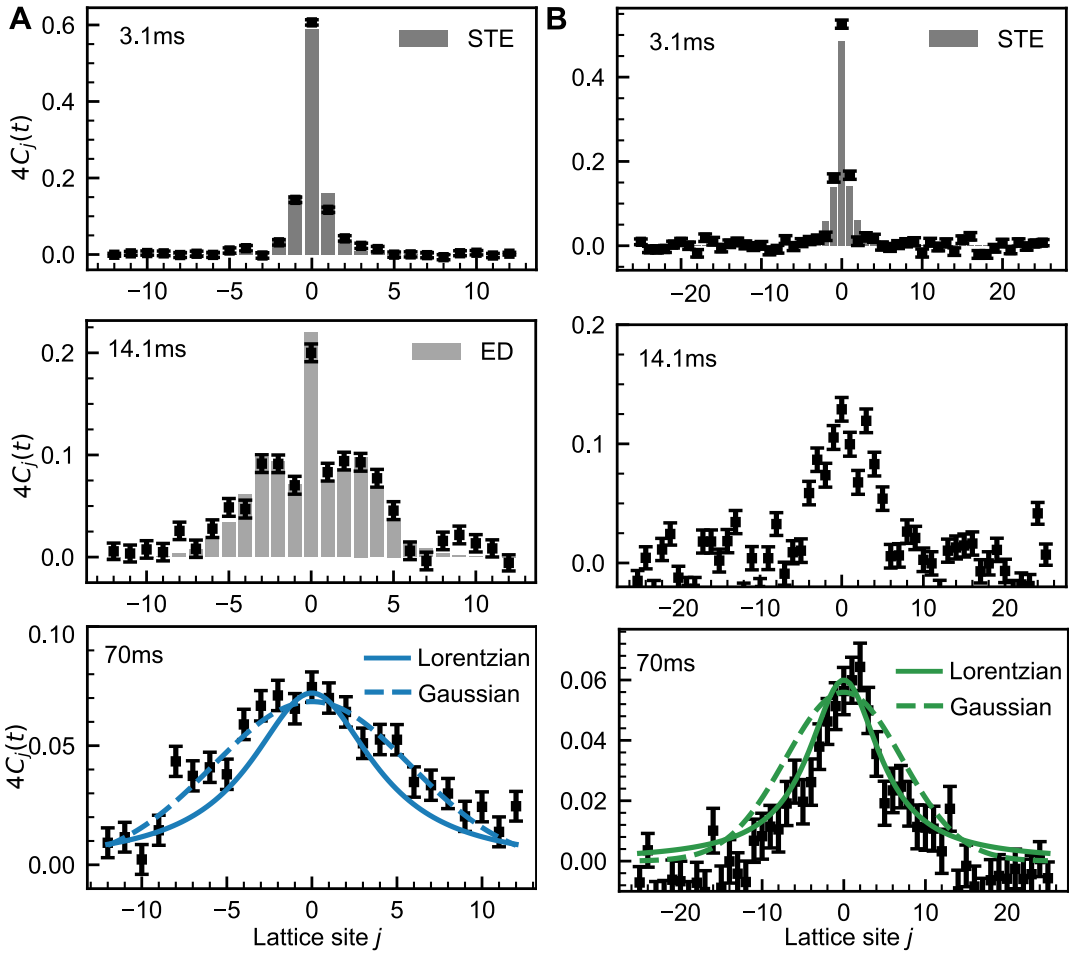

Figure 6.9: **Spatial correlation profiles measured in the trapped ion simulator.** Spatially resolved correlations for column A) $\alpha = 1.5$ and column B) $\alpha = 1.1$. The spatial correlations are measured at short times (left), intermediate times (middle), and in the hydrodynamic late-time regime (right). STE: analytic short-time expansion, ED: exact diagonalization accessible only for the shorter chain of 25 ions. In the hydrodynamic regime (right) the measured profiles are compared to predictions from Lévy flights. The spatial profile in A) is compatible with a Gaussian (dashed) and in B) with a Lorentzian (solid), as supported by the reduced χ^2 values of the fit: A) $\chi^2_{\mathrm{L}} = 3.9$, $\chi^2_{\mathrm{G}} = 1.3$; B) $\chi^2_{\mathrm{L}} = 1.1$, $\chi^2_{\mathrm{G}} = 3.6$ (obtained by fitting over the central 27 sites).

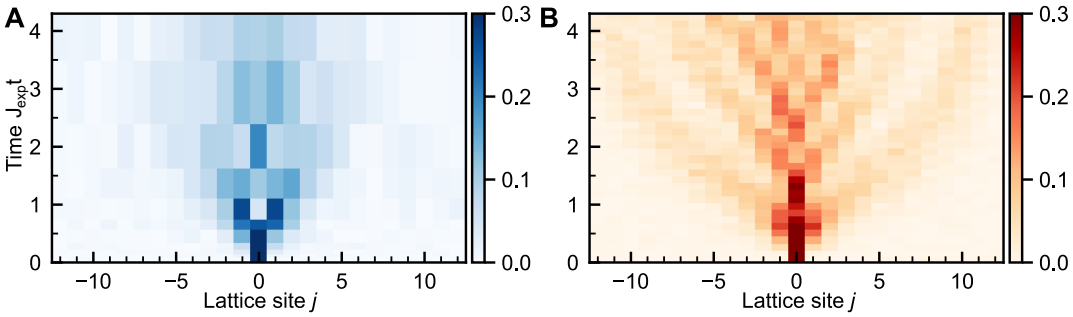

Figure 6.10: **Contrasting the infinite temperature background with the spin polarized background in the trapped ion simulator.** A) The deterministically prepared excitation of the central ion strongly interacts with all the other excitations of the infinite temperature background and slowly spreads through the system following the laws of classical hydrodynamics. B) By contrast, a single excitation on top of the fully down-polarized state $|\downarrow\cdots\downarrow\uparrow\downarrow\cdots\downarrow\rangle$ has no other excitations to scatter off and therefore spreads freely, exhibiting quantum interference patterns. Data is measured for 25 ions with power-law exponent $\alpha = 1.5$.

the experiment, two values of the long-range exponent, $\alpha = 1.5$ with 25 ions and, $\alpha = 1.1$ with 51 ions, were realized to test the diffusive and superdiffusive regimes, respectively. In Fig 6.9 we show the corresponding results. At early times (3.1ms) the quantum dynamics is well-described by an analytic short-time expansion of the equations of motion, see section 6.5. At intermediate times (14.1ms), the excitation starts spreading through the system, but some quantum coherence remains, indicated by the spatial oscillations. For 25 ions, the measured dynamics compares well with results obtained from exact diagonalization, demonstrating the coherence of the simulator.

At the latest times shown, interactions have entangled local degrees of freedom with the rest of the system. Quantum interference patterns are averaged out and the hydrodynamic regime is entered. This becomes even more apparent in the space-time correlations; Fig. 6.10A. By contrast, a single excitation on top of a spin-polarized state cannot scatter, and the associated correlations exhibit coherent space-time oscillation patterns instead [187]; Fig. 6.10B.

The measured hydrodynamic profiles are compatible with a Lorentzian for $\alpha = 1.1$ ($f_{\alpha=1.1}$ is still very close to a Lorentzian) and with a Gaussian for $\alpha = 1.5$, see χ^2 analysis in Fig. 6.9 (right panels), in agreement with Eq. (6.52).

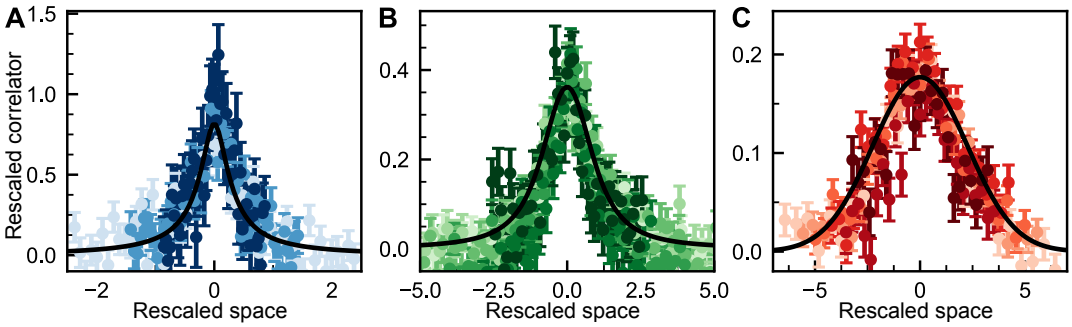

Figure 6.11: **Self-similar scaling and exctraction of transport coefficients.** At late times the correlations exhibit a self-similar scaling, relating space and time with a microscopic transport coefficient D_α. Rescaled correlations $\tau_x C_j(t)$ as a function of rescaled space j/τ_x, where $\tau_x = (J_{\text{exp}}t)^{1/(2\alpha-1)}$. A) $\alpha = 0.9$, 51 ions, B) $\alpha = 1.1$, 51 ions, and C) $\alpha = 1.5$, 25 ions. Correlations are shown for times $J_{\text{exp}}t > 5$ (darker colors correspond to later times).

6.6.3 *Self-similarity*

One of the most striking predictions of hydrodynamics is the self-similar scaling of the correlations, relating time and space by a universal dynamical scaling exponent, given by $1/(2\alpha - 1)$, and a non-universal constant, the transport coefficient D_α. In analogy with the universal scaling of correlation functions near a second-order equilibrium phase transition, the hydrodynamic scaling indicates the proximity of the dynamics to a thermal fixed point. The scaling collapse of the 2PI data in Fig. 6.8 b), f) shows good agreement with classical Lévy flights, Eq. (6.52), at late times. This is also true for the experimental data, Fig. 6.11.

Interestingly, we find heavy tails even for $\alpha \geq 1.5$ in spin 2PI. We explain these by sub-leading corrections to the scaling ansatz Eq. (6.52) present in the Master equation, see section 6.7. They survive up to algebraically long times for $\alpha > 1.5$, turning to a logarithmic correction at $\alpha = 1.5$ [427].

For $\alpha \gtrsim 2$ we furthermore find signs of peaks propagating ballistically for intermediate times in the dTWA scaling functions, which survive longer as α increases. These peaks are remnants of the integrable point at $\alpha = \infty$, see section 6.8. Such behaviour is not present in the spin-2PI data as this method is not able to capture integrable behaviour [215].

6.6.4 *Generalized diffusion constant*

While the scaling form of the data is universal and can be predicted from purely hydrodynamic reasoning, the transport coefficient D_α depends on the full quantum many-body spectrum and is therefore challenging to predict from analytical or

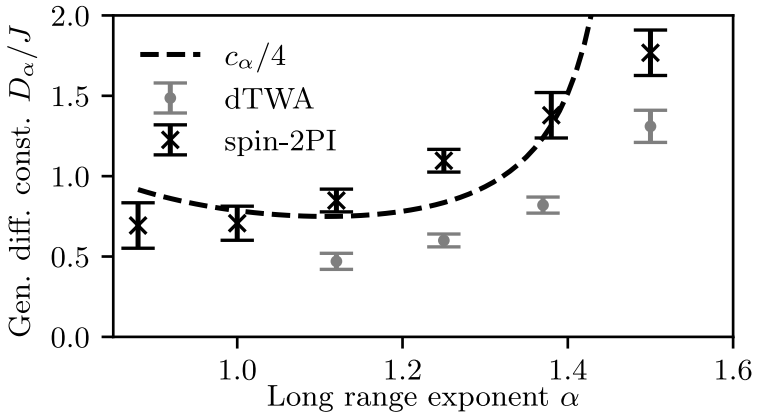

Figure 6.12: **Generalized diffusion constant.** The α dependence of the diffusion constant obtained from fits with the scaling function of Lévy flights, Eq. (6.52). The qualitative behavior follows the Lévy flight prediction $D_\alpha \sim c_\alpha$ for $\alpha < 1.5$.

numerical methods. We obtain D_α from the fits to the scaling function. In Fig. 6.12 we show the thus obtained approximate theoretical data. The leading α dependence of D_α can be explained by $D_\alpha \sim c_\alpha$ for $\alpha < 1.5$ [5], hence the prefactor λ^{-1}, constituting the *quantum* many-body time scale, depends only weakly on α. As expected from their differing approximate treatment of the quantum fluctuations in the system, we find slight differences between the values of λ determined by spin-2PI and dTWA, $\lambda_{\mathrm{2PI}} \approx 0.25$ and $\lambda_{\mathrm{dTWA}} \approx 0.15$. For $\alpha > 1.5$ we find considerable differences between the dTWA and spin-2PI results, because the emergent ballistic peaks, stemming from the nearby integrable point, accelerate the spreading in the dTWA simulations. In contrast to the regime $\alpha < 1.5$, the dTWA results for the quantum many-body time scale λ show a strong α dependence, with D_α increasing as a function of α due to the approach to the integrable point at $\alpha \to \infty$.

From similar fits to the scaling functions in the experiment, Fig. 6.11, $D_\alpha / J_{\mathrm{exp}} = 0.5^{+0.2}_{-0.1}, 0.8^{+0.3}_{-0.2}, 2.6^{+0.9}_{-0.7}$ for $\alpha = 0.9, 1.1, 1.5$ were found. Note that a direct comparison to the theoretical values is not possible because the D_α are very sensitive to differences in the microscopic model, which in the trapped ion experiment result from deviations from the pure algebraic form of the interactions.

6.7 CORRECTIONS TO HYDRODYNAMIC SCALING

For finite times, the two terms in Eq. (6.17) compete, leading to corrections to the leading-order scaling ansatz. As we show below, these corrections survive until algebraically long times for $\alpha > 1.5$, and they add a logarithmic correction to the

5 The spurious divergence of c_α in the limit $\alpha = 1.5$ is cured by logarithmic corrections to scaling, see section 6.7. Furthermore, without the normalisation $N_{L,\alpha}$, $D(\alpha) \sim N_{L,\alpha} \to \infty$ for $\alpha \to 0.5$.

scaling ansatz at the threshold value $\alpha = 1.5$, explaining all major deviations from leading-order scaling we observe in our numerical data.

DIFFUSIVE REGIME, $\alpha > 1.5$ Taking into account both terms in Eq. (6.17), then rescaling as $k \to k\sqrt{D_\alpha t}$ and $j \to y = j/\sqrt{D_\alpha t}$ where $D_\alpha = \lambda/(2\alpha - 3)$, and finally expanding the remaining time dependent term for $t \to \infty$, we arrive at

$$\begin{aligned}\sqrt{D_\alpha t}\, f_j(t) &\approx \frac{1}{4}\int \frac{dk}{2\pi}\, \exp\left(iky - k^2\right)\left(1 - (D_\alpha t)^{-\alpha+3/2}\, c_\alpha(2\alpha-3)|k|^{2\alpha-1}\right) \\ &= G(y) - (D_\alpha t)^{-\alpha+3/2}\, \frac{c_\alpha(2\alpha-3)\Gamma(\alpha)}{16\,\pi}\, {}_1F_1\left[\alpha, \frac{1}{2}, -\frac{y^2}{4}\right], \end{aligned} \tag{6.62}$$

with ${}_1F_1\left[\cdot,\cdot,\cdot\right]$ denoting the Kummer confluent hypergeometric function. Most importantly, the latter exhibits heavy tails $\sim y^{-2\alpha}$ for $y \to \infty$, reproducing the finite time data for $\alpha = 2$ in Fig. 6.13.

We show this behaviour more explicitly in Fig. 6.13, where we compare our numerical results to a scaling function involving a single fit parameter D_2,

$$\sqrt{D_2 t}\, f_j(t) \approx G(y) - \frac{1}{96\sqrt{D_2 t}}\, {}_1F_1\left[\alpha, \frac{1}{2}, -\frac{y^2}{4}\right], \tag{6.63}$$

following from Eq. (6.62) using $\lim_{\alpha\to 2} \sin(\alpha\pi)\Gamma(1-2\alpha) = \pi/12$. Furthermore, according to Eq. (6.62) the approach to Gaussian scaling is algebraically slow with exponent $1.5 - \alpha \to 0$ for $\alpha \to 1.5$. As we show in the following, at this special value $\alpha = 1.5$ this algebraic convergence to scaling is replaced by a persistent logarithmic correction to the scaling ansatz.

CROSSOVER POINT $\alpha = 1.5$ In the limit $\alpha \to 1.5$, both prefactors in Eq. (6.17), c_α and $1/(3-2\alpha)$, diverge with their difference remaining finite, $-c_\alpha + 1/(3-2\alpha) \to \gamma - 3/2 \approx -0.92$, with γ denoting the Euler-Mascheroni constant, resulting in a Gaussian leading order term, $\partial_t f(k) \approx -0.92\,\lambda\, k^2$. However, an additional logarithmic correction from $\lim_{\alpha\to 1.5} c_\alpha(|k|^{2\alpha-1} - k^2) = 0.5k^2 \log k^2$ also contributes. Following the derivation in Ref. [427], we rescale k as $k \to k\sqrt{\lambda t\, \Omega(\lambda t)/2}$, with $\Omega(\lambda t)$ a function to be determined, and get

$$\begin{aligned}&\sqrt{\lambda t\, \Omega(\lambda t)/2} f_j(t) \\ &\approx \frac{1}{4}\int \frac{dk}{2\pi} \exp(ik\tilde{y}) \exp\left(\frac{k^2}{\Omega(\lambda t)} \ln\left(2\frac{\exp(2\gamma-3)}{\lambda t\, \Omega(\lambda t)}\right) + \frac{k^2}{\Omega(\lambda t)}\ln(k^2)\right)\end{aligned} \tag{6.64}$$

with scaling variable $\tilde{y} = j/\sqrt{\lambda t\, \Omega(\lambda t)/2}$. The function $\Omega(\lambda t)$ is chosen in such a way that the first term in the exponent is equal to $-k^2$, reproducing the leading order Gaussian behavior [427]. This leads to

$$\Omega(\lambda t) = \left| W_{-1}\left(-\frac{2\exp(2\gamma-3)}{\lambda t}\right)\right|, \tag{6.65}$$

with W_{-1} the secondary branch of the Lambert W-function. As discussed in Ref. [427], this gives $\Omega(\lambda t) \approx \ln(\lambda t) \sim \ln t$, for $t \to \infty$, yielding a logarithmic correction to the scaling ansatz. Finally, we expand the resulting expression for large time $\Omega(\lambda t) \sim \ln(\lambda t) \gg 1$ and arrive at

$$\sqrt{\lambda t\, \Omega(\lambda t)/2} f_j(t) \approx \frac{1}{4} \int \frac{dk}{2\pi} \exp(ik\tilde{y}) \exp(-k^2) \left(1 + \frac{k^2}{\Omega(\lambda t)} \ln(k^2)\right) \tag{6.66}$$

$$= G(\tilde{y}) \Bigg(1 + \frac{1}{4\,\Omega(\lambda t)} \left((-2 + \tilde{y}^2)\left(-2 + \gamma + \ln(4)\right)\right.$$

$$\left. + 2 \exp\left(\tilde{y}^2/4\right) {}_1F_1^{(1,0,0)} \left[\frac{3}{2}, \frac{1}{2}, -\frac{\tilde{y}^2}{4}\right]\right)\Bigg), \tag{6.67}$$

with the superscript $(1,0,0)$ denoting the derivative with respect to the first argument. This expression shows the logarithmically slow convergence towards the Gaussian scaling function for $\alpha = 1.5$, as well as a persistent logarithmic correction to the scaling form, with scaling variable $\tilde{y} = j/\sqrt{\lambda t\, \Omega(\lambda t)}$. Furthermore, for finite t, the above function exhibits a heavy tail $\sqrt{\lambda t\, \Omega(\lambda t)}\, f_{j,\alpha=1.5}(t) \sim y^{-3}$ and matches our 2PI results as shown in Fig. 6.13, using the single fitting parameter λ. As times were note large enough in the simulations to be in the regime where $\Omega(\lambda t) \approx \ln(t)$, we used the full expression in Eq. (6.65) for $\Omega(\lambda t)$ to fit the unrescaled $f_j(t)$ at a fixed time t.

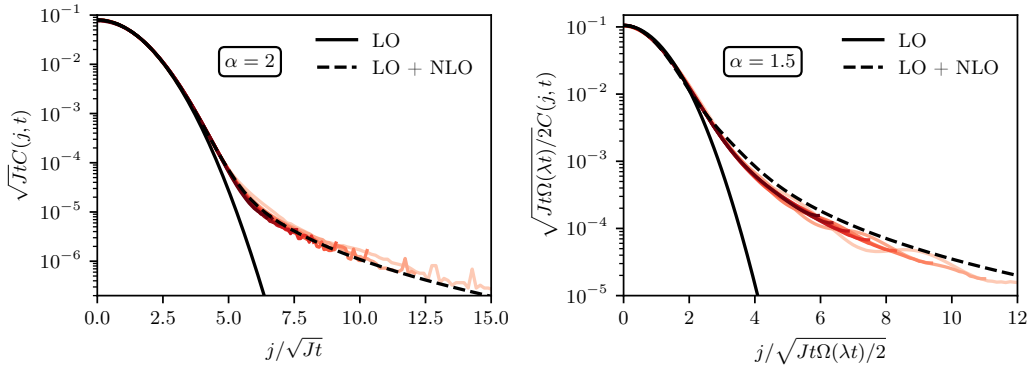

Figure 6.13: **Corrections to scaling.** The heavy tails found in the scaling functions for $\alpha \geq 1.5$ are completely captured by the finite time corrections to scaling in the classical Master equation, with fit functions given in Eqs. (6.63) and (6.67). Note that there is only a single fit parameter (given by the quantum many body time scale $1/\lambda$), with its numerical value being approximately equal in the fit to the (scaling) functions obtained from the leading order (LO) and next-to-leading order (LO+NLO) in a simultaneous $k \to 0$, $t \to \infty$ expansion.

SUPERDIFFUSIVE REGIME, $\alpha < 1.5$ While there are no qualitative corrections to the scaling function in this regime, the term $\sim k^2$ in Eq. (6.17) leads to a correction

to the exponent of the hydrodynamic tail as $\alpha \nearrow 1.5$. When evaluating the Fourier transform numerically with the full expression in Eq. (6.17) for $\alpha \lesssim 1.5$, we still find an approximate hydrodynamic tail with a modified exponent reproducing the finite-time dTWA and spin-2PI results more closely than the 'bare' expression β_α and hence accounting for the slight deviations between the numerical results and β_α. For example, we get $\beta_{\alpha=1.5} \approx 0.57$ from this procedure, in agreement with 2PI ($\beta^{\text{2PI}}_{\alpha=1.5} \approx 0.58 \pm 0.02$) and dTWA ($\beta^{\text{dTWA}}_{\alpha=1.5} \approx 0.59 \pm 0.02$).

6.8 INTEGRABLE LIMIT $\alpha \to \infty$

The long-range XY model converges to an integrable point with increasing exponent $\alpha \to \infty$, where the diffusive hydrodynamic description is expected to break down. Here we discuss the influence of the vicinity of this integrable point on the spin transport.

The integrable point at $\alpha \to \infty$ corresponds to the nearest-neighbor interacting XY model with Hamiltonian

$$\hat{H} = -\frac{J}{2}\frac{1}{\mathcal{N}_{\alpha\to\infty}} \sum_{\langle i,j \rangle} \left(\hat{S}^x_i \hat{S}^x_j + \hat{S}^y_i \hat{S}^y_j \right). \tag{6.68}$$

Using $\mathcal{N}_{\alpha\to\infty} = \sqrt{2}$ and applying a Jordan-Wigner transformation $\hat{S}^x_i = \frac{1}{2}(\hat{c}^\dagger_i + \hat{c}_i)$, $\{\hat{c}_i, \hat{c}^\dagger_i\} = 1$, we arrive after a Fourier transformation $\hat{c}_j = \sum_k e^{ikj}\hat{c}_k/\sqrt{L}$ at

$$\hat{H} = -\frac{J}{\sqrt{2}} \sum_k \cos(k) \hat{c}^\dagger_k \hat{c}_k. \tag{6.69}$$

This means that for $\alpha \to \infty$ we expect ballistic spin transport with a velocity given by the group velocity $v_g = \max_k(\partial_k(J\cos(k)/\sqrt{2})) = J/\sqrt{2}$.Note that while we employed periodic boundary conditions here, the same result could have been obtained with open boundary conditions where the eigenfunctions are not plain waves of the form e^{ikj} but standing waves $\sim \sin(kj)$ with $k = n\pi/(L+1), n \in \{1, .., L\}$ [187].

In Fig. 6.14 we show the spin correlation function $C(j,t)$ obtained from dTWA for $\alpha = 3$. For short times, we find ballistically propagating peaks that get gradually damped as they move towards the edges of the chain. From the time evolution of the position of the peaks we can deduce the propagation velocity and find $v_{\alpha=3} \approx 0.5J$, which is not too far from the nearest-neighbour result of $\sqrt{2}J \approx 0.7J$. As we found this discrepancy not to change as α is increased, we interpret it as a short-coming of this method, which is expected to work less well as the interactions become shorter ranged [420].

At later times, the center of the correlation function again indicates diffusive scaling, showing that interactions between particles are still strong enough to

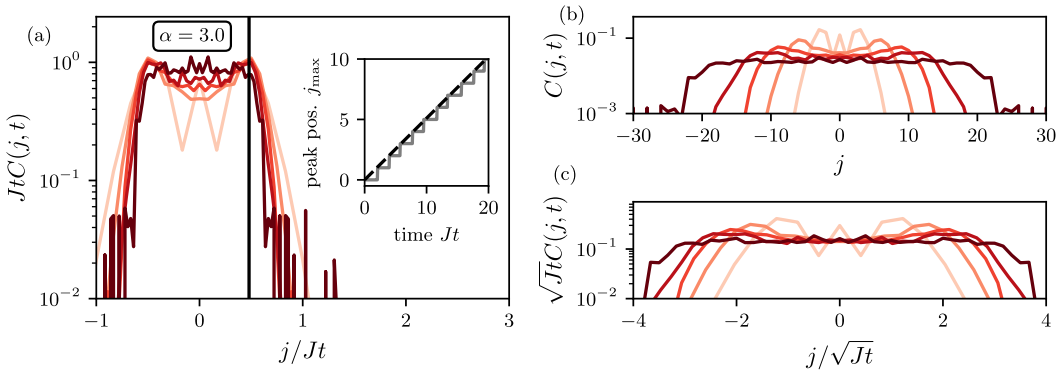

Figure 6.14: **Ballistic spreading at short times for $\alpha = 3$ from dTWA.–** At short times ($Jt \in \{6, 12, 18, 24, 36\}$) the spin correlation function shows ballistic peaks propagating towards the boundaries of the chain. (a) The scaling collapse of $C(j,t)$ when rescaling with Jt as well as a linear growth of the peak position (inset) indicates ballistic transport. The black line indicates the velocity $v \approx 0.5J$ extracted from the growth of the peak position (dashed line in the inset). (b) Unrescaled plot showing the propagation of the peaks. (c) Diffusive rescaling showing the late time crossover to diffusive behavior at the center of the chain.

effectively dephase the system, leading to classical hydrodynamical transport at late times. We expect the time at which diffusive transport is restored to diverge as $\alpha \to \infty$. Whether the crossover to undamped ballistic transport happens at any finite α, i.e. whether the long-range interacting XY model becomes integrable at $\alpha < \infty$ is an open question.

We do not find any such peaks revealing the nearby integrable point in spin-2PI simulations, in line with the previous finding that this method is not able to capture integrable dynamics in the XXZ spin chain [215].

6.9 CONCLUSIONS

In this chapter, we have shown that spin transport at high temperatures in long-range interacting XY-chains is well described by Lévy flights for long-range interaction exponents $0.5 < \alpha \leq 1.5$, effectively realizing a random walk with infinite variance of step sizes. In particular, we have shown that the scaling function of the unequal time spin correlation function covers the stable symmetric distributions, in accordance with the generalized central limit theorem. While the system relaxes instantly for $\alpha < 0.5$, standard diffusion was recovered for $\alpha > 1.5$, with heavy tails from finite time corrections surviving until extremely long times. We demonstrated the non-trivial dependence of the generalized diffusion coefficient D_α on α, and found that it is captured by classical Lévy flights, with the quantum many body time scale being approximately independent of α.

We have tested our theoretical predictions by comparison to results obtained in a trapped ion quantum simulator by the Innsbruck trapped ions group. The measurement of the full spatio-temporal profile of the hydrodynamic scaling functions experimentally established the tunable family of transport ranging from conventional diffusion to anomalous superdiffusion predicted by our analytical and numerical methods.

While we only studied one-dimensional systems, we expect this phenomenon to generalize straightforwardly to $d > 1$ dimensions. Assuming the effective classical Lévy flight picture persists, superdiffusive behaviour would be found for $d/2 < \alpha < 1 + d/2$ with the exponent of the hydrodynamic tails given by $d/(2\alpha - d)$. Furthermore, we indicated that Lévy flights also imply a non-linear-response of the spin current to magnetic field gradients.

An exciting prospect is to investigate transport in models with enhanced symmetries, which can be realized in trapped ions by suitably designed Floquet protocols [428]. Moreover, our tools for measuring high-temperature correlations can be readily applied to other quantum devices with local control, including quantum gas microscopes, Rydberg atom arrays, and superconducting qubits. New classes of hydrodynamics can be realized and probed in that way.

6.10 OUTLOOK: KINETIC EQUATIONS FROM SPIN 2PI

Here we seek to derive kinetic equations for the spin one-point function from the Schwinger boson Spin 2PI approach developed in Ref. [215]. The derivation is in analogy to the usual derivation of self-consistent kinetic equations from 2PI and might ultimately lead to an analytic derivation of the effective hydrodynamics from first principles. In the short term, kinetic equations could be solved for more elaborate approximations then the one employed here, for example probing the convergence of the diffusion coefficient in a perturbative expansion.

In our case, there is no contribution from the LO term and no magnetic field, hence the evolution equations for the Schwinger boson (SB) (anti-)commutator F/ρ with self-energies $\Sigma^{F/\rho}$ become

$$\partial_{t_1} F_i(t_1, t_2) = \int_{t_0}^{t_1} \mathrm{d}t\, A \circ \Sigma_i^{\rho}(t_1, t) \circ F_i(t, t_2) - \int_{t_0}^{t_2} \mathrm{d}t\, A \circ \Sigma_i^{F}(t_1, t) \circ \rho_i(t, t_2), \tag{6.70}$$

$$\partial_{t_1} \rho_i(t_1, t_2) = \int_{t_2}^{t_1} \mathrm{d}t\, A \circ \Sigma_i^{\rho}(t_1, t) \circ \rho_i(t, t_2), \tag{6.71}$$

where we defined $A \equiv \left[\mathbb{1} \otimes i\sigma_y\right]$ and made the SB indices explicit by denoting the matrix product in SB space by $\circ$.

The evolution equations for the second time index t_2 can be obtained by renaming $t_1 \leftrightarrow t_2$ in above equations and using that F, Σ^F are symmetric and ρ, Σ^ρ, A are antisymmetric, resulting in

$$\partial_{t_2} F_i(t_1,t_2) = \int_{t_0}^{t_2} \mathrm{d}t\, F_i(t_1,t) \circ \Sigma_i^\rho(t,t_2) \circ A - \int_{t_0}^{t_1} \mathrm{d}t\, \rho_i(t_1,t) \circ \Sigma_i^F(t,t_2) \circ A, \tag{6.72}$$

$$\partial_{t_2} \rho_i(t_1,t_2) = -\int_{t_2}^{t_1} \mathrm{d}t\, \rho_i(t_1,t) \circ \Sigma_i^\rho(t,t_2) \circ A. \tag{6.73}$$

By introducing retarded and advanced components as

$$G_i^R(t_1,t_2) = \Theta(t_1-t_2)\rho(t_1,t_2)_i, \qquad G_i^A(t_1,t_2) = -\Theta(t_2-t_1)\rho(t_1,t_2)_i, \tag{6.74}$$

we can furthermore write the sum of Eqs. (6.70), (6.72) and Eqs. (6.71), (6.73) as

$$\begin{aligned}(\partial_{t_1}+\partial_{t_2})F_i(t_1,t_2) = \int_{-\infty}^{\infty} \mathrm{d}t\, \Theta(t-t_0) \Big\{ A \circ \Big(&\Sigma_i^R(t_1,t) \circ F_i(t,t_2) \\ &- \Sigma_i^F(t_1,t) \circ G_i^A(t,t_2) \Big) \\ - \Big(F_i(t_1,t) \circ \Sigma_i^A(t,t_2) &- G_i^R(t_1,t) \circ \Sigma_i^F(t,t_2) \Big) \circ A \Big\},\end{aligned} \tag{6.75}$$

$$\begin{aligned}(\partial_{t_1}+\partial_{t_2})\rho_i(t_1,t_2) = \int_{-\infty}^{\infty} \mathrm{d}t \Big\{ A \circ \Big(&\Sigma_i^R(t_1,t) \circ \rho_i(t,t_2) + \Sigma_i^\rho(t_1,t) \circ G_i^A(t,t_2) \Big) \\ - \Big(G_i^R(t_1,t) \circ \Sigma_i^\rho(t,t_2) &+ \rho_i(t_1,t) \circ \Sigma_i^A(t,t_2) \Big) \circ A \Big\}.\end{aligned} \tag{6.76}$$

In the equation for ρ we have used the identity $\int_{t_2}^{t_1} dt = \int_{-\infty}^{\infty} dt(\Theta(t_1-t) - \Theta(t_2-t))$. Note that in order to derive Eqs. (6.76), (6.75) we have not employed any approximations yet.

In order to derive kinetic equations for the late time dynamics, we assume the initial time to be in the distant past, i.e. $t_0 \to -\infty$, transform to Wigner coordinates $(T,\tau) = (\frac{1}{2}(t_1+t_2), t_1-t_2)$ and employ both a Fourier transform with respect to the relative time τ and a gradient expansion with respect to the central time T. The latter two can be done simultaneously by using the identity [210]

$$\int \mathrm{d}\tau \exp(i\omega\tau) \int \mathrm{d}t f(t_1,t) g(t,t_2) \approx f(T,\omega) g(T,\omega) \tag{6.77}$$

to lowest order in the gradient expansion. We hence get

$$\partial_T F_i(T,\omega) = A \circ \left(\Sigma_i^R \circ F_i - \Sigma_i^F \circ G_i^A \right) - \left(F_i \circ \Sigma_i^A - G_i^R \circ \Sigma_i^F \right) \circ A \tag{6.78}$$

$$\partial_T \rho_i(T,\omega) = A \circ \left(\Sigma_i^R \circ \rho_i + \Sigma_i^\rho \circ G_i^A \right) - \left(G_i^R \circ \Sigma_i^\rho + \rho_i \circ \Sigma_i^A \right) \circ A, \tag{6.79}$$

where we have suppressed the (T, ω) dependence of all two point functions on the RHS. Note that contrary to O(N) symmetric relativistic scalar field theories [210], the spectral function does not appear to be trivially constant to lowest order in the gradient expansion due to the matrix structure in this theory, although we can't exclude that there is some non-obvious identity leading to the vanishing of the right hand side.

From Eq. (6.78) we can now deduce the kinetic equation for the local magnetizations by using that they are related to the equal-time SB anticommutator by $\langle \hat{S}_i^\alpha(t) \rangle = \frac{1}{4} \operatorname{Tr}\{\mathcal{K}^\alpha F_i(t,t)\}$, where $\mathcal{K}^\alpha_{ab} = [\sigma_x \otimes \mathbb{1}]^{ab} \delta^{\alpha x} - [\sigma_y \otimes \sigma_y]^{ab} \delta^{\alpha y} + [\sigma_z \otimes \mathbb{1}]^{ab} \delta^{\alpha z}$ and $\alpha \in \{x, y, z\}$ is the spin component. Hence,

$$\partial_T \langle \hat{S}_i^\alpha(T) \rangle = \int \frac{\mathrm{d}\omega}{8\pi} \operatorname{Tr}\Big\{ \mathcal{K}^\alpha \circ A \circ (\Sigma_i^R \circ F_i - \Sigma_i^F \circ G_i^A - F_i \circ \Sigma_i^A + G_i^R \circ \Sigma_i^F) \Big\}, \quad (6.80)$$

where we have used the cyclicity of the trace and that $\mathcal{K}^\alpha A = A \mathcal{K}^\alpha$. By comparing the above result to the corresponding result in the O(N) model (c.f. Eq.(3.95) in [210]), one may identify the local magnetization as the 'occupation number' appearing in the Boltzmann equation by analogy.

So far the only approximation we made is the gradient expansion. In the following, we will now make approximations for the self-energy Σ, employing the $1/N$ expansion presented in [215].

Self-energies to NLO in 1/N

For our later purposes it will be advantageous to define the auxiliary field correlator slightly differently to how it's done in Ref. [215]. This will also lead to an improvement on the numerical evaluation of the full Kadanoff-Baym equations, improving the scaling with system size from quadratic to linear. We thank Asier Piñeiro-Orioli for pointing this trick out to us.

We start by replacing Eq. (64) in Ref. [215] with

$$D_{ij}^{\alpha\beta}(t_1, t_2) = i J_{ij}^\alpha \delta^{\alpha\beta} \delta_{\mathcal{C}}(t_1 - t_2) + \hat{D}_{ij}^{\alpha\beta}(t_1, t_2). \quad (6.81)$$

Inserting this into Eq. (45) and decomposing $\hat{D}(t_1, t_2) = D^F(t_1, t_2) - \frac{i}{2} \operatorname{sgn}_{\mathcal{C}}(t_1 - t_2) D^\rho(t_1, t_2)$, we obtain

$$\begin{aligned} D_{ij}^{F,\alpha\beta}(t_1, t_2) = \sum_k J_{ik}^\alpha \Big\{ &- \Pi_k^{F,\alpha\beta}(t_1, t_2) J_{kj}^\beta + \int_0^{t_1} \mathrm{d}t \sum_\delta \Pi_k^{\rho,\alpha\delta}(t_1, t) D_{kj}^{F,\delta\beta}(t, t_2) \\ &- \int_0^{t_2} \mathrm{d}t \sum_\delta \Pi_k^{F,\alpha\delta}(t_1, t) D_{kj}^{\rho,\delta\beta}(t, t_2) \Big\}, \end{aligned} \quad (6.82)$$

$$D_{ij}^{\rho,\alpha\beta}(t_1, t_2) = \sum_k J_{ik}^\alpha \Big\{ - \Pi_k^{\rho,\alpha\beta}(t_1, t_2) J_{kj}^\beta + \int_{t_2}^{t_1} \mathrm{d}t \sum_\delta \Pi_k^{\rho,\alpha\delta}(t_1, t) D_{kj}^{\rho,\delta\beta}(t, t_2) \Big\}. \quad (6.83)$$

The SB self energies become,

$$\Sigma_i^F(t_1,t_2) = -\frac{1}{4}\sum_{\alpha\beta}\mathcal{K}^\alpha \circ \left(F_i(t_1,t_2)D_{ii}^{F,\alpha\beta}(t_1,t_2) - \frac{1}{4}\rho_i(t_1,t_2)D_{ii}^{\rho,\alpha\beta}(t_1,t_2)\right)\circ\mathcal{K}^\beta, \tag{6.84}$$

$$\Sigma_i^\rho(t_1,t_2) = -\frac{1}{4}\sum_{\alpha\beta}\mathcal{K}^\alpha \circ \left(\rho_i(t_1,t_2)D_{ii}^{F,\alpha\beta}(t_1,t_2) + F_i(t_1,t_2)D_{ii}^{\rho,\alpha\beta}(t_1,t_2)\right)\circ\mathcal{K}^\beta, \tag{6.85}$$

i.e. contrary to the expressions in Ref. [215], no sums over lattice indices are involved here and the only expression in which the interaction matrix J appears is in the auxiliary field one- and two-point functions. The auxiliary field self energies stay the same, but we note them here for completeness:

$$\Pi_i^{F,\alpha\beta}(t_1,t_2) = -\frac{1}{8}\operatorname{Tr}\left\{\mathcal{K}^\alpha \circ \left(F_i(t_1,t_2)\circ\mathcal{K}^\beta\circ F_i(t_1,t_2) + \frac{1}{4}\rho_i(t_1,t_2)\circ\mathcal{K}^\beta\circ\rho_i(t_1,t_2)\right)\right\}, \tag{6.86}$$

$$\Pi_i^{\rho,\alpha\beta}(t_1,t_2) = \frac{1}{4}\operatorname{Tr}\left\{\mathcal{K}^\alpha\circ F_i(t_1,t_2)\circ\mathcal{K}^\beta\circ\rho_i(t_1,t_2)\right\}, \tag{6.87}$$

where the trace is over the SB indices.

Furthermore, the connected spin two point functions

$$F_{ij}^{S,\alpha\beta}(t_1,t_2) \equiv \frac{1}{2}\left\langle\left\{\hat{S}_i^\alpha(t_1),\hat{S}_j^\beta(t_2)\right\}\right\rangle_c, \tag{6.88}$$

$$\rho_{ij}^{S,\alpha\beta}(t_1,t_2) \equiv i\left\langle\left[\hat{S}_i^\alpha(t_1),\hat{S}_j^\beta(t_2)\right]\right\rangle. \tag{6.89}$$

can be expressed in terms of the connected auxiliary field correlators as

$$F_{ij}^{S,\alpha\beta}(t_1,t_2) = \sum_{k,l}[J^{-1}]_{ik}^\alpha D_{kl}^{F,\alpha\beta}(t_1,t_2)[J^{-1}]_{lj}^\beta, \tag{6.90}$$

$$\rho_{ij}^{S,\alpha\beta}(t_1,t_2) = \sum_{k,l}[J^{-1}]_{ik}^\alpha D_{kl}^{\rho,\alpha\beta}(t_1,t_2)[J^{-1}]_{lj}^\beta. \tag{6.91}$$

This is directly obvious from following the derivation in appendix D of Ref. [215] with the modified expression for D.

Gradient expansion of the self-energies to NLO in 1/N

In order to perform a gradient expansion of the memory integrals in Eq. (6.83), we note that

$$\Theta(t_1-t_2)\int_{t_2}^{t_1}\mathrm{d}t = \int_{-\infty}^{\infty}\mathrm{d}t\Theta(t_1-t)\Theta(t-t_2), \tag{6.92}$$

$$\Theta(t_2-t_1)\int_{t_2}^{t_1}\mathrm{d}t = -\int_{-\infty}^{\infty}\mathrm{d}t\Theta(t_2-t)\Theta(t-t_1). \tag{6.93}$$

It follows to first order in the gradient expansion that

$$D^{R,\alpha\beta} = \sum_{\delta} \left[\mathbb{1} - J\Pi^{R}\right]^{-1,\alpha\delta} \times \left(-J^{\delta}\Pi^{R,\delta\beta} \times J^{\beta}\right), \tag{6.94}$$

$$D^{A,\alpha\beta} = \sum_{\delta} \left[\mathbb{1} - J\Pi^{A}\right]^{-1,\alpha\delta} \times \left(-J^{\delta}\Pi^{A,\delta\beta} \times J^{\beta}\right), \tag{6.95}$$

where $\times$ denotes the matrix product with respect to spatial indices. There is no matrix product between matrices without $\times$, e.g. $[J^{\delta}\Pi^{A,\delta\beta}]_{ij} = J^{\delta}_{ij}\Pi^{A,\delta\beta}_{jj}$ (no sum convention).

Proceeding similarly for D^{F}, we find

$$D^{F,\alpha\beta} = \sum_{\delta} [\mathbb{1} - J\Pi^{R}]^{-1,\alpha\delta} \times \left(-J^{\delta}\Pi^{F,\delta\beta} \times J^{\beta} + \sum_{\gamma} J^{\delta}\Pi^{F,\delta\gamma} \times D^{A,\gamma\beta}\right) \tag{6.96}$$

While analytical results were difficult to derive from this derivation, it might be instructive to solve these kinetic equations numerically, as they might give access to diffusion coefficients in a larger variety of models. Furthermore, the 2PI approximation could be made more elaborate, up to the point where a full solution of the Kadanoff-Baym equations are difficult. Then, the simpler structure of the kinetic equations might be advantageous.

Part II

NONEQUILIBRIUM PROBES OF QUANTUM MATTER

While the previous part was focussed on far-from-equilibrium settings, we will study situations closer to, but still out of equilibrium in this part. In particular, we will use some of the intuitions and methods developed while studying thermalization dynamics to learn about equilibrium phases of matter and their stability.

7

SCREENED HARTREE-FOCK THEORY OF THE DISORDERED ELECTRON GAS

7.1 INTRODUCTION

The interplay of disorder, interactions and Fermionic statistics is at the heart of condensed matter physics. For instance, the scattering rates of electrons on impurities (as well as phonons) determines the resistivity of metals in a semi-classical model. More extremely, Anderson [429] showed that strong disorder can even lead to a full localization of electronic wavefunctions due to quantum-mechanical interference. Doped semiconductors exhibit a quantum phase transition from a metal to an insulator as a function of the doping density, i.e. the density of (disordered) charge carriers. While frequently, Anderson's model is invoked in these materials, the presence of strong, long-range Coulomb interactions challenges this interpretation [430, 431]. In particular, it remains unclear whether well-defined quasiparticles exist on the insulating side of the transition [432] and whether screening of the Coulomb interactions plays an important role. Recently, non-linear spectroscopy techniques have been employed to study phosphorous-doped silicon in more detail [433] which found that such well-defined electronic excitations do indeed *not* exist. Due to linear-in-frequency scaling of the found optical excitations they dubbed this phase an "marginal Fermi glass". The authors argued that dipoles corresponding to particle-hole excitations are the dominant excitations at very large disorder and interaction strength. However, numerical evidence based on a microscopic theory which can also describe the transition into the metallic side has so far not been obtained.

Here, we [1] make steps towards describing this state of matter by developing a screened Hartree Fock theory of the disordered three-dimensional electron gas, with which the ground state can be obtained self-consistently. We furthermore construct an effective Hamiltonian for the one-particle-hole sector above the HF ground state as a first step towards a microscopic theory of the marginal Fermi glass.

1 This project was conducted in collaboration with Sarang Gopalakrishnan and Michael Knap.

7.2 MODEL

Phosphorous dopants have five electrons in their outermost shells. When doping, tetrahedrally bonded silicon atoms are replaced by phosphorous atoms. Four of the phosphorous valence electrons are used for the bonds to the surrounding silicon atoms. The dynamics of the remaining "surplus" electrons of many phosphorous dopants can then be modelled by a Hubbard-type model [434], where the sites represent the locations of the phosphorous atoms,

$$\hat{H}_{\text{random}} = \sum_{i \neq j} J_{ij} \hat{c}_i^\dagger \hat{c}_j + \sum_i \mu_i \hat{c}_i^\dagger \hat{c}_i + \frac{1}{2} \sum_{i \neq j} U_{ij} \hat{c}_i^\dagger \hat{c}_i \hat{c}_j^\dagger \hat{c}_j, \tag{7.1}$$

with $U_{ij} \sim 1/|\mathbf{r}_i - \mathbf{r}_j|$ are the Coulomb interactions between the sites at locations $\mathbf{r}_i$ and the $J_{ij} \sim \exp(-\text{const.}|\mathbf{r}_i - \mathbf{r}_j|)$ are exponentially decaying hopping strengths. The on-site potential $\mu_i = -\mu + h_i^{\text{ion}}$ consists out of a global chemical potential μ and a potential resulting from the interactions with the positive charges of the phosphorous ions [435], $h_i^{\text{ion}} = -\sum_{j \neq i} U_{ij} K$ with $K = N_e/N$ the filling. As the dopants are randomly positioned, the hopping strengths and interactions strengths between neighbouring sites are in principle random. However, one can replace this substitutionally disordered model with a model on the square lattice and on-site disorder by perturbatively considering the effects of the random couplings, see e.g. section III.B.1. in Ref. [433]. This way, we consider

$$\hat{H} = \sum_{i \neq j} J_{ij} \hat{c}_i^\dagger \hat{c}_j + \sum_i \mu_i \hat{c}_i^\dagger \hat{c}_i + \frac{1}{2} \sum_{i \neq j} U_{ij} \hat{c}_i^\dagger \hat{c}_i \hat{c}_j^\dagger \hat{c}_j, \tag{7.2}$$

where $J_{ij} = -t\delta_{\langle i,j \rangle}$ is a nearest-neighbour hopping on the square lattices and $U_{ij} = U/|\vec{r}_i - \vec{r}_j|$ is the Coulomb interaction. The chemical potential is modified $\mu_i \to \mu_i + h_i$ with random fields h_i phenomenologically replacing the substitutional disorder. It is sampled from a uniform distribution with width Δ and mean 0, i.e. $h_i \in [-\Delta/2, \Delta/2]$.

7.3 SCREENED HARTREE-FOCK APPROACH

We combine a Hartree-Fock approximation with screened interactions. The self-consistency loop proceeds as follows:

1. Initialize the screened interaction with the bare interaction $W = U$.
2. Solve the Hartree-Fock problem self-consistently (see section 7.3.1), obtaining the eigenvalues ϵ_p and matrix of eigenvectors V.

3. Determine the static retarded susceptibility (see section 7.3.2 for a derivation)

$$\chi^R_{ij} = \sum_{k,k'} (V^*_{jk} V_{ik} V^*_{ik'} V_{jk'}) \frac{n_{k'} - n_k}{\epsilon_{k'} - \epsilon_k + i\eta}. \tag{7.3}$$

with number of electrons N_e and from that the screened interaction by

$$W = [1 - U\chi^R]^{-1} U. \tag{7.4}$$

4. Iterate steps 2-3 until convergence.

7.3.1 *Self-consistent solution of Hartree-Fock problem*

After having initialized the single particle density matrix $D_{ij} = \langle \hat{c}^\dagger_j \hat{c}_i \rangle$ with some initial guess fulfilling $\sum_i D_{ii} = N$, the self-consistency loop proceeds as follows

1. **Construct Hartree-Fock Hamiltonian.** The approximate Hamiltonian within HF is given by $\hat{H} = \sum_{ij} H^{\text{eff}}_{ij} \hat{c}^\dagger_i \hat{c}_j$ with

$$H^{\text{eff}}_{ij} = J_{ij} + (\mu_i + \sum_k U_{ik} D_{kk}) \delta_{ij} - W_{ij} D_{ij}, \tag{7.5}$$

where we replaced the bare interactions with screened interactions $U_{ij} \to W_{ij}$ in the Fock term, but not in the Hartree term. This is because this would lead to double counting (polarization insertions in Hartree diagram are generated by the self-consistency loop as they are equivalent to self-energy insertions).

2. **Diagonalize HF Hamiltonian** By diagonalizing $H^{\text{eff}} = V H^{\text{diag}} V^\dagger$ with eigenvalues ϵ_p, the diagonal many-body Hamiltonian is given by $\hat{H}^{\text{diag}} = \sum_p \epsilon_p \tilde{c}^\dagger_p \tilde{c}_p$ with the new creation/annihilation operators following as $\tilde{c}^\dagger_p = \sum_i V_{ip} c^\dagger_i, c^\dagger_i = \sum_p V^*_{ip} \tilde{c}^\dagger_p$

3. **Thermal single particle density matrix.** We can now calculate D_{ij} in a thermal ensemble $\hat{\rho}$ by

$$\begin{aligned} D_{ij} &= \sum_{k,k'} V^*_{jk} V_{ik'} \operatorname{Tr}\left(\hat{\rho} \tilde{c}^\dagger_k \tilde{c}_{k'}\right) && (7.6)\\ &= \sum_k V^*_{jk} V_{ik} n_{\beta,\mu}(\epsilon_k) && (7.7)\\ &\overset{\beta\to\infty}{=} \sum_{k \le N_e} V^*_{jk} V_{ik}, && (7.8) \end{aligned}$$

with the Fermi-Dirac distribution $n_{\beta,\mu}(\omega) = 1/(e^{\beta(\omega-\mu)} + 1)$ and the number of electrons N_e.

4. **Determine chemical potential** By solving

$$N_e = \sum_k n_{\beta,\mu}(\epsilon_k) \tag{7.9}$$

for μ. For $\beta = \infty$, this reduces to setting μ to the Fermi energy, i.e. the Nth eigenvalue.In fact, there is an ambiguity, as any choice between the Nth and $N+1$th eigenvalue leads to this normalization, as noted in Ref. [436]. We set it to a random value between the two.

5. **Convergence** Iterate steps 2-4 until convergence has reached for D within $\sim 10^{-4}$ relative error.

7.3.2 *Screening from Lindhard function*

We construct the Lindhard function corresponding to the effective (Hartree-Fock renormalized) free Fermion Hamiltonian to calculate a screened interaction. The HF-Hamiltonian is diagonalized by $\hat{H}^{\text{diag}} = \sum_p \epsilon_p \tilde{c}_p^\dagger \tilde{c}_p$ with the diagonalized creation/annihilation operators being connected to the real space ones by $\tilde{c}_p^\dagger = \sum_i V_{ip} c_i^\dagger, c_i^\dagger = \sum_p V_{ip}^* \tilde{c}_p^\dagger$. One can then show that the lesser/greater Green's functions are given by

$$\begin{aligned} G_{ij}^<(t,t') &\equiv i \operatorname{Tr}(\rho c_j^\dagger(t') c_i(t)) && (7.10)\\ &= i \sum_k V_{jk}^* V_{ik} e^{-i\epsilon_k(t-t')} n_k, && (7.11)\\ G_{ij}^>(t,t') &\equiv -i \operatorname{Tr}(\rho c_i(t) c_j^\dagger(t')) && (7.12)\\ &= -i \sum_k V_{jk}^* V_{ik} e^{-i\epsilon_k(t-t')} (1-n_k), && (7.13) \end{aligned}$$

with the occupation numbers $n_k = 1/(e^{\beta(\epsilon_k-\mu)}+1)$ at inverse temperature β and chemical potential μ and ρ is the density matrix of the system. The greater/lesser components of the density susceptibility are given by $\chi_{ij}^{\gtrless}(t,t') = -iG_{ij}^{\gtrless}(t,t')G_{ji}^{\lessgtr}(t',t)$, from which in turn the retarded susceptibility $\chi^R = \Theta(t)(\chi^> - \chi^<)$ can be determined to

$$\chi_{ij}^R(t-t') = -i\Theta(t-t') \sum_{k,k'} V_{jk}^* V_{ik} V_{ik'}^* V_{jk'} e^{-i(\epsilon_k-\epsilon_{k'})(t-t')} \left((1-n_k)n_{k'} - (1-n_{k'})n_k\right). \tag{7.14}$$

Finally, using $\Theta(t) = i\int \frac{d\omega}{2\pi} \frac{\exp(-i\omega t)}{\omega+i\eta}$, we find the frequency dependent retarded susceptibility $\chi^R(\omega) = \int dt e^{i\omega t} \chi^R(t)$ to be given by

$$\chi_{ij}^R(\omega) = \sum_{k,k'} V_{jk}^* V_{ik} V_{ik'}^* V_{jk'} \frac{(1-n_k)n_{k'} - (1-n_{k'})n_k}{\omega - (\epsilon_k - \epsilon_{k'}) + i\eta}. \tag{7.15}$$

We take the static limit $\omega \to 0$, such that

$$\chi^R_{ij} = \sum_{k,k'} (V^*_{jk} V_{ik} V^*_{ik'} V_{jk'}) \frac{n_{k'} - n_k}{\epsilon_{k'} - \epsilon_k + i\eta}. \tag{7.16}$$

The screened interaction then follows as

$$W = [1 - U\chi^R]^{-1} U. \tag{7.17}$$

Continuum limit

In the limit of no disorder $\Delta \to 0$, the system is translationally invariant and the screening procedure is expected to yield the familiar Thomas-Fermi result. In the following, we review how to recover this limit.

Ignoring interaction effects, the wavefunctions are given by the Fourier factors $V_{jk} = \exp(-i(2\pi/L)kj)/N$, with total volume $N = L^3$ and the retarded susceptibility in Fourier space becomes the familiar Lindhard function

$$\chi^R_q = \frac{1}{N} \sum_k \frac{n_{k+q} - n_k}{\epsilon_{k+q} - \epsilon_k + i\eta}. \tag{7.18}$$

The Lindhard function can be evaluated by expanding for small $q \ll k_F$ around the Fermi energy, yielding

$$\chi^R_q \approx -\frac{1}{N} \sum_k \delta(\epsilon_k - \epsilon_F) \equiv -\mathrm{DOS}(\epsilon_F). \tag{7.19}$$

This yields the effective interaction by using that in an infinite continuum system, the Fourier transform of the Coulomb interaction $U(r) = U/r$ is given by $U(q) = 4\pi U/q^2$,

$$W_q = \frac{U_q}{1 - U_q \chi^R_q} = \frac{4\pi U}{q^2 + 4\pi U\, \mathrm{DOS}(\epsilon_F)}, \tag{7.20}$$

or equivalently in real space

$$W(r) = \frac{U}{r} \exp(-r/l_{\mathrm{TF}}) \tag{7.21}$$

with the Thomas-Fermi screening length $l_{\mathrm{TF}} = 1/\sqrt{4\pi U\, \mathrm{DOS}(\epsilon_F)}$.

7.4 SCREENING IN THE PRESENCE OF DISORDER

While screening in the three-dimensional electron gas is by now textbook knowledge, less is known when disorder is present. In the following, we will study properties of the screened electron gas with the self-consistent Hartree-Fock scheme we developed in the previous section. We fix the linear system size to $L = 6$ and consider periodic

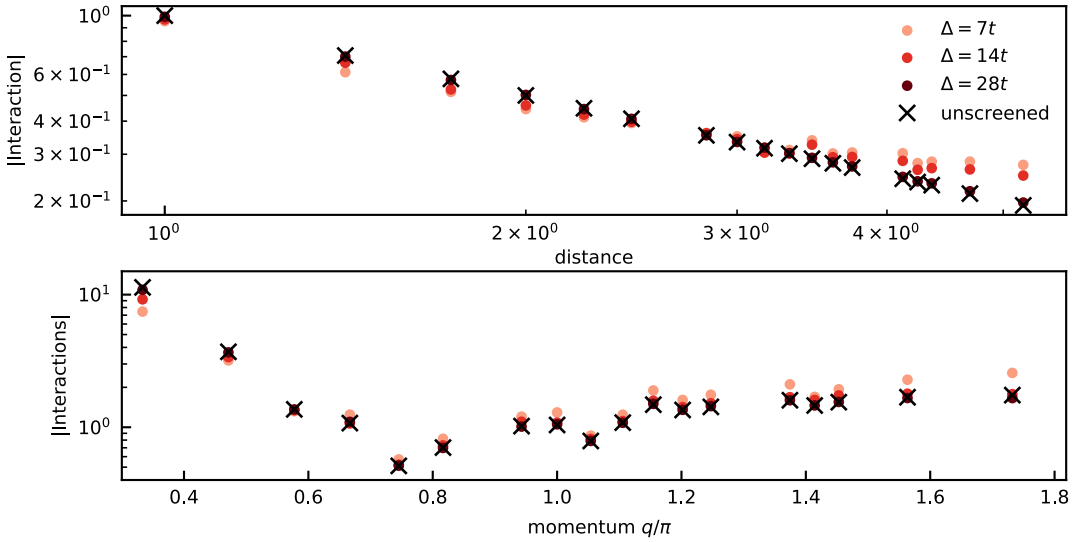

Figure 7.1: Self-consistent screened interactions as a function of real-space distance (top) and pseudo-momentum (bottom), see text for definition of the latter. Interaction strength $U = t$. All quantities averaged over radii before taking the absolute value.

boundary conditions. In Fig. 7.1 we show the screened interactions W as a function of disorder strength. As expected, the effect of screening is stronger for smaller disorder as wavefunctions become more extended. In particular, we recover the unscreened interactions for $\Delta \approx 28t$. Strong finite size effects are present in the small systems we consider. For instance, the expected exponential decay of the interactions at large distances is not directly visible. To define some notion of screening in keeping with the translationally invariant case, we define a pseudo-Fouriertransform by fixing a site $i = 0$, calculating

$$W_q = \sum_j e^{-i\mathbf{r}_j\mathbf{q}} W_{j0} \tag{7.22}$$

and averaging over the angular components of the momentum $\mathbf{q}$. The resulting "momentum space" screened interaction is displayed in the bottom of Fig. 7.1. We find that the screened interactions are diminished at smaller momentum, which is the expected behaviour from screening in the continuum limit, c.f. Eq. (7.20). At larger momenta, there is an oscillation due to the fact that we sharply cut-off the $1/r$ potential at the system's boundaries, i.e. this oscillations is the well known Gibbs phenomena in Fourier transforms.

In Fig. 7.2 we study the dependence of the screening effect on the relative strength of the Coulomb interactions. We find that it increases as the interactions are increased, even when renormalizing the interactions by the overall prefactor U.

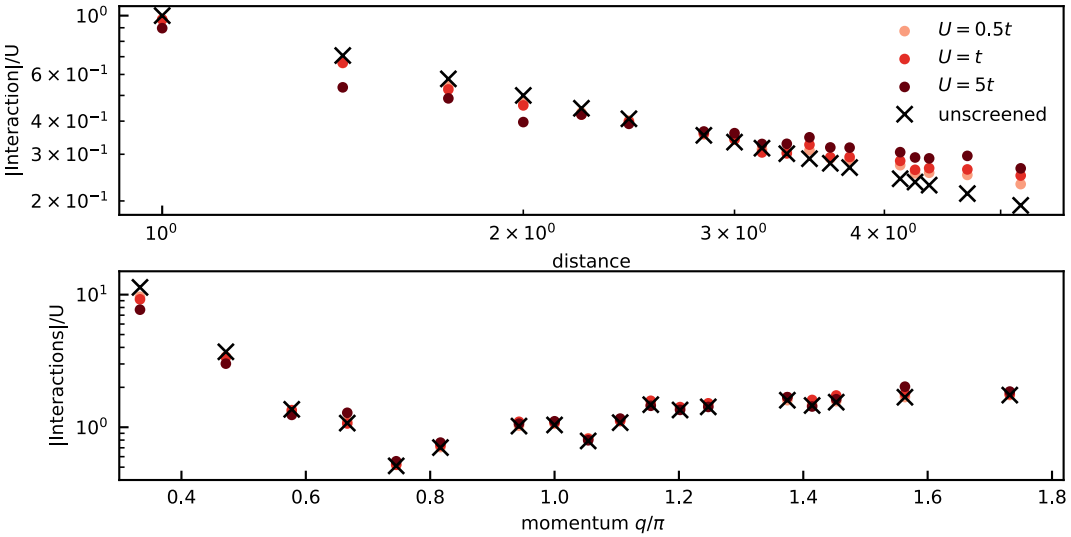

Figure 7.2: Self-consistent screened interactions as a function of real-space distance (top) and pseudo-momentum (bottom), see text for definition of the latter. Note that all interactions are normalized by the interaction prefactor U. Disorder strength $W = 14t$. All quantities averaged over radii before taking the absolute value.

7.5 SINGLE ELECTRON PROPERTIES IN PRESENCE OF SCREENING

Having studied how the interactions are modified by screening, we will now discuss how single-electron properties are altered. First, we discuss the density of states before moving over to localization properties of the Hartree-Fock wavefunctions.

7.5.1 *Density of states*

The density of states is given by

$$\mathrm{DOS}(\epsilon) = \frac{1}{L^3}\sum_i \delta(\epsilon_i - \epsilon), \tag{7.23}$$

where ϵ_i are the HF eigenenergies. Most importantly, the DOS signals the Efros-Shklovskii [430] pseudogap $\mathrm{DOS}(\epsilon) \sim \epsilon^2$ created by Coulomb interactions between localized orbitals in the interacting insulator. Importantly, this is a purely classical effect. Contrarily, the DOS shows a behaviour $\mathrm{DOS}(\epsilon) \sim |\epsilon|^{1/2}$ in the metal induced by quantum corrections discussed by Altshuler et al. [437] Beyond the localization transition, the DOS at the Fermi energy ($\epsilon = 0$ in our case) becomes finite[2]. We show in Fig. 7.3 the DOS for a fixed interaction strength as a function of disorder, showing that screening does not make a big difference for $U = t$. Note that the finite value of the DOS at the Fermi energy is due to the large finite size gap at

2 See Ref. [436] for a more complete discussion of the expected behaviour of the DOS.

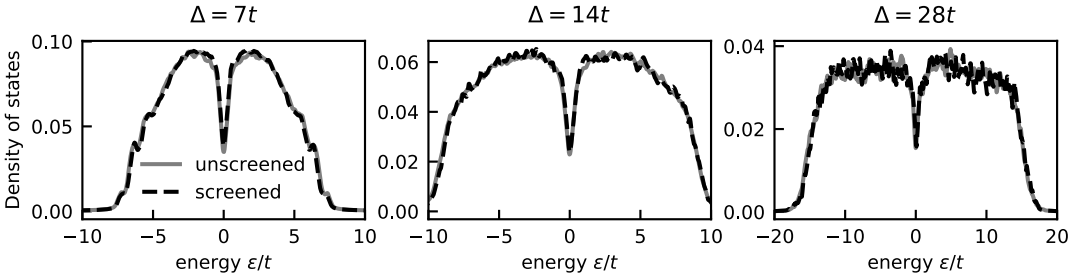

Figure 7.3: Density of states for fixed interaction strength $U = t$, comparing screened and unscreened results.

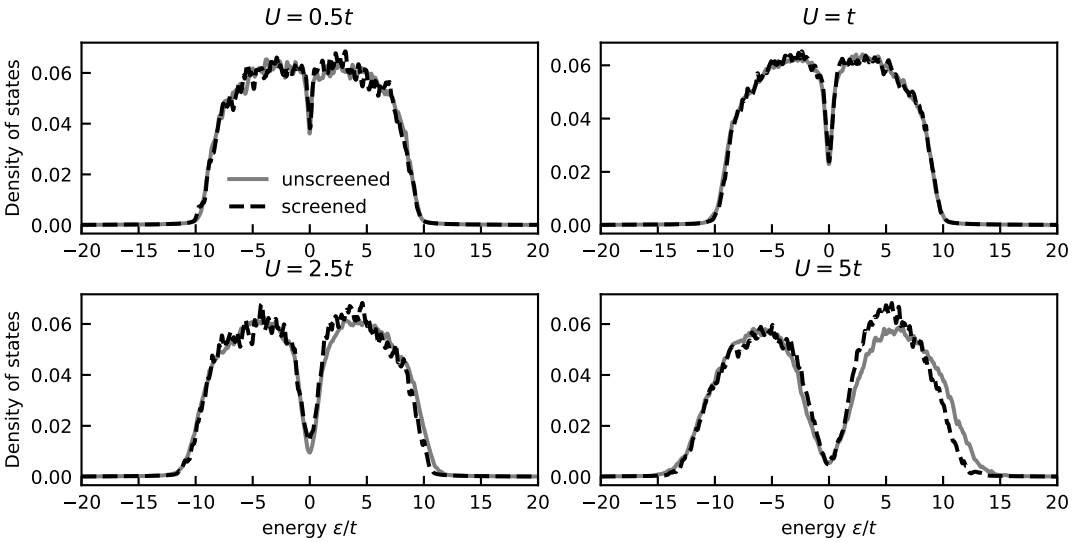

Figure 7.4: Density of states for fixed disorder strength $\Delta = 14t$, comparing screened and unscreened results.

our small system sizes. In this regime, we find the gap to behave according to the discontinuous quantum behaviour, in accordance with Ref. [436]. When fixing the disorder strength, see Fig. 7.4 we again find little effect of screening for small values of the interaction strength. For $U > 2$ we find the gap to gradually move over to the classical ϵ^2 behaviour as expected. For large U we find a larger effect of the interactions, in particular we find an asymmetry of the density of states around $\epsilon = 0$.

7.5.2 *Localization*

Moving on to study the localization of wavefunctions, we use the spatial correlations of the wavefunctions as in Ref. [436],

$$K(R_j, \epsilon_n) = \frac{\langle \sum_{\mathbf{r}} |V_n(\mathbf{r})|^2 |V_n(\mathbf{r}+\mathbf{R})|^2 \rangle}{\langle \sum_{\mathbf{r}} |V_n(\mathbf{r})|^2 \rangle}. \tag{7.24}$$

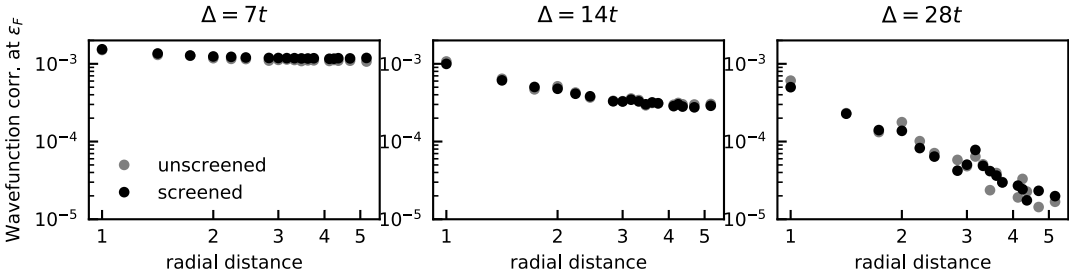

Figure 7.5: Wavefunction correlations for fixed interaction strength $U = t$, comparing screened and unscreened results.

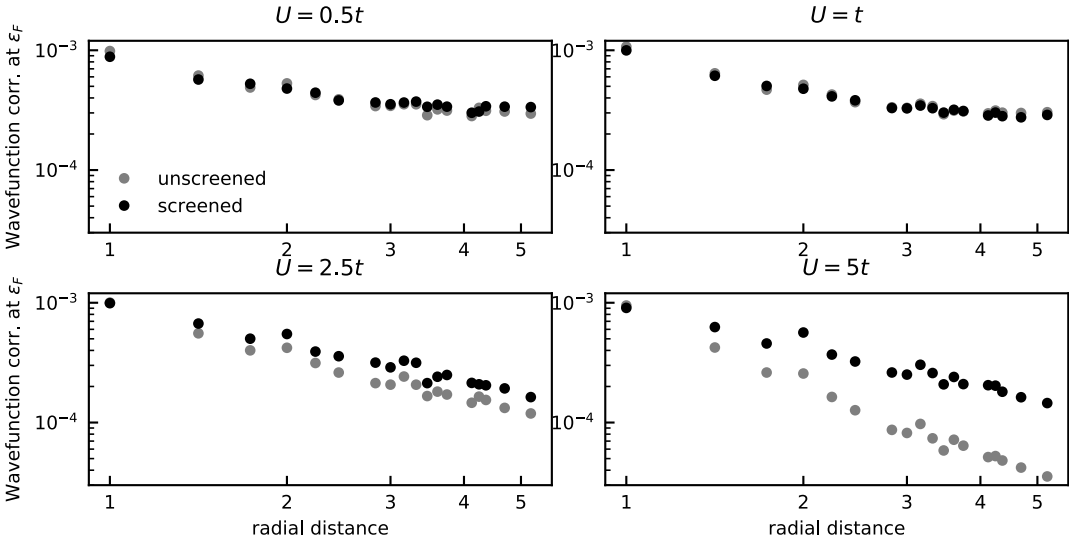

Figure 7.6: Wavefunction correlations for fixed disorder strength $\Delta = 14t$, comparing screened and unscreened results.

In the metallic phase, K saturates to a constant at long distances while it decays exponentially for all distances in the insulating phase. We study K for fixed interaction strength for $\epsilon_n = 0$, see Fig. 7.5, again finding little difference between screened and unscreened interactions. We find as expected that for the lower two disorder strengths the system is a metal. Note that $\Delta \approx 16.5t$ corresponds to the localization transition for $U = 0$ [438]. Contrarily, we find by fixing $\Delta = 14t$ the interaction induced metal to insulator transition, c.f. Fig. 7.6, which is expected to appear at around $U \approx 0.9$ [436]. Again, for $U = 2.5, 5$ we find differences between screened and unscreened interactions, indicating a delocalizing effect of the screening.

7.6 PARTICLE-HOLE HAMILTONIAN

In order to enable the role of particle-hole excitations in this system, we construct the effective Hamiltonian within the one particle-hole subsector in the following.

To do so, we first rewrite the Hamiltonian in terms of the creation and annihilation operators of Hartee-Fock states $\hat{d}/\hat{d}^\dagger$, which are obtained from the bare ones through

$$\hat{c}_i = \sum_k V_{ik}\hat{d}_k, \qquad \hat{c}_i^\dagger = \sum_k V_{ik}^* \hat{d}_k^\dagger. \tag{7.25}$$

The Hamiltonian (with screened interactions) can then be rewritten as

$$\hat{H} = \sum_{k_1 \neq k_2} \tilde{J}_{k_1 k_2} \hat{d}_{k_1}^\dagger \hat{d}_{k_2} + \frac{1}{2} \sum_{k_1 k_2 k_3 k_4} \tilde{W}_{k_1 k_2 k_3 k_4} \hat{d}_{k_1}^\dagger \hat{d}_{k_2}^\dagger \hat{d}_{k_3} \hat{d}_{k_4} \tag{7.26}$$

with $\tilde{J} = V^\dagger (J + \mathrm{diag}(\mu)) V$ and $\tilde{W}_{k_1 k_2 k_3 k_4} = \sum_{ij} V_{ik_1}^* V_{jk_2}^* W_{ij} V_{jk_3} V_{ik_4}$.

The Hartree-Fock ground state with N_e electrons is given by the Fermi sea $|\Psi_0\rangle = \Pi_{k \leq N_e} d_k^\dagger |0\rangle$. Creating an electron at site i while destroying one at site m leads to a superposition of Hartree-Fock particle hole states as

$$\hat{c}_l^\dagger \hat{c}_m |\Psi_0\rangle \tag{7.27}$$

$$= \sum_{a > N_e} \sum_{i \leq N_e} V_{la}^* V_{mi} \hat{d}_a^\dagger \hat{d}_i |\Psi_0\rangle \tag{7.28}$$

$$\equiv |\Psi_i^a\rangle , \tag{7.29}$$

where we used the properties of the Fermi sea. From now on we use $i, j, l, \ldots$ for hole indices (fulfilling $i \leq N_e$) and $a, b, c, \ldots$ for particle indices ($a > N_e$). In order to subtract the interaction effects taken into account within Hartree-Fock, we calculate the effective Hamiltonian within the particle-hole sector with respect to $\hat{H} - \hat{F}$. Particle-hole states are eigenstate of the Hartree-Fock Hamiltonian $\hat{F} = \sum_k \epsilon_k \hat{d}_k^\dagger \hat{d}_k$ with eigenenergies $E_i^a = \sum_{k \leq N_e} \epsilon_k - \epsilon_i + \epsilon_a$.

It is convenient to define new particle-hole operators $\hat{b}$ by

$$\hat{b}_i^\dagger = \hat{d}_i, \quad \hat{b}_a^\dagger = \hat{d}_a^\dagger, \tag{7.30}$$

such that the Fermi-sea is the vacuum of these new operators, i.e. $\hat{b} |\Psi_0\rangle = 0$ and $|\Psi_i^a\rangle = \hat{b}_a^\dagger \hat{b}_i^\dagger |\Psi_0\rangle$. This enables the straightforward use of Wick's theorem to evaluate multi-point correlation functions. As a last step before constructing the one-particle-hole Hamiltonian, we need to rewrite the Hamiltonian in Eq. 7.26 in terms of the new operators $\hat{b}$ while only keeping terms with an even number of both particles and holes, giving

$$\hat{H} = \sum_i \tilde{J}_{ii} - \sum_{ij} \tilde{J}_{ij} \hat{b}_j^\dagger \hat{b}_i + \sum_{ab} \left(\tilde{J}_{ab} - 2 \sum_i \tilde{W}_{aibi} \right) \hat{b}_a^\dagger \hat{b}_b + \frac{1}{2} \sum_{abcd} \tilde{W}_{abcd} \hat{b}_a^\dagger \hat{b}_b^\dagger \hat{b}_c \hat{b}_d$$
$$+ \frac{1}{2} \sum_{ijlm} \tilde{W}_{ijlm} \hat{b}_i \hat{b}_j \hat{b}_l^\dagger \hat{b}_m^\dagger + \sum_{aibj} \frac{1}{2} \tilde{W}_{ajbi} \hat{b}_a^\dagger \hat{b}_b \hat{b}_i^\dagger \hat{b}_j. \tag{7.31}$$

Finally, we evaluate the matrix elements by using Wick's theorem, for example

$$\langle \Psi_p^f | \hat{b}_a^\dagger \hat{b}_b \hat{b}_i^\dagger \hat{b}_j | \Psi_q^g \rangle = \langle \Psi_0 | \hat{b}_p \hat{b}_f \hat{b}_a^\dagger \hat{b}_b \hat{b}_i^\dagger \hat{b}_j \hat{b}_g^\dagger \hat{b}_q^\dagger | \Psi_0 \rangle \tag{7.32}$$

$$= \delta_{af}\delta_{bg}\delta_{pi}\delta_{jq}, \tag{7.33}$$

where we used that $\langle \Psi_0 | \hat{b}_a \hat{b}_b^\dagger | \Psi_0 \rangle = \delta_{ab}$, $\langle \Psi_0 | \hat{b}_i \hat{b}_j^\dagger | \Psi_0 \rangle = \delta_{ij}$ and $\langle \Psi_0 | \hat{b}_a \hat{b}_i^\dagger | \Psi_0 \rangle = 0$. This way, we obtain the matrix elements of the one particle-hole Hamiltonian as

$$\langle \Psi_p^f | \hat{H} | \Psi_q^g \rangle = \left(\tilde{J}_{fg} - 2\sum_i \tilde{W}_{figi} \right) \delta_{pq} - \left(\tilde{J}_{pq} - 2\sum_j \tilde{W}_{qjpj} \right) \delta_{fg} + \left(\sum_i \tilde{J}_{ii} + \sum_{ij} \tilde{W}_{ijji} \right) \delta_{fg}\delta_{pq} + 2\tilde{W}_{fqgp}. \tag{7.34}$$

We introduce new two-particle operators $\hat{C}_\alpha = \hat{C}_{(ij)} \equiv \hat{d}_a^\dagger \hat{d}_i$ and write the one-particle-hole Hamiltonian as

$$\hat{H}_{\text{1p.h.}} = \sum_{\alpha\beta} \hat{C}_\alpha^\dagger H_{\alpha\beta} \hat{C}_\beta, \tag{7.35}$$

with $\hat{H}_{\alpha\beta} = \hat{H}_{(ai)(bj)} = \langle \Psi_0 | \hat{d}_i^\dagger \hat{d}_a \hat{H} \hat{d}_b^\dagger \hat{d}_j | \Psi_0 \rangle$. We can again diagonalize this matrix by introducing

$$\hat{C}_\alpha = \sum_\beta V_{\alpha\beta}^{ph} \hat{D}_\beta, \quad \hat{C}_\alpha^\dagger = \sum_\beta V_{\alpha\beta}^{ph,*} \hat{D}_\beta^\dagger, \tag{7.36}$$

with which the Hamiltonian is diagonal with $\hat{H} = \sum_\alpha \xi_\alpha \hat{D}_\alpha^\dagger \hat{D}_\alpha$.

REAL SPACE PARTICLE-HOLE EIGENFUNCTIONS. We transform the particle hole eigenstates back to real space by using Eq. 7.28,

$$V_{ij}^{ph}(\gamma) = \sum_{a=0}^{N_s} \sum_{k=0}^{N_s} V_{i,a+N_e}^* V_{j,N_e-k} V_{aN_s+j,\gamma}^{ph}, \tag{7.37}$$

where we restricted to N_s states above and below the Fermi level N_e and redefined the indices relative to N_e.

7.7 CONCLUSIONS AND OUTLOOK

In this chapter, we have introduced an extended Hartree Fock theory for the disordered three-dimensional electron gas, by incorporating a self-consistent screening procedure. We have numerically demonstrated its use by determining the screened interactions in small systems. We found that screening is largest for smaller disorder. For strong disorder, the unscreened interactions are recovered. When fixing the disorder strength, the screening effect is larger when the interactions are increased. We

did not find a strong effect of screening on physical quantities such as the density of states and the localization of the Hartree Fock wavefunctions except for large interaction strengths, where we found a delocalizing effect on the wavefunctions.

We have furthermore constructed an effective description of particle hole excitations in the Coulomb gas, which enables a study of their role in recent optical spectroscopy experiments on doped silicon [433].

8

UNIVERSAL DECAY OF SPIN SPIRAL ORDER IN THE HEISENBERG MODEL

This chapter is based on the preprint

- Joaquin F. Rodriguez-Nieva, Alexander Schuckert, Dries Sels, Michael Knap, Eugene Demler: "Transverse instability and universal decay of spin spiral order in the Heisenberg model" – [arXiv:2011.07058]

Text and figures have been adapted and expanded here. Discrete truncated Wigner approximation (dTWA) results were obtained by Joaquin F. Rodriguez-Nieva. Sections 1.1.1, 1.2.3, 1.3.1, 1.3.2, 1.4, 1.6.2 and 1.6.3 including the data presented in the figures contained in these sections have not been previously published.

We analyze the stability of spin spiral states in the two-dimensional Heisenberg model. Our analysis reveals that the SU(2) symmetric point hosts a dynamic instability that is enabled by the existence of energetically favorable transverse deformations - both in real and spin space - of the spiral order. The instability is universal in the sense that it applies to systems with any spin number, spiral wavevector, and spiral amplitude. Unlike the Landau or modulational instabilities which require impurities or periodic potential modulation of an optical lattice, quantum fluctuations alone are sufficient to trigger the transverse instability. We analytically find the most unstable mode and its growth rate, and compare our analysis with phase space methods. We show that the same instability also exists in 1D using exact matrix product state methods, giving credibility to our approximate treatments in two spatial dimensions. Using an exact short time expansion, we show that the instability is not present from the shortest possible time scales but is only built up at non-perturbatively long times. We study this crossover from short-time to instability regime with two-particle irreducible effective action method for spin systems (spin-2PI) methods. By adding an easy plane exchange coupling that reduces the Hamiltonian symmetry from SU(2) to U(1), the stability boundary is shown to continuously interpolate between the modulational instability and the transverse instability. This suggests that the transverse instability is also an important mechanism that hinders long-range phase coherence even in the presence of exchange anisotropy.

8.1 INTRODUCTION

Characterizing the mechanisms responsible for the breakdown of phase coherence in quantum systems is a fundamental problem with broad implications in quantum science and technology. The interplay between kinetic effects, interactions, and disorder gives rise to a wide range of phase relaxation mechanisms. In the simplest scenario, the phase coherence in a superfluid is subject to the Landau criterion [439] which defines an upper limit for the superfluid velocity: when the superfluid moves faster than the sound velocity, a spatially localized defect can trigger a superfluid instability that globally destroys phase coherence [440]. In the case of a Bose-Einstein condensate (BEC) in an optical lattice with spacing a, the characteristic lattice modulation $q_1 = \pi/2a$ sets another limit for the superfluid wavevector above which a modulational instability occurs [441, 442]. Such instability can be enhanced in the presence of strong interactions [443, 444]. Rich physics and diverse mechanisms that destroy—and sometimes stabilize—the phase coherence have been discussed in the context of counterflowing superfluids [445], multicomponent [446] and spinor BECs [447–449], superconductors [450–453], in the presence of extended disorder [454–457], dipolar interactions [458–460], and driving [461–465].

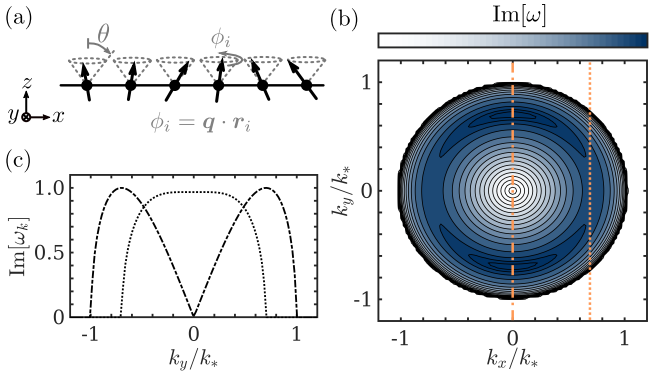

Figure 8.1: (a) Schematics of a spin spiral parametrized by a wavevector $\mathbf{q}$ and angular amplitude θ. (b) Imaginary part of the frequency of Bogoliubov modes. The wavevectors $k_{x,y}$ are relative to $\mathbf{q}$, which is assumed to be pointing in the x-direction ($k_* = q \sin\theta$). The fastest growing modes are transverse to $\mathbf{q}$, with $k_y \approx k_*/\sqrt{2}$. (c) Slice of panel (b) plotted at the linecuts $k_x/k_* = 0$ (dotted-dashed line) and $k_x/k_* = 0.75$ (dotted line) and normalized with $1/\tau_*$ in Eq.(8.1). Parameters used: $\theta = \pi/4$, $q_x a = 0.5$, $q_y = 0$.

Here we inquire about the fate of a spin spiral state in the two-dimensional Heisenberg model, see Fig. 8.1(a). Understanding the stability and dynamics of such states is of relevance in many important scenarios. The non-equilibrium dynamics of spin spirals has recently been in the spotlight of several cold atom experiments [161, 162, 466]. By tuning the wavevector $\mathbf{q}$ and angular amplitude θ of

the spin spiral, we can tune the energy and magnetization of the system and trigger interesting far-from-equilibrium phenomena, such as quantum turbulence [467, 468], prethermalization [48], universal self-similar relaxation [50, 210], and anomalous transport [163]. In addition, the stability of spin superfluids in ferromagnetic materials, promising for dissipationless spintronic applications [469–474], hinges on the stability of long-range coherence of a spin spiral. As such, our results are useful to understand the relevant modes that lead to spin superfluid decay.

Our analysis reveals that the SU(2) symmetry of the Hamiltonian gives rise to a dynamic instability with different characteristics from previously-studied instabilities. In particular, the instability (i) is enabled by gapless symmetry-allowed deformations of the order parameter rather than kinematic effects, (ii) is triggered by quantum fluctuations without the need for defects, disorder or a lattice, and (iii) is universal in the sense that it affects systems with arbitrary spin number S, spiral wavevector, and spiral amplitude. The main physics can be understood by noticing that the SU(2) symmetry relaxes the topological constraint that protects the U(1) phase in superfluids [469]: while in usual superfluids the thermally-activated creation of vortex-antivortex pairs or large kinematic fluctuations destroy coherence, the SU(2) symmetry alone furnishes additional 'directions' (or rotation generators) in which the phase coherence can be destroyed. As indicated in Fig. 8.1(b), the instability evolves by unwinding the spiral via growth of modes in a ring around the wavevector $\mathbf{q}$. Assuming $\mathbf{q} = (q_x, 0)$, the fastest growing mode has transverse wavevector $k_\perp \approx k_*/\sqrt{2}$, and grows with a rate $1/\tau_*$, with

$$k_* = |\mathbf{q}| \sin\theta, \quad \frac{1}{\tau_*} = JS \sin^2\theta [1 - \cos(q_x a)], \tag{8.1}$$

and J the exchange coupling. In addition, numerical simulations show that the constraint $\hat{S}_j^2 = S(S+1)$ of each spin regulates the instability growth, which peaks in a time $t \approx 4\tau_*$ (largely independent of $\mathbf{q}$, θ, and S).

We analytically discuss dynamics in the SU(2) symmetric Heisenberg model for large S, but our conclusion are far more general. In particular, below we numerically show that the imprint of the ring of unstable modes survives even in the $S = 1/2$ limit for sufficiently small wavevectors. In addition, we show that the effect of the instability pervades away from the SU(2) symmetric point. Indeed, in the presence of anisotropic exchange that reduces the Hamiltonian symmetry to U(1), we observe a strong reduction of the critical wavevector for modulation instabilities (*i*.e., $|\mathbf{q}_c| = \pi/2a$) for a wide range of values of the exchange anisotropy. As such, manifestations of the transverse instability still exist in the presence of exchange anisotropy.

MODEL We consider the two-dimensional Heisenberg model on a square lattice with exchange anisotropy:

$$\hat{H} = -\sum_{\langle j,j'\rangle} J\left(\hat{S}_j^x \hat{S}_{j'}^x + \hat{S}_j^y \hat{S}_{j'}^y\right) + J_z \hat{S}_j^z \hat{S}_{j'}^z, \tag{8.2}$$

where $\langle j, j'\rangle$ denotes summation over nearest neighbours. Each site contains a spin S degree of freedom and periodic boundary conditions in each spatial direction are assumed. Our analysis is not affected by a Zeeman field, which is present in many relevant experiments: although a Zeeman field breaks the SU(2) symmetry of the Hamiltonian, its effect on dynamics can be removed by using a rotating frame. The initial condition is a spin spiral

$$\langle \hat{S}_j^{\pm}\rangle = S\sin\theta e^{\pm i\mathbf{q}\cdot\mathbf{r}_j}, \quad \langle \hat{S}_j^z\rangle = S\cos\theta, \tag{8.3}$$

with $\hat{S}_j^{\pm} = \hat{S}_j^x \pm i\hat{S}_j^y$.

8.1.1 *Hamiltonian in rotating frame*

In the following, we will sometimes employ a description of the problem in the rotating frame of the spiral. To do so, we write the spiral as

$$|\Psi_0\rangle = \exp\left(i\sum_j \mathbf{Q}_j\mathbf{R}_j\hat{S}_j^z\right)\exp\left(i\Theta\sum_j \hat{S}_j^y\right)|\uparrow\cdots\uparrow\rangle_x \tag{8.4}$$

$$\equiv \hat{U}_1^\dagger\hat{U}_2^\dagger|\uparrow\cdots\uparrow\rangle_x. \tag{8.5}$$

We distinguish "diagonal" spirals with wavevector $\mathbf{Q} = (Q, Q)$ and "x-spirals" with wavevector $\mathbf{Q} = (Q, 0)$. $\Theta \in [-\pi/2, \pi/2]$ is the tilt angle of the spiral, with $\Theta = \pm\pi/2$ corresponding to fully polarized states in the z-direction as $\exp\left(i\frac{\pi}{2}\hat{S}^y\right)|\uparrow\rangle_x = |\uparrow\rangle$. $\Theta = 0$ corresponds to the spirals studied theoretically in 3D in Ref. [48] and experimentally in 1D in Ref. [162]. Note that we have changed the reference point of the tilt angle to the previous sections, with $\Theta = \theta + \frac{\pi}{2}$.

We can unwind the spiral by the unitary transformation

$$|\Psi_0\rangle \to \hat{U}_2\hat{U}_1|\Psi_0\rangle = |\uparrow\cdots\uparrow\rangle_x, \tag{8.6}$$

$$\hat{H} \to \hat{U}_2\hat{U}_1\hat{H}\hat{U}_1^\dagger\hat{U}_2^\dagger. \tag{8.7}$$

Assuming $Jz = 1$, we can use the result from Ref. [48],

$$\hat{U}_1\hat{H}\hat{U}_1^\dagger = -J\sum_{\langle i,j\rangle}\Big[\hat{S}_i^z\hat{S}_j^z + \cos\left(\mathbf{Q}\cdot(\mathbf{R}_i - \mathbf{R}_j)\right)\left(\hat{S}_i^x\hat{S}_j^x + \hat{S}_i^y\hat{S}_j^y\right) \tag{8.8}$$

$$-\sin\left(\mathbf{Q}\cdot(\mathbf{R}_i - \mathbf{R}_j)\right)\left(\hat{S}_i^x\hat{S}_j^y - \hat{S}_i^y\hat{S}_j^x\right)\Big].$$

Furthermore, from the BCH formula $e^X Y e^{-X} = Y + [X,Y] + \frac{1}{2}[X,[X,Y]] + \dots$ we can derive the following identities:

$$\hat{U}_2 \hat{S}_j^z \hat{U}_2^\dagger = \cos\Theta \hat{S}_j^z + \sin\Theta \hat{S}_j^x, \tag{8.9}$$

$$\hat{U}_2 \hat{S}_j^x \hat{U}_2^\dagger = \cos\Theta \hat{S}_j^x - \sin\Theta \hat{S}_j^z, \tag{8.10}$$

$$\hat{U}_2 \hat{S}_j^y \hat{U}_2^\dagger = \hat{S}_j^y. \tag{8.11}$$

Combining the above with Eq. (8.9) we arrive at

$$\begin{aligned} U_2 \hat{U}_1 \hat{H} \hat{U}_1^\dagger \hat{U}_2^\dagger = -J \sum_{\langle i,j \rangle} \Big[& \cos^2\Theta \hat{S}_i^z \hat{S}_j^z + \sin^2\Theta \hat{S}_i^x \hat{S}_j^x + \cos\Theta \sin\Theta \left(\hat{S}_i^x \hat{S}_j^z + \hat{S}_j^x \hat{S}_i^z \right) \\ & + \cos\left(\mathbf{Q} \cdot (\mathbf{R}_i - \mathbf{R}_j)\right) \Big(\cos^2\Theta \hat{S}_i^x \hat{S}_j^x + \sin^2\Theta \hat{S}_i^z \hat{S}_j^z \\ & \qquad - \cos\Theta \sin\Theta \left(\hat{S}_i^x \hat{S}_j^z + \hat{S}_j^x \hat{S}_i^z \right) + \hat{S}_i^y \hat{S}_j^y \Big) \\ & - \sin\left(\mathbf{Q} \cdot (\mathbf{R}_i - \mathbf{R}_j)\right) \left(\cos\Theta \left(\hat{S}_i^x \hat{S}_j^y - \hat{S}_i^y \hat{S}_j^x \right) - \sin\Theta \left(\hat{S}_i^z \hat{S}_j^y - \hat{S}_i^y \hat{S}_j^z \right) \right) \Big] \end{aligned} \tag{8.12}$$

In Fourier space, we finally arrive at

$$\hat{U}_2 \hat{U}_1 \hat{H} \hat{U}_1^\dagger \hat{U}_2^\dagger = \sum_{\mathbf{k}} \sum_{\alpha\beta} J_{\mathbf{k}}^{\alpha\beta} S_{\mathbf{k}}^\alpha \hat{S}_{-\mathbf{k}}^\beta, \tag{8.13}$$

with

$$J_{\mathbf{k}}^{xx} = -2J \sum_d \left(\sin^2\Theta + \cos Q_d \cos^2\Theta \right) \cos k_d, \tag{8.14}$$

$$J_{\mathbf{k}}^{xy} = -J_{\mathbf{k}}^{yx} = -2Ji \sum_d \sin Q_d \sin k_d \cos\Theta, \tag{8.15}$$

$$J_{\mathbf{k}}^{xz} = J_{\mathbf{k}}^{zx} = -2J \sum_d \left(\cos\Theta \sin\Theta (1 - \cos Q_d) \right) \cos k_d, \tag{8.16}$$

$$J_{\mathbf{k}}^{yy} = -2J \sum_d \cos Q_d \cos k_d, \tag{8.17}$$

$$J_{\mathbf{k}}^{yz} = -J_{\mathbf{k}}^{zy} = -2Ji \sum_d \sin Q_d \sin k_d \sin\Theta, \tag{8.18}$$

$$J_{\mathbf{k}}^{zz} = -2J \sum_d \left(\cos^2\Theta + \cos Q_d \sin^2\Theta \right) \cos k_d, \tag{8.19}$$

where $Q_d = \mathbf{Q}\mathbf{e_d}$ is the projection of $\mathbf{Q}$ on the lattice unit vector $\mathbf{e_d}$.

Observables

Here, we show how to construct expectation values with respect to the wavefunction $|\Psi\rangle$ in the unrotated frame from the expectation values in the rotated frame.

SPIRAL MAGNETIZATION The spiral magnetization is given by

$$S_\perp(\mathbf{Q}) = \frac{1}{N}\sum_j e^{i\mathbf{Q}\mathbf{R}_j}\langle\Psi|\hat{S}_j^+|\Psi\rangle \tag{8.20}$$

$$= \frac{1}{N}\sum_j e^{i\mathbf{Q}\mathbf{R}_j}\langle\tilde{\Psi}|\hat{U}_2\hat{U}_1\hat{S}_j^+\hat{U}_1^\dagger\hat{U}_2^\dagger|\tilde{\Psi}\rangle \tag{8.21}$$

$$= \cos(\Theta)\langle\tilde{\Psi}|\hat{S}^x|\tilde{\Psi}\rangle - \sin(\Theta)\langle\tilde{\Psi}|\hat{S}^z|\tilde{\Psi}\rangle + i\langle\tilde{\Psi}|\hat{S}^y|\tilde{\Psi}\rangle \tag{8.22}$$

Z MAGNETIZATION Similarly, we get for the total z magnetization

$$\langle\Psi|\hat{S}^z|\Psi\rangle = \cos\Theta\langle\tilde{\Psi}|\hat{S}^z|\tilde{\Psi}\rangle + \sin\Theta\langle\tilde{\Psi}|\hat{S}^x|\tilde{\Psi}\rangle\,, \tag{8.23}$$

which is constant under the Heisenberg Hamiltonian.

CORRELATIONS Denoting $C_{\mathbf{k}}^{\alpha\beta}$ the correlations between spin component α and β at wavevector $\mathbf{k}$ in the unrotated frame, and $\tilde{C}$ the ones in the rotated frame, we find

$$C_{\mathbf{k}}^{zz} = \cos^2\Theta\,\tilde{C}_{\mathbf{k}}^{zz} + \sin\Theta\cos\Theta(\tilde{C}_{\mathbf{k}}^{xz} + \tilde{C}_{\mathbf{k}}^{zx}) + \sin^2\Theta\,\tilde{C}_{\mathbf{k}}^{xx} \tag{8.24}$$

$$\begin{aligned} C_{\mathbf{k}}^{+-} &= \cos^2\Theta\,\tilde{C}_{\mathbf{k}-\mathbf{Q}}^{xx} + \sin^2\Theta\,\tilde{C}_{\mathbf{k}-\mathbf{Q}}^{zz} + \tilde{C}_{\mathbf{k}-\mathbf{Q}}^{yy} - \cos\Theta\sin\Theta\left(\tilde{C}_{\mathbf{k}-\mathbf{Q}}^{xz} + \tilde{C}_{\mathbf{k}-\mathbf{Q}}^{zx}\right) \\ &\quad + i\cos\Theta\left(\tilde{C}_{\mathbf{k}-\mathbf{Q}}^{yx} - \tilde{C}_{\mathbf{k}-\mathbf{Q}}^{xy}\right) + i\sin\Theta\left(\tilde{C}_{\mathbf{k}-\mathbf{Q}}^{zy} - \tilde{C}_{\mathbf{k}-\mathbf{Q}}^{yz}\right) \end{aligned} \tag{8.25}$$

These relations hold for both equal and unequal time correlation functions.

ENERGY The energy density of the tilted spiral is given by

$$E = \frac{\langle\hat{H}\rangle}{N} = -\frac{J}{2}\sum_{i=1}^{d}\left(\sin^2\Theta + \cos\left(\mathbf{Q}\mathbf{e}_i\right)\cos^2\Theta\right), \tag{8.26}$$

where $\mathbf{e}_i$ denotes unit vector i.

8.2 STABILITY ANALYSIS

We study the stability of the spiral state by expanding the equations of motion around the classical steady state value. Moreover, we will use two complentary approaches: an analysis of the continuum theory and a Holstein-Primakoff analysis in the rotating frame of the spiral. As it turns out that all those methods will

yield the same result for the unstable modes, we will use "Bogoliubov dispersion", "Holstein-Primakoff analysis" and "stability analysis" interchangeably in the following sections.

8.2.1 *Equations of motion*

Here we inquire about the stability of the spin spiral state by expanding the equations of motion around the spiral steady state.

The equations of motion of the spin operators are given by $\partial_t \hat{\mathbf{S}}_j = J \sum_{j' \in \mathcal{N}_j} \hat{\mathbf{S}}_j \times (\hat{\mathbf{S}}_{j'} + \epsilon \hat{S}^z_{j'} \mathbf{z})$, with $\epsilon = (J_z - J)/J$, $\mathcal{N}_j$ the nearest neighbors of site j, and $\mathbf{z}$ a unit vector. We first analyze the linearized dynamics at short times using the approximation $\langle \hat{S}^\alpha_j \hat{S}^\beta_{j'} \rangle \approx \langle \hat{S}^\alpha_j \rangle \langle \hat{S}^\beta_{j'} \rangle$, which gives rise to the equations of motion

$$\begin{aligned} \dot{S}^\pm_j &= \mp iJ \sum_{j' \in \mathcal{N}_j} \left[(1+\epsilon) S^\pm_j S^z_{j'} - S^\pm_{j'} S^z_j \right], \\ \dot{S}^z_j &= \frac{iJ}{2} \sum_{j' \in \mathcal{N}_j} \left[S^+_j S^-_{j'} - S^-_j S^+_{j'} \right], \end{aligned} \tag{8.27}$$

with $\langle \hat{S}^\alpha_j \rangle = S^\alpha_j$. Hereafter, energy and inverse time are expressed in units of JS and wavevectors in units of $1/a$. Using the initial conditions in Eq. (8.3), it can be shown that the solution $\bar{S}^\pm_j(t) = S \sin\theta e^{\pm i(\mathbf{q}\cdot\mathbf{r}_j + \mu t)}$, $\bar{S}^z_j = S\cos\theta$, is a steady-state solution of Eq.(8.27), with oscillation frequency $\mu = 2\cos\theta[(1+\epsilon)2 - \cos q_x - \cos q_y]$. Therefore, one needs to incorporate quantum fluctuations to obtain non-trivial dynamics.

We proceed to analyze the stability of the spiral in the isotropic exchange case, $\epsilon = 0$. We parametrize fluctuations on top of the steady-state solution using the xy components of magnetization, $S^\pm_j = \bar{S}^\pm_j + \delta S^\pm_j$; this implies that our parametrization is singular at $\theta = \pi/2$, but taking the limit $\theta \to \pi/2$ at the end still yields the correct result (a parametrization in polar coordinates that is non-singular at $\theta = \pi/2$, but more cumbersome, is discussed in subsection 8.2.1). Going into momentum space and expressing modes relative to the wavevector and frequency of the spiral, $\delta S^\pm_j = e^{\pm i(\mathbf{q}\cdot\mathbf{r}_j + \mu t)} \sum_{\mathbf{k}} e^{i(\mathbf{k}\cdot\mathbf{r}_j + \omega_{\mathbf{k}} t)} \delta S^\pm_{\mathbf{k}\pm\mathbf{q}}$.

We begin our analysis by parametrizing the spin degrees of freedom on the upper hemisphere of the Bloch sphere, $S^z_j = \sqrt{S^2 - |S_j|^2}$. The resulting equations of motion are

$$\dot{S}^\pm_j = \pm i \sum_{j' \in \mathcal{N}_j} \left[S^\pm_j \sqrt{S^2 - |S_{j'}|^2} - S^\pm_{j'} \sqrt{S^2 - |S_j|^2} \right], \tag{8.28}$$

with energy and inverse time in units of JS. Taking small deviation over the steady-state solution $\bar{S}_j$, $S^\pm_j = \bar{S}^\pm_j + \delta S^\pm_j$, Eq. (8.28) reads

$$i\delta\dot{S}^\pm_j = \pm \sum_{j' \in \mathcal{N}_j} \cos\theta \left[\delta S^\pm_{j'} + \frac{\bar{S}^\pm_{j'} \left(\bar{S}^+_j \delta S^-_j + \bar{S}^-_j \delta S^+_j \right)}{2\cos^2\theta} - (j \leftrightarrow j') \right]. \tag{8.29}$$

Because $\bar{S}_j^{\pm}$ is both time and position-dependent, it is convenient to write fluctuations relative to the wavevector and frequency of $\bar{S}_j$, i.e.

$$\delta S_j^{\pm} = e^{\pm i(\mathbf{q}\cdot\mathbf{r}_j+\mu t)} \sum_{\mathbf{k}} e^{i(\mathbf{k}\cdot\mathbf{r}_j+\omega_{\mathbf{k}} t)} \delta S^{\pm}_{\mathbf{q}\pm\mathbf{k}} \tag{8.30}$$

. The linearized equations of motion can thus be written as

$$(\omega_{\mathbf{k}} \pm \mu)\delta S^{\pm}_{\mathbf{q}\pm\mathbf{k}} = \mp \cos\theta \Bigg[\left(\gamma_0 - \gamma_{\mathbf{q}\pm\mathbf{k}} - \frac{\tan^2\theta(\gamma_{\mathbf{k}} - \gamma_{\mathbf{q}})}{2} \right) \delta S^{\pm}_{\mathbf{q}\pm\mathbf{k}} - \frac{\tan^2\theta(\gamma_{\mathbf{k}} - \gamma_{\mathbf{q}})}{2} \delta S^{\mp}_{\mathbf{q}\mp\mathbf{k}} \Bigg], \tag{8.31}$$

with $\gamma_{\mathbf{q}} = \sum_{\mathbf{a}} e^{i\mathbf{q}\cdot\mathbf{a}}$ ($\mathbf{a}$: unit vectors of the lattice). Defining $\varepsilon_{\mathbf{p}} = \cos\theta(\gamma_0 - \gamma_{\mathbf{p}})$ and $\Delta_{\mathbf{k}} = -\sin\theta\tan\theta(\gamma_{\mathbf{k}} - \gamma_{\mathbf{q}})$ leads to

$$\begin{pmatrix} \omega_{\mathbf{k}} + \varepsilon_{\mathbf{q}+\mathbf{k}} + \frac{\Delta_{\mathbf{k}}}{2} - \mu & \frac{\Delta_{\mathbf{k}}}{2} \\ -\frac{\Delta_{\mathbf{k}}}{2} & \omega_{\mathbf{k}} - \varepsilon_{\mathbf{q}-\mathbf{k}} - \frac{\Delta_{\mathbf{k}}}{2} + \mu \end{pmatrix} \delta\mathbf{S} = 0. \tag{8.32}$$

Adding an anisotropic term to the Heisenberg Hamiltonian, $\delta\hat{H} = -\epsilon \sum_{\langle jj'\rangle} \hat{S}_j^z \hat{S}_{j'}^z$, and repeating the same procedure above leads to the same form of Eq. (8.32) with modified energy and pairing

$$\varepsilon_{\mathbf{p}} = \cos\theta\left[(1+\epsilon)\gamma_0 - \gamma_{\mathbf{p}}\right], \quad \Delta_{\mathbf{k}} = -\sin\theta\tan\theta\left[(1+\epsilon)\gamma_{\mathbf{k}} - \gamma_{\mathbf{q}}\right]. \tag{8.33}$$

Note that, in the long-wavelength, limit, the pairing becomes hard-core and repulsive if $\epsilon < 0$, *i*.e., $\Delta_{\mathbf{k}} \approx |\epsilon| \sin\theta\tan\theta$. Note that the Bogoliubov analysis can be easily generalized to next nearest neighbor interactions by modifying the definition of $\gamma_{\mathbf{k}}$ accordingly. We note that the value of μ is $\mu = \varepsilon_{\mathbf{q}}$. The frequencies of the Bogoliubov modes are

$$\omega_{\mathbf{k}} = \frac{\varepsilon_{\mathbf{q}+\mathbf{k}} - \varepsilon_{\mathbf{q}-\mathbf{k}}}{2} \pm \frac{1}{2}\sqrt{\Delta\varepsilon(\Delta\varepsilon + 2\Delta_{\mathbf{k}})}, \tag{8.34}$$

where $\Delta\varepsilon = \varepsilon_{\mathbf{q}+\mathbf{k}} + \varepsilon_{\mathbf{q}-\mathbf{k}} - 2\varepsilon_{\mathbf{q}}$ can be interpreted as the kinetic energy cost of unbinding two quasiparticles from mode $\mathbf{q}$. For large spiral wavevectors, $q_x, q_y > \pi/2$, $\Delta\varepsilon$ can be negative because of the negative mass of bare particles and gives rise to the previously studied modulational instability [441]. For $q_x, q_y < \pi/2$, however, $\Delta\varepsilon$ is strictly positive and the condition for the mode $S^+_{\mathbf{q}+\mathbf{k}}$ to be unstable (*i*.e., $\omega''_{\mathbf{k}} = Im[\omega_{\mathbf{k}}] \neq 0$) is given by

$$\varepsilon_{\mathbf{q}+\mathbf{k}} + \varepsilon_{\mathbf{q}-\mathbf{k}} - 2\varepsilon_{\mathbf{q}} + 2\Delta_{\mathbf{k}} < 0. \tag{8.35}$$

It is instructive to analyze the condition (8.35) in the limit of small $\mathbf{q}$ and θ, and contrast it with the usual Landau instability. In this case, Eq.(8.35) is an energy balance equation resulting from unbinding two magnons of energy $\varepsilon_{\mathbf{q}\pm\mathbf{k}} \approx JSa^2(\mathbf{p} \pm$

$\mathbf{q})^2$ and with a *m*omentum-dependent pairing energy $\Delta_{\mathbf{k}} \approx -JSa^2 \sin^2\theta(\mathbf{q}^2 - \mathbf{k}^2)$. Importantly, $\Delta_{\mathbf{k}}$ is attractive in a ring of radius $|\mathbf{k}| \lesssim |\mathbf{q}|$. Attractive magnon-magnon interactions are known to give rise to magnon bound states in 1D [475] and its momentum dependence has been shown to result in unusual quasiparticle relaxation [476] and hydrodynamic behavior [477, 478]. Equation (8.35) dictates that, independently of S, the growth of modes with small wavevectors $\mathbf{k}$ relative to $\mathbf{q}$ is energetically favorable (a large value of $\mathbf{k}$, on the other hand, is penalized by a large kinetic energy cost, $\varepsilon_{\mathbf{q}+\mathbf{k}} + \varepsilon_{\mathbf{q}-\mathbf{k}} - 2\varepsilon_{\mathbf{q}} \propto \mathbf{k}^2$). Condition (8.35) needs to be contrasted with the superfluid stability condition where $\Delta_{\mathbf{k}} = gn > 0$ is momentum independent and repulsive, thus ensuring stability of the superfluid in the long wavelength limit (g: local interaction, n: density).

More generally, Eq.(8.35) gives rise to unstable modes for any value of $\mathbf{q}$ and θ. To analytically find the most unstable mode when $\mathbf{q} = (q_x, 0)$, we maximize $\omega''_{\mathbf{k}}$ under the constraint $k_x = 0$ [note that the fastest growing mode in Fig. 8.1(a) is transverse to $\mathbf{q}$]. In this case, we obtain

$$\omega''_{\mathbf{k}} = 2\sqrt{(1-\cos k_y)\left[(1-\cos k_y) - \sin^2\theta\,(1-\cos q_x)\right]}. \tag{8.36}$$

From this, we see that the maximum of $\omega''_{\mathbf{k}}$ occurs at $k_y = \tilde{k}_y$, with $\tilde{k}_y$ satisfying $1 - \cos\tilde{k}_y = \sin^2\theta(1-\cos q_x)/2$, and such mode grows with a rate $max\,(\omega''_{\mathbf{k}}) = \frac{1}{\tau_*}$ in Eq.(8.1). Equation (8.36) also defines the volume in phase space of unstable modes, which is bounded by the wavevector k_* satisfying the condition $1 - \cos k_* = \sin^2\theta[1 - \cos q_x]$. In the limit of small q_x, we obtain $\tilde{k}_y \approx k_*/\sqrt{2}$, with k_* defined in Eq.(8.1).

Spherical coordinates

The previous derivation has the disadvantage that the parametrization is singular at $\theta = \pi/2$. In order to avoid the singular behaviour in the physically interesting case $\theta = \pi/2$, we can use polar coordinates, $\mathbf{\Omega}_j = (\sin\theta_j\cos\phi_j, \sin\theta_j\sin\phi_j, \cos\theta_j)$, to parametrize the spin orientation. As we will see, this does not change the end result when we take the limit $\theta \to \pi/2$. The equation of motion are

$$i\dot{\Omega}^{\pm}_j = \pm \sum_{j'\in\mathcal{N}_j} [\Omega^{\pm}_j \Omega^z_{j'} - \Omega^{\pm}_{j'}\Omega^z_j], \tag{8.37}$$

with mean field solution

$$\bar{\Omega}^{\pm}_j = \sin\theta e^{\pm i(\mathbf{q}\cdot\mathbf{r}_j - \mu t)}, \quad \bar{\Omega}^z_j = \cos\theta, \tag{8.38}$$

and $\mu = \cos\theta(\gamma_0 - \gamma_{\mathbf{q}})$. Fluctuations on top of the mean-field equations are parametrized by

$$\delta\Omega^{\pm}_j = e^{\pm i(\mathbf{q}\cdot\mathbf{r}_j - \mu t)}\left(\pm i\delta\phi_j + \cos\theta_j\delta\theta_j\right), \quad \delta\Omega^z_j = -\sin\theta_j\delta\theta_j. \tag{8.39}$$

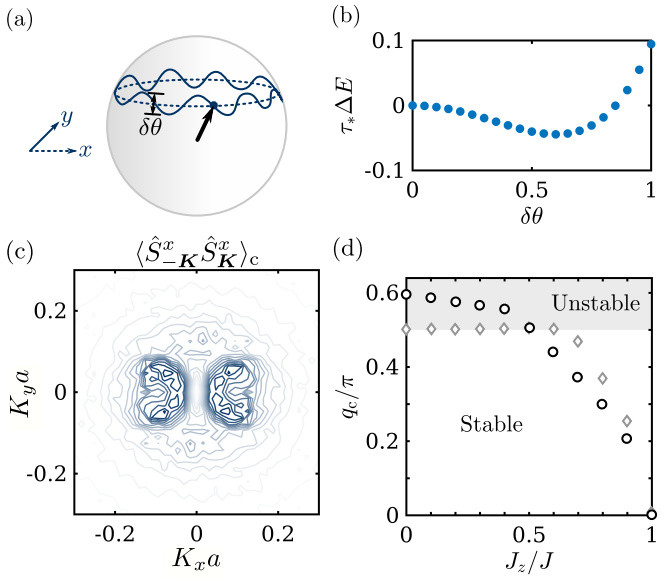

Figure 8.2: (a) Schematics of the most favorable deformation of the spin spiral order and (b) the corresponding energy shift with respect to the spiral state. Shown in (a) is the trajectory of the magnetization vector by moving on the lattice in the x (dotted line) and y (solid line) directions, and $\delta\theta$ is the amplitude of deformation, see definition in text. (c) Contour plot showing the connected component of $\langle \hat{S}^x_{-\mathbf{K}} \hat{S}^x_{\mathbf{K}} \rangle$ for $S = 1/2$, $q_x a = 0.12$, and $\theta = \pi/2$. (d) Stability boundary showing the critical momentum q_c as a function of exchange anisotropy for a spiral amplitude of $\theta = \pi/4$ (black circles), $\theta = 0.1$ (gray diamonds), and $S \to \infty$. The shaded area indicates the parameter space region of the modulational instability.

By replacing Eq.(8.39) into Eq.(8.37), we find

$$\pm\mu \cos\theta \delta\theta_j \mp \delta\dot{\phi}_j + i(\mu\delta\phi_j + \cos\theta\delta\dot{\theta}_j) = \pm \sum_{j'\in\mathcal{N}_j} \Big[-\sin^2\theta(\delta\theta_{j'} - e^{\pm i\mathbf{q}\cdot\mathbf{r}_{jj'}}\delta\theta_j) \\ \pm i\cos\theta(\delta\phi_j - e^{\pm i\mathbf{q}\cdot\mathbf{r}_{jj'}}) + \cos^2\theta(\delta\theta_j - e^{\pm i\mathbf{q}\cdot\mathbf{r}_{jj'}}\delta\theta_{j'}) \Big], \tag{8.40}$$

where $\mathbf{r}_{jj'} = \mathbf{r}_{j'} - \mathbf{r}_j$ and $\mathcal{N}_j$ denotes the neareset neighbor of j. The real and imaginary parts of this equation are given by

$$\delta\dot{\phi}_j = \sum_{j'\in\mathcal{N}_j} \big[\sin^2\theta(\delta\theta_{j'} - \cos(\mathbf{q}\cdot\mathbf{r}_{jj'})\delta\theta_j) - \cos^2\theta(\delta\theta_j - \cos(\mathbf{q}\cdot\mathbf{r}_{jj'})\delta\theta_{j'}) \\ - \cos\theta\sin(\mathbf{q}\cdot\mathbf{r}_{jj'})\delta\phi_{j'} + \mu\cos\theta\delta\theta_j \big], \tag{8.41}$$

$$\delta\dot{\theta}_j = \sum_{j'\in\mathcal{N}_j} \left[(\delta\phi_j - \cos(\mathbf{q}\cdot\mathbf{r}_{jj'})\delta\phi_{j'}) - \frac{\mu}{\cos\theta}\delta\phi_j - \cos\theta\sin(\mathbf{q}\cdot\mathbf{r}_{jj'})\delta\theta_{j'} \right].$$

Going into Fourier space and using the relations $\sum_{\mathbf{a}} \cos(\mathbf{q}\cdot\mathbf{a}) e^{i\mathbf{k}\cdot\mathbf{a}} = \frac{\gamma_{\mathbf{q}+\mathbf{k}}+\gamma_{\mathbf{q}-\mathbf{k}}}{2}$ and $\sum_{\mathbf{a}} \sin(\mathbf{q}\cdot\mathbf{a}) e^{i\mathbf{k}\cdot\mathbf{a}} = \frac{\gamma_{\mathbf{q}+\mathbf{k}}-\gamma_{\mathbf{q}-\mathbf{k}}}{2i}$, results in

$$\begin{aligned}
\delta\dot{\phi}_{\mathbf{k}} &= \left[\cos^2\theta\left(\frac{\gamma_{\mathbf{q}+\mathbf{k}}+\gamma_{\mathbf{q}-\mathbf{k}}}{2}-\gamma_{\mathbf{q}}\right)+\sin^2\theta(\gamma_{\mathbf{k}}-\gamma_{\mathbf{q}})\right]\delta\theta_{\mathbf{k}} \\
&- \cos\theta\left(\frac{\gamma_{\mathbf{q}+\mathbf{k}}-\gamma_{\mathbf{q}-\mathbf{k}}}{2i}\right)\delta\phi_{\mathbf{k}}, \\
\delta\dot{\theta}_{\mathbf{k}} &= -\left(\frac{\gamma_{\mathbf{q}+\mathbf{k}}+\gamma_{\mathbf{q}-\mathbf{k}}}{2}-\gamma_{\mathbf{q}}\right)\delta\phi_{\mathbf{k}} \\
&\quad - \cos\theta\left(\frac{\gamma_{\mathbf{q}+\mathbf{k}}-\gamma_{\mathbf{q}-\mathbf{k}}}{2i}\right)\delta\theta_{\mathbf{k}}.
\end{aligned} \tag{8.42}$$

If we define $\Delta\varepsilon' = \gamma_{\mathbf{q}+\mathbf{k}} + \gamma_{\mathbf{q}-\mathbf{k}} - 2\gamma_{\mathbf{q}}$ and $\Delta'_{\mathbf{k}} = \gamma_{\mathbf{k}} - \gamma_{\mathbf{q}}$. The imaginary part of the eigenvalue equation is given by

$$\mathrm{Im}[\omega_{\mathbf{k}}] = \frac{1}{2}\sqrt{\Delta\varepsilon'[\Delta\varepsilon'\cos^2\theta + \sin^2\theta\Delta'_{\mathbf{k}}]} \tag{8.43}$$

which coincides with the expression in Eq. 8.32 after identifying $\Delta\varepsilon = \Delta\varepsilon'\cos\theta$ and $\Delta_{\mathbf{k}} = -\sin\theta\cos\theta\Delta'_{\mathbf{k}}$.

8.2.2 *Long-wavelength theory*

To make the connection with the usual BEC theory more crisp, we make a one-to-one comparison between the long wavelength effective theory of the Heisenberg model and a weakly interacting Bose gas in the limit $\mathbf{q} \to 0$ and $\theta \to 0$. This analysis also shows that the results above are a generic feature of SU(2) symmetry rather than a peculiarity of the nearest-neighbour Heisenberg model in Eq.(2), and that the underlying lattice is not essential as in the modulational instability. Assuming small deviations from the ferromagnetic ground state $|F\rangle$ and performing a Holstein-Primakoff transformation $\hat{S}^+_j = \sqrt{2S - \hat{\psi}^\dagger_j\hat{\psi}_j}\hat{\psi}_j$ and $\hat{S}^z_j = S - \hat{\psi}^\dagger_j\hat{\psi}_j$, to quartic order in the bosonic operators $\hat{\psi}_j$ leads to the long-wavelength Hamiltonian

$$\hat{H} = JSa^2\int_{\mathbf{x}}\left(\nabla\hat{\psi}^\dagger_{\mathbf{x}}\nabla\hat{\psi}_{\mathbf{x}} + \frac{1}{4S}\hat{\psi}^\dagger_{\mathbf{x}}\hat{\psi}^\dagger_{\mathbf{x}}\nabla\hat{\psi}_{\mathbf{x}}\nabla\hat{\psi}_{\mathbf{x}} + h.c.\right). \tag{8.44}$$

Unlike the usual Bose gas with hard core collisions, here the collision amplitude of two quasiparticles with momentum $\mathbf{k}$ and $\mathbf{p}$ is $\propto -(\mathbf{k}\cdot\mathbf{p})$. This reflects the SU(2) symmetry of the Hamiltonian: collisions become negligible at small momenta because a $\mathbf{k} \to 0$ magnon state, $\hat{\psi}^\dagger_{\mathbf{k}}|\mathrm{F}\rangle \approx \frac{\hat{S}^+_{\mathbf{k}}}{\sqrt{2S}}|\mathrm{F}\rangle$, is effectively a global rotation of $|\mathrm{F}\rangle$ that would not affect the dynamics of a second incoming magnon. Furthermore, unlike the BEC theory that contains a characteristic velocity $v_* = \sqrt{gn/m}$ that quantifies the sound velocity of linearly-dispersing quasiparticles and the resulting Landau criterion (n: condensate density, m: mass), there is no emergent velocity

in Eq.(8.44)—this results in the well-known fact that the Goldstone modes of the ferromagnet do not have sound-like dispersion.

In the presence of a condensate $\langle \hat{\psi}^{\pm}_{\mathbf{x}} \rangle = \psi_0 e^{\pm i(\mathbf{q}\cdot\mathbf{x}+\mu t)}$, linearization of the equation of motion leads to

$$i\partial_t \delta\psi = \begin{pmatrix} \varepsilon^0_{\mathbf{q}+\mathbf{k}} - 2Ja^2\mathbf{q}\cdot(\mathbf{q}+\mathbf{k})|\psi_0|^2 - \mu & -Ja^2\psi_0^2(\mathbf{q}+\mathbf{k})\cdot(\mathbf{q}-\mathbf{k}) \\ Ja^2\psi_0^2(\mathbf{q}+\mathbf{k})\cdot(\mathbf{q}-\mathbf{k}) & -\varepsilon^0_{\mathbf{q}-\mathbf{k}} + 2Ja^2\psi_0^2\mathbf{q}\cdot(\mathbf{q}-\mathbf{k}) \end{pmatrix} \delta\psi, \tag{8.45}$$

where $\delta\psi^t = (\delta\psi_{\mathbf{q}+\mathbf{k}}, \delta\bar{\psi}_{\mathbf{k}-\mathbf{q}})$, μ is the chemical potential $\mu = JSa^2\mathbf{q}^2 - Ja^2\psi_0^2\mathbf{q}^2$, and $\varepsilon^0_{\mathbf{p}}$ is the bare magnon energy defined as $\varepsilon^0_{\mathbf{p}} = JSa^2\mathbf{p}^2$. First, we re-arrange the terms in the diagonal of the matrix:

$$\varepsilon^0_{\mathbf{q}\pm\mathbf{k}} - 2Ja^2\psi_0^2\mathbf{q}\cdot(\mathbf{q}\pm\mathbf{k}) - \mu = \varepsilon^0_{\mathbf{q}\pm\mathbf{k}} - Ja^2\psi_0^2(\mathbf{q}\pm\mathbf{k})^2 - Ja^2\psi_0^2(\mathbf{q}^2-\mathbf{k}^2) - \mu. \tag{8.46}$$

Second, we define the renormalized energy $\varepsilon_{\mathbf{q}\pm\mathbf{k}} = \varepsilon^0_{\mathbf{q}\pm\mathbf{k}} - Ja^2\psi_0^2(\mathbf{q}\pm\mathbf{k})^2$ and the binding energy $\Delta_{\mathbf{k}}/2 = -Ja^2\psi_0^2(\mathbf{q}^2-\mathbf{k}^2)$. The value of ψ_0 is related to θ through $\sqrt{2S-\psi_0^2}\psi_0 = S\sin\theta$, or $\psi_0 \approx \sqrt{\frac{S}{2}}\sin\theta$. This results in the pairing energy $\Delta_{\mathbf{k}} = -JSa^2\sin^2\theta(\mathbf{q}^2-\mathbf{k}^2)$, consistent with the long-wavelength expansion of Eq. (8.32).

Terms that reduce the symmetry from SU(2) to U(1), such as the exchange anisotropy $\epsilon < 0$ in Eq.(2), give rise to hard-core collisions in Eq.(8.44) with strength $g = -\epsilon J$, leading to a repulsive and hard-core pairing $\Delta_{\mathbf{k}} = |\varepsilon| J\sin^2\theta$ in the easy-plane case.

8.2.3 *Holstein-Primakoff analysis in rotating frame of spiral*

So far, we have investigated the stability of the spiral from the perspective of the classical equations of motion by linearizing them around the steady-state solution given by the mean-field precession of the spiral. In the following, we will show that the same results can be obtained from a Holstein-Primakoff analysis.

For a well-defined Holstein-Primakoff stability analysis, we need to expand around a fully polarized state. However, for $\Theta \neq 0$, there is a mean-field precession of the spiral given by $\langle \hat{S}^{\pm}_{\mathbf{Q}}(t)\rangle = \langle \hat{S}^{\pm}_{\mathbf{Q}}(0)\rangle e^{\mp iBt}$ with $B = 2J\sin\Theta\sum_d(1-\cos Q_d)$, i.e. an effective magnetic field in z-direction. Ignoring this precession would lead to a rapid break-down of the Holstein-Primakoff expansion as the mean field rotates the state away from the completely polarized state. Therefore, we need to go into the time-dependent rotating frame of this precession before applying U_1, U_2 by applying the unitary transformation $\hat{H} \to \hat{U}_0(t)\hat{H}\hat{U}_0^\dagger(t) + i\frac{d\hat{U}_0}{dt}\hat{U}_0^\dagger(t)$ with

$\hat{U}_0 = \exp\left(-iBt\sum_i \hat{S}_i^z\right)$ and $B = 2J\sin\Theta\sum_d(1-\cos Q_d)$. As $\hat{U}_0(t)\hat{H}\hat{U}_0^\dagger(t) = \hat{H}$ we get after all three transformations

$$\hat{H} \to \hat{U}_2\hat{U}_1\hat{H}\hat{U}_1^\dagger\hat{U}_2^\dagger + 2J\sin\Theta\sum_d(1-\cos Q_d)\left(\cos\Theta\sum_i \hat{S}_i^z + \sin\Theta\sum_i \hat{S}_i^x\right) \quad (8.47)$$

The spiral initial state is then transformed into the x-polarized state rotating according to the mean field evolution.

We introduce Holstein Primakoff Bosons $\hat{a}$ around the completely polarized state by

$$\hat{S}_i^x = \frac{1}{2} - \hat{a}_i^\dagger\hat{a}_i, \quad \hat{S}_i^z = \frac{1}{2}\left(\hat{a}_i^\dagger + \hat{a}_i\right), \quad \hat{S}_i^y = \frac{i}{2}\left(\hat{a}_i - \hat{a}_i^\dagger\right), \quad (8.48)$$

or equivalently in Fourier space (N is number of spins)

$$\hat{S}_{\mathbf{k}}^x = \frac{\sqrt{N}}{2}\delta(\mathbf{k}) - \frac{1}{\sqrt{N}}\sum_{\mathbf{q}}\hat{a}_{\mathbf{q}-\mathbf{k}}^\dagger\hat{a}_{\mathbf{q}}, \quad \hat{S}_{\mathbf{k}}^z = \frac{1}{2}\left(\hat{a}_{-\mathbf{k}}^\dagger + \hat{a}_{\mathbf{k}}\right), \quad \hat{S}_{\mathbf{k}}^y = \frac{i}{2}\left(\hat{a}_{\mathbf{k}} - \hat{a}_{-\mathbf{k}}^\dagger\right). \quad (8.49)$$

Keeping only up to quadratic terms and dropping constants, we arrive at

$$\hat{H}_{\mathrm{HP}} = \sum_{\mathbf{k}}\Delta_{\mathbf{k}}(\hat{a}_{\mathbf{k}}^\dagger\hat{a}_{-\mathbf{k}}^\dagger + \hat{a}_{\mathbf{k}}\hat{a}_{-\mathbf{k}}) + (\epsilon_{\mathbf{k}} + \mu)\hat{a}_{\mathbf{k}}^\dagger\hat{a}_{\mathbf{k}} + (\epsilon_{-\mathbf{k}} + \mu)\hat{a}_{-\mathbf{k}}\hat{a}_{-\mathbf{k}}^\dagger, \quad (8.50)$$

with

$$\Delta_{\mathbf{k}} = -\frac{J}{2}\sum_d\left(\cos^2\Theta(1-\cos Q_d)\right)\cos k_d, \quad (8.51)$$

$$\epsilon_{\mathbf{k}} = -\frac{J}{2}\sum_d\left(\left(\cos^2\Theta + \cos Q_d\left(\sin^2\Theta + 1\right)\right)\cos k_d - 2\sin Q_d\sin k_d\sin\Theta\right), \quad (8.52)$$

$$\mu = J\sum_d\cos Q_d. \quad (8.53)$$

Note in particular that $\epsilon_{\mathbf{k}} \neq \epsilon_{-\mathbf{k}}$ which is due to complex hopping terms arising from the J^{zy} components for nonzero Θ.

BOGOLIUBOV TRANSFORMATION Due to $\epsilon_{\mathbf{k}} \neq \epsilon_{-\mathbf{k}}$, the required Bogoliubov transformation is somewhat non-standard, so we go in some detail here. Setting for the moment $h = 0$, the Hamiltonian can be rewritten as

$$\hat{H}_{\mathrm{HP}} = \sum_{\mathbf{k}}\bar{A}_{\mathbf{k}}\mathcal{H}(\mathbf{k})A_{\mathbf{k}}, \quad (8.54)$$

with

$$A_{\mathbf{k}} = \begin{pmatrix} a_{\mathbf{k}} \\ -a_{-\mathbf{k}}^\dagger \end{pmatrix}, \qquad \bar{A}_{\mathbf{k}} = A_{\mathbf{k}}^\dagger\sigma_z, \qquad \mathcal{H}(\mathbf{k}) = \begin{pmatrix} J_{\mathbf{k}} & -\Delta_{\mathbf{k}} \\ \Delta_{\mathbf{k}} & -J_{-\mathbf{k}} \end{pmatrix}. \quad (8.55)$$

By defining a Bogoliubov rotation with

$$U_{\pm}(\mathbf{k}) = \begin{pmatrix} u_{\mathbf{k}}^{*} & \pm v_{\mathbf{k}} \\ \pm v_{\mathbf{k}}^{*} & u_{\mathbf{k}} \end{pmatrix}, \qquad U_{+}(\mathbf{k})U_{-}^{\dagger}(\mathbf{k}) = \mathbb{1}, \tag{8.56}$$

we can diagonalize the Hamiltonian by defining new operators $\bar{B}_{\mathbf{k}} = (b_{\mathbf{k}}^{\dagger} \quad b_{-\mathbf{k}})$ such that

$$A_{\mathbf{k}} = U_{+}(\mathbf{k})B_{\mathbf{k}}, \qquad \bar{A}_{\mathbf{k}} = \bar{B}_{\mathbf{k}}U_{-}^{\dagger}(\mathbf{k}). \tag{8.57}$$

Inserting Eq. 8.57 into the Hamiltonian in Eq. 8.54 and demanding that the result should be equal to

$$\hat{H} = \sum_{\mathbf{k}} E_{\mathbf{k}} b_{\mathbf{k}}^{\dagger} b_{\mathbf{k}} + E_{-\mathbf{k}} b_{-\mathbf{k}} b_{-\mathbf{k}}^{\dagger} \tag{8.58}$$

results in the Bogoliubov-de-Gennes equations

$$\mathcal{H}(\mathbf{k})U_{+}(\mathbf{k}) = U_{+}(\mathbf{k}) \begin{pmatrix} E_{\mathbf{k}} & 0 \\ 0 & -E_{-\mathbf{k}} \end{pmatrix} \tag{8.59}$$

which may be rewritten as two equivalent eigenvalue problems

$$(\mathcal{H}(\mathbf{k}) - E_{\mathbf{k}}\mathbb{1}) \begin{pmatrix} u_{\mathbf{k}}^{*} \\ v_{\mathbf{k}}^{*} \end{pmatrix} = 0, \qquad (\mathcal{H}(\mathbf{k}) + E_{-\mathbf{k}}\mathbb{1}) \begin{pmatrix} v_{\mathbf{k}} \\ u_{\mathbf{k}} \end{pmatrix} = 0. \tag{8.60}$$

Solving these finally gives

$$E_{\mathbf{k}} = \frac{1}{2}\left(\epsilon_{\mathbf{k}} - \epsilon_{-\mathbf{k}} \pm \sqrt{(\epsilon_{\mathbf{k}} + \epsilon_{-\mathbf{k}} + 2\mu)^2 - 4\Delta_{\mathbf{k}}^2}\right). \tag{8.61}$$

For $\Theta = 0$, this expression reduces to the one found in Refs. [48, 162] for the untilted spiral.

After some algebra, one can show that this expression is indeed equivalent to the result obtained from the stability of the equations of motion, Eq. (8.34).

8.3 EXACT SHORT TIME DYNAMICS

In order to get a first feeling for the quantum dynamics of the spiral, we here derive exact results for the first stage of the dynamics: the perturbative short time regime. We will first discuss the decay of the spiral magnetization for the tilted spiral discussed in this chapter. Then, we will move to the case of finite Jz anisotropy, where we discuss the short time dynamics of a recently realized xz-spiral (for finite anisotropy, the plane of the spiral winding matters). Finally, we will discuss the short time dynamics of the spiral fluctuations, which is most relevant for the discussion in the remainder of the chapter.

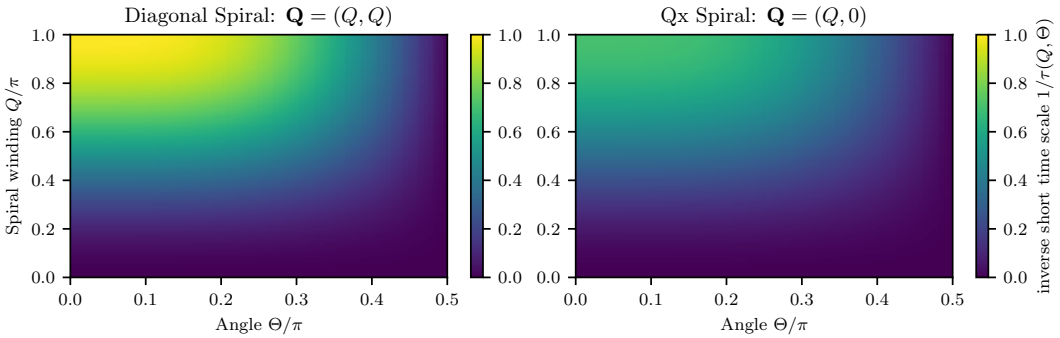

Figure 8.3: Short time decay constants of the spiral magnetization as a function of spiral wavenumber Q and tilt angle Θ.

8.3.1 *Spiral magnetization for tilted spiral*

We calculate the short time dynamics of the spiral magnetization $\hat{S}_\perp = \hat{S}^x_{\mathbf{Q}} + i\hat{S}^y_{\mathbf{Q}}$ by expanding $e^{iHt}\hat{S}_\perp e^{-iHt} \approx \hat{S}_\perp - \frac{t^2}{2}[\hat{H},[\hat{H},\hat{S}_\perp]]$. This expression is most conveniently evaluated in the rotating frame of the spiral. This gives

$$\hat{S}_\perp(t) \approx \frac{1}{2}\sin(\theta) - \left(\frac{t}{\tau(Q,\Theta)}\right)^2. \tag{8.62}$$

DIAGONAL SPIRALS For diagonal spirals $\mathbf{Q} = (Q, Q)$ we find

$$\begin{aligned}\frac{1}{\tau(Q,\Theta)^2} = \frac{1}{4}\Big[&\cos(Q)^2 - 2\cos(Q)\cos(\Theta)^2 + \cos(\Theta)^4 - 2\cos(Q)^2\sin(\Theta)^2 \\ &+ 2\cos(\Theta)^2\sin(\Theta)^2 - 2\cos(Q)\cos(\Theta)^2\sin(\Theta)^2 \\ &+ 2\cos(Q)^2\cos(\Theta)^2\sin(\Theta)^2 + \cos(Q)^2\sin(\Theta)^4\Big].\end{aligned} \tag{8.63}$$

For $\Theta \to 0$ this expression reduces to

$$\frac{1}{\tau(Q,\Theta)^2} = \frac{1}{4}(1-\cos(Q))^2, \tag{8.64}$$

which is the expression found in Ref. [48].

X-SPIRALS For x spirals we find

$$\begin{aligned}\frac{1}{\tau(Q,\Theta)^2} = \frac{1}{8}\Big[&\cos(Q)^2 - 2\cos(Q)\cos(\Theta)^2 + \cos(\Theta)^4 - 2\cos(Q)^2\sin(\Theta)^2 \\ &+ 2\cos(\Theta)^2\sin(\Theta)^2 - 2\cos(Q)\cos(\Theta)^2\sin(\Theta)^2 \\ &+ 2\cos(Q)^2\cos(\Theta)^2\sin(\Theta)^2 + \cos(Q)^2\sin(\Theta)^4 + 1 - 2\cos(\Theta)^2 \\ &+ \cos(\Theta)^4 - 2\sin(\Theta)^2 + 2\cos(\Theta)^2\sin(\Theta)^2 + \sin(\Theta)^4\Big].\end{aligned} \tag{8.65}$$

In Fig. 8.3 we show $1(\tau(Q,\Theta)$ for both the diagonal and x-spiral. Both spirals show a qualitatively similar behaviour, with $Q = 0$ and the $\Theta = \pi/2$ indicating

cases in which the spiral is an exact eigenstate of the Hamiltonian while the decay rate increases when going away from these limits. The x-spiral decays slower overall.

8.3.2 *Spiral magnetization for xz spirals in XXZ model*

Here we discuss the short time dynamics of the xz-spiral in the XXZ model, i.e. with a finite anisotropy Δ, defined via the Hamiltonian

$$\hat{H} = J \sum_i \left(S_i^x S_{i+1}^x + S_i^y S_{i+1}^y + \Delta S_i^z S_{i+1}^z \right) \tag{8.66}$$

with periodic boundary conditions. In this case, the plane in which the spiral winds matters. Here we discuss the x-z spiral recently realized in a cold-atom experiment [163],

$$|\psi_0\rangle = \Pi_i \left(\cos(\pi Q i/L) \, |\uparrow\rangle_i + \sin(\pi Q i/L) \, |\downarrow\rangle_i \right). \tag{8.67}$$

As before, we calculate the short time dynamics of the spiral magnetization $\hat{S}_\perp = \hat{S}_Q^z + i\hat{S}_Q^x$ giving the perturbative time scale

$$\begin{aligned}
\frac{1}{\tau(Q,\Delta)^2} = \frac{1}{256}\frac{1}{L}\sum_{k=0}^{L-1}\Big[& 32 - 32\cos(Q) - 32\Delta\cos(Q) \\
& + 8\cos^2(Q) + 16\Delta\cos^2(Q) \\
& + 8\Delta^2\cos^2(Q) - 16\cos(Q-2kQ) + 16\Delta\cos(Q-2kQ) \\
& + 8\cos(Q)\cos(Q-2kQ) - 8\Delta^2\cos(Q)\cos(Q-2kQ) \\
& + 4\cos^2(Q-2kQ) - 8\Delta\cos^2(Q-2kQ) \\
& + 4\Delta^2\cos^2(Q-2kQ) - 16\cos(Q+2kQ) \\
& + 16\Delta\cos(Q+2kQ) \\
& + 8\cos(Q)\cos(Q+2kQ) - 8\Delta^2\cos(Q)\cos(Q+2kQ) \\
& + 4\cos^2(Q+2kQ) - 8\Delta\cos^2(Q+2kQ) \\
& + 4\Delta^2\cos^2(Q+2kQ) + 4\sin^2((-1+2k)Q) \\
& - 8\Delta\sin^2((-1+2k)Q) + 4\Delta^2\sin^2((-1+2k)Q) \\
& + 8\sin((-1+2k)Q)\sin(Q+2kQ) \\
& - 16\Delta\sin((-1+2k)Q)\sin(Q+2kQ) \\
& + 8\Delta^2\sin((-1+2k)Q)\sin(Q+2kQ) + 4\sin^2(Q+2kQ) \\
& - 8\Delta\sin^2(Q+2kQ) + 4\Delta^2\sin^2(Q+2kQ)\Big]
\end{aligned} \tag{8.68}$$

For $\Delta \to 1$ this again reduces to the expression found in Ref. [48]. In Fig. 8.4 we show that time evolving block decimation (TEBD) data, exactly simulating the open

chain, collapses when we rescale time with our perturbative time scale, showing that the short-time universality indeed holds. Moreover, in Fig. 8.5 we show the perturbative timescale for several spiral wavenumbers as a function of anisotropy Δ. It is clearly visible that as the wavenumber vanishes ($Q \to 0$ or wavenumber $\lambda \to \infty$), the perturbative time scale diverges at $\Delta = 0$ due to the fact that the totally polarized state is an eigenstate of the Hamiltonian. However, even away from this limit the timescale can reach $10 - 100\,(1/J)$. This renders it difficult to reach timescales beyond this perturbative limit in current experiments.

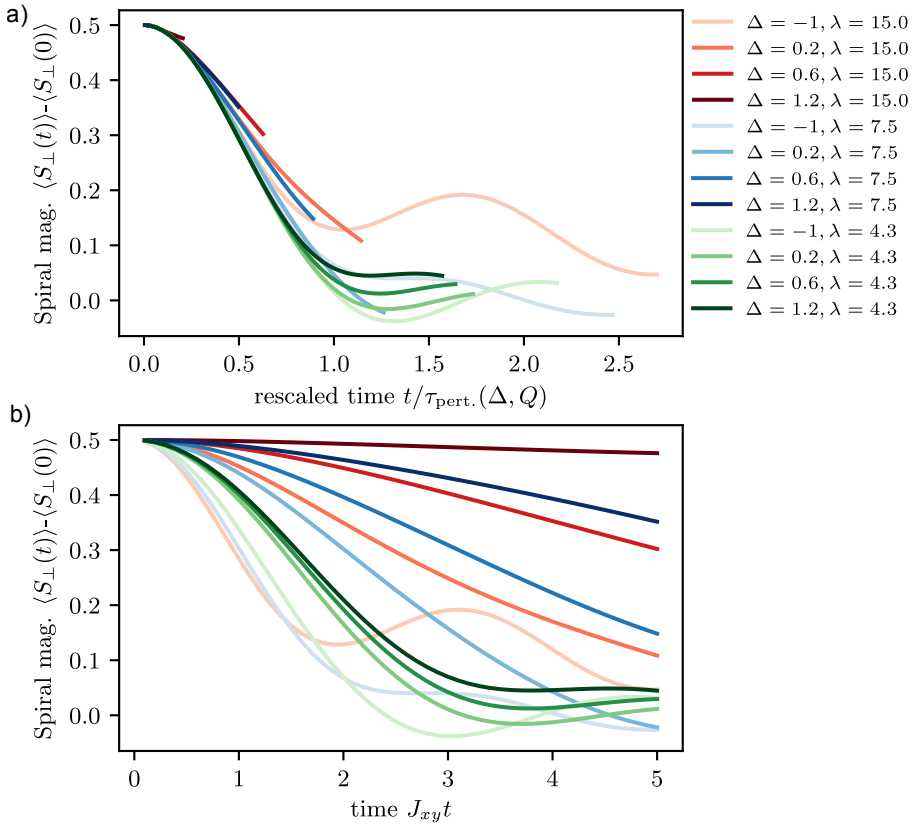

Figure 8.4: Short time scaling collapse of xz spiral dynamics. Obtained with TEBD-MPS, open boundary conditions, system size $L = 30$ and spiral wavevector given by $Q = \pi/\lambda$. All curves have been evolved to $5Jt$. Deviations from the collapse are due to the differing boundary conditions, are more strongly pronounced as $Q \to 0, \Delta \to 1$ and less pronounced as L is increased. b) Unrescaled data

8.3.3 *Fluctuations*

We consider the general Heisenberg model

$$\hat{H} = \sum_{i \neq j} J_{ij} \left(\hat{S}_i^+ \hat{S}_j^- + \hat{S}_i^z \hat{S}_j^z \right), \tag{8.69}$$

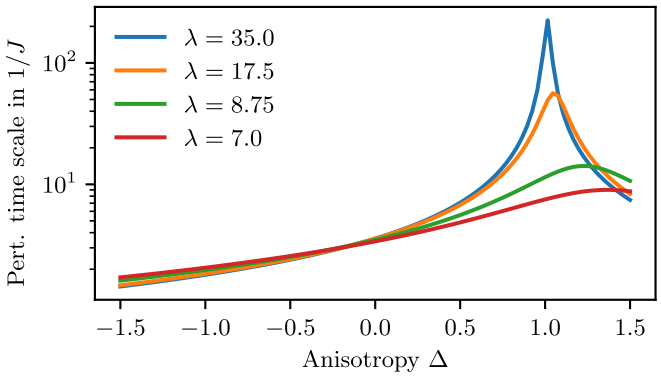

Figure 8.5: Perturbative time scale as a function of anisotropy for several spiral wavevectors given by $Q = \pi/\lambda$. System size $L = 35$.

where $\hat{S}_i^+ = \hat{S}_i^x + i\hat{S}_i^y$ and we assume real couplings $J_{ij} = J_{ji}$. We calculate the short time dynamics of the zz-fluctuations $C_{\mathbf{k}}^{zz} = \frac{1}{N}\sum_{i,j} e^{i\mathbf{k}(\mathbf{r}_i - \mathbf{r}_j)} \langle\Psi(t)|\hat{S}_i^z\hat{S}_j^z|\Psi(t)\rangle$ by expanding

$$C_{\mathbf{k}}^{zz}(t) \approx C_{\mathbf{k}}^{zz}(0) - \frac{t^2}{2}\frac{1}{N}\sum_{i,j} e^{i\mathbf{k}(\mathbf{r}_i - \mathbf{r}_j)} \langle\Psi(0)|[\hat{H},[\hat{H},\hat{S}_i^z\hat{S}_j^z]]|\Psi(0)\rangle\,. \tag{8.70}$$

The expression can be easiest evaluated for the spiral initial state by introducing the unwinding transformation U as $\langle\Psi(0)|U^\dagger U[\hat{H},[\hat{H},\hat{S}_i^z\hat{S}_j^z]]U^\dagger U|\Psi(0)\rangle$ with $U|\Psi(0)\rangle = |\uparrow\cdots\uparrow\rangle_x$ and $US_i^\pm U^\dagger = e^{\mp i\mathbf{Q}\mathbf{r}_i}S_i^\pm$, $US_i^zU^\dagger = S_i^z$ *after* calculating the double commutator. The general result is

$$\begin{aligned}\langle\Psi(0)|[\hat{H},[\hat{H},\hat{S}_k^z\hat{S}_l^z]]|\Psi(0)\rangle = &-\frac{1}{4}J_{kl}\sum_j(J_{kj}+J_{jl})(\cos(\mathbf{Q}\mathbf{r}_{jk})+\cos(\mathbf{Q}\mathbf{r}_{jl})\\ &+\frac{1}{2}J_{kl}^2\left(\cos(\mathbf{Q}\mathbf{r}_{kl})-\cos^2(\mathbf{Q}\mathbf{r}_{kl})\right)\\ &+\frac{1}{4}\sum_j J_{lj}J_{jk}\left(\cos(\mathbf{Q}\mathbf{r}_{jl})+\cos(\mathbf{Q}\mathbf{r}_{jk})-2\cos(\mathbf{Q}\mathbf{r}_{jk})\cos(\mathbf{Q}\mathbf{r}_{jl})\right)\\ &+\frac{1}{2}J_{kl}\cos(\mathbf{Q}\mathbf{r}_{kl})\left(\sum_j J_{lj}\cos(\mathbf{Q}\mathbf{r}_{jl})+\sum_j J_{jk}\cos(\mathbf{Q}\mathbf{r}_{jk})\right),\end{aligned} \tag{8.71}$$

where $\mathbf{r}_{jk} = \mathbf{r}_j - \mathbf{r}_k$.

NEAREST NEIGHBOUR 1D Evaluating this expression for 1D nearest neighbour interactions $J_{ij} = \delta_{j,i+1} + \delta_{j,i-1}$, we find

$$C_k^{zz}(t) \approx \frac{1}{4} - \frac{t^2}{2}\Big\{\left(\cos(k)-\cos(2k)\right)\left(\cos^2 Q - \cos Q\right)\Big\}. \tag{8.72}$$

The short time scale in angle brackets vanishes for both $k = 0$ and $Q = 0$ as expected and agrees with an exact MPS simulation at short times, see Fig. 8.6. Importantly, the location of the maximum of the short time scale is *independent* of Q and located at $k = \pm\text{atan}(\sqrt{15}) \approx \pm 0.42\pi$.

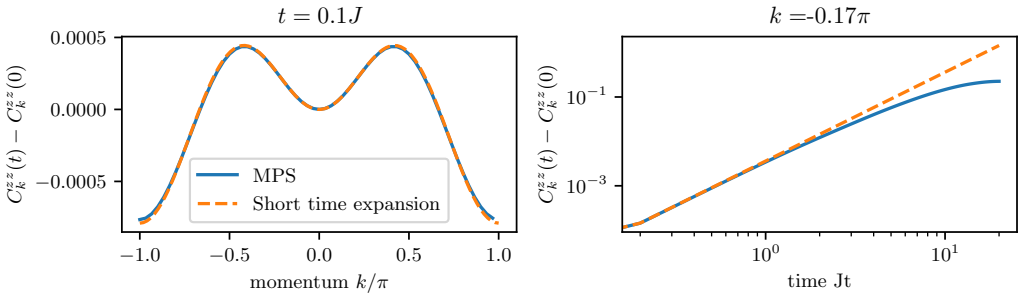

Figure 8.6: Comparison between Eq. 8.72 and an iTEBD simulation for $Q = 0.13\pi$.

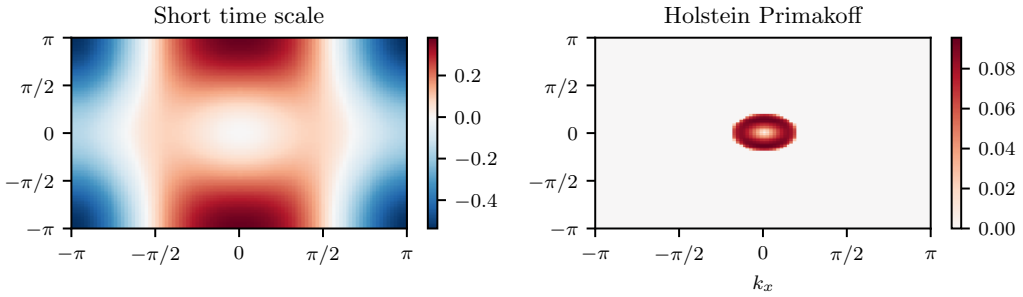

Figure 8.7: Comparison of inverse short time scale for fluctuations and the imaginary part of the Holstein-Primakoff dispersion $\mathrm{Im}(E(k))$. $\mathbf{Q} = (0.2\pi, 0), \Theta = 0$.

NEAREST NEIGHBOUR 2D For nearest neighbour interactions in 2D we find for a general spiral with wavevector $\mathbf{Q} = (Q_x, Q_y)$

$$\begin{aligned}
&\frac{1}{4} - C^{zz}_{\mathbf{k}}(t) \\
&\approx \frac{t^2}{2}\Big\{ \cos(k_x)\left(-\cos(Q_x) - 2\cos(Q_y) + \cos^2(Q_x) + 2\cos(Q_x)\cos(Q_y)\right) \\
&\quad + \cos(k_y)\left(-\cos(Q_y) - 2\cos(Q_x) + \cos^2(Q_y) + 2\cos(Q_x)\cos(Q_y)\right) \\
&\quad + \cos(2k_x)\left(\cos(Q_x) - \cos^2(Q_x)\right) \\
&\quad + \cos(2k_y)\left(\cos(Q_y) - \cos^2(Q_y)\right) \\
&\quad + 2\cos(k_x)\cos(k_y)\left(\cos(Q_x) + \cos(Q_y) - 2\cos(Q_y)\cos(Q_x)\right)\Big\}. \qquad (8.73)
\end{aligned}$$

In Fig. 8.7 we compare the short time scale of the fluctuations to the imaginary part of the Holstein Primakoff dispersion, showing that they are different. This shows that the instability predicted by the Holstein Primakoff analysis is indeed a non-perturbative phenomenon. As the short time expansion is exact, this also means that there will be a crossover at intermediate times between the domination of the $(0, \pm\pi)$ mode at short times and the small momentum modes at longer times, when the Holstein Primakoff instability becomes important. In the following, we

will study this intermediate time regime within 2PI before studying the instability for small spiral wavevector Q in more detail with semi-classical methods.

8.4 CROSSOVER FROM SHORT TIME TO INSTABILITY DYNAMICS FROM SPIN 2PI

We solve the full quantum dynamics of the spiral within the GW expansion employed in spin 2PI [48], which we introduced in section 2.2. We will elucidate to which extent the decay of the spiral contrast and the growth of spin fluctuations reflect the instabilities predicted by the Holstein-Primakoff analysis. We note that the mean field equations only show a precession of the magnetization for $\Theta \neq 0$, equivalent to an effective magnetic field term $2J\sum_d(\cos Q_d - 1)\sin\Theta\sum_i \hat{S}_i^z$ in the Hamiltonian. All observables considered below show no dynamics in the mean field approximation, i.e. all results shown here exclusively result from the treatment of quantum fluctuations by including the GW diagram.

8.4.1 *Decay of the spiral contrast*

Due to translational invariance and conservation of the total magnetization $\langle \hat{S}^z \rangle = \frac{1}{2}\sin(\Theta)$, the spiral contrast, defined as

$$S_\perp(\mathbf{Q}) = \frac{1}{N}\left|\sum_j e^{i\mathbf{Q}\mathbf{R}_j}\langle\Psi|\hat{S}_j^+|\Psi\rangle\right| \tag{8.74}$$

with $\hat{S}_j^+ = \hat{S}_j^x + i\hat{S}_j^y$ is the only single-spin observable [48] for $\Theta = 0$. Oscillations around the z axis due to the mean-field precession for $\Theta \neq 0$ are not visible in this observable as they would only show up in $\langle \hat{S}^{x/y} \rangle$. Here, we are however mainly interested in the decay of the contrast rather than the oscillation.

Within spin-2PI, we find an exponential decay of the spiral contrast for most values of $\mathbf{Q}$ and Θ. Only for diagonal spirals with $\mathbf{Q} \lesssim 0.9\pi$ and $\Theta \lesssim 0.2\pi$ we find a pronounced linear decay for intermediate times $Jt \lesssim 20$ as we show in Fig. 8.8, reminiscent of the prethermal plateau found in 3D [48]. We do not find such a plateau for x-spirals.

In Fig. 8.9 we show the decay rate of the spiral scanned across the $\mathbf{Q}$,Θ plane for both diagonal and x-spirals, obtained by a fit $S_\perp(t) \sim \exp(-\gamma t)$ at times $10 > Jt > 5$. Comparing with the imaginary part of the Holstein Primakoff dispersion in Fig. 8.3 we find good agreement of the qualitative features for the x-spiral. However, while the Holstein-Primakoff analysis predicts similar behaviour for diagonal and x-spirals, we find a dip of the decay rate around $Q = \pi, \Theta = 0$ due to the emergence of the plateau-like structure discussed previously. For small $Q \ll \pi/2$, the decay

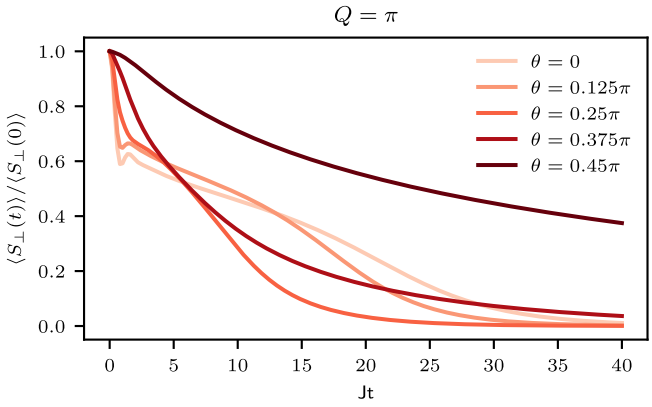

Figure 8.8: **Slow decay of spiral contrast for diagonal spirals with $\mathbf{Q} = (\pi, \pi)$.–** The spiral contrast shows a two-stage decay process, where the first, slow stage becomes less pronounced as the tilt increases. We only find this slow stage for $Q \gtrsim 0.9\pi$. The late time behaviour is given by an exponential decay.

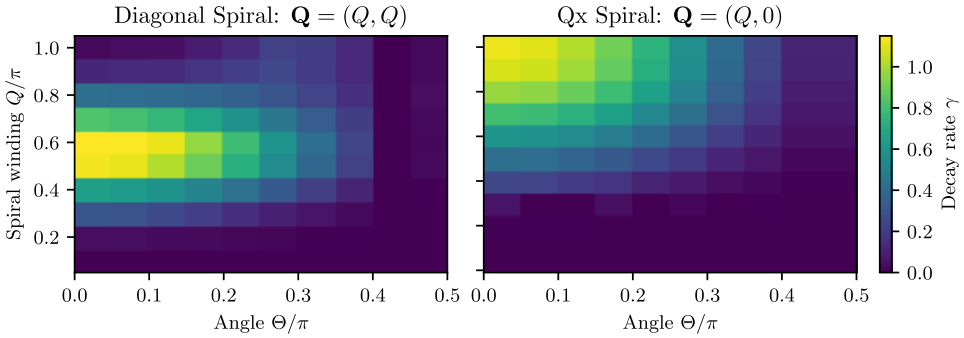

Figure 8.9: **Decay rate γ of the spiral magnetization from spin 2PI.–** Obtained by fitting the spiral magetization with an exponential decay $S_\perp(t) \sim \exp(-\gamma t)$ for times $5 < Jt < 10$. The Q, Θ dependence of the decay rate resembles the stability phase diagrams of the Holstein Primakoff Bosons.

rate however does decrease monotonically for Q decreasing and Θ increasing for both spiral types, as predicted from the Holstein-Primakoff analysis.

In order to elucidate whether the instabilities predicted in the Holstein-Primakoff analysis are really the underlying mechanisms of the spiral decay and whether and how they are regulated by interactions, we will look at the growth of spin fluctuations in the following.

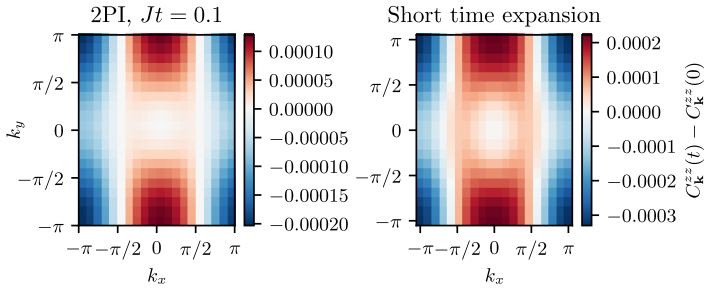

Figure 8.10: Comparison between Eq. 8.73 and a 2PI simulation for $Q_x = 0.159\pi, Q_y = 0$. Note the different color scales.

8.4.2 *Fluctuations*

Here we study the "out-of-plane" and "in-plane" connected spin correlation functions defined by

$$C^{zz}_{\mathbf{k}}(t) = \frac{1}{N}\sum_{i,j} e^{i\mathbf{k}(\mathbf{R}_i - \mathbf{R}_j)} \left(\langle \hat{S}^z_i(t)\hat{S}^z_j(t)\rangle - \langle \hat{S}^z_i(t)\rangle \langle \hat{S}^z_j(t)\rangle \right), \tag{8.75}$$

$$C^{+-}_{\mathbf{k}}(t) = \frac{1}{N}\sum_{i,j} e^{i\mathbf{k}(\mathbf{R}_i - \mathbf{R}_j)} \left(\langle \hat{S}^+_i(t)\hat{S}^-_j(t)\rangle - \langle \hat{S}^+_i(t)\rangle \langle \hat{S}^-_j(t)\rangle \right). \tag{8.76}$$

Due to the operator identity $(\hat{S}^\alpha_j)^2 = 1/4$ for $\alpha \in \{x, y, z\}$, both $C^{zz}_{\mathbf{k}}(0) = \frac{1}{4}\cos^2(\Theta)$ and $C^{+-}_{\mathbf{k}}(0) = \frac{1}{4}(1 + \sin^2(\Theta))$ are nonzero initially even for this product state, but homogeneous in $\mathbf{k}$ space. Moreover, C^{zz} fulfills the non-equilibrium sum rule

$$\frac{1}{N}\sum_{\mathbf{k}} C^{zz}_{\mathbf{k}}(t) = \frac{1}{4}\cos^2(\Theta), \tag{8.77}$$

with $C^{+-}_{\mathbf{k}}(t)$ left unconstrained [1].

SHORT-TIME DYNAMICS In order to benchmark our 2PI simulation, we first compare the short time dynamics to the exact result. We find qualitative agreemeent of the main structures, see Fig. 8.10, i.e. a growth of modes around $k_x = 0, k_y = \pm\pi$ and a decay around $k_x = \pm\pi, k_y = \pm\pi$. However, there are quantitative differences, for example in the ring-like structure around $k_x = 0, k_y = 0$.

Within spin 2PI, we extract the connected spin correlation functions from the auxiliary field correlator introduced by the GW approximation, see section 2.1.4. It can be shown that this is equivalent to solving the Bethe-Salpeter equation for the Majorana vertex up to leading order in 1/N, i.e. up to the RPA diagram for the vertex [48]. We checked for some cases that there are no qualitative differences when

1 While the sum rule is exactly fulfilled for the Majorana Green's function in spin 2PI for all times and for the spin correlators extracted from the auxiliary field correlator at the initial time by construction, we found some deviations for the latter at finite times.

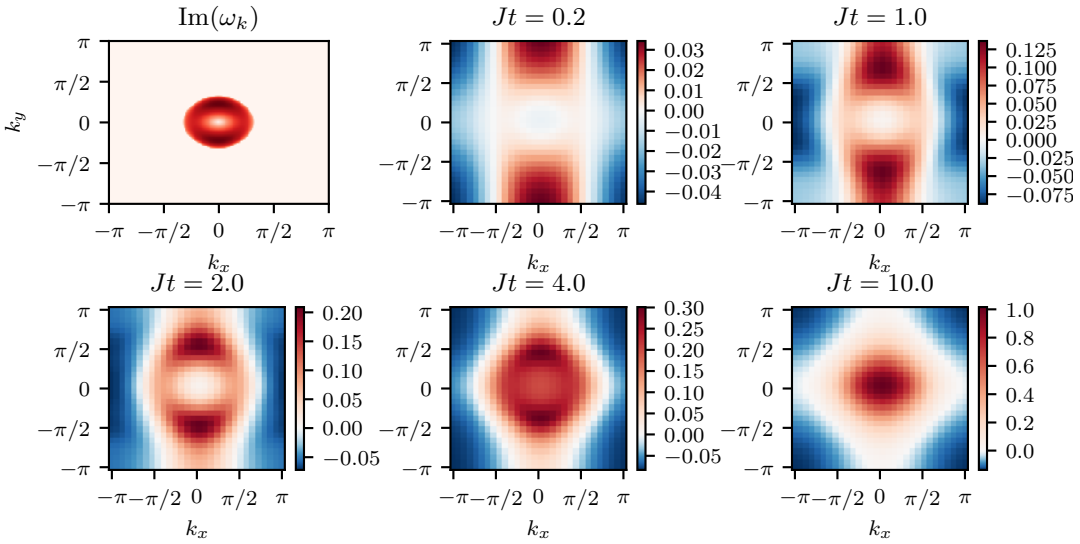

Figure 8.11: Crossover from short time dynamics to instability from spin 2PI as measured by the C^{zz} flucutations. Leftmost plot is the imaginary part of the Holstein Primakoff dispersion, Eq. 8.43. x-spiral with wavenumber $Qx = 0.323\pi.\Theta = 0$.

also including part of the NLO contribution to the vertex, i.e. the Maki-Thompson diagram.

BUILD-UP OF THE INSTABILITY In the short time analysis we saw that spin fluctations do not reflect the instabilities predicted by the Holstein-Primakoff analysis from the shortest possible times. In Fig. 8.11 we show that instead, the fluctuations only slowly get dominated slowly by the modes predicted to be most unstable. The largest wavenumber moves continuously from $(0, \pm\pi)$ to smaller momenta as time evolves. Due to the sum rule in Eq. 8.77, some modes have to become negative as the unstable modes grow. These are at the corners of the Brillouin zone. Although it is to be expected that the largest mode moves up to the mode predicted by the Holstein-Primakoff analysis and then stops there, we see a contuous move up until $(0, 0)$ within spin 2PI. Contrastingly, within TWA and MPS we will see this behaviour in the coming sections.

The spurious behaviour within 2PI is hence an artefact of the method as the $(0, 0)$ mode needs to vanish for all times due to spin conservation. As we discussed in the introductory chapters about spin 2PI, this violation of a sum rule is most likely due to the fact that the correspondence between the auxiliary field correlators and the spin correlation function does not hold exactly any more when employing approximations.

In Fig. 8.12 we show the time evolution of a momentum space cut at $k_x = 0$ for various spiral parameters alongside the imaginary part of the Holstein-Primaoff dispersion. While qualitatively, the latter gives similar results, the spin 2PI analysis

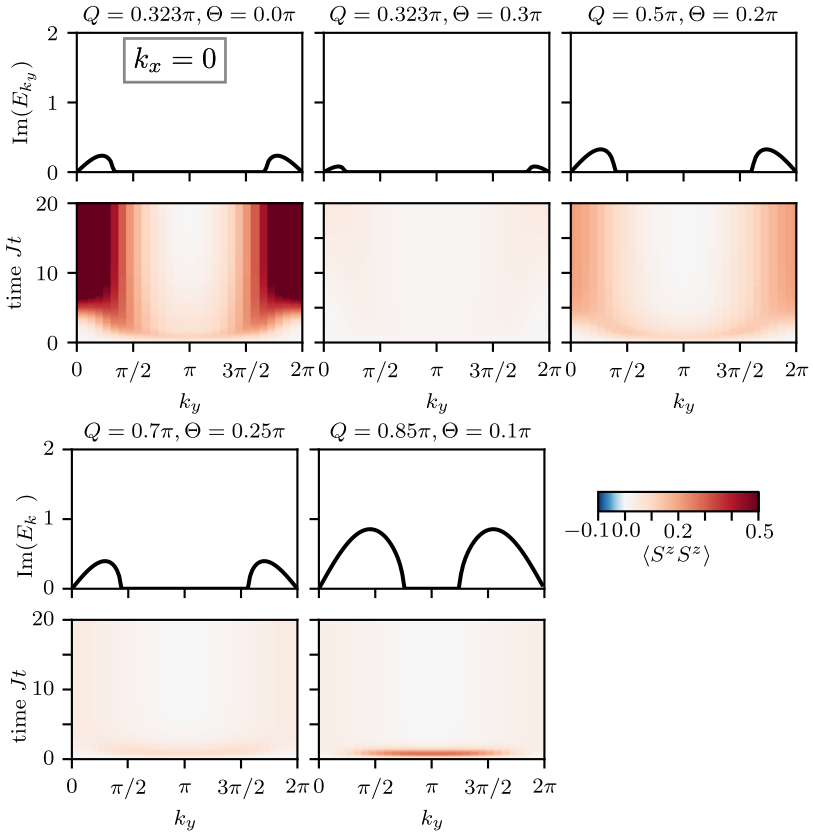

Figure 8.12: Time evolution of the fluctuations for different spiral wavenumbers and tilts Θ.

predicts that the spiral is more stable than expected from the imaginary part of the dispersion - the modes initially start growing around $k_y = 0$ but then start decaying again. However, these results are to be taken with care due to the challenges for interpreting fluctuation data from spin 2PI discussed above.

8.5 INSTABILITY DYNAMICS FROM SEMICLASSICAL METHODS

To complement the Bogoliubov analysis, we compute real time dynamics of the spiral decay by incorporating quantum fluctuations using the Truncated Wigner Approximation[419]. Defining $\langle \hat{\mathbf{S}}_j^{\perp} \rangle$ as the transverse magnetization of the initial condition (8.3), we assume Gaussian fluctuations of $\hat{\mathbf{S}}_j^{\perp}$ given by $\langle \hat{\mathbf{S}}_j^{\perp} \rangle = 0$ and $\langle \hat{\mathbf{S}}_j^{\perp} \cdot \hat{\mathbf{S}}_j^{\perp} \rangle = S$.

Figure 8.13(a) shows a single realization of TWA noise for a spin spiral with parameters $\theta = \pi/4$ and $q_x = 0.5$ (same parameters as in Fig.8.1). Independently of the spin number S, we consistently observe growth of unstable modes that lead to a disordered state. Analysis of the connected correlation $\langle \hat{S}^x_{-\mathbf{K}} \hat{S}^x_{\mathbf{K}} \rangle_c = \langle \hat{S}^x_{-\mathbf{K}} \hat{S}^x_{\mathbf{K}} \rangle - \langle \hat{S}^x_{-\mathbf{K}} \rangle \langle \hat{S}^x_{\mathbf{K}} \rangle$ [shown in Fig.8.13(b), with $\mathbf{K}$ the absolute wavevector] reveals that the spiral state is primarily decaying into modes located in a ring around the wavevector

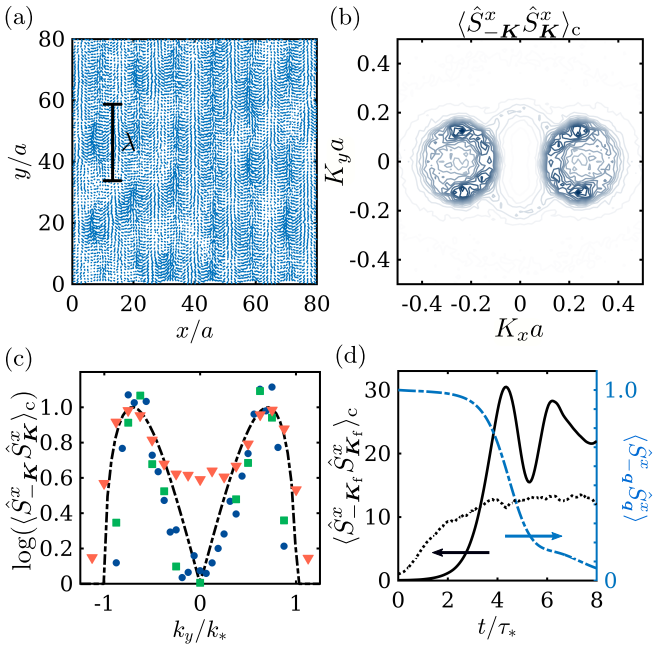

Figure 8.13: Real space snapshot of a single TWA realization at $t/\tau_* = 3.5$, see Eq.(8.1). Shown are snapshots of the spins $\hat{\mathbf{S}}_j$ projected on the xy plane. Indicated with a bar is the wavelength in the y direction of the fastest growing mode. (b) Contour plot showing the connected correlation $\langle \hat{S}^x_{-\mathbf{K}} \hat{S}^x_{\mathbf{K}} \rangle_c$ corresponding to panel (a). Consistent with the Bogoliubov analysis, the plot exhibits a ring of unstable modes around $\mathbf{q}$ with size $k_* \approx q_x \sin\theta$ and a maximal amplitude transverse to $\mathbf{q}$. Parameters used in panel (a,b): $\theta = \pi/4$, $q_x = 0.25$, $q_y = 0$, $S = 10$ averaged over 50 realizations. (c) Spatial-temporal scaling of $\langle \hat{S}^x_{-\mathbf{K}} \hat{S}^x_{\mathbf{K}} \rangle_c$. Shown is the log of $\langle \hat{S}^x_{-\mathbf{K}} \hat{S}^x_{\mathbf{K}} \rangle_c$ for $\mathbf{K} = (q_x, k_y)$ and $t/\tau_* = 3.5$, and for different initial conditions: $(q_x, \theta) = (0.25, \pi/2)$ (circles), $(0.5, \pi/2)$ (squares) and $(0.25, \pi/4)$ (triangles) and $S = 10$. The dotted-dashed line is the Bogoliubov $Im[\omega]$ in Eq.(8.36) as a guide to the eye. (d) Growth of the most unstable mode, $\mathbf{K}_f = (q_x, \tilde{k}_y)$, showing saturation and subsequent oscillations for $S = 10$ (solid line) and $S = 1/2$ (dotted lines). Also shown is the depletion of the spin spiral (dashed-dotted line).

$\mathbf{q}$, preferentially in the direction perpendicular to $\mathbf{q}$, thus confirming the Bogoliubov analysis above.

In addition, Fig.8.13(c) shows the scaling of fluctuations for wavectors $\mathbf{K} = (q_x, k_y)$ and various initial conditions at the rescaled time $t/\tau_* = 3.5$. Given that we expect unstable modes to grow as $S^+_{\mathbf{K}}(t) \approx S^+_{\mathbf{K}}(0) e^{t/\tau_{\mathbf{K}}}$, the y axis is plotted in log scale and the correlation $\langle \hat{S}^x_{-\mathbf{K}} \hat{S}^x_{\mathbf{K}} \rangle_c$ is normalized with the maximum value as a function of k_y for each initial condition. We observe excellent agreement with the Bogoliubov analysis for all $\mathbf{q}$ and θ.

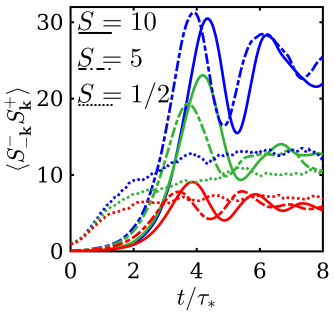

Figure 8.14: Growth of the most unstable mode showing saturation and subsequent oscillations plotted for different initial conditions and spin number S. The colorcode indicates simulations with different $\boldsymbol{q}$: $q_x a = 0.25$ (blue), $q_x a = 0.37$ (green), and $q_x a = 0.5$ (red). The linestyle indicates models with different value of S. All figures use $\theta = \pi/2$.

INSTABILITY GROWTH AND SELF-REGULARIZATION Going beyond the linear stability analysis, we inquire about the intermediate timescale dynamics of instability growth. Figure 8.13(d) shows the decay of the spin spiral and multiple stages in the evolution of the most unstable mode: (i) initial growth compatible with the Bogoliubov analysis above, (ii) saturation, (iii) coherent oscillations prior to equilibration. Unlike usual instabilities in BEC where unstable modes grow exponentially for long times, the local constraint $\hat{S}_j^2 = S(S+1)$ and the conservation of total magnetization regulates the growth of the transverse spin modulation at relatively short times, analogously to Refs. [48, 49, 479]. We observe that saturation occurs at $t \approx 4\tau_*$, irrespective of the value of S, $\mathbf{q}$ and θ. In Figure 8.14, we show this behavior for various initial conditions and values of the spin number S.

The existence of unstable modes in the linearized analysis and the small oscillations in Fig.8.13(d) are linked to the existence of smooth, symmetry-allowed deformations of the spin spiral order with a valley-shaped potential. Using the insights gained from the Bogoliubov analysis, we propose a simple Ansatz for a transverse spin texture given by $S_j^{\pm} = S \sin\theta_i e^{\pm i \mathbf{q}\cdot\mathbf{r}_j}$ and $S_j^z = S\cos\theta_j$, with $\theta_j = \bar{\theta} + 2\delta\theta \cos(\tilde{k}_y y_i)$ and $\tilde{k}_y$ defined below Eq.(8.36) [see Fig.8.2(a)]. The value of $\delta\theta$ controls the amplitude of transverse spin deformations around $\bar{\theta}$ and is modulated by the transverse wavevector $\tilde{k}_y$. This ansatz trivially satisfies $\sum_j S_j^{\pm} = 0$ for all values of $\bar{\theta}$ and $\delta\theta$, and the condition $\frac{1}{N}\sum_j S_j^z = S\cos\theta$ defines a constraint that links $\bar{\theta}$ and $\delta\theta$. Because we recover Eq.(8.3) when $\bar{\theta} = \theta$ and $\delta\theta = 0$, our Ansatz is smoothly connected to the original spiral and preserves its total magnetization. Figure 8.2(b) shows that increasing the transverse modulation $\delta\theta$ reduces the energy of the spin spiral. In addition, the observed oscillations in Fig.8.13(d) can be interpreted as amplitude oscillations on a valley-shaped potential. The same argument

can be applied to any value of $\mathbf{k}$ that satisfies the instability condition (8.35), but the valley is deepest for $\mathbf{K} = (q_x, \tilde{k}_y)$.

CROSSOVER TO THE QUANTUM REGIME The stability analysis above relies on a $1/S$ expansion of the equations of motion, opening the question on its validity in the experimentally relevant $S = 1/2$ case. The competition between quantumness in the $S \to 1/2$ limit and classicality in the $\mathbf{q} \to 0$ limit suggests that a smeared, but still observable, ring of unstable modes is obtained for finite but small $\mathbf{q}$ and $S = 1/2$. Indeed, our numerics reveal that strong quantum fluctuations supress the exponential growth of unstable modes and smear out coherent oscillations in the two-point correlation function [see Fig.8.13(d)], but the latter still exhibits an imprint of the ring of unstable modes, see Fig.8.2(c). Remarkably, we also find that our simple semiclassical picture essentially survives in the one-dimensional Heisenberg model despite integrability and reduced dimensionality, as shown with Matrix Product States and TWA in the Supplement (in this case, the most unstable modes are necessarily collinear with q_x).

CROSSOVER TO MODULATIONAL INSTABILITY To study the crossover between the transverse instability in the Heisenberg model ($J_z = J$) to the modulational instability that characterizes a superfluid on a lattice, we extend the Bogoliubov analysis for values of $J_z < J$ (see details in the Supplement). Tuning J_z can be realized experimentally using Feshbach resonances, dipolar interactions or lattice shacking [160, 206, 480–482]. The anisotropic exchange energetically penalizes the transverse deformation of the spin spiral order. In the language of the stability condition in Eq.(8.35), the pairing $\Delta_{\mathbf{k}}$ becomes repulsive, $\Delta_{\mathbf{k}} \approx (J - J_z)$. While breaking the SU(2) symmetry has a stabilizing effect on the spin spiral state, there is still a strong reduction of the critical wavevector far from the SU(2) symmetric point, as shown in Fig.8.2(d). This suggests that the instability mechanism that we describe is also relevant for materials with anisotropic exchange.

8.6 SPIN SPIRALS IN 1D USING MATRIX PRODUCT STATE METHODS

8.6.1 *Transverse instability*

Here we show that the dynamics described previously for two-dimensional spin spirals in the large S limit are also relevant for $S = 1/2$ in 1D. We focus on

full spirals with $\theta = \pi/2$. In Fig. 8.15 we display the connected spin correlation functions

$$\begin{aligned} C^{zz}_k(t) &\equiv \langle \hat{S}^z_k(t)\hat{S}^z_{-k}(t)\rangle, \\ C^{+-}_k(t) &\equiv \langle \hat{S}^+_k(t)\hat{S}^-_{-k}(t)\rangle - \langle \hat{S}^+_k(t)\rangle\langle \hat{S}^-_{-k}(t)\rangle, \end{aligned} \tag{8.78}$$

for a spiral wavelength $Q = 0.13\pi$ obtained from MPS-iTEBD simulations employing the TeNPy package [89], with a unit cell chosen large enough to fit the spiral (here: $L = 90$). For very short times, pertubartive short time dynamics dominate, see derivation below. At around $Jt = 5$, the dynamic instability takes over, leading to a growth of fluctuations with momenta around the spiral wavelength, $k = \pm Q$. The distribution of fluctuations in momentum space approximately agree with the imaginary part of the Bogoliobov dispersion. We find similar signatures of the instability in the C^{+-} correlations. However, we find the that low-momentum part ($k \leq Q$) of the "double lobe" structure of the Bogoliubov dispersion dominates over the large-momentum part ($k > Q$).

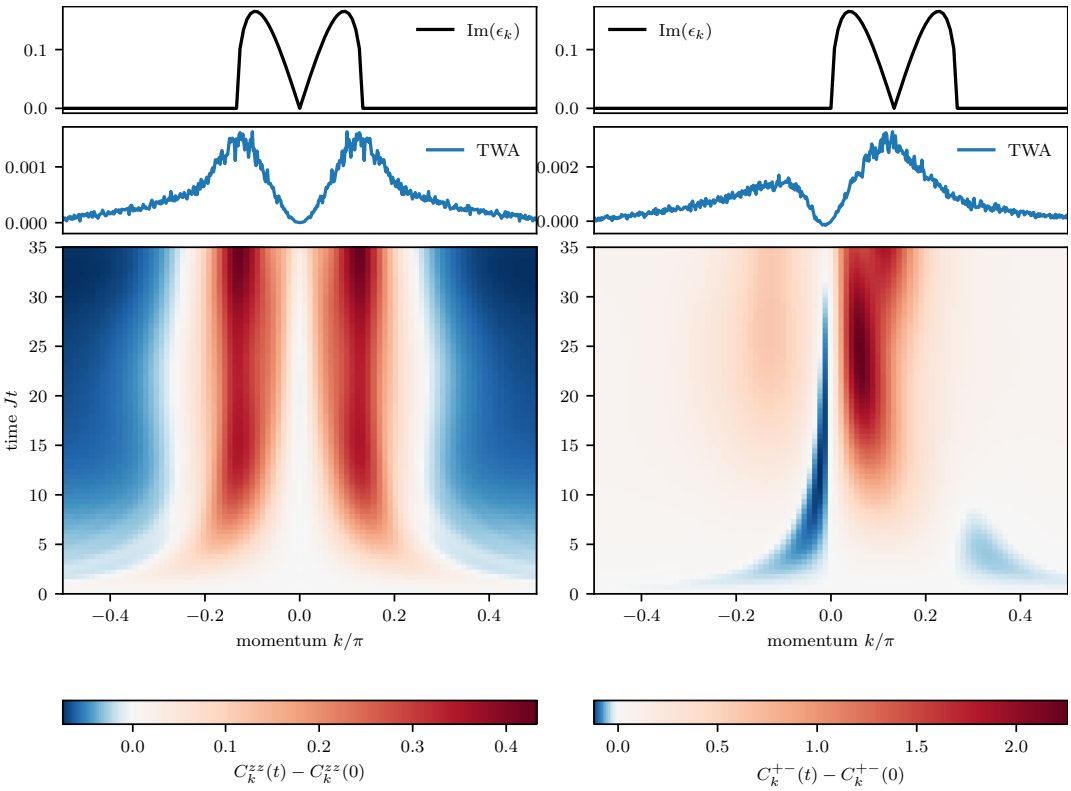

Figure 8.15: Growth of spiral fluctations in 1D. Shown are the $C^{zz}_{\mathbf{k}}$ and $C^{+-}_{\mathbf{k}}$ correlations for a spiral wavelength $Q = 0.13\pi$, obtained from iTEBD-MPS simulations. The upper panels show the results of the Bogoliubov analysis, and TWA calculations for $tJ = 15$.

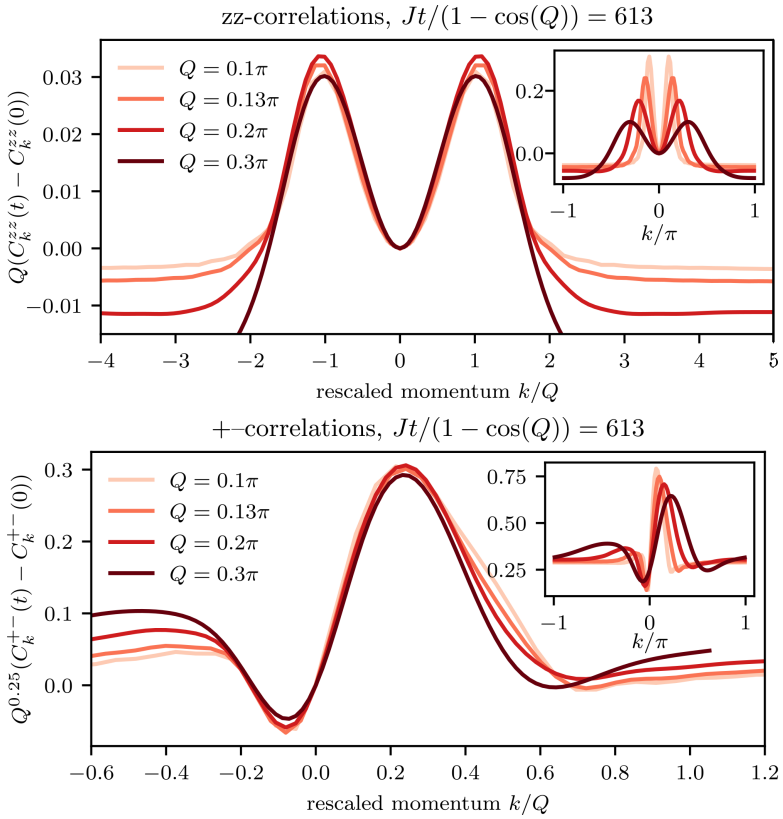

Figure 8.16: Spatial-temporal scaling of spin fluctuations. Shown is the C^{+-} and C^{zz} correlations as defined in Eq. (8.78) rescaled according to the scaling function in Eq. (8.79), with the rescaled time $Jt/(1-\cos(Q))$ fixed. Insets: Unrescaled correlation functions.

In analogy with the scaling of fluctuations shown in in Fig. 8.13(c), we also find scaling in the growth of fluctuations. As shown in Fig. 8.16, the scaling relation is given by

$$C_k^{ab}\left(\frac{Jt}{1-\cos(Q)}\right) - C_k^{ab}(0) = Q^{-\alpha} f\left(\frac{k}{Q^{\beta}}\right). \tag{8.79}$$

While the time and momentum rescaling factors $\beta = 1$ are obtained analytically from the Bogoliubov treatment, we find $\alpha \approx 0.25$ for $ab = +-$ and $\alpha \approx 1$ for $ab = zz$ numerically from our MPS simulations. Note that our results can not be explained by a simple perturbative short time scaling. Indeed, we analytically show next that the perturbative short time scale is *Q-independent*, in contrast to the k/Q dependence we find here.

8.6.2 *Benchmark for spin 2PI*

We can also use the one-dimensional case to benchmark our 2PI simulations. In Fig. 8.17 we show the comparison between exact TEBD simulations and Majorna

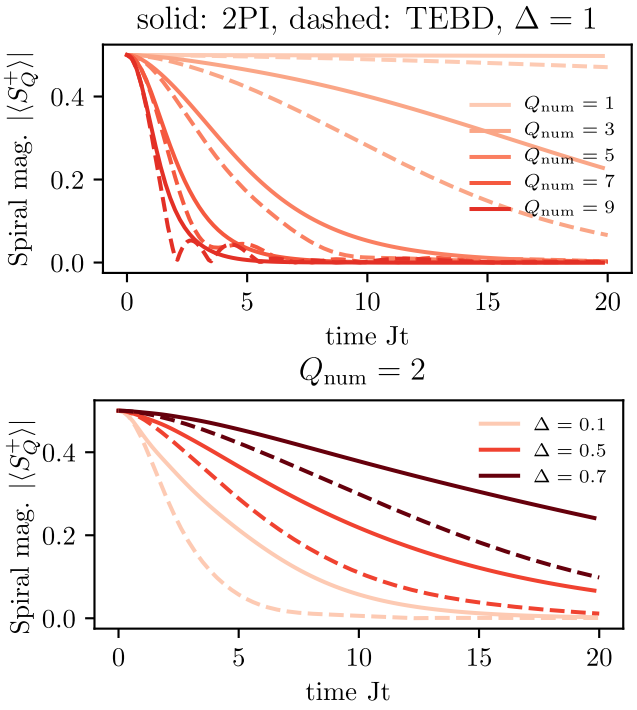

Figure 8.17: Comparison of TEBD and 2PI for a spiral of wavevector $Q = Q_{\text{num}} \times 2\pi/30$, i.e. a system with $L = 30$ sites. The spiral is winding around the z-axis, i.e. in the xy plane.

spin 2PI for the decay of the spiral magnetization in the anisotropic Heisenberg model

$$\hat{H} = J \sum_i \left(S_i^x S_{i+1}^x + S_i^y S_{i+1}^y + \Delta S_i^z S_{i+1}^z \right). \tag{8.80}$$

While quantitative differences are clearly visible, the qualitative trends, i.e. parameter dependencies on Q and Δ seem to be reproduced. Note that 1D nearest neighbour interactions are in a sense the hardest case for 2PI: The approach develops onto the mean-field limit, which becomes more valid as the dimensionality and/or range of the interactions is increased. Hence, we expect 2PI to work better in the two-dimensional case we discussed previously.

8.6.3 *Imperfections in quantum simulators of spiral dynamics*

The decay of spiral states has been recently studied [162, 163] in cold atom quantum simulators, where the two spin 1/2 spin states are encoded in the two hyperfine states of the Bosonic atoms. In the Mott insulating regime at large on-site interactions and unit filling, the charge dynamics are frozen and the spin dynamics are effectively described by a Heisenberg model [483–485]. The anisotropy Δ can be tuned by the ratio between interstate and intrastate on-site interactions. In the following, we will

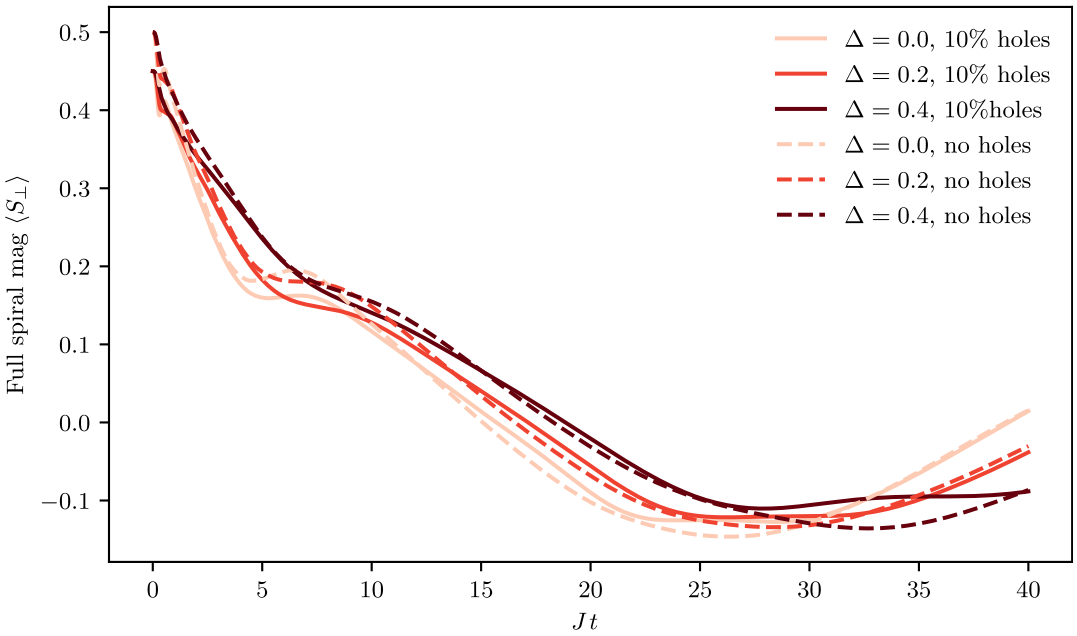

Figure 8.18: Comparison of spiral magnetization dynamics with and without holes. Obtained from MPS simulations of the two-component Bose Hubbard model truncated to three states per site. Spiral wavenumber $Q = 2\pi/40$, on-site interaction $U = 10$, system size $L = 40$, averaging over 10 ralizations of randomly sprinkling four holes over the system.

study two imperfection in this simulation scheme which can lead to a deviation of the experimental measurement from the expected results in the spin model.

HOLES The Mott insulating state can have defects in the form of holes propagating through the system. In this case, the spiral dynamics can be altered due to the charge dynamics. In Fig. 8.18 we simulate the full two-component Bose Hubbard model taking into account three states per site to study the spiral dynamics in the presence of holes in 1D. While we find some deviations, the influence is only very slight is most directly expressed in the initial spiral magnetization. The fact that holes only influence the spin dynamics in a negligible way may be interpreted as an effect of spin-charge separation in this one-dimensional system [147, 486, 487]. In chapter 9 we will study this effect in more detail.

CHAIN LENGTH AVERAGING Cold atom experiments use three-dimensional optical lattices which can be reduced to one-dimensional tubes by making the intensity pattern anisotropic. However, it is challenging to only measure a single tube, and therefore, many tubes are averaged over [163]. Due to the Gaussian envelope of the trapping lasers, not all tubes will have the same length. As the spiral wavelength is however the same in all tubes, this leads to differing magnetizations

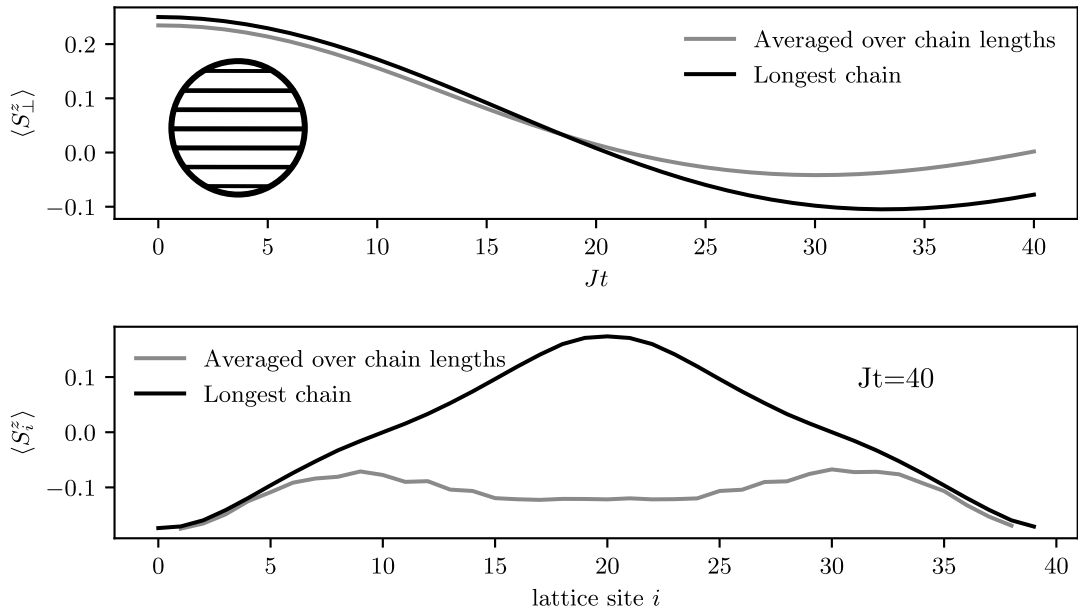

Figure 8.19: Simulation of the effect of randomly averaging over many tubes of different lengths. We assume a circular geometry of the tubes, see inset in top plot. The longest chain has length $L = 40$, wavenumber is $Q = 2\pi/L$, $\Delta = 0.5$. We measure the spiral magnetization projected onto the z-axis as in the Experiment in Ref. [163].

in each tube and a deviation from the exact dynamics. In Fig. 8.19 we simulate the tube averaging while approximating the envelope by a spherical geometry. We only find a rather small effect on the spiral magnetization while the profile at the longest times does deviate substantially. In Ref. [163] it has also been noted that this effect does indeed have a substantial impact on the measured data.

8.7 CONCLUSIONS

We analyzed the dynamics of spin spiral states in the two-dimensional Heisenberg model using several complementary analytical and numerical methods. By employing a Holstein-Primakoff stability analysis, we discovered a new class of dynamic instability which is enabled by the topology of the order parameter manifold rather than kinematic effects. From an exact short-time analysis, we showed that the instability does not govern the dynamics from the shortest possible timescales. Instead, it is built up non-perturbatively, which we showed by employing spin 2PI and truncated Wigner simulations. At late times, the instability is regularized by the spin length constraint. We also show using the numerically exact MPS-TEBD algorithm, that the same mechanism is happening in one-dimensional spin 1/2

chain. We conjecture that this instability is an important mechanism that governs the decay of spin superfluids.

While the mechanism that we discuss is intrinsic to the Heisenberg model, open problems include understanding the enhancement of the instability in the presence of disorder and long-range interactions, and understanding the mechanisms of decay in systems with different lattice types. In addition, extending our simulations to longer timescales in order to obtain a wholistic perspective of thermalization, which captures the growth of unstable modes and subsequent quasiparticle relaxation, remains an important challenge. While 2PI would be a contender for such a method, we showed that there are some problems in the interpretation of higher order correlation functions when employing approximations. A possible solution could be to employ a multi-channel GW approximation as done in Ref. [488]. Alternatively, using MPS methods on cylinders might lead to numerically exact results. However, the expected drastic entanglement growth due to the global quench might render this challenging.

9

VISUALIZING SPINON FERMI SURFACES WITH TIME-DEPENDENT SPECTROSCOPY

This chapter is based on the preprint

- Alexander Schuckert*, Annabelle Bohrdt*, Eleanor Crane, Fabian Grusdt: "Visualizing spinon Fermi surfaces with time-dependent spectroscopy" – [arXiv:2105.13366]

The text has been adapted here. * indicates equal contribution.

Quantum simulation experiments have started to explore regimes that are not accessible with exact numerical methods. In order to probe these systems and enable new physical insights, the need for measurement protocols arises that can bridge the gap to solid state experiments, and at the same time make optimal use of the capabilities of quantum simulation experiments. Here we propose applying time-dependent photo-emission spectroscopy, an established tool in solid state systems, in cold atom quantum simulators. Concretely, we suggest combining the method with large magnetic field gradients, unattainable in eeriments on real materials, to drive Bloch oscillations of spinons, the emergent quasiparticles of spin liquids. We show in exact diagonalization simulations of the one-dimensional $t-J$ model that the spinons start to populate previously unoccupied states in an effective band structure, thus allowing to visualize states invisible in the equilibrium spectrum. The dependence of the spectral function on the time after the pump pulse reveals collective interactions among spinons. In numerical simulations of small two-dimensional systems, spectral weight appears at the ground state energy at momentum $\mathbf{q} = (\pi, \pi)$, where the equilibrium spectral response is strongly suppressed up to higher energies, indicating a possible route towards solving the mystery of the Fermi arcs in the cuprate materials.

9.1 INTRODUCTION

Just like the back side of the moon is invisible from the earth, certain quantum states may be hidden from standard measurement tools in condensed matter physics. For example, states may be unoccupied at low temperatures or associated with strongly suppressed matrix elements. Akin to the fascination induced by the back side of the

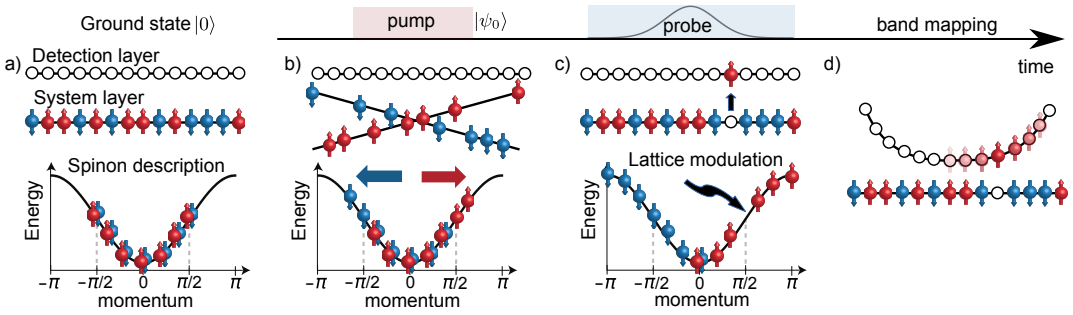

Figure 9.1: **Time-dependent photoemission-spectroscopy in quantum gases.** a) A half-filled 1D Fermi-Hubbard chain in the ground state, corresponding to a spinon Fermi sea, is prepared in the system layer while the detection layer is empty. b) A strong magnetic field gradient is applied, leading to Bloch oscillations in opposite directions of the two spinon species. c) After the field is switched off, a weak lattice modulation is applied, exciting an atom to the detection layer. d) Finally, the momentum of the excited atom in the detection layer is measured, e.g. in a harmonic potential by a quarter-period oscillation, using time-of-flight or another adiabatic band mapping scheme.

moon in popular culture, the back side of the Fermi arcs in the elusive pseudogap phase of the cuprate materials has excited condensed matter physicists for decades.

The cuprates exhibit superconductivity [115] at high temperatures, and fully understanding their phase diagram has become something like a holy grail in the community. One particularly intriguing part of this phase diagram is the pseudogap phase. One of its many fascinating properties is the observation of Fermi arcs in angle-resolved photoemission spectroscopy (ARPES) [489]: around the nodal points $\mathbf{k} = (\pm\pi/2, \pm\pi/2)$, arcs of high spectral weight appear in the spectral function, and in principle could be part of a small Fermi surface [490, 491]. However, these arcs appear to have two endpoints, and the backside of the putative Fermi surface is invisible. An important question is thus whether there exist states on the backside of the Fermi arcs, which are invisible in ARPES measurements. If this is the case, Luttinger's theorem [492] would be violated, as the area enclosed by the putative Fermi surface would be too small, indicating either a thus far unknown broken translational symmetry or topological excitations [493].

Here we propose a scheme to probe unoccupied states [494, 495] in the spectral function of strongly correlated many-body systems, realizable in quantum simulators. It is based on pump-probe spectroscopy, which has recently emerged as a valuable tool in solid state experiments to study non-equilibrium properties of materials [496–501]. Quantum simulators such as ultracold atoms have several advantages: for example, the absence of phonons leads to long coherence times and the Hamiltonian parameters are well known and tunable. In particular, a different toolbox for possible probe pulses is available, such as magnetic field gradients with

strengths unattainable in solid state experiments. For these reasons, our scheme is an important complement to existing pump-probe experiments. Our proposal to implement time-dependent ARPES (td-ARPES) to visualize spinon states in cold atoms is within reach of current quantum gas microscopy experiments, which have recently realized all the required building blocks: a magnetic field gradient [502], angle-resolved photoemission spectroscopy [503] and Bloch oscillations [504–506].

Applying our td-ARPES scheme to the Fermi-Hubbard model, which has been realized with cold atoms in several quantum gas microscopes [148, 502, 507, 508], directly enables the study of fractionalized excitations: In the one-dimensional (1D) Fermi-Hubbard model, the electron is effectively split into *independent* charge and spin excitations, called chargon and spinon, respectively [147, 486, 509]. The single-particle spectra of the 1D Fermi-Hubbard and $t-J$ models exhibit a strong asymmetry [510], which can be associated with the fermionic statistics of spinons and their Fermi sea [95].

In this chapter, we demonstrate by numerical simulations that td-ARPES combined with strong external field gradient pulses can shed light on spinon states not occupied in the ground state of the 1D $t-J$ model, up to the highest momentum $k=\pi$, see Fig. 9.1. In two dimensions, we show that a magnetic field gradient pulse along the diagonal direction yields spectral weight at low energies at $k=(\pi,\pi)$. This provides a hint that the missing weight on the back side of the Fermi arcs may be related to a spinon Fermi sea picture [86].

9.2 TIME DEPENDENT SPECTROSCOPY IN QUANTUM SIMULATORS

Our protocol combines the equilibrium ARPES protocol [95, 503] for quantum simulators with the solid state td-ARPES protocol [511]. First, a system in equilibrium is prepared in one layer of an optical lattice. A neighboring layer ("detection layer") is left empty with a gradient along the transverse direction inhibiting tunneling between the layers due to the energy difference Δ induced by the gradient, Fig. 9.1a). Subsequently, a non-equilibrium state $|\psi_0\rangle$ is prepared by a quench, such as the application of an external field. Here, we propose to apply a strong magnetic field gradient for a time t_B, Fig. 9.1b). Magnetic field gradients have been realized in quantum gas microscopy experiments for example to study spin transport [502].

To measure the time-dependent ARPES spectrum $A_{\mathbf{q}}(T,\omega)$, we suggest to apply a weak lattice modulation between system and detection layers with frequency $\tilde{\omega}$ and a Gaussian envelope centered around time T with variance Σ^2, Fig. 9.1c). In the weak modulation limit, this allows a single atom of energy $\epsilon_{\mathbf{q}}$ and spin σ to tunnel resonantly into the detection layer if $\tilde{\omega}=\epsilon_{\mathbf{q}}+\Delta$. Alternatively to the detection layer,

a non-interacting third hyperfine state can be used, with the lattice modulation replaced by a radio-frequency (RF) pulse [503]. This enables the application of our protocol in continuum quantum gases, where RF spectroscopy in equilibrium is routinely performed [512–514].

Finally, one of the band mapping schemes described in [95] can be used to measure the momentum of the atom in the detection layer at long times after the pulse has subsided, i.e. $t \gg T + \Sigma$, Fig. 9.1d). We show below that the momentum space occupation number in the detection layer is proportional to the time-dependent hole spectral function $A_{\mathbf{q}\sigma}(T, \omega)$

$$A_{\mathbf{q}\sigma}(T,\omega) = \int d\tau e^{i\omega\tau} \left\langle \psi_0 \middle| \hat{c}^\dagger_{\mathbf{q},\sigma}(T+\tau/2)\hat{c}_{\mathbf{q},\sigma}(T-\tau/2) \middle| \psi_0 \right\rangle \tag{9.1}$$

at frequency $\omega = \tilde{\omega} - (\epsilon_{\mathbf{q}} + \Delta)$ and central time T. Here, $\hat{c}^{(\dagger)}_{\mathbf{q},\sigma}$ annihilates (creates) a fermion or boson of spin σ and momentum $\mathbf{q}$. The particle spectral function $\int d\tau e^{i\omega\tau} \mathrm{Tr}(\rho \hat{c}_{\mathbf{q}\sigma}(T+\tau/2)\hat{c}^\dagger_{\mathbf{q}\sigma}(T-\tau/2))$ can be measured by the same protocol by initially preparing the detection layer in a band-insulator. The modulation leads in this case to an assisted tunneling of an atom from the detection layer into the system, whose momentum can be obtained by band-mapping of the resulting hole in the detection layer. In the solid state, this protocol is known as angle-resolved-inverse-photoemission-spectroscopy.

In the following, we will derive the above results in more detail, combining the ARPES protocol presented in Bohrdt et al. [95] to arbitrary initial states, closely following the theoretical description of time resolved ARPES in the solid state by Freericks et al. [515]. We then generalize the protocols to ARIPES. Our protocol is applicable for fermionic and bosonic systems.

9.2.1 *Linear and quadratic response*

Consider a system with many-body Hamiltonian $\hat{H}_0$ and probe Hamiltonian $\hat{V}$ (e.g. containing a lattice modulation or RF pulse), such that the total Hamiltonian is given by $\hat{H} = \hat{H}_0 + \hat{V}$. We work in an interaction picture with respect to $\hat{H}_0$ such that operators are evolved according to $\hat{A}_I(t) = \hat{U}_0^\dagger(t)\hat{A}\hat{U}_0(t)$, with $\hat{U}_0(t) = \mathcal{T}\exp(-i\int dt' \hat{H}_0(t'))$. The initial density matrix $\hat{\rho}_0$ is evolved according to $\hat{\rho}(t) = \hat{U}(t)\hat{\rho}_0\hat{U}^\dagger(t)$ with $\hat{U}(t) = \mathcal{T}\exp(-i\int_0^t \hat{V}_I(t')dt')$. Up to second order in $\hat{V}$, the time evolution operator is given by

$$\hat{U}(t) = \mathbb{1} - i\int_0^t dt_1 \hat{V}_I(t_1) - \int_0^t dt_1 \int_0^{t_1} dt_2 \hat{V}_I(t_1)\hat{V}_I(t_2) + \mathcal{O}(V^3). \tag{9.2}$$

The expectation value of an observable $\hat{A}$ at time t, $\langle \hat{A}(t) \rangle \equiv \mathrm{Tr}\left(\hat{\rho}(t)\hat{A}_I(t)\right)$, is then given by

$$\begin{aligned}\langle \hat{A}(t) \rangle - \langle \hat{A}(t) \rangle_{V=0} = -i \int_0^t dt_1 \, \langle \left[\hat{A}_I(t), \hat{V}_I(t_1)\right] \rangle \\ + \int_0^t dt_1 \int_0^t dt_2 \, \langle \hat{V}_I(t_1)\hat{A}_I(t)\hat{V}_I(t_2) \rangle \\ - \int_0^t dt_1 \int_0^{t_1} dt_2 \, \langle \hat{V}_I(t_2)\hat{V}_I(t_1)\hat{A}_I(t) + \hat{A}_I(t)\hat{V}_I(t_1)\hat{V}_I(t_2) \rangle + \mathcal{O}(V^3),\end{aligned} \tag{9.3}$$

where $\langle \hat{A}(t) \rangle_{V=0}$ is the expectation value in the absence of a probe pulse.

The above expression is valid for any density matrix $\hat{\rho}_0$, in particular also for thermal equilibrium $\hat{\rho}_0 = \frac{1}{Z} e^{-\beta \hat{H}_0}$ with $Z = \mathrm{Tr}(e^{-\beta \hat{H}_0})$. Moreover, it offers a unified perspective on non-equilibrium dynamics between cold atom experiments, where usually $\hat{\rho}_0$ is thought off as some (product) initial state, given by the ground state of some Hamiltonian different to $\hat{H}_0$, i.e. a " quantum quench", and condensed matter pump-probe experiments, where $\hat{\rho}_0 = \frac{1}{Z} e^{-\beta \hat{H}_0}$, but there is an additional strong, time dependent pump term during the time evolution $\hat{H}_0 \to \hat{H}_0 + \hat{H}_{\mathrm{pump}}(t)$. In fact, these two perspectives are equivalent if the pump pulse only acts up to some time t^* before the probe is turned on, as then the action of the pump pulse can be absorbed into the initial density matrix by $\hat{\rho}_0 = \hat{U}_0(t^*) \frac{1}{Z} e^{-\beta \hat{H}_0} \hat{U}_0^\dagger(t^*)$.

In the following, we will specify this expression to the cases of the probe pulse coupling the atom creation/annihilation operator $c/c^\dagger$, which yields the cold-atom analogues of time-resolved ARPES and ARIPES, probing the two-time correlation functions $\langle \hat{c}_{\mathbf{q}}^\dagger(t_1)\hat{c}_{\mathbf{q}}(t_2) \rangle$, $\langle \hat{c}_{\mathbf{q}}(t_1)\hat{c}_{\mathbf{q}}^\dagger(t_2) \rangle$ respectively, with momentum $\mathbf{q}$ and lattice site j.

9.2.2 *Time dependent ARPES*

The protocol consists in coupling the "system" optical lattice to another tube/layer representing a "detection" lattice, which is initially empty. The detection lattice is offset by an energy Δ, which is the analogue of the work function in condensed matter ARPES. An analogue of a photopulse is created by modulating the lattice depth between system and detection layer, resulting in a coupling Hamiltonian

$$\hat{V}_I(t) = -t_y s(t) e^{-i\omega t} \sum_{\mathbf{k}} \hat{d}_{\mathbf{k}\sigma}^\dagger \hat{c}_{\mathbf{k}\sigma} + h.c., \tag{9.4}$$

where $d_{\mathbf{k}\sigma}^\dagger$, $\hat{c}_{\mathbf{k}\sigma}$ creates/annihilates an atom with spin σ in the detection/system layer; t_y is the amplitude of the modulation, which needs to be small compared to the tunneling within the system; ω is the modulation frequency. The detection system is assumed to be non-interacting, such that $\hat{H}_d = \sum_{\mathbf{q}} (\epsilon_{\mathbf{q}} + \Delta) \hat{d}_{\mathbf{q}\sigma}^\dagger \hat{d}_{\mathbf{q}\sigma}$ with $\epsilon_{\mathbf{q}}$

the non-interacting dispersion of the detection lattice. The operator measured in this scheme is the momentum space occupation number in the detection system $\hat{A} = \hat{n}_{\mathbf{q}\sigma} \equiv \hat{d}^\dagger_{\mathbf{q}\sigma}\hat{d}_{\mathbf{q}\sigma}$, which may be obtained from the band-mapping schemes in Ref. [95]. The total initial density matrix $\hat{\rho}_0$ is a product state of the empty detection system and the system density matrix $\hat{\rho}_0 = |0\rangle\langle 0|_d \otimes \hat{\rho}_s$.

Inserting $\hat{A}$ and $\hat{V}_I$ into Eq. 9.3, we directly see that the linear term in $\hat{V}_I$ vanishes as it contains a vacuum expectation value of an odd number of detection system creation/annihilation operators. Furthermore, the terms in the second line of Eq. 9.3 also vanish as $\hat{A}_I(t) = \hat{n}_{\mathbf{q}\sigma}(t)$ acting on the empty detection initial state gives zero. Moreover, in the absence of system-detection layer tunneling, the occupation number in the detection system stays zero, such that $\langle \hat{n}_{\mathbf{q}\sigma}(t)\rangle_{t_y=0} = 0$ at all times. The last remaining term then finally gives

$$\begin{aligned}
\langle \hat{n}_{\mathbf{q}\sigma}(t)\rangle &= t_y^2 \int_0^t dt_1 \int_0^t dt_2\, s(t_1)s(t_2)\times \\
&\quad \sum_{\mathbf{k}'\mathbf{k}'',\sigma'\sigma''} \langle 0|\hat{d}_{\mathbf{k}'\sigma'}(t_1)\hat{n}_{\mathbf{q}\sigma}(t)\hat{d}^\dagger_{\mathbf{k}''\sigma''}(t_2)|0\rangle \,\mathrm{Tr}(\hat{\rho}_s \hat{c}^\dagger_{\mathbf{k}'\sigma'}(t_1)\hat{c}_{\mathbf{k}''\sigma''}(t_2)) e^{i\omega(t_1-t_2)} \\
&= t_y^2 \int_0^t dt_1 \int_0^t dt_2 s(t_1)s(t_2) e^{i(\omega-\epsilon_{\mathbf{q}}-\Delta)(t_1-t_2)} \,\mathrm{Tr}(\hat{\rho}_s \hat{c}^\dagger_{\mathbf{q}\sigma}(t_1)\hat{c}_{\mathbf{q}\sigma}(t_2)) \quad (9.5) \\
&= t_y^2 \int_0^t dT \int_{-\tau_{\max}(T)}^{\tau_{\max}(T)} d\tau s\left(T-\frac{\tau}{2}\right) s\left(T+\frac{\tau}{2}\right) e^{i(\omega-\epsilon_{\mathbf{q}}-\Delta)\tau} A(T,\tau), \quad (9.6)
\end{aligned}$$

where we defined center of mass time $T = \frac{1}{2}(t_1+t_2)$, and relative time τ as well as the "lesser" Green's function $A(T,\tau) = \mathrm{Tr}(\hat{\rho}_s \hat{c}^\dagger_{\mathbf{q}\sigma}(T+\tau/2)\hat{c}_{\mathbf{q}\sigma}(T-\tau/2))$. The maximum relative time is $\tau_{\max} = 2T$ for $T \leq t/2$ and $\tau_{\max} = 2t$ for $T > t/2$. In most situations however, we can send $\tau_{\max} \to \infty$ due to the rapid decay of $A(T,\tau)$. We note that this expression is valid for both Fermionic and Bosonic species because we assumed the detection system to be initially empty.

In the following, we will discuss a few instructive limits of the above general expression.

EQUILIBRIUM LIMIT We can recover the equilibrium result of Ref. [95] by inserting $s(t) = 1$ as well as using that in equilibrium, $\hat{\rho}_s = \frac{1}{Z}e^{-\beta\hat{H}_0}$, $A(T,\tau)$ only depends on τ. The rate of tunneling to the detection system is then given by

$$\begin{aligned}
\Gamma_{\mathbf{q}\sigma}(\omega) &= \frac{1}{t}\langle \hat{n}_{\mathbf{q}\sigma}(t)\rangle & (9.7)\\
&= t_y^2 \int_{-\infty}^{\infty} dt e^{i(\omega-\epsilon_{\mathbf{q}}-\Delta)t} \frac{1}{Z}\,\mathrm{Tr}(e^{-\beta\hat{H}_0}\hat{c}^\dagger_{\mathbf{q}\sigma}(t)\hat{c}_{\mathbf{q}\sigma}) & (9.8)\\
&= t_y^2 A_{\mathbf{q}\sigma}(\omega-\epsilon_{\mathbf{q}}-\Delta). & (9.9)
\end{aligned}$$

$A_{\mathbf{q}\sigma}(\omega)$ is the hole spectral function

$$A_{\mathbf{q}\sigma}(\omega) = \frac{1}{Z}\sum_{nm} e^{-\beta E_n} |\langle m|\hat{c}_{\mathbf{k}\sigma}|n\rangle|^2 \delta(\omega-(E_m-E_n)). \quad (9.10)$$

GAUSSIAN PULSE A (normalized) Gaussian pulse centred around $t = t_p$ as $s(t) = \frac{1}{\sqrt{2\pi\sigma^2}} \exp(-(t-t_p)^2/2\sigma^2)$, leads to

$$2\pi\sigma^2 \langle \hat{n}_{\mathbf{q}\sigma}(t) \rangle = \int_0^t dT \int_{-t_{\max}}^{t_{\max}} d\tau \exp\left(-\frac{(T-t_p)^2}{\sigma^2/2}\right) \exp\left(-\frac{\tau^2}{8\sigma^2}\right) e^{i(\omega-\epsilon_{\mathbf{q}}-\Delta)\tau} A(T,\tau), \quad (9.11)$$

Typically, $A(T,\tau)$ decays rapidly as a function of τ (with the decay rate corresponding to the lifetime of excitations in the system), such that we can extend the integral boundaries for the τ integral to $\pm\infty$. Then we can interpret the τ integral as a Fourier transform, with a broadening introduced by the finite pulse length, leading to

$$\langle \hat{n}_{\mathbf{q}\sigma}(t) \rangle = \sqrt{\frac{2}{\pi\sigma^2}} \int_0^t dT \exp\left(-\frac{(T-t_p)^2}{\sigma^2/2}\right) \times \int \frac{d\tilde{\omega}}{2\pi} \exp\left(-2\sigma^2\tilde{\omega}^2\right) A(T, \omega - \epsilon_{\mathbf{q}} - \Delta - \tilde{\omega}). \quad (9.12)$$

Hence, a Gaussian pulse centred around t_p measures the time dependent lesser Green's function averaged over a time and frequency window fulfilling the "uncertainty relation" $\sigma_T^2 \sigma_\omega^2 = \frac{1}{16}$.

9.2.3 *Time dependent ARIPES*

Here we show how to measure the time dependent particle spectral function in angle-resolve inverse photo-emission spectroscopy, in which atoms are injected rather than ejected from the system layer.

To measure the ARIPES spectrum, we propose to prepare the detection layer in a bandinsulator, i.e. all momenta are initially filled. Then, the same coupling term as in the ARPES protocol is turned on. In this case, the second line in Eq. 9.3 is not zero, however for Fermions it cancels with another contribution from the second term in the first line. In total, we get for Fermions

$$1 - \langle \hat{n}_{\mathbf{q}\sigma}(t) \rangle = t_y^2 \int_0^t dT \int_{-\tau_{\max}(T)}^{\tau_{\max}(T)} d\tau s\left(T - \frac{\tau}{2}\right) s\left(T + \frac{\tau}{2}\right) e^{-i(\omega-\epsilon_{\mathbf{q}}-\Delta)\tau} A^{>}_{\mathbf{q}\sigma}(T,\tau), \quad (9.13)$$

i.e. in this case the hole propagation in the detection layer needs to be measured. The result involves the particle spectral function

$$A^{>}_{\mathbf{q}\sigma}(t_1,t_2) = \mathrm{Tr}(\hat{\rho}_s \hat{c}_{\mathbf{q}\sigma}(t_1)\hat{c}^\dagger_{\mathbf{q}\sigma}(t_2)), \quad (9.14)$$

which measures the unoccupied states in the system. The same manipulations as above go through analogously to obtain the equilibrium limits and the case of a Gaussian pulse.

9.2.4 *Extracting $|A|$ from two copies of the same state*

Here we give an alternative protocol based on Ref. [40]. It consists in evolving two copies of the system, acting with some operators on them and interfering them in the end.

First, prepare two copies of the same initial state $|\Psi\rangle \otimes |\Psi\rangle$ and let them evolve under the same Hamiltonian $\hat{H}$ for time t_1, such that we get $\exp(-i\hat{H}t_1)|\Psi\rangle \otimes \exp(-i\hat{H}t_1)|\Psi\rangle$. Then, remove a particle in the first copy at site i, evolve for time $(t_2 - t_1)$ with $t_2 > t_1$ and remove a particle in the second copy at site j. Thus, we end up in the state $\exp(-i\hat{H}(t_2 - t_1))\hat{c}_i \exp(-i\hat{H}t_1)|\Psi\rangle \otimes \hat{c}_j \exp(i\hat{H}t_2)|\Psi\rangle$. Finally, measure the swap operator SWAP by tunnel-coupling the two copies and measuring the parity-projected particle number, leading to

$$\langle \text{SWAP} \rangle_{t_1 < t_2} = |\langle \hat{c}_j^\dagger(t_2)\hat{c}_i(t_1)\rangle|^2, \tag{9.15}$$

9.3 OCCUPYING HIGHER MOMENTUM SPINON STATES BY BLOCH OSCILLATIONS

Here, we use our tdARPES protocol it to probe unoccupied spinon states in the $t - J$ model,

$$\hat{\mathcal{H}}_{t-J} = -t \sum_{\langle i,j\rangle,\sigma} \mathcal{P}\left(\hat{c}_{i,\sigma}^\dagger \hat{c}_{j,\sigma} + \text{h.c.}\right)\mathcal{P} + J \sum_{\langle i,j\rangle} \hat{\mathbf{S}}_i \cdot \hat{\mathbf{S}}_j, \tag{9.16}$$

where $\mathcal{P}$ denotes projection on the Hilbert space without double occupancies, $\langle i,j\rangle$ denotes neighboring sites, and $\hat{\mathbf{S}}_j$ are spin-1/2 operators.

The 1D $t - J$ model exhibits spin-charge separation [486]. This can be made explicit by writing the original fermionic operators as $\hat{c}_{i,\sigma} = \hat{h}_i^\dagger \hat{f}_{i,\sigma}$, where the spin operators $\hat{\mathbf{S}}_i$ are related to the fermionic spinon operators as $\hat{\mathbf{S}}_i = \frac{1}{2}\sum_{\alpha,\beta} \hat{f}_{i,\alpha}^\dagger \boldsymbol{\sigma}_{\alpha,\beta} \hat{f}_{i,\beta}$ and $\hat{h}_i$ denotes the bosonic chargon operator [516, 517]. On a mean-field level, the time dependent spectral function can be approximated as a convolution of spinon and chargon contribution,

$$A_{q\sigma}(T,\omega) = \sum_{k_h} \int d\nu A^s_{q-k_h\sigma}(T,\omega-\nu) A^c_{k_h}(T,\nu). \tag{9.17}$$

This representation serves in particular to determine the positions at which spectral weight should appear as it explicitly satisfies momentum and energy conservation. Note that due to spin-charge separation, the chargon can be approximated as a free particle with dispersion $\epsilon_h(k) = -2t\cos(k)$ when $t \gg J$ [518].

To gain a better understanding of the spinon contribution to the spectrum, we express the spin part of the Hamiltonian in Eq. (9.16) in terms of the spinons [519]:

$$\hat{\mathcal{H}}_J = -\frac{1}{2}\sum_{\langle i,j\rangle,\alpha} \hat{f}^\dagger_{i,\alpha}\hat{f}_{j,\alpha}\left[J_\perp \hat{f}^\dagger_{j,\bar{\alpha}}\hat{f}_{i,\bar{\alpha}} + J_z \hat{f}^\dagger_{j,\alpha}\hat{f}_{i,\alpha}\right] \tag{9.18}$$

where, $\bar{\uparrow} = \downarrow$ and $\bar{\downarrow} = \uparrow$. This expression is exact within the subspace satisfying $\sum_\alpha \hat{f}^\dagger_{i,\alpha}\hat{f}_{i,\alpha} = 1$ [95, 519].

In a mean-field description of the $SU(2)$ invariant model with $J_\perp = J_z$, we replace the operator $\hat{f}^\dagger_{i,\alpha}\hat{f}_{j,\alpha}$ by its ground state expectation value, leading to the formation of a Fermi sea of the spinons $\hat{f}_{i,\sigma}$ [95]. In standard ARPES, fermions can only be removed from formerly occupied states, and thus spectral weight only appears for spinon momenta within the Fermi sea. For an undoped spin chain this corresponds to $k_F = \pm\pi/2$. At momenta $|k| > \pi/2$, states of the many body system exist, but are not occupied and therefore do not yield any weight in the spectral function.

Here, we want to probe these unoccupied spinon states of the 1D $t-J$ model at zero temperature by driving the system out of equilibrium before measuring the time dependent one-hole ARPES spectrum, akin to solid state pump-probe experiments. We do so by applying a magnetic field gradient, described by the Hamiltonian

$$\hat{\mathcal{H}}_B = -B\sum_j j\hat{S}^z_j, \tag{9.19}$$

for a time t_B, starting from the $B = 0$ ground state. Numerically, we consider periodic boundary conditions for a cleaner signal and apply a time-dependent unitary transformation in order to restore translational invariance. After time t_B, we switch the gradient field off and calculate the td-ARPES spectrum of the resulting non-equilibrium state with exact diagonalization.

In the following, we show how to obtain a translationally invariant rotating frame.

9.3.1 *Restoring translational invariance*

Leaving initial state invariant

In order to restore translational invariance for our numerics, we apply a time-dependent unitary transformation

$$\hat{U}(t) = \exp\left(-iBt\sum_j j\hat{S}^z_j\right), \tag{9.20}$$

such that the transformed Hamiltonian $\hat{H}_J + \hat{H}_B \to \hat{H}'$ is given by

$$\hat{H}' = \hat{U}\hat{H}\hat{U}^\dagger + i\frac{\partial \hat{U}}{\partial t}\hat{U}^\dagger \tag{9.21}$$

$$= J\sum_j \frac{1}{2}\left(e^{-iBt}\hat{S}^+_{j+1}\hat{S}^-_j + e^{iBt}\hat{S}^-_{j+1}\hat{S}^+_j\right) + \hat{S}^z_{j+1}\hat{S}^z_j. \tag{9.22}$$

In this interaction picture, time evolution is governed by the Schrödinger equation

$$i\frac{d}{dt}\left|\psi'(t)\right\rangle = H'(t)\left|\psi'(t)\right\rangle, \tag{9.23}$$

with initial state $|\psi'(0)\rangle = \hat{U}(0)\,|0\rangle = |0\rangle$. Therefore, the time evolved state in the *unrotated* frame is given by

$$|\psi_0\rangle = \hat{U}^\dagger(t_B)\mathcal{T}e^{-i\int_0^{t_B} H'(t)dt}\,|0\rangle \tag{9.24}$$

After preparation of the state $|\psi_0\rangle$ we calculate the td-ARPES function $A_{k\sigma}(t_1, t_2) = \langle\psi_0|\hat{c}^\dagger_{k\sigma}t_1)\hat{c}_{k\sigma}(t_2)|\psi_0\rangle$, which contains time evolution under the tJ model. The tJ Hamiltonian is transformed with $U(t_B)$, such that time evolution is generated by

$$\hat{H}'_{tJ} = \mathcal{P}\Bigg[-t\sum_{\langle j,l\rangle,\sigma} e^{-i\frac{Bt_B}{2}(j-l)\sigma}\hat{c}^\dagger_{j,\sigma}\hat{c}_{l,\sigma} + J\sum_j \frac{1}{2}\left(e^{-iBt_B}\hat{S}^+_{j+1}\hat{S}^-_j + e^{iBt_B}\hat{S}^-_{j+1}\hat{S}^+_j\right) + \hat{S}^z_{j+1}\hat{S}^z_j\Bigg]\mathcal{P}. \tag{9.25}$$

Moreover, we need to transform the operators $\hat{c}^\dagger_{k\sigma}$ via $\hat{U}(t_B)\hat{c}^\dagger_{k,\sigma}\hat{U}^\dagger(t_B) = \hat{c}^\dagger_{k-\sigma\theta/2,\sigma}$, such that the td-ARPES function in the lab frame can be written as

$$A_{k\sigma}(t_1, t_2) = \langle\psi_0|\hat{U}^\dagger(t_B)\hat{c}^\dagger_{k-\sigma\theta/2,\sigma}(t'_1)\hat{c}_{k-\sigma\theta/2,\sigma}(t'_2)\hat{U}(t_B)|\psi_0\rangle, \tag{9.26}$$

where we marked the times with a prime to make explicit that time evolution is done under $\hat{H}'_{tJ}$. Finally, inserting the time evolved state in Eq. (9.24), we can rewrite this as

$$A_{k\sigma}(t_1, t_2) = \langle\overline{\psi_0}|\hat{c}^\dagger_{k-\sigma\theta/2,\sigma}(t'_1)\hat{c}_{k-\sigma\theta/2,\sigma}(t'_2)|\overline{\psi_0}\rangle \tag{9.27}$$

where $|\overline{\psi_0}\rangle = \mathcal{T}e^{-i\int_0^{t_B} H'(t)dt}\,|0\rangle$ is the ground state evolved under the rotated Hamiltonian. Using this expression, we never need to explicitly act with the unitary $\hat{U}$ on the state.

Eliminating the phase in the hopping term

For numerical reasons, we want to additionally eliminate the phase in front of the hopping term in Eq. (9.25). We can do so by shifting the unitary transformation by the corresponding constant phase, such that

$$\hat{U}(t) = \exp\left(iB(t_B - t)\sum_j j\hat{S}^z_j\right), \tag{9.28}$$

and

$$\hat{H}''(t) = J\sum_j \frac{1}{2}\left(e^{iB(t_B-t)}\hat{S}^+_{j+1}\hat{S}^-_j + e^{-iB(t_B-t)}\hat{S}^-_{j+1}\hat{S}^+_j\right) + \hat{S}^z_{j+1}\hat{S}^z_j. \tag{9.29}$$

Now, the initial state in the rotated frame is given by $|\psi'(0)\rangle = \hat{U}(0)\,|0\rangle$, with $\hat{U}(0) = \exp\left(iBt_B\sum_j j\hat{S}^z_j\right) \neq \mathbb{1}$ such that contrary to before we need to act with a unitary on the initial state. We do this by preparing the ground state of the Hamiltonian $\hat{H}''(t=0)$ at time 0.

The other steps performed above go through as before. Notably, $U(t_B) = \mathbb{1}$, such that both the tJ Hamiltonian and the operators $\hat{c}_k$ for the time evolution in $A_{k\sigma}(t_1, t_2)$ are unchanged. Hence, the full expression can be written as

$$A_{k\sigma}(t_1, t_2) = \langle\overline{\psi_0}|\hat{c}^\dagger_{k,\sigma}(t_1)\hat{c}_{k,\sigma}(t_2)|\overline{\psi_0}\rangle \tag{9.30}$$

where $|\overline{\psi_0}\rangle = \mathcal{T}e^{-i\int_0^{t_B} H''(t)dt}\,|0''\rangle$ is the ground state of $H''(t=0)$ evolved under $H''(t)$ in Eq. (9.29).

To summarize, we prepare the ground state of Hamiltonian $\hat{H}''(t=0)$, evolve it under the time dependent Hamiltonian $\hat{H}''(t)$ until time $t = t_B$ and then calculate the spectrum according to Eq. (9.30), where the time evolution is performed under the (unrotated) t-J model.

Before showing the numerical results, we discuss the expectation from the mean field picture.

9.3.2 *Shift of spinon occupation by a magnetic field gradient within mean field theory*

Here we want to show that the magnetic field gradient protocol leads to a shift of the occupation of the spinon dispersion in the Heisenberg chain. We first start with a simple example where a similar effect happens: spinless non-interacting Fermions in an electric field. We then go on to discuss the spinon mean field theory.

Warmup: Noninteracting Fermions in an electric field

We consider a single fermionic band in 1D in an electric field, described by Hamiltonian

$$\hat{H} = -J\sum_i(\hat{c}^\dagger_i\hat{c}_{i+1} + h.c.) + \Delta\sum_j j\hat{n}_j. \tag{9.31}$$

By using the same rotating frame as in the previous section, here created by unitary $\hat{U}(t) = \exp(-i\Delta(t_B - t)\sum_j j\hat{n}_j)$, the Hamiltonian in momentum space becomes

$$\hat{H}'(t) = -2J\sum_k \cos(k - \Delta(t_B - t))\hat{c}^\dagger_k\hat{c}_k. \tag{9.32}$$

We then follow the same procedure as in the t-J model: We prepare the ground state of $\hat{H}'(t)$ at time $t = 0$, given by

$$|0\rangle = \prod_{|k-\Delta t_B|\leq k_F} \hat{c}_k^\dagger |0\rangle , \tag{9.33}$$

where k_F is the Fermi momentum in the absence of a tilt. The time evolution of this state under the time dependent Hamiltonian $\hat{H}'$ until time t_B can be calculated by noting that $\hat{c}_k^\dagger(t_B) = \exp(-2Ji\int_0^{t_B}\cos(k-\Delta(t_B-t'))dt')\hat{c}_k^\dagger$ and hence

$$\overline{|\psi_0\rangle} \equiv \mathcal{T}\exp\left(-i\int_0^{t_B}\hat{H}'(t')dt'\right)|0\rangle \tag{9.34}$$

$$= \prod_{|k-\Delta t_B|\leq k_F} \exp\left(-\frac{2Ji}{\Delta}\left(\sin(k)-\sin(k-\Delta t_B)\right)\right) c_k^\dagger |0\rangle . \tag{9.35}$$

The ARPES spectrum then follows as

$$A_k(\omega) \equiv \int d(t_1-t_2)e^{i\omega(t_1-t_2))}\overline{\langle\psi_0|}\hat{c}_k^\dagger(t_1)\hat{c}_k(t_2)\overline{|\psi_0\rangle} \tag{9.36}$$

$$= 2\pi\delta(\omega-2J\cos(k))\overline{\langle\psi_0|}\hat{c}_k^\dagger\hat{c}_k\overline{|\psi_0\rangle} \tag{9.37}$$

$$= 2\pi\delta(\omega-2J\cos(k))\Theta(|k-\Delta t_B|-k_F). \tag{9.38}$$

This result shows some of the main features of the numerical results for the tJ model in a gradient magnetic field: One can scan along the whole dispersion by changing Δt_B, occupying states which are not occupied in the ground state without the field. However, in contrast to the tJ model, the result is both independent of central time $t_1 + t_2$ and of the strength of the tilt field Δ. Furthermore, the above result can be easily generalized to spinful Fermions in a magnetic field gradient: they just get shifted in opposite directions by $\pm\Delta t_B/2$, where the factor of one-half comes from the fact that $\hat{S}^z = \frac{1}{2}(\hat{n}_\uparrow - \hat{n}_\downarrow)$. In the following, we show how essentially the same result emerges in the Heisenberg model

9.3.3 *Constrained Fermion mean field theory with a gradient*

We start from the Heisenberg model in a magnetic field gradient

$$H = J\sum_i \frac{1}{2}\left(S_i^+ S_{i+1}^- + S_i^- S_{i+1}^+\right) + \hat{S}_i^z\hat{S}_{i+1}^z - B\sum_j j\hat{S}_j^z \tag{9.39}$$

Introducing constrained Fermion operators by $\hat{S}_i^+ = \hat{f}_{i\uparrow}^\dagger\hat{f}_{i\downarrow}$, $\hat{S}_i^z = \frac{1}{2}\left(\hat{f}_{i\uparrow}^\dagger\hat{f}_{i\uparrow} - \hat{f}_{i\downarrow}^\dagger\hat{f}_{i\downarrow}\right)$ with constraint $\sum_\alpha \hat{f}_{i,\alpha}^\dagger\hat{f}_{i,\alpha} = 1$, we get

$$\hat{H} = -\frac{J}{2}\sum_{i,\alpha}\hat{f}_{i,\alpha}^\dagger\hat{f}_{i+1,\alpha}\left(f_{i+1,\bar{\alpha}}^\dagger\hat{f}_{i,\bar{\alpha}} + f_{i+1,\alpha}^\dagger\hat{f}_{i,\alpha}\right) - \frac{B}{2}\sum_\alpha \alpha\sum_j j\hat{f}_{j\alpha}^\dagger\hat{f}_{j\alpha}. \tag{9.40}$$

Here, we defined $\alpha = +/-$ for $\uparrow$ / $\downarrow$ and $\bar{\uparrow} = \downarrow, \bar{\downarrow} = \uparrow$. Moreover, we neglected all constant terms.

In order to decouple the interactions, we introduce a spin-dependent mean field

$$\chi_\alpha = \langle \hat{f}^\dagger_{i,\alpha} \hat{f}_{i+1,\alpha} \rangle \tag{9.41}$$

and neglect all terms quadratic in the fluctuations around this mean field, arriving at

$$\hat{H} = -\frac{JL}{2} \sum_\alpha \chi_\alpha (\chi^\dagger_{\bar{\alpha}} + \chi^\dagger_\alpha) - \frac{J}{2} \sum_{i,\alpha} \left((\chi_\alpha + \chi_{\bar{\alpha}}) \hat{f}^\dagger_{i+1,\alpha} \hat{f}_{i,\alpha} + h.c. \right) - \frac{B}{2} \sum_\alpha \alpha \sum_j j \hat{f}^\dagger_{j\alpha} \hat{f}_{j\alpha}. \tag{9.42}$$

In order to follow the protocol, we move into the rotating frame of the magnetic field gradient with the unitary

$$\hat{U} = \exp\left(i \frac{B}{2} (t_B - t) \sum_\alpha \alpha \sum_j j \hat{f}^\dagger_{j,\alpha} \hat{f}_{j,\alpha} \right), \tag{9.43}$$

such that

$$\hat{f}_{j\alpha} \to U f_{j\alpha} U^\dagger = \exp\left(-i \frac{\alpha B j}{2} (t_B - t) \right) \hat{f}_{j,\alpha}. \tag{9.44}$$

Defining $f_j = \frac{1}{\sqrt{L}} \sum_k e^{-ikj} f_k$, and taking the infinite system size limit $(1/L) \sum_k = (1/2\pi) \int dk$ the Hamiltonian density becomes

$$\hat{H}(t) = -\frac{JL}{2} \sum_\alpha \chi_\alpha(t) (\chi^\dagger_{\bar{\alpha}}(t) + \chi^\dagger_\alpha(t)) + \int_{-\pi}^{\pi} dk \sum_\alpha \epsilon_\alpha(k,t) \hat{f}^\dagger_{k\alpha} \hat{f}_{k\alpha} \tag{9.45}$$

with dispersion

$$\epsilon_\alpha(k,t) = -\frac{J}{2} \left((\chi_\alpha + \chi_{\bar{\alpha}}) e^{i(k + \frac{\alpha B}{2}(t_B - t))} + c.c. \right). \tag{9.46}$$

Moreover, using that in the ground state $\langle \hat{f}^\dagger_k \hat{f}_{k'} \rangle \sim \delta_{kk'}$, the mean field transforms to

$$\chi_\alpha(t) = \frac{1}{2\pi} \int_{-\pi}^{\pi} dk e^{-i(k + \frac{\alpha B}{2}(t_B - t))} \langle \hat{f}^\dagger_{k,\alpha} \hat{f}_{k,\alpha} \rangle. \tag{9.47}$$

In order to find the ground state solution for $t = 0$, we need to minimize $\langle \hat{H} \rangle$ self-consistently under the constraint (9.47). To do so, we set the phase of $\chi_\alpha + \chi_{\bar{\alpha}}$ to zero (without loss of generality as the ground state is degenerate with respect to this phase) such that

$$\epsilon_\alpha(k, t = 0) = -J \left(|\chi_\alpha + \chi_{\bar{\alpha}}| \cos\left(k + \frac{\alpha B}{2} t_B \right) \right). \tag{9.48}$$

The ground state is hence given by a Fermi sea with the Fermi momenta given by $|k_F + \alpha \frac{B}{2} t_B| = \frac{\pi}{2}$. Inserting this into (9.47), we find

$$\chi_\alpha(t=0) = \frac{1}{2\pi} \int_{(-\pi-\alpha B t_B)/2}^{(\pi-\alpha B t_B)/2} dk\, e^{-i(k+\frac{\alpha B}{2} t_B)} \tag{9.49}$$

$$= \frac{1}{\pi} \tag{9.50}$$

independent of α and we get our final result for the spinon dispersion

$$\epsilon_\alpha(k, t=0) = -\frac{2J}{\pi} \cos\left(k + \frac{\alpha B}{2} t_B\right). \tag{9.51}$$

Having found the ground state at $t = 0$, we can now proceed with time evolving the state until $t = t_B$ to then calculate the spinon spectral function as in the previous example for free Fermions, yielding

$$A^s_{k,\alpha}(\omega) \equiv \int d(t_1 - t_2) e^{i\omega(t_1 - t_2))} \overline{\langle \psi_0 |} \hat{f}^\dagger_k(t_1) \hat{f}_k(t_2) \overline{| \psi_0 \rangle} \tag{9.52}$$

$$= 2\pi\delta\left(\omega + \frac{2J}{\pi} \cos(k)\right) \Theta(|k + \alpha B t_B/2| - \frac{\pi}{2}). \tag{9.53}$$

In the slave-particle mean-field picture introduced above, the magnetic field gradient hence exerts an equal but opposite force on the two spinon species, shifting their occupation along the mean-field spinon dispersion. The duration t_B is chosen such that these Bloch oscillations lead to a total shift $\theta = B t_B$, such that after the application of the magnetic field, states with momentum $-\pi/2 \mp \theta/2 \leq k \leq \pi/2 \mp \theta/2$ are occupied by up and down spinons, respectively. The spinons only experience half the total shift since Eq. (9.19) introduces a coupling of $\mp B/2$ to the density of up/down spinons.

The resulting spinon spectrum then reveals the shifted Fermi seas: spectral weight is obtained for momenta q which are now occupied and were previously empty in the ground state. Within mean-field theory, the positions of spectral lines can be obtained by inserting the known spinon and chargon dispersions [486, 520, 521] into Eq. (9.17).

In Fig. 9.2, we show the numerically obtained spectral function after applying a magnetic field gradient pulse of different strengths, yielding different shifts $\theta/2$. We always remove a spin down particle, thus probing only one of the two spinon Fermi seas. Comparing the numerical results to the spectral building principle [520, 521] – where shifts due to the magnetic field gradient are explicitly taken into account – yields perfect agreement, providing strong evidence that the slave-particle mean-field theory remains an accurate description beyond the ground state. However, while the mean-field picture predicts a shift of spectral weight in only one direction along the dispersion by $+\theta/2$, we find weight appearing on *both* sides at $\pm\theta/2$. In the following, we show that this is due to a time dependence of the spectrum

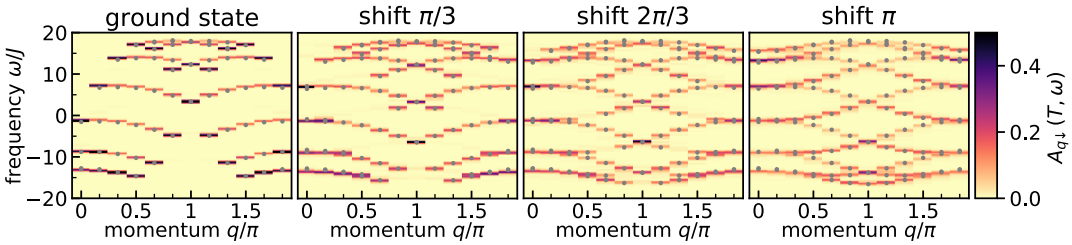

Figure 9.2: **Occupying spinon states by magnetic field gradient pulses.** The non-equilibrium one-hole spectral function for a system with $L = 12$ sites at $t/J = 8$ is shown after a magnetic field gradient was applied. The shift in momentum space is given by the product of magnetic field strength and duration of the gradient, $\theta = Bt_B$, with $t_B = 10/J$. Gray dots denote the points where spectral weight is expected from our out-of-equilibrium extension of the spectral building principle. The momentum shift due to the magnetic field gradient has been explicitly taken into account in the spinon properties while the chargon stays unaffected. Central times shown are $JT = 12.5, 15, 15$ for shift $\theta = \pi/3, 2\pi/3, \pi$.

induced by interactions among spinons.

9.4 COHERENT OSCILLATIONS OF THE SPECTRUM

In the slave-particle mean-field theory, the shifted Fermi sea is still an eigenstate of the Hamiltonian and we thus do not expect to find any dependence on the central time T. For sufficiently small magnetic field gradients, the spectral function $A_{q\sigma}(T,\omega)$ indeed does not exhibit a dependence on T. However, if the magnetic field gradient is strong, with $B \sim J$, coherent oscillations of the spectral weight emerge, Fig. 9.3.

In particular, the spectral weight in momentum space oscillates between the occupied momenta for up and down spinons, with the spectra for up and down fermions oscillating exactly out of phase, see Fig. 9.4. However, the position of the spectral lines does not change.

We can further analyze the spectrum by using the Lehmann representation of the spectral function

$$A_{\mathbf{q}\sigma}(T,\omega) = \int d\tau e^{i\omega\tau} \left\langle \psi_0 \left| \hat{c}^\dagger_{\mathbf{q},\sigma}(T+\tau/2)\hat{c}_{\mathbf{q},\sigma}(T-\tau/2) \right| \psi_0 \right\rangle, \tag{9.54}$$

where τ is the relative time between creation and annihilation of a Fermion and $|\psi_0\rangle$ is the non-equilibrium initial state. It can be decomposed into time dependent and thermal parts according to

$$A_{\mathbf{q}\sigma}(T,\omega) = A^{\mathrm{th}}_{\mathbf{q}\sigma}(\omega) + A^{\mathrm{td}}_{\mathbf{q}\sigma}(T,\omega) \tag{9.55}$$

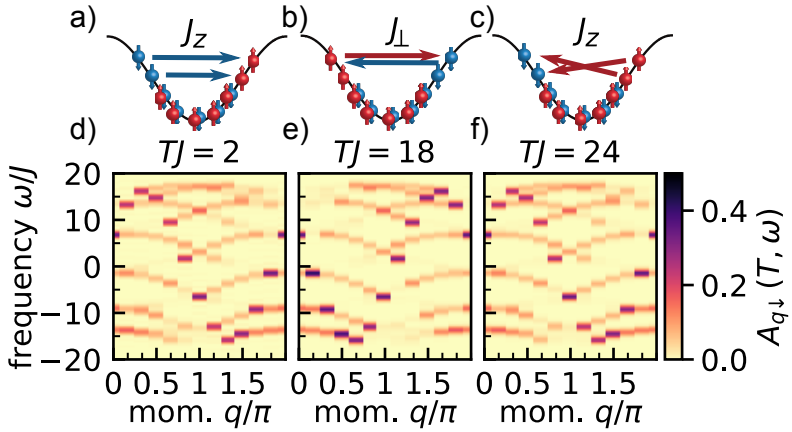

Figure 9.3: **Coherent oscillations of the spectral weight.** a) Resonant scattering processes leading to a redistribution of spectral weight between the shifted Fermi surfaces. b-d) The spectral function $A_{q\downarrow}(T,\omega)$ is shown as a function of momentum and frequency for three central times T in a system with $L = 12$ sites for the case of shift $2\pi/3$ shown in Fig. 9.2. Comparing the spectral function at different central times shows the oscillations of the spectral weight from one side of the visible arcs to the other, corresponding to the Fermi surfaces of the up and down spinon Fermi seas.

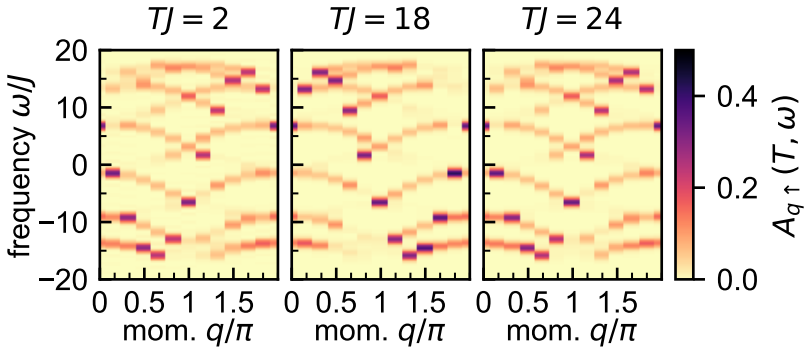

Figure 9.4: **Oscillations of ↑ spectrum.** Here, we use the same parameters as in Fig.1.3.

with

$$A^{\text{th}}_{\mathbf{q}\sigma}(\omega) = \sum_n |\langle\psi_0|n^N\rangle|^2 \sum_l |\langle l^{N-1}|c_{\mathbf{q}\sigma}|n^N\rangle|^2 \delta(\omega - (E_l^{N-1} - E_n^N)), \tag{9.56}$$

$$A^{\text{td}}_{\mathbf{q}\sigma}(T,\omega) = \sum_{n,m\neq n} \langle\psi_0|n^N\rangle \langle m^N|\psi_0\rangle e^{i(E_n^N - E_m^N)T} \times$$
$$\sum_l \langle n^N|c^\dagger_{\mathbf{q}\sigma}|l^{N-1}\rangle \langle l^{N-1}|c_{\mathbf{q}\sigma}|m^N\rangle \delta\left(\omega - \frac{1}{2}\left(E_l^{N-1} - E_m^N\right) - \frac{1}{2}\left(E_l^{N-1} - E_n^N\right)\right). \tag{9.57}$$

A^{th} is the expected steady state spectral function from the diagonal ensemble. The only time dependence is contained in the phase factors in A^{td}. Remarkably, they only depend on eigenstates with occupation N, i.e. the system before inserting a hole. In our case, this corresponds to the ground state of the half-filled t-J model,

i.e. the Heisenberg spin system. This shows that the only dependence on the time T enters through the eigenstates of the *half-filled* system without a hole. Therefore, the time-dependence of the spectral function further probes the properties of the spinons in the Heisenberg model.

9.4.1 *Gaussian states fail to reproduce time dependence*

While our mean-field picture reproduces the numerical observation that the spin up/down components are shifted in opposite directions by $Bt_B/2$, it does not contain any time dependence. Hence, we can attribute these effects to beyond-mean field interaction effects of the spinons. In the following, we show that even a more general Gaussian state ansatz can not explain the time dependence.

Spinon Hamiltonian in momentum space

We transform the spinon Hamiltonian

$$\hat{H} = -\frac{J_\perp}{2}\sum_{i\sigma}\hat{f}^\dagger_{i\sigma}\hat{f}^\dagger_{i+1\bar{\sigma}}\hat{f}_{i\bar{\sigma}}\hat{f}_{i+1\sigma} - \frac{J_z}{2}\sum_{i\sigma}\hat{f}^\dagger_{i\sigma}\hat{f}^\dagger_{i+1\sigma}\hat{f}_{i\sigma}\hat{f}_{i+1\sigma} \tag{9.58}$$

into momentum space by defining

$$\hat{f}_{k\sigma} = \frac{1}{\sqrt{L}}\sum_j e^{ikj}\hat{f}_{j\sigma}, \tag{9.59}$$

arriving at

$$\hat{H} = -\frac{1}{2L}\sum_{kk'q,\sigma}\cos(q)\left[J_\perp\hat{f}^\dagger_{k+q\sigma}\hat{f}^\dagger_{k'-q\bar{\sigma}}\hat{f}_{k\bar{\sigma}}\hat{f}_{k'\sigma} + J_z\hat{f}^\dagger_{k+q\sigma}\hat{f}^\dagger_{k'-q\sigma}\hat{f}_{k\sigma}\hat{f}_{k'\sigma}\right]. \tag{9.60}$$

Gaussian variational ansatz

In an attempt to explain the oscillations observed, we introduce a variational state

$$\begin{aligned}|\Psi(t)\rangle = &\prod_{k_-\le k\le k_+}\left(\alpha_k|k,\uparrow\rangle + \beta_k|-k,\uparrow\rangle\right)\times\\ &\prod_{k_-\le k\le k_+}\left(\beta_k|k,\downarrow\rangle + \alpha_k|-k,\downarrow\rangle\right)\prod_{0<k<k_-}|k,-k,\uparrow\rangle|k,-k,\downarrow\rangle,\end{aligned} \tag{9.61}$$

where in this definition $\pi > k \ge 0$ (in the following $\pi > k \ge -\pi$) and $|k,\sigma\rangle = \hat{f}^\dagger_{k\sigma}|0\rangle$, $|k,-k,\sigma\rangle = \hat{f}^\dagger_{k\sigma}\hat{f}^\dagger_{-k\sigma}|0\rangle$. From the normalisation of the state it follows that $|\alpha_k|^2 + |\beta_k|^2 = 1$. All parameters are time dependent, i.e. $\alpha_k = \alpha_k(t)$, $\beta_k = \beta_k(t)$.

Due to the product nature of the state, a generalized Wick's theorem holds in which all higher order correlation functions can be decomposed in two-point correlation functions, which we calculate in the following.

Two point correlation functions

The pairing and cross-spin correlation functions vanish,

$$\langle \hat{f}^\dagger_{k\sigma} \hat{f}^\dagger_{k'\sigma} \rangle = \langle \hat{f}_{k\sigma} \hat{f}_{k'\sigma} \rangle = \langle \hat{f}^\dagger_{k\sigma} \hat{f}_{k'\bar{\sigma}} \rangle = 0. \tag{9.62}$$

Moreover, the only remaining combination is nonzero only if $k = k'$ or $k = -k'$, i.e.

$$\langle \hat{f}^\dagger_{k\sigma} \hat{f}_{k'\sigma} \rangle = \delta_{k,k'} \langle \hat{f}^\dagger_{k\sigma} \hat{f}_{k\sigma} \rangle + \delta_{k,-k'} \langle \hat{f}^\dagger_{k\sigma} \hat{f}_{-k\sigma} \rangle . \tag{9.63}$$

Finally, the two terms on the right hand side can be evaluated in the variational state, yielding

$$\langle \hat{f}^\dagger_{k\uparrow} \hat{f}_{k\uparrow} \rangle = \begin{cases} 1 & \text{for } |k| < k_- \\ |\beta_k|^2 & \text{for } -k_+ \leq k \leq -k_- \\ |\alpha_k|^2 & \text{for } k_- \leq k \leq k_+ \\ 0 & \text{for } |k| > k_+ \end{cases}, \tag{9.64}$$

$$\langle \hat{f}^\dagger_{k\downarrow} \hat{f}_{k\downarrow} \rangle = \begin{cases} 1 & \text{for } |k| < k_- \\ |\alpha_k|^2 & \text{for } -k_+ \leq k \leq -k_- \\ |\beta_k|^2 & \text{for } k_- \leq k \leq k_+ \\ 0 & \text{for } |k| > k_+ \end{cases}, \tag{9.65}$$

$$\langle \hat{f}^\dagger_{k\uparrow} \hat{f}_{-k\uparrow} \rangle = \begin{cases} 0 & \text{for } |k| < k_- \\ \alpha_k \beta^*_k & \text{for } -k_+ \leq k \leq -k_- \\ \alpha^*_k \beta_k & \text{for } k_- \leq k \leq k_+ \\ 0 & \text{for } |k| > k_+ \end{cases}, \tag{9.66}$$

$$\langle \hat{f}^\dagger_{k\downarrow} \hat{f}_{-k\downarrow} \rangle = \begin{cases} 0 & \text{for } |k| < k_- \\ \alpha^*_k \beta_k & \text{for } -k_+ \leq k \leq -k_- \\ \alpha_k \beta^*_k & \text{for } k_- \leq k \leq k_+ \\ 0 & \text{for } |k| > k_+ \end{cases}. \tag{9.67}$$

From the above, we note the following symmetries between the spin correlation functions:

$$\langle \hat{f}^\dagger_{k\uparrow} \hat{f}_{k\uparrow} \rangle = \langle \hat{f}^\dagger_{-k\downarrow} \hat{f}_{-k\downarrow} \rangle , \tag{9.68}$$

$$\langle \hat{f}^\dagger_{k\uparrow} \hat{f}_{-k\uparrow} \rangle = \langle \hat{f}^\dagger_{-k\downarrow} \hat{f}_{k\downarrow} \rangle = \langle \hat{f}^\dagger_{k\downarrow} \hat{f}_{-k\downarrow} \rangle^* , \tag{9.69}$$

such that we can follow that there are in fact only two independent correlation functions,

$$n_k = \langle \hat{n}_k \rangle \equiv \langle \hat{f}^\dagger_{k\uparrow} \hat{f}_{k\uparrow} \rangle \tag{9.70}$$

$$m_k = \langle \hat{m}_k \rangle \equiv \langle \hat{f}^\dagger_{k\uparrow} \hat{f}_{-k\uparrow} \rangle \tag{9.71}$$

Equations of motion

We can now derive the equations of motion for the correlators n_k and m_k from Heisenberg equations of motion for $\hat{n}_k$, $\hat{m}_k$,

$$-i\partial_t \hat{n}_k = [\hat{H}, \hat{n}_k] \tag{9.72}$$

$$= -\frac{1}{L} \sum_{k',q} \cos(q) \big(J_\perp \hat{f}^\dagger_{k'+q\uparrow} \hat{f}^\dagger_{k-q\downarrow} \hat{f}_{k'\downarrow} \hat{f}_{k\uparrow} - J_\perp \hat{f}^\dagger_{k'+q\downarrow} \hat{f}^\dagger_{k\uparrow} \hat{f}_{k'\uparrow} \hat{f}_{k+q\downarrow} + J_z \hat{f}^\dagger_{k'+q\uparrow} \hat{f}^\dagger_{k-q\uparrow} \hat{f}_{k'\uparrow} \hat{f}_{k\uparrow} - J_z \hat{f}^\dagger_{k'+q\uparrow} \hat{f}^\dagger_{k\uparrow} \hat{f}_{k'\uparrow} \hat{f}_{k+q\uparrow} \big), \tag{9.73}$$

$$-i\partial_t \hat{m}_k = [\hat{H}, \hat{m}_k] \tag{9.74}$$

$$= -\frac{1}{L} \sum_{k',q} \cos(q) \big(J_\perp \hat{f}^\dagger_{k'+q\uparrow} \hat{f}^\dagger_{k-q\downarrow} \hat{f}_{k'\downarrow} \hat{f}_{-k\uparrow} - J_\perp \hat{f}^\dagger_{k'+q\downarrow} \hat{f}^\dagger_{k\uparrow} \hat{f}_{k'\uparrow} \hat{f}_{-k+q\downarrow} + J_z \hat{f}^\dagger_{k'+q\uparrow} \hat{f}^\dagger_{k-q\uparrow} \hat{f}_{k'\uparrow} \hat{f}_{-k\uparrow} - J_z \hat{f}^\dagger_{k'+q\uparrow} \hat{f}^\dagger_{k\uparrow} \hat{f}_{k'\uparrow} \hat{f}_{-k+q\uparrow} \big). \tag{9.75}$$

Evaluating these equations of motion with respect to the variational state while employing Wicks theorem, i.e.

$$\langle f^\dagger_{k_1\sigma_1} f^\dagger_{k_2\sigma_2} f_{k_3\sigma_3} f_{k_4\sigma_4} \rangle \approx \langle f^\dagger_{k_1\sigma_1} f_{k_4\sigma_4} \rangle \langle f^\dagger_{k_2\sigma_2} f_{k_3\sigma_3} \rangle - \langle f^\dagger_{k_1\sigma_1} f_{k_3\sigma_3} \rangle \langle f^\dagger_{k_2\sigma_2} f_{k_4\sigma_4} \rangle , \tag{9.76}$$

we get

$$\partial_t \langle \hat{n}_k \rangle = 0, \tag{9.77}$$

showing that this variational state does not suffice to explain the time dependence seen.

9.4.2 *Non-Gaussian state ansatz*

In the previous sections we have demonstrated that a Gaussian ansatz does not suffice to explain time dependent spinon occupation numbers. Here, we construct a new variational state taking into account some non-Gaussian correlations while stile retaining both energy and momentum conservation with the shifted Fermi sea as a reference state.

The state is defined by

$$
\begin{aligned}
|\psi\rangle = \prod_{0\leq k<k_-} & |-k\uparrow k\uparrow -k\downarrow k\downarrow\rangle \\
& \prod_{\frac{\pi}{2}\leq k\leq k_+} \Big[\alpha_k^{(1)}\,|k\uparrow\tilde{k}\uparrow -k\downarrow -\tilde{k}\downarrow\rangle + \alpha_k^{(2)}\,|-k\uparrow -\tilde{k}\uparrow k\downarrow\tilde{k}\downarrow\rangle \\
& \quad + \beta_k^{(1)}\,|-k\uparrow\tilde{k}\uparrow k\downarrow -\tilde{k}\downarrow\rangle + \beta_k^{(2)}\,|k\uparrow -\tilde{k}\uparrow -k\downarrow\tilde{k}\downarrow\rangle \\
& \quad + \gamma_k^{(1)}\,|-k\uparrow -\tilde{k}\uparrow -k\downarrow -\tilde{k}\downarrow\rangle + \gamma_k^{(2)}\,|k\uparrow\tilde{k}\uparrow k\downarrow\tilde{k}\downarrow\rangle \\
& \quad + \delta_k^{(1)}\,|\tilde{k}\uparrow -\tilde{k}\uparrow k\downarrow -k\downarrow\rangle + \delta_k^{(2)}\,|k\uparrow -k\uparrow\tilde{k}\downarrow -\tilde{k}\downarrow\rangle\Big],
\end{aligned}
\tag{9.78}
$$

where $\tilde{k} = \pi - k$ and $k_\pm = \pi/2 \pm \theta$.

Hamiltonian $\langle\hat{H}\rangle$

In the following, we will evaluate $\langle\psi|\hat{H}|\psi\rangle$. As the state conserves energy explicitly, with the non-interacting dispersion satisfying $\epsilon(k) \sim \cos(k)$, we obtain a constraint for the three momenta k, q, k' in Eq. 9.60, given by the three options

$$
q = 0 \text{ or } k' = \pi - k = \tilde{k} \text{ or } k' = q + k. \tag{9.79}
$$

We calculate $\langle\hat{H}\rangle$ for all three combinations separately, with the overall Hamiltonian given by

$$
\langle\hat{H}\rangle = \langle\hat{H}\rangle_{q=0} + \langle H_\perp\rangle_{k'=k+qk,q\neq 0} + \langle H_z\rangle_{k'=k+q,q\neq 0} + \langle H_\perp\rangle_{k'=\tilde{k},q\neq 0} + \langle H_z\rangle_{k'=\tilde{k},q\neq 0} \tag{9.80}
$$

Q=0 In this case,

$$
\hat{H}_{q=0} = -\frac{J_z}{2} + \frac{J_z L}{4} - \frac{J_\perp}{L}\sum_{k,k'} \hat{f}^\dagger_{k\uparrow}\hat{f}^\dagger_{k'\downarrow}\hat{f}_{k\downarrow}\hat{f}_{k'\uparrow}, \tag{9.81}
$$

where we used that $\sum_k \hat{f}^\dagger_{k\sigma}\hat{f}_{k\sigma} = \frac{L}{2}$. Evaluating with respect to the variational state, we obtain

$$
\begin{aligned}
\langle\hat{H}\rangle_{q=0} = & -\frac{J_z}{2} + \frac{J_z L}{4} - \frac{J_\perp}{L}\sum_{|k|<k_-} \\
& - \frac{J_\perp}{L}\sum_{\frac{\pi}{2}\leq k\leq k_+} \Big[2|\gamma_k^{(1)}|^2 + 2|\gamma_k^{(2)}|^2 \\
& \quad + \left(\alpha_k^{(1)} + \alpha_k^{(2)}\right)\left(\beta_k^{(1),*} + \beta_k^{(2),*} + \gamma_k^{(1),*} + \gamma_k^{(2),*}\right) + c.c. \\
& \quad - \left(\beta_k^{(1)} + \beta_k^{(2)}\right)\left(\delta_k^{(1),*} + \delta_k^{(2),*}\right) + c.c.\Big]
\end{aligned}
\tag{9.82}
$$

$q \neq 0$, $k' = k + q$ The $J_\perp$ term corresponds to a pure interspecies density-density interaction,

$$\langle H_\perp \rangle_{k'=k+q,q\neq 0} = -\frac{J_\perp}{L} \sum_{k,q\neq 0} \langle \hat{n}_{k+q\downarrow} \hat{n}_{k\uparrow} \rangle \tag{9.83}$$

$$\begin{aligned} &= -\frac{2J_\perp}{L} \sum_{0\leq k<k_-} \cos(2k) \\ &\quad - \frac{2J_\perp}{L} \sum_{\frac{\pi}{2}\leq k\leq k_+} \left(|\alpha_k^{(1)}|^2 + |\alpha_k^{(2)}|^2 \right) (\cos(2k) - 1) \\ &\quad + \frac{2J_\perp}{L} \sum_{\frac{\pi}{2}\leq k\leq k_+} \left(|\gamma_k^{(1)}|^2 + |\gamma_k^{(2)}|^2 \right) \cos(2k) \\ &\quad + \frac{2J_\perp}{L} \sum_{\frac{\pi}{2}\leq k\leq k_+} \left(|\delta_k^{(1)}|^2 + |\delta_k^{(2)}|^2 \right) (\cos(2k) + 1) \end{aligned} \tag{9.84}$$

The J_z term corresponds to the intraspecies interaction,

$$\langle H_z \rangle_{k'=k+q,q\neq 0} = -\frac{J_z}{2L} \sum_{k,q\neq 0,\sigma} \langle \hat{n}_{k+q,\sigma} \hat{n}_{k,\sigma} \rangle \tag{9.85}$$

$$\begin{aligned} &= -\frac{2J_z}{L} \sum_{0\leq k<k_-} \cos(2k) \\ &\quad + \frac{2J_z}{L} \sum_{\frac{\pi}{2}\leq k\leq k_+} \left(|\alpha_k^{(1)}|^2 + |\alpha_k^{(2)}|^2 \right) \cos(2k) \\ &\quad + \frac{2J_z}{L} \sum_{\frac{\pi}{2}\leq k\leq k_+} \left(|\beta_k^{(1)}|^2 + |\beta_k^{(2)}|^2 \right) \\ &\quad + \frac{2J_z}{L} \sum_{\frac{\pi}{2}\leq k\leq k_+} \left(|\gamma_k^{(1)}|^2 + |\gamma_k^{(2)}|^2 \right) \cos(2k) \\ &\quad - \frac{2J_z}{L} \sum_{\frac{\pi}{2}\leq k\leq k_+} \left(|\delta_k^{(1)}|^2 + |\delta_k^{(2)}|^2 \right) \cos(2k) \end{aligned} \tag{9.86}$$

$q \neq 0$, $k' = \pi - k = \tilde{k}$ Inserting $k' = \pi - k = \tilde{k}$, we get

$$\langle H_\perp \rangle_{k'=\tilde{k},q\neq 0} = -\frac{J_\perp}{L} \sum_{q\neq 0,k} \langle \hat{f}^\dagger_{k+q\downarrow} \hat{f}^\dagger_{\tilde{k}-q\uparrow} \hat{f}_{k\uparrow} \hat{f}_{\tilde{k}\downarrow} \rangle \tag{9.87}$$

$$= \frac{J_\perp}{L} \sum_{\frac{\pi}{2}\leq k\leq k_+} \left[\sum_{a,b=1}^{2} \beta_k^{(a)} \gamma_k^{(b),*} + \cos(2k) \left(\sum_{a,b=1}^{2} \gamma_k^{(a)} \delta_k^{(b),*} + c.c. \right) \right] \tag{9.88}$$

for the $J_\perp$ term.

Correspondingly, we get

$$\langle H_z \rangle_{k'=\tilde{k},q\neq 0} = -\frac{J_z}{2L} \sum_{q\neq 0,k,\sigma} \langle \hat{f}^\dagger_{k+q,\sigma} \hat{f}^\dagger_{\tilde{k}-q,\sigma} \hat{f}_{k\sigma} \hat{f}_{\tilde{k}\sigma} \rangle \tag{9.89}$$

$$= \frac{J_z}{L} \sum_{\frac{\pi}{2}\leq k\leq k_+} (\cos(2k) + 1) \left(\sum_{a,b=1}^{2} \alpha_k^{(a)} \gamma_k^{(b),*} + c.c. \right) \tag{9.90}$$

for the J_z term.

Equations of motion

The equations of motion for the state can be derived from Dirac's time dependent variational principle, which uses the extremization of the action, $\delta S = \delta \int dt L(t) = 0$, with the Lagrangian given by

$$L(t) = \langle \psi(t) | i\partial_t - \hat{H} | \psi(t) \rangle \,. \tag{9.91}$$

This leads to the Euler-Lagrange equations

$$\frac{d}{dt} \frac{\partial L}{\partial(\partial_t \alpha_k^{(1)})} - \frac{\partial L}{\partial \alpha_k^{(1)}} = 0, \tag{9.92}$$

and

$$i\partial_t \alpha_k^{(1)} = \frac{\partial \langle \hat{H} \rangle}{\partial \alpha_k^{(1),*}} \tag{9.93}$$

for $\pi/2 \leq k \leq k_+$ and equivalently for all other parameters. Evaluating the right hand side, we get the effective Schrödinger equation

$$i\partial_t |\psi_k\rangle = \hat{H}_k |\psi_k\rangle \text{ for } \pi/2 \leq k \leq k_+ \tag{9.94}$$

with $|\psi_k\rangle = (\alpha_k^{(1)}, \alpha_k^{(2)}, \beta_k^{(1)}, \beta_k^{(2)}, \gamma_k^{(1)}, \gamma_k^{(2)}, \delta_k^{(1)}, \delta_k^{(2)})^T$ and

$$\hat{H}_k = \frac{1}{L}\begin{pmatrix}
(-2J_\perp + 2J_z)\cos(2k) + 2J_\perp & 0 & -J_\perp \\
0 & (-2J_\perp + 2J_z)\cos(2k) + 2J_\perp & -J_\perp \\
-J_\perp & -J_\perp & 2J_z \\
-J_\perp & -J_\perp & 0 \\
-J_\perp + J_z(\cos(2k)+1) & -J_\perp + J_z(\cos(2k)+1) & J_\perp \\
-J_\perp + J_z(\cos(2k)+1) & -J_\perp + J_z(\cos(2k)+1) & J_\perp \\
0 & 0 & J_\perp \\
0 & 0 & J_\perp
\end{pmatrix}$$

$$\begin{pmatrix}
-J_\perp & J_z(\cos(2k)+1) - J_\perp & J_z(\cos(2k)+1) - J_\perp \\
-J_\perp & J_z(\cos(2k)+1) - J_\perp & {}_z(\cos(2k)+1) - J_\perp \\
0 & J_\perp & J_\perp \\
2J_z & J_\perp & J_\perp \\
J_\perp & (2J_\perp + 2J_z)\cos(2k) - 2J_\perp & 0 \\
J_\perp & 0 & (2J_\perp + 2J_z)\cos(2k) - 2J_\perp \\
J_\perp & J_\perp\cos(2k) & J_\perp\cos(2k) \\
J_\perp & J_\perp\cos(2k) & J_\perp\cos(2k)
\end{pmatrix}$$

$$\begin{pmatrix}
0 & 0 & \\
J0 & 0 & \\
J_\perp & J_\perp & \\
J_\perp & J_\perp & \\
J_\perp\cos(2k) & J_\perp\cos(2k) & \\
 & J_\perp\cos(2k) & J_\perp\cos(2k) \\
(2J_\perp - 2J_z)\cos(2k) + 2J_\perp & 0 & \\
0 & (2J_\perp - 2J_z)\cos(2k) + 2J_\perp &
\end{pmatrix}. \quad (9.95)$$

The initial conditions are given by $|\psi_k\rangle = (1,0,0,0,0,0,0,0)^T$.

OBSERVABLES The most relevant observable for us are the momentum occupations given by

$$\langle \hat{f}^\dagger_{k\uparrow}\hat{f}_{k\uparrow}\rangle = \begin{cases} |\alpha_k^{(1)}|^2 + |\beta_k^{(2)}|^2 + |\gamma_k^{(2)}|^2 + |\delta_k^{(2)}|^2 & \text{for } \pi/2 \le k \le k_+ \\ |\alpha_k^{(1)}|^2 + |\beta_k^{(1)}|^2 + |\gamma_k^{(2)}|^2 + |\delta_k^{1)}|^2 & \text{for } k_- \le k < \pi/2 \end{cases} \quad (9.96)$$

Despite the considerably higher complexity of the ansatz, the oscillations we have seen in our numerics can still not be explained by the ansatz due to the absence of cross-momentum scattering. However, we can use the intuition gained from these trials to come up with a more heuristic picture for the processes leading to the oscillations, which we will do in the following.

9.4.3 *Beyond mean-field interactions lead to oscillations*

Since the time-dependence observed in the spectrum goes beyond a mean-field description, we conclude that interactions between the spinons are relevant, see also [522]. To understand this effect in more detail we examine the quartic slave-particle Hamiltonian in Eq. (9.18). First, we consider the J_z term in the Hamiltonian, reading $-J_z/(2L)\sum_{\sigma,qkk'}\cos(q)\hat{f}^\dagger_{k+q\sigma}\hat{f}^\dagger_{k'-q\sigma}\hat{f}_{k'\sigma}\hat{f}_{k\sigma}$ in momentum space. Enforcing energy conservation on the level of the mean-field dispersion, only processes involving $q = 0$, $k' = \pi - k$ or $k' = q + k$ are allowed, examples of which are sketched in Fig. 9.3a),c). This picture is confirmed by switching $J_\perp = 0$ after the application of the magnetic field gradient and shifting by $\theta/2 = 2\pi/L$, which yields perfect sinusoidal oscillations of the up/down Fermi seas. For $J_\perp = J_z$, we find *two* frequency components of the oscillations, which we attribute to the additional resonant coupling of the two Fermi seas by $J_\perp$ processes as sketched in Fig. 9.3b). In the following, we discuss this picture in more detail.

For a shift by a single momentum point, $\Delta k = 2\pi/L$, there are only very few processes allowed by the spinon Hamiltonian when imposing both momentum and energy conservation. This becomes particularly extreme in the case when $J_\perp = 0$. Then, only one state has the same energy as the shifted Fermi sea and is also connected to the shifted Fermi sea by a momentum-conserving process: its "conjugate" partner, i.e. the Fermi sea shifted in the opposite direction in momentum space. Within this picture, the spectrum is expected to perform Rabi oscillations between the shifted Fermi sea and its conjugate partner. In Fig. 9.5 we show the time evolution of the spectrum when switching $J_\perp = 0$ after t_B. The Fermi sea then performs perfect sinusoidal oscillations with frequency J_z, as we show by looking at the spectral weight of a single line (all others perform the same oscillations). This supports the picture discussed above. However, when looking at snapshots of the whole spectrum, we see that the conjugate state is never fully reached, which may be attributed to a detuning between the shifted Fermi sea and its conjugate introduced by non-energy-conserving processes not included in this picture.

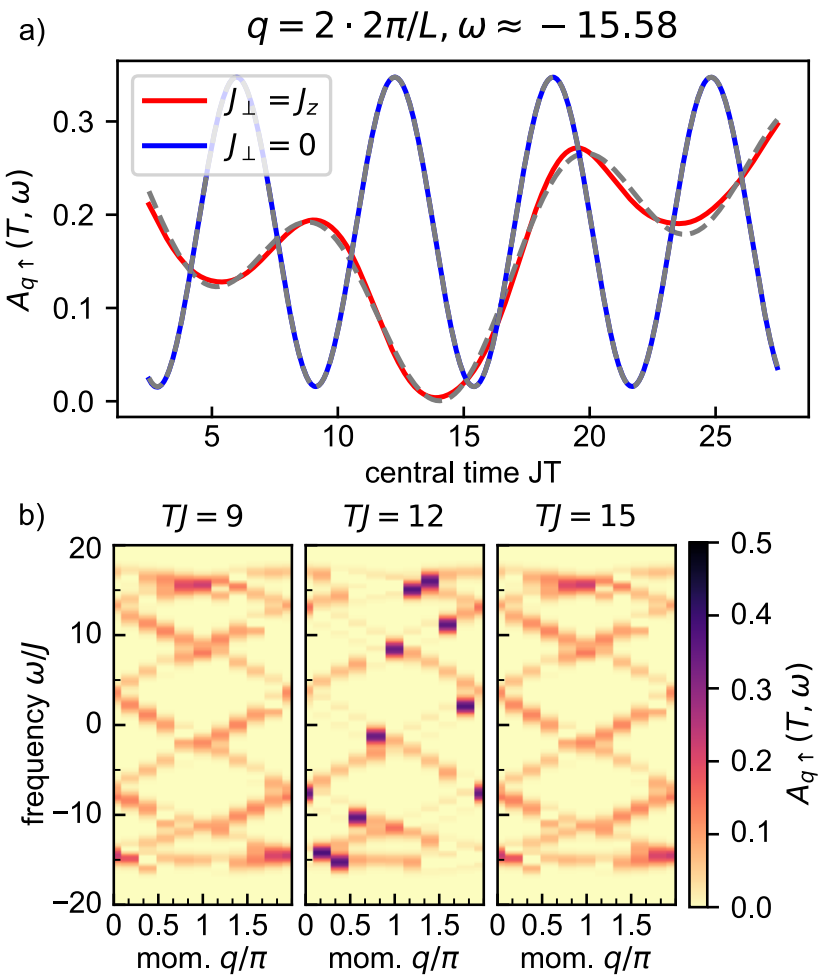

Figure 9.5: **Comparing coherent oscillations of spectrum with and without $J_\perp$.** a) Central time dependence of the spectral line with lowest frequency for a single momentum. Grey dashed lines indicate a fit with a single sine function with frequency $\approx 1J_z$ for $J_\perp = 0$ and a sum of two sine functions with frequencies $0.25J$ and $0.64J$ b) Snapshots of the spectrum at the maxima and minima of the oscillations for $J_\perp = 0$. $L = 10$, $t = 8J$. Total shift $\Theta = 2 \cdot 2\pi/L$.

Contrarily, when keeping $J_\perp = J_z$, we find an oscillation with a superposition of two sine functions, which we attribute to the coupling of the two oscillating Fermi seas by $J_\perp$.

9.5 TWO-DIMENSIONAL $t-J$ MODEL

The same protocol can also be applied in a 2D system. In Fig. 9.6, we show numerical results for the spectral function $A_{\mathbf{q}\downarrow}(T,\omega)$ in the $t-J$ model on a 4×4 torus at momentum $\mathbf{q} = (\pi,\pi)$. In equilibrium, the spectral weight is strongly suppressed at this momentum at low energies. A possible explanation involves binding of a light chargon to a heavy fermionic spinon from a Fermi sea [86]. This suggests that

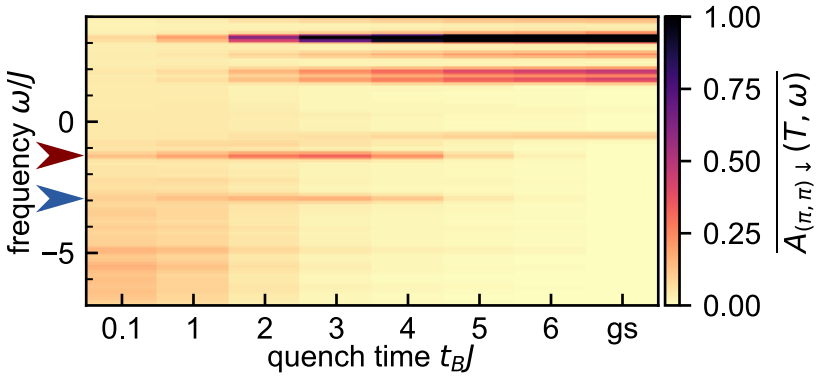

Figure 9.6: **Time-dependent ARPES in two dimensions.** The spectral function $A_{\mathbf{q}\downarrow}(T,\omega)$ in the $t-J$ model on a 4×4 torus at $t/J=2$ evaluated at momentum $\mathbf{q}=(\pi,\pi)$ calculated for a magnetic field gradient along the diagonal of strength $Bt_B=\pi/2$ for different quench times t_B. We average over central times $10\leq JT\leq 20$, indicated by the overline. The magnetic polaron ground state (gs) energy at momentum $q=(\pi,\pi)[q=(\pi/2,\pi/2)]$, $\omega\approx -2.93J$ $[\omega\approx -1.28J]$ is indicated by a red(blue) arrow.

additional spectral weight should appear at low energies when the magnetic field gradient is switched on and the putative spinon Fermi surface is displaced.

When employing a very strong magnetic field gradient with pulse duration $t_B<1/J$ and total shift is $\Theta=(\pi,\pi)$, we find the spectrum to be identical to the one of a free particle hopping with dispersion $-2t(\cos(q_x)+\cos(q_y))$, see Fig. 9.7. We can explain this by considering the strong magnetic field gradient limit, in which we can neglect the Heisenberg Hamiltonian during the dynamics and the system only evolves due to the gradient field. The initial state of the dynamics is given by the ground state of the Heisenberg model in 2D, which shows antiferromagnetic correlations. Now, when a (π,π) pulse is applied, these correlations get rotated around the z-axis such that in the xy plane there are now ferromagnetic correlations. In a ferromagnet, an injected hole can move freely as there is no energy cost related to the reshuffling of spins associated to the movement of the hole. Hence, the spectrum becomes identical to the one of a free particle.

More interestingly, a quench with $\theta=\pi/2$ at moderate speeds leads to the appearance of spectral weight around the ground state energy of a single hole in the $t-J$ model, indicated by arrows in Fig. 9.6. We interpret this feature as a signature of a spinon Fermi sea in two dimensions. Finally, for very slow quenches, finite-size gaps prevent any interesting dynamics and the obtained spectrum resembles the ground state result.

In Fig. 9.6 we only showed part of the frequency range in order to emphasize the low-energy feature we attribute to the magnetic polaron ground state energy. In Fig. 9.8 we show the full frequency range, in particular showing a high energy

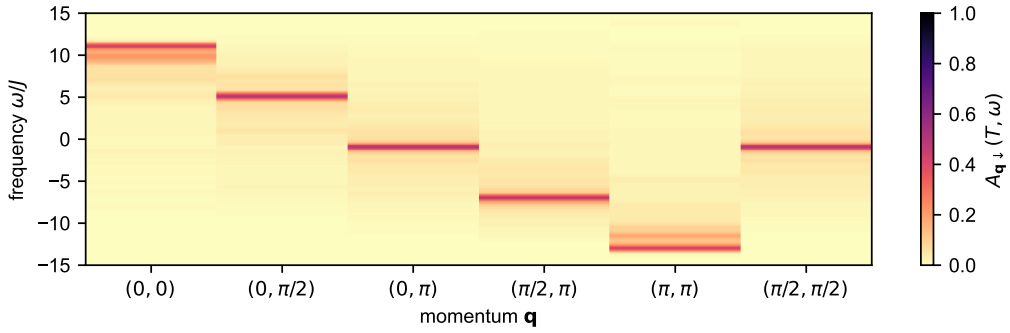

Figure 9.7: **Emergence of free particle spectrum for (π, π) shift in 2D.** Here, we use $t = 3J$ as well as $t_B = 1/J$.

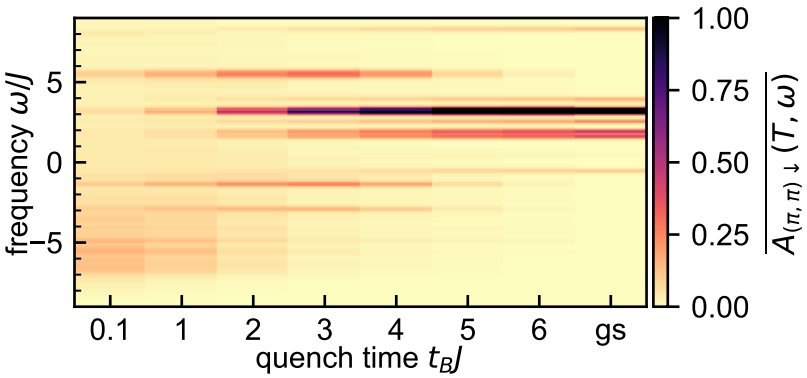

Figure 9.8: **Full frequency range of Fig.1.6.**

feature around $\omega \approx 5$ appearing for the same values of t_B at which the above mentioned low-energy feature appears.

9.6 CONCLUSIONS

We propose a measurement scheme to reveal unoccupied spinon states in the one-hole spectral function. Our numerical results for the 1D $t - J$ model show that a strong magnetic field gradient leads to spinon Bloch oscillations, where the spinons occupy previously empty momentum states. These can then be probed by time-dependent spectroscopy, revealing beyond mean-field interactions among spinons. Extending our results to small 2D systems, we are able to visualize the ground state of the magnetic polaron at momentum $\mathbf{q} = (\pi, \pi)$ in the spectral function, which has no spectral weight in the equilibrium spectrum [86].

A promising future direction is to perform similar numerical simulations of the time-dependent spectral function for extended 2D systems. The perhaps most interesting candidates are the 2D Fermi-Hubbard or $t - J$ models at finite doping, where our protocol can help to resolve the long-standing question concerning the existence of (unoccupied) states on the back side of the Fermi arcs. As numerical

calculations in this regime are challenging, experimental realizations become essential. Measuring the particle spectral function, which is challenging in solids, could lead to an alternative route to probing unoccupied states. Apart from the square lattice $t-J$ model discussed here, pump-probe spectroscopy with strong magnetic fields also enables new insights into the properties of spinons in other models and geometries, such as triangular and Kagomé lattices or the J_1-J_2 model [523]. Graphene, simulable in hexagonal lattice quantum simulators, exhibits a d-wave superconducting state due to a Van-Hove singularity, which could be probed by shifting the band structure occupation akin to our protocol [524].

9.7 OUTLOOK: THEORY-INDEPENDENT THERMOMETRY IN FERMI GASES

Most schemes to measure temperature rely on comparison with a model, for example by fitting the density distribution in a harmonic trap to a Thomas Fermi profile [525] or a virial expansion [526] or the mean energy per particle to Nozière-Schmitt-Rink theory [525]. However, for strong interactions, the theories compared with are not exact and hence introduce systematic uncertainties in the temperature measurement. Recently, a theory-independent scheme using the fluctuation-dissipation-relation has been presented [320] and recently demonstrated in a quantum gas microscope [321]. It is based on a relation between the compressibility and density correlations. While it only requires a measurement of the spatially resolved density, a non-uniform trap (e.g. linear or harmonic) is needed such that a homogeneous gas would first have to be adiabatically transferred into an inhomogeneous trap. Here, we present a scheme that enables a direct measurement based on ARPES and ARIPES spectra, which removes the necessity to take into account details of the trap.

9.7.1 *Compressibility scheme*

It can be shown [320] that the iso-thermal compressibility at density n, $\kappa = \frac{1}{n^2}\frac{\partial\langle\hat{n}(\mathbf{r})\rangle}{\partial\mu}\big|_T$, is related to the density fluctuations by

$$k_B T \frac{\partial \langle n(\mathbf{r})\rangle}{\partial\mu}\bigg|_T = \langle n(\mathbf{r})n\rangle - \langle n(\mathbf{r})\rangle \langle n\rangle \,, \tag{9.97}$$

where n on the right hand side is still operator valued, i.e. $n(\mathbf{r})$ needs to be multiplied with the total density in the same shot *before* averaging to get $\langle n(\mathbf{r})n\rangle$. In an inhomogenous trap with potential $V(\mathbf{r})$, the chemical potential μ is dependent on $\mathbf{r}$, such that $\mu = \mu_{\text{hom}} - V(\mathbf{r})$. Using the known $V(\mathbf{r})$, we can bring Eq. (9.97)

into a more useful form. In particular, by applying a linear gradient $V(x) = \delta x$ along the x-direction additionally to the homogeneous box trap, we get

$$-\frac{k_B T}{\delta}\frac{\partial \langle n(\mathbf{r})\rangle}{\partial x} = \langle n(\mathbf{r})n\rangle - \langle n(\mathbf{r})\rangle \langle n\rangle . \tag{9.98}$$

The homogeneous gas needs to be adiabatically transferred into the new trap. After that, the spatial dependence of the density is measured and the temperature extracted from the above formulas.

9.7.2 *RF scheme*

Here we use the fluctuation-dissipation relation between the ejection spectrum $A(\omega)$ and the injection spectrum $A^{>}(\omega)$, given by

$$A(\omega) = e^{-\omega/k_B T} A^{>}(\omega), \tag{9.99}$$

which again can be used as a thermometer without theory input. We have discussed this possibility at length in chapter 4 for Hermitian operators, for which the fluctuation-dissipation relation takes a slightly different form. Here, we shortly recapitulate its derivation from the properties of the thermal density matrix and the cyclicity of the trace,

$$A(k,t) = \frac{1}{Z}\operatorname{Tr}(e^{-\beta H} c_k^\dagger(t) c_k) = \frac{1}{Z}\operatorname{Tr}(e^{-\beta H} c_k c_k^\dagger(t+i\beta)) = A^{>}(k, t+i\beta). \tag{9.100}$$

Fourier transforming both sides we get

$$A(k,\omega) = e^{\beta\omega} A^{>}(k,\omega). \tag{9.101}$$

Ejection and injection RF spectroscopy

The following derivations follow Refs. [489, 515, 527–530] employing Fermi's golden rule. This corresponds to an alternative derivation of the equilibrium limit of the time-dependent protocols discussed in section 9.2, leading to equivalent results. The measurement of the spectrum uses a third, initially unoccupied state, which is coupled to one of the two science states with an RF pulse with a small Rabi frequency $\Omega \ll E_F$ and frequency ω. This pulse induces a coupling Hamiltonian

$$V = \frac{\hbar\Omega}{2}\cos(\omega t)\sum_k d_k^\dagger c_k + c_k^\dagger d_k, \tag{9.102}$$

where d_k destroys an atom with momentum k in the third state and c_k destroys an atom in one of the two science states.

Within Fermi's golden rule, the transition rate from an initial state i to a final state f within the subsector of N atoms is given by

$$\Gamma(\omega)_{i\to f} = 2\pi |\langle f^N|V|i^N\rangle|^2 \delta(\hbar\omega - (E_f^N - E_i^N)) \tag{9.103}$$

As the third state is assumed not to interact with the science states, both initial and final states are tensor product states of the form $|n^N\rangle = |n_d^{N-M}\rangle \otimes |n_c^M\rangle$ and the eigenstates are given by $E_n^N = E_{d,n}^{N-M} + E_{c,n}^M$ where we indicated the number of Fermions in the superscript. A single particle state in the third state has energy $\epsilon_k + \Delta$, where Δ is the Zeeman splitting between the third state and the system and $\epsilon_k = k^2/2m$. The measurement of injection and ejection spectra then correspond to situations in which the third state is either fully occupied (in the sense of having a Fermi Energy much larger than the energy scales in the system) or unoccupied, respectively. This means that the first/second term in Eq. 9.102 do not contribute in Eq. 9.103.

EJECTION SPECTRUM Assuming that initially the system is in its ground state with N atoms and the third state is empty, the initial energy is given by $E_i^N = E_{c,0}^N$. The final states then have energy $E_f^N = \epsilon_k + \Delta + E_{c,f}^{N-1}$. Summing over all possible final states, we get that the ARPES spectrum (i.e. the momentum resolved transition rate of an atom of momentum k to the third state) is given by

$$\Gamma^-(k,\omega) = 2\pi \left|\frac{\hbar\Omega}{2}\right|^2 \sum_f |\langle f_c^{N-1}|c_k|0_c^N\rangle|^2 \delta(\hbar\omega - (\epsilon_k + \Delta + E_{c,f}^{N-1} - E_{c,0}^N)) \tag{9.104}$$

$$= \left|\frac{\hbar\Omega}{2}\right|^2 A(k, \omega - (\epsilon_k + \Delta)/\hbar), \tag{9.105}$$

where in the last step we defined the ejection/hole spectral function by

$$A(k,\omega) = 2\pi \sum_f |\langle f_c^{N-1}|c_k|0_c^N\rangle|^2 \delta(\hbar\omega - (E_{c,f}^{N-1} - E_{c,0}^N)). \tag{9.106}$$

INJECTION SPECTRUM Contrastingly, in injection spectroscopy the third state is assumed to be completely filled such that the initial energy is $E_i^N = E_{c,0}^N + \sum_{k=0}^{k_F}(\epsilon_k + \Delta)$, with k_F the Fermi momentum of the third state and in slight abuse of notation we only indicate the occupation of the system state. After injecting an

atom with momentum k from the detection to the third state, the energy is given by $E_f^N = \sum_{k=0}^{k_F}(\epsilon_k + \Delta) + E_{c,f}^{N+1} - (\epsilon_k + \Delta)$. Hence we get for the transition rate

$$\Gamma^+(k,\omega) = 2\pi \left|\frac{\hbar\Omega}{2}\right|^2 \sum_f |\langle f_c^{N+1}|c_k^\dagger|0_c^N\rangle|^2 \delta(\hbar\omega - (\epsilon_k + \Delta - (E_{c,f}^{N+1} - E_{c,0}^N))) \tag{9.107}$$

$$= \left|\frac{\hbar\Omega}{2}\right|^2 A^>(k, \omega - (\epsilon_k + \Delta)/\hbar), \tag{9.108}$$

and we defined the injection/particle spectral function

$$A^>(k,\omega) = 2\pi \sum_f |\langle f_c^{N+1}|c_k^\dagger|0_c^N\rangle|^2 \delta(\hbar\omega + (E_{c,f}^{N+1} - E_{c,n}^N)). \tag{9.109}$$

Above, we calculated all expressions in a momentum-resolved way. The RF spectra without momentum resolution are obtained by summming over all momenta.

9.7.3 *Thermometry in presence of particle-hole symmetry*

The schemes discussed above can of course equally be used in lattice models. Here, we show that in the presence of a particle-hole symmetry, only the ARPES spectrum needs to be measured for thermometry, as the ARIPES spectrum can be obtained from it.

The Hubbard model

$$\hat{H} = -t \sum_{\langle ij\rangle,\sigma} \left(\hat{c}_{i\sigma}^\dagger \hat{c}_{j\sigma} + \hat{c}_{j\sigma}^\dagger \hat{c}_{i\sigma}\right) + U \sum_i \left(\hat{n}_{i\uparrow} - \frac{1}{2}\right)\left(\hat{n}_{i\downarrow} - \frac{1}{2}\right) + \mu \sum_{i,\sigma} \left(\hat{n}_{i\sigma} - \frac{1}{2}\right) \tag{9.110}$$

on bipartite lattices is invariant under a particle hole transformation up to a flip of the chemical potential $\mu \to -\mu$. It is given by

$$\hat{c}_\uparrow^\dagger \to \pm\hat{c}_\downarrow, \qquad \hat{c}_\downarrow^\dagger \to \mp\hat{c}_\uparrow, \tag{9.111}$$

$$\hat{c}_\uparrow \to \pm\hat{c}_\downarrow^\dagger, \qquad \hat{c}_\downarrow \to \mp\hat{c}_\downarrow^\dagger, \tag{9.112}$$

where the top/bottom sign is for the A/B sublattice respectively. Under this transformation, composite operators transform as

$$\hat{n}_{i\sigma} \to 1 - \hat{n}_{i\bar{\sigma}}, \qquad \hat{S}^\alpha \to \hat{S}^\alpha \tag{9.113}$$

with the spin operators ($\alpha \in x, y, z$) defined as usual and $\bar{\sigma}$ indicating the opposite spin.

The lesser and greater Green's functions

$$G_{ij,\sigma}^<(t_1,t_2) = \mathrm{Tr}\left(\rho_0 \hat{c}_{i\sigma}^\dagger(t_1)\hat{c}_{j\sigma}(t_2)\right), \qquad G_{ij,\sigma}^>(t_1,t_2) = \mathrm{Tr}\left(\rho_0 \hat{c}_{j\sigma}(t_2)\hat{c}_{i\sigma}^\dagger(t_1)\right), \tag{9.114}$$

which determine what is measured in ARPES, and ARIPES, respectively, transform as

$$G^{<}_{ij,\sigma}(t_1, t_2) \to \pm \tilde{G}^{>}_{ji,\bar{\sigma}}(t_2, t_1), \tag{9.115}$$

where the tilde indicates evaluation with the particle-hole transformed initial state $\rho_0 \to \Gamma \rho_0 \Gamma^\dagger$ and the top/bottom sign holds if i, j are on the same/different sublattice.

Transforming to central and relative times, and Fourier transforming with respect to the latter we can follow

$$G^{<}_{ij,\sigma}(T, \omega) \to \pm \tilde{G}^{>}_{ji,\bar{\sigma}}(T, -\omega). \tag{9.116}$$

If the initial state is particle-hole symmetric, for example a thermal equilibrium state or the ground state at half filling perturbed by a unitary $\sim \exp(i\alpha S^\alpha)$ then $G^>$ can be directly obtained from $G^<$.

Here, we assumed that $\mu = 0$, $\mu \neq 0$ only leads to a shift of the frequency zero (LHS and RHS shifted oppositely due to $\mu \to -\mu$ after the particle-hole transformation).

In equilibrium, we can drop the central time (T) dependence. The fluctuation dissipation relation then dictates that

$$\sum_\sigma G^{<}_{ii,\sigma}(-\omega) = e^{-\beta\omega} \sum_\sigma G^{<}_{ii,\sigma}(\omega), \tag{9.117}$$

i.e. the sought-after relation from which the temperature β can be extracted. The equal-site Green's function can be obtained from the sum over all momenta of the ARPES spectrum.

10

CONCLUSIONS AND OUTLOOK

In the first part of the thesis, we studied several aspects of the thermalization dynamics of quantum many-body systems, ranging from the spreading of many-body chaos close to a thermal phase transition over the theory-independent probing of eigenstate thermalization in quantum simulators and gauge theories to the emergence of hydrodynamics in long-range systems, which all necessitated the study of two-time correlation functions.

We showed that the out-of-time-ordered correlation function (OTOC) increases exponentially with time in a relativistic scalar field theory. In particular, this qualitative behaviour persisted near the thermal phase transition, which was surprising given the fact that single particle relaxation slows down drastically at this point. Moreover, the OTOC spreads ballistically in space, showing a maximum of the velocity near the phase transition. An interesting future direction would be to study how the OTOC behaves in a true non-equilibrium setting, in which it is likely to become dependent on the central time. We have made a first step in this direction by generalizing our semi-classical method to non-equilibrium settings. In particular, it would be intriguing to see whether the OTOC shows unusual behaviour near non-thermal fixed points [50].

In chapter 4 we developed a protocol to probe thermalization without theory input in quantum simulation experiments: by using two-time correlation functions and a test of the fluctuation dissipation relations (FDRs). In particular, we stressed that this probes the *off-diagonal* part of eigenstate thermalization hypothesis (ETH), which is challenging to do by other means. We showed that not only the emergence of equilibrium can be tested in that way, but also the approach to equilibrium in settings in which the system takes a "detour". In particular, prethermalization can be characterized by the emergence of FDRs with an effective temperature corresponding to the *prethermal* Hamiltonian. Moreover, we showed that non-thermal excitations can be directly characterized using two-time correlation functions, which we examined in the context of confined excitations. Naturally, it would be interesting to see whether this protocol also works for other settings with non-thermal excitations. We have for instance made first steps towards characterizing many-body scars in this way. Moreover, the spectroscopic nature of our protocols may enable an energy-resolved study of Hilbert space fragmentation [61] by also varying the energy of the initial state and hence the overlap with different fragmented sectors.

In chapter 9 of the second part, we developed a further protocol for studying two-time correlation functions in experiment, building on the ideas we developed in this part.

In chapter 5 we extended our study of two-time correlation functions to the lattice Schwinger model by employing two-particle irreducible effective action methods (2PIs). This constitutes an important technical progress as this technique has so far not been successfully applied to studying gauge theories. While we made first steps towards characterizing the thermalization of strings in a high-temperature regime at weak coupling, further study is warranted to study thermalization in different settings. Most importantly, the thermalization of strings created on top of the interacting vacuum would be most interesting. Moreover, strong electric fields can create pairs out of the vacuum, a phenomenon called the Schwinger effect [531–533]. It would be interesting how these pairs scatter and finally thermalize. Moreover, the thermalization of non-abelian gauge fields is of importance to gain intuition for collider experiments. We made first steps in this direction by developing a systematic $1/N$ expansion for SU(N) gauge theories in one dimension. We furthermore developed a technique to directly calculate infinite temperature spectral functions within 2PI. These could also be applied to studying the stability of strong zero modes [534–537].

In chapter 6 we showed the emergence of hydrodynamic transport in the late time regime of quantum systems, which had so far been elusive. In particular, we showed that spin transport in long-range interacting spin systems is superdiffusive, behaving according to the theory of Lévy flights. We employed the Schwinger Boson two-particle irreducible effective action method for spin systems (spin-2PI), which we further developed in the context of this thesis, as well as the discrete truncated Wigner approximation (dTWA) method. Several interesting aspects emerge from the Lévy flight picture. For instance, we showed that linear response theory breaks down, which makes the usual way of probing transport in condensed matter systems challenging. In a collaboration with a trapped ion quantum simulation experiment, a different route was taken by directly measuring the infinite temperature spin correlation function. We were able to confirm the Lévy flight picture by comparison to the experiment and extract the diffusion coefficients. Several future research directions are openend up by these results. For instance, the long-range exponents at which superdiffusive behaviour is found are different to the exponents at which Lieb-Robinson bounds do not behave according to the short-range expectation [178]. It would therefore be interesting to study the recently found connection between transport and Rény entropy growth [538], as well as their connection to operator spreading in this long-range model. Moreover, the dynamics of non-thermal fixed points crucially depends on dimensionality [539]. Hence, long-range interactions

should lead to a novel class of far-from-equilibrium universality with tunable scaling exponents. Our protocol to study transport in quantum simulation experiments can be readily applied to other experimental setups, enabling the routine extraction of diffusion coefficients from experiment.

In the second part we have applied non-equilibrium methods to study phases of matter, showing that some of the intuitions gained while asking fundamental questions around the thermalization of quantum systems can be applied to studying equilibrium properties in condensed-matter systems and quantum simulators.

We made first steps towards describing the disordered electron gas in the presence of screening in the metallic phase on a microscopic level. We extended Hartree Fock theory with a screening procedure and showed that in most regimes, screening does not play a large role. We developed an effective theory of particle hole excitations building on the screened Hartree Fock theory and showed how to extract the non-linear spectrum in this theory. In the future, the numerical evaluation of the particle hole Hamiltonian could enable a characterization of the nature of the particle hole excitations. In particular, the most pressing question is whether their properties could already give a hint at the signals seen in the experiment in Ref. [433].

In chapter 8 we showed that spin spiral states are unstable in the one- and two-dimensional Heisenberg model. The instability was characterized from several perspectives: With a short time expansion, we analyzed the initial decay due to perturbative quantum effects. Intermediate time scales were analyzed using the spin-2PI method, in which we showed the crossover to the instability dynamics. The latter were derived from a Holstein-Primakoff expansion and numerically verified with both matrix product state and dTWA methods. The instability was identified as a "transverse" one, i.e. fluctuations in the spin components transverse to the spiral grow quickly and destabilize it. We connected our results to usual instabilities in bosonic superfluids by varying the anisotropy of the spin interactions, showing that they are smoothly connected. Our results give some indications for the stability of spin superfluids: Despite the spiral being a classical steady state, we showed that quantum fluctuations render this state unstable. Recently, it has been shown that the large fluctuations built up during the instability dynamics can lead to the emergence of a non-thermal fixed point of the dynamics [476, 540]. It would be interesting to see whether such behaviour also emerges in long-range interacting systems, which would also enable immediate study in trapped ion quantum simulators. In particular, as non-thermal fixed point behaviour is connected to turbulent transport [50, 468], it would be interesting how the Lévy flight behaviour we found in chapter 6 modifies this picture.

In the last chapter, we developed a protocol to measure time-dependent angle-resolved photoemission spectra in cold atom quantum simulators. We showed

that combining this technique with strong magnetic field gradients enables the study of spinon excitations in one-dimensional quantum magnets which are not occupied in the ground state. Moreover, we showed that oscillations in the spectral weight indicate beyond mean-field interactions between spinons. Lastly, we obtained first indications that in two spatial dimensions, spinon excitations get occupied at momentum (π, π), indicating that the missing ground state spectral weight is indeed due to the formation of a spinon Fermi sea. Further study is implied by these results. Firstly, using matrix product state methods on cylinders would enable a confirmation of the 2D results in larger systems. Repeating the same study with finite doping, a rather challenging numerical setting, could enable a resolution of the riddle behind Fermi arcs - spectral weight appearing after the application of a magnetic field gradient would give strong indications that the missing weight on the backside of Fermi arcs is indeed due to the presence of a spinon Fermi sea and hence a quantum spin liquid. Using an electric field gradient instead of a magnetic one could help to discern effects due to charge and spin excitations. Repeating our protocol in a triangular lattice could furthermore lead to insights into the unoccupied spinon states in two-dimensional quantum spin liquids. Our protocols are not limited to lattice systems. In continuum Fermi gases, time dependent angle-resolved photoemission spectroscopy (ARPES) enables the study of non-equilibrium dynamics in the unitary regime, including the emergence of fluctuation-dissipation relations as discussed in chapter 4 in the first part.

BIBLIOGRAPHY

[1] L. Boltzmann, *Weitere Studien über das Wärmegleichgewicht unter Gasmolekülen*, Sitzungsberichte der Akademie der Wissenschaften zu Wien **66**, 275 (1872).

[2] J. Loschmidt, *Über den Zustand des Wärmgleichgewichtes eines Systemes von Körpern mit Rücksicht auf die Schwerkraft*, Sitzungsberichte der Akademie der Wissenschaften zu Wien **73**, 128 (1876).

[3] A. Eddington, *The nature of the physical world* (The Macmillan Company, New York, 1928).

[4] P. W. Anderson, *More Is Different*, Science **177**, 393 (1972).

[5] W. Haber, Handbuch fr̈ Planung, Gestaltung und Schutz der Umwelt, Band 1 : Die Umwelt des Menschen, (BLV Verlagsgesellschaft Müchen Bern Wien, 1978) Chap. Begriff und System menschlicher Umwelt, p. 74.

[6] D. Levesque and L. Verlet, *Molecular dynamics and time reversibility*, Journal of Statistical Physics **72**, 519 (1993).

[7] L. DÁlessio, Y. Kafri, A. Polkovnikov, and M. Rigol, *From Quantum Chaos and Eigenstate Thermalization to Statistical Mechanics and Thermodynamics*, Advances in Physics **65**, 239 (2016).

[8] E. N. Lorenz, *Deterministic nonperiodic flow*, Journal of Atmospheric Sciences **20**, 130 (1963).

[9] A. Lichtenberg and M. Liebermann, *Regular and Chaotic Dynamics* (Springer, Berlin, 1992).

[10] P. Cvitanovic, R. Artuso, R. Mainieri, G. Tanner, and G. Vattay, *Chaos: Classical and Quantum, ChaosBook.org* (Niels Bohr Institute, Copenhagen, 2012).

[11] O. Penrose, *Foundations of Statistical Mechanics* (Pergamon, Oxford, 1970).

[12] Y. Sinai, *On the foundations of the ergodic hypothesis for a dynamical system of statistical mechanics*, Sov. Math. Dokl. **4**, 1818 (1963).

[13] Y. Sinai, *Dynamical systems with elastic reflections: ergodic properties of dispersing billiards*, Russ. Math. Surv. **25**, 137 (1970).

[14] L. Bunimovich, *On the ergodic properties of nowhere dispersing billiards*, Commun. Math. Phys. **65**, 295 (1979).

[15] N. Simanyi, *Proof of the ergodic hypothesis for typical hard ball systems*, Ann. Henri Poincaré **5**, 203 (2004).

[16] D. Poulin, A. Qarry, R. Somma, and F. Verstraete, *Quantum simulation of time-dependent hamiltonians and the convenient illusion of hilbert space*, Phys. Rev. Lett. **106**, 170501 (2011).

[17] J. von Neumann, *Beweis des Ergodensatzes und desH-Theorems in der neuen Mechanik*, Zeitschrift für Physik **57**, 30 (1929).

[18] J. von Neumann, *Proof of the ergodic theorem and the H-theorem in quantum mechanics*, The European Physical Journal H **35**, 201 (2010).

[19] T. Guhr, A. Müller–Groeling, and H. A. Weidenmüller, *Random-matrix theories in quantum physics: common concepts*, Physics Reports **299**, 189 (1998).

[20] M. Mehta, *Random Matrices* (Elsevier/Academic Press, Amsterdam, 2004).

[21] E. P. Wigner, *Characteristic vectors of bordered matrices with infinite dimensions*, Annals of Mathematics **62**, 548 (1955).

[22] R. Verresen, R. Moessner, and F. Pollmann, *Avoided quasiparticle decay from strong quantum interactions*, Nature Physics **15**, 750 (2019).

[23] M. V. Berry, M. Tabor, and J. M. Ziman, *Level clustering in the regular spectrum*, Proceedings of the Royal Society of London. A. Mathematical and Physical Sciences **356**, 375 (1977).

[24] M. Srednicki, *The approach to thermal equilibrium in quantized chaotic systems*, Journal of Physics A: Mathematical and General **32**, 1163 (1999).

[25] J. M. Deutsch, *Quantum statistical mechanics in a closed system*, Phys. Rev. A **43**, 2046 (1991).

[26] M. Srednicki, *Chaos and quantum thermalization*, Phys. Rev. E **50**, 888 (1994).

[27] M. Rigol, V. Dunjko, and M. Olshanii, *Thermalization and its mechanism for generic isolated quantum systems*, Nature **452**, 854 (2008).

[28] G. De Palma, A. Serafini, V. Giovannetti, and M. Cramer, *Necessity of eigenstate thermalization*, Phys. Rev. Lett. **115**, 220401 (2015).

[29] A. N. Wenz, G. Zürn, S. Murmann, I. Brouzos, T. Lompe, and S. Jochim, *From few to many: Observing the formation of a fermi sea one atom at a time*, Science **342**, 457 (2013).

[30] P. Calabrese and J. Cardy, *Evolution of entanglement entropy in one-dimensional systems*, Journal of Statistical Mechanics: Theory and Experiment **2005**, P04010 (2005).

[31] A. Nahum, J. Ruhman, S. Vijay, and J. Haah, *Quantum entanglement growth under random unitary dynamics*, Phys. Rev. X **7**, 031016 (2017).

[32] T. Zhou and A. Nahum, *Entanglement membrane in chaotic many-body systems*, Phys. Rev. X **10**, 031066 (2020).

[33] T. Zhou and A. Nahum, *Emergent statistical mechanics of entanglement in random unitary circuits*, Phys. Rev. B **99**, 174205 (2019).

[34] M. Knap, *Entanglement production and information scrambling in a noisy spin system*, Phys. Rev. B **98**, 184416 (2018).

[35] S. H. Shenker and D. Stanford, *Black holes and the butterfly effect*, Journal of High Energy Physics **2014**, 67 (2014).

[36] I. L. Aleiner, L. Faoro, and L. B. Ioffe, *Microscopic model of quantum butterfly effect: Out-of-time-order correlators and traveling combustion waves*, Annals of Physics **375**, 378 (2016).

[37] D. Chowdhury and B. Swingle, *Onset of many-body chaos in the $O(N)$ model*, Physical Review D **96**, 065005 (2017).

[38] A. A. Patel, D. Chowdhury, S. Sachdev, and B. Swingle, *Quantum Butterfly Effect in Weakly Interacting Diffusive Metals*, Physical Review X **7**, 031047 (2017).

[39] V. Khemani, D. A. Huse, and A. Nahum, *Velocity-dependent lyapunov exponents in many-body quantum, semiclassical, and classical chaos*, Phys. Rev. B **98**, 144304 (2018).

[40] A. Bohrdt, C. B. Mendl, M. Endres, and M. Knap, *Scrambling and thermalization in a diffusive quantum many-body system*, New Journal of Physics **19**, 063001 (2017).

[41] A. Nahum, S. Vijay, and J. Haah, *Operator spreading in random unitary circuits*, Phys. Rev. X **8**, 021014 (2018).

[42] C. W. von Keyserlingk, T. Rakovszky, F. Pollmann, and S. L. Sondhi, *Operator hydrodynamics, otocs, and entanglement growth in systems without conservation laws*, Phys. Rev. X **8**, 021013 (2018).

[43] T. Rakovszky, F. Pollmann, and C. W. von Keyserlingk, *Diffusive hydrodynamics of out-of-time-ordered correlators with charge conservation*, Phys. Rev. X **8**, 031058 (2018).

[44] E. Leviatan, F. Pollmann, J. H. Bardarson, D. A. Huse, and E. Altman, *Quantum thermalization dynamics with Matrix-Product States*, arXiv:1702.08894 (2017).

[45] T. Rakovszky, C. W. von Keyserlingk, and F. Pollmann, *Dissipation-assisted operator evolution method for capturing hydrodynamic transport*, arXiv:2004.05177 .

[46] J. Berges, S. Borsányi, and C. Wetterich, *Prethermalization*, Phys. Rev. Lett. **93**, 142002 (2004).

[47] M. Gring, M. Kuhnert, T. Langen, T. Kitagawa, B. Rauer, M. Schreitl, I. Mazets, D. A. Smith, E. Demler, and J. Schmiedmayer, *Relaxation and prethermalization in an isolated quantum system*, Science **337**, 1318 (2012).

[48] M. Babadi, E. Demler, and M. Knap, *Far-from-equilibrium field theory of many-body quantum spin systems: Prethermalization and relaxation of spin spiral states in three dimensions*, Phys. Rev. X **5**, 041005 (2015).

[49] J. Berges, A. Rothkopf, and J. Schmidt, *Nonthermal fixed points: Effective weak coupling for strongly correlated systems far from equilibrium*, Phys. Rev. Lett. **101**, 041603 (2008).

[50] A. Piñeiro Orioli, K. Boguslavski, and J. Berges, *Universal self-similar dynamics of relativistic and nonrelativistic field theories near nonthermal fixed points*, Physical Review D **92**, 025041 (2015).

[51] M. Prüfer, P. Kunkel, H. Strobel, S. Lannig, D. Linnemann, C.-M. Schmied, J. Berges, T. Gasenzer, and M. K. Oberthaler, *Observation of universal dynamics in a spinor Bose gas far from equilibrium*, Nature **563**, 217 (2018).

[52] D. Basko, I. Aleiner, and B. Altshuler, *Metal-insulator transition in a weakly interacting many-electron system with localized single-particle states*, Annals of Physics **321**, 1126 (2006).

[53] A. Pal and D. A. Huse, *Many-body localization phase transition*, Phys. Rev. B **82**, 174411 (2010).

[54] R. Vosk, D. A. Huse, and E. Altman, *Theory of the many-body localization transition in one-dimensional systems*, Phys. Rev. X **5**, 031032 (2015).

[55] K. Agarwal, E. Altman, E. Demler, S. Gopalakrishnan, D. A. Huse, and M. Knap, *Rare-region effects and dynamics near the many-body localization transition*, Annalen der Physik **529**, 1600326 (2017).

[56] S. Gopalakrishnan, K. R. Islam, and M. Knap, *Noise-Induced Subdiffusion in Strongly Localized Quantum Systems*, Physical Review Letters **119**, 046601 (2017).

[57] Luitz David J. and Lev Yevgeny Bar, *The ergodic side of the manybody localization transition*, Annalen der Physik **529**, 1600350 (2017).

[58] C. J. Turner, A. A. Michailidis, D. A. Abanin, M. Serbyn, and Z. Papić, *Weak ergodicity breaking from quantum many-body scars*, Nature Physics **14**, 745 (2018).

[59] H. Bernien, S. Schwartz, A. Keesling, H. Levine, A. Omran, H. Pichler, S. Choi, A. S. Zibrov, M. Endres, M. Greiner, V. Vuletić, and M. D. Lukin, *Probing many-body dynamics on a 51-atom quantum simulator*, Nature **551**, 579 (2017).

[60] N. Pancotti, G. Giudice, J. I. Cirac, J. P. Garrahan, and M. C. Bañuls, *Quantum east model: Localization, nonthermal eigenstates, and slow dynamics*, Phys. Rev. X **10**, 021051 (2020).

[61] P. Sala, T. Rakovszky, R. Verresen, M. Knap, and F. Pollmann, *Ergodicity breaking arising from hilbert space fragmentation in dipole-conserving hamiltonians*, Phys. Rev. X **10**, 011047 (2020).

[62] T. Rakovszky, P. Sala, R. Verresen, M. Knap, and F. Pollmann, *Statistical localization: From strong fragmentation to strong edge modes*, Phys. Rev. B **101**, 125126 (2020).

[63] J. P. Bouchaud, *Weak ergodicity breaking and aging in disordered systems*, J. Phys. I France **2**, 1705 (1992).

[64] J. P. Garrahan, *Aspects of non-equilibrium in classical and quantum systems: Slow relaxation and glasses, dynamical large deviations, quantum non-ergodicity, and open quantum dynamics*, Physica A: Statistical Mechanics and its Applications **504**, 130 (2018).

[65] J. Feldmeier, P. Sala, G. De Tomasi, F. Pollmann, and M. Knap, *Anomalous diffusion in dipole- and higher-moment-conserving systems*, Phys. Rev. Lett. **125**, 245303 (2020).

[66] A. W. Sandvik, *Computational Studies of Quantum Spin Systems*, AIP Conference Proceedings **1297**, 135 (2010).

[67] M. R. Garey and D. S. Johnson, *Computers and Intractability: A Guide to the Theory of NP-Completeness* (W. H. Freeman and Co., San Francisco, 1979).

[68] B. Rudiak-Gould, *The sum-over-histories formulation of quantum computing*, arXiv:quant-ph/0607151 (2006).

[69] E. Bernstein and U. Vazirani, *Quantum Complexity Theory*, SIAM Journal on Computing **26**, 1411 (1997).

[70] S. Aaronson and L. Chen, in *32nd Computational Complexity Conference (CCC 2017)*, Leibniz International Proceedings in Informatics (LIPIcs), Vol. 79, edited by R. O'Donnell (Schloss Dagstuhl–Leibniz-Zentrum fuer Informatik, Dagstuhl, Germany, 2017) pp. 22:1–22:67.

[71] R. Feynman, *Feynman's Thesis — A New Approach to Quantum Theory*, edited by L. M. Brown (World Scientific, 2005).

[72] R. P. Feynman, *Space-time approach to non-relativistic quantum mechanics*, Rev. Mod. Phys. **20**, 367 (1948).

[73] P. A. M. Dirac, *The lagrangian in quantum mechanics*, Physikalische Zeitschrift der Sowjetunion **3**, 64 (1933).

[74] Y. Manin, *Computable and Uncomputabl* (Sovetskoye Radio Press, 1980).

[75] R. P. Feynman, *Simulating physics with computers*, International Journal of Theoretical Physics **21**, 467 (1982).

[76] S. R. White, *Density matrix formulation for quantum renormalization groups*, Phys. Rev. Lett. **69**, 2863 (1992).

[77] M. Fannes, B. Nachtergaele, and R. F. Werner, *Finitely correlated states on quantum spin chains*, Communications in Mathematical Physics **144**, 443 (1992).

[78] M. B. Hastings, *An area law for one-dimensional quantum systems*, Journal of Statistical Mechanics: Theory and Experiment **2007**, P08024 (2007).

[79] U. Schollwöck, *The density-matrix renormalization group in the age of matrix product states*, Annals of Physics January 2011 Special Issue, **326**, 96 (2011).

[80] J. Haegeman, J. I. Cirac, T. J. Osborne, I. Pizorn, H. Verschelde, and F. Verstraete, *Time-dependent variational principle for quantum lattices*, Phys. Rev. Lett. **107**, 070601 (2011).

[81] J. Haegeman, C. Lubich, I. Oseledets, B. Vandereycken, and F. Verstraete, *Unifying time evolution and optimization with matrix product states*, Phys. Rev. B **94**, 165116 (2016).

[82] B. Zunkovic, M. Heyl, M. Knap, and A. Silva, *Dynamical quantum phase transitions in spin chains with long-range interactions: Merging different concepts of nonequilibrium criticality*, Phys. Rev. Lett. **120**, 130601 (2018).

[83] M. P. Zaletel, R. S. K. Mong, C. Karrasch, J. E. Moore, and F. Pollmann, *Time-evolving a matrix product state with long-ranged interactions*, Phys. Rev. B **91**, 165112 (2015).

[84] M. Gohlke, R. Verresen, R. Moessner, and F. Pollmann, *Dynamics of the kitaev-heisenberg model*, Phys. Rev. Lett. **119**, 157203 (2017).

[85] R. Verresen, F. Pollmann, and R. Moessner, *Quantum dynamics of the square-lattice heisenberg model*, Phys. Rev. B **98**, 155102 (2018).

[86] A. Bohrdt, E. Demler, F. Pollmann, M. Knap, and F. Grusdt, *Parton theory of angle-resolved photoemission spectroscopy spectra in antiferromagnetic mott insulators*, Phys. Rev. B **102**, 035139 (2020).

[87] A. Bohrdt, F. Grusdt, and M. Knap, *Dynamical formation of a magnetic polaron in a two-dimensional quantum antiferromagnet*, New Journal of Physics **22**, 123023 (2020).

[88] G. Vidal, *Efficient simulation of one-dimensional quantum many-body systems*, Phys. Rev. Lett. **93**, 040502 (2004).

[89] J. Hauschild and F. Pollmann, *Efficient numerical simulations with Tensor Networks: Tensor Network Python (TeNPy)*, SciPost Phys. Lect. Notes , 5 (2018).

[90] F. Verstraete, J. J. García-Ripoll, and J. I. Cirac, *Matrix Product Density Operators: Simulation of Finite-Temperature and Dissipative Systems*, Physical Review Letters **93**, 207204 (2004).

[91] S. R. White and A. E. Feiguin, *Real-time evolution using the density matrix renormalization group*, Phys. Rev. Lett. **93**, 076401 (2004).

[92] F. Verstraete, V. Murg, and J. Cirac, *Matrix product states, projected entangled pair states, and variational renormalization group methods for quantum spin systems*, Advances in Physics **57**, 143 (2008).

[93] U. Schollwöck, *The density-matrix renormalization group*, Rev. Mod. Phys. **77**, 259 (2005).

[94] T. Barthel, *Precise evaluation of thermal response functions by optimized density matrix renormalization group schemes*, New Journal of Physics **15**, 073010 (2013).

[95] A. Bohrdt, D. Greif, E. Demler, M. Knap, and F. Grusdt, *Angle-resolved photoemission spectroscopy with quantum gas microscopes*, Phys. Rev. B **97**, 125117 (2018).

[96] N. N. Bogoliubov, *Kinetic equations*, Journal of Experimental and Theoretical Physics **16**, 691 (1946).

[97] M. Born and H. S. Green, *A general kinetic theory of liquids i. the molecular distribution functions*, Proceedings of the Royal Society of London. Series A. Mathematical and Physical Sciences **188**, 10 (1946).

[98] J. G. Kirkwood, *The statistical mechanical theory of transport processes i. general theory*, The Journal of Chemical Physics **14**, 180 (1946).

[99] J. G. Kirkwood, *The statistical mechanical theory of transport processes ii. transport in gases*, The Journal of Chemical Physics **15**, 72 (1947).

[100] J. Yvon, *La Théorie Statistique des Fluids et l'Équation d'État* (Hermann & Cie, Paris, 1935) p. 180.

[101] L. Kadanoff and G. Baym, *Quantum Statistical Mechanics* (Westview Press, 1994).

[102] J. Berges, in *AIP Conference Proceedings*, Vol. 739 (AIP, Rio de Janeiro (Brazil), 2004) pp. 3–62.

[103] A. Barenco, C. H. Bennett, R. Cleve, D. P. DiVincenzo, N. Margolus, P. Shor, T. Sleator, J. A. Smolin, and H. Weinfurter, *Elementary gates for quantum computation*, Phys. Rev. A **52**, 3457 (1995).

[104] N. Wiebe, D. W. Berry, P. Høyer, and B. C. Sanders, *Simulating quantum dynamics on a quantum computer*, Journal of Physics A: Mathematical and Theoretical **44**, 445308 (2011).

[105] H. Lamm and S. Lawrence, *Simulation of nonequilibrium dynamics on a quantum computer*, Phys. Rev. Lett. **121**, 170501 (2018).

[106] A. Smith, M. S. Kim, F. Pollmann, and J. Knolle, *Simulating quantum many-body dynamics on a current digital quantum computer*, npj Quantum Information **5**, 106 (2019).

[107] Y. Zhou, E. M. Stoudenmire, and X. Waintal, *What limits the simulation of quantum computers?* Phys. Rev. X **10**, 041038 (2020).

[108] S. B. Bravyi and A. Y. Kitaev, *Quantum codes on a lattice with boundary*, arXiv:quant-ph/9811052 (1998).

[109] M. H. Freedman and D. A. Meyer, *Projective Plane and Planar Quantum Codes*, Foundations of Computational Mathematics **1**, 325 (2001).

[110] E. Dennis, A. Kitaev, A. Landahl, and J. Preskill, *Topological quantum memory*, Journal of Mathematical Physics **43**, 4452 (2002).

[111] S.-H. Lin, R. Dilip, A. G. Green, A. Smith, and F. Pollmann, *Real- and imaginary-time evolution with compressed quantum circuits*, PRX Quantum **2**, 010342 (2021).

[112] F. Barratt, J. Dborin, M. Bal, V. Stojevic, F. Pollmann, and A. G. Green, *Parallel quantum simulation of large systems on small NISQ computers*, npj Quantum Information **7**, 79 (2021).

[113] S. Gopalakrishnan and A. Lamacraft, *Unitary circuits of finite depth and infinite width from quantum channels*, Phys. Rev. B **100**, 064309 (2019).

[114] N. F. Mott, *Metal-Insulator Transitions* (Taylor & Francis, London, 1974).

[115] J. G. Bednorz and K. A. Müller, *Possible high T_c superconductivity in the Ba-La-Cu-O system*, Zeitschrift fur Physik B Condensed Matter **64**, 189 (1986).

[116] P. W. Anderson, *The Resonating Valence Bond State in La2CuO4 and Superconductivity*, Science **235**, 1196 (1987).

[117] F. C. Zhang and T. M. Rice, *Effective hamiltonian for the superconducting cu oxides*, Phys. Rev. B **37**, 3759 (1988).

[118] A. Altland and B. Simons, *Condensed Matter Field Theory* (Cambridge Unviversity Press, 2010).

[119] R. S. Markiewicz, S. Sahrakorpi, M. Lindroos, H. Lin, and A. Bansil, *One-band tight-binding model parametrization of the high-T_c cuprates including the effect of k_z dispersion*, Phys. Rev. B **72**, 054519 (2005).

[120] A. L. Cavalieri, N. Müller, T. Uphues, V. S. Yakovlev, A. Baltuška, B. Horvath, B. Schmidt, L. Blümel, R. Holzwarth, S. Hendel, M. Drescher, U. Kleineberg, P. M. Echenique, R. Kienberger, F. Krausz, and U. Heinzmann, *Attosecond spectroscopy in condensed matter*, Nature **449**, 1029 (2007).

[121] Bose, *Plancks Gesetz und Lichtquantenhypothese*, Zeitschrift für Physik **26**, 178 (1924).

[122] A. Einstein, *Quantentheorie des einatomigen idealen gases*, Sitzungsberichte der Preussischen Akademie der Wissenschaften **1**, 3 (1925).

[123] M. H. Anderson, J. R. Ensher, M. R. Matthews, C. E. Wieman, and E. A. Cornell, *Observation of Bose-Einstein Condensation in a Dilute Atomic Vapor*, Science **269**, 198 (1995).

[124] K. B. Davis, M. O. Mewes, M. R. Andrews, N. J. van Druten, D. S. Durfee, D. M. Kurn, and W. Ketterle, *Bose-Einstein Condensation in a Gas of Sodium Atoms*, Physical Review Letters **75**, 3969 (1995).

[125] M. Greiner, O. Mandel, T. Esslinger, T. W. Hänsch, and I. Bloch, *Quantum phase transition from a superfluid to a Mott insulator in a gas of ultracold atoms*, Nature **415**, 39 (2002).

[126] I. Bloch, J. Dalibard, and W. Zwerger, *Many-body physics with ultracold gases*, Reviews of Modern Physics **80**, 885 (2008).

[127] S. Trotzky, Y.-A. Chen, A. Flesch, I. P. McCulloch, U. Schollwöck, J. Eisert, and I. Bloch, *Probing the relaxation towards equilibrium in an isolated strongly correlated one-dimensional Bose gas*, Nature Physics **8**, 325 (2012).

[128] A. Mazurenko, C. S. Chiu, G. Ji, M. F. Parsons, M. Kanász-Nagy, R. Schmidt, F. Grusdt, E. Demler, D. Greif, and M. Greiner, *A cold-atom Fermi–Hubbard antiferromagnet*, Nature **545**, 462 (2017).

[129] M. Schreiber, S. S. Hodgman, P. Bordia, H. P. Lüschen, M. H. Fischer, R. Vosk, E. Altman, U. Schneider, and I. Bloch, *Observation of many-body localization of interacting fermions in a quasirandom optical lattice*, Science **349**, 842 (2015).

[130] M. Schemmer, I. Bouchoule, B. Doyon, and J. Dubail, *Generalized hydrodynamics on an atom chip*, Phys. Rev. Lett. **122**, 090601 (2019).

[131] F. Møller, C. Li, I. Mazets, H.-P. Stimming, T. Zhou, Z. Zhu, X. Chen, and J. Schmiedmayer, *Extension of the generalized hydrodynamics to the dimensional crossover regime*, Phys. Rev. Lett. **126**, 090602 (2021).

[132] N. Malvania, Y. Zhang, Y. Le, J. Dubail, M. Rigol, and D. S. Weiss, *Generalized hydrodynamics in strongly interacting 1D Bose gases*, arXiv: 2009.06651 (2020).

[133] W. S. Bakr, J. I. Gillen, A. Peng, S. Fölling, and M. Greiner, *A quantum gas microscope for detecting single atoms in a hubbard-regime optical lattice*, Nature **462**, 74–77 (2009).

[134] J. F. Sherson, C. Weitenberg, M. Endres, M. Cheneau, I. Bloch, and S. Kuhr, *Single-atom-resolved fluorescence imaging of an atomic mott insulator*, Nature **467**, 68–72 (2010).

[135] M. F. Parsons, F. Huber, A. Mazurenko, C. S. Chiu, W. Setiawan, K. Wooley-Brown, S. Blatt, and M. Greiner, *Site-resolved imaging of fermionic* ^{6}Li *in an optical lattice*, Phys. Rev. Lett. **114**, 213002 (2015).

[136] A. Omran, M. Boll, T. A. Hilker, K. Kleinlein, G. Salomon, I. Bloch, and C. Gross, *Microscopic observation of pauli blocking in degenerate fermionic lattice gases*, Phys. Rev. Lett. **115**, 263001 (2015).

[137] L. W. Cheuk, M. A. Nichols, M. Okan, T. Gersdorf, V. V. Ramasesh, W. S. Bakr, T. Lompe, and M. W. Zwierlein, *Quantum-gas microscope for fermionic atoms*, Phys. Rev. Lett. **114**, 193001 (2015).

[138] G. J. A. Edge, R. Anderson, D. Jervis, D. C. McKay, R. Day, S. Trotzky, and J. H. Thywissen, *Imaging and addressing of individual fermionic atoms in an optical lattice*, Phys. Rev. A **92**, 063406 (2015).

[139] E. Haller, J. Hudson, A. Kelly, D. A. Cotta, B. Peaudecerf, G. D. Bruce, and S. Kuhr, *Single-atom imaging of fermions in a quantum-gas microscope*, Nature Physics **11**, 738 (2015).

[140] D. Greif, M. F. Parsons, A. Mazurenko, C. S. Chiu, S. Blatt, F. Huber, G. Ji, and M. Greiner, *Site-resolved imaging of a fermionic Mott insulator*, Science **351**, 953 (2016).

[141] P. T. Brown, D. Mitra, E. Guardado-Sanchez, R. Nourafkan, A. Reymbaut, C.-D. Hébert, S. Bergeron, A.-M. S. Tremblay, J. Kokalj, D. A. Huse, P. Schauß, and W. S. Bakr, *Bad metallic transport in a cold atom Fermi-Hubbard system*, Science **363**, 379 (2019).

[142] C. S. Chiu, G. Ji, A. Bohrdt, M. Xu, M. Knap, E. Demler, F. Grusdt, M. Greiner, and D. Greif, *String patterns in the doped Hubbard model*, Science **365**, 251 (2019).

[143] A. Bohrdt, C. S. Chiu, G. Ji, M. Xu, D. Greif, M. Greiner, E. Demler, F. Grusdt, and M. Knap, *Classifying snapshots of the doped Hubbard model with machine learning*, Nature Physics **15**, 921 (2019).

[144] T. Esslinger, *Fermi-hubbard physics with atoms in an optical lattice*, Annual Review of Condensed Matter Physics **1**, 129 (2010), https://doi.org/10.1146/annurev-conmatphys-070909-104059 .

[145] A. Bohrdt, L. Homeier, C. Reinmoser, E. Demler, and F. Grusdt, *Exploration of doped quantum magnets with ultracold atoms*, arXiv:2107.08043 (2021).

[146] A. M. Kaufman, M. E. Tai, A. Lukin, M. Rispoli, R. Schittko, P. M. Preiss, and M. Greiner, *Quantum thermalization through entanglement in an isolated many-body system*, Science **353**, 794 (2016).

[147] J. Vijayan, P. Sompet, G. Salomon, J. Koepsell, S. Hirthe, A. Bohrdt, F. Grusdt, I. Bloch, and C. Gross, *Time-resolved observation of spin-charge deconfinement in fermionic hubbard chains*, Science **367**, 186 (2020).

[148] G. Ji, M. Xu, L. H. Kendrick, C. S. Chiu, J. C. Brüggenjürgen, D. Greif, A. Bohrdt, F. Grusdt, E. Demler, M. Lebrat, and M. Greiner, *Coupling a mobile hole to an antiferromagnetic spin background: Transient dynamics of a magnetic polaron*, Phys. Rev. X **11**, 021022 (2021).

[149] A. Rubio-Abadal, M. Ippoliti, S. Hollerith, D. Wei, J. Rui, S. L. Sondhi, V. Khemani, C. Gross, and I. Bloch, *Floquet prethermalization in a bose-hubbard system*, Phys. Rev. X **10**, 021044 (2020).

[150] S. Scherg, T. Kohlert, P. Sala, F. Pollmann, B. Hebbe Madhusudhana, I. Bloch, and M. Aidelsburger, *Observing non-ergodicity due to kinetic constraints in tilted Fermi-Hubbard chains*, Nature Communications **12**, 4490 (2021).

[151] N. D. Oppong, G. Pasqualetti, O. Bettermann, P. Zechmann, M. Knap, I. Bloch, and S. Fölling, *Probing transport and slow relaxation in the mass-imbalanced Fermi-Hubbard model*, arXiv:2011.12411 (2020).

[152] P. Bordia, H. Lüschen, S. Scherg, S. Gopalakrishnan, M. Knap, U. Schneider, and I. Bloch, *Probing slow relaxation and many-body localization in two-dimensional quasiperiodic systems*, Phys. Rev. X **7**, 041047 (2017).

[153] A. Lukin, M. Rispoli, R. Schittko, M. E. Tai, A. M. Kaufman, S. Choi, V. Khemani, J. Léonard, and M. Greiner, *Probing entanglement in a many-body–localized system*, Science **364**, 256 (2019).

[154] J.-y. Choi, S. Hild, J. Zeiher, P. Schauß, A. Rubio-Abadal, T. Yefsah, V. Khemani, D. A. Huse, I. Bloch, and C. Gross, *Exploring the many-body localization transition in two dimensions*, Science **352**, 1547 (2016).

[155] A. Rubio-Abadal, J.-y. Choi, J. Zeiher, S. Hollerith, J. Rui, I. Bloch, and C. Gross, *Many-body delocalization in the presence of a quantum bath*, Phys. Rev. X **9**, 041014 (2019).

[156] T. Kohlert, S. Scherg, X. Li, H. P. Lüschen, S. Das Sarma, I. Bloch, and M. Aidelsburger, *Observation of many-body localization in a one-dimensional system with a single-particle mobility edge*, Phys. Rev. Lett. **122**, 170403 (2019).

[157] P. Bordia, H. Lüschen, U. Schneider, M. Knap, and I. Bloch, *Periodically driving a many-body localized quantum system*, Nature Physics **13**, 460 (2017).

[158] H. P. Lüschen, P. Bordia, S. S. Hodgman, M. Schreiber, S. Sarkar, A. J. Daley, M. H. Fischer, E. Altman, I. Bloch, and U. Schneider, *Signatures of many-body localization in a controlled open quantum system*, Phys. Rev. X **7**, 011034 (2017).

[159] M. Rispoli, A. Lukin, R. Schittko, S. Kim, M. E. Tai, J. Léonard, and M. Greiner, *Quantum critical behaviour at the many-body localization transition*, Nature **573**, 385 (2019).

[160] S. Trotzky, P. Cheinet, S. Fölling, M. Feld, U. Schnorrberger, A. M. Rey, A. Polkovnikov, E. A. Demler, M. D. Lukin, and I. Bloch, *Time-resolved observation and control of superexchange interactions with ultracold atoms in optical lattices*, Science **319**, 295 (2008).

[161] R. C. Brown, R. Wyllie, S. B. Koller, E. A. Goldschmidt, M. Foss-Feig, and J. V. Porto, *Two-dimensional superexchange-mediated magnetization dynamics in an optical lattice*, Science **348**, 540 (2015).

[162] S. Hild, T. Fukuhara, P. Schauß, J. Zeiher, M. Knap, E. Demler, I. Bloch, and C. Gross, *Far-from-equilibrium spin transport in heisenberg quantum magnets*, Phys. Rev. Lett. **113**, 147205 (2014).

[163] P. N. Jepsen, J. Amato-Grill, I. Dimitrova, W. W. Ho, E. Demler, and W. Ketterle, *Spin transport in a tunable heisenberg model realized with ultracold atoms*, Nature **588**, 403 (2020).

[164] A. Signoles, T. Franz, R. Ferracini Alves, M. Gärttner, S. Whitlock, G. Zürn, and M. Weidemüller, *Glassy dynamics in a disordered heisenberg quantum spin system*, Phys. Rev. X **11**, 011011 (2021).

[165] A. Piñeiro Orioli, A. Signoles, H. Wildhagen, G. Günter, J. Berges, S. Whitlock, and M. Weidemüller, *Relaxation of an isolated dipolar-interacting rydberg quantum spin system*, Phys. Rev. Lett. **120**, 063601 (2018).

[166] A. Ashkin, *Acceleration and trapping of particles by radiation pressure*, Phys. Rev. Lett. **24**, 156 (1970).

[167] A. Ashkin, J. M. Dziedzic, J. E. Bjorkholm, and S. Chu, *Observation of a single-beam gradient force optical trap for dielectric particles*, Opt. Lett. **11**, 288 (1986).

[168] A. Browaeys and T. Lahaye, *Many-body physics with individually controlled Rydberg atoms*, Nature Physics **16**, 132 (2020).

[169] D. Barredo, S. de Léséleuc, V. Lienhard, T. Lahaye, and A. Browaeys, *An atom-by-atom assembler of defect-free arbitrary two-dimensional atomic arrays*, Science **354**, 1021 (2016).

[170] S. Ebadi, T. T. Wang, H. Levine, A. Keesling, G. Semeghini, A. Omran, D. Bluvstein, R. Samajdar, H. Pichler, W. W. Ho, S. Choi, S. Sachdev, M. Greiner, V. Vuletić, and M. D. Lukin, *Quantum phases of matter on a 256-atom programmable quantum simulator*, Nature **595**, 227 (2021).

[171] G. Semeghini, H. Levine, A. Keesling, S. Ebadi, T. T. Wang, D. Bluvstein, R. Verresen, H. Pichler, M. Kalinowski, R. Samajdar, A. Omran, S. Sachdev, A. Vishwanath, M. Greiner, V. Vuletic, and M. D. Lukin, *Probing Topological Spin Liquids on a Programmable Quantum Simulator*, arXiv:2104.04119 [cond-mat, physics:physics, physics:quant-ph] (2021), arXiv: 2104.04119.

[172] A. Keesling, A. Omran, H. Levine, H. Bernien, H. Pichler, S. Choi, R. Samajdar, S. Schwartz, P. Silvi, S. Sachdev, P. Zoller, M. Endres, M. Greiner, V. Vuletić, and M. D. Lukin, *Quantum Kibble–Zurek mechanism and critical dynamics on a programmable Rydberg simulator*, Nature **568**, 207 (2019).

[173] J. Zeiher, J.-y. Choi, A. Rubio-Abadal, T. Pohl, R. van Bijnen, I. Bloch, and C. Gross, *Coherent many-body spin dynamics in a long-range interacting ising chain*, Phys. Rev. X **7**, 041063 (2017).

[174] H. Häffner, C. F. Roos, and R. Blatt, *Quantum computing with trapped ions*, Physics Reports **469**, 155 (2008).

[175] C. Monroe, W. C. Campbell, L.-M. Duan, Z.-X. Gong, A. V. Gorshkov, P. W. Hess, R. Islam, K. Kim, N. M. Linke, G. Pagano, P. Richerme, C. Senko, and N. Y. Yao, *Programmable quantum simulations of spin systems with trapped ions*, Rev. Mod. Phys. **93**, 025001 (2021).

[176] P. Richerme, Z.-X. Gong, A. Lee, C. Senko, J. Smith, M. Foss-Feig, S. Michalakis, A. V. Gorshkov, and C. Monroe, *Non-local propagation of correlations in quantum systems with long-range interactions*, Nature **511**, 198 (2014).

[177] E. H. Lieb and D. W. Robinson, *The finite group velocity of quantum spin systems*, Communications in Mathematical Physics **28**, 251 (1972).

[178] M. C. Tran, A. Y. Guo, C. L. Baldwin, A. Ehrenberg, A. V. Gorshkov, and A. Lucas, *The lieb-robinson light cone for power-law interactions*, arXiv:2103.15828 (2021).

[179] J. Smith, A. Lee, P. Richerme, B. Neyenhuis, P. W. Hess, P. Hauke, M. Heyl, D. A. Huse, and C. Monroe, *Many-body localization in a quantum simulator with programmable random disorder*, Nature Physics **12**, 907 (2016).

[180] E. A. Martinez, C. A. Muschik, P. Schindler, D. Nigg, A. Erhard, M. Heyl, P. Hauke, M. Dalmonte, T. Monz, P. Zoller, and R. Blatt, *Real-time dynamics of lattice gauge theories with a few-qubit quantum computer*, Nature **534**, 516 (2016).

[181] P. Jurcevic, H. Shen, P. Hauke, C. Maier, T. Brydges, C. Hempel, B. P. Lanyon, M. Heyl, R. Blatt, and C. F. Roos, *Direct observation of dynamical quantum phase transitions in an interacting many-body system*, Phys. Rev. Lett. **119**, 080501 (2017).

[182] J. Zhang, G. Pagano, P. W. Hess, A. Kyprianidis, P. Becker, H. Kaplan, A. V. Gorshkov, Z.-X. Gong, and C. Monroe, *Observation of a many-body dynamical phase transition with a 53-qubit quantum simulator*, Nature **551**, 601 (2017).

[183] B. Neyenhuis, J. Zhang, P. W. Hess, J. Smith, A. C. Lee, P. Richerme, Z.-X. Gong, A. V. Gorshkov, and C. Monroe, *Observation of prethermalization in long-range interacting spin chains*, Science Advances **3**, e1700672 (2017).

[184] C. Noel, P. Niroula, D. Zhu, A. Risinger, L. Egan, D. Biswas, M. Cetina, A. V. Gorshkov, M. J. Gullans, D. A. Huse, and C. Monroe, *Observation of measurement-induced quantum phases in a trapped-ion quantum computer*, arXiv:2106.05881 (2021).

[185] C. Maier, T. Brydges, P. Jurcevic, N. Trautmann, C. Hempel, B. P. Lanyon, P. Hauke, R. Blatt, and C. F. Roos, *Environment-assisted quantum transport in a 10-qubit network*, Phys. Rev. Lett. **122**, 050501 (2019).

[186] M. K. Joshi, A. Elben, B. Vermersch, T. Brydges, C. Maier, P. Zoller, R. Blatt, and C. F. Roos, *Quantum information scrambling in a trapped-ion quantum simulator with tunable range interactions*, Phys. Rev. Lett. **124**, 240505 (2020).

[187] P. Jurcevic, B. P. Lanyon, P. Hauke, C. Hempel, P. Zoller, R. Blatt, and C. F. Roos, *Quasiparticle engineering and entanglement propagation in a quantum many-body system*, Nature **511**, 202 (2014).

[188] J. Koch, T. M. Yu, J. Gambetta, A. A. Houck, D. I. Schuster, J. Majer, A. Blais, M. H. Devoret, S. M. Girvin, and R. J. Schoelkopf, *Charge-insensitive qubit design derived from the cooper pair box*, Phys. Rev. A **76**, 042319 (2007).

[189] J. A. Schreier, A. A. Houck, J. Koch, D. I. Schuster, B. R. Johnson, J. M. Chow, J. M. Gambetta, J. Majer, L. Frunzio, M. H. Devoret, S. M. Girvin, and R. J. Schoelkopf, *Suppressing charge noise decoherence in superconducting charge qubits*, Phys. Rev. B **77**, 180502 (2008).

[190] C. Neill, P. Roushan, K. Kechedzhi, S. Boixo, S. V. Isakov, V. Smelyanskiy, A. Megrant, B. Chiaro, A. Dunsworth, K. Arya, R. Barends, B. Burkett, Y. Chen, Z. Chen, A. Fowler, B. Foxen, M. Giustina, R. Graff, E. Jeffrey, T. Huang, J. Kelly, P. Klimov, E. Lucero, J. Mutus, M. Neeley, C. Quintana, D. Sank, A. Vainsencher, J. Wenner, T. C. White, H. Neven, and J. M. Martinis, *A blueprint for demonstrating quantum supremacy with superconducting qubits*, Science **360**, 195 (2018).

[191] F. Arute, K. Arya, R. Babbush, D. Bacon, J. C. Bardin, R. Barends, R. Biswas, S. Boixo, F. G. S. L. Brandao, D. A. Buell, B. Burkett, Y. Chen, Z. Chen, B. Chiaro, R. Collins, W. Courtney, A. Dunsworth, E. Farhi, B. Foxen, A. Fowler, C. Gidney, M. Giustina, R. Graff, K. Guerin, S. Habegger, M. P. Harrigan, M. J. Hartmann, A. Ho, M. Hoffmann, T. Huang, T. S. Humble, S. V. Isakov, E. Jeffrey, Z. Jiang, D. Kafri, K. Kechedzhi, J. Kelly, P. V. Klimov, S. Knysh, A. Korotkov, F. Kostritsa, D. Landhuis, M. Lindmark, E. Lucero, D. Lyakh, S. Mandrà, J. R. McClean, M. McEwen, A. Megrant, X. Mi, K. Michielsen, M. Mohseni, J. Mutus, O. Naaman, M. Neeley, C. Neill, M. Y. Niu, E. Ostby, A. Petukhov, J. C. Platt, C. Quintana, E. G. Rieffel, P. Roushan, N. C. Rubin, D. Sank, K. J. Satzinger, V. Smelyanskiy, K. J. Sung, M. D. Trevithick, A. Vainsencher, B. Villalonga, T. White, Z. J. Yao, P. Yeh, A. Zalcman, H. Neven, and J. M. Martinis, *Quantum supremacy using a programmable superconducting processor*, Nature **574**, 505 (2019).

[192] K. J. Satzinger, Y. Liu, A. Smith, C. Knapp, M. Newman, C. Jones, Z. Chen, C. Quintana, X. Mi, A. Dunsworth, C. Gidney, I. Aleiner, F. Arute, K. Arya, J. Atalaya, R. Babbush, J. C. Bardin, R. Barends, J. Basso, A. Bengtsson, A. Bilmes, M. Broughton, B. B. Buckley, D. A. Buell, B. Burkett, N. Bushnell, B. Chiaro, R. Collins, W. Courtney, S. Demura, A. R. Derk, D. Eppens, C. Erickson, E. Farhi, L. Foaro, A. G. Fowler, B. Foxen, M. Giustina, A. Greene, J. A. Gross, M. P. Harrigan, S. D. Harrington, J. Hilton, S. Hong, T. Huang, W. J. Huggins, L. B. Ioffe, S. V. Isakov, E. Jeffrey, Z. Jiang, D. Kafri, K. Kechedzhi, T. Khattar, S. Kim, P. V. Klimov, A. N. Korotkov, F. Kostritsa, D. Landhuis,

P. Laptev, A. Locharla, E. Lucero, O. Martin, J. R. McClean, M. McEwen, K. C. Miao, M. Mohseni, S. Montazeri, W. Mruczkiewicz, J. Mutus, O. Naaman, M. Neeley, C. Neill, M. Y. Niu, T. E. O'Brien, A. Opremcak, B. Pató, A. Petukhov, N. C. Rubin, D. Sank, V. Shvarts, D. Strain, M. Szalay, B. Villalonga, T. C. White, Z. Yao, P. Yeh, J. Yoo, A. Zalcman, H. Neven, S. Boixo, A. Megrant, Y. Chen, J. Kelly, V. Smelyanskiy, A. Kitaev, M. Knap, F. Pollmann, and P. Roushan, *Realizing topologically ordered states on a quantum processor,* arXiv:2104.01180 (2021).

[193] P. Roushan, C. Neill, J. Tangpanitanon, V. M. Bastidas, A. Megrant, R. Barends, Y. Chen, Z. Chen, B. Chiaro, A. Dunsworth, A. Fowler, B. Foxen, M. Giustina, E. Jeffrey, J. Kelly, E. Lucero, J. Mutus, M. Neeley, C. Quintana, D. Sank, A. Vainsencher, J. Wenner, T. White, H. Neven, D. G. Angelakis, and J. Martinis, *Spectroscopic signatures of localization with interacting photons in superconducting qubits,* Science **358**, 1175 (2017).

[194] B. Chiaro, C. Neill, A. Bohrdt, M. Filippone, F. Arute, K. Arya, R. Babbush, D. Bacon, J. Bardin, R. Barends, S. Boixo, D. Buell, B. Burkett, Y. Chen, Z. Chen, R. Collins, A. Dunsworth, E. Farhi, A. Fowler, B. Foxen, C. Gidney, M. Giustina, M. Harrigan, T. Huang, S. Isakov, E. Jeffrey, Z. Jiang, D. Kafri, K. Kechedzhi, J. Kelly, P. Klimov, A. Korotkov, F. Kostritsa, D. Landhuis, E. Lucero, J. McClean, X. Mi, A. Megrant, M. Mohseni, J. Mutus, M. McEwen, O. Naaman, M. Neeley, M. Niu, A. Petukhov, C. Quintana, N. Rubin, D. Sank, K. Satzinger, A. Vainsencher, T. White, Z. Yao, P. Yeh, A. Zalcman, V. Smelyanskiy, H. Neven, S. Gopalakrishnan, D. Abanin, M. Knap, J. Martinis, and P. Roushan, *Direct measurement of non-local interactions in the many-body localized phase*, arXiv: 1910.06024 (2019).

[195] R. Hanson, L. P. Kouwenhoven, J. R. Petta, S. Tarucha, and L. M. K. Vandersypen, *Spins in few-electron quantum dots,* Rev. Mod. Phys. **79**, 1217 (2007).

[196] Y. Nagaoka, *Ferromagnetism in a narrow, almost half-filled s band,* Phys. Rev. **147**, 392 (1966).

[197] J. P. Dehollain, U. Mukhopadhyay, V. P. Michal, Y. Wang, B. Wunsch, C. Reichl, W. Wegscheider, M. S. Rudner, E. Demler, and L. M. K. Vandersypen, *Nagaoka ferromagnetism observed in a quantum dot plaquette,* Nature **579**, 528 (2020).

[198] B. E. Kane, *A silicon-based nuclear spin quantum computer,* Nature **393**, 133 (1998).

[199] P. Greenland, S. A. Lynch, A. Van der Meer, B. Murdin, C. Pidgeon, B. Redlich, N. Vinh, and G. Aeppli, *Coherent control of Rydberg states in silicon*, Nature **465**, 1057 (2010).

[200] E. Crane, A. Schuckert, N. H. Le, and A. J. Fisher, *Rydberg entangling gates in silicon*, Phys. Rev. Research **3**, 033086 (2021).

[201] T. Hensgens, T. Fujita, L. Janssen, X. Li, C. J. Van Diepen, C. Reichl, W. Wegscheider, S. Das Sarma, and L. M. K. Vandersypen, *Quantum simulation of a Fermi–Hubbard model using a semiconductor quantum dot array*, Nature **548**, 70 (2017).

[202] S. Choi, J. Choi, R. Landig, G. Kucsko, H. Zhou, J. Isoya, F. Jelezko, S. Onoda, H. Sumiya, V. Khemani, C. von Keyserlingk, N. Y. Yao, E. Demler, and M. D. Lukin, *Observation of discrete time-crystalline order in a disordered dipolar many-body system*, Nature **543**, 221 (2017).

[203] C. Zu, F. Machado, B. Ye, S. Choi, B. Kobrin, T. Mittiga, S. Hsieh, P. Bhattacharyya, M. Markham, D. Twitchen, A. Jarmola, D. Budker, C. R. Laumann, J. E. Moore, and N. Y. Yao, *Emergent hydrodynamics in a strongly interacting dipolar spin ensemble*, arXiv:2104.07678 (2021).

[204] A. Periwal, E. S. Cooper, P. Kunkel, J. F. Wienand, E. J. Davis, and M. Schleier-Smith, *Programmable Interactions and Emergent Geometry in an Atomic Array*, arXiv:2106.04070 (2021).

[205] J. Zeiher, J. Wolf, J. A. Isaacs, J. Kohler, and D. M. Stamper-Kurn, *Tracking evaporative cooling of a mesoscopic atomic quantum gas in real time*, arXiv:2012.01280 (2020).

[206] B. Yan, S. A. Moses, B. Gadway, J. P. Covey, K. R. A. Hazzard, A. M. Rey, D. S. Jin, and J. Ye, *Observation of dipolar spin-exchange interactions with lattice-confined polar molecules*, Nature **501**, 521 (2013).

[207] K. R. A. Hazzard, B. Gadway, M. Foss-Feig, B. Yan, S. A. Moses, J. P. Covey, N. Y. Yao, M. D. Lukin, J. Ye, D. S. Jin, and A. M. Rey, *Many-body dynamics of dipolar molecules in an optical lattice*, Phys. Rev. Lett. **113**, 195302 (2014).

[208] J.-R. Li, W. G. Tobias, K. Matsuda, C. Miller, G. Valtolina, L. D. Marco, R. R. W. Wang, L. Lassablière, G. Quéméner, J. L. Bohn, and J. Ye, *Controlling anisotropic dipolar interaction with shielding resonance in a three-dimensional molecular quantum gas*, arXiv:2103.06246 (2021).

[209] J. M. Cornwall, R. Jackiw, and E. Tomboulis, *Effective action for composite operators*, Phys. Rev. D **10**, 2428 (1974).

[210] J. Berges, *Nonequilibrium quantum fields: From cold atoms to cosmology*, arXiv:1503.02907 (2015).

[211] N. Schlünzen, S. Hermanns, M. Scharnke, and M. Bonitz, *Ultrafast dynamics of strongly correlated fermions—nonequilibrium Green functions and selfenergy approximations*, Journal of Physics: Condensed Matter **32**, 103001 (2019).

[212] G. Stefanucci and R. V. Leeuwen, *Nonequilibrium Many-Body Theory of Quantum Systems* (Cambridge University Press, 2013).

[213] H. O. John W. Negele, *Quantum many-particle systems*, edited by D. Pines (Westview Press, 1998).

[214] G. Aarts, D. Ahrensmeier, R. Baier, J. Berges, and J. Serreau, *Far-from-equilibrium dynamics with broken symmetries from the $1/N$ expansion of the 2PI effective action*, Physical Review D **66**, 045008 (2002).

[215] A. Schuckert, A. Piñeiro Orioli, and J. Berges, *Nonequilibrium quantum spin dynamics from two-particle irreducible functional integral techniques in the schwinger boson representation*, Phys. Rev. B **98**, 224304 (2018).

[216] L. Shen, J. Berges, J. M. Pawlowski, and A. Rothkopf, *Thermalization and dynamical spectral properties in the quark-meson model*, Phys. Rev. D **102**, 016012 (2020).

[217] N. Schluenzen, J.-P. Joost, F. Heidrich-Meisner, and M. Bonitz, *Nonequilibrium dynamics in the one-dimensional Fermi-Hubbard model: A comparison of the nonequilibrium Green functions approach and the density matrix renormalization group method*, Physical Review B **95**, 165139 (2017).

[218] S. Tan, *Large momentum part of a strongly correlated Fermi gas*, Annals of Physics **323**, 2971 (2008).

[219] S. Tan, *Generalized virial theorem and pressure relation for a strongly correlated Fermi gas*, Annals of Physics **323**, 2987 (2008).

[220] S. Tan, *Energetics of a strongly correlated Fermi gas*, Annals of Physics **323**, 2952 (2008).

[221] W. Zwerger, in *Proceedings of the International School of Physics "Enrico Fermi"*, Vol. 191, edited by Inguscio, Ketterle, Stringari, and Roati (2016) p. 63.

[222] S. A. Weidinger and M. Knap, *Floquet prethermalization and regimes of heating in a periodically driven, interacting quantum system*, Scientific Reports **7**, 45382 (2017).

[223] F. Kugler, *Renormalization group approaches to strongly correlated electron systems*, Ph.D. thesis, Ludwig-Maximilians-Universität München (2019).

[224] A. Auerbach, *Interacting Electrons and Quantum Magnetism* (Springer-Verlag New York, 1994).

[225] P. Barmettler, M. Punk, V. Gritsev, E. Demler, and E. Altman, *Quantum quenches in the anisotropic spin-1/2 Heisenberg chain: Different approaches to many-body dynamics far from equilibrium*, New Journal of Physics **12**, 055017 (2010), arXiv:0911.1927 .

[226] M. Heyl, *Dynamical Quantum Phase Transitions in Systems with Broken-Symmetry Phases*, Physical Review Letters **113**, 205701 (2014).

[227] M. Heyl, *Scaling and universality at dynamical quantum phase transitions*, Phys. Rev. Lett. **115**, 140602 (2015).

[228] M. Heyl, A. Polkovnikov, and S. Kehrein, *Dynamical quantum phase transitions in the transverse-field ising model*, Phys. Rev. Lett. **110**, 135704 (2013).

[229] P. Barmettler, M. Punk, V. Gritsev, E. Demler, and E. Altman, *Relaxation of antiferromagnetic order in spin-1/2 chains following a quantum quench*, Phys. Rev. Lett. **102**, 130603 (2009).

[230] J. Zinn-Justin, *Quantum Field Theory and Critical Phenomena* (Oxford University Press, 2002).

[231] S. A. Weidinger, M. Heyl, A. Silva, and M. Knap, *Dynamical quantum phase transitions in systems with continuous symmetry breaking*, Phys. Rev. B **96**, 134313 (2017).

[232] N. Y. Yao, C. R. Laumann, S. Gopalakrishnan, M. Knap, M. Müller, E. A. Demler, and M. D. Lukin, *Many-body localization in dipolar systems*, Phys. Rev. Lett. **113**, 243002 (2014).

[233] K. Agarwal, S. Gopalakrishnan, M. Knap, M. Müller, and E. Demler, *Anomalous diffusion and griffiths effects near the many-body localization transition*, Phys. Rev. Lett. **114**, 160401 (2015).

[234] J. H. Bardarson, F. Pollmann, and J. E. Moore, *Unbounded Growth of Entanglement in Models of Many-Body Localization*, Physical Review Letters **109**, 017202 (2012).

[235] S. A. Weidinger, S. Gopalakrishnan, and M. Knap, *Self-consistent hartree-fock approach to many-body localization*, Phys. Rev. B **98**, 224205 (2018).

[236] R. Singh, J. H. Bardarson, and F. Pollmann, *Signatures of the many-body localization transition in the dynamics of entanglement and bipartite fluctuations*, New Journal of Physics **18**, 023046 (2016).

[237] A. Kamenev and A. Andreev, *Electron-electron interactions in disordered metals: Keldysh formalism*, Phys. Rev. B **60**, 2218 (1999).

[238] J. Berges, S. Borsanyi, and J. Serreau, *Thermalization of fermionic quantum fields*, Nucl. Phys. **B660**, 51 (2003).

[239] J. Berges and J. Cox, *Thermalization of quantum fields from time-reversal invariant evolution equations*, Physics Letters B **517**, 369 (2001).

[240] A. I. Larkin and Y. N. Ovchinnikov, *Quasiclassical Method in the Theory of Superconductivity*, Soviet Physics JETP **28**, 1200 (1969).

[241] B. V. Fine, T. A. Elsayed, C. M. Kropf, and A. S. de Wijn, *Absence of exponential sensitivity to small perturbations in nonintegrable systems of spins 1/2*, Phys. Rev. E **89**, 012923 (2014).

[242] D. A. Roberts and D. Stanford, *Diagnosing Chaos Using Four-Point Functions in Two-Dimensional Conformal Field Theory*, Physical Review Letters **115**, 131603 (2015).

[243] J. Maldacena, S. H. Shenker, and D. Stanford, *A bound on chaos*, Journal of High Energy Physics **2016**, 106 (2016).

[244] M. Blake, *Universal charge diffusion and the butterfly effect in holographic theories*, Phys. Rev. Lett. **117**, 091601 (2016).

[245] P. Hosur, X.-L. Qi, D. A. Roberts, and B. Yoshida, *Chaos in quantum channels*, Journal of High Energy Physics **2016**, 4 (2016).

[246] J. Polchinski and V. Rosenhaus, *The spectrum in the Sachdev-Ye-Kitaev model*, Journal of High Energy Physics **2016**, 1 (2016).

[247] D. Stanford, *Many-body chaos at weak coupling*, Journal of High Energy Physics **2016**, 9 (2016).

[248] A. A. Patel and S. Sachdev, *Quantum chaos on a critical Fermi surface*, Proceedings of the National Academy of Sciences **114**, 1844 (2017).

[249] Y. Werman, S. A. Kivelson, and E. Berg, *Quantum chaos in an electron-phonon bad metal*, arXiv:1705.07895 (2017).

[250] Y. Gu, X.-L. Qi, and D. Stanford, *Local criticality, diffusion and chaos in generalized Sachdev-Ye-Kitaev models*, Journal of High Energy Physics **2017**, 125 (2017).

[251] I. Kukuljan, S. Grozdanov, and T. Prosen, *Weak quantum chaos*, Physical Review B **96**, 060301 (2017).

[252] A. Chan, A. De Luca, and J. Chalker, *Solution of a Minimal Model for Many-Body Quantum Chaos*, Physical Review X **8**, 041019 (2018).

[253] X. Chen, T. Zhou, D. A. Huse, and E. Fradkin, *Out-of-time-order correlations in many-body localized and thermal phases*, Annalen der Physik **529**, 1600332 (2017).

[254] D. J. Luitz and Y. Bar Lev, *Information propagation in isolated quantum systems*, Physical Review B **96**, 020406 (2017).

[255] S. Sahu, S. Xu, and B. Swingle, *Scrambling dynamics across a thermalization-localization quantum phase transition*, Phys. Rev. Lett. **123**, 165902 (2019).

[256] K. Hémery, F. Pollmann, and D. J. Luitz, *Matrix product states approaches to operator spreading in ergodic quantum systems*, Phys. Rev. B **100**, 104303 (2019).

[257] P. Calabrese and J. Cardy, *Time dependence of correlation functions following a quantum quench*, Phys. Rev. Lett. **96**, 136801 (2006).

[258] A. Hallam, J. G. Morley, and A. G. Green, *The Lyapunov spectra of quantum thermalisation*, Nature Communications **10**, 2708 (2019).

[259] T. Bilitewski, S. Bhattacharjee, and R. Moessner, *Temperature dependence of the butterfly effect in a classical many-body system*, Phys. Rev. Lett. **121**, 250602 (2018).

[260] A. Das, S. Chakrabarty, A. Dhar, A. Kundu, D. A. Huse, R. Moessner, S. S. Ray, and S. Bhattacharjee, *Light-cone spreading of perturbations and the butterfly effect in a classical spin chain*, Physical Review Letters **121**, 024101 (2018).

[261] T. Scaffidi and E. Altman, *Chaos in a classical limit of the sachdev-ye-kitaev model*, Phys. Rev. B **100**, 155128 (2019).

[262] S. Sachdev, *Theory of finite-temperature crossovers near quantum critical points close to,or above, their upper-critical dimension*, Physical Review B **55**, 142 (1997).

[263] J. Berges, S. Schlichting, and D. Sexty, *Dynamic critical phenomena from spectral functions on the lattice*, Nuclear Physics B **832**, 228 (2010).

[264] G. Aarts, *Spectral function at high temperature in the classical approximation*, Physics Letters B **518**, 315 (2001).

[265] G. Aarts and J. Berges, *Classical aspects of quantum fields far from equilibrium*, Phys. Rev. Lett. **88**, 041603 (2002).

[266] G. Aarts and J. Smit, *Finiteness of Hot Classical Scalar Field Theory and the Plasmon Damping Rate*, Physics Letters B **393**, 395 (1997).

[267] S. Sachdev, *Universal relaxational dynamics near two-dimensional quantum critical points*, Physical Review B **59**, 14054 (1999).

[268] J. Rammensee, J. D. Urbina, and K. Richter, *Many-body quantum interference and the saturation of out-of-time-order correlators*, Phys. Rev. Lett. **121**, 124101 (2018).

[269] M. Kardar, G. Parisi, and Y.-C. Zhang, *Dynamic scaling of growing interfaces*, Phys. Rev. Lett. **56**, 889 (1986).

[270] G. Aarts and J. Smit, *Classical approximation for time dependent quantum field theory: diagrammatic analysis for hot scalar fields*, Nuclear Physics B **511**, 451 (1998).

[271] W. Buchmuller and A. Jakovac, *Classical Statistical Mechanics and Landau Damping*, Physics Letters B **407**, 39 (1997).

[272] P. C. Hohenberg and B. I. Halperin, *Theory of dynamic critical phenomena*, Rev. Mod. Phys. **49**, 435 (1977).

[273] J. Berges and T. Gasenzer, *Quantum versus classical statistical dynamics of an ultracold bose gas*, Phys. Rev. A **76**, 033604 (2007).

[274] G. Aarts, G. F. Bonini, and C. Wetterich, *Exact and Truncated Dynamics in Nonequilibrium Field Theory*, Physical Review D **63**, 025012 (2000).

[275] W. Loinaz and R. S. Willey, *Monte carlo simulation calculation of the critical coupling constant for two-dimensional continuum φ^4 theory*, Physical Review D **58**, 076003 (1998).

[276] K. Boguslavski, A. Kurkela, T. Lappi, and J. Peuron, *Spectral function for overoccupied gluodynamics from real-time lattice simulations*, Phys. Rev. D **98**, 014006 (2018).

[277] A. Piñeiro Orioli and J. Berges, *Breaking the fluctuation-dissipation relation by universal transport processes*, Phys. Rev. Lett. **122**, 150401 (2019).

[278] S. Duane, A. D. Kennedy, B. J. Pendleton, and D. Roweth, *Hybrid monte carlo*, Physics letters B **195**, 216 (1987).

[279] R. M. Neal, *MCMC using Hamiltonian dynamics*, Handbook of Markov Chain Monte Carlo **2**, 11 (2011).

[280] V. Ambegaokar and M. Troyer, *Estimating errors reliably in Monte Carlo simulations of the Ehrenfest model*, American Journal of Physics **78**, 150 (2010).

[281] J. Shao and D. Tu, *The Jackknife and Bootstrap* (Springer, New York, 1995).

[282] K. Binder, *Finite size scaling analysis of ising model block distribution functions*, Z.Phys. B **43**, 119 (1981).

[283] H. H. W. Blöte, E. Luijten, and J. R. Heringa, *Journal of physics a: Mathematical and general ising universality in three dimensions: a monte carlo study*, Journal of Physics A: Mathematical and General **28**, 6289 (1995).

[284] E. Wang and U. Heinz, *Plasmon in hot φ^4 theory*, Phys. Rev. D **53**, 899 (1996).

[285] L. Onsager, *Crystal statistics. i. a two-dimensional model with an order-disorder transition*, Phys. Rev. **65**, 117 (1944).

[286] E. Nakano, V. Skokov, and B. Friman, *Transport coefficients of $o(n)$ scalar field theories close to the critical point*, Phys. Rev. D **85**, 096007 (2012).

[287] E. Ott, *Chaos in Dynamical Systems* (Cambridge University Press, 2002).

[288] A. S. de Wijn, B. Hess, and B. V. Fine, *Chaotic properties of spin lattices near second-order phase transitions*, Physical Review E **92**, 062929 (2015).

[289] R. J. Lewis-Swan, A. Safavi-Naini, J. J. Bollinger, and A. M. Rey, *Unifying scrambling, thermalization and entanglement through measurement of fidelity out-of-time-order correlators in the Dicke model*, Nature Communications **10**, 1581 (2019).

[290] B. A. Huberman and J. Rudnick, *Scaling Behavior of Chaotic Flows*, Physical Review Letters **45**, 154 (1980).

[291] A. Bonasera, V. Latora, and A. Rapisarda, *Universal Behavior of Lyapunov Exponents in Unstable Systems*, Physical Review Letters **75**, 3434 (1995).

[292] J. Deng, S. Schlichting, R. Venugopalan, and Q. Wang, *Off-equilibrium infrared structure of self-interacting scalar fields: Universal scaling, vortex-antivortex superfluid dynamics, and bose-einstein condensation*, Phys. Rev. A **97**, 053606 (2018).

[293] P. Butera and G. Caravati, *Phase transitions and Lyapunov characteristic exponents*, Physical Review A **36**, 962 (1987).

[294] V. Latora, A. Rapisarda, and S. Ruffo, *Lyapunov Instability and Finite Size Effects in a System with Long-Range Forces*, Physical Review Letters **80**, 692 (1998).

[295] S.-J. Chang, *Existence of a second-order phase transition in a two-dimensional φ^4 field theory*, Phys. Rev. D **13**, 2778 (1976).

[296] A. Jakovac, *Viscosity of the Scalar Fields from the Classical Theory*, Physics Letters B **446**, 203 (1999).

[297] S. Jeon, *Hydrodynamic Transport Coefficients in Relativistic Scalar Field Theory*, Physical Review D **52**, 3591 (1995).

[298] R. J. Deissler, *One-dimensional strings, random fluctuations, and complex chaotic structures*, Physics Letters A **100**, 451 (1984).

[299] R. J. Deissler and K. Kaneko, *Velocity-dependent Lyapunov exponents as a measure of chaos for open-flow systems*, Physics Letters A **119**, 397 (1987).

[300] K. Kaneko, *Lyapunov analysis and information flow in coupled map lattices*, Physica D: Nonlinear Phenomena **23**, 436 (1986).

[301] A. E. Tarkhov and B. V. Fine, *Estimating ergodization time of a chaotic many-particle system from a time reversal of equilibrium noise*, New Journal of Physics **20**, 123021 (2018).

[302] M. Prähofer and H. Spohn, *Universal distributions for growth processes in $1+1$ dimensions and random matrices*, Phys. Rev. Lett. **84**, 4882 (2000).

[303] G. Aarts and J. M. M. Resco, *Shear Viscosity in the O(N) Model*, Journal of High Energy Physics **2004**, 061 (2004).

[304] J. Berges, A. Rothkopf, and J. Schmidt, *Non-thermal fixed points: effective weak-coupling for strongly correlated systems far from equilibrium*, Physical Review Letters **101**, 041603 (2008).

[305] J. Berges, K. Boguslavski, S. Schlichting, and R. Venugopalan, *Universal attractor in a highly occupied non-abelian plasma*, Phys. Rev. D **89**, 114007 (2014).

[306] Y. Tang, W. Kao, K.-Y. Li, S. Seo, K. Mallayya, M. Rigol, S. Gopalakrishnan, and B. L. Lev, *Thermalization near integrability in a dipolar quantum newton's cradle*, Phys. Rev. X **8**, 021030 (2018).

[307] T. Brydges, A. Elben, P. Jurcevic, B. Vermersch, C. Maier, B. P. Lanyon, P. Zoller, R. Blatt, and C. F. Roos, *Probing Rényi entanglement entropy via randomized measurements*, Science **364**, 260 (2019).

[308] T. Kinoshita, T. Wenger, and D. S. Weiss, *A quantum Newton's cradle*, Nature **440**, 900 (2006).

[309] T. Schweigler, V. Kasper, S. Erne, I. Mazets, B. Rauer, F. Cataldini, T. Langen, T. Gasenzer, J. Berges, and J. Schmiedmayer, *Experimental characterization of a quantum many-body system via higher-order correlations*, Nature **545**, 323 (2017).

[310] T. V. Zache, T. Schweigler, S. Erne, J. Schmiedmayer, and J. Berges, *Extracting the field theory description of a quantum many-body system from experimental data*, Phys. Rev. X **10**, 011020 (2020).

[311] M. Prüfer, T. V. Zache, P. Kunkel, S. Lannig, A. Bonnin, H. Strobel, J. Berges, and M. K. Oberthaler, *Experimental extraction of the quantum effective action for a non-equilibrium many-body system*, Nature Physics **16**, 1012 (2020).

[312] P. Reimann, *Foundation of Statistical Mechanics under Experimentally Realistic Conditions*, Physical Review Letters **101**, 190403 (2008).

[313] C. Nation and D. Porras, *Quantum chaotic fluctuation-dissipation theorem: Effective brownian motion in closed quantum systems*, Phys. Rev. E **99**, 052139 (2019).

[314] H. B. Kaplan, L. Guo, W. L. Tan, A. De, F. Marquardt, G. Pagano, and C. Monroe, *Many-body dephasing in a trapped-ion quantum simulator*, Phys. Rev. Lett. **125**, 120605 (2020).

[315] H. B. Callen and T. A. Welton, *Irreversibility and generalized noise*, Phys. Rev. **83**, 34 (1951).

[316] E. Khatami, G. Pupillo, M. Srednicki, and M. Rigol, *Fluctuation-Dissipation Theorem in an Isolated System of Quantum Dipolar Bosons after a Quench*, Physical Review Letters **111**, 050403 (2013).

[317] F. Randi, M. Esposito, F. Giusti, O. Misochko, F. Parmigiani, D. Fausti, and M. Eckstein, *Probing the fluctuations of the optical properties in time-resolved spectroscopy*, Physical Review Letters **119**, 187403 (2017).

[318] C. Kuhlenkamp and M. Knap, *Periodically driven sachdev-ye-kitaev models*, Phys. Rev. Lett. **124**, 106401 (2020).

[319] K. Mallayya and M. Rigol, *Heating rates in periodically driven strongly interacting quantum many-body systems*, Phys. Rev. Lett. **123**, 240603 (2019).

[320] Q. Zhou and T.-L. Ho, *Universal thermometry for quantum simulation*, Phys. Rev. Lett. **106**, 225301 (2011).

[321] T. Hartke, B. Oreg, N. Jia, and M. Zwierlein, *Doublon-hole correlations and fluctuation thermometry in a fermi-hubbard gas*, Phys. Rev. Lett. **125**, 113601 (2020).

[322] D. Yang, A. Grankin, L. M. Sieberer, D. V. Vasilyev, and P. Zoller, *Quantum non-demolition measurement of a many-body Hamiltonian*, Nature Communications **11**, 775 (2020).

[323] M. Knap, A. Kantian, T. Giamarchi, I. Bloch, M. D. Lukin, and E. Demler, *Probing real-space and time-resolved correlation functions with many-body ramsey interferometry*, Phys. Rev. Lett. **111**, 147205 (2013).

[324] P. Uhrich, S. Castrignano, H. Uys, and M. Kastner, *Noninvasive measurement of dynamic correlation functions*, Physical Review A **96**, 022127 (2017).

[325] A. Elben, B. Vermersch, M. Dalmonte, J. I. Cirac, and P. Zoller, *Rényi entropies from random quenches in atomic hubbard and spin models*, Phys. Rev. Lett. **120**, 050406 (2018).

[326] A. M. Rey, P. B. Blakie, G. Pupillo, C. J. Williams, and C. W. Clark, *Bragg spectroscopy of ultracold atoms loaded in an optical lattice*, Physical Review A **72**, 023407 (2005).

[327] L. Foini, A. Gambassi, R. Konik, and L. F. Cugliandolo, *Measuring effective temperatures in a generalized gibbs ensemble*, Phys. Rev. E **95**, 052116 (2017).

[328] M. Rigol, *Quantum quenches and thermalization in one-dimensional fermionic systems*, Physical Review A **80**, 053607 (2009).

[329] J. D. Noh, T. Sagawa, and J. Yeo, *Numerical verification of the fluctuation-dissipation theorem for isolated quantum systems*, Phys. Rev. Lett. **125**, 050603 (2020).

[330] K. Chou, Z. Su, B. Hao, and L. Yu, *Equilibrium and Nonquilibrium Formalisms Made Unified*, Phys. Rep. **118**, 1 (1985).

[331] A. Lupaşcu, S. Saito, T. Picot, P. C. d. Groot, C. J. P. M. Harmans, and J. E. Mooij, *Quantum non-demolition measurement of a superconducting two-level system*, Nature Physics **3**, 119 (2007).

[332] J. P. Covey, I. S. Madjarov, A. Cooper, and M. Endres, *2000-times repeated imaging of strontium atoms in clock-magic tweezer arrays*, Phys. Rev. Lett. **122**, 173201 (2019).

[333] W. Nagourney, J. Sandberg, and H. Dehmelt, *Shelved optical electron amplifier: Observation of quantum jumps*, Phys. Rev. Lett. **56**, 2797 (1986).

[334] T. Sauter, W. Neuhauser, R. Blatt, and P. E. Toschek, *Observation of quantum jumps*, Phys. Rev. Lett. **57**, 1696 (1986).

[335] S. J. van Enk and C. W. J. Beenakker, *Measuring* $\mathrm{Tr}\rho^n$ *on single copies of* ρ *using random measurements*, Phys. Rev. Lett. **108**, 110503 (2012).

[336] M. Ohliger, V. Nesme, and J. Eisert, *Efficient and feasible state tomography of quantum many-body systems*, New Journal of Physics **15**, 015024 (2013).

[337] A. Ketterer, N. Wyderka, and O. Gühne, *Characterizing multipartite entanglement with moments of random correlations*, Phys. Rev. Lett. **122**, 120505 (2019).

[338] B. Vermersch, A. Elben, L. M. Sieberer, N. Y. Yao, and P. Zoller, *Probing scrambling using statistical correlations between randomized measurements*, Phys. Rev. X **9**, 021061 (2019).

[339] Y. Nakata, C. Hirche, M. Koashi, and A. Winter, *Efficient quantum pseudorandomness with nearly time-independent hamiltonian dynamics*, Phys. Rev. X **7**, 021006 (2017).

[340] D. M. Stamper-Kurn, A. P. Chikkatur, A. Görlitz, S. Inouye, S. Gupta, D. E. Pritchard, and W. Ketterle, *Excitation of Phonons in a Bose-Einstein Condensate by Light Scattering*, Physical Review Letters **83**, 2876 (1999).

[341] J. Stenger, S. Inouye, A. P. Chikkatur, D. M. Stamper-Kurn, D. E. Pritchard, and W. Ketterle, *Bragg Spectroscopy of a Bose-Einstein Condensate*, Physical Review Letters **82**, 4569 (1999).

[342] C. Menotti, M. Krämer, L. Pitaevskii, and S. Stringari, *Dynamic structure factor of a bose-einstein condensate in a one-dimensional optical lattice*, Phys. Rev. A **67**, 053609 (2003).

[343] M. A. Norcia, A. W. Young, W. J. Eckner, E. Oelker, J. Ye, and A. M. Kaufman, *Seconds-scale coherence on an optical clock transition in a tweezer array*, Science **366**, 93 (2019).

[344] M. Norcia, A. Young, and A. Kaufman, *Microscopic Control and Detection of Ultracold Strontium in Optical-Tweezer Arrays*, Physical Review X **8**, 041054 (2018).

[345] P. M. Preiss, R. Ma, M. E. Tai, J. Simon, and M. Greiner, *Quantum gas microscopy with spin, atom-number, and multilayer readout*, Phys. Rev. A **91**, 041602 (R) (2015).

[346] J. Koepsell, S. Hirthe, D. Bourgund, P. Sompet, J. Vijayan, G. Salomon, C. Gross, and I. Bloch, *Robust bilayer charge pumping for spin- and density-resolved quantum gas microscopy*, Phys. Rev. Lett. **125**, 010403 (2020).

[347] P. Uhrich, C. Gross, and M. Kastner, *Probing unitary two-time correlations in a neutral atom quantum simulator*, Quantum Science and Technology **4**, 024005 (2019).

[348] A. Kantian, U. Schollwöck, and T. Giamarchi, *Lattice-Assisted Spectroscopy: A Generalized Scanning Tunneling Microscope for Ultracold Atoms*, Physical Review Letters **115**, 165301 (2015).

[349] D. Abanin, W. De Roeck, W. W. Ho, and F. Huveneers, *A Rigorous Theory of Many-Body Prethermalization for Periodically Driven and Closed Quantum Systems*, Communications in Mathematical Physics **354**, 809 (2017).

[350] E. T. Jaynes, *Information theory and statistical mechanics*, Phys. Rev. **106**, 620 (1957).

[351] F. H. L. Essler, S. Evangelisti, and M. Fagotti, *Dynamical Correlations After a Quantum Quench*, Physical Review Letters **109**, 247206 (2012).

[352] J. De Nardis, M. Panfil, A. Gambassi, L. F. Cugliandolo, R. Konik, and L. Foini, *Probing non-thermal density fluctuations in the one-dimensional Bose gas*, SciPost Physics **3**, 023 (2017).

[353] P. Hauke and L. Tagliacozzo, *Spread of correlations in long-range interacting quantum systems*, Phys. Rev. Lett. **111**, 207202 (2013).

[354] P. Jurcevic, P. Hauke, C. Maier, C. Hempel, B. P. Lanyon, R. Blatt, and C. F. Roos, *Spectroscopy of interacting quasiparticles in trapped ions*, Phys. Rev. Lett. **115**, 100501 (2015).

[355] M. Kormos, M. Collura, G. Takács, and P. Calabrese, *Real-time confinement following a quantum quench to a non-integrable model*, Nature Physics **13**, 246 (2017).

[356] A. J. James, R. M. Konik, and N. J. Robinson, *Nonthermal States Arising from Confinement in One and Two Dimensions*, Physical Review Letters **122**, 130603 (2019).

[357] P. P. Mazza, G. Perfetto, A. Lerose, M. Collura, and A. Gambassi, *Suppression of transport in nondisordered quantum spin chains due to confined excitations*, Physical Review B **99**, 180302 (R) (2019).

[358] F. Liu, R. Lundgren, P. Titum, G. Pagano, J. Zhang, C. Monroe, and A. V. Gorshkov, *Confined Quasiparticle Dynamics in Long-Range Interacting Quantum Spin Chains*, Physical Review Letters **122**, 150601 (2019).

[359] A. Lerose, B. Žunkovič, A. Silva, and A. Gambassi, *Quasilocalized excitations induced by long-range interactions in translationally invariant quantum spin chains*, Physical Review B **99**, 121112 (R) (2019).

[360] K. G. Wilson, *Confinement of quarks*, Phys. Rev. D **10**, 2445 (1974).

[361] Z. Lenarcic, E. Altman, and A. Rosch, *Activating many-body localization in solids by driving with light*, Phys. Rev. Lett. **121**, 267603 (2018).

[362] D. Hérisson and M. Ocio, *Fluctuation-dissipation ratio of a spin glass in the aging regime*, Phys. Rev. Lett. **88**, 257202 (2002).

[363] J. Feldmeier, F. Pollmann, and M. Knap, *Emergent glassy dynamics in a quantum dimer model*, Phys. Rev. Lett. **123**, 040601 (2019).

[364] M. Eckstein and M. Kollar, *Theory of time-resolved optical spectroscopy on correlated electron systems*, Physical Review B **78**, 205119 (2008).

[365] A. Arrizabalaga and J. Smit, *Gauge-fixing dependence of Phi-derivable approximations*, Physical Review D **66**, 065014 (2002).

[366] J. Kogut and L. Susskind, *Hamiltonian formulation of Wilson's lattice gauge theories*, Physical Review D **11**, 395 (1975).

[367] P. Sala, T. Shi, S. Kühn, M. C. Bañuls, E. Demler, and J. I. Cirac, *Variational study of u(1) and su(2) lattice gauge theories with gaussian states in* $1+1$ *dimensions*, Phys. Rev. D **98**, 034505 (2018).

[368] T. Zache, *Quantum simulation of high-energy physics with ultracold atoms*, Ph.D. thesis, Heidelberg University (2020).

[369] U. Reinosa and J. Serreau, *Ward identities for the 2pi effective action in QED*, Journal of High Energy Physics **2007**, 097 (2007).

[370] U. Reinosa and J. Serreau, *2pi effective action for gauge theories: renormalization*, Journal of High Energy Physics **2006**, 028 (2006).

[371] G. Aarts and J. M. M. Resco, *Transport coefficients in large N_f gauge theories with massive fermions*, Journal of High Energy Physics **2005**, 074 (2005).

[372] E. Mottola, *Gauge Invariance in 2PI Effective Actions*, Strong and Electroweak Matter 2002 , 432 (2003).

[373] J. Berges, *Controlled nonperturbative dynamics of quantum fields out of equilibrium*, Nuclear Physics A **699**, 847 (2002).

[374] S. Sachdev, *Quantum Phase Transitions* (Cambridge University Press, 2011).

[375] S. A. Hartnoll and A. P. Mackenzie, *Planckian Dissipation in Metals*, arXiv:2107.07802 (2021).

[376] A. Eberlein, V. Kasper, S. Sachdev, and J. Steinberg, *Quantum quench of the sachdev-ye-kitaev model*, Phys. Rev. B **96**, 205123 (2017).

[377] T. Chanda, J. Zakrzewski, M. Lewenstein, and L. Tagliacozzo, *Confinement and lack of thermalization after quenches in the bosonic schwinger model*, Phys. Rev. Lett. **124**, 180602 (2020).

[378] A. Stan, N. E. Dahlen, and R. van Leeuwen, *Time propagation of the Kadanoff–Baym equations for inhomogeneous systems*, The Journal of Chemical Physics **130**, 224101 (2009).

[379] T. V. Zache, F. Hebenstreit, F. Jendrzejewski, M. K. Oberthaler, J. Berges, and P. Hauke, *Quantum simulation of lattice gauge theories using Wilson fermions*, Quantum Science and Technology **3**, 034010 (2018).

[380] V. Kasper, F. Hebenstreit, M. Oberthaler, and J. Berges, *Schwinger pair production with ultracold atoms*, Physics Letters B **760**, 742 (2016).

[381] E. Zohar, J. I. Cirac, and B. Reznik, *Quantum simulations of gauge theories with ultracold atoms: Local gauge invariance from angular-momentum conservation*, Phys. Rev. A **88**, 023617 (2013).

[382] A. Mil, T. V. Zache, A. Hegde, A. Xia, R. P. Bhatt, M. K. Oberthaler, P. Hauke, J. Berges, and F. Jendrzejewski, *A scalable realization of local u(1) gauge invariance in cold atomic mixtures*, Science **367**, 1128 (2020).

[383] A. V. Gorshkov, M. Hermele, V. Gurarie, C. Xu, P. S. Julienne, J. Ye, P. Zoller, E. Demler, M. D. Lukin, and A. M. Rey, *Two-orbital S U(N) magnetism with ultracold alkaline-earth atoms*, Nature Physics **6**, 289 (2010).

[384] M. Babadi, *Non-equilibrium dynamics of artificial quantum matter*, Ph.D. thesis, Harvard University (2013).

[385] J. G. Bohnet, B. C. Sawyer, J. W. Britton, M. L. Wall, A. M. Rey, M. Foss-Feig, and J. J. Bollinger, *Quantum spin dynamics and entanglement generation with hundreds of trapped ions*, Science **352**, 1297 (2016).

[386] E. Guardado-Sanchez, A. Morningstar, B. M. Spar, P. T. Brown, D. A. Huse, and W. S. Bakr, *Subdiffusion and heat transport in a tilted two-dimensional Fermi-Hubbard system*, Phys. Rev. X **10**, 011042 (2020).

[387] S. Erne, R. Bücker, T. Gasenzer, J. Berges, and J. Schmiedmayer, *Universal dynamics in an isolated one-dimensional Bose gas far from equilibrium*, Nature **563**, 225 (2018).

[388] J. Lux, J. Müller, A. Mitra, and A. Rosch, *Hydrodynamic long-time tails after a quantum quench*, Physical Review A **89**, 053608 (2014).

[389] S. Mukerjee, V. Oganesyan, and D. Huse, *Statistical theory of transport by strongly interacting lattice fermions*, Phys. Rev. B **73**, 035113 (2006).

[390] M. Medenjak, K. Klobas, and T. Prosen, *Diffusion in deterministic interacting lattice systems*, Physical Review Letters **119**, 110603 (2017).

[391] V. Khemani, A. Vishwanath, and D. A. Huse, *Operator spreading and the emergence of dissipative hydrodynamics under unitary evolution with conservation laws*, Phys. Rev. X **8**, 031057 (2018).

[392] D. E. Parker, X. Cao, A. Avdoshkin, T. Scaffidi, and E. Altman, *A universal operator growth hypothesis*, Phys. Rev. X **9**, 041017 (2019).

[393] O. A. Castro-Alvaredo, B. Doyon, and T. Yoshimura, *Emergent hydrodynamics in integrable quantum systems out of equilibrium*, Phys. Rev. X **6**, 041065 (2016).

[394] B. Bertini, M. Collura, J. De Nardis, and M. Fagotti, *Transport in out-of-equilibrium xxz chains: Exact profiles of charges and currents*, Phys. Rev. Lett. **117**, 207201 (2016).

[395] S. Gopalakrishnan and R. Vasseur, *Kinetic Theory of Spin Diffusion and Superdiffusion in XXZ Spin Chains*, Physical Review Letters **122**, 127202 (2019).

[396] M. Ljubotina, L. Zadnik, and T. Prosen, *Ballistic spin transport in a periodically driven integrable quantum system*, Phys. Rev. Lett. **122**, 150605 (2019).

[397] M. Ljubotina, M. Znidaric, and T. Prosen, *Kardar-parisi-zhang physics in the quantum heisenberg magnet*, Phys. Rev. Lett. **122**, 210602 (2019).

[398] P. Prelovsek, J. Bonca, and M. Mierzejewski, *Transient and persistent particle subdiffusion in a disordered chain coupled to bosons*, Phys. Rev. B **98**, 125119 (2018).

[399] M. Sroda, P. Prelovsek, and M. Mierzejewski, *Instability of subdiffusive spin dynamics in strongly disordered hubbard chain*, Phys. Rev. B **99**, 121110(R) (2019).

[400] A. C. Potter, R. Vasseur, and S. A. Parameswaran, *Universal properties of many-body delocalization transitions*, Phys. Rev. X **5**, 031033 (2015).

[401] C. Cao, E. Elliott, J. Joseph, H. Wu, J. Petricka, T. Schäfer, and J. E. Thomas, *Universal quantum viscosity in a unitary Fermi gas*, Science **331**, 58 (2011).

[402] A. Sommer, M. Ku, G. Roati, and M. W. Zwierlein, *Universal spin transport in a strongly interacting Fermi gas*, Nature **472**, 201 (2011).

[403] U. Schneider, L. Hackermüller, J. P. Ronzheimer, S. Will, S. Braun, T. Best, I. Bloch, E. Demler, S. Mandt, D. Rasch, and A. Rosch, *Fermionic transport and out-of-equilibrium dynamics in a homogeneous Hubbard model with ultracold atoms*, Nature Physics **8**, 213 (2012).

[404] D. A. Bandurin, I. Torre, R. K. Kumar, M. Ben Shalom, A. Tomadin, A. Principi, G. H. Auton, E. Khestanova, K. S. Novoselov, I. V. Grigorieva, L. A. Ponomarenko, A. K. Geim, and M. Polini, *Negative local resistance caused by viscous electron backflow in graphene*, Science **351**, 1055 (2016).

[405] J. Crossno, J. K. Shi, K. Wang, X. Liu, A. Harzheim, A. Lucas, S. Sachdev, P. Kim, T. Taniguchi, K. Watanabe, T. A. Ohki, and K. C. Fong, *Observation of the Dirac fluid and the breakdown of the Wiedemann-Franz law in graphene*, Science **351**, 1058 (2016).

[406] P. J. W. Moll, P. Kushwaha, N. Nandi, B. Schmidt, and A. P. Mackenzie, *Evidence for hydrodynamic electron flow in $PdCoO_2$*, Science **351**, 1061 (2016).

[407] A. Gromov, A. Lucas, and R. M. Nandkishore, *Fracton hydrodynamics*, Phys. Rev. Research **2**, 033124 (2020).

[408] M. Ljubotina, M. Žnidarič, and T. Prosen, *Spin diffusion from an inhomogeneous quench in an integrable system*, Nature Communications **8**, 16117 (2017).

[409] V. B. Bulchandani, S. Gopalakrishnan, and E. Ilievski, Superdiffusion in spin chains, (2021).

[410] A. Schuckert, I. Lovas, and M. Knap, *Nonlocal emergent hydrodynamics in a long-range quantum spin system*, Phys. Rev. B **101**, 020416 (2020).

[411] V. Zaburdaev, S. Denisov, and J. Klafter, *Lévy walks*, Reviews of Modern Physics **87**, 483 (2015).

[412] R. Bachelard and M. Kastner, *Universal threshold for the dynamical behavior of lattice systems with long-range interactions*, Phys. Rev. Lett. **110**, 170603 (2013).

[413] P. Hauke and L. Tagliacozzo, *Spread of correlations in long-range interacting quantum systems*, Physical Review Letters **111**, 207202 (2013).

[414] M. B. Hastings and T. Koma, *Spectral Gap and Exponential Decay of Correlations*, Communications in Mathematical Physics **265**, 781 (2006).

[415] J. Eisert, M. Van Den Worm, S. R. Manmana, and M. Kastner, *Breakdown of quasilocality in long-range quantum lattice models*, Physical Review Letters **111**, 260401 (2013).

[416] M. C. Tran, A. Y. Guo, Y. Su, J. R. Garrison, Z. Eldredge, M. Foss-Feig, A. M. Childs, and A. V. Gorshkov, *Locality and digital quantum simulation of power-law interactions*, Phys. Rev. X **9**, 031006 (2019).

[417] B. Kloss and Y. Bar Lev, *Spin transport in a long-range-interacting spin chain*, Phys. Rev. A **99**, 032114 (2019).

[418] W. K. Wootters, *A Wigner-function formulation of finite-state quantum mechanics*, Annals of Physics **176**, 1 (1987).

[419] A. Polkovnikov, *Phase space representation of quantum dynamics*, Annals of Physics **325**, 1790 (2010).

[420] J. Schachenmayer, A. Pikovski, and A. M. Rey, *Many-body quantum spin dynamics with monte carlo trajectories on a discrete phase space*, Phys. Rev. X **5**, 011022 (2015).

[421] L. Pucci, A. Roy, and M. Kastner, *Simulation of quantum spin dynamics by phase space sampling of bogoliubov-born-green-kirkwood-yvon trajectories*, Phys. Rev. B **93**, 174302 (2016).

[422] C. Bartsch and J. Gemmer, *Dynamical typicality of quantum expectation values*, Phys. Rev. Lett. **102**, 110403 (2009).

[423] D. Forster, *Hydrodynamic Fluctuations, Broken Symmetry, And Correlation Functions* (Westview Press, 1994).

[424] V. E. Arkhincheev, *Nonlinear relation between diffusion and conductivity for Levy flights*, AIP Conference Proceedings **553**, 231 (2001).

[425] W. H. Lee, *Continuous and Discrete Properties of Stochastic Processes*, Ph.D. thesis, University of Nottingham (2010).

[426] B. Gnedenko and A. N. Kolmogorov, *Limit Distributions for Sums of Independent Random Variables* (Addison-Wesley, 1954).

[427] L. Zarfaty, A. Peletskyi, E. Barkai, and S. Denisov, *Infinite horizon billiards: Transport at the border between gauss and lévy universality classes*, Phys. Rev. E **100**, 042140 (2019).

[428] S. Birnkammer, A. Bohrdt, F. Grusdt, and M. Knap, *Characterizing topological excitations of a long-range Heisenberg model with trapped ions*, arXiv:2012.09185 (2020).

[429] P. W. Anderson, *Absence of Diffusion in Certain Random Lattices*, Phys. Rev. **109**, 1492 (1958).

[430] A. L. Efros and B. I. Shklovskii, *Coulomb gap and low temperature conductivity of disordered systems*, Journal of Physics C: Solid State Physics **8**, L49 (1975).

[431] L. Fleishman and P. W. Anderson, *Interactions and the anderson transition*, Phys. Rev. B **21**, 2366 (1980).

[432] R. M. Nandkishore and S. L. Sondhi, *Many-Body Localization with Long-Range Interactions*, Phys. Rev. X **7**, 041021 (2017).

[433] F. Mahmood, D. Chaudhuri, S. Gopalakrishnan, R. Nandkishore, and N. P. Armitage, *Observation of a marginal Fermi glass*, Nature Physics **17**, 627 (2021).

[434] N. H. Le, A. J. Fisher, and E. Ginossar, *Extended Hubbard model for mesoscopic transport in donor arrays in silicon*, Physical Review B **96**, 245406 (2017).

[435] F. Epperlein, M. Schreiber, and T. Vojta, *Quantum coulomb glass within a hartree-fock approximation*, Phys. Rev. B **56**, 5890 (1997).

[436] M. Amini, V. E. Kravtsov, and M. Müller, *Multifractality and quantum-to-classical crossover in the Coulomb anomaly at the Mott–Anderson metal–insulator transition*, New Journal of Physics **16**, 015022 (2014).

[437] A. Altshuler, B .and Aronov, A. Efros, and M. Pollak, *Electron–electron Interactions in Disordered Systems* (Elsevier, Amerstdam, 1985).

[438] K. Slevin and T. Ohtsuki, *Corrections to scaling at the anderson transition*, Phys. Rev. Lett. **82**, 382 (1999).

[439] L. Landau, *Theory of the superfluidity of helium ii*, Phys. Rev. **60**, 356 (1941).

[440] Z. Dutton, M. Budde, C. Slowe, and L. V. Hau, *Observation of quantum shock waves created with ultra- compressed slow light pulses in a bose-einstein condensate*, Science **293**, 663 (2001).

[441] B. Wu and Q. Niu, *Landau and dynamical instabilities of the superflow of bose-einstein condensates in optical lattices*, Phys. Rev. A **64**, 061603 (2001).

[442] L. Fallani, L. De Sarlo, J. E. Lye, M. Modugno, R. Saers, C. Fort, and M. Inguscio, *Observation of dynamical instability for a bose-einstein condensate in a moving 1d optical lattice*, Phys. Rev. Lett. **93**, 140406 (2004).

[443] A. Polkovnikov, E. Altman, E. Demler, B. Halperin, and M. D. Lukin, *Decay of superfluid currents in a moving system of strongly interacting bosons*, Phys. Rev. A **71**, 063613 (2005).

[444] E. Altman, A. Polkovnikov, E. Demler, B. I. Halperin, and M. D. Lukin, *Superfluid-insulator transition in a moving system of interacting bosons*, Phys. Rev. Lett. **95**, 020402 (2005).

[445] A. A. Norrie, R. J. Ballagh, and C. W. Gardiner, *Quantum turbulence in condensate collisions: An application of the classical field method*, Phys. Rev. Lett. **94**, 040401 (2005).

[446] H. Takeuchi, S. Ishino, and M. Tsubota, *Binary quantum turbulence arising from countersuperflow instability in two-component bose-einstein condensates*, Phys. Rev. Lett. **105**, 205301 (2010).

[447] R. W. Cherng, V. Gritsev, D. M. Stamper-Kurn, and E. Demler, *Dynamical instability of the xy spiral state of ferromagnetic condensates*, Phys. Rev. Lett. **100**, 180404 (2008).

[448] R. W. Cherng and E. Demler, *Magnetoroton softening in rb spinor condensates with dipolar interactions*, Phys. Rev. Lett. **103**, 185301 (2009).

[449] K. Fujimoto and M. Tsubota, *Counterflow instability and turbulence in a spin-1 spinor bose-einstein condensate*, Phys. Rev. A **85**, 033642 (2012).

[450] J. S. Langer and V. Ambegaokar, *Intrinsic resistive transition in narrow superconducting channels*, Phys. Rev. **164**, 498 (1967).

[451] D. E. McCumber and B. I. Halperin, *Time scale of intrinsic resistive fluctuations in thin superconducting wires*, Phys. Rev. B **1**, 1054 (1970).

[452] D. E. Sheehy and P. M. Goldbart, *Intrinsic resistivity and the so(5) theory of high-temperature superconductors*, Phys. Rev. B **57**, R8131 (1998).

[453] B. I. Halperin, G. Refael, and E. Demler, *Resistance in superconductors*, International Journal of Modern Physics B **24**, 4039 (2010).

[454] T. Paul, P. Schlagheck, P. Leboeuf, and N. Pavloff, *Superfluidity versus anderson localization in a dilute bose gas*, Phys. Rev. Lett. **98**, 210602 (2007).

[455] M. Albert, T. Paul, N. Pavloff, and P. Leboeuf, *Dipole oscillations of a bose-einstein condensate in the presence of defects and disorder*, Phys. Rev. Lett. **100**, 250405 (2008).

[456] M. Albert, T. Paul, N. Pavloff, and P. Leboeuf, *Breakdown of the superfluidity of a matter wave in a random environment*, Phys. Rev. A **82**, 011602 (2010).

[457] T. Haga and M. Ueda, *Effective temperature of a superfluid flowing in a random potential*, Phys. Rev. Research **2**, 043316 (2020).

[458] L. Santos, G. V. Shlyapnikov, P. Zoller, and M. Lewenstein, *Bose-einstein condensation in trapped dipolar gases*, Phys. Rev. Lett. **85**, 1791 (2000).

[459] K. Góral and L. Santos, *Ground state and elementary excitations of single and binary bose-einstein condensates of trapped dipolar gases*, Phys. Rev. A **66**, 023613 (2002).

[460] L. Santos, G. V. Shlyapnikov, and M. Lewenstein, *Roton-maxon spectrum and stability of trapped dipolar bose-einstein condensates*, Phys. Rev. Lett. **90**, 250403 (2003).

[461] G. Bertotti, I. Mayergoyz, and C. Serpico, *Spin-wave instabilities in landau–lifshitz–gilbert dynamics*, Physica B: Condensed Matter **306**, 106 (2001).

[462] A. J. E. Kreil, D. A. Bozhko, H. Y. Musiienko-Shmarova, V. I. Vasyuchka, V. S. L'vov, A. Pomyalov, B. Hillebrands, and A. A. Serga, *From kinetic instability to bose-einstein condensation and magnon supercurrents*, Phys. Rev. Lett. **121**, 077203 (2018).

[463] K. Wintersperger, M. Bukov, J. Näger, S. Lellouch, E. Demler, U. Schneider, I. Bloch, N. Goldman, and M. Aidelsburger, *Parametric instabilities of interacting bosons in periodically driven 1d optical lattices*, Phys. Rev. X **10**, 011030 (2020).

[464] M. Bukov, S. Gopalakrishnan, M. Knap, and E. Demler, *Prethermal floquet steady states and instabilities in the periodically driven, weakly interacting bose-hubbard model*, Phys. Rev. Lett. **115**, 205301 (2015).

[465] T. Boulier, J. Maslek, M. Bukov, C. Bracamontes, E. Magnan, S. Lellouch, E. Demler, N. Goldman, and J. V. Porto, *Parametric heating in a 2d periodically*

driven bosonic system: Beyond the weakly interacting regime, Phys. Rev. X **9**, 011047 (2019).

[466] A. B. Bardon, S. Beattie, C. Luciuk, W. Cairncross, D. Fine, N. S. Cheng, G. J. A. Edge, E. Taylor, S. Zhang, S. Trotzky, and J. H. Thywissen, *Transverse demagnetization dynamics of a unitary fermi gas*, Science **344**, 722 (2014).

[467] M. Tsubota, *Quantum turbulence—from superfluid helium to atomic bose–einstein condensates*, Journal of Physics: Condensed Matter **21**, 164207 (2009).

[468] J. F. Rodriguez-Nieva, *Turbulent relaxation after a quench in the heisenberg model*, arXiv:2009.11883 (2020).

[469] E. Sonin, *Spin currents and spin superfluidity*, Advances in Physics **59**, 181 (2010).

[470] D. A. Bozhko, A. A. Serga, P. Clausen, V. I. Vasyuchka, F. Heussner, G. A. Melkov, A. Pomyalov, V. S. L'vov, and B. Hillebrands, *Supercurrent in a room-temperature bose-einstein magnon condensate*, Nature Physics **12**, 1057 (2016).

[471] S. Takei and Y. Tserkovnyak, *Superfluid spin transport through easy-plane ferromagnetic insulators*, Phys. Rev. Lett. **112**, 227201 (2014).

[472] K. Nakata, K. A. van Hoogdalem, P. Simon, and D. Loss, *Josephson and persistent spin currents in bose-einstein condensates of magnons*, Phys. Rev. B **90**, 144419 (2014).

[473] C. Sun, T. Nattermann, and V. L. Pokrovsky, *Unconventional superfluidity in yttrium iron garnet films*, Phys. Rev. Lett. **116**, 257205 (2016).

[474] E. B. Sonin, *Spin superfluidity and spin waves in yig films*, Phys. Rev. B **95**, 144432 (2017).

[475] D. C. Mattis, *The Theory of Magnetism Made Simple* (WORLD SCIENTIFIC, 2006).

[476] S. Bhattacharyya, J. F. Rodriguez-Nieva, and E. Demler, *Universal prethermal dynamics in heisenberg ferromagnets*, Phys. Rev. Lett. **125**, 230601 (2020).

[477] E. Iacocca, T. J. Silva, and M. A. Hoefer, *Breaking of galilean invariance in the hydrodynamic formulation of ferromagnetic thin films*, Phys. Rev. Lett. **118**, 017203 (2017).

[478] J. F. Rodriguez-Nieva, D. Podolsky, and E. Demler, *Hydrodynamic sound modes and galilean symmetry breaking in a magnon fluid*, arXiv:1810.12333 (2018).

[479] J. Berges and J. Serreau, *Parametric resonance in quantum field theory*, Phys. Rev. Lett. **91**, 111601 (2003).

[480] C. V. Parker, L.-C. Ha, and C. Chin, *Direct observation of effective ferromagnetic domains of cold atoms in a shaken optical lattice*, Nature Physics **9**, 769 (2013).

[481] C.-L. Hung, A. González-Tudela, J. I. Cirac, and H. J. Kimble, *Quantum spin dynamics with pairwise-tunable, long-range interactions*, Proceedings of the National Academy of Sciences **113**, E4946 (2016).

[482] E. J. Davis, G. Bentsen, L. Homeier, T. Li, and M. H. Schleier-Smith, *Photon-mediated spin-exchange dynamics of spin-1 atoms*, Phys. Rev. Lett. **122**, 010405 (2019).

[483] L.-M. Duan, E. Demler, and M. D. Lukin, *Controlling spin exchange interactions of ultracold atoms in optical lattices*, Phys. Rev. Lett. **91**, 090402 (2003).

[484] A. B. Kuklov and B. V. Svistunov, *Counterflow superfluidity of two-species ultracold atoms in a commensurate optical lattice*, Phys. Rev. Lett. **90**, 100401 (2003).

[485] E. Altman, W. Hofstetter, E. Demler, and M. D. Lukin, *Phase diagram of two-component bosons on an optical lattice*, New Journal of Physics **5**, 113 (2003).

[486] T. Giamarchi, *Quantum Physics in One Dimension*, International Series of Monographs on Physics (Clarendon Press, 2003).

[487] F. D. M. Haldane, *Luttinger liquid theory of one-dimensional quantum fluids. i. properties of the luttinger model and their extension to the general 1d interacting spinless fermi gas*, Journal of Physics C: Solid State Physics **14**, 2585 (1981).

[488] S. Bock, A. Liluashvili, and T. Gasenzer, *Buildup of the kondo effect from real-time effective action for the anderson impurity model*, Phys. Rev. B **94**, 045108 (2016).

[489] A. Damascelli, Z. Hussain, and Z.-X. Shen, *Angle-resolved photoemission studies of the cuprate superconductors*, Rev. Mod. Phys. **75**, 473 (2003).

[490] K. M. Shen, F. Ronning, D. H. Lu, F. Baumberger, N. J. C. Ingle, W. S. Lee, W. Meevasana, Y. Kohsaka, M. Azuma, M. Takano, H. Takagi, and Z.-X. Shen, *Nodal quasiparticles and antinodal charge ordering in* $ca_{2-x}na_xcuo_2cl$, Science **307**, 901 (2005).

[491] S. Sachdev and D. Chowdhury, *The novel metallic states of the cuprates: Topological fermi liquids and strange metals*, Progress of Theoretical and Experimental Physics **2016**, 12C102 (2016).

[492] J. M. Luttinger, *Fermi surface and some simple equilibrium properties of a system of interacting fermions*, Phys. Rev. **119**, 1153 (1960).

[493] M. Oshikawa, *Topological approach to luttinger's theorem and the fermi surface of a kondo lattice*, Phys. Rev. Lett. **84**, 3370 (2000).

[494] A. F. Kemper, M. Sentef, B. Moritz, C. C. Kao, Z. X. Shen, J. K. Freericks, and T. P. Devereaux, *Mapping of unoccupied states and relevant bosonic modes via the time-dependent momentum distribution*, Phys. Rev. B **87**, 235139 (2013).

[495] N. Bittner, D. Golez, H. U. R. Strand, M. Eckstein, and P. Werner, *Coupled charge and spin dynamics in a photoexcited doped mott insulator*, Phys. Rev. B **97**, 235125 (2018).

[496] A. Schuckert and M. Knap, *Probing eigenstate thermalization in quantum simulators via fluctuation-dissipation relations*, Phys. Rev. Research **2**, 043315 (2020).

[497] M. Babadi, M. Knap, I. Martin, G. Refael, and E. Demler, *Theory of parametrically amplified electron-phonon superconductivity*, Phys. Rev. B **96**, 014512 (2017).

[498] C. Giannetti, M. Capone, D. Fausti, M. Fabrizio, F. Parmigiani, and D. Mihailovic, *Ultrafast optical spectroscopy of strongly correlated materials and high-temperature superconductors: a non-equilibrium approach*, Advances in Physics **65**, 58 (2016).

[499] C. L. Smallwood, R. A. Kaindl, and A. Lanzara, *Ultrafast angle-resolved photoemission spectroscopy of quantum materials*, EPL **115**, 27001 (2016).

[500] D. Fausti, R. I. Tobey, N. Dean, S. Kaiser, A. Dienst, M. C. Hoffmann, S. Pyon, T. Takayama, H. Takagi, and A. Cavalleri, *Light-induced superconductivity in a stripe-ordered cuprate*, Science **331**, 189 (2011).

[501] L. Perfetti, P. A. Loukakos, M. Lisowski, U. Bovensiepen, H. Eisaki, and M. Wolf, *Ultrafast electron relaxation in superconducting* $\mathrm{bi_2sr_2cacu_2o_{8+\delta}}$ *by time-resolved photoelectron spectroscopy*, Phys. Rev. Lett. **99**, 197001 (2007).

[502] M. A. Nichols, L. W. Cheuk, M. Okan, T. R. Hartke, E. Mendez, T. Senthil, E. Khatami, H. Zhang, and M. W. Zwierlein, *Spin transport in a Mott insulator of ultracold fermions*, Science **363**, 383 (2019).

[503] P. T. Brown, E. Guardado-Sanchez, B. M. Spar, E. W. Huang, T. P. Devereaux, and W. S. Bakr, *Angle-resolved photoemission spectroscopy of a Fermi–Hubbard system*, Nature Physics **16**, 26 (2020).

[504] M. Ben Dahan, E. Peik, J. Reichel, Y. Castin, and C. Salomon, *Bloch oscillations of atoms in an optical potential*, Phys. Rev. Lett. **76**, 4508 (1996).

[505] P. M. Preiss, R. Ma, M. E. Tai, A. Lukin, M. Rispoli, P. Zupancic, Y. Lahini, R. Islam, and M. Greiner, *Strongly correlated quantum walks in optical lattices*, Science **347**, 1229 (2015).

[506] F. Meinert, M. Knap, E. Kirilov, K. Jag-Lauber, M. B. Zvonarev, E. Demler, and H.-C. Naegerl, *Bloch oscillations in the absence of a lattice*, Science **356**, 945 (2017).

[507] J. Koepsell, D. Bourgund, P. Sompet, S. Hirthe, A. Bohrdt, Y. Wang, F. Grusdt, E. Demler, G. Salomon, C. Gross, and I. Bloch, *Microscopic evolution of doped mott insulators from polaronic metal to fermi liquid*, arXiv:2009.04440 (2020).

[508] E. Guardado-Sanchez, B. M. Spar, P. Schauss, R. Belyansky, J. T. Young, P. Bienias, A. V. Gorshkov, T. Iadecola, and W. S. Bakr, *Quench dynamics of a fermi gas with strong nonlocal interactions*, Phys. Rev. X **11**, 021036 (2021).

[509] T. A. Hilker, G. Salomon, F. Grusdt, A. Omran, M. Boll, E. Demler, I. Bloch, and C. Gross, *Revealing hidden antiferromagnetic correlations in doped hubbard chains via string correlators*, Science **357**, 484 (2017).

[510] C. Kim, A. Y. Matsuura, Z.-X. Shen, N. Motoyama, H. Eisaki, S. Uchida, T. Tohyama, and S. Maekawa, *Observation of spin-charge separation in one-dimensional* $srcuo_2$, Phys. Rev. Lett. **77**, 4054 (1996).

[511] B. Moritz, T. P. Devereaux, and J. K. Freericks, *Time-resolved photoemission of correlated electrons driven out of equilibrium*, Phys. Rev. B **81**, 165112 (2010).

[512] S. Gupta, Z. Hadzibabic, M. W. Zwierlein, C. A. Stan, K. Dieckmann, C. H. Schunck, E. G. M. van Kempen, B. J. Verhaar, and W. Ketterle, *Radio-frequency spectroscopy of ultracold fermions*, Science **300**, 1723 (2003).

[513] M. Greiner, C. A. Regal, and D. S. Jin, *Probing the Excitation Spectrum of a Fermi Gas in the BCS-BEC Crossover Regime*, Physical Review Letters **94**, 070403 (2005).

[514] M. Cetina, M. Jag, R. S. Lous, I. Fritsche, J. T. M. Walraven, R. Grimm, J. Levinsen, M. M. Parish, R. Schmidt, M. Knap, and E. Demler, *Ultrafast many-body interferometry of impurities coupled to a fermi sea*, Science **354**, 96 (2016).

[515] J. K. Freericks, H. R. Krishnamurthy, and T. Pruschke, *Theoretical description of time-resolved photoemission spectroscopy: Application to pump-probe experiments*, Phys. Rev. Lett. **102**, 136401 (2009).

[516] G. Baskaran, Z. Zou, and P. Anderson, *The resonating valence bond state and high-tc superconductivity - a mean field theory*, Solid State Communications **63**, 973 (1987).

[517] P. Coleman, *New approach to the mixed-valence problem*, Phys. Rev. B **29**, 3035 (1984).

[518] M. Ogata and H. Shiba, *Bethe-ansatz wave function, momentum distribution, and spin correlation in the one-dimensional strongly correlated hubbard model*, Phys. Rev. B **41**, 2326 (1990).

[519] X.-G. Wen, *Quantum Field Theory of Many-body Systems* (Oxford University Press, 2004).

[520] R. Eder and Y. Ohta, *Photoemission spectra of the t-j model in one and two dimensions: Similarities and differences*, Phys. Rev. B **56**, 2542 (1997).

[521] R. N. Bannister and N. d'Ambrumenil, *Spectral functions of half-filled one-dimensional hubbard rings with varying boundary conditions*, Phys. Rev. B **61**, 4651 (2000).

[522] A. Keselman, L. Balents, and O. A. Starykh, *Dynamical signatures of quasiparticle interactions in quantum spin chains*, Phys. Rev. Lett. **125**, 187201 (2020).

[523] F. Ferrari and F. Becca, *Spectral signatures of fractionalization in the frustrated heisenberg model on the square lattice*, Phys. Rev. B **98**, 100405 (2018).

[524] A. M. Black-Schaffer and C. Honerkamp, *Chiral d-wave superconductivity in doped graphene*, Journal of Physics: Condensed Matter **26**, 423201 (2014).

[525] E. D. Kuhnle, S. Hoinka, P. Dyke, H. Hu, P. Hannaford, and C. J. Vale, *Temperature Dependence of the Universal Contact Parameter in a Unitary Fermi Gas*, Physical Review Letters **106**, 170402 (2011).

[526] Z. Yan, P. B. Patel, B. Mukherjee, R. J. Fletcher, J. Struck, and M. W. Zwierlein, *Boiling a Unitary Fermi Liquid*, Physical Review Letters **122**, 093401 (2019).

[527] W. Ketterle and M. W. Zwierlein, *Making, probing and understanding ultracold Fermi gases*, La Rivista del Nuovo Cimento **31**, 247 (2008).

[528] J. T. Stewart, J. P. Gaebler, and D. S. Jin, *Using photoemission spectroscopy to probe a strongly interacting Fermi gas*, Nature **454**, 744 (2008).

[529] G. Baym, C. J. Pethick, Z. Yu, and M. W. Zwierlein, *Coherence and clock shifts in ultracold Fermi gases with resonant interactions*, Physical Review Letters **99**, 190407 (2007).

[530] M. Punk and W. Zwerger, *Theory of rf-Spectroscopy of Strongly Interacting Fermions*, Physical Review Letters **99**, 170404 (2007).

[531] F. Sauter, *Über das Verhalten eines Elektrons im homogenen elektrischen Feld nach der relativistischen Theorie Diracs*, Zeitschrift für Physik **69**, 742 (1931).

[532] W. Heisenberg and H. Euler, *Folgerungen aus der Diracschen Theorie des Positrons*, Zeitschrift für Physik **98**, 714 (1936).

[533] J. Schwinger, *On gauge invariance and vacuum polarization*, Phys. Rev. **82**, 664 (1951).

[534] D. V. Else, P. Fendley, J. Kemp, and C. Nayak, *Prethermal Strong Zero Modes and Topological Qubits*, Physical Review X **7**, 041062 (2017).

[535] P. Fendley, *Parafermionic edge zero modes inZn-invariant spin chains*, Journal of Statistical Mechanics: Theory and Experiment **2012**, P11020 (2012).

[536] P. Fendley, *Strong zero modes and eigenstate phase transitions in the XYZ/interacting Majorana chain*, Journal of Physics A: Mathematical and Theoretical **49**, 30LT01 (2016).

[537] J. Kemp, N. Y. Yao, C. R. Laumann, and P. Fendley, *Long coherence times for edge spins*, Journal of Statistical Mechanics: Theory and Experiment **2017**, 063105 (2017).

[538] T. Rakovszky, F. Pollmann, and C. W. von Keyserlingk, *Sub-ballistic growth of rényi entropies due to diffusion*, Phys. Rev. Lett. **122**, 250602 (2019).

[539] L. Gresista, T. V. Zache, and J. Berges, *Dimensional crossover for universal scaling far from equilibrium*, arXiv:2107.11749 (2021).

[540] J. F. Rodriguez-Nieva, A. P. Orioli, and J. Marino, *Universal prethermal dynamics and self-similar relaxation in the two-dimensional heisenberg model*, arXiv:2106.00023 (2021).

[541] G. Guennebaud, B. Jacob, *et al.*, Eigen v3, http://eigen.tuxfamily.org (2010).

[542] J. D. Hunter, *Matplotlib: A 2d graphics environment*, Computing in Science & Engineering **9**, 90 (2007).

[543] P. Weinberg and M. Bukov, *QuSpin: a Python Package for Dynamics and Exact Diagonalisation of Quantum Many Body Systems part I: spin chains*, SciPost Phys. **2**, 003 (2017).

[544] P. Weinberg and M. Bukov, *QuSpin: a Python Package for Dynamics and Exact Diagonalisation of Quantum Many Body Systems. Part II: bosons, fermions and higher spins*, SciPost Phys. **7**, 20 (2019).

[545] C. R. Harris, K. J. Millman, S. J. van der Walt, R. Gommers, P. Virtanen, D. Cournapeau, E. Wieser, J. Taylor, S. Berg, N. J. Smith, R. Kern, M. Picus, S. Hoyer, M. H. van Kerkwijk, M. Brett, A. Haldane, J. F. del Río, M. Wiebe, P. Peterson, P. Gérard-Marchant, K. Sheppard, T. Reddy, W. Weckesser, H. Abbasi, C. Gohlke, and T. E. Oliphant, *Array programming with NumPy*, Nature **585**, 357 (2020).

[546] P. Virtanen, R. Gommers, T. E. Oliphant, M. Haberland, T. Reddy, D. Cournapeau, E. Burovski, P. Peterson, W. Weckesser, J. Bright, S. J. van der Walt, M. Brett, J. Wilson, K. J. Millman, N. Mayorov, A. R. J. Nelson, E. Jones, R. Kern, E. Larson, C. J. Carey, İ. Polat, Y. Feng, E. W. Moore, J. VanderPlas, D. Laxalde, J. Perktold, R. Cimrman, I. Henriksen, E. A. Quintero, C. R. Harris, A. M. Archibald, A. H. Ribeiro, F. Pedregosa, P. van Mulbregt, and SciPy 1.0 Contributors, *SciPy 1.0: Fundamental Algorithms for Scientific Computing in Python*, Nature Methods **17**, 261 (2020).

COLOPHON

This document was typeset using the typographical look-and-feel `classicthesis` developed by André Miede and Ivo Pletikosić. The style was inspired by Robert Bringhurst's seminal book on typography "*The Elements of Typographic Style*". `classicthesis` is available for both LaTeX and LyX: https://bitbucket.org/amiede/classicthesis/. Happy users of `classicthesis` usually send a real postcard to the author, a collection of postcards received so far is featured here: http://postcards.miede.de/

Numerical calculations employed parts of the GNU Scientific Library available at http://www.gnu.org/software/gsl as well as the Eigen [541] template library for linear algebra operations: http://eigen.tuxfamily.org.
All plots in this thesis were made with Matplotlib [542]: https://matplotlib.org/.
MPS calculations have been done using the TeNPy library [89].
ED calculations were performed with the QuSpin library [543, 544].
All illustrations have been made with InkScape https://inkscape.org.
Numerical Fourier transformations were done using the FFTW template library http://fftw.org and NumPy [545] and SciPy [546] were heavily employed.
Citation managing has been done using the JabRef reference manager acquirable at http://jabref.sourceforge.net/ and the Zotero manager: https://www.zotero.org/.